

PAPER • OPEN ACCESS

## Can mesoscale models capture the effect from cluster wakes offshore?

To cite this article: Miguel Sanchez Gomez *et al* 2024 *J. Phys.: Conf. Ser.* **2767** 062013

View the [article online](#) for updates and enhancements.

You may also like

- [Charging of multiple grains in subsonic and supersonic plasma flows](#)  
D Block and W J Miloch
- [Enhanced Wind Farm Maintenance Scheduling Including Wake Effects](#)  
R B Santos Pereira, C Bussolati, F C Fonseca et al.
- [Scalable SCADA-Based Calibration for Analytical Wake Models Across an Offshore Cluster](#)  
Diederik van Binsbergen, Pieter-Jan Daems, Timothy Verstraeten et al.



**ECS** The Electrochemical Society  
Advancing solid state & electrochemical science & technology

**ECS UNITED**

**247th ECS Meeting**  
Montréal, Canada  
May 18-22, 2025  
*Palais des Congrès de Montréal*

**Showcase your science!**

**Abstracts due  
December  
6th**

# Can mesoscale models capture the effect from cluster wakes offshore?

Miguel Sanchez Gomez<sup>1</sup>, Georgios Deskos<sup>1</sup>, Julie K. Lundquist<sup>1,2</sup> and Timothy W. Juliano<sup>3</sup>

<sup>1</sup> National Renewable Energy Laboratory, Golden, Colorado, USA

<sup>2</sup> University of Colorado, Boulder, Colorado, USA

<sup>3</sup> U.S. NSF National Center for Atmospheric Research, Boulder, Colorado, USA

E-mail: ██████████@nrel.gov

**Abstract.** Long wakes from offshore wind turbine clusters can extend tens of kilometers downstream, affecting the wind resource of a large area. Given the ability of mesoscale numerical weather prediction models to capture important atmospheric phenomena and mechanisms relevant to wake evolution, they are often used to simulate wakes behind large wind turbine clusters and their impact over a wider region. Yet, uncertainty persists regarding the accuracy of representing cluster wakes via mesoscale models and their wind turbine parameterizations. Here, we evaluate the accuracy of the Fitch wind farm parameterization in the Weather Research and Forecasting model in capturing cluster-wake effects using two different options to represent turbulent mixing in the planetary boundary layer. To this end, we compare operational data from an offshore wind farm in the North Sea that is fully or partially waked by an upstream array against high-resolution mesoscale simulations. In general, we find that mesoscale models accurately represent the effect of cluster wakes on front-row turbines of a downstream wind farm. However, the same models may not accurately capture cluster-wake effects on an entire downstream wind farm, due to misrepresenting internal-wake effects.

## 1. Introduction

Wakes from offshore wind turbine clusters, also referred to as cluster wakes, can propagate long distances, reducing the power production of downstream wind farms [1, 2]. Power losses associated with the effect of cluster wakes have historically been underestimated, leading to uncertainty in energy yield estimates [3].

Analytical and numerical models can be used to estimate losses from cluster wakes and reduce uncertainty in wind farms' energy production assessments. Due to their low computational cost, engineering wake models are commonly used to quantify both wake and power losses. However, these simplified models do not account for some key physical mechanisms that can modify wake evolution in an offshore environment [4, 5]. High-fidelity simulations, like large-eddy simulations (LES), can provide a more complete representation of wake physics [6]; however, at a considerably higher computational cost. Mesoscale numerical weather prediction models, on the other hand, represent well the physical conditions (such as atmospheric stability) that may impact wake evolution—and at a lower computational cost than LES. Nevertheless, uncertainty persists regarding the precision of mesoscale models in accurately representing the impact of wind turbines in the atmospheric boundary layer [7, 8, 9, 10].





Mesoscale simulations rely on the assumption that the size of the most energetic turbulent structures ( $l$ ) is much smaller than the horizontal grid spacing ( $\Delta x$ ) of the model (i.e.,  $\Delta x \gg l$ ); as such, the effects of turbulence are parameterized. Vertical turbulence mixing at the subgrid scale is typically modeled by assuming horizontal homogeneity using planetary boundary-layer (PBL) parameterizations. In coarse mesoscale simulations ( $\Delta x \sim 10$  km), the horizontal gradients of momentum and heat are small compared to their vertical gradients. However, in high-resolution mesoscale simulations ( $\Delta x \sim l$ ), commonly referred to as *gray zone* or *terra incognita* simulations, the most energetic turbulent eddies are not fully parameterized and horizontal gradients of mean quantities become important [11, 12, 13]. Wind turbine and wind farm wakes are characterized by large horizontal and vertical momentum gradients. Consequently, horizontal gradients of turbulence statistics become non-negligible and the three-dimensional effects of turbulence should be considered. In addition, turbine-scale effects (i.e., momentum extraction and enhanced turbulence mixing), which are on the order of 100 m, must also be parameterized. Wind turbines in mesoscale models are typically parameterized as momentum sinks, such as in the Fitch Wind Farm Parameterization (WFP) [14] and the Explicit Wake Parameterization (EWP) [15], or as enhanced surface roughness [16], which misrepresents the wake structure downstream of the turbines [17].

In this study, we evaluate the ability of the Fitch WFP to represent wakes from offshore wind turbines. In particular, we investigate its ability—when used in conjunction with two different PBL schemes, namely the MYNN [18] and the three-dimensional (3D) PBL [13, 19] schemes—to estimate power losses due to external and internal wakes as compared with operational data from an offshore wind farm. The remainder of this paper is organized as follows. In Section 2, we describe the wind farm operational data used to validate the mesoscale simulations. Section 3 provides an overview of the numerical methods employed herein. The climatology of winds around the wind farms of interest is outlined in Section 4. The effects of cluster wakes on downstream wind farms is detailed in Section 5, and a summary and next steps are provided in Section 6.

## 2. Wind turbine power data

We use wind turbine operational data from offshore wind farms in the North Sea to validate cluster-wake effects in mesoscale models. Specifically, we assess the interaction between the Westernmost Rough and Humber Gateway wind farms. Westernmost Rough is located approximately 19 km northwest of the Humber Gateway wind farm (Figure 1). The Westernmost Rough wind farm comprises 35 Siemens 6-MW wind turbines with hub height at 102 m and 154-m rotor diameter. The Humber Gateway wind farm comprises 73 Vestas 3-MW wind turbines with hub height at 80 m and 112-m rotor diameter. Turbine power data from the Supervisory Control and Data Acquisition system (SCADA) from Westernmost Rough between January and December, 2017, are used to validate power production estimates calculated by the mesoscale model. Power production, nacelle wind speed, turbine yaw angle, and fault conditions are provided by the wind farm operator for each turbine as 10-min averages. All turbines in Humber Gateway are assumed to be operating normally for the analysis.

SCADA data filtering is performed using the FLOW Redirection and Induction in Steady State (FLORIS)-based Analysis for SCADA data (FLASC) tool [20]. We filter out power outliers for each turbine based on curtailment, mean-power-curve outliers, sensor-stuck faults, and non-normal operations. On average for all turbines in the wind farm, 77.9% of the data remain valid after discarding outliers. Furthermore, the yaw angle for each turbine is calibrated to true north in FLASC using FLORIS with the Gaussian wake model.

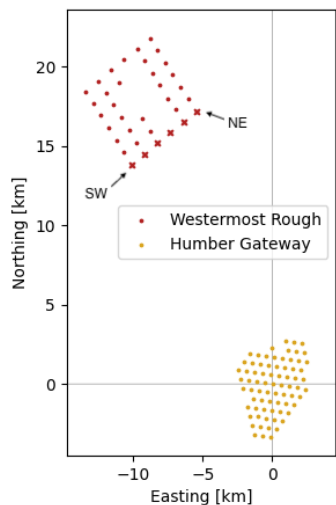


**Figure 1.** Relative location of the Westermost Rough and Humber Gateway wind farms. Front-row turbines in Westermost Rough for southeasterly winds are shown with crosses. The Southwest (SW) and Northeast (NE) front-row turbines (for southeasterly winds) of Westermost Rough are shown for reference. Relative distances are calculated from the center of the Humber Gateway wind farm.

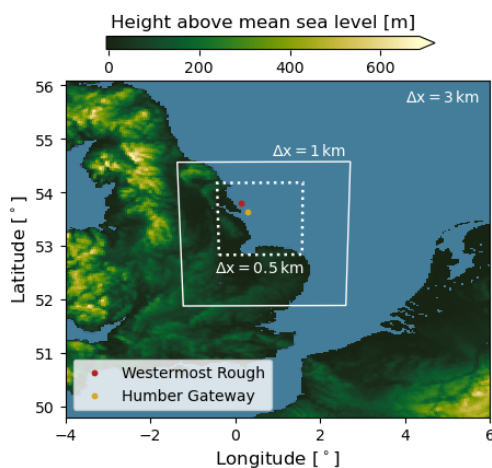


**Figure 2.** Domain layout for the WRF simulations. The solid and dotted white rectangles represent the location and size of the nested domain for the  $\Delta x = 1$  km and  $\Delta x = 0.5$  km simulations, respectively, within the parent domain ( $\Delta x = 3$  km).

### 3. Numerical Models

We simulate atmospheric flow around these two wind farms in the North Sea using the Weather Research and Forecasting (WRF) model (Version 4.4) using a two-domain, one-way nesting setup (Figure 2). ERA5 reanalysis [21] provides initial and boundary conditions to the outer ( $\Delta x = 3$  km) mesoscale domain. For the nested mesoscale domain, we perform simulations using two horizontal grid spacings, one with  $\Delta x = 1$  km (solid white line in Figure 2) and another with  $\Delta x = 0.5$  km (dotted white line in Figure 2). The physical characteristics and modeling options of the domains are provided in Table 1.

Two boundary-layer parameterizations are used to model turbulent mixing in the lowest portion of the atmosphere. The one-dimensional 2.5-MYNN boundary-layer parameterization (MYNN from hereafter) [18] is used with  $\Delta x = 1$  km, whereas a 3D boundary-layer parameterization (3D PBL from hereafter) [13, 19] is employed with  $\Delta x = 0.5$  km. For completeness, we also perform simulations using the 3D PBL for a nested domain with  $\Delta x = 1$  km. The MYNN parameterization estimates vertical turbulent mixing using the vertical turbulent stress divergence, whereas horizontal mixing is computed with a Smagorinsky-like approach. In contrast, the 3D PBL explicitly computes both the vertical and horizontal turbulent flux divergence for momentum, heat, and moisture. Here, we use the “boundary-layer approximation” to the 3D PBL, where vertical turbulent fluxes are calculated like in MYNN,

Domain	$\Delta x$ [km]	$\Delta z_s$ [m]	$(n_x, n_y, n_z)$	$\alpha$ [-]	PBL Model
d01	3.0	8	(241, 241, 79)	-	MYNN
d02	1.0	8	(265, 301, 79)	[0.0, 0.5, 1.0]	MYNN
	0.5	8	(265, 301, 79)	1.0	3D PBL

**Table 1.** Simulation setup, including horizontal grid resolution ( $\Delta x$ ), vertical resolution at the surface ( $\Delta z_s$ ), number of grid cells along each direction ( $n_i$ ), correction factor for the fraction of turbine-added TKE ( $\alpha$ ), and boundary-layer parameterization for each domain.

and the horizontal turbulent fluxes are calculated analytically following [22], as in [23, 24]. We found the full matrix solution to the turbulent fluxes to be numerically unstable in our test cases. Model closure constants and the master length scale follow the original Mellor–Yamada model [22]. Additional information on the “full” 3D PBL and its “boundary-layer approximation” can be found in Juliano et al. [13].

We simulate the wind turbines exclusively in the nested domain (d02) using the Fitch WFP [14, 25, 23]. The Fitch parameterization represents the effect of wind turbines through a momentum sink and a source of turbulence kinetic energy (TKE). The drag from the turbines on the flow is a function of the thrust coefficient, the number of turbines per grid cell, and the turbine size (i.e., rotor diameter  $D$ ). The Fitch wind farm parameterization postulates that a fraction of the energy from the flow is converted into increased turbulent motions; thus, the parameterization adds a source to the TKE tendency equation as well. Turbine-added TKE is regulated in the model as  $C_{TKE} = \alpha(C_T - C_P)$ , where  $\alpha$  is a correction factor, and  $C_T$  and  $C_P$  are the turbine’s thrust and power coefficients, respectively, which in turn are a function of inflow wind speed. We explore the sensitivity to the turbine-added TKE in the MYNN simulations by varying  $\alpha$  between 0 and 1. Because the average turbine spacing in Westermost Rough and Humber Gateway is 945 m and 580 m, respectively, multiple wind turbines are expected to occupy one grid cell for the  $\Delta x = 1$  km domain (Figure 3a). Furthermore, due to the domain discretization and because the effect of the turbines is placed at the grid cell center, the effective wind farm layout of Westermost Rough and Humber Gateway in our simulations (Figure 3) may differ from their physical location (Figure 1). A more accurate representation of each farm’s layout is obtained with finer resolution (Figure 3b).

#### 4. Climatology of winds in the region

We characterize the climatology of winds in the region using nacelle-anemometer wind speed and turbine yaw angle (corrected to true north) recorded in SCADA for the turbines in Westermost Rough. Cluster wakes from Humber Gateway are expected to impact Westermost Rough for wind directions between  $130^\circ$  and  $170^\circ$  [26], when both wind farms are partially or fully aligned. Consequently, we focus on these wind sectors. Furthermore, we focus our analysis on winds above cut-in speed and below rated speed ( $4 \text{ m s}^{-1}$  and  $13 \text{ m s}^{-1}$ , respectively, for the Siemens 6-MW turbine). Rather than replicating the observations on a case-by-case basis, which is highly sensitive to accurately reproducing the temporal evolution of atmospheric conditions, we use ERA5 reanalysis to find times when the statistics of wind speed and direction are comparable to SCADA and simulate those cases in WRF.

To evaluate the capability of mesoscale models in representing cluster wakes, we perform numerical simulations of 42 cases in 2017 that reproduce the statistics of wind speed and direction near the Westermost Rough wind farm. For each case, the parent domain spins up for 14 hr before initializing the nested domain. We discard the first 5 hr of simulation data for the

nested domain. Three-dimensional wind speed and temperature fields, as well as turbine power production, are output every 5 min for 10 hr after spinup of both domains is complete. Note that winds in the mesoscale simulations are expected to be different from the ERA5 reanalysis. ERA5 data is obtained from the ECMWF's Integrated Forecasting System, which employs a different dynamical core, grid resolution, and parameterizations of physical processes from WRF. Thus, even though WRF is forced using ERA5 data, it will reach its own resolved state away from the domain boundaries.

We use the Perkins Skill Score (PSS) [27] to determine a continuous range of wind speeds and directions where wind statistics in the observations and simulations are similar. The PSS is defined as the cumulative minimum value of two distributions of a binned value, measuring the common area between two probability distributions. Here, we compare the conditional probability distributions for wind speed ( $U_i$ ) and wind direction ( $\phi_j$ ) bins from observations ( $Z_o$ ) and model results ( $Z_m$ ), as shown in Eq. 1. For the mesoscale simulations, we use wind speed and direction for the grid points closest to the front-row turbines in Westermost Rough.

$$PSS = \sum_{U_i} \sum_{\phi_j} \min\{Z_m(U_i, \phi_j), Z_o(U_i, \phi_j)\} \quad (1)$$

The climatology of winds (i.e., wind speed and direction) near the Westermost Rough wind farm is well represented in the WRF simulations for a range of wind speeds and directions. We calculate the PSS score for different combinations of wind speed and wind direction bins, then find the continuous range of wind speed and directions that maximize the correspondence between the simulations and observations (i.e., PSS score). Note that variations in the cluster-wake effect may influence the model's ability to reproduce the climatology of this site. The PSS score for the conditional probabilities from WRF and SCADA is 0.75 for wind speeds between  $[6 \text{ m s}^{-1}, 9.5 \text{ m s}^{-1}]$  and wind directions between  $[130^\circ, 170^\circ]$ , suggesting simulations capture about 75% of the observed probability density functions. Kolmogorov-Smirnov and Chi-Squared tests indicate the statistics of winds in the MYNN and 3D PBL simulations match the statistics of the SCADA data at a 95% confidence level. Moreover, even though the  $\Delta x = 0.5 \text{ km}$  domain is smaller than the  $\Delta x = 1 \text{ km}$  domain, resulting in different boundary conditions, the statistics of wind speed and direction are still well captured. Approximately 1900 data points of filtered data from SCADA (10-min averages) lay within these wind speed and direction ranges. Similarly, more than 1300 data points from the WRF simulations (data every 5 min) satisfy

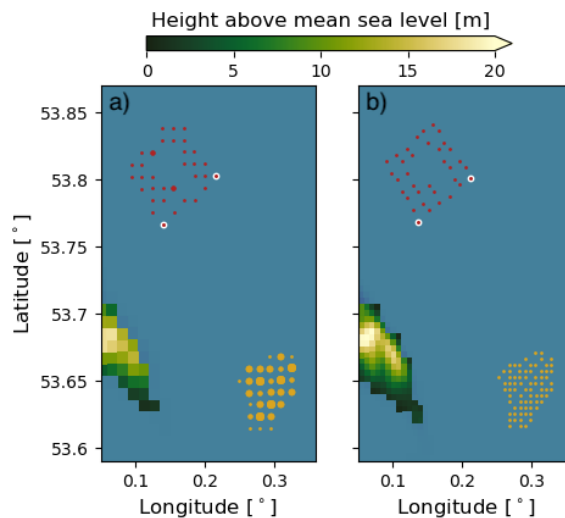


**Figure 3.** Simulated turbine locations in the WRF grid for the  $\Delta x = 1 \text{ km}$  (a) and  $\Delta x = 0.5 \text{ km}$  (b) simulations. Multiple turbines located on the same grid cell are represented by larger circles. The edge-most turbines in the front row of Westermost Rough (for southeasterly winds) are highlighted using white circles.

these wind conditions. Note that we use ERA5 reanalysis to find cases when winds at 100 m are between  $4 \text{ m s}^{-1}$  and  $13 \text{ m s}^{-1}$ . However, the mesoscale simulations only capture the statistics accurately for wind speeds between  $6 \text{ m s}^{-1}$  and  $9.5 \text{ m s}^{-1}$ . The remaining analysis is restricted to winds with a speed between  $6 \text{ m s}^{-1}$  and  $9.5 \text{ m s}^{-1}$  and direction between  $130^\circ$  and  $170^\circ$  only.

## 5. Cluster-wake effects

### 5.1. Front-row turbines

We quantify cluster-wake effects from Humber Gateway on downstream wind turbines using the average of the ratio of power production from the edge-most, front-row turbines in the Westernmost Rough wind farm (turbines SW and NE in Figure 1). This power-ratio metric is accurate for quantifying partially waked conditions for Westernmost Rough [26]. The southwest turbine in the front row of Westernmost Rough ( $P_{SW}$ ) is expected to generate more power than the northeast turbine in the front row ( $P_{NE}$ ) for wind directions around  $145^\circ$ , and vice versa for wind directions around  $165^\circ$  [26].

Mesoscale simulations accurately represent cluster-wake effects on front-row turbines in the Westernmost Rough wind farm (Figure 4). In general, all mesoscale simulations display the same trend in the power ratio when compared to SCADA data. The southwest turbine (SW) in Westernmost Rough is waked by Humber Gateway for wind direction sectors between  $130^\circ$  and  $155^\circ$ , whereas the northeast turbine (NE) is waked by Humber Gateway for wind direction sectors between  $155^\circ$  and  $170^\circ$ .

The MYNN ( $\alpha = 1$ ) and 3D PBL ( $\Delta x = 1 \text{ km}$ ) model configurations show the best agreement with the observational data (Figure 4). The power ratio obtained from SCADA is statistically different (95% confidence) from the power ratio predicted using MYNN ( $\alpha = 1$ ) only when the winds have a strong easterly component ( $\phi \in [130^\circ, 134^\circ]$ ). Similarly, SCADA data are only statistically different from the 3D PBL simulations ( $\Delta x = 1 \text{ km}$ ) for wind sectors  $\phi \in [130^\circ, 134^\circ]$  and  $\phi = 161^\circ \pm 1^\circ$ . Surprisingly, an increased grid resolution while using the 3D PBL (i.e.,  $\Delta x = 0.5 \text{ km}$ ) negatively impacts the ability of the mesoscale model to represent cluster-wake effects on front-row turbines, displaying the least skill in reproducing observations. It is likely that the horizontal gradients of the mean velocities become increasingly important for the wake evolution with the finer grid spacing. Thus, the “full” 3D PBL model instead of its “boundary-layer approximation” may be better suited for modeling the wake evolution downstream of a wind farm using the smaller grid spacing. Despite some studies suggesting turbine-added TKE may affect wind farm wake evolution [25, 23, 8], our data show that power losses due to cluster-wake effects are minimally impacted by  $\alpha$ , similar to previous results [28]. Nonetheless, neglecting the turbine-added TKE (i.e.,  $\alpha = 0$ ) yields the largest differences between the mesoscale model predictions with MYNN and the SCADA data.

Mesoscale simulations can represent differences in cluster-wake effects caused by different atmospheric stability regimes (Figure 5). For the SCADA data, we quantify stability using the bulk Richardson number between the surface and 150 m derived from ERA5 reanalysis. For WRF, stable conditions are defined using the surface heat flux. For the wind conditions described in Section 4, about 60% (67%) of the cases in WRF (SCADA) are stable and 40% (32%) are unstable. All simulations display increased power losses during stable conditions compared to unstable conditions, just like the SCADA data. The 3D PBL ( $\Delta x = 1 \text{ km}$ ) better captures cluster-wake effects on front-row turbines for stable and unstable conditions than the other model configurations. Conversely, the 3D PBL ( $\Delta x = 0.5 \text{ km}$ ) evidences the least agreement with SCADA data for both stable and unstable conditions. Mean cluster-wake effects are similar between the stable and unstable simulations for winds with a strong southerly component ( $\phi \sim 165^\circ$ ). Winds from the south have a long fetch over land, where atmospheric stability can be different (and in many cases opposite) from offshore, and so an internal boundary layer develops with stably stratified winds aloft a weakly unstable surface layer that can persist



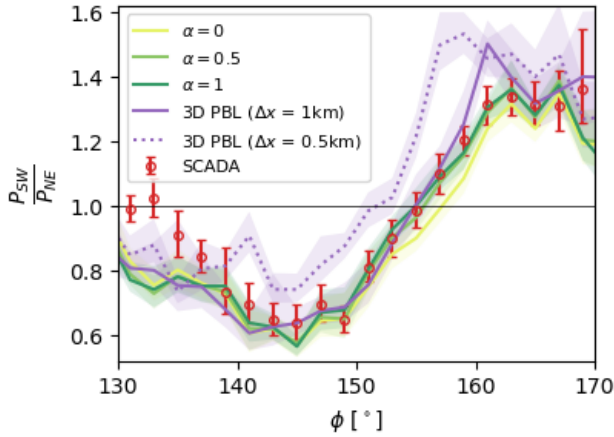


**Figure 4.** Ratio of power production between the southwest (SW) and northeast (NE) front-row turbines (as shown in Figure 1) of Westermost Rough for simulations and observations. Data are shown for wind speeds between  $[6 \text{ m s}^{-1}, 9.5 \text{ m s}^{-1}]$  and wind directions between  $[130^\circ, 170^\circ]$  in  $2^\circ$  bins. The shaded area/error bars represent the 95% confidence interval obtained from a bootstrapping method.

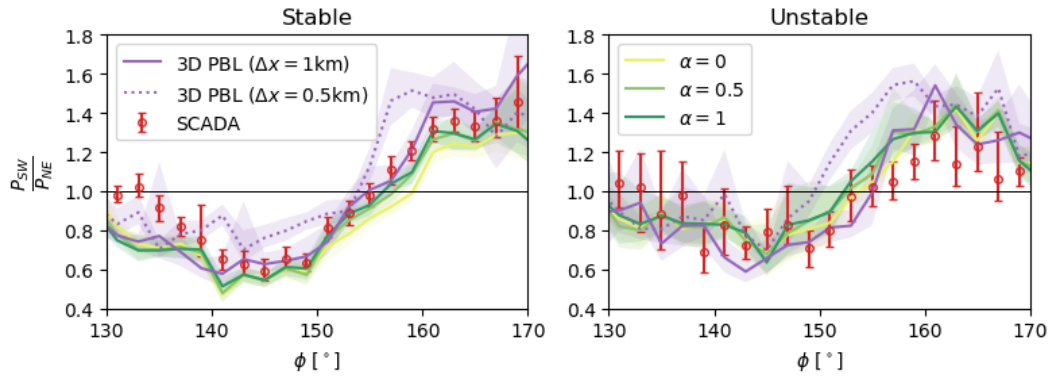


**Figure 5.** Same as Figure 4 but for stable (left) and unstable (right) atmospheric stability conditions.

for long distances and affect cluster-wake evolution.

### 5.2. Wind farm

Even though mesoscale simulations accurately represent cluster-wake effects on front-row turbines (Section 5.1), they do not necessarily capture the effect on the entire downstream wind farm. We quantify the model’s accuracy in representing the effect from internal and external wakes using the error metric  $\mathbb{E}$  defined in Eq. 2, where  $\hat{P}_o$  and  $\hat{P}_m$  are the average normalized power production of each turbine from SCADA and WRF, respectively, for the wind speed  $U_i$  and direction  $\phi_j$  sectors. The normalized power production of each turbine in Westermost Rough for a combination of wind speed and direction  $(U_i, \phi_j)$  is estimated as  $\hat{P} = P/P_{FR}$ , where  $P_{FR}$  is the average power production of the front-row turbines.  $\mathbb{E}$  provides a measure of the mismatch between WRF and SCADA for a set of inflow wind conditions. Based on Eq. 2, WRF overestimates wake effects when  $\mathbb{E} > 0$ , and underestimates wake effects when  $\mathbb{E} < 0$ . Figure 6 illustrates the mismatch between WRF and SCADA for two sets of wind directions: when the wind turbine columns are aligned with the incoming flow (Figure 6a-c), and when they are staggered (Figure 6d-f). Note that we do not include results from MYNN for  $\alpha = 0, 0.5$  in Figure 6 because they are nearly identical to the results from MYNN with  $\alpha = 1$ .

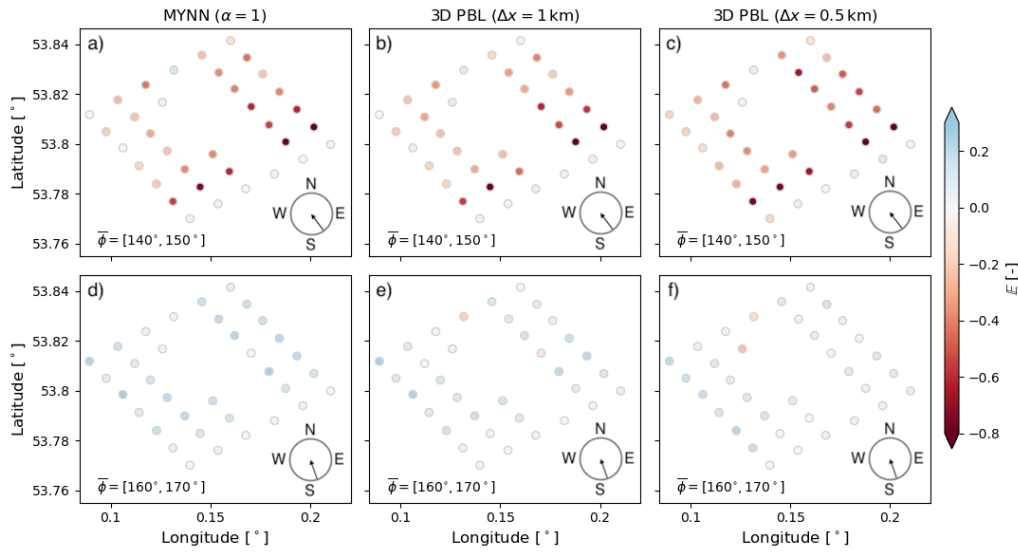


**Figure 6.** Normalized difference between measured and simulated power production for each wind turbine in Westermost Rough. Data are shown for wind speeds between  $[6 \text{ m s}^{-1}, 9.5 \text{ m s}^{-1}]$ . The top panels (a-c) correspond to wind directions within  $[140^\circ, 150^\circ]$ , and the bottom panels (d-f) to wind directions within  $[160^\circ, 170^\circ]$ . Panels (a,d) show the difference between SCADA and WRF with MYNN ( $\alpha = 1$ ), panels (b,e) the difference between SCADA and WRF with the 3D PBL ( $\Delta x = 1 \text{ km}$ ), and panels (c,f) the difference between SCADA and WRF with the 3D PBL ( $\Delta x = 0.5 \text{ km}$ ). The arrows in the bottom right of each panel illustrate the range of wind directions considered.

$$\mathbb{E}(U_i, \phi_j) = \frac{\hat{P}_o(U_i, \phi_j) - \hat{P}_m(U_i, \phi_j)}{\hat{P}_o(U_i, \phi_j)} \quad (2)$$

Mesoscale simulations underestimate (overestimate) internal-wake effects when the wind direction results in an aligned (staggered) array layout within Westermost Rough (Figure 6). All model configurations display the same trend when compared to the observations. Power production from WRF is generally larger than SCADA for aligned conditions (Figure 6a-c), and consistently larger for the second turbine row in Westermost Rough, suggesting WRF predicts smaller velocity deficits than the observations. Conversely, the simulations predict larger internal-wake velocity deficits when the wind direction results in a staggered layout, as depicted by reduced power production compared to SCADA (Figure 6d-f). Differences between SCADA and WRF are minimal for front-row turbines, as shown in Section 5.1, suggesting cluster wakes from Humber Gateway are accurately represented in the simulations.

Internal-wake effects are not accurately captured in the mesoscale simulations because the velocity deficits are distributed over a grid cell that is much larger than the individual wakes. As a result, the velocity deficit is reduced for aligned conditions ( $\phi \approx 146^\circ$ ), minimizing internal-wake effects on downstream turbines. For the same reasons, power reductions from internal wakes are overestimated in a staggered layout ( $\phi \approx 165^\circ$ ) because individual turbine wakes affect a wider downstream area. Furthermore, turbines may occupy adjacent grid cells in the staggered layout; thus, individual-turbine wakes can propagate to a nearby turbine even if it is not immediately downstream. Given that internal-wake effects are not accurately captured in mesoscale simulations, it can be argued that total wake-related power losses that includes both internal- and cluster-wake effects can be misrepresented.

## 6. Summary and Conclusions

Wakes from offshore wind turbine clusters can propagate long distances, reducing the power production of downstream wind farms. Power losses from cluster wakes have historically been underestimated, leading to uncertainty in energy yield estimates. Mesoscale numerical weather prediction models can be used to estimate losses from cluster wakes and reduce uncertainty in wind farms' energy production assessments. However, there is still uncertainty regarding the accuracy and calibration parameters of the wind turbine parameterizations within them. Here, we investigate the ability of the mesoscale Fitch wind turbine parameterization to represent offshore cluster wakes using two boundary-layer parameterizations. We perform high-resolution mesoscale simulations of two offshore wind farms in the North Sea using the Weather Research and Forecasting model. Wind turbine operational data from the downstream wind farm are used to investigate the ability of the mesoscale model to capture internal- and external-wake effects.

Mesoscale models accurately represent cluster-wake effects on the front-row turbines of the downstream wind farm, but fail to capture the internal-wake effects. The one-dimensional and three-dimensional boundary-layer parameterizations yield accurate estimates for cluster-wake-induced power losses on the front-row turbines of a waked offshore wind farm (Figure 4). Inherently, stable atmospheric conditions exhibit increased power losses compared to unstable atmospheric stability regimes (Figure 5), a feature that is well-captured by the mesoscale simulations. However, mesoscale models fail to capture the cumulative power reductions for an entire wind farm when it is being waked by an upstream turbine cluster because internal wakes are not well represented. Due to the numerical grid resolution used in the mesoscale simulations, power losses due to internal wakes are overestimated (underestimated) when the wind is staggered (aligned) with the turbine columns of the wind farm (Figure 6). It is likely that an even finer grid spacing is required to accurately represent internal-wake effects in mesoscale simulations. However, the horizontal gradients in the wake of the wind farm may become non-negligible with the smaller grid spacing, highlighting the importance of further development of the "full" 3D PBL for high-resolution mesoscale modeling of wind farms. Future studies could use a hybrid approach and combine engineering models or large-eddy simulations with mesoscale models to evaluate internal-wake effects on power production of the offshore wind farm. Mesoscale models may also be used to estimate cluster-wake effects when observations are not available or for planning purposes. To this end, mesoscale model results may be employed to tune engineering wake models for farm-to-farm wakes for a variety of wind speeds, wind directions, and atmospheric stability conditions that represent the climatology of a given site, which is cost-prohibitive if only using large-eddy simulations.

## 7. Acknowledgments

The authors would like to thank Ørsted for providing access to operational and measurement data from the Westernmost Rough offshore wind farm. This work was authored in part by the National Renewable Energy Laboratory, operated by Alliance for Sustainable Energy, LLC, for the U.S. Department of Energy (DOE) under Contract No. DE-AC36-08GO28308. Partial funding was provided by DOE's Office of Energy Efficiency and Renewable Energy Wind Energy Technologies Office and funded in part by the Bureau of Ocean Energy Management through an interagency agreement with DOE. Partial funding was also provided by partially funded by the National Offshore Wind Research and Development Consortium (NOWRDC) to carry out a Joint Industry Project investigating Multi-fidelity Modeling of Offshore Wind Inter-array Wake Impacts to Inform Future U.S. Atlantic Offshore Wind Energy Area Development under CRD-23-24539-0. The US government retains certain rights in intellectual property under CRD-23-24539-0. This publication does not necessarily reflect the views of NOWRDC or the US government, and NOWRDC nor the US government makes no representations or

warranties and has no liability for any of its contents. Timothy W. Juliano was supported by the U.S. Department of Energy Wind Technology Office Contract #DE-A05-76RL01830 to Pacific Northwest National Laboratory (PNNL). The National Center for Atmospheric Research (NCAR) is a subcontractor to PNNL under Contract #659135. NCAR is a major facility sponsored by the National Science Foundation under Cooperative Agreement No. 1852977. The research was performed using computational resources sponsored by DOE and located at the National Renewable Energy Laboratory.

## References

- [1] Platis A, Siedersleben S K, Bange J, Lampert A, Bärfuss K, Hankers R, Cañadillas B, Foreman R, Schulz-Stellenfleth J, Djath B, Neumann T and Emeis S 2018 *Sci Rep* **8** 2163 ISSN 2045-2322
- [2] Schneemann J, Rott A, Dörenkämper M, Steinfeld G and Kühn M 2020 *Wind Energ. Sci.* **5** 29–49 ISSN 2366-7451
- [3] Lee J C Y and Fields M J 2021 *Wind Energ. Sci.* **6** 311–365 ISSN 2366-7451
- [4] Stieren A and Stevens R J 2022 *Flow* **2** E21 ISSN 2633-4259
- [5] Doekemeijer B M, Simley E and Fleming P 2022 *Energies* **15** 1964 ISSN 1996-1073
- [6] Maas O 2023 *Wind Energ. Sci.* **8** 535–556 ISSN 2366-7451
- [7] Eriksson O, Baltscheffsky M, Breton S P, Söderberg S and Ivanell S 2017 *J. Phys.: Conf. Ser.* **854** 012012 ISSN 1742-6588, 1742-6596
- [8] Ali K, Schultz D M, Revell A, Stallard T and Ouro P 2023 *Monthly Weather Review* **151** 2333–2359 ISSN 0027-0644, 1520-0493
- [9] Fischereit J, Schaldemose Hansen K, Larsén X G, Van Der Laan M P, Réthoré P E and Murcia Leon J P 2022 *Wind Energ. Sci.* **7** 1069–1091 ISSN 2366-7451
- [10] Peña A, Mirocha J D and Van Der Laan M P 2022 *Monthly Weather Review* **150** 3051–3064 ISSN 0027-0644, 1520-0493
- [11] Wyngaard J C 2004 *Journal of the Atmospheric Sciences* **61** 1816–1826 ISSN 0022-4928, 1520-0469
- [12] Rai R K, Berg L K, Kosović B, Haupt S E, Mirocha J D, Ennis B L and Draxl C 2019 *Monthly Weather Review* **147** 1007–1027 ISSN 0027-0644, 1520-0493
- [13] Juliano T W, Kosović B, Jiménez P A, Eghdami M, Haupt S E and Martilli A 2022 *Monthly Weather Review* **150** 1585–1619 ISSN 0027-0644, 1520-0493
- [14] Fitch A C, Olson J B, Lundquist J K, Dudhia J, Gupta A K, Michalakes J and Barstad I 2012 *Monthly Weather Review* **140** 3017–3038 ISSN 0027-0644, 1520-0493
- [15] Volker P J H, Badger J, Hahmann A N and Ott S 2015 *Geosci. Model Dev.* **8** 3715–3731 ISSN 1991-9603
- [16] Keith D W, DeCarolis J F, Denkenberger D C, Lenschow D H, Malyshev S L, Pacala S and Rasch P J 2004 *Proc. Natl. Acad. Sci. U.S.A.* **101** 16115–16120 ISSN 0027-8424, 1091-6490
- [17] Fitch A C, Olson J B and Lundquist J K 2013 *Journal of Climate* **26** 6439–6458 ISSN 0894-8755, 1520-0442
- [18] Nakanishi M and Niino H 2009 *Journal of the Meteorological Society of Japan* **87** 895–912 ISSN 0026-1165, 2186-9057
- [19] Kosović B, Jimenez Munoz P, Juliano T W, Martilli A, Eghdami M, Barros A P and Haupt S E 2020 *J. Phys.: Conf. Ser.* **1452** 012080 ISSN 1742-6588, 1742-6596
- [20] NREL 2022 Flasc. version 1.0 URL <https://github.com/NREL/flasc>
- [21] Hersbach H, Bell B, Berrisford P, Biavati G, Horányi A, Muñoz Sabater J, Nicolas J, Peubey C, Radu R, Rozum I, Schepers D, Simmons A, Soci C, Dee D and Thépaut J N 2023 ERA5 hourly data on pressure levels from 1940 to present
- [22] Mellor G L and Yamada T 1982 *Reviews of Geophysics* **20** 851–875 ISSN 8755-1209, 1944-9208
- [23] Rybchuk A, Juliano T W, Lundquist J K, Rosencrans D, Bodini N and Optis M 2022 *Wind Energ. Sci.* **7** 2085–2098 ISSN 2366-7451
- [24] Arthur R S, Juliano T W, Adler B, Krishnamurthy R, Lundquist J K, Kosović B and Jiménez P A 2022 *Journal of Applied Meteorology and Climatology* **61** 685–707 ISSN 1558-8424, 1558-8432
- [25] Archer C L, Wu S, Ma Y and Jiménez P A 2020 *Monthly Weather Review* **148** 4823–4835 ISSN 0027-0644, 1520-0493
- [26] Nygaard N G, Steen S T, Poulsen L and Pedersen J G 2020 *J. Phys.: Conf. Ser.* **1618** 062072 ISSN 1742-6588, 1742-6596
- [27] Perkins S E, Pitman A J, Holbrook N J and McAneney J 2007 *Journal of Climate* **20** 4356–4376 ISSN 1520-0442, 0894-8755
- [28] Rosencrans D, Lundquist J K, Optis M, Rybchuk A, Bodini N and Rossol M 2024 *Wind Energ. Sci.* **9** 555–583 ISSN 2366-7443



---

**Estimating Long-Range External Wake Losses  
in Energy Yield and Operational Performance Assessments Using the  
WRF Wind Farm Parameterization**

---

Mark Stoelinga, Ph.D.  
Miguel Sanchez-Gomez, MS<sup>1</sup>  
Gregory S. Poulos, Ph.D.  
Jerry Crescenti, M.S.

ArcVera Renewables  
1301 Arapahoe Street, Suite 105  
Golden, Colorado 80401 USA

---

<sup>1</sup> Miguel Sanchez-Gomez is a graduate student at the University of Colorado who worked for ArcVera Renewables.



## DOCUMENT HISTORY

**Preparer(s):** Mark Stoelinga, Lead, Atmospheric Science Innovation and Applications

**Reviewer(s):** Jerry Crescenti, Director, Wind Energy Analysis Team, Technical Editor, Emily Coulter

**Final Review and Approval by:** Greg Poulos, CEO, Principal Atmospheric Scientist

Version	Date	Comments
1.0	08/09/2022	Initial issue

## Disclaimer

The information, opinions and analysis contained herein are based on sources believed to be reliable, but no representation, expressed or implied, is made as to its accuracy, completeness, or correctness. Neither ArcVera Renewables, nor any of its employees, contractors, or subcontractors (i) makes any warranty, express or implied, including warranties of merchantability, non-infringement or fitness for a particular purpose, (ii) assumes any legal liability or responsibility for the accuracy, completeness, correctness or any use or the results of such use of any information, apparatus, product, or process disclosed in the report, or (iii) represents that the report or its use would not infringe privately owned rights. Reference herein to any specific commercial product, process, or service by trade name, trademark, manufacturer, or otherwise, does not necessarily constitute or imply its endorsement, recommendation, or favoring by ArcVera Renewables. This report is for the use by the named recipient only and may not be used or relied on by any third party without obtaining the prior written consent of ArcVera Renewables.

<b>Report:</b> Document 1.0	<b>Key to Report Standard</b>  Research Result: Description of the subject of the report, including methods and conclusions with review from senior-level staff
<b>Report Standard:</b> Research Result	Review: A brief description without details for general use.
<b>Classification:</b> Confidential	<b>Key to Classification</b>  Strictly Confidential: For recipients only
<b>Status:</b> Final	Confidential: Can be distributed within client's organization  Internal: Not to be distributed outside ArcVera Renewables  Client's Discretion: Distribution at the client's discretion  Published: No restriction

© 2022 ArcVera Renewables

**ABSTRACT**

ArcVera Renewables carried out a study of long-range (> 50 rotor diameters) external wakes, with emphasis on the tendency of existing engineering wake models to greatly underpredict the strength and longevity of external wind farm wake losses on other projects under some atmospheric conditions. Three wind farm case studies are presented; two onshore in the central United States, and one offshore in the New York Bight lease areas recently auctioned for wind energy development. The first case study demonstrates the inadequacy of standard engineering wake models to capture the magnitude of long-range external wake losses. With that result as motivation, the second case study was used to demonstrate the utility of the WRF mesoscale model with the Wind Farm Parameterization (WFP) to model the wake impacts of distant external turbines more accurately than existing engineering wake models. WRF-WFP produced average external wake losses much closer to, 16% higher than, that derived from SCADA data. In contrast, two engineering wake loss models failed to come close to the actual wake loss deficit; these models under-predicted external wake losses as a small fraction,  $\frac{1}{3}$  or less, of that derived from SCADA data.

As a further demonstration of the capabilities of WRF-WFP, and to give a view into the potential for large project-to-project wake impacts in the recently auctioned New York Bight offshore lease areas, ArcVera presented a third offshore wind energy case study. ArcVera Renewables designed WRF-WFP simulations of hypothetical wind project turbine arrays that might be built in those areas approximately 5-10 years from today. The simulations were run for a set of 16 days, with winds from the prevailing southwesterly wind direction, selected to maximize the wakening of arrays aligned in a southwest to northeast direction. The simulations produced dramatic hub-height project-scale wake swaths that extended over 50 km downwind, with a specific example showing a waked wind speed deficit of 7% extending 100 km downwind from the array of turbines that produced it. When averaged over the selected 16 simulation days, the energy loss at the target lease area due to external wakes from arrays to its southwest was 28.9%. While the 16-day result undoubtedly greatly exceeds the long-term external wake loss for winds from all directions, it is nonetheless illustrative of the potential for much greater external wake losses than have been accounted for in development planning for the New York Bight lease areas; and, as in the two onshore long-distance wake loss case studies, are much larger than engineering wake models predict for the same conditions.

---

The implications of this study of long-range wakes on the assessment of energy production (or shortfalls thereof) of existing and anticipated future wind farms is material and significant, as unexpectedly large impacts may well be present, and existing non-WRF-WFP-based engineering long-range wake loss methods are shown to be inadequate. The inadequacy of these models for long-distance wakes may be remedied in the future with further validation time-series modeling and concomitantly accurate assessment of time periods when atmospheric stability is high. Still larger implications are clear for long-term project valuation risk, the analysis and assessment of hybrid projects, battery usage risk, and around-the-clock reliable renewable energy power production. Offshore wind farms are equally strongly affected, and the extensive global plans for proximal deployment of offshore wind projects should account for such impacts.

**TABLE OF CONTENTS**

DOCUMENT HISTORY **2**

ABSTRACT **2**

TABLE OF CONTENTS **3**

LIST OF FIGURES **4**

LIST OF TABLES **4**

LIST OF ACRONYMS AND ABBREVIATIONS **5**

INTRODUCTION **6**

CASE STUDY 1: THE PROBLEM **7**

A POTENTIAL SOLUTION: MESOSCALE MODELING WITH A WIND FARM PARAMETERIZATION **8**

CASE STUDY 2: A DEMONSTRATION OF WRF-WFP **9**

CASE STUDY 3: EXTERNAL WAKES FROM HYPOTHETICAL WIND FARMS IN THE NEW YORK BIGHT LEASE AREAS **12**

    CONFIGURATION **12**

    RESULTS **13**

    SENSITIVITY TESTS **15**

CONCLUSIONS **16**

REFERENCES **17**

**LIST OF FIGURES**

Figure 1. Schematic of the two projects studied in Case Study 1. 8

Figure 2. Schematic of the two projects studied in Case Study 2. 11

Figure 3. Waked wind speed deficit at hub height from the WRF-WFP, in m/s (color scale at bottom), at 10 pm local time on a mid-summer day at the projects in Case Study 2. 13

Figure 4. Map of New York Bight offshore lease areas (orange outlines). 16

Figure 5. Waked wind speed deficit at hub height (m/s, color scale at bottom), from the WRF-WFP simulations of the New York Bight lease areas, at 1530 EST, 24 Feb 2020. 17

**LIST OF TABLES**

Table 1. SCADA-derived and modeled long-range annual-average external wake losses at Target Project for Case Study 1. 9

Table 2. SCADA-derived and modeled long-range external wake losses at Target Project for Case 2 for the selected 1300 hours of northerly wind direction, with separate results by stability class. 13

Table 3. Modeled long-range external wake losses at New York Bight Lease Area 0538 for the 16 selected days of primarily southwest wind direction. 18

Table 4. Sensitivity test results. 19

## LIST OF ACRONYMS AND ABBREVIATIONS

COD	Commercial Operation Date
D	Rotor Diameter
ECMWF	European Centre for Medium-Range Weather Forecasts
ERA5	ECMWF Reanalysis, Version 5
EST	Eastern Standard Time
EV-DAWM	Eddy-Viscosity / Deep Array Wake Model
IEA	International Energy Agency
LES	Large-Eddy Simulation
MW	megawatt
SAR	Synthetic aperture radar
SCADA	Supervisory Control and Data Acquisition
TKE	Turbulent Kinetic Energy
WFP	Wind Farm Parameterization
WRF	Weather Research and Forecast Model



## 1 INTRODUCTION

When wind energy resource assessments are conducted for planned wind energy projects, one of the most significant and uncertain contributors to that estimate is the energy loss due to wind turbine wakes. Typically, the wake losses are calculated separately for those coming from wakes generated within the project (internal wakes) and those generated by turbines outside the project (external wakes). Until recently the same models have been used for both. These models often predict negligible waked wind speed deficits just a few tens of rotor diameters downwind of the wakening turbines. Aggregate effects of wakes from a large array of turbines acting in concert can extend this farm-scale wake effect, but, the general sense in the industry was that wakes from external turbines more than roughly 50D (“D” refers to the rotor diameter of the wake-generating turbine) from the project of interest could be ignored. In Brazil, for example, local renewable energy regulations require compensation for lost energy from new wind farms installed within 20 wind turbine tip-heights (~24D).

Historical work in the 1980’s (Nierenberg, 1989, Nierenberg and Kline, 1989) documented significant wake effects 250D downwind in California’s passes. More recently, observational evidence gathered over the last decade has begun to change this view. For onshore wakes, the “far wake” region was thought to extend no more than about 15D downwind (McCay et al. 2012). Scanning Doppler radar revealed wakes from single turbines extending at least 30D (Hirth et al. 2012). The offshore environment has always been understood to be more conducive than onshore to wake longevity, because turbines tend to be larger (producing larger wakes), atmospheric conditions tend to be more stable (which slows wake recovery), and the wind flow is less disturbed by underlying surface irregularities. Offshore wakes were thought to extend perhaps as far as 15 km (McCay et al. 2012), corresponding to approximately 125D. However, recent evidence from satellite-based synthetic aperture radar (SAR) measurements over the North Sea (Hasagar et al. 2015; Djath et al. 2018); as well as aircraft measurements in the same region (Platis et al. 2018) have shown wind farm-scale wakes with wind speed deficits of 5-10% extending 50 km or more (> 400D).

This white paper brings to light the significant impacts on energy production due to long-range wakes. We present evidence from two pairs of wind farms in the central United States, in which SCADA data from a downwind “target” wind farm is analyzed before and after a new upwind project was built. We also show the insufficiency of existing wake models to capture the energy losses caused by the distant upwind farm. We describe the accuracy potential of the Wind farm Parameterization (WFP), designed and implemented in the Weather Research and Forecast (WRF) model by Fitch et al. (2012), as a commercially viable tool for estimating the impacts of long-range external wakes and external wake production risk. For the second pair of onshore projects, we demonstrate that WRF-WFP predicts external wake losses much closer to the SCADA-derived values than the conventional engineering models.

Finally, as in recent studies focused on the lease areas offshore of Massachusetts (Rosencrans et al. 2022; Pryor et al. 2022), we apply the WRF-WFP to hypothetical future wind development in the New York Bight Lease Areas recently auctioned in February 2022, to demonstrate the

potential for strong, long-range wakes from these lease areas to negatively affect energy production at neighboring wind farms, even those many tens of kilometers away. These hypothetical simulations use the largest reference turbine defined in the IEA Wind reference turbine family, assuming that turbines of this capacity (or larger) will eventually be installed when construction begins in 5-10 years. The results are material to heretofore seldom considered wind energy resource assessment production long-range wake loss risk; in terms of distance downwind (50-100 km) wakes with speed deficits greater than 1 m/s persist and directly impact other lease areas. These predictions are preliminary, considering there is no operational history for these very large turbines with which to validate the long-range wakes they produce within the WRF-WFP. However, confidence in the WRF-WFP has been accumulating based on validation studies already conducted by the research community (see below) and the onshore results presented in the first part of this report. ArcVera already commercially utilizes this tool to assess and reduce risk, and anticipates that tools like the WFP, or other wind farm-aware mesoscale model applications, will become a key part of the wind energy resource assessment (WERA) wind farm-atmosphere interaction (WFAI)/wake loss modeling toolbox.

## **2 CASE STUDY 1: THE PROBLEM**

The challenge of correctly estimating long-range wake impacts can be illustrated with Case Study 1, depicted schematically in Figure 1. Case Study 1 involves a smaller, new project being built 13 km north of an existing larger project in the central United States. Details of the turbine layouts, project capacities, and turbine models are withheld to maintain the projects' anonymity. The existing project is the “target project” at which the impact of external wakes from the new project is evaluated. Four years of SCADA data were available at the target project, with the first two years occurring before the COD of the new project, and the second two years after. While southerlies are the prevailing wind direction, northerlies occupy a secondary frequency peak (see wind rose in Figure 1) and would lead to a project-scale wake impinging upon the target project a substantial portion of the time.

An operational assessment was performed for the target project, using SCADA data from the two separate periods, to determine the long-term energy yield based on the performance of the target project during each period. Reasonable corrections for curtailment, availability, and windiness were made during the period assessed, relative to the long-term, to assure comparability of different periods of record. No other project development occurred within the vicinity during the 4-year study period.

In addition to the operational assessment, wake model experiments were run in which the same project wind climate was applied, but in one experiment, the new project was included, and in the other, it was excluded, and the difference in energy yield at the target project evaluated. This experiment was repeated with two wake models: The Eddy Viscosity / Deep-Array Wake Model (EV-DAWM) available in OpenWind, and the ArcVera Wind Farm-Atmosphere Interaction (WFAI) Model (Poulos et al. 2022). The WFAI model is an empirical loss model built upon and validated against numerous data sets of energy production and measured wind speeds before and after wind farm installations. It was originally developed

under the auspices of U.S. Department of Energy scientific research (DOE 1987, 1990), continually upgraded, and commercially used on numerous WERAs at ArcVera for many years.

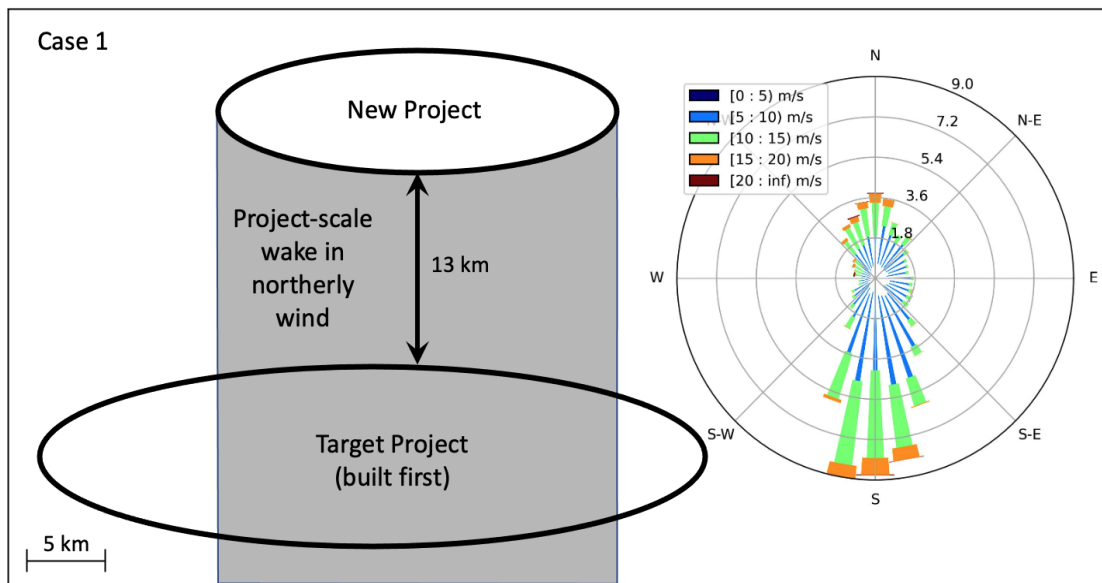


**Figure 1. Schematic of the two projects studied in Case Study 1. Ellipses indicate outlines and relative locations of projects. The wind rose is derived from a hub-height met tower within the target project.**

Table 1 provides the results of the before and after SCADA-based operational assessment, and the wake model predictions. While the SCADA analysis indicated that the presence of the new wind farm reduced production at the target wind farm by 3.6%, both the wake models indicated a nearly negligible impact of the new wind farm. The wake models were unable to predict even a small fraction of the observed wake loss from an external wind farm 13 km away.

**Table 1. SCADA-derived and modeled long-range annual-average external wake losses at Target Project for Case Study 1. Losses are expressed as the percent of gross energy.**

Source of Estimate	Long-Range External Wake Loss
SCADA	3.6%
EV-DAWM	0.1%
WFAI Model	< 0.1%

While these engineering wake loss models have been well validated against internal wake and WFAI losses of wind farms based on production data, they have been less well, or unvalidated, at long-range. This long-range wake loss weakness is exposed in this case study.

### 3 A POTENTIAL SOLUTION: MESOSCALE MODELING WITH A WIND FARM PARAMETERIZATION

The Weather Research and Forecasting model (WRF, Skamarock et al. 2019) is a numerical weather prediction model that has been in use globally by academic and national research institutions, national weather prediction agencies, and private companies with weather and

climate concerns since it was first developed and released in 2000. It is classified as a “mesoscale model,” which means it is designed to simulate weather phenomena covering spatial scales from 2 km to 2000 km (numerically resolved with grid spacing of 200 m to 200 km Chapter 10, Pielke, 1984), but has been used successfully at both larger scales and smaller scales, in the latter case as a “large eddy simulation” or LES model, with a grid spacing of 10 m or less). It is used routinely in the wind energy industry for short-term energy forecasting and retrospective energy assessment. ArcVera Renewables has over 45 years combined experience using WRF and similar mesoscale models for various applications, including using WRF and WRF-LES in wind energy forecasting and assessment for over a decade.

In 2012, in response to the increasing interest in wind energy development and the potential physical interactions between wind farms and the weather and climate of the surrounding region, Fitch et al. (2012) developed and implemented in WRF a capability referred to as the Wind Farm Parameterization (WFP), which models the deceleration of winds by turbines within a WRF model grid box, based on the turbine thrust characteristics. The kinetic energy removed by the turbines is distributed between electric power generation and turbulence production. The wind deceleration interacts with the full atmospheric dynamics simulated by WRF, allowing for downwind transport of the waked wind speed deficits, and feedbacks to the flow such as upwind blockage from the simulated combined induction zone effects of wind turbines, flow deflection around wind farms, gravity wave development and impacts on wind flow patterns,, and the complex movement and distortion of wake swaths within time-dependent curved or sheared wind flows. Importantly, the roles of time-varying atmospheric stability, particularly stable atmospheric conditions, and turbulence on wake recovery are realistically represented in meteorological physics within WRF with WFP.

The waked wind speed deficits simulated by WRF-WFP have been validated in several research studies, mostly at North Sea offshore wind projects, including Fitch et al. (2012), Hasagar et al. (2015), Platis et al. (2018), and Siedersleben et al. (2018). In addition, many studies have conducted sensitivity and other tests with WFP, leading to improvements and recommendations for best use (Lee and Lundquist 2017; Archer et al. 2020; Siedersleben et al. 2020; Tomaszewski and Lundquist 2020; and Larsén and Fischereit 2020). Based on these studies, the WFP has been modified and improved and continues to be actively developed in the research community. Therefore, the WFP should be considered a well-validated tool that continues to improve as part of ongoing active research and development. ArcVera’s work and the research cited above provides ample validating evidence that WRF-WFP captures the fundamental physics of wind turbine interactions with the atmosphere.

#### **4 CASE STUDY 2: A DEMONSTRATION OF WRF-WFP**

Case Study 2 is similar to Case Study 1, in that it involves an existing project, and a new project built to its north (Figure 2). Two key differences from Case Study 1 are that the new project is much larger than the target project; and that the new project is closer to the target project (only 5 km away, as opposed to 13 km in Case Study 1). The wind rose in Figure 2 indicates that a project-scale wake from the new project would impinge on the target project a substantial portion of the time. In Case Study 2, rather than performing a long-term-adjusted operational

assessment for the before and after periods, we evaluated 10-minute SCADA energy production data from the Target Project and ran model simulations only during a selection of days in which maximum waking of the target project by the new project was expected. Maximum waking was expected in northerly flow conditions, with wind speeds in the steep, non-linear section of the target project’s power curve. Care was taken to select a set of times in which the wind speed distributions in the before and after period matched, so as not to skew the result due to different wind climates. A total of 1300 hours (~54 days) of SCADA production and simulated winds were used.

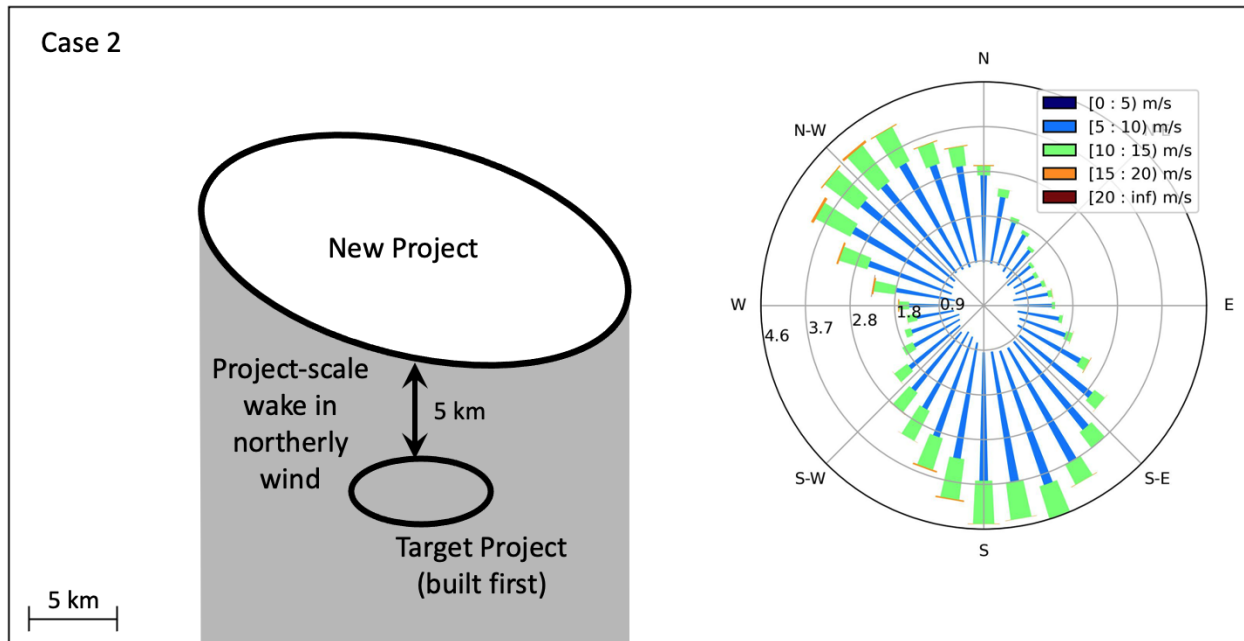


**Figure 2. Schematic of the two projects studied in Case Study 2. Ellipses indicate approximate outlines and relative locations of projects. The wind rose is derived from an ERA5 Reanalysis node within the target project.**

For Case Study 2, wake model simulations were also performed for the “before” and “after” periods (i.e., with and without wakes from the New Project), using both EV-DAWM and ArcVera WFAI. In addition, WRF-WFP was run for the same selected set of times, with three simulations performed for each of the selected dates, one with no turbines, one with only the target project turbines, and one with new project and target project turbines. We used WRF version 4.2.1, which includes a key code correction for the WFP identified by Archer et al. (2020).

The study used WRF model grid with 1.0-km spacing and obtained initial and boundary conditions from the ERA5 Reanalysis data set (Hersbach et al. 2020). Waked wind speed deficits due to the new project were evaluated from the difference between the “new and target turbines” run and the “only target turbines” run. For illustration, an example of waked wind speed deficit simulated by WRF-WFP at one time is shown in Figure 3. It depicts all wakes from both projects by showing the difference between the “new and target turbines” run and the “no turbines” run during a time of north-northeasterly wind flow. Note that the project-scale wake swath from the new project not only envelopes the smaller target project but continues with



substantial magnitude (at least 1 m/s) to the domain boundary over 30 km south-southwest of the new project.

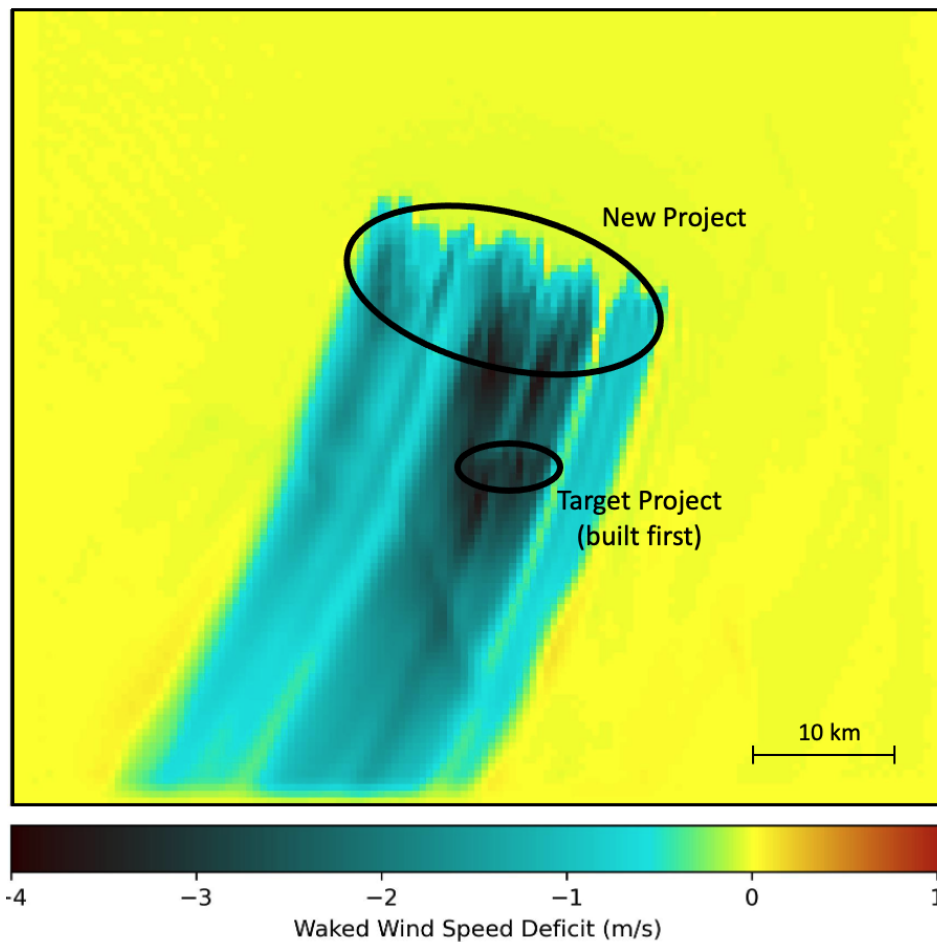


**Figure 3.** Waked wind speed deficit at hub height from the WRF-WFP, in m/s (color scale at bottom), at 10 pm local time on a mid-summer day at the projects in Case Study 2. Ellipses indicate approximate outlines and relative locations of projects. Hub height wind speed at this time was 9.5 m/s.

The average wake loss during the selected periods is shown in Table 2. Because the times were selected to maximize the wake impacts of the new project on the target project, the loss numbers are much higher than the long-term mean values shown for Case Study 1. Additionally, the time points were segregated into unstable and stable categories based on negative or positive values of the bulk Richardson number. The SCADA analysis indicates a large external wake impact of 23.8% by the new project on the target project, averaged over the selected time points. As expected, the SCADA analysis also shows wake impacts to be stronger during stable periods than during unstable periods. The WRF-WFP model overpredicts the external wake loss during the selected time points, but only by a factor of 1.16 (16% overprediction). It also correctly identifies the stronger wake impact during stable conditions. Meanwhile, as in Case Study 1, the engineering wake loss models underpredict the effect by a large amount; they predict only a small fraction of the SCADA-derived wake loss in energy.

**Table 2. SCADA-derived and modeled long-range external wake losses at Target Project for Case 2 for the selected 1300 hours of northerly wind direction, with separate results by stability class. Losses are expressed as the percent of gross energy. Percent frequency of occurrence of stable and unstable conditions are shown in column headings.**

Source of Estimate	Long-Range External Wake Loss		
	All Times	Stable Conditions (67.5%)	Unstable Conditions (32.5%)
SCADA	23.8%	29.1%	12.8%
EV-DAWM	5.7%	not tested	not tested
ArcVera WFAI Model	0.2%	not tested	not tested
WRF-WFP	27.7%	32.6%	17.5%

**5 CASE STUDY 3: EXTERNAL WAKES FROM HYPOTHETICAL WIND FARMS IN THE NEW YORK BIGHT LEASE AREAS**

**5.1 CONFIGURATION**

As a further demonstration of the capabilities of WRF-WFP, and to give a view into the potential for large project-to-project wake impacts in the recently auctioned New York Bight offshore lease areas, ArcVera Renewables ran WRF-WFP simulations of hypothetical wind projects that might be built in those areas perhaps 5-10 years from today. The hypothetical arrays, depicted in Figure 4, were designed as follows. The turbine is the IEA Wind 15-MW Reference Turbine, with a hub height of 150 m and a rotor diameter of 240 m. Turbines of this size and capacity are now starting to be commercially marketed. In 5-10 years, offshore wind energy projects may utilize turbines of this size or larger. We designed the arrays with a turbine spacing of 1.0 nautical miles (1.85 km) in the east-west direction, and 0.75 nautical miles (1.39 km) in the north-south direction, based on our current understanding of what the relevant jurisdictional agencies will require and the measured wind rose. 10 km (42D) gaps were enforced between turbine arrays; there are 3 km gaps between lease areas. Prevailing winds are southwesterly.

Three arrays were designed:

- Northern Array
  - Lease Area 0538
  - 85 turbines
  - Treated as the target project
- Central Array
  - Lease Area 0539
  - 118 turbines
  - Treated as an external project
- Southern Array
  - Lease Areas 0541 and 0542
  - 157 turbines
  - Treated as an external project

The WRF model was configured similarly to Case Study 2, except with slightly finer horizontal grid resolution (800 m). 16 case study dates were selectively chosen to provide maximum time with winds from the 190°-240° sector and speed in the range of 6-11 m/s. Under these conditions, the wakening of the target array (0538) by areas 0539, 0541, and 0542 is maximum, not only because they are directionally aligned with the wind, but because in southwesterly flow (the prevailing direction, especially in the warm season), typically there is warm air moving over colder water, resulting in stabilization of the flow and longer-lived wakes. The wind speed range, positioned in the steepest part of the turbine power curve, was chosen to maximize the energy sensitivity to the waked wind speed deficits. The annual wind rose at floating lidar E06 (Figure 4, right side) indicates that the conditions described above frequently occur, though the chosen set of times have much higher wake losses than a long-term mean that accounts for the entire wind rose. For each simulation day, the model was run for 24 h starting at 7:00 AM EST, with a 6-h spin-up period from 1:00 AM to 7:00 AM EST. Model output was produced every 10 minutes.

For each chosen day, three simulations were run, which included the effects of:

- 1. No turbines (Simulation 1)
- 2. Turbines at the Southern (0541/0542) Array only (Simulation 2)
- 3. Turbines at both the Central (0539) and Southern Arrays (Simulation 3)

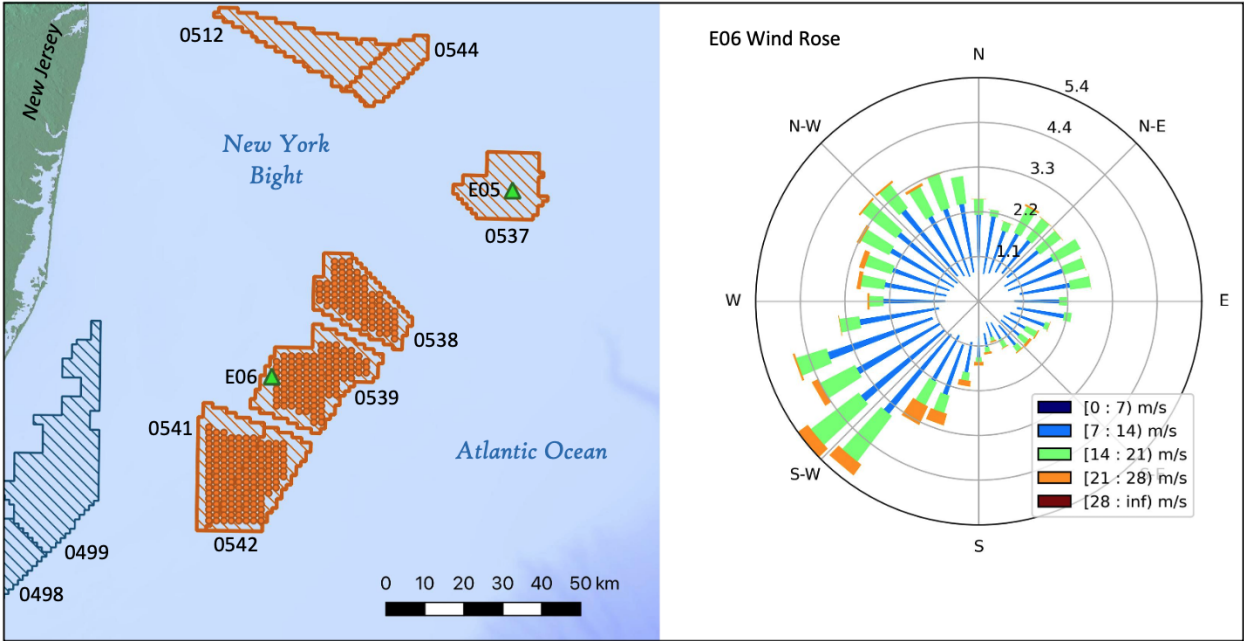


Figure 4. Map of New York Bight offshore lease areas (orange outlines). New Jersey lease areas are also shown (blue outlines). Orange dots indicate hypothetical turbine arrays in lease areas 0538, 0539, 0541, and 0542. Green triangles indicate floating lidar sites E05 and E06. The wind rose in the right panel is from lidar measurements at site E06.

Wind speed deficits on the Northern Array (Lease Area 0538) due to external wakes from the Southern Array only were evaluated from Simulation 2 minus Simulation 1. Wind speed deficits

due to external wakes from the Central and Southern Arrays only were evaluated from Simulation 3 minus Simulation 1.

## 5.2 RESULTS

An example of waked wind speed deficit from the WRF-WFP simulations is shown in Figure 5. The left panel shows the effect of turbines in only the Southern Array, whereas the right panel shows the effect of turbines in both the Southern and Central Arrays. The dominant feature of these plots is the long-range project-scale wake swath extending from the arrays to the north-northeast. Even at the northern edge of the domain, over 100 km downwind of the Southern Array, the long-range wake from the Southern Array only (left panel) maintains a 0.7 m/s (or 7%) hub-height wind speed deficit; and 80 km downwind of the Central Array, the long-range wake from the Southern and Central Arrays combined (right panel) maintains a 1.0 m/s (or 10%) wind speed deficit. The waked speed deficits within the target (0538, Northern) array are 1.6 m/s (16%) from the Southern Array only, and 2.5 m/s (25%) from the combination of the Southern and Central Arrays. Note that no turbines from the Northern Array were included in the simulations, so the entire speed deficit within the Northern array is due to external wakes from the Southern and Central Arrays.

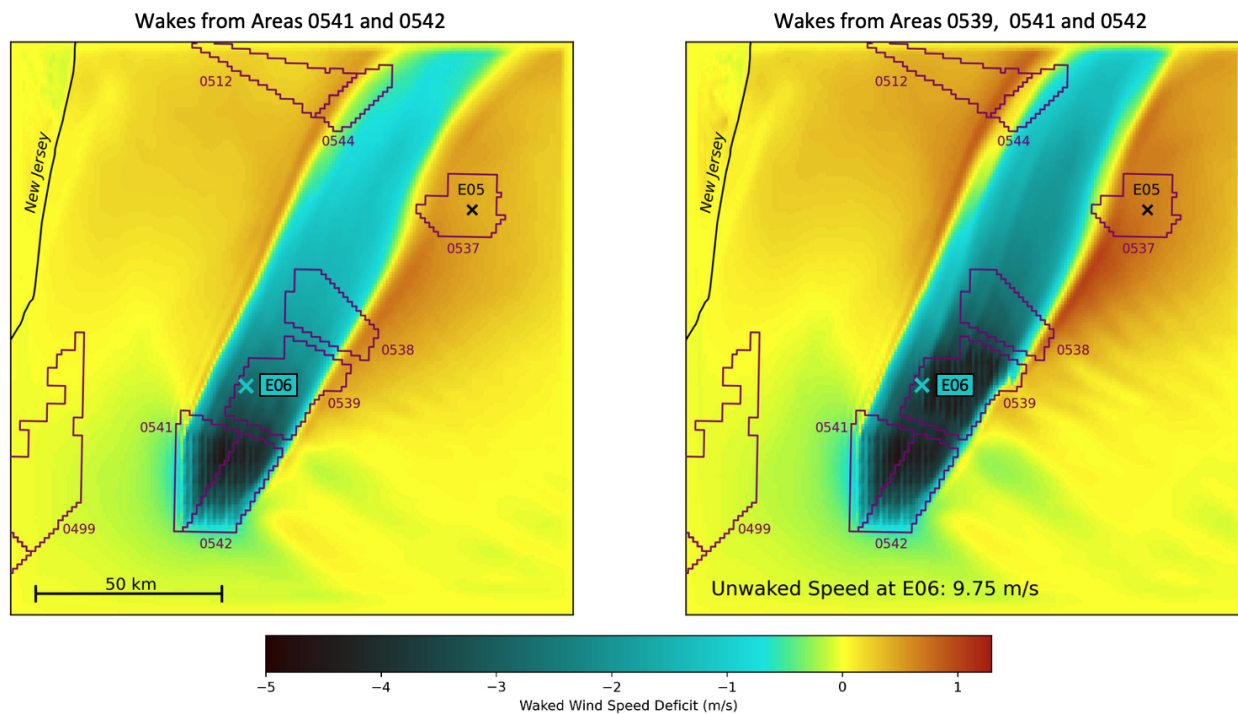


**Figure 5. Waked wind speed deficit at hub height (m/s, color scale at bottom), from the WRF-WFP simulations of the New York Bight lease areas, at 1530 EST, 24 Feb 2020. “x” symbols indicate the locations of floating lidars.**

In addition to the project-scale wake, other prominent WFAI features emerge in these plots. A region of speed deficit upwind of the projects indicates project-scale blockage, up to 0.5 m/s in some locations, with wave-like structures embedded in it. Downwind, the wake swath is flanked by areas of significant speed enhancement ( $> 0.5$  m/s), which are a subject of future

scientific study. Over the long term, when these flanking wind acceleration zones pass over downwind projects, the accelerations partially offset the wake losses incurred at other times, reducing the long-term mean external wake loss.

Energy-based losses at the Northern Array due to external wakes at the Central and Southern Arrays for the 16 days of the simulation were calculated, along with corresponding predictions from the EV-DAWM and ArcVera WFAI models. Results are shown in Table 3. No validation of the results is possible due to the hypothetical nature of the turbine arrays. However, the results illustrate the potential for large external wake losses. Even if the long-term mean external wake loss at the Northern Array is, for example, one-quarter of the loss from this set of 16-days with enhanced waking conditions, that still represents a very large loss due only to external wakes. But equally important is the result, consistent with those of the first two case studies, that the engineering wake models estimate only a small fraction of the external wake loss predicted by the WRF-WFP.

**Table 3. Modeled long-range external wake losses at New York Bight Lease Area 0538 for the 16 selected days of primarily southwest wind direction, with separate results for wakes from Lease Area 0539 only, and from the combination of Lease Areas 0539, 0541, and 0542. Losses are expressed as the percent of gross energy.**

Source of Estimate	Long-Range External Wake Loss at Area 0538	
	From 0539 only	From 0539, 0541, & 0542
EV-DAWM	0.5%	5.3%
ArcVera WFAI Model	< 0.1%	0.2%
WRF-WFP	13.0%	28.9%

### 5.3 SENSITIVITY TESTS

Considering the large magnitude and length of wakes predicted by WRF-WFP in the New York Bight lease areas, and lack of validating data for the large hypothetical wind turbines used in the simulations, ArcVera consulted with Professor Julie Lundquist’s research group at the University of Colorado to consider the uncertainty in these model predictions of large, long-range wakes. A suggestion that emerged was to test the sensitivity of the wakes to two configurable parameters that recent studies have demonstrated are important for the magnitude of wakes predicted by WRF-WFP: the number of vertical levels beneath the rotor layer, and the amount of turbine-produced turbulence that is injected into the model simulation.

Tomaszewski and Lundquist (2020) found that using more vertical levels reduces mixing and increases wake longevity (though they found the sensitivity modest). We used only 2 vertical levels beneath the rotor, so we tested increasing that to 4 levels.

The turbulent kinetic energy (TKE) factor (a tunable parameter) scales the amount of turbine-induced turbulence injected into the model flow. A value of 0.0 injects no turbine-induced turbulence, whereas a value of 1.0 injects the full amount consistent with the turbine power and thrust curves. The appropriate amount is not a settled matter, with the original Fitch (2012) paper injecting the full amount (but testing sensitivity to half or double the

full amount). Archer et al. (2020) recommended only one-quarter of the full amount be injected to best match large-eddy simulations that they conducted, and Larsén and Fischereit (2021) found that a value of 1.0 validated better than 0.25. Others have argued that none of the turbine-induced turbulence should be injected into the model flow at the scales resolved by the model (Jacobson and Archer 2012; Volker et al. 2015). In our simulations for both Case Studies 2 and 3, we used a TKE factor of 0.0, so we tested higher values, up to 1.0.

Table 4 shows the parameter values tested in the sensitivity experiments, and the resulting relative change in wake strength compared to the control experiment (green highlight, 0.0%), which used the configuration indicated in the upper left cell of the table (zero turbulence injected, and two model vertical levels below the rotor layer). The wake strength was defined as the area-integrated wind speed difference within the wind speed deficit swath north and east of lease area 0539 . This definition yields a higher value if either the wake's magnitude or areal size increases.

**Table 4. Sensitivity test results. The control configuration (green highlight) is the upper left cell in the table, with 2 model levels beneath the rotor layer, and a TKE factor of 0.0%. The value in each cell represents the change in wake strength relative to that of the control configuration. All values are positive, meaning that all sensitivity tests produced stronger wakes than in the control configuration.**

		Turbine TKE Injection Factor			
		0.00	0.25	0.50	1.00
Number of model levels beneath rotor	2	0.0%	not tested	not tested	8.0%
	4	0.7%	6.6%	7.7%	8.4%

The increase in vertical levels beneath the rotor slightly increased the wake strength, consistent with Tomaszewski and Lundquist (2020). The increase in turbulence also increased the wake strength. The latter result is counterintuitive considering that greater turbulence would be expected to enhance wake recovery, and this does occur within the waking turbine array, but downwind of it the opposite occurs: the wake is enhanced. Fitch et al. (2012) and Rybchuk et al. (2021) found the same counterintuitive result. In summary, the original configuration actually produced the *weakest* wakes of all the configurations tested. A TKE injection factor of 0.0 was found to produce rather accurate results in Case Study 2, and an increase in TKE injection factor could reduce accuracy based on these sensitivity tests.

## 6 CONCLUSIONS

ArcVera Renewables carried out a study of long-range (> 50 rotor diameters) external wakes, with emphasis on the tendency of existing engineering wake models to greatly underpredict the strength and longevity of external wind farm wake losses on other projects under some atmospheric conditions. Three wind farm case studies are presented; two onshore in the central United States, and one offshore in the New York Bight lease areas recently auctioned for wind energy development. The first case study demonstrates the inadequacy of standard engineering wake models to capture the magnitude of long-range external wake losses. With



that result as motivation, the second case study was used to demonstrate the utility of the WRF mesoscale model with the Wind Farm Parameterization (WFP) to model the wake impacts of distant external turbines more accurately than existing engineering wake models. WRF-WFP produced average external wake losses much closer to, 16% higher than, that derived from SCADA data. In contrast, two engineering wake loss models failed to come close to the actual wake loss deficit; these models under-predicted external wake losses as a small fraction,  $\frac{1}{3}$  or less, of that derived from SCADA data.

As a further demonstration of the capabilities of WRF-WFP, and to give a view into the potential for large project-to-project wake impacts in the recently auctioned New York Bight offshore lease areas, ArcVera presented a third offshore wind energy case study. ArcVera Renewables designed WRF-WFP simulations of hypothetical wind project turbine arrays that might be built in those areas approximately 5-10 years from today. The simulations were run for a set of 16 days, with winds from the prevailing southwesterly wind direction, selected to maximize the wakening of arrays aligned in a southwest to northeast direction. The simulations produced dramatic hub-height project-scale wake swaths that extended over 50 km downwind, with a specific example showing a waked wind speed deficit of 7% extending 100 km downwind from the array of turbines that produced it. When averaged over the selected 16 simulation days, the energy loss at the target lease area due to external wakes from arrays to its southwest was 28.9%. While the 16-day result undoubtedly greatly exceeds the long-term external wake loss for winds from all directions, it is nonetheless illustrative of the potential for much greater external wake losses than have been accounted for in development planning for the New York Bight lease areas; and, as in the two onshore long-distance wake loss case studies, are much larger than engineering wake models predict for the same conditions.

---

The implications of this study of long-range wakes on the assessment of energy production (or shortfalls thereof) of existing and anticipated future wind farms is material and significant, as unexpectedly large impacts may well be present, and existing non-WRF-WFP-based engineering long-range wake loss methods are shown to be inadequate. The inadequacy of these models for long-distance wakes may be remedied in the future with further validation time-series modeling and concomitantly accurate assessment of time periods when atmospheric stability is high. Still larger implications are clear for long-term project valuation risk, the analysis and assessment of hybrid projects, battery usage risk, and around-the-clock reliable renewable energy power production. Offshore wind farms are equally strongly affected, and the extensive global plans for proximal deployment of offshore wind projects should account for such impacts.

## REFERENCES

- Archer, C. L., Wu, S., Ma, Y., & Jiménez, P. A., 2020: Two Corrections for Turbulent Kinetic Energy Generated by Wind Farms in the WRF Model. *Mon. Wea. Rev.*, 148, 4823–4835, <https://doi.org/10.1175/MWR-D-20-0097.1>.
- Brower, M. C., and N. M. Robinson, 2012: The Openwind Deep-Array Model—Development and Validation. AWS Truepower Report.
- DOE SBIR Program U.S. Department of Energy. "United Industries Report No. 8701: Numerical Model for Predicting Turbine Array Performance in Complex Terrain, Phase 1." Washington D.C., 1987.
- DOE SBIR Program U.S. Department of Energy. "United Industries Report No. 8917: Numerical Model for Predicting Turbine Array Performance in Complex Terrain, Phase 2: Final Technical Report." Washington D.C., 1990.
- Djath, B., Schulz-Stellenfleth, J., and Cañadillas, B., 2018: Impact of atmospheric stability on X-band and C-band synthetic aperture radar imagery of offshore windpark wakes, *J. Renew. Sustain. Ener.*, 10, 043301, <https://doi.org/10.1063/1.5020437>.
- Fitch, A. C., Olson, J. B., Lundquist, J. K., Dudhia, J., Gupta, A. K., Michalakes, J., and Barstad, I., 2012: Local and Mesoscale Impacts of Wind Farms as Parameterized in a Mesoscale NWP Model, *Mon. Weather Rev.*, 140, 3017–3038, <https://doi.org/10.1175/MWRD-11-00352.1>.
- Hasager, C., P. Vincent, H. Vincent, R. Husson, A. Mouche, M. Badger, A. Peña, P. Volker, J. Badger, A Di Bella, A. Palomares, E. Cantero, P. Correia, 2015: Comparing satellite SAR and wind farm wake models. *Journal of Physics: Conference Series*. 625. 10.1088/1742-6596/625/1/012035.
- Hersbach, H., and Coauthors, 2020: The ERA5 global reanalysis. *Quart. J. Roy. Meteor. Soc.*, 146, 1999–2049, <https://doi.org/10.1002/qj.3803>.
- Hirth, B. D., J. L. Schroeder, W. S. Gunter, and J. G. Guynes, 2012: Measuring a utility-scale turbine wake using the TTU Ka mobile research radars. *J. Atmos. Oceanic Technol.*, 29, 766–771.
- Jacobson, M. Z., and C. L. Archer, 2012: Saturation wind power potential and its implications for wind energy. *Proc. Natl. Acad. Sci.*, 109(39), 15681.
- Larsén, X.G., and J. Fischereit, 2021: A case study of wind farm effects using two wake parameterizations in the Weather Research and Forecasting (WRF) model (V3. 7.1) in the presence of low-level jets. *Geoscientific Model Development*, 14(6): 3141-3158.
- Lee, J. C. Y., and Lundquist, J. K., 2017: Evaluation of the Wind Farm Parameterization in the Weather Research and Forecasting Model (Version 3.8.1) with meteorological and turbine power data, *Geoscientific Model Development*, 10, 4229–4244, <https://doi.org/10.5194/gmd-10-4229-2017>.
- Mckay, P., R. Carriveau, D. S-K Ting, and T. Newson, 2012: Turbine Wake Dynamics. *Advances in Wind Power*: 65–84. INTECH. Web.
- Nierenberg, R. and J. Kline, 1989: Macro-scale wake effects. *WindStats Newsletter*. Spring 1989. Vol. 2, No. 2, ISSN 0903-5648, 2 pp.
- Nierenberg, R., 1989: Macro-scale wake effects. *Windpower*, 1989, San Francisco, CA, September, 9 pp.



- Pielke, R. A., 1984: Mesoscale Meteorological Modeling. New York, N. Y.: Academic Press, 612 pp.
- Platis, A., Siedersleben, S. K., Bange, J., Lampert, A., Baerfuss, K., Hankers, R., Cañadillas, B., Foreman, R., Schulz-Stellenfleth, J., Djath, B., Neuman, T., and Emeis, S., 2018: First in situ evidence of wakes in the far field behind offshore wind farms, *Sci. Rep.*, 8, 2163, <https://doi.org/10.1038/s41598-018-20389-y>.
- Poulos, G. S., E. Jones, and J. Crescenti, 2022: Validation: Replacing wake loss modeling with wind farm-atmosphere interaction loss modeling. *Journal of Energy in Southern Africa*, August, 28 pp.
- Pryor, S. C., R. J. Barthelmie, T. J. Shepherd, A. N. Hahmann, and O. M. Garcia Santiago, 2022: Wakes in and between very large offshore arrays. *J. Phys.: Conf. Ser.* 2265 022037
- Rosencrans, D. J., J. K. Lundquist, M. Optis, and N. Bodini, 2022: Quantifying the uncertainty of wake impacts across the Atlantic outer continental shelf. 13th Conference on Weather, Climate, and the New Energy Economy. Houston, Texas, American Meteor. Soc. <https://ams.confex.com/ams/102ANNUAL/meetingapp.cgi/Session/60432>
- Rybchuk, A., T. Juliano, J. Lundquist, D. Rosencrans, N. Bodini, M. Optis, 2021: The sensitivity of the Fitch wind farm parameterization to a three-dimensional planetary boundary layer scheme. 10.5194/wes-2021-127.
- Siedersleben, S. K., Platis, A., Lundquist, J. K., Djath, B., Lampert, A., Bärfuss, K., Cañadillas, B., Schulz-Stellenfleth, J., Bange, J., Neumann, T., and Emeis, S., 2020: Turbulent kinetic energy over large offshore wind farms observed and simulated by the mesoscale model WRF (3.8.1), *Geoscientific Model Development*, 13, 249–268, <https://doi.org/10.5194/gmd-13-249-2020>.
- Siedersleben, S. K., Platis, A., Lundquist, J. K., Lampert, A., Bärfuss, K., Cañadillas, B., Djath, B., Schulz-Stellenfleth, J., Bange, J., Neumann, T., and Emeis, S., 2018: Evaluation of a wind farm parametrization for mesoscale atmospheric flow models with aircraft measurements, *Meteorol. Z.*, 27, 401–415, <https://doi.org/10.1127/metz/2018/0900>.
- Skamarock, W. C., J. B. Klemp, J. Dudhia, D. O. Gill, Z. Liu, J. Berner, W. Wang, J. G. Powers, M. G. Duda, D. M. Barker, and X.-Y. Huang, 2019: A Description of the Advanced Research WRF Version 4. NCAR Tech. Note NCAR/TN-556+STR, 145 pp. doi:10.5065/1dfh-6p97.
- Tomaszewski, J. M., and Lundquist, J. K., 2020: Simulated wind farm wake sensitivity to configuration choices in the Weather Research and Forecasting Model Version 3.8.1, *Geoscientific Model Development*, 13, 2645–2662, <https://doi.org/10.5194/gmd-13-2645-2020>.
- Volker, P. J. H., J. Badger, A. N. Hahmann, and S. Ott, 2015: The Explicit Wake Parametrisation V1.0: a wind farm parametrisation in the mesoscale model WRF, *Geosci. Model Dev.*, 8, 3715–3731, <https://doi.org/10.5194/gmd-8-3715-2015>, 2015.



# Investigating energy production and wake losses of multi-gigawatt offshore wind farms with atmospheric large-eddy simulation

Peter Baas<sup>1</sup>, Remco Verzijlbergh<sup>1,2</sup>, Pim van Dorp<sup>1</sup>, and Harm Jonker<sup>1,3</sup>

<sup>1</sup>Whiffle, Molengraaffsingel 8, 2629 JD Delft, the Netherlands

<sup>2</sup>Department of Engineering Systems and Services, Delft University of Technology, Jaffalaan 5, 2628 BX Delft, the Netherlands

<sup>3</sup>Department of Geoscience and Remote Sensing, Delft University of Technology, Stevinweg 1, 2628 CN Delft, the Netherlands

**Correspondence:** Peter Baas (redacted)@whiffle.nl)

Received: 12 December 2022 – Discussion started: 20 December 2022

Revised: 7 March 2023 – Accepted: 24 April 2023 – Published: 22 May 2023

**Abstract.** As a consequence of the rapid growth of the globally installed offshore wind energy capacity, the size of individual wind farms is increasing. This poses a challenge to models that predict energy production. For instance, the current generation of wake models has mostly been calibrated on existing wind farms of much smaller size. This work analyzes annual energy production and wake losses for future, multi-gigawatt wind farms with atmospheric large-eddy simulation. To that end, 1 year of actual weather has been simulated for a suite of hypothetical 4 GW offshore wind farm scenarios. The scenarios differ in terms of applied turbine type, installed capacity density, and layout. The results suggest that production numbers increase significantly when the rated power of the individual turbines is larger while keeping the total installed capacity the same. Even for turbine types with similar rated power but slightly different power curves, significant differences in production were found. Although wind speed was identified as the most dominant factor determining the aerodynamic losses, a clear impact of atmospheric stability and boundary layer height has been identified. By analyzing losses of the first-row turbines, the yearly average global-blockage effect is estimated to be between 2 and 3 %, but it can reach levels over 10 % for stably stratified conditions and wind speeds around  $8 \text{ m s}^{-1}$ . Using a high-fidelity modeling technique, the present work provides insights into the performance of future, multi-gigawatt wind farms for a full year of realistic weather conditions.

## 1 Introduction

As part of the transition to renewable energy sources, the European offshore wind energy capacity is expanding rapidly. For example, the offshore wind energy capacity in Dutch, Belgian, Danish, and German parts of the North Sea is anticipated to reach the 65 GW mark in the year 2030 and 150 GW in the year 2050 (The Esbjerg Declaration, 2022), whereas the European-wide target for offshore wind in 2050 is 300 GW (European Commission, 2020).

Ten years ago, the largest offshore wind farms had a capacity of around 500 MW. Nowadays this number has in-

creased to 1500 MW, and before the year 2030, wind farms of 4000 MW will be no exception. In fact, already today clusters of wind farms with a joint capacity of several gigawatts exist. In parallel, the wind turbines themselves have been increasing in size. The current generation of offshore wind turbines have a nominal power of 10 to 12 MW, but this could increase to as much as 20 MW for the year 2030. Offshore wind energy is thus entering a new phase on three levels: the total installed capacity, the size of the wind farms, and the size of the individual wind turbines.

Veers et al. (2019), among others, have pointed out the need for a better understanding of atmospheric flows through

wind farms. In particular the growth of wind farm size poses a challenge for models that predict energy production. The current generation of wake models has been extensively validated on wind farms in the 100-to-500 MW range. Using these model to make predictions for the future generation of multi-gigawatt wind farms forces them to operate well outside their validation range. This could at least add significant uncertainty to their predictions. It could therefore be argued that more physics-based models have higher fidelity in this “terra incognita”.

One such modeling technique is large-eddy simulation (LES). By numerically integrating the filtered conservation equations of mass, momentum, temperature, and moisture, LES is able to capture the essential aspects of wind farm flow dynamics in a physically sound way. The “global-blockage” phenomenon is a fitting example: the presence of a wind farm induces spatial gradients in the modeled pressure field, leading to forces upwind of the wind farm, thus “informing” the flow about the “obstacle” ahead and causing the flow to deflect (around and/or over the wind farm).

LES has been at the forefront of wind farm flow physics research for some time; see for example the reviews in Mehta et al. (2014), Stevens and Meneveau (2017), and Porté-Agel et al. (2020). Owing to the increase in wind turbine and wind farm scales, a number of recent studies have explored atmospheric flows through large wind farms. Maas and Raasch (2022) have studied the wake effects of a cluster of offshore wind farms in the German Bight, exploring aspects like (far-)wake effects, boundary layer structure, turbulence, and entrainment of kinetic energy for a selection of cases with different atmospheric stabilities. Verzijlbergh (2021) discussed some aspects of modeling flows through large wind farms with illustrative LES results of a 4 GW wind farm in the North Sea.

The present work aims to explore the energy production and internal wake effects for a suite of hypothetical 4 GW offshore wind farm scenarios. The scenarios differ in terms of applied turbine type, capacity density, and layout. Furthermore, we study how wake losses depend on atmospheric stability and we discuss the global-blockage phenomenon. Amongst others, we address questions like the following: how large are wake and blockage losses in 4 GW wind farms and how do these depend on wind speed, wind direction, and atmospheric stability? What is the impact of turbine size and power density? How are losses distributed over the wind farms for different layouts and geometries?

To this end, for a total of six hypothetical wind farm scenarios we simulate 1 year of actual weather with the GRASP (GPU-Resident Atmospheric Simulation Platform) LES model. This is done by driving the LES with data from ECMWF’s ERA5 reanalysis dataset (Hersbach et al., 2020). In this way, we obtain representative distributions of, for example, wind speed, stability, and baroclinicity in a natural way (Schalkwijk et al., 2015b). The resulting dataset can be regarded as a consistent, three-dimensional, 1-year dataset

of pseudo-observations of meteorological variables (including wake effects) and power production (at turbine level). As such, the present work allows for a more statistical approach to studying wind farm dynamics compared to other LES studies that have mostly considered a set of idealized case studies.

This paper is organized as follows. In Sect. 2 the model is introduced. The different scenarios are described in Sect. 3. Section 4 presents the results. After a discussion in Sect. 5, the conclusions are summarized in Sect. 6.

## 2 Model description and simulation strategy

The model simulations are carried out with the GPU-Resident Atmospheric Simulation Platform (GRASP). GRASP is an LES code that runs almost entirely on GPUs; see Schalkwijk et al. (2012). The origin of GRASP can be traced back to the Dutch Atmospheric Large-Eddy Simulation (DALES) model, which is extensively described in Heus et al. (2010).

### 2.1 Governing equations

We present the most important governing equations below. More details can be found in Heus et al. (2010), Böing (2014), and Schalkwijk et al. (2015a). We follow Einstein’s summation notation, with  $x_1, x_2, x_3 = x, y, z$  for the coordinates and  $u_1, u_2, u_3 = u, v, w$  for the wind components. The continuity equation reads

$$\frac{\partial \rho_b u_j}{\partial x_j} = 0. \quad (1)$$

In the anelastic approximation employed in GRASP, the density  $\rho_b = \rho_b(z)$  represents a base density profile depending on height only.

$$\rho_b \frac{\partial u_i}{\partial t} = - \frac{\partial \rho_b u_i u_j}{\partial x_j} - \frac{\partial \tau_{ij}}{\partial x_j} - \frac{\partial p'}{\partial x_i} + \delta_{i3} \rho_b B + \epsilon_{ij3} f_c (u_j - u_{\text{geo},j}) + \left( \frac{\partial \rho_b u_i}{\partial t} \right)_{\text{sources}} \quad (2)$$

In the Navier–Stokes equation above, we denote buoyancy with  $B$ . In the buoyancy calculation a height-dependent reference temperature is used. The large-scale pressure gradient term has been written as a geostrophic wind  $u_{\text{geo}}$ . Further,  $f_c$  denotes the Coriolis parameter and  $p'$  the pressure fluctuations. The subgrid-scale turbulent stress,  $\tau_{ij}$ , needs to be modeled with an appropriate turbulence closure. In this study we apply the Rozema model (Rozema et al., 2015), which is a minimum-dissipation eddy-viscosity model specifically developed for anisotropic grids. As such,  $\tau_{ij}$  is modeled as

$$\tau_{ij} = -2K_m S_{ij}, \quad (3)$$

where

$$S_{ij} = \frac{1}{2} \left( \frac{\partial u_i}{\partial x_j} + \frac{\partial u_j}{\partial x_i} \right) \quad (4)$$

is (the symmetric part of) the velocity-gradient tensor. The eddy viscosity/diffusivity,  $K_m$ , is given by

$$K_m = (c_s \Delta)^2 f(S_{ij}), \quad (5)$$

with a term containing the grid resolution,  $\Delta$ ; a prefactor,  $c_s$ ; and some function of the velocity-gradient tensor. The prefactor  $c_s$  is named after the so-called Smagorinsky constant in the traditional Smagorinsky subgrid model.

Transport of heat is described by

$$\rho_b \frac{\partial \vartheta_l}{\partial t} = - \frac{\partial \rho_b u_j \vartheta_l}{\partial x_j} - \frac{\partial F_j^\vartheta}{\partial x_j} + S_{\vartheta_l}. \quad (6)$$

Sources/sinks of temperature are, e.g., related to diabatic processes such as radiative transfer. Radiative transfer calculations are carried out offline based on the ERA5 input profiles of the relevant variables.

We use a temperature,

$$\vartheta_l = \frac{h_1}{c_p}, \quad (7)$$

which is based on moist static energy  $h_1$ :

$$h_1 = c_p T + gz - L_v q_l - L_i q_i. \quad (8)$$

This is a conserved variable for moist adiabatic ascent. Here  $c_p = 1005 \text{ kJ kg}^{-1} \text{ K}^{-1}$  denotes the specific heat capacity of air (at constant pressure),  $L_v = 2.25 \times 10^6 \text{ J kg}^{-1}$  the latent heat of vaporization of water, and  $L_i = 2.84 \times 10^6 \text{ J kg}^{-1} \text{ K}^{-1}$  the latent heat of sublimation of ice.

Transport of moisture is described by

$$\rho_b \frac{\partial q_t}{\partial t} = - \frac{\partial \rho_b u_j q_t}{\partial x_j} - \frac{\partial F_j^q}{\partial x_j} + S_{q_t}, \quad (9)$$

where  $q_t = q_v + q_l + q_i$  denotes the conserved variable total specific humidity, being the sum of vapor, liquid, and ice water. Subgrid fluxes of humidity are denoted  $F_j^q$ . Local sources/sinks of humidity, denoted by  $S_{q_t}$ , are related to microphysics.

An ‘‘all-or-nothing’’ cloud adjustment scheme is used that assumes that no cloud water/ice is present in unsaturated grid boxes, while all moisture exceeding the local saturated vapor pressure is considered liquid water or ice. In addition, the Grabowski (1998) ice microphysics scheme is used. A single precipitating prognostic variable,  $q_r$ , is used. The partitioning towards water, snow, and graupel is diagnosed with a temperature criterion. Autoconversion, the initial stage of raindrop formation, is modeled according the Kessler–Lin formulation (Khairoutdinov and Randall, 2003).

## 2.2 Boundary conditions

### 2.2.1 Large-scale meteorological conditions

In this study, the LES is coupled to ECMWF’s ERA5 reanalysis dataset. As we apply periodic lateral boundary conditions, no large-scale gradients can be resolved by the LES (a model version with open boundary conditions is currently being developed). Initial conditions and large-scale (LS) tendencies are extracted from ERA5 by means of spatial and temporal interpolation and prescribed to GRASP as a function of height only (i.e., homogeneous over the domain). To account for the large-scale tendencies, several model terms are adjusted and/or added:

$$\begin{aligned} \rho_b \frac{\partial u_i}{\partial t} = & \dots + \epsilon_{ij3} f \left( u_j - u_{\text{geo},j}^{\text{LS}} \right) - \rho_b u_i^{\text{LS}} \frac{\partial u_j^{\text{LS}}}{\partial x_j} \\ & - w^{\text{LS}} \frac{\partial u_i}{\partial z} + \frac{1}{\tau} \left( u_i^{\text{LS}} - \overline{u_i} \right). \end{aligned} \quad (10)$$

And for any scalar  $\phi_i$ ,

$$\rho_b \frac{\partial \phi_i}{\partial t} = \dots - \rho_b u_i^{\text{LS}} \frac{\partial \phi_j^{\text{LS}}}{\partial x_j} - w^{\text{LS}} \frac{\partial \phi_i}{\partial z} + \frac{1}{\tau} \left( \phi_i^{\text{LS}} - \overline{\phi_i} \right). \quad (11)$$

The final terms of Eqs. (10) and (11) represent nudging to the large-scale model: the slab-averaged model fields ( $\overline{u_i}$ ,  $\overline{\phi_i}$ ) are nudged to ERA5 with a nudging timescale,  $\tau$ , of 6 h. This timescale is long enough to give the LES physics enough freedom to establish its own unique state but short enough to make the simulation follow slow large-scale disturbances such as weather fronts (Neggers et al., 2012). In the upper quarter of the domain, the nudging timescale to ERA5 is gradually decreased (i.e., stronger nudging) towards a value of 60 s at the domain top.

### 2.2.2 Lower-boundary conditions

Over water surfaces (as in the present study), GRASP uses a prescribed surface temperature  $T_s$ . At the surface, saturation is assumed:

$$q_{ts} = q_{\text{sat}}(T_s, p_s). \quad (12)$$

The surface roughness lengths for momentum and heat,  $z_{0m,h}$ , are parameterized following the ECMWF IFS documentation (ECMWF, 2017):

$$z_{0m} = \alpha_m \frac{\nu}{u_*} + \alpha \frac{u_*^2}{g}, \quad (13)$$

$$z_{0h} = \alpha_h \frac{\nu}{u_*}, \quad (14)$$

where  $\alpha$  is the Charnock parameter, taken as 0.0185. Furthermore,  $g = 9.81 \text{ m s}^{-2}$  is the gravitational constant;  $\nu = 1.5 \times 10^{-5} \text{ m}^2 \text{ s}^{-1}$  is the kinematic viscosity of air,  $\alpha_m = 0.11$ , and  $\alpha_h = 0.4$ . For momentum, this parameterization follows Charnock (1955) with viscous effects for light wind conditions added.

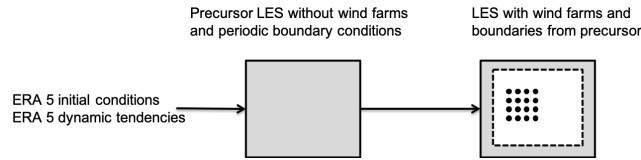


**Figure 1.** Schematic view of ERA5 boundary conditions, a precursor simulation, and a nested domain with turbines.

### 2.2.3 Upper-boundary conditions

At the top of the domain, we take

$$\frac{\partial u}{\partial z} = \frac{\partial v}{\partial z} = 0, \quad w = 0, \quad \frac{\partial \phi_i}{\partial z} = \text{constant in time.} \quad (15)$$

Fluctuations of velocity and scalars are damped out in the upper part of the domain by a sponge layer through additional forcing/source terms added to the right-hand side of the governing equations:

$$\rho_b \frac{\partial u_i}{\partial t} = \dots - \alpha^{\text{sp}} \rho_b (u_i - \bar{u}_i), \quad (16)$$

$$\rho_b \frac{\partial \phi_i}{\partial t} = \dots - \alpha^{\text{sp}} \rho_b (\phi_i - \bar{\phi}_i), \quad (17)$$

with  $\alpha^{\text{sp}}$  being a height-dependent relaxation rate (units  $\text{s}^{-1}$ ) that varies from  $2.75 \times 10^{-3} \text{ s}^{-1}$  at the top of the domain to 0 at the height where the sponge layer starts, which is at 75 % of the domain height (i.e., the sponge layer comprises the upper quarter of the domain).

### 2.2.4 Lateral boundary conditions

In the present setup we apply periodic boundary conditions. To prevent the recirculation of wind farm wakes, we make use of a concurrent-precursor simulation (Stevens et al., 2014). This is a simulation without wind turbines that runs in parallel with the “actual” simulation. Over a boundary region, the values of the actual simulation are strongly nudged towards the precursor simulation (with an adaptive nudging timescale on the order of the model time step). A schematic overview of this setup is shown in Fig. 1.

### 2.3 Wind turbine parameterization

Wind turbines are modeled by a so-called actuator-disk model. This models each turbine as a semi-permeable disk that exerts forces on the flow that are consistent with the thrust curve of the wind turbine. In this way, wind farm wake effects are taken into account. In addition, using the turbine power curve, the turbine parameterization allows us to directly model power output per turbine at a high temporal resolution. The actuator-disk model is implemented following Meyers and Meneveau (2010) and Calaf et al. (2010). Within this parameterization, the total drag force exerted on the flow by a wind turbine is modeled as

$$F_t = -\frac{1}{2} \rho A C_t' \overline{M_D}^2, \quad (18)$$

where  $\rho$  is the disk-averaged air density,  $A = \pi R^2$  the frontal area of the rotor, and  $C_t'$  the thrust coefficient based on the disk-averaged wind speed  $M_D$ . Wind turbine power is given by

$$P_t = -\frac{1}{2} \rho A C_p' \overline{M_D}^3, \quad (19)$$

with  $C_p'$  being the disk-based power coefficient. The disk-based power and thrust coefficients are determined from the manufacturer’s power and thrust curves by means of an off-line simulation. This additional step is required, since the manufacturer curves are based on a free-stream wind speed,  $M_\infty$ ; a reference density,  $\rho_0$ ; and a reference turbulent intensity,  $\text{TI}_{\text{ref}}$ . An additional advantage of this approach is that the turbines by definition produce the correct power and thrust for the given grid configuration. The present implementation of the actuator-disk model has been tested extensively in operational practice and shows good performance for a wide range of numerical grid settings.

In order to quantify aerodynamic losses, we compare the energy production of the wind turbines with the production of so-called thrustless turbines. These thrustless turbines are embedded in the concurrent-precursor simulation. The disk-based power coefficients for the thrustless turbines are obtained by means of a separate offline simulation with the thrust coefficients set to 0. As a result, a power production of the thrustless turbines can be determined, but they do not exert drag on the flow. Thus, each thrustless turbine produces power as if it were a single isolated turbine. Furthermore, the simulations with thrustless turbines and those with the active turbines experience exactly the same turbulent wind fields at the boundaries. As such, the difference between the production of the thrustless turbines and the active turbines is a measure of the aerodynamic loss.

### 2.4 Simulation strategy

For each of the wind farm scenarios (Sect. 3.1), the year 2015 was simulated. For this year, observations from the meteorological mast (metmast) “Metemast IJmuiden” were available for basic validation. The year-long simulations consist of concatenated daily simulations with a spin-up of 2 h. For each day, GRASP is initialized at 22:00 UTC the previous day. Model output valid between 00:00 and 24:00 (UTC) is used for the analysis.

The model domain consists of  $640 \times 640 \times 48$  grid points. The horizontal grid spacing is 120 m; the lowest grid box has a height of 30 m. The horizontal domain size extends to 76 800 m. Vertical grid stretching was applied to obtain a domain height of 3000 m (i.e., a uniform growth factor of 2.845 %). Sensitivity experiments discussed in Sect. 5 indi-



cate that this domain size is sufficiently large. The model domain is centered around  $52.8659^\circ$  N,  $3.5364^\circ$  E. This corresponds to a location in the North Sea, roughly 100 km from the Dutch coast within the planned 4000 MW wind farm IJmuiden Ver.

Compared to other LES studies (Wu and Porté-Agel, 2017; Maas and Raasch, 2022; Strickland et al., 2022), the horizontal resolution of 120 m is relatively coarse. This choice results from a trade-off between computational cost and accuracy and has been tested extensively in an operational setting. As such, it follows from our ambition to simulate a full year of realistic weather conditions, rather than the common approach of running a suite of targeted (idealized) case studies. To provide insights into the effect of the applied resolution, the sensitivity of the results to the grid spacing is discussed in Sect. 5.

As a basic validation of the model's capability to represent the local wind conditions, Fig. 2a compares modeled versus observed wind speed at a height of 92 m. In this case, the modeled (horizontal) wind speed is taken from a virtual metmast placed at the location of the actual metmast. The correspondence between model and tower observations is satisfactory, with error metrics within the expected range for wind resource assessments. Figure 2b shows the distribution of the modeled 92 m wind speed, with a Weibull function fitted to the data. For comparison, grey dots indicate the distribution of the observations. Figure 2c presents the (modeled) wind rose, indicating that southwesterly winds have the highest frequency of occurrence and are generally stronger than winds from other sectors.

### 3 Wind farm scenarios and turbine characteristics

In this section, the six hypothetical 4000 MW wind farm scenarios and details of the applied turbine types will be introduced.

#### 3.1 Scenarios

Layouts of the six considered scenarios are given in Fig. 3. The rationale for the first five scenarios is the same: each layout consists of four sites of roughly 10 km by 10 km, separated by 3 km wide corridors. Each of the four sites within each scenario has an installed capacity of approximately 1000 MW (Scenario 1 to 4). The number of turbines depends on the rated power of the applied turbine. As Scenario 5 has only half the capacity density of the other scenarios ( $5 \text{ MW km}^{-2}$  instead of  $10 \text{ MW km}^{-2}$ ), each of its four sites has only half the installed capacity (i.e., 500 MW). Scenario 6 is based on the actual site boundaries of the planned IJmuiden Ver wind farm for which a tender is expected to open in 2023 (RVO, 2022). The installed capacity of 4000 MW corresponds to the actual plans.

#### 3.2 Turbine types

To study the impact of using different turbine types while keeping the total installed power approximately the same, four different turbine types have been applied. Three reference wind turbines were used with data taken from <https://nrel.github.io/turbine-models/Offshore.html> (last access: 18 May 2023; the DTU\_10MW\_178\_RWT turbine (10.6 MW, labeled as DTU10), the IEA\_10MW\_198\_RWT turbine (10.6 MW, labeled as IEA10), and the IEA\_15MW\_240\_RWT turbine (15 MW, labeled as IEA15)). In addition, a 21.4 MW turbine was constructed by using the power and thrust curves from the IEA15 turbine but increasing the rotor diameter to obtain the desired rated power. Power and thrust curves for the four wind turbines are given in Fig. 4. The rated wind speed of the IEA10 is lower than that of the DTU10. Instead, the latter produces lower thrust. Differences between the  $c_p$  and  $c_t$  curves of the IEA10 and IEA15 turbines are small.

An overview of the scenarios and turbine characteristics is given in Table 1. The installed capacity of the first four scenarios is close to 4200 MW. For Scenario 5, with half the capacity density, this is 2100 MW. The installed capacity for the IJmuiden Ver scenario (Scenario 6) is a little lower than for the other scenarios. Turbine spacing is between 5.6 and 6.2  $D$  for the  $10 \text{ MW km}^{-2}$  scenarios and 8.3  $D$  for the  $5 \text{ MW km}^{-2}$  scenario. These values are in the range of values that occur in existing offshore wind farms. The baseline capacity density of  $10 \text{ MW km}^{-2}$  corresponds to the target set for future wind farms in the Dutch part of the North Sea. In the following, we consider Scenario 3 a reference, for which more detailed analyses will be presented.

### 4 Results

In this section we discuss the differences in energy production between the six scenarios. We distinguish between production of the thrustless turbines (also called “free-stream production” or “gross power”) and the actual production (“net power”). We designate the difference between the two as the “aerodynamic losses”. Depending on the application, we present either absolute aerodynamic losses (in MW or MW h) or relative aerodynamic losses (dimensionless) where the absolute losses are normalized with the free-stream production.

After analyzing the dependence of the aerodynamic losses on the wind speed, we discuss the impact of atmospheric stability and boundary layer height. Next, losses of the first-row turbines (i.e., turbines which have no other turbines upstream) will be considered, which gives an indication of the impact of blockage effects. We will also break down our results for bins of wind direction. Apart from showing the impact of wind farm layout, this illustrates that for understanding directional differences, a proper separation of the wind speed effect and the stability effect is crucial. Finally, we il-

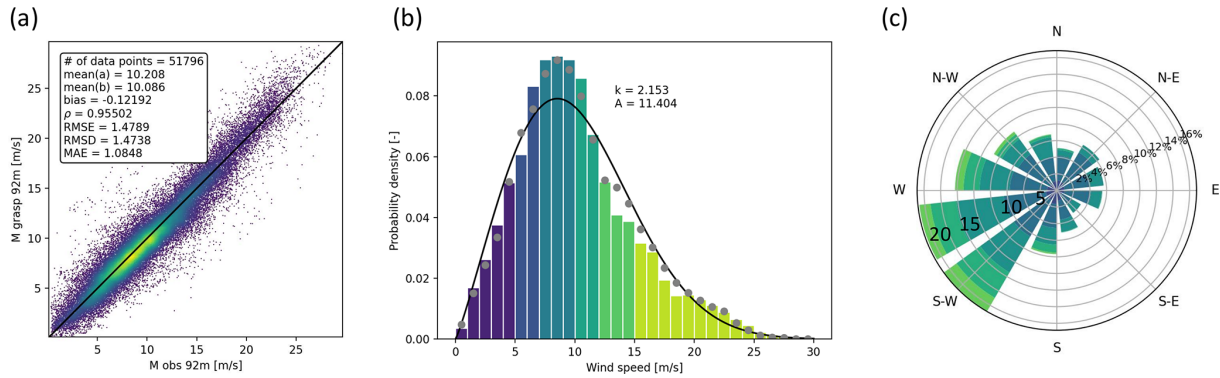


**Figure 2.** Validation results of GRASP versus offshore tall mast IJmuiden. **(a)** Modeled versus observed wind speed at 92 m. **(b)** Weibull plot of GRASP 92 m wind speed. Grey dots represent the observations. **(c)** Modeled wind rose at 92 m. Colors indicate  $5 \text{ m s}^{-1}$  intervals.

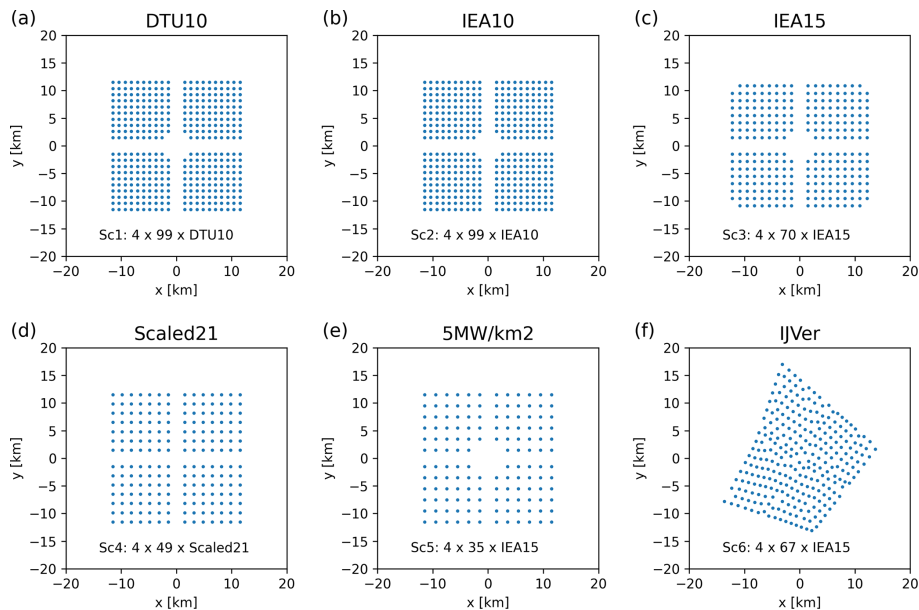


**Figure 3.** Layouts of the six wind farm scenarios. Panel titles refer to the scenario labels in Table 1. For each scenario the number and type of the applied turbine are indicated.

illustrate the results with a selection of composite maps showing spatial variations in wind speed and aerodynamic losses over the wind farms.

Figure 5 presents the overall energy production and the aerodynamic losses for each of the six scenarios. The aerodynamic losses vary between 12 % and 18 % for the 4 GW wind farms, whereas the 2 GW variant has losses of around 6 %. Several noticeable differences between the scenarios become apparent.

First, although the DTU10 and IEA10 turbine have the same rated power, the actual production of the IEA10 turbine is 7.7 % larger. This significant difference is the result of higher “free-stream” production numbers. These more than compensate for the slightly higher aerodynamic losses. Both the higher production and the higher aerodynamic losses for the IEA10 scenario can be related to a difference in the ro-

tor diameter and a different behavior of the respective power curves (see Fig. 4).

Second, while keeping the same installed power, it appears to pay off to apply fewer but more powerful turbines. This is shown by comparing the IEA10, IEA15, and Scaled21 scenarios. While these three scenarios have similar free-stream production, their actual production varies significantly: for IEA10, production is 5.3 % less than for IEA15, and for Scaled21, the production is 2.8 % more. In terms of aerodynamic losses, this implies a reduction from 18.4 % for IEA10 to 11.8 % for Scaled21. At the same time, Table 1 indicates that the turbine spacing in terms of rotor diameters is approximately the same for these three scenarios. This suggests that the (relative) reduction in the number of turbines that is hampered by wakes of other turbines is a major factor contributing to higher production (for instance, the ratio of the

**Table 1.** Overview of the six scenarios, including turbines characteristics. Turbine radius is denoted by  $r$ , turbine rated power by  $P_{\text{rated}}$ , the wind farm installed capacity by  $P_{\text{installed}}$ , and the number of installed turbines by  $N$ . Turbine spacing is given in number of rotor diameters,  $D$ .

Scenario	Label	Turb. type	Hub height [m]	$r$ [m]	$P_{\text{rated}}$ [MW]	$N$ [-]	$P_{\text{installed}}$ [MW]	Spacing	Density [MW km <sup>-2</sup> ]
1	DTU10	DTU_10MW_178_RWT	119	89	10.6	396	4198	6.2 $D$	10.5
2	IEA10	IEA_10MW_198_RWT	119	98	10.6	396	4198	5.6 $D$	10.5
3	IEA15	IEA_15MW_240_RWT	150	120	15.0	280	4200	5.6 $D$	10.5
4	Scaled21	Scaled_21.4MW_WT	173	143	21.4	196	4194	5.8 $D$	10.5
5	5MW/km2	IEA_15MW_240_RWT	150	120	15.0	140	2100	8.3 $D$	5.4
6	IJVer	IEA_15MW_240_RWT	150	120	15.0	268	4020	5.3 $D$	10.4

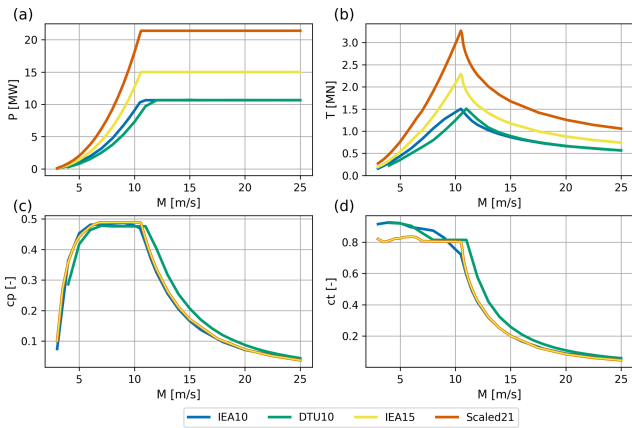


**Figure 4.** Power and thrust curves for the applied turbine types.

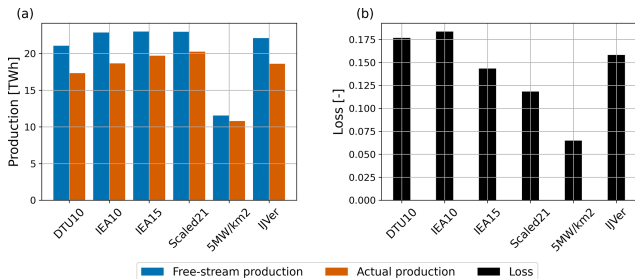


**Figure 5.** Total free-stream and actual production (a) and aerodynamic losses (b) for the six scenarios.

number of first-row turbines over “wake-impacted” turbines will increase (beneficially) when the total number of turbines becomes smaller).

Third, Fig. 5 illustrates the impact of varying the installed capacity per square kilometer. As expected, in the 5 MW km<sup>-2</sup> scenario, the free-stream production is reduced by 50 % compared to the reference IEA15 scenario. However, the actual production decreases only by 45.2 %. The aerodynamic losses decrease drastically from 14.3 % to 6.5 %.

Fourth, the results of the IJVer scenario are comparable to the IEA15 scenario. Its free-stream production is a bit less, because the installed capacity is slightly lower. Also, its aerodynamic losses are slightly higher, which is mainly related to the absence of the 3 km wide corridors (see Fig. 3).

In summary, the present results indicate that expected aerodynamic losses for a 4 GW offshore wind farm are in the range of 12 % to 18 %, where the exact value is determined by the rated power of the applied turbines (or, the number of installed turbines). Moreover, turbines of the same rated capacity but different numbers may give significantly different production numbers. We emphasize that absolute numbers are related to the prevalent wind conditions in the simulated year 2015. To obtain annual energy production (AEP) estimates that are representative of a longer period, additional statistical postprocessing of the data is required, but this is out of the scope of the present work.

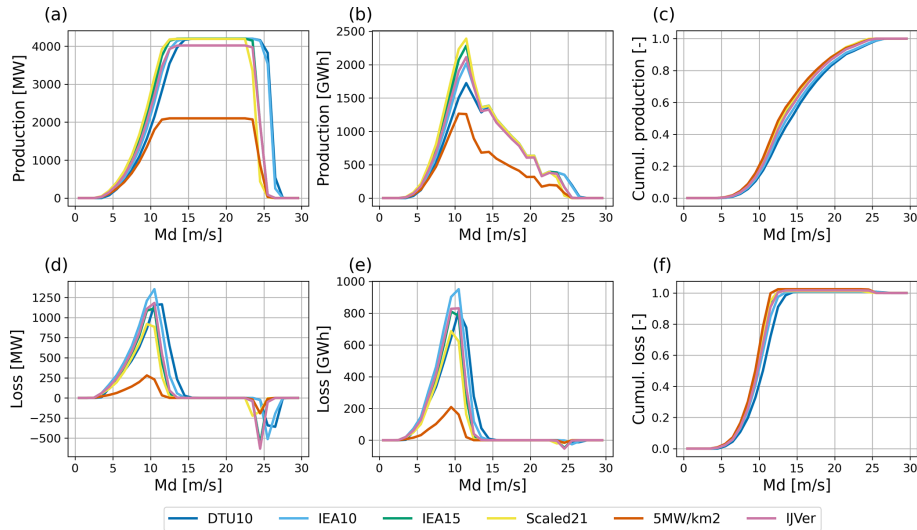
#### 4.1 Wind speed dependence of production and losses

Figure 6 considers energy production and aerodynamic loss as a function of the free-stream disk-averaged wind speed (i.e., the disk-averaged wind speed from the thrustless turbines in the concurrent-precursor simulation). From left to right, the top panels represent averaged instantaneous wind farm production over the year, total energy production, and normalized cumulative production, respectively. The bottom panels show the equivalent aerodynamic losses. The results presented here are representative of the wind climate and the specific turbine design choices. A few interesting observations can be made.

First, Fig. 6a indicates that for wind speeds stronger than 14 m s<sup>-1</sup>, all scenarios operate at rated power. For these strong wind conditions, which generate 50 % of the total energy production (Fig. 6c), the energy content of the flow is so large that aerodynamic losses are negligible.

Second, Fig. 6d–f illustrate that 80 % of all aerodynamic losses occur within a narrow wind speed range of 8 to 12 m s<sup>-1</sup>. For lower wind speeds, production and losses are low anyway; for higher wind speeds, all turbines operate





**Figure 6.** (a–c) Year-averaged wind farm power production (a), total energy production for  $1 \text{ m s}^{-1}$  bins (b), and normalized cumulative production (c) as a function of the free-stream disk-averaged wind speed. (d–f) Year-averaged wind farm power losses (d), total aerodynamic losses for  $1 \text{ m s}^{-1}$  bins (e), and normalized cumulative losses (f) as a function of the free-stream disk-averaged wind speed.

at (or close to) rated power. Around cut-out wind speeds, substantial instantaneous negative losses occur (Fig. 6d). This remarkable feature is caused by the fact that for these wind speeds, as a result of subtle wake effects, the number of power-producing turbines in the simulations with actual (thrust-generating) turbines is larger than in the simulations with the thrustless turbines. As the frequency of occurrence of these specific wind conditions is low, the impact of this effect on the integrated losses is small (Fig. 6e).

Third, the total energy production peaks around a wind speeds of approximately  $12 \text{ m s}^{-1}$ . This can be understood by interpreting the total energy production as a function of wind speed as a multiplication of the wind speed probability density (Fig. 2b) and the power curves.

Differences between the six scenarios are small. They are consistent with the total production numbers of Fig. 5 and can be explained by the differences in the turbine power curves (Fig. 4).

#### 4.2 Impact of stability and boundary layer height

In this sub-section, we attempt to isolate the impact of stability and boundary layer height from the impact of the wind speed itself. For clarity reasons, mainly results for the IEA15 reference scenario are presented.

The impact of atmospheric stability on wake losses of wind farms has been widely reported in the scientific literature; see, e.g., Stevens and Meneveau (2017). As a stability parameter, we choose the bulk Richardson number,  $R_b$ , over the rotor blade of the IEA15 turbine, i.e., between heights of 270 and 30 m:

$$R_b = \frac{g}{\vartheta_l} \frac{\Delta z \Delta \vartheta_l}{(\Delta u)^2 + (\Delta v)^2}. \quad (20)$$

Values of  $R_b$  are taken from the precursor simulation. As such, they represent free-stream (or undisturbed) conditions. We consider three classes of stability, separated by the percentiles 33.3 and 66.6 of the year-round distribution of  $R_b$ , which have values of  $-0.04$  and  $0.44$ , respectively. As such, the stability class with the 33.3 % of lowest  $R_b$  values represents convective conditions, while the class with the 33.3 % of highest  $R_b$  values represents significantly stable conditions. The class of intermediate stability contains neutral conditions but is dominated by weakly stratified conditions.

Figure 7 presents the aerodynamic losses as a function of the free-stream disk-averaged wind speed for the three stability classes for the IEA15 scenario. For a wide range of wind conditions, the impact of stability is small. However, just in the wind speed range where most of the actual losses occur, a clear impact of stability is observed. Here, for the most stably stratified conditions, relative losses are roughly 10 percentage points larger than for convective conditions. For higher wind speeds, losses quickly reduce to zero, irrespective of stability. For lower wind speeds, absolute losses (and production) are small.

The strong dependency of aerodynamic losses on the wind speed may easily obscure an analysis of the impact of stability. The relevant wind speed range for considering the impact of stability seems to be between  $6$  and  $10 \text{ m s}^{-1}$ . This narrow range of wind speeds is characterized by near-constant relative losses, which allows for a fair comparison between stability conditions. As can be seen in Fig. 4, this specific wind speed range coincides with the power and thrust curves being at their maximum. In the following, to indicate any impact of stability, we include only data for which the wind speed is between  $6$  and  $10 \text{ m s}^{-1}$ .

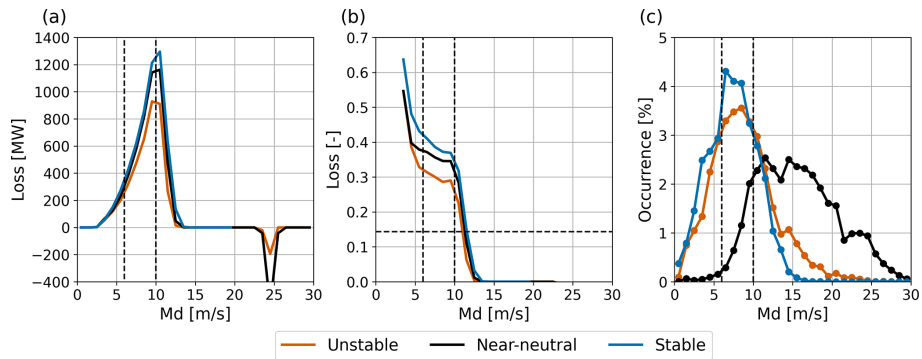


**Figure 7.** Combined effect of wind speed and stability on wind farm aerodynamic losses. (a) Power losses in megawatts (MW). (b) Relative aerodynamic losses. (c) Frequency of occurrence of the three stability classes. Dashed lines at 6 and 10 m s<sup>-1</sup> indicate the wind speed interval for which the aerodynamic losses are relatively constant. The horizontal dashed line in (b) indicates the overall aerodynamic loss.

**Table 2.** Relative aerodynamic losses per scenario for free-stream disk-averaged wind speeds between 6 and 10 m s<sup>-1</sup>, for the three stability classes.

Scenario	Unstable	Neutral	Stable
DTU10	0.29	0.37	0.45
IEA10	0.34	0.41	0.48
IEA15	0.29	0.35	0.38
Scaled21	0.26	0.29	0.32
MW km <sup>-2</sup>	0.14	0.18	0.20
IJVer	0.32	0.36	0.41

Table 2 summarizes the relative aerodynamic losses for all six scenarios for disk-averaged wind speeds between 6 and 10 m s<sup>-1</sup>. Considerable differences between scenarios exist: the higher the overall aerodynamic losses (cf. Fig. 5), the larger the impact of stability. For example, the impact of stability is clearly smaller for the Scaled21 and 5 MW km<sup>-2</sup> scenarios.

To summarize, the impact of stability is only significant for a small range of wind speed conditions. However, it is exactly this range that is also most relevant for aerodynamic losses.

Apart from stability, other LES wind farm studies indicate that the boundary layer height, *h*, may have substantial impact on wakes and wind farm production (e.g., Maas and Raasch, 2022). Here, we examine the influence of the boundary layer height on the aerodynamic losses for the IEA15 scenario. To that end, we diagnosed the boundary layer height from model output of the precursor simulation (undisturbed conditions). We take *h* as the height at which the magnitude of the momentum flux becomes less than 5 % of its surface value.

We distinguish three classes of *h*, separated by the percentiles 33.3 and 66.6 of the year-round distribution of *h*, which have values of 341 and 955 m, respectively. Figure 8 presents the aerodynamic losses as a function of the free-

**Table 3.** Contingency table showing the simultaneous frequency of occurrence (in %) of the three classes of stability (unstable, neutral, stable) and boundary layer height (low, medium, high).

	Low	Medium	High	Total
Unstable	0.3	13.9	19.1	33.3
Neutral	6.1	15.8	11.4	33.3
Stable	24.6	5.2	3.6	33.3
Total	31.0	34.9	34.1	100.0

stream disk-averaged wind speed for the three classes of boundary layer height. The results show remarkable resemblance with the stability analysis (Fig. 7). Also here, the impact is mostly confined to the wind speed range between 6 and 10 m s<sup>-1</sup>. Within this range, aerodynamic losses for shallow boundary layers are clearly (around 10 percentage points) higher than for deep boundary layers.

Obviously, stability and boundary layer height are related. This is illustrated in Table 3, which shows the simultaneous occurrence of the three classes of stability and boundary layer height. Especially the shallow boundary layers clearly coincide with stably stratified conditions.

### 4.3 First-row losses

As with any obstacle placed in a flow, wind farms will have an impact on the flow itself. The air will tend to flow around and over the obstacle, and in front of the wind farm a reduction in wind speed is expected. This will lead to a reduction in power production of the turbines that are not in the wake of other turbines (i.e., located in the “first row”). This phenomenon is known as the global-blockage effect (Bleeg et al., 2018). As the wind speed reduction will propagate to downstream (“waked”) turbines, separating the blockage effect from wake effects is virtually impossible. This is especially true for observations and physically based modeling studies like LES. Therefore, in this study we focus on losses

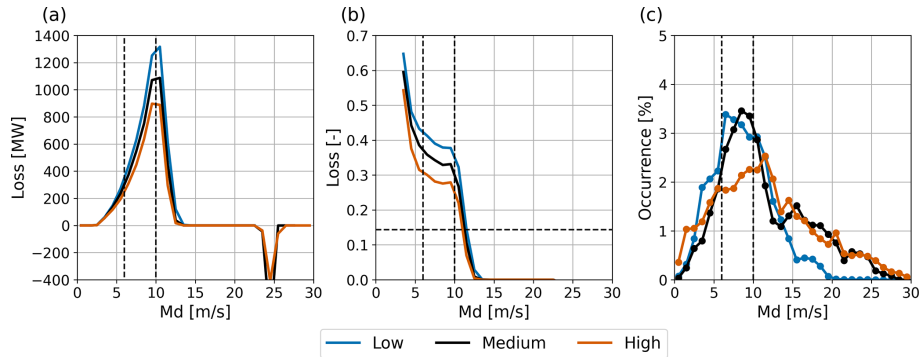


**Figure 8.** Combined effect of wind speed and boundary layer height on wind farm aerodynamic losses. **(a)** Power losses in megawatts (MW). **(b)** Relative aerodynamic losses. **(c)** Frequency of occurrence of the three boundary layer height classes. Dashed lines at  $6$  and  $10 \text{ m s}^{-1}$  indicate the wind speed interval for which the aerodynamic losses are relatively constant. The horizontal dashed line in **(b)** indicates the overall aerodynamic loss.

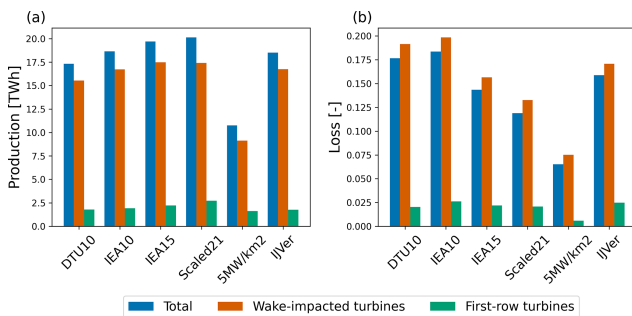


**Figure 9.** **(a)** Total production, production of “wake-affected” turbines, and production of first-row turbines for all six scenarios. **(b)** Aerodynamic losses.

of the first-row turbines, which can be interpreted as a conservative estimate for the blockage effect.

We determine the first-row losses as follows: given the wind direction, for each time step we verify if any other turbines are located within a  $60^\circ$  wide sector opposite to the flow direction. If this is not the case, a turbine is classified as a first-row turbine for that particular time step.

Figure 9 presents the year-round production numbers and relative aerodynamic losses for the first-row turbines and all other (waked) turbines. The actual production of the first-row turbines is between 2 % and 3 % lower than their corresponding thrustless (or free-stream) production. Although the applied definitions and metrics can be discussed, these values are not inconsistent with values of the blockage effect reported in the literature (e.g., Wu and Porté-Agel, 2017; Allaerts et al., 2018; Blegg et al., 2018; Schneemann et al., 2021). Consistently, the losses of the non-first-row, or other, turbines are a bit higher than the overall losses.

As with the overall aerodynamic losses above, we can also assess the impact of both wind speed and stability on the first-row losses. Figure 10 shows that, consistently with the above results (e.g., Fig. 6), also the first-row losses are

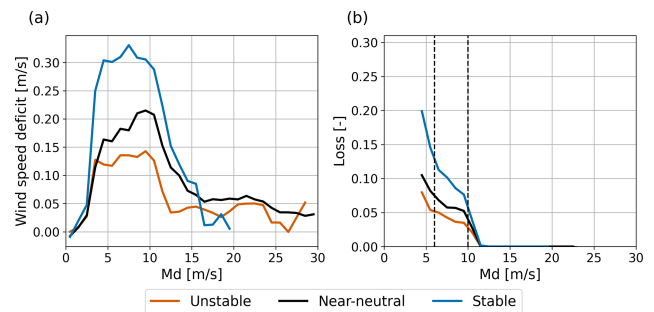


**Figure 10.** The reduction in the first-row 140 m wind speed compared to the free-stream wind speed **(a)** and the relative aerodynamic losses of first-row turbines **(b)** as a function of wind speed and stability.

negligible for wind speeds over  $12 \text{ m s}^{-1}$ . Interestingly, the first-row wind speed deficit with respect to free-stream conditions continues towards much higher wind speeds. The majority of the first-row losses occur for wind speeds between  $6$  and  $10 \text{ m s}^{-1}$ . Values range from 4 % in convective conditions to 8 % in the most stable conditions. The corresponding first-row wind speed deficits vary from approximately  $0.12$  to  $0.30 \text{ m s}^{-1}$ . Relative first-row losses are even higher for wind speeds below  $6 \text{ m s}^{-1}$ , but these are less relevant in an absolute sense (not shown).

We conclude that first-row losses are on average between 2 % and 3 %. However, for the wind speed range where most of the losses occur these numbers can be more than twice as high. Also, first-row losses are significantly larger for stably stratified conditions (cf. Strickland et al., 2022).

#### 4.4 Directional effects

An analysis of aerodynamic losses per wind direction reveals how the respective impacts of wind speed and stability are

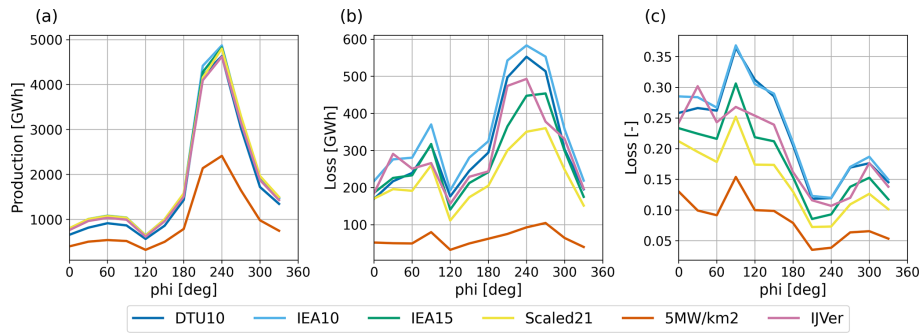


**Figure 11.** Directional dependence of total energy production (a), absolute aerodynamic losses (b), and relative losses (c) for the six scenarios.

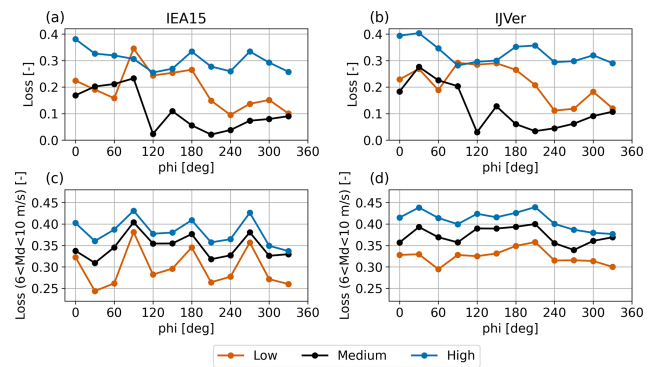
entangled. Moreover, it shows the impact of difference in the layout and geometry of the wind farm scenarios.

Figure 11 shows energy production and aerodynamic losses as a function of the wind direction. The first element that stands out is the overwhelming dominance of the contribution of southwesterly winds to the total energy production. This is the cumulative effect of both the higher frequency of occurrence and the generally stronger wind speeds (see Fig. 2c), in combination with a strongly non-linear character of the turbine power curves.

Figure 11b and c show that while the absolute losses are largest for the southwesterly direction, the relative losses are much higher for easterly directions. From this figure, it cannot be determined if the difference in relative losses is mainly a wind speed effect or if stability is important here. Interestingly, the five hypothetical layouts closely follow the same pattern, but the IJVer scenario behaves differently. Comparison with Fig. 3 suggests that this difference is related to the different layout of the IJVer scenario: while other scenarios form north–south- and west–east-facing squares, the IJVer layout is significantly rotated (but still resembling a clear “square-like” shape). Inspection of Fig. 11b and c indicates that aerodynamic losses are higher/lower when the flow is directed towards the faces/corners of the wind farm layouts.

For two of the scenarios, IEA15 and IJVer, Fig. 12 breaks down the directional losses into stability and wind speed. Figure 12a and b present the relative aerodynamic losses for the three stability classes defined above, irrespective of the wind speed. Losses for stably stratified conditions are the largest, but the losses for convective conditions are also large. Because of generally higher wind speeds (i.e., lower thrust coefficients), the losses for the near-neutral class are much smaller, even when omni-direction numbers are considered (not shown).

As a next step, the bottom panels of Fig. 12 present stability-dependent losses like before but now only including wind speeds between 6 and 10 m s<sup>-1</sup>. By doing so, a clear organization of the data occurs, with the lowest losses occurring for convective conditions and the highest losses for the most stably stratified conditions. Moreover, a clear di-



**Figure 12.** Directional dependence of total aerodynamic losses for different stability classes for the IEA15 (a, c) and IJVer (b, d) scenarios. The top panels (a, b) are based on all data; the bottom panels (c, d) only include wind speeds between 6 and 10 m s<sup>-1</sup>.

rectional pattern is revealed, in particular for the IEA15 scenario, with much higher losses when the flow is directed to the sides of the wind farm and lower losses when the flow faces the corners of the wind farm. This pattern is clearly visible for all three stability classes. For the IJVer scenario the directional pattern is more obscured.

In summary, Fig. 12 demonstrates that an assessment of the impact of stability on wind farm losses is not straightforward. It can only be isolated if the data are also conditioned over a particular, carefully selected wind speed range. This is because both the turbine thrust curves and the stability depend on the wind speed but in different ways. To avoid the impact of wind speed as much as possible, this range should not be too broad, as small differences in wind speed can have a large impact on both absolute and relative aerodynamic losses (Fig. 7).

#### 4.5 Spatial patterns

So far, we have only considered power production and aerodynamic losses for the wind farms as a whole. In the following section, we consider spatial variations in wind speed,

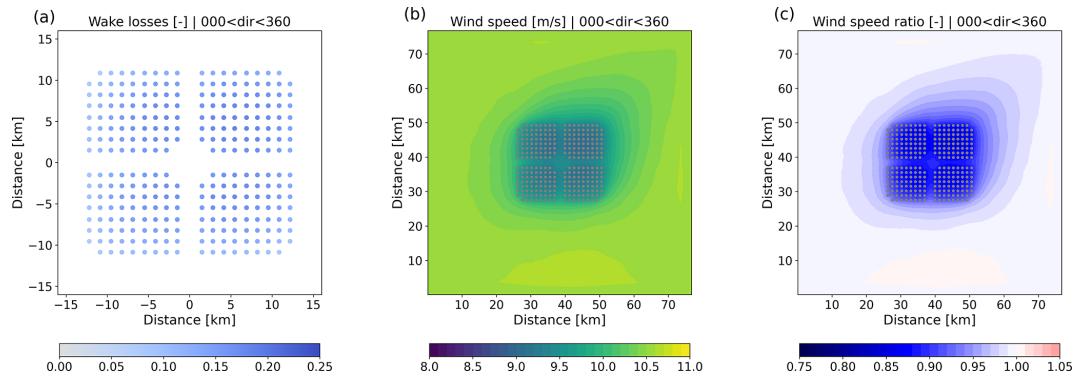


**Figure 13.** Aerodynamic losses (a), mean 140 m wind speed (b), and ratio of actual to free-stream wind speed (c) for the IEA15 scenario (including all data).

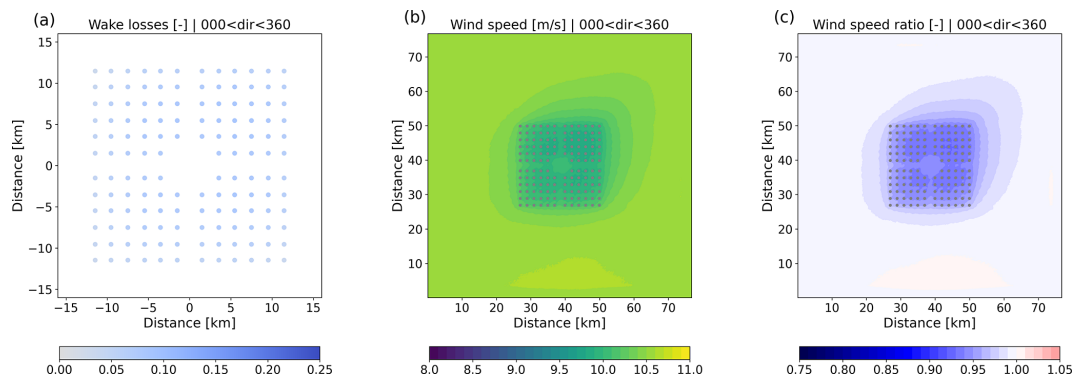


**Figure 14.** Same as Fig. 13 but for the  $5 \text{ MW km}^{-2}$  scenario (including all data).

power production, and aerodynamic losses over the wind farms. By breaking down the dataset into bins of wind direction, wind speed, and stability classes, the impact of different atmospheric conditions can be examined. A selection of composite maps of aerodynamic losses, wind speed, and the ratio of actual to free-stream wind speed (taken from the precursor simulation) are presented.

Figure 13 shows aerodynamic losses, mean wind speed, and velocity deficit compared to the free-stream flow for the IEA15 scenario, averaged over the entire year and all wind directions. Losses vary from around 6 % for turbines located at the outer parts of the wind farm to 20 % for turbines in the interior of the wind farm. The dominance of stronger south-westerly winds is reflected in lower losses in the southwestern part of the wind farm and a clear asymmetry in the composite wind fields. The impact of the wind farm on the year-round, omni-directional wind field is on the order of 20 km, after which a velocity deficit of less than 1 % is observed.

For comparison, Fig. 14 shows the results for the  $5 \text{ MW km}^{-2}$  scenario. As expected, losses are much lower compared to IEA15, which has a capacity density of around  $10 \text{ MW km}^{-2}$ . This is the combined effect of larger distance between the turbines and the fact that only half the number of turbines is involved. The impact on the mean wind field and

the corresponding velocity deficit is smaller as well: in the center of the wind farm the velocity deficit is 6 %, compared to 12 % in the  $10 \text{ MW km}^{-2}$  case.

Figure 15 presents composite maps for the IEA15 scenario again but now only including data with a wind direction between  $15$  and  $45^\circ$ . In this case, a clear wake is visible, which is still present as the flow reaches the southern edge of the domain. Clearly, for studying wake lengths behind wind farms of this size, much larger domains are required than the present 80 km. Upstream, the wind speed is already reduced before the flow reaches the wind farm, which signals the presence of blockage. Along the sides, a clear flow acceleration is visible. The distribution of aerodynamic losses over the wind farm shows interesting patterns. Although not in the wake of any other turbines, the first-row turbines in the northeastern corner of the wind farm produce 10 % less power than their “thrustless” equivalents. On the other hand, the turbines in the southeastern part profit from the flow acceleration around the wind farm and produce up to 5 % more power than if they had operated in isolation.

Comparison of Fig. 15 with Fig. 16 clearly illustrates the difference in the flow being oriented to the corner of the wind farm or directly towards the one of the sides. In the case of the latter, the numbers of turbines that are facing undisturbed



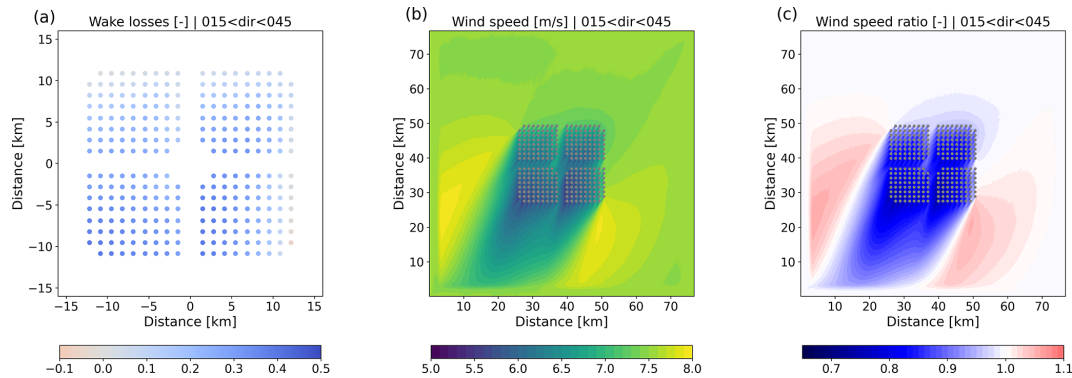


**Figure 15.** Same as Fig. 13 but only including wind directions between 15 and 45°.

conditions (apart from blockage effects) is much less, resulting in larger aerodynamic losses (cf. Fig. 12).

The different layout of the IJVer scenario results in relatively low aerodynamic losses for easterly flow (Fig. 17). Also here, flow acceleration around the wind farm leads to increased production for, in this particular case, the northernmost turbines.

Finally, Figs. 18 and 19 illustrate the impact of convective and stable conditions, respectively. To enable a “fair” comparison, only conditions with wind speeds between 6 and 10 m s<sup>-1</sup> are included. As shown before, in this wind speed range the aerodynamic losses are much higher than average. In stably stratified conditions, deeper wakes occur that extend further downstream. Also, the wind speed reduction upstream of the wind farm is larger in stable conditions. This is reflected in larger first-row losses compared to convective conditions. Moreover, going deeper into the wind farm, losses increase faster for stable than for convective conditions: near the southern edge of the wind farm, turbine losses increase to around 60 % for stable conditions, while they are confined to approximately 40 % in convective conditions.

## 5 Discussion and sensitivity study

To assess production numbers and aerodynamic losses for a suite of hypothetical 4 GW offshore wind farms, a full year of simulations with the LES model GRASP have been performed. Even though GRASP has a relatively high computational performance due to its implementation on GPUs, the computational costs of the simulations are significant. That is to say, in order to enable the atmospheric simulations of large wind farms covering an entire year, the configuration of both the model grid and the domain needs to be carefully selected to limit computational cost while maintaining physically sound results.

Because the applied horizontal grid spacing of 120 m might be considered coarse for an atmospheric LES model and/or for the actuator-disk model that is used, we consider an assessment of the sensitivity of the modeling results ap-

propriate. Therefore, additional simulations have been performed in which we varied the resolution, the prefactor of the subgrid model (governing the magnitude of the subgrid-scale diffusion), and the domain size (both height and horizontal extent). The sensitivity experiments were performed on a smaller domain of 30 720 m. A wind farm of around 770 MW was included. To assess if relative differences between scenarios remained the same, each sensitivity experiment was carried out twice: once with 72 of the IEA10 turbines (regular 9 by 8 array, spacing of 5.6  $D$ ) and once with 36 of the Scaled21 turbines (regular 6 by 6 array, spacing of 5.8  $D$ ). The sensitivity experiments were not run for the entire year but for a representative subset of 100 d. The 100 d was selected by a  $k$ -means clustering method based on the daily mean of the longitudinal and latitudinal components of the ERA5 100 m wind.

Specifically, the following sensitivity experiments have been performed:

- *REF*. This is a reference simulation on a 30 720 m domain of 3000 m height. The horizontal grid spacing was 120 m and the height of the lowest grid box 30 m (as in the main simulations). The number of grid points was 256 in the horizontal and 48 in the vertical.
- *HR*. This is the same as REF but with the horizontal grid spacing set to 60 m. To keep the domain size the same, the number of grid points in the horizontal was increased to 512.
- *C<sub>s</sub>*. This is the same as REF but with the  $c_s$  prefactor of the subgrid-scale eddy diffusivity increased by 50 % (see Eq. 5).
- *2L<sub>x</sub>*. This is the same as REF but with a twice as large horizontal domain of 61 440 m using 512 grid points in both horizontal directions.
- *2L<sub>z</sub>*. This is the same as REF but with the domain height increased to 6000 m using 68 vertical levels.

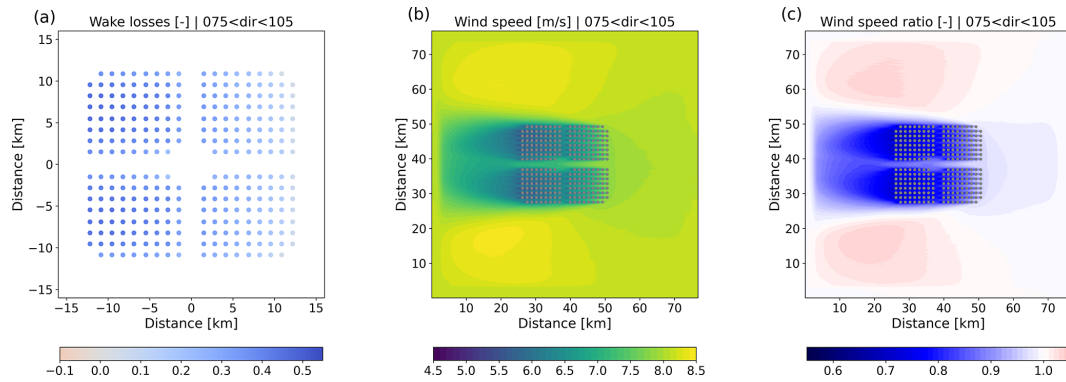


**Figure 16.** Same as Fig. 13 but only including wind directions between 75 and 105°.

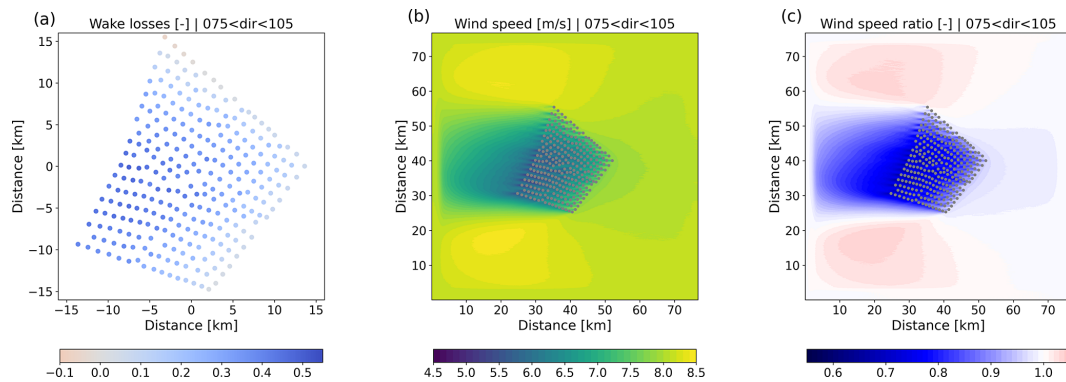


**Figure 17.** Same as Fig. 13 but for the IJVer scenario, only including wind directions between 75 and 105°.

- $5L_z$ . This is the same as REF but with the domain height increased to 14 500 m using 96 vertical levels.

Modifying the modeling setup may impact both the ambient conditions (which will change the thrustless production numbers) and the interaction between the turbines of the wind farm (changing the aerodynamic losses). Figure 20 presents the relative differences between each sensitivity experiment and the REF experiment. Differences in free-stream (thrustless) production are mostly less than 1 %. The same is true for the actual production numbers. Naturally, the aerodynamic losses of the sensitivity experiment are smaller than in the main simulations as the installed capacity is smaller.

Increasing the resolution from 120 to 60 m leads to slightly lower aerodynamic losses. This is expected as at finer resolutions, turbine wakes are more accurately resolved and less smeared out over the grid. Still, the impact is relatively small, especially given the factor-of-8 difference in computational cost (number of points in the domain and a 50 % reduction in the model time step). Increasing the prefactor of the subgrid-scale eddy diffusivity  $c_s$  by 50 % increases the subgrid-scale diffusion, logically leading to a decrease in resolved fluctuations. As shown by the  $c_s$  experiment, the impact on the aerodynamic losses is small. A common way to assess the validity of a large-eddy simulation is to consider the fraction

of resolved turbulence. In our main simulation, the resolved fraction of the momentum flux is larger than 80 % for 70 % of the time (at a height of 150 m, which is the hub height of the IEA15 turbine). For stably stratified conditions the contribution of the subgrid-scale fluxes is larger, but situations where all turbulent fluctuations disappear are rare. In practice, a relatively large (fractional) subgrid-scale contribution may have limited effect, as the absolute values of the turbulent fluxes are small.

The sensitivity experiments were performed for two contrasting wind farm scenarios in order to verify the robustness of the relative differences between the scenarios. Figure 20b indicates that while the aerodynamic losses may change a bit between the sensitivity experiments, the two scenarios show similar patterns. This gives confidence in the comparison between different scenarios in Sect. 4.

It can be argued that the impact of the sensitivity experiments as discussed above is masked by the fact that for wind speed above  $14 \text{ m s}^{-1}$  (related to 50 % of the production), losses are negligible anyway (cf. Fig. 6). Therefore, Fig. 21 presents relative aerodynamic losses for disk-averaged wind speeds between 6 and  $10 \text{ m s}^{-1}$ . As expected, aerodynamic losses for this specific wind speed range are higher than the overall losses, as are the differences between the scenarios. Still, differences with the REF simulations remain within

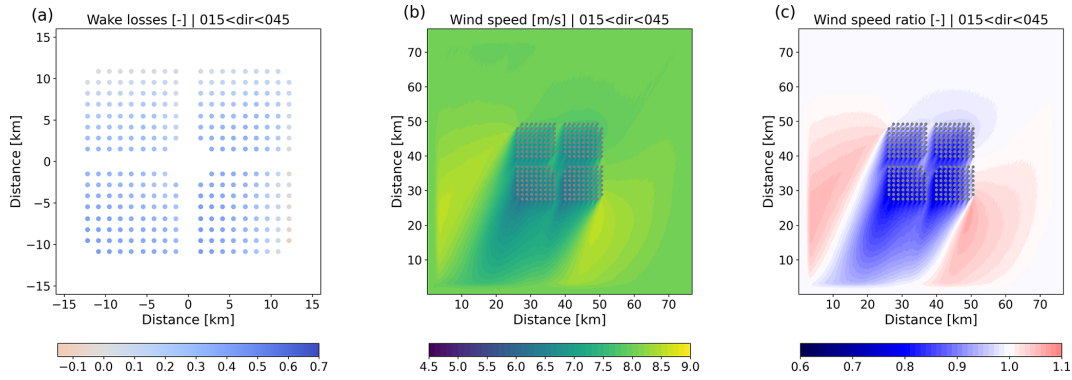


**Figure 18.** Same as Fig. 13 but only including convective conditions, wind speeds between 6 and 10 m s<sup>-1</sup>, and wind directions between 15 and 45°.

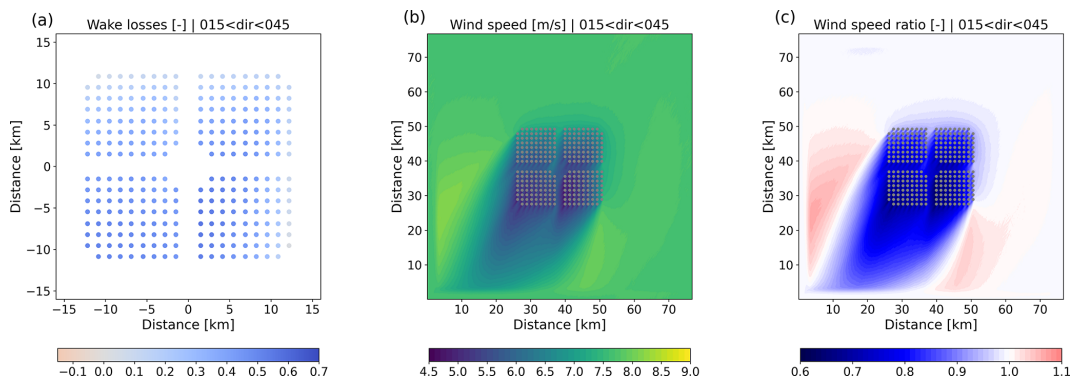


**Figure 19.** Same as Fig. 13 but only including stable conditions, wind speeds between 6 and 10 m s<sup>-1</sup>, and wind directions between 15 and 45°.

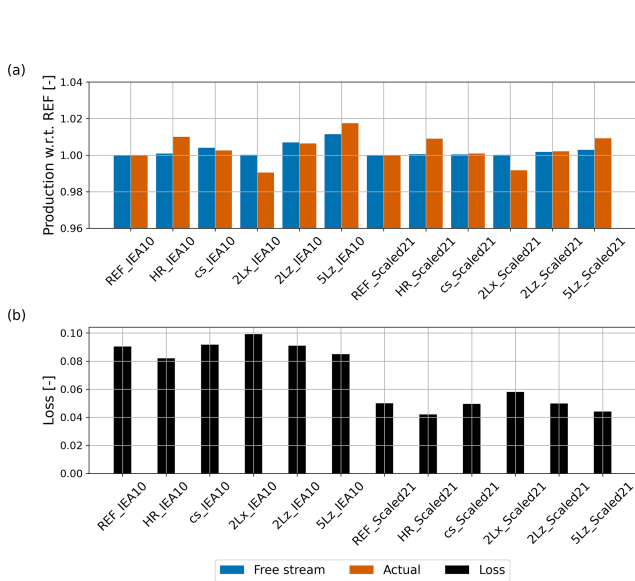


**Figure 20.** Free-stream and actual production of the sensitivity experiments with respect to REF (a) and the corresponding aerodynamic losses (b).

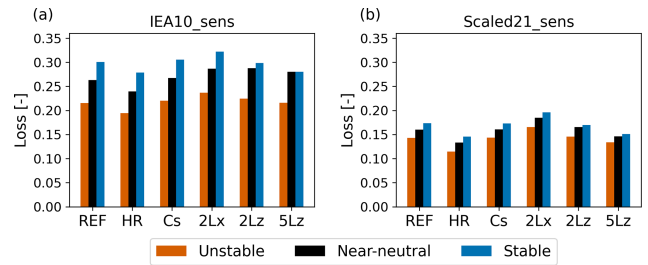


**Figure 21.** Stability-dependent aerodynamic losses for disk-averaged wind speeds between 6 and 10 m s<sup>-1</sup> for the IEA10 (a) and Scaled21 (b) sensitivity experiments.

reasonable limits. Presented numbers are for the three stability classes defined above. The differences between the stability classes are similar for the different sensitivity experiments. This gives confidence in the analysis on the impact of stability in the main Results section.

Increasing the horizontal and increasing the vertical extent of the domain both have a modest impact on the production numbers and aerodynamic losses. With a twice-as-large horizontal domain, the aerodynamic losses become slightly



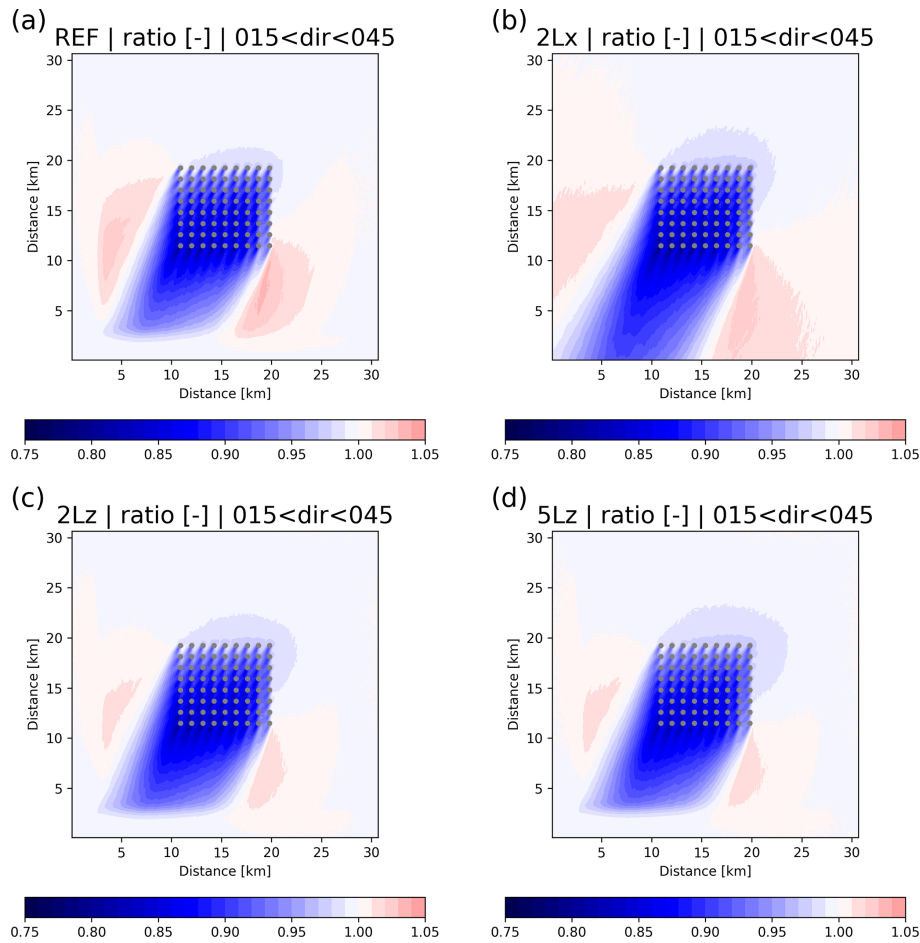


**Figure 22.** Ratio of actual to free-stream 142 m wind speed for the REF (a), the  $2L_x$  (b), the  $2L_z$  (c), and the  $5L_z$  (d) IEA10 sensitivity experiments for wind directions between 15 and 45°.

higher. This may be related to the additional space around the wind farms, reducing the tendency of the flow to accelerate along the wind farm's edges.

Recently, several LES wind farm studies have argued that for a proper modeling of flow through large wind farms, large domain heights (usually more than 10 km) are required. In particular, these large domain heights would be needed for a proper modeling of wind-farm-induced gravity waves and their impact on blockage effects and production numbers (e.g., Allaerts and Meyers, 2017; Lanzilao and Meyers, 2022). Therefore, we performed two sensitivity simulations with increased domain height: one with a height of 6 km ( $2L_z$ ) and one with a height of 14.5 km ( $5L_z$ ). The results presented in Figs. 20 and 21 do not indicate a significant sensitivity of our results to the domain height (in contrast, explorative model simulations in the early stages of the present study indicated that reducing the domain height to, for instance, 2000 m does have a clear impact on the results).

In addition, Fig. 22 shows the impact of the domain configuration on the ratio of actual to free-stream 140 m wind speeds for wind directions between 15 and 45°. For com-

parison, the results of the  $2L_x$  simulation are cropped to the extent of the REF domain. While the evolution of the wake is comparable to the REF simulation, in the  $2L_x$  simulation the flow acceleration along the edges of the wind farm is weaker. The same effect can be seen when the domain height is increased from 3000 to 6000 m ( $2L_z$ ). Increasing the domain height even further, to 14 500 m ( $5L_z$ ), has a negligible effect on the flow field. This is true for both the downstream evolution of the wake and the reduction in the wind speed upstream of the wind farm.

The relatively small impact of the domain height reported here may be somewhat surprising given the findings of the studies cited above. However, it could well be that in our study the impact of, for instance, gravity waves is masked by the large variety of synoptic forcings and boundary layer conditions associated with 1 year of actual weather.

The sensitivity experiments discussed in this section give a clear indication of the robustness of the presented results: modifying grid spacing, settings of the subgrid model, and the extent of the domain within reasonable margins will likely change the results to several percent at maximum.

Overall, we argue that the sensitivity experiments presented here do not invalidate the reasoning and conclusions discussed in the Results section.

Also, from a broader perspective, the sensitivities described here are not larger than, for instance, sensitivities that are reported in studies with mesoscale models that use wind farm parameterizations like the Fitch et al. (2012) parameterization and/or the explicit wake parameterization of Volker et al. (2015) as discussed in, for example, Pryor et al. (2019) and Fischereit et al. (2022). In addition, engineering models rely on calibration on wind farms with much smaller installed capacities as discussed in the present work, and extrapolation to large wind farms is not straightforward. For example, Maas and Raasch (2022) demonstrate that flow dynamics for multi-gigawatt wind farms may differ significantly from those for smaller-scale wind farms.

## 6 Conclusions

In this work we studied production numbers and aerodynamic losses for six hypothetical 4 GW offshore wind farm scenarios using the GRASP large-eddy simulation model. The six scenarios differed in terms of applied turbine type (e.g.,  $2n \times 10$  MW turbines versus  $n \times 20$  MW turbines), installed capacity density ( $5 \text{ MW km}^{-2}$  versus  $10 \text{ MW km}^{-2}$ ), and layout. For each scenario, a 1-year GRASP simulation was performed using 2015 meteorological large-scale conditions taken from ECMWF's ERA5 reanalysis dataset.

The results suggest that, for the simulated year, aerodynamic losses for a 4 GW offshore wind farm vary from 12 % for 21 MW turbines to 18 % for 10 MW turbines. Moreover, even for turbine types with similar rated capacity but slightly different power and thrust curves, energy production may vary by as much as 7.7 %.

For all considered scenarios, 80 % of the aerodynamic losses occur in a narrow wind speed range of 8 to  $12 \text{ m s}^{-1}$ . On the other hand, 50 % of the energy production occurs without any aerodynamic losses when all turbines operate at rated capacity. Naturally, these specific numbers should be viewed in the context of the wind speed probability density function considered and the wind turbine design choices (power curves).

Although wind speed is identified as the most important factor determining aerodynamic losses, we were able to isolate the impact of stability. A fair assessment of this impact seemed possible by only considering wind speeds between 6 and  $10 \text{ m s}^{-1}$ . In this wind speed range, aerodynamic losses may be 10 percentage points larger for stably stratified conditions compared to convective conditions. Numbers vary per scenario with larger differences for scenarios with higher overall losses.

Losses of first-row turbines, which are related to the global-blockage effect, were found to be 2 % to 3 % in general. These values are consistent with values of the blockage

effect reported in the literature. As with the general losses, also the first-row losses occur in a narrow range of disk-averaged wind speeds. Also, a clear impact of stability is identified. For example, for disk-averaged wind speeds between 6 and  $10 \text{ m s}^{-1}$ , first-row losses may increase to almost 10 % in stably stratified conditions.

The complexity of disentangling the effect of wind speed and stability is illustrated by considering direction-dependent aerodynamic losses. Only when selecting proper wind speed conditions does a clear impact of stability and of the geometry of the respective scenarios become apparent. For instance, when the flow is facing the corners of a square-shaped wind farm, losses are clearly lower than when the flow is directed towards the faces of the wind farm.

Sensitivity experiments were carried out to better understand the impact of various modeling choices such as resolution and domain height. Results suggest that overall energy production varies with 1 % to 2 % depending on model settings and/or the domain configuration. Relative differences between the IEA10 and Scaled21 turbine scenario are robust.

In summary, using a high-fidelity modeling technique, the results presented in this explorative study provide a clear indication of the performance of future, multi-gigawatt wind farms for 1 year of realistic weather conditions. Further research could address several open questions like the influence of the lateral boundary conditions, inter-wind-farm wake effects, and more validation against meteorological observations and wind farm data. More elaborate validation studies could also shed more light on the resolution dependence of the aerodynamic losses.

**Data availability.** The GRASP large-eddy simulation dataset is available from the authors on request.

**Author contributions.** PB performed the model simulation, analyzed the results, and wrote the manuscript. RV, PvD, and HJ provided ideas, corrections, and modifications. PvD implemented and calibrated the actuator-disk model. HJ is the main developer of the GRASP model.

**Competing interests.** The contact author has declared that none of the authors has any competing interests.

**Disclaimer.** Publisher's note: Copernicus Publications remains neutral with regard to jurisdictional claims in published maps and institutional affiliations.

**Acknowledgements.** The MSc projects of Sebastiaan Ettema and Thijs Bon (Delft University of Technology) on the global-blockage phenomenon provided inspiration and insights for the present work. The constructive comments of the referees are highly appreciated.

**Financial support.** This research has been supported by the Rijksdienst voor Ondernemend Nederland via the Top Sector Energy project Winds of the North Sea in 2050 (WINS50) (grant no. TEWZ119007).

**Review statement.** This paper was edited by Cristina Archer and reviewed by Oliver Maas and three anonymous referees.

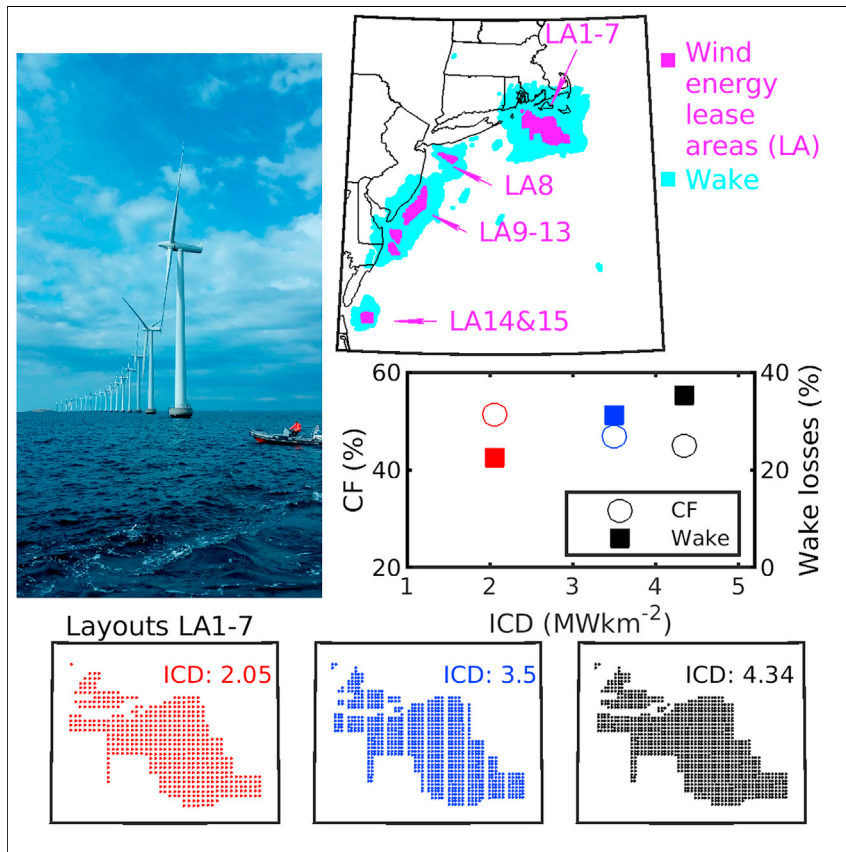
## References

- Allaerts, D. and Meyers, J.: Boundary-layer development and gravity waves in conventionally neutral wind farms, *J. Fluid Mech.*, 814, 95–130, <https://doi.org/10.1017/jfm.2017.11>, 2017.
- Allaerts, D., Vanden Broucke, S., Van Lipzig, N., and Meyers, J.: Annual impact of wind-farm gravity waves on the Belgian–Dutch offshore wind-farm cluster, *J. Phys.: Conf. Ser.*, 1037, 072006, <https://doi.org/10.1088/1742-6596/1037/7/072006>, 2018.
- Bleeg, J., Purcell, M., Ruisi, R., and Traiger, E.: Wind farm blockage and the consequences of neglecting its impact on energy production, *Energies*, 11, 1609, <https://doi.org/10.3390/en11061609>, 2018.
- Böing, S.: The interaction between deep convective clouds and their environment, PhD thesis, TU Delft, <https://doi.org/10.4233/uuid:aa9e6037-b9cb-4ea0-9eb0-a47bf1dfc940>, 2014.
- Calaf, M., Meneveau, C., and Meyers, J.: Large eddy simulation study of fully developed wind-turbine array boundary layers, *Phys. Fluids*, 22, 1–16, <https://doi.org/10.1063/1.862466>, 2010.
- Charnock, H.: Wind stress on a water surface, *Q. J. Roy. Meteorol. Soc.*, 81, 639–640, 1955.
- ECMWF: IFS Manual Part IV: Physical Processes. IFS Documentation Cy43R3, Tech. rep., ECMWF, <https://www.ecmwf.int/en/elibrary/17736-part-iv-physical-processes> (last access: 18 May 2023), 2017.
- European Commission: Offshore Renewable Energy Strategy, [https://energy.ec.europa.eu/topics/renewable-energy/eu-strategy-offshore-renewable-energy\\_en](https://energy.ec.europa.eu/topics/renewable-energy/eu-strategy-offshore-renewable-energy_en) (last access: 18 May 2023), 2020.
- Fischereit, J., Brown, R., Gia Larsen, X., Badger, J., and Hawkes, G.: Wind farm wakes simulated using WRF, *Bound.-Lay. Meteorol.*, 182, 175–224, 2022.
- Fitch, A., Olson, J., Lundquist, J., Dudhia, J., Gupta, A., Michalak, J., and Barstad, I.: Local and mesoscale impacts of wind farms as parameterized in a mesoscale NWP Model, *Mon. Weather Rev.*, 140, 3017–3038, <https://doi.org/10.1175/MWR-D-11-00352.1>, 2012.
- Grabowski, W.: Toward Cloud Resolving Modeling of Large-Scale Tropical Circulations: A Simple Cloud Microphysics Parameterization, *J. Atmos. Sci.*, 55, 3283–3298, 1998.
- Hersbach, H., Bell, B., P., B., Hirahara, S., Horányi, A., Muñoz-Sabater, J., Nicolas, J., Peubey, C., Radu, R., Schepers, D., Simmons, A., Soci, C., Abdalla, S., Abellan, X., Balsamo, G., Bechtold, P., Biavati, G., Bidlot, J., Bonavita, De Chiara, G., Dahlgren, P., Dee, D., Diamantakis, M., Dragani, R., Flemming, J., Forbes, R., Fuentes, M., Geer, A., Haimberger, L., Healy, S., Hogan, R., Hólm, E., Janisková, M., Keeley, S.,
- Laloyaux, P., Lopez, P., Lupu, C., Radnoti, G., De Rosnay, P., Rozum, I., Vamborg, F., Villaume, S., and Thépaut, J.: The ERA5 global reanalysis, *Q. J. Roy. Meteorol. Soc.*, 146, 1999–2049, <https://doi.org/10.1002/qj.3803>, 2020.
- Heus, T., Van Heerwaarden, C. C., Jonker, H. J. J., Siebesma, A. P., Axelsen, S., Van Den Dries, K., Geoffroy, O., Moene, A. F., Pino, D., De Roode, S. R., and Vila-Guerau de Arellano, J.: Formulation of the Dutch Atmospheric Large-Eddy Simulation (DALES) and overview of its applications, *Geosci. Model Dev.*, 3, 415–444, <https://doi.org/10.5194/gmd-3-415-2010>, 2010.
- Khairoutdinov, M. and Randall, D.: Cloud Resolving Modeling of the ARM Summer 1997 IOP: Model Formulation, Results, Uncertainties, and Sensitivities, *J. Atmos. Sci.*, 60, 607–625, 2003.
- Lanzilao, L. and Meyers, J.: Effects of self-induced gravity waves on finite wind-farm operations using a large-eddy simulation framework, *J. Phys.: Conf. Ser.*, 2265, 022043, <https://doi.org/10.1088/1742-6596/2265/2/022043>, 2022.
- Maas, O. and Raasch, S.: Wake properties and power output of very large wind farms for different meteorological conditions and turbine spacings: A large-eddy simulation case study for the German Bight, *Wind Energ. Sci.*, 7, 715–739, <https://doi.org/10.5194/wes-7-715-2022>, 2022.
- Mehta, D., van Zuijlen, A. H., Koren, B., Holierhoek, J. G., and Bijl, H.: Large Eddy Simulation of wind farm aerodynamics: A review, *J. Wind Eng. Indust. Aerodynam.*, 133, 1–17, <https://doi.org/10.1016/j.jweia.2014.07.002>, 2014.
- Meyers, J. and Meneveau, C.: Large Eddy Simulations of Large Wind-Turbine Arrays in the Atmospheric Boundary Layer, in: 48th AIAA Aerospace Sciences Meeting Including the New Horizons Forum and Aerospace Exposition, 4–7 January 2010, Orlando, Florida, USA, 1–10, <https://doi.org/10.2514/6.2010-827>, 2010.
- Neggens, R. A. J., Siebesma, A. P., and Heus, T.: Continuous single-column model evaluation at a permanent meteorological supersite, *B. Am. Meteorol. Soc.*, 93, 1389–1400, <https://doi.org/10.1175/BAMS-D-11-00162.1>, 2012.
- Porté-Agel, F., Bastankhah, M., and Shamsoddin, S.: Wind-Turbine and Wind-Farm Flows: A Review, *Bound.-Lay. Meteorol.*, 174, 1–59, <https://doi.org/10.1007/s10546-019-00473-0>, 2020.
- Pryor, S., Shepard, T., Bartherlmie, R., Hahmann, A., and Volker, P.: Wind farm wakes simulated using WRF, *J. Phys.: Conf. Ser.*, 1256, 012025, <https://doi.org/10.1088/1742-6596/1256/1/012025>, 2019.
- Rozema, W., Bae, H. J., Moin, P., and Verstappen, R.: Minimum-dissipation models for large-eddy simulation, *Phys. Fluids*, 27, 085107, <https://doi.org/10.1063/1.4928700>, 2015.
- RVO: General Information IJmuiden Ver, <https://offshorewind.rvo.nl/cms/view/5c06ac88-c12f-4903-89f3-27d66937b7e9/general-information-ijmuiden-ver> (last access: 18 May 2023), 2022.
- Schalkwijk, J., Griffith, E. J., Post, F. H., and Jonker, H. J. J.: High-performance simulations of turbulent clouds on a desktop PC, *B. Am. Meteorol. Soc.*, 93, 307–314, 2012.
- Schalkwijk, J., Jonker, H., Siebesma, A., and Van Meijgaard, E.: Weather forecasting using GPU-based large-eddy simulations, *B. Am. Meteorol. Soc.*, 96, 715–723, <https://doi.org/10.1175/BAMS-D-14-00114.1>, 2015a.
- Schalkwijk, J., Jonker, H. J. J., Siebesma, A. P., and Bosveld, F. C.: A Year-Long Large-Eddy Simulation of the Weather

- over Cabauw: an Overview, *Mon. Weather Rev.*, 143, 828–844, <https://doi.org/10.1175/MWR-D-14-00293.1>, 2015b.
- Schneemann, J., Theuer, F., Rott, A., Dörenkämper, M., and Kühn, M.: Offshore wind farm global blockage measured with scanning lidar, *Wind Energ. Sci.*, 6, 521–538, <https://doi.org/10.5194/wes-6-521-2021>, 2021.
- Stevens, R. J. and Meneveau, C.: Flow Structure and Turbulence in Wind Farms, *Annu. Rev. Fluid Mech.*, 49, 311–339, <https://doi.org/10.1146/annurev-fluid-010816-060206>, 2017.
- Stevens, R. J., Graham, J., and Meneveau, C.: A concurrent precursor inflow method for Large Eddy Simulations and applications to finite length wind farms, *Renew. Energy*, 68, 46–50, <https://doi.org/10.1016/j.renene.2014.01.024>, 2014.
- Strickland, J., Srinidhi, N., and Stevens, R.: Wind farm blockage in a stable atmospheric boundary layer, *Renew. Energy*, 197, 50–58, <https://doi.org/10.1016/j.renene.2022.07.108>, 2022.
- The Esbjerg Declaration: The Esbjerg Declaration on The North Sea as a Green Power Plant of Europe, <https://open.overheid.nl/documenten/ronl-1e299d084fbc5bfc2968d934ca2f4a97b3931d9f/pdf> (last access: 18 May 2023), 2022.
- Veers, P., Dykes, K., Lantz, E., Barth, S., Bottasso, C. L., Carlson, O., Clifton, A., Green, J., Green, P., Holttinen, H., Laird, D., Lehtomäki, V., Lundquist, J. K., Manwell, J., Marquis, M., Meneveau, C., Moriarty, P., Munduate, X., Muskulus, M., Naughton, J., Pao, L., Paquette, J., Peinke, J., Robertson, A., Rodrigo, J. S., Sempreviva, A. M., Smith, J. C., Tuohy, A., and Wiser, R.: Grand challenges in the science of wind energy, *Science*, 366, eaau2027, <https://doi.org/10.1126/science.aau2027>, 2019.
- Verzijlbergh, R. A.: Atmospheric flows in large wind farms, *Europhys. News*, 52, 20–23, <https://doi.org/10.1051/eprn/2021502>, 2021.
- Volker, P., Badger, J., Hahmann, A., and Ott, S.: The explicit wake parametrisation V1.0: a wind farm parametrisation in the mesoscale model WRF, *Geosci. Model Dev.*, 8, 3715–3731, <https://doi.org/10.5194/gmd-8-3715-2015>, 2015.
- Wu, K. and Porté-Agel, F.: Flow Adjustment Inside and Around Large Finite-Size Wind Farms, *Energies*, 10, 2164, <https://doi.org/10.3390/en10122164>, 2017.

Article

# Wind power production from very large offshore wind farms



Many countries are planning development of very large offshore wind farms to aid decarbonization of the energy sector. High-resolution numerical simulations are performed to quantify power production (capacity factors [CFs]) and the spatial scale and effects of downstream wakes (areas of disturbed flow) from lease areas that are under development along the U.S. east coast. Descriptions of wake extent and power as a function of prevailing meteorology and wind-farm layout (installed capacity density [ICD]) are presented.

Sara C. Pryor, Rebecca J. Barthelmie, Tristan J. Shepherd  
 @cornell.edu

**Highlights**  
 Current U.S. east coast offshore wind lease areas can supply 3% of electricity

On average wakes extend over nearly 3-times footprint of the wind turbine arrays

Power and wakes are nonlinear functions of wind turbine density and meteorology

Guidance is provided for layouts of large offshore wind farms around the world





## Article

# Wind power production from very large offshore wind farms

Sara C. Pryor,<sup>1,3,\*</sup> Rebecca J. Barthelmie,<sup>2</sup> and Tristan J. Shepherd<sup>1</sup>

## SUMMARY

We provide the first quantitative assessment of power production and wake generation from offshore wind energy lease areas along the U.S. east coast. Deploying 15-MW wind turbines, with spacing equal to the European average, yields electricity production of 116 TWh/year or 3% of current national supply. However, power production is reduced by one-third due to wakes caused by upwind wind turbines and wind farms. Under some flow conditions whole wind-farm wakes can extend up to 90 km downwind of the largest lease areas, and the frequency-weighted average area with a 5% velocity deficit is 2.6 times the footprint of the lease areas. Simulations including maritime corridors demonstrate reduction in the wake effects leading to power-efficiency gains and may offer contingent benefits. First-order scaling rules are developed that describe how “wake shadows” from large offshore wind farms scale with prevailing meteorology and wind turbine installed densities.

## INTRODUCTION

The move to reduce energy-related greenhouse gas emissions is gathering international momentum fueled by both the urgent need to reduce anthropogenic forcing of climate<sup>1–3</sup> and rapid declines in the cost of renewable generation sources.<sup>4</sup> The government of the United Kingdom has committed to net zero greenhouse gas emissions by 2030. A critical part of that commitment is to deploy 40 GW of offshore wind, sufficient to power every home in the United Kingdom by 2030.<sup>5</sup> The European Commission’s long-term strategy for decarbonization assumes the installation of 400 to 450 GW of offshore wind capacity within European waters by 2050.<sup>6</sup> In March 2021, the White House made a commitment to deploy 30 GW of offshore wind as part of a move to reduce U.S. greenhouse gas emissions by 50% from 2005 levels in 2030 and a carbon-pollution-free power sector by 2035 (see White House briefing at; <https://www.whitehouse.gov/briefing-room/>). China has also committed to increasing the installed capacity of wind and solar power to over 1,200 GW by 2030 from 414 GW in 2019 (see press coverage at <https://www.reuters.com/article/climate-change-un-china/chinas-xi-targets-steeper-cut-in-carbon-intensity-by-2030-idUSKBN28M0ND>). This unprecedented and rapid expansion of offshore wind energy deployments affords opportunities to reduce anthropogenic climate forcing. It also raises challenges in terms of how to optimally locate wind turbines offshore at the scale required to achieve electricity-generation goals. This article provides timely and critical information to guide both U.S. and global offshore wind-energy deployments.

Estimated technically feasible potential electricity generation from U.S. offshore wind resources exceeds 7,000 Terra-Watt hours per year (TWh/year).<sup>7</sup> This surpasses current total national electricity generation of ~4,000 TWh/year.<sup>8</sup> As of May 2021, the U.S.

## Context & scale

Massive upscaling of wind turbine deployments offshore is critical to achieving global and national goals to decarbonize the electricity supply. The excellent wind resource and proximity to large markets along the U.S. east coast mean it is the focus of America’s first-phase offshore-wind projects. Thousands of physically larger and higher capacity wind turbines will be deployed over areas of unprecedented scale. The scale of these installations and those planned by other countries raises questions regarding potential reductions of electrical-power-production efficiency due to the operation of wind turbines in disturbed flow (wakes) from upwind wind turbines and wind farms. In this work, guidance is provided regarding the optimal layout of this new generation of wind farms to harness offshore wind resources in a manner that maximizes electricity production and minimizes the levelized cost of energy.



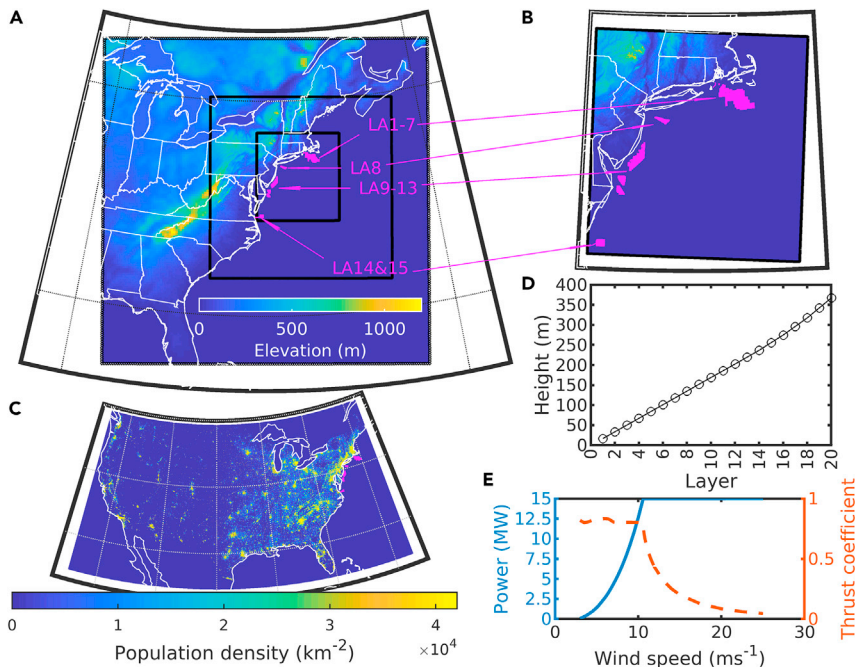


**Figure 1. Overview of the simulations with the Weather Research and Forecasting (WRF) model and the locations of offshore wind-farm lease areas (LAs) along the U.S. east coast**

(A) The outer WRF simulation domain (d01) has a grid resolution of 16.67 km. The second domain (d02) has a grid resolution of 5.56 km. Two inner domains (d03 and d04) comprise 340 × 361 grid cells and use a grid resolution of 1.85 km. The 15 offshore lease areas analyzed herein are shown by the magenta shading.

(B) The inner-most domain (d03 and d04) showing the lease area (LA) clusters.

(C) Proximity of the offshore lease areas to major demand centers as illustrated by the population density per km<sup>2</sup> according to the 2010 census (<https://www.census.gov/data/tables/time-series/demo/popest/2010s-state-total.html>) and the location of the 15 offshore lease areas (magenta).

(D) Mean height of the lowest 20 wind-speed levels computed for all water grid cells within d03.

(E) Wind turbine power and thrust coefficients as a function of wind speed (WS) for the IEA 15-MW reference turbine used in this analysis. This wind turbine has a HH of 150 m and rotor diameter of 240 m.<sup>12</sup> Power production begins at 4 ms<sup>-1</sup> and ceases at WSs > 25 ms<sup>-1</sup>, thus no power production or thrust coefficients are plotted for WSs outside of the range of 4–25 ms<sup>-1</sup>.

had one 30-MW offshore wind farm operating at Block Island, Rhode Island, and two research turbines in Virginia.<sup>9</sup> However, the current total U.S. offshore wind pipeline (to 2030) is over 26 GW, much of which is focused on 16 lease areas (LAs) along the east coast<sup>10</sup> (Figures 1A and 1B). Realizing this pipeline would increase current U.S. wind turbine installed capacity (IC) by over 20% and almost double total global offshore installed capacity, which was 28 GW at the end of 2019.<sup>11</sup>

Expansion of the U.S. offshore wind industry represents a substantial financial investment. Data from Germany indicate the total installed project cost for offshore wind turbines of US\$ 1,910 per kilo-Watt (kW) during 2019.<sup>13</sup> Projections for fixed bottom offshore wind turbines in the U.S. made in 2019 indicate total capital expenditure of US\$ 4,077 per kW.<sup>14</sup> Using these cost estimates, installation of 26–29 GW in the 16 LAs off the U.S. east coast, equates to a direct investment of ~US\$ 50 to 120 billion.

The global trend toward increased deployment of wind turbines offshore is associated with declining levelized cost of energy (LCoE), and offshore projects in the mature markets of Germany and the Netherlands are now subsidy free.<sup>13</sup> The

<sup>1</sup>Department of Earth and Atmospheric Sciences, Cornell University, Ithaca, NY 14853, USA

<sup>2</sup>Sibley School of Mechanical and Aerospace Engineering, Cornell University, Ithaca, NY 14853, USA

<sup>3</sup>Lead contact

\*Correspondence: [redacted]@cornell.edu

<https://doi.org/10.1016/j.joule.2021.09.002>

transition to offshore deployments is driven by multiple factors. First, wind speeds are generally higher and more persistent than over land surfaces, leading to higher efficiency of electrical-power production.<sup>11</sup> The variation of electrical-power production from wind turbines with wind speed is described using a power curve (Figure 1E). Power production increases as wind speeds increase from cut-in when power production begins (commonly about  $4 \text{ ms}^{-1}$ ) to a threshold at which the power production reaches the rated power and no longer continues to increase with increasing wind speed. This rated power thus describes the amount of electrical power in watts (i.e., joules per second) a wind turbine generates if it is operating at optimal wind speeds. Due to factors such as lower surface roughness and the absence of orographic barriers, wind turbines deployed offshore generally operate more frequently at rated power than those located onshore. Second, many major urban areas are located in coastal areas, providing nearby load centers for the electricity generated by offshore wind farms. For example, the Boston-Washington corridor, encompassing New York City, has a population over 50 million and is located close to the U.S. east coast offshore LAs (Figure 1C).

A major source of uncertainty in designing offshore wind turbine arrays (wind farms) and optimal spacing between wind farms derives from power-production losses<sup>15,16</sup> and enhanced fatigue loading<sup>17</sup> caused by operation of a wind turbine or wind farm in the wake of an upstream wind turbine or wind farm.<sup>18</sup> Wakes are flow regions behind wind turbines and wind farms that are characterized by lower wind speeds and higher turbulence levels and are caused by the extraction of momentum by wind turbines. The magnitude of these wakes and the downstream distance necessary for them to be eroded by mixing with surrounding high-momentum air is primarily determined by: (1) wind speed across the wind turbine rotor. This determines the efficiency of momentum extraction. The wind turbine thrust coefficient describes the magnitude of the wind-speed reduction and amount of turbulence introduced by the rotor as a nonlinear function of the incident wind speed (Figure 1E).<sup>15</sup> (2) Turbulence from mechanical and thermal sources. The turbulence intensity and the depth of the planetary boundary layer dictate the rate at which kinetic energy can be transferred down the velocity gradient into the wind turbine wake. For a given wind turbine or wind farm, as shown herein, these three atmospheric variables; wind speed, turbulence intensity, and boundary layer depth are largely responsible for dictating the downwind distance necessary for the flow to return to its undisturbed condition, i.e., for the wake to recover.<sup>15,16,19</sup> The rate at which kinetic energy can be transferred in the atmosphere limits the amount of energy that can be extracted by wind turbines per unit of surface area.<sup>20–22</sup> Low transfer rates can reduce power production from wind turbines in the interior of large offshore wind farms to approximately 60% of what would be achievable if all wind turbines experienced undisturbed air flow.<sup>15,16</sup> Low turbulence and planetary boundary layer depths offshore also mean that cumulative wind-farm wakes persist over longer downwind distances<sup>23,24</sup> and that wake-induced power loss within wind farms are also larger than in onshore wind farms.<sup>15,16</sup> (3) Wind turbine spacing: closer spacing means more wind turbines operate in the wake of upstream turbines and thus experience lower wind speeds and generate less electrical power. For example, the Horns Rev I offshore wind farm in Denmark has an IC of 166 MW, a turbine spacing of  $7 \times 7$  rotor diameters (D) and mean reduction in power production due to wakes from upstream turbines impinging on downstream wind turbines (wake losses) of 12.4%.<sup>25</sup> Conversely, Lillgrund, in the coastal waters of Sweden, which has a similar IC (of 110 MW) but uses a smaller distance between wind turbines (a spacing of 3.3 to 4.3 D), exhibits wake losses of 23%.<sup>25</sup> (4) Wind direction: wind direction determines the likelihood that wind turbine wakes within an array interact with each other and whether the wake from one wind turbine array will be advected over another.<sup>23,26</sup>



The number of global offshore wind farms, the size and rated capacity of the wind turbines, and the total IC within individual arrays are increasing. For example, the mean IC of European offshore wind farms doubled from 321 to 621 MW between 2010 and 2019.<sup>27</sup> The largest operating offshore wind array is Hornsea Project One. It has a total IC of 1.2 GW over a deployment area of 630 km<sup>2</sup>.<sup>28</sup> Despite the growth in installed capacities, the most recently built European offshore wind farms continued to employ wind turbine spacing of 4 to 11 rotor diameters (D) with a mean of 7.7D.<sup>29</sup> Offshore wind farms operating in Europe have installed capacity densities (ICDs), i.e., the rated power of the installed wind turbines per square kilometer of ground area) of 2.5 to 12 MWkm<sup>-2</sup>.<sup>30</sup> An additional analysis of data from offshore wind farms in Europe indicates mean ICDs of 3 to 7.2 MWkm<sup>-2</sup>, depending on the definition of wind farm areal extent.<sup>31</sup> There has also been a pronounced trend toward deployment of physically larger and higher-rated power wind turbines.<sup>32</sup> These industry trends are causing an increased probability of large wake losses within individual wind farms and an increased probability of wake interactions between offshore wind-turbine arrays.<sup>33,34</sup> Further, a recent meta-analysis identified wake-induced power losses as the primary source of uncertainty in preconstruction estimates of annual energy production from wind turbine arrays and a major contributor to excess project financing costs.<sup>35</sup> Improved understanding of wind turbine and wind-farm wakes is thus essential to ensuring the planned global investments in offshore wind achieve the electricity-generation goals and do so at the lowest possible cost.

The objective of this work is to characterize power production, wind-farm wake intensity and extent, and wake-induced power losses from planned very large offshore wind farms. This work is focused on much larger offshore wind turbine arrays than are currently operational but have a scale equal to those that are anticipated to be developed in the U.S., Europe, and China. It thus extends the literature that has previously focused primarily on smaller wind turbine arrays or has considered the limit case of nearly infinite wind farms. This work also includes an analysis of the sensitivity of power production and wake effects to both wind-farm ICD and meteorology for a wide range of atmospheric conditions that prevail offshore. Two methodological innovations are presented. A flow-scenario method is introduced to efficiently develop robust assessments of power production, wake extent and intensity, and wake-induced power losses. The concept of the normalized wake extent is also introduced and statistical models of this property as a function of prevailing meteorology are developed. The numerical simulations are performed for the existing offshore LAs along the U.S. east coast but the study findings have relevance to the global offshore wind-energy industry.

### Offshore wind LAs along the U.S. east coast

LAs for possible offshore wind development in the U.S. are auctioned and managed by the Bureau of Ocean Energy Management (BOEM). The 15 offshore LAs considered here lie along the coasts of the Northeast and Atlantic U.S. states (Figures 1A and 1B<sup>10</sup>). Each has a unique alpha-numeric identifier; OCS-A-NNNN, where NNNN is unique to the LAs. LAs 1–7 are treated as a LA cluster herein. All seven lie within a coherent area along the coast of Massachusetts and Rhode Island and collectively cover 3,675 km<sup>2</sup>. These include OCS-A 0487, 0500, 0501, 0520, 0521, 0522 (listed west to east) that are adjacent to one another, while OCS-A 0486 is separated from 0487 by a channel that is 2.4 km wide. LA 8 (0512) is located off the coast of New York state and covers an area of 321 km<sup>2</sup>. LAs 9–13 cover a total area of 2,105 km<sup>2</sup>. Two of these LAs are adjacent and are offshore from New Jersey (OCS-A 0499 and 0498). They are 23 km north of two LAs east of Delaware (OCS-A 0482 and 0519), that are 11 km north and east of the

sole Maryland LA (OCS-A 0490). These five LAs are not all adjacent but are treated as a cluster here because, as shown herein, under certain flow conditions the wake from these LAs exhibit substantial overlap. LAs 14 and 15 (OCS-A 0483 and 0497) are adjacent, cover an area of 465 km<sup>2</sup> and are located off the coast of Virginia. The final LA, OCS-A 0508, lies further south off the coast of North Carolina. It is not included in the innermost simulation domain and is thus excluded from consideration in this analysis.

The total extent of the LAs considered here is 6,566 km<sup>2</sup>. This, and the spatial scale of the individual and contiguous offshore LAs along the U.S. east coast, greatly exceeds that of current European offshore wind farms. However, they are representative of the scale of future wind turbine deployments needed to meet the expressed goals of the United Kingdom, the European Union, the United States of America, and China. Quantifying power losses due to wakes as a function of atmospheric conditions (e.g., wind speed, planetary boundary layer height, and ambient turbulent kinetic energy) and ICD will inform wind turbine array layouts, and aid power-production forecasting and grid-integration planning in both the U.S. and beyond. The close proximity of these current LAs (Figures 1A and 1B) and prospective future LA offerings along the U.S. east coast<sup>36</sup> and the planned expansion of wind turbine deployments in the North Sea<sup>6</sup> further emphasize the need to quantify possible array-array interactions, particularly as adjacent LAs are owned and operated by different companies or consortia.

Simulations with the Weather Research and Forecasting (WRF) model are performed using nested domains resolved with high horizontal and vertical resolution (Figures 1A, 1B, and 1D). The modified Fitch wind-farm parameterization is used to quantify power production and wakes.<sup>37,38</sup> Wind-farm parameterizations such as Fitch seek to treat the bulk aerodynamic effects caused by wind turbines within and downwind of the grid cell(s) in which they are located. An estimate of the power produced by the wind turbine(s) in each grid cell and model time step is computed from the wind turbine power curve (Figure 1E) and the grid-cell-averaged incident wind-speed profile across the rotor plane. The wind turbine(s) within a given grid cell impose a drag force across the rotor plane that is determined by the wind turbine thrust coefficient (Figure 1E) and the incident wind-speed profile. This drag force removes kinetic energy from the flow resulting in a modified wind-speed profile that is advected to adjacent grid cells. Turbulent kinetic energy is added to the flow at a rate proportional to the fraction of kinetic energy extracted by the wind turbine and not converted into electrical power. It too is advected into adjacent grid cells. The wind-farm parameterization thus requires information regarding wind turbine physical dimensions, along with power and thrust coefficients that are often held confidential by wind turbine manufacturers. Therefore, the International Energy Agency (IEA) reference turbine<sup>12</sup> is employed, having a similar hub height (HH) and rotor diameter (D) to the G.E. Haliade-X 13-MW wind turbine (HH ~ 140 m, D ~ 220 m) that has been selected for LA 1.

The methodology used to efficiently generate a robust assessment of likely power production and wake losses from the U.S. east coast LAs is derived from earlier work on wind-resource assessment.<sup>39</sup> We identify dominant modes of relevant atmospheric flow conditions and then perform simulations for real 5-day periods that reflect those flow scenarios (Figure 2). The results from these simulations are weighted by the frequency with which each flow scenario occurs to derive climatologically representative power-production and wake statistics. The flow scenarios are abbreviated using the following nomenclature: WDWS (where WD is the wind direction and WS is the wind speed e.g., NE4-10 for northeasterly flow in the

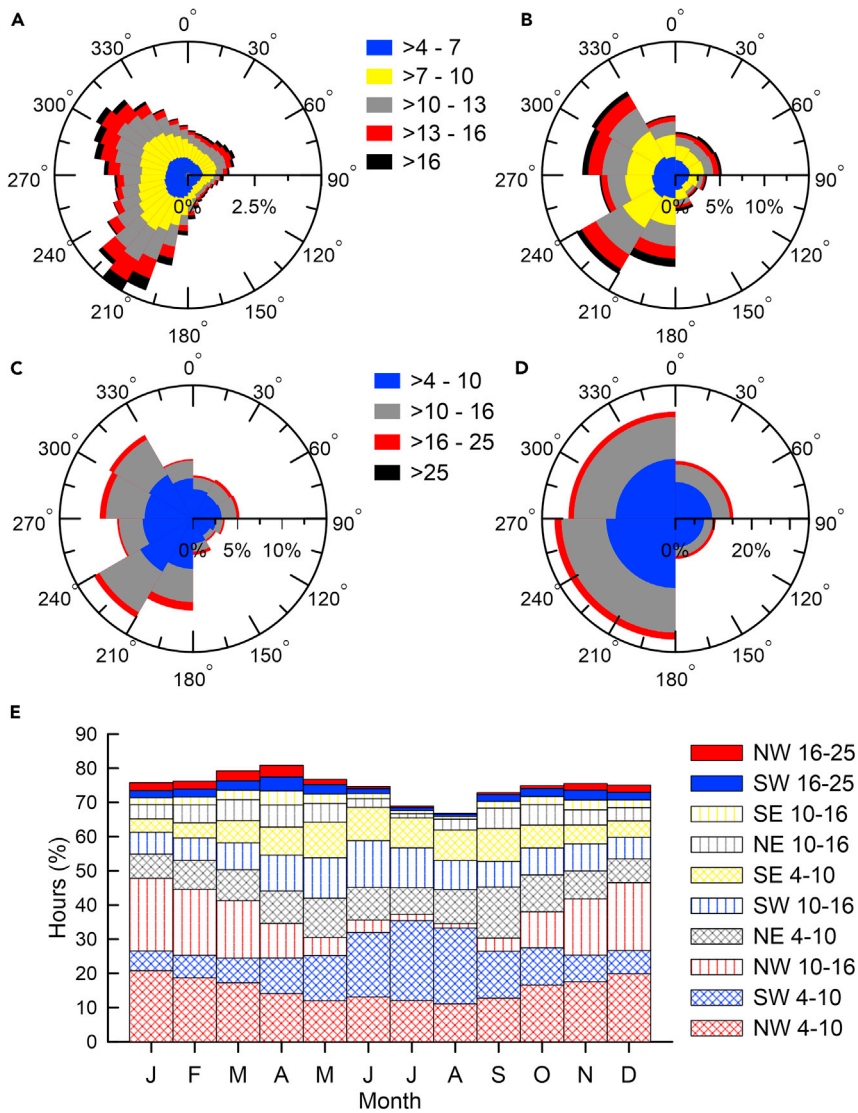


**Figure 2. Overview of hourly wind speeds and directions at 100 m height in lease area 8 and the aggregation approach used to define the flow scenarios and characterize their frequency and seasonality**

(A) Wind rose of all ERA5 hourly observations from 1979–2018 for the grid cell containing lease area 8 (Figures 1A and 1B) wherein the wind speeds (WSs) are discretized into  $3 \text{ ms}^{-1}$  classes for all values above  $4 \text{ ms}^{-1}$ , and wind directions (WDs) are discretized into  $10^\circ$  classes.

(B) As in (A) but using  $30^\circ$  wind direction sectors.

(C) As in (A) but for WSs in  $6 \text{ ms}^{-1}$  classes.

(D) As in (A) but using  $90^\circ$  wind direction sectors.

In each (A–D), the radial axis denotes the percentage of hours with wind speeds between 4 and  $25 \text{ ms}^{-1}$  that fall into the specified flow class. The ten most frequently observed combinations of wind direction and speed (denoted by WDWS) are (in rank order); SW4-10, SW10-16, NW4-10, NW4-10, NE4-10, SE4-10, NE10-16, SE10-16, SW16-25 and NW16-25.

(E) Frequency of the flow scenarios by calendar month as a percentage of hours in each month. The flow scenarios are ordered by frequency with the most frequent at the bottom. Red shading denotes northwesterly (NW) flow, blue for southwesterly (SW), black for northeasterly (NE), and yellow for southeasterly (SE) flow. Crosshatching indicates wind speeds (WS) of 4 to  $10 \text{ ms}^{-1}$ , vertical lines denote WS between 10 and  $16 \text{ ms}^{-1}$ , and the solid shading indicates WS between 16 and  $25 \text{ ms}^{-1}$ .

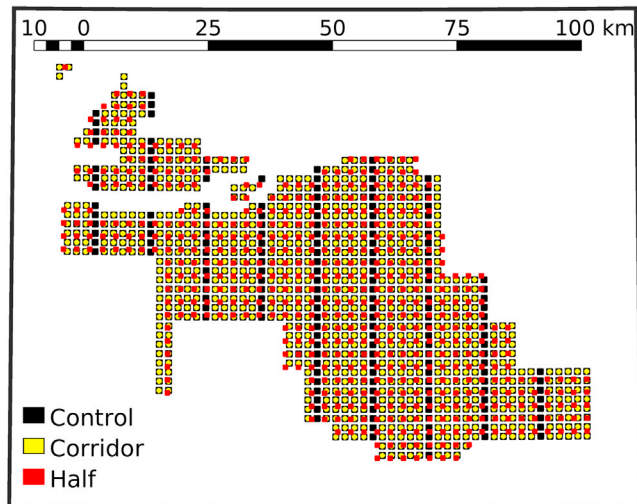


**Figure 3.** Illustration of the three wind-turbine deployment layouts for the lease areas 1–7 cluster (see location in Figure 1)

The black squares denote the placement of wind turbines within this cluster of lease areas in the control deployment layout with wind turbine separation of 1.85 km (for a mean installed capacity density of  $4.34 \text{ MWkm}^{-2}$ ). The yellow circles denote placement of wind turbines in this cluster of lease areas in the maritime-corridor deployment layout (i.e., where the sixth north-south row of wind turbines from the control are removed). The red squares denote placement of wind turbines in this cluster of lease areas in the half-density deployment layout.

wind-speed class  $4\text{--}10 \text{ ms}^{-1}$ ). The simulation periods are referred to here use the date; YYYY-MM-DD (i.e., year-month-day) of the first day of each 5-day period.

Simulations are performed for three different wind turbine layouts and ICD (Figure 3): (1) a control layout using the average wind turbine spacing from Europe (i.e., 7.7 wind-turbine rotor diameters), which means that the distance between each wind turbine is 1.85 km. This spacing has been selected for LAs 1 through 7. It yields a total IC of 28.8 GW from 1922 wind turbines of 15 MW each. For this wind turbine layout the mean ICD across the four clusters of LAs is  $4.34 \text{ MWkm}^{-2}$ . (2) A maritime-corridor layout where the sixth north-south “column” of wind turbines in each LA is removed. This reduces the total IC to 24.1 GW. (3) A half-density layout for a total installed of 14.5 GW. The ICD for this layout ( $\sim 2.1 \text{ MWkm}^{-2}$ ) is at the lower end of current offshore wind farms in Europe.

The distribution of wind turbines between the LA clusters are as follows. In the control simulations there are 1,073 wind turbines deployed in LAs 1 through 7, 89 in LA 8, 624 in LAs 9 through 13, and 136 in LAs 14 and 15. When the maritime corridors are introduced, the total number of wind turbines in each LA cluster drops to 900, 74, 521, and 109, respectively. In the half-density layout the wind turbines are separated by  $\sim 2.8 \text{ km}$ , and the equivalent wind turbine numbers deployed in each LA cluster are, respectively, 532, 47, 318, and 71.

Output from each of the eleven, 5-day simulations of the control layout is weighted using the relative frequency of the flow conditions it represents to derive robust estimates of expected power production and a wake climatology from the U.S. east coast LAs. The same analysis is performed for simulations of the other wind-farm layouts. Model output for the control and half-density wind-farm layouts are also used to develop first-order scaling rules that describe how the area influenced by wakes

from an offshore wind farm depends on the prevailing atmospheric conditions and the density of wind turbines within the wind farm.

## RESULTS

### Estimated power production from the U.S. offshore LAs

After applying frequency weighting to output from the 5-day simulations of each of the 11 flow scenarios, the expected electric-power production for the control layout is 116 TWh/year or 3% of current national supply. Electric-power production from wind turbines is summarized using capacity factors (CFs) computed as the ratio of the amount of power produced normalized by the potential power produced if all wind turbines run at their rated capacity (in this case, 15 MW). The mean CF for the control layout, where the wind turbines are spaced at the mean value from operating offshore wind farms in Europe, is 45.8% (Table 1). Power losses due to transmission, curtailment for grid operation, and operations and maintenance actions for onshore wind farms decrease CFs in the U.S. by an average of 4 percentage points.<sup>40</sup> Assuming that this estimate is also appropriate for offshore wind turbine arrays, the resulting estimated net-CF for these U.S. east coast offshore LAs is ~42%. This is comparable with, or better than, values reported for European (38% during 2019<sup>41</sup> and 40.8% cited in a meta-analysis<sup>31</sup>) and global (40% to 42%<sup>11</sup>) offshore wind farms. Thus, this modeling suggests that if the U.S. LAs are developed using wind turbines similar to the IEA 15-MW reference wind turbine laid out at a spacing equal to the mean in European offshore wind farms, they would operate with the same, or higher, CFs than those in smaller offshore wind farms in Europe that have been shown to be highly viable economically.

There is substantial variability in power production across the flow scenarios with, as expected, higher freestream wind speeds being associated with higher CFs (Figure 4A; Table 1). The higher CFs for the northern LAs (LA cluster 1–7 and LAs 8; Figures 4A and 5A) are due to: (1) higher wind speeds and thus better wind resources (Figure 5B) and (2) smaller wake losses in the smallest contiguous LA of wind turbine deployments (lease area 8, LA8) (Figures 4B and 5A). The south-north gradient of increasing wind-resource magnitude implied in the 11 simulations of the individual flow scenarios is consistent with wind-resource estimations from long-term reanalyses,<sup>10</sup> mesoscale simulations, and satellite-derived wind climates.<sup>42</sup> The most northern and largest cluster of LAs (1 through 7; see Figure 1B) exhibit a frequency-weighted mean CF of 46%, while in LA 8 it is 56%, in lease areas 9–13 it is 45% and lease areas 14 and 15 have a mean CF of 40% (Table 1; Figures 4B and 5).

Each of the LA clusters exhibits different CFs for the diverse flow scenarios due in part to variations in wind direction, and hence the over-water fetch and the resulting levels of turbulent kinetic energy (TKE) and wind speeds at the wind turbine HH (Figure 4C). For example, LAs 14 and 15 exhibit the highest mean CFs for the northeasterly flow scenarios (NE10-16 and NE4-10, represented by simulation periods that commence on 1985-11-28 and 2012-11-17) and lowest mean CFs for flow directions that are from land (NW4-10 and SW4-10, represented by simulation periods that commence on 1988-07-04 and 1998-06-04) (Figure 4B).

Two sets of sensitivity simulations for different wind turbine layouts are performed for a subset of atmospheric flow conditions. Implementation of maritime corridors reduces overall power production due to the decrease in the number of wind turbines (from 1,922 to 1,604) but increases mean CFs by 2 percentage points due to the reduction in wake losses (Figure 4A; Table 1). Reducing the wind turbine

**Table 1. Summary of the flow scenarios and simulation results**

Flow scenario	Start date of 5 day	ERA5: lease area 8 centroid				Control					Corridor		Half		
		% of obs.	100-m WS class ( $\text{ms}^{-1}$ )	100-m wind direction class ( $^{\circ}$ )	# of hours out of 120 in class	Mean CF (%)	Mean wake loss (%)	Area of d04 with $\langle v_d \rangle$ of 2% (%)	Area of d04 with $\langle v_d \rangle$ of 5% (%)	Area of d04 with $\langle v_d \rangle$ of 10% (%)	Mean CF (%)	Mean wake loss (%)	Mean CF (%)	Mean wake loss (%)	
NW4-10	1979-10-26	7.85	4-10	270-360	66	26.7	34.4	4.1	2.3	1.3	28.3	30.5	32.1	21.2	
SW16-25	1981-04-04	1.6	16-25	180-270	43	76.0	13.5	7.7	3.7	1.7	-	-	-	-	
SE4-10	1981-08-29	7.5	4-10	90-180	78	22.9	65.5	8.8	5.6	3.8	-	-	-	-	
NE10-16	1985-11-28	4.6	10-16	0-90	64	73.6	17.5	7.6	3.3	1.6	-	-	-	-	
SW10-16	1986-03-26	9.1	10-16	180-270	69	53.0	31.1	12.3	6.2	3.6	56.2	27.0	63.4	17.4	
SW4-10	1988-07-04	12.5	4-10	180-270	84	9.0	64.7	14.1	4.7	2.7	10.1	60.3	13.6	47.0	
NW4-10	1998-06-04	7.85	4-10	270-360	78	42.8	34.6	5.6	3.4	2.2	-	-	-	-	
NW16-25	2000-01-17	1.4	16-25	270-360	32	60.7	6.8	3.6	1.6	0.2	-	-	-	-	
NW10-16	2007-02-05	11	10-16	270-360	84	88.7	4.2	2.8	1.4	0.3	89.6	3.3	91.0	1.7	
SE10-16	2011-05-15	2.3	10-16	90-180	37	63.3	20.7	7.7	5.0	2.9	-	-	-	-	
NE4-10	2012-11-17	9.6	4-10	0-90	90	49.1	34.4	10.3	3.9	2.0	52.0	30.5	59.9	20.1	
Frequency-weighted means. Two values are given for the control.						45.8 <sup>a</sup>	35.3 <sup>a</sup>	34.7 <sup>b</sup>	-	-	-	46.9	31.3	51.4	22.5

Columns on the left define the flow scenarios and the 11 5-day periods used to represent each scenario (by start date). Subsequent columns show the flow-scenario frequency based on ERA5 WS and wind direction at 100 m from the grid cell containing lease area 8 (LA8), along with the number of hours in the 5-day period that fall within the flow class. Results of the WRF simulations are shown for three different wind-turbine layouts: control in which the lease areas are fully occupied by wind turbines deployed with a 1.85 km spacing. Corridor where every sixth north-south row of wind turbines is omitted. Half (for half-installed capacity density) where the wind-turbine spacing is increased to 2.6 km (see details in Figure 3). The mean CF shown is derived from 10-min power production output from wind turbines in all lease areas. Mean wake losses are computed using the power production from the wind-farm parameterization and the maximum power possible if all wind turbines experienced the freestream WS. For the control layout the percentage of the grid cells in the innermost domain that exhibits a mean velocity deficit ( $v_d$ ) of 2, 5, and 10% is also shown. Slightly over 1.5% of simulation domain d04 grid cells contain wind turbines in the control simulations.

<sup>a</sup>Frequency weighting across all flow scenarios.

<sup>b</sup>Frequency weighting of only flow scenarios also used in Corridor and half simulations.



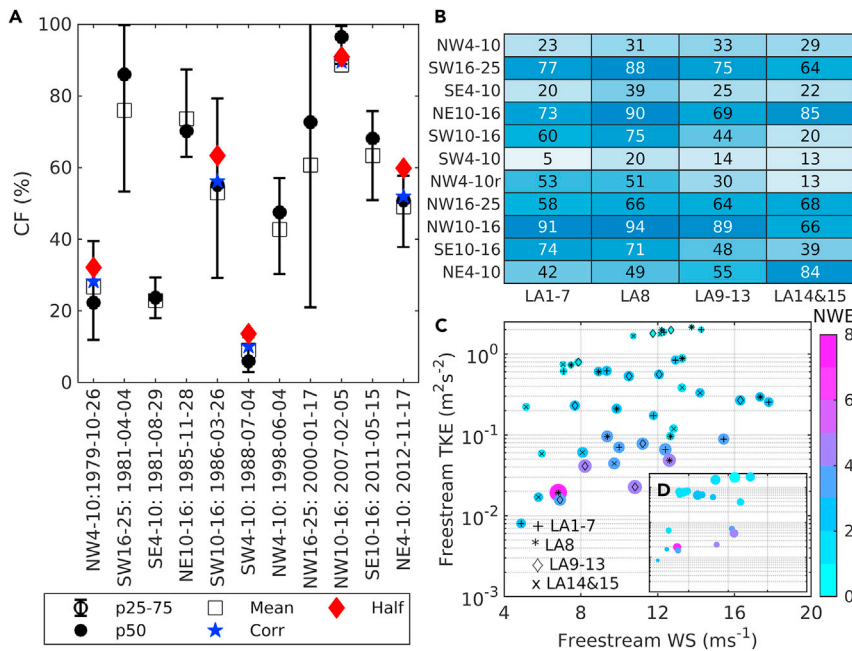


**Figure 4. Capacity factors (CFs, in %) and wake extents for each of the 5-day periods that represent the 11 flow scenarios**

(A) Mean, median (p50), and interquartile range (p25–75) of 10-min systemwide CFs (i.e., all lease areas) for each flow scenario in the control simulations (black). Also shown are mean capacity factors for simulations of wind turbine layouts including maritime corridors (blue stars) and half wind turbine density (red diamonds). Labels on the bottom axis indicate the flow scenario and start date of each 5-day simulation period.

(B) A heat map of mean capacity factors (CFs, in %) in each lease-area (LA) cluster for each flow scenario from the control simulations. Note: two cases are simulated for the most common flow scenario; northwesterly flow with WSs from 4 to 10  $\text{ms}^{-1}$  (NW4-10), one in fall and one in summer (denoted by the r). The first lease area cluster (LA1–7) is located south of Massachusetts. Lease area 8 (LA8) is located off the coast of New York state. Lease areas 9–13 (LA9-13) are located offshore of New Jersey, Delaware, and Maryland. Lease areas 14 and 15 (LA14&15) are located off the coast of Virginia (Figures 1A and 1B).

(C) Normalized wake extent (NWE) calculated as the area covered by a mean velocity deficits of over 5% ( $v_d \leq -0.05$ ) divided by the spatial extent of the lease-area cluster that generates the wake using Equation 6) for the control simulations plotted as a function of the mean freestream wind speed (WS) and turbulent kinetic energy (TKE) at 150 m in height over each lease-area cluster. There are 11 simulations and 4 lease-area clusters, thus 44 data points are plotted. The symbol size and color denote the normalized wake extent (NWE), and the marker in each NWE estimate denotes the lease-area cluster for which it is derived.

(D) (Inset to C) Difference in NWE ( $\Delta\text{NWE}$ , Equation 7) plotted as a function of the mean freestream WS and TKE at 150 m over each lease-area cluster. Symbol size scales with the magnitude of  $\Delta\text{NWE}$  between the control layout and half-density simulations (range 0.15–0.95), while the color denotes normalized wake extent (NWE) in the control simulations.

installed density to half of that used in the control simulations (968 wind turbines) further reduces power production but again increases mean CFs (Figure 4A; Table 1). Frequency-weighted mean CFs based on this subset of five flow scenarios increases from 45% in the control, to 46.9% in the corridor layout, and to 51.4% in the half-density layout (Table 1). This demonstrates the highly nonlinear dependence of power production and wake losses on atmospheric conditions and wind turbine spacing. Simulations such as those presented herein, which consider different wind turbine layouts, have high value in guiding development of large offshore wind farms in spatially limited LAs, particularly when they address other stakeholder interests (e.g., corridors to enable fishing and shipping) and can contribute to life-cycle financial analyses.<sup>44</sup>

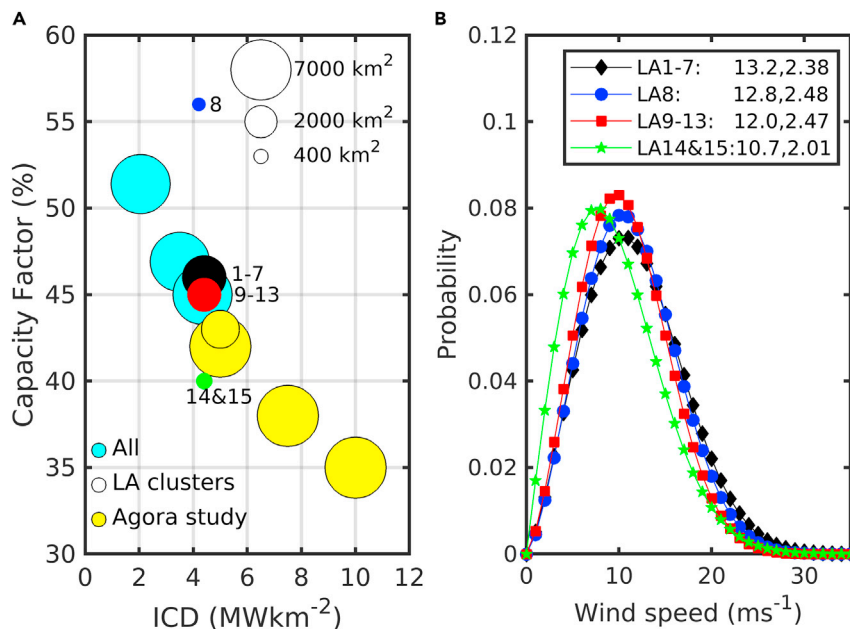


**Figure 5. Capacity factors and wind speed probability distributions for the U.S. east coast lease area clusters**

(A) Mean capacity factor (CFs in %) versus installed capacity density (ICD in MWkm<sup>-2</sup>) for varying wind turbine deployment layouts and across the four lease-area (LA) clusters. The symbol diameter in (A) scales with the area over which the wind turbines are deployed (see legend, upper right). Results from this study are shown accumulated over all four lease-area clusters (cyan) for the three wind-turbine deployments—control, maritime corridors, and half-installed capacity density—(ICD), and for each the four lease-area (LA) clusters (colors as in B) from the control deployment (ICD ~ 4.34 MWkm<sup>-2</sup>) with the numbers indicating the lease-area clusters (LAs 1–7, 8, 9–13, and 14 and 15) (see Figures 1A and 1B). Also shown are results of a study for projected developments in the German Bight area of the North Sea from the Agora study.<sup>6</sup> Both analyses are based on simulations with the Weather Research and Forecasting (WRF) model, but use different wind-farm parameterizations; Fitch<sup>37,38</sup> is shown here and the Explicit Wake Parameterization (EWP)<sup>43</sup> in the Agora study. Results from the Agora study are shown for 12-MW wind turbines deployed at an installed capacity density (ICD) of 5 MWkm<sup>-2</sup> over an area of 2,767 km<sup>2</sup>, with an installed capacity (IC) of 13.8 GW, and in two large arrays covering areas of 2,767 km<sup>2</sup> and 4,473 km<sup>2</sup> (total IC of 36.2 GW), and for those two deployment areas at ICD of 7.5 MWkm<sup>-2</sup> (total IC of 54.3 GW) and of 10 MWkm<sup>-2</sup> (total IC of 72.4 GW).

(B) Probability distributions from a two-parameter Weibull fit to modeled freestream wind speeds (WSs) at a height of 153 m a.s.l. in the center of each lease-area (LA) cluster. The numbers in the legend in (B) indicate the Weibull A and Weibull k parameters derived using maximum likelihood estimation and Equation 3.

### Estimated wake intensity and spatial extent

Despite the relatively high CFs that measure the actual energy output relative to the maximum possible, these model simulations also indicate substantial loss of potential power production due to the impingement of wakes on downstream wind turbines within individual LAs and between LAs (Figure 6). Individual LAs, and not only those that are immediately adjacent, are projected to be frequently operating in the “wind shadow” of upstream wind farms (Figure 6). This not only reduces power production but will be associated with increased mechanical loading on the wind turbines.

Frequency-weighted wake-induced power losses averaged over all LAs are 35.3% (Table 1). Thus, over a third of potential electrical-power production that could be achieved if all wind turbines operated in freestream (undisturbed) flow is lost due

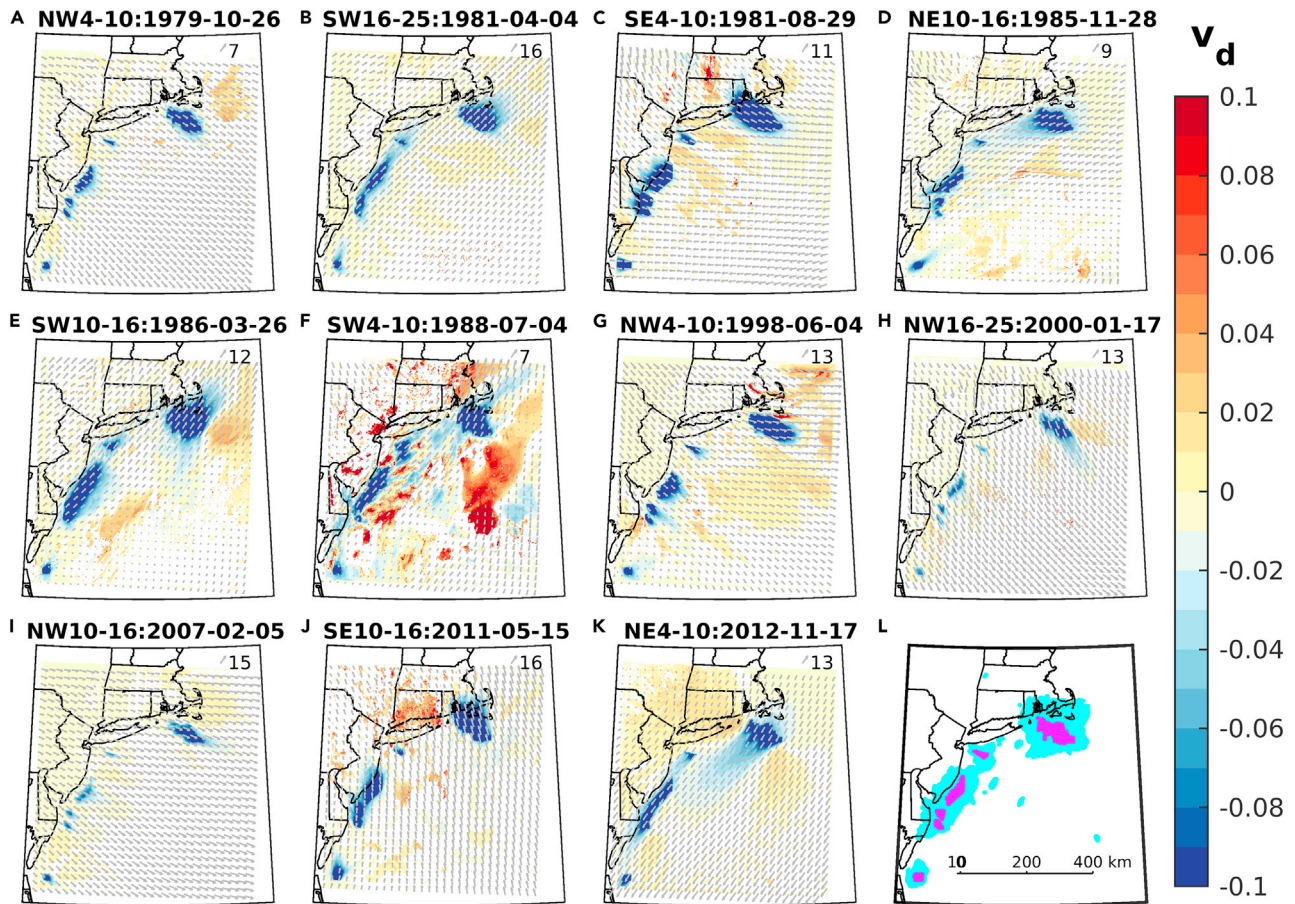


**Figure 6.** Mean velocity deficit ( $v_d$ ) in each grid cell for each of the 5-day flow-scenario simulations (Table 1)

(A–K) The title of each panel denotes the flow scenario (the first two letters denote the wind direction and the digits indicate the WS class) and first day of each 5-day simulation period (date is written as year-month-day). The mean velocity deficit is the mean normalized difference in WS in each grid cell at each time step (i) in output from simulation domain d04 (operating wind turbines) to output from simulation domain d03 (no wind turbines) (see Equation 4). The overlying quivers are the mean WS and direction computed using output from the simulation domain d03 that describes the freestream conditions. For legibility, the quivers are plotted at the 12<sup>th</sup> grid cell in both the latitude and longitude positions and are scaled to prevent overlap. The maximum length of each quiver in each panel is set to the maximum mean WS plot for each case (shown in the upper right of the panel and expressed in  $\text{ms}^{-1}$ ).

(L) Composite of all grid cells that have a mean velocity deficit of 5% or more ( $v_d \leq -0.05$ ) in one or more of the flow cases (cyan) and the location of grid cells containing wind turbines (magenta).

to their operation within wakes from upstream wind turbines and wind farms. This value greatly exceeds wake losses from current European offshore wind farms<sup>25</sup> in part because of the very large extent of the wind-farm clusters and unprecedented number of wind turbines deployed.

Velocity deficits ( $v_d$ ) are used here as a metric of wake intensity and extent. They represent the reduction in wind speed relative to what would be observed if no upstream wind turbines are present. These velocity deficits are calculated using wind speeds at the wind turbine HH from simulation domain d04 output with the action of wind turbines included ( $WS_{WT}$ ) and output from simulation domain d03 where no wind turbines are included ( $WS_{NoWT}$ ) (see methods). The concept of the normalized wake extent (NWE) is introduced to describe the areal extent of disturbed flow caused by a given wind farm. It is the ratio of the spatial extent of the wind shadow generated by a wind farm to the area of the wind farm. The NWE is naturally a

function of the threshold of velocity deficit used to define the wake. The area covered by mean velocity deficits of 2% (i.e.,  $v_d \leq -0.02$ , Equation 4) for the 11 flow scenarios with the control layout ranges from 2.8% to 14.1% of the innermost model domain where wind turbines are operating (d04), while the area covered by wind turbines is 1.5% (Table 1). Thus, the mean NWE using this velocity deficit threshold varies depending on the prevailing atmospheric conditions but is between two times and nearly ten times the spatial extent of the wind farms. Similar mean NWEs computed for the different flow scenarios using a velocity deficit ( $v_d$ ) of 5% range from one to four, with a weighted mean of 2.6. Using a velocity deficit ( $v_d$ ) of 10% to define the area covered by a wake, the mean NWE in each 5-day simulation ranges from 0.15 to nearly three (Table 1). These values indicate that, consistent with expectations, wind turbine deployments within these LAs will generate substantial downstream “wind shadows” (Figure 6). As discussed further below, large, NWEs are associated with simulations of flow conditions characterized by moderate wind speeds, low ambient turbulence, and low planetary boundary layer depths.

The NWE is substantially smaller in the half-density simulations for all LA clusters and all values of freestream wind speed, planetary boundary layer height, and TKE (Figure 7). The mean difference in normalized spatial wake extents in the control and half-density simulations ( $\Delta$ NWE, computed using Equation 7) is 0.48. Thus, the area covered by mean velocity deficit of at least 5% reduces to half the value from the control simulations when a half-density wind turbine layout is simulated. Thus, on average, there is a systemwide benefit from minimizing wind shadows from upstream LAs by locating wind turbines with greater spacing. However, the range of  $\Delta$ NWE extends from 0.12 to 0.96, indicating that under some atmospheric flow conditions the NWE is only modestly influenced by the density of wind turbine deployments in the LAs. The difference in NWE in the half-density simulations relative to the control is maximized for periods with high ambient turbulence (Figure 4D). Thus, the decrease in wake extent due to the reduction in ICD is disproportionately weighted toward periods with relatively small, NWEs in the control simulations. The BOEM intends to auction additional LAs close to these existing LAs. While adoption of lower ICD will reduce revenues to individual LA operators, it may have benefits in terms of reducing systemwide power losses and wind turbine fatigue loading due to wakes within wind farms and between wind farms.

An alternative metric of the wind-farm wake extent is the maximum distance downwind from LA clusters aligned with the mean wind direction to which a mean velocity deficit of at least 5% ( $v_d \leq -0.05$ ) extends (Figure 6L). For the control simulations, the minimum downwind wake extent from the largest LA cluster (LAs 1–7) is 14 km. It is associated with northwesterly flow scenarios (represented by simulations commencing on 1979-10-26 and 2007-02-05) (Figure 6A–6K). These simulations exhibit flow from over land to this LA cluster with relatively low freestream wind speeds ( $5\text{--}8\text{ ms}^{-1}$  at the center of these LAs at  $\sim 150\text{ m}$  in height) and moderate freestream TKE of  $\sim 1\text{ m}^2\text{s}^{-2}$ . The maximum wake extent from the LAs 1–7 of 90 km is found for the SW10-16 flow scenario (the simulation starting on 1986-03-26) and the NE4-10 flow scenario (represented by the simulation that starts on 2012-11-17) (Figure 6). The SW10-16 case exhibits higher wind speeds (freestream wind speed at  $\sim 150\text{ m}$  at the center of the LA cluster of  $\sim 10\text{ ms}^{-1}$ ) but has a long over-water fetch, which results in low freestream TKE  $< 0.07\text{ m}^2\text{s}^{-2}$  that contributes to slow wake recovery and large wake-propagation distances. By contrast, the NE4-10 case exhibits higher TKE  $< 0.4\text{ m}^2\text{s}^{-2}$ , but lower wind speeds (WSs  $\sim 7.8\text{ ms}^{-1}$ ) and higher thrust coefficients, which also lead to larger wake extents. For cases with southerly, southwesterly mean flow, i.e.,



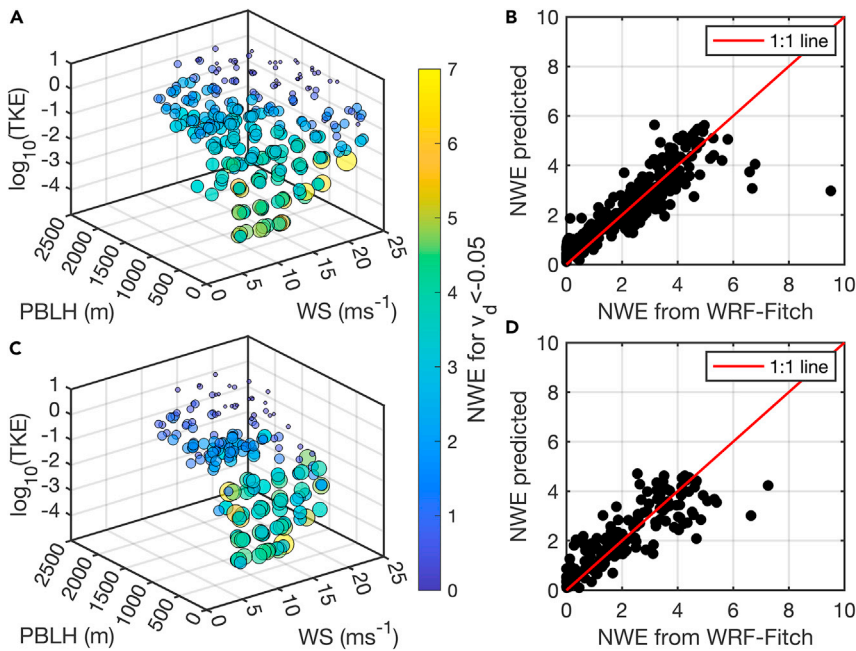


**Figure 7. Spatial extent of disturbed flow (wakes) from offshore wind farms shown as a function of prevailing meteorology**

(A and C) 3D bubble plots of the normalized wake extent (NWE, for a velocity deficit threshold 5%, i.e.,  $v_d < -0.05$ ) from each of the four lease-area clusters as a function of freestream wind speed (WS) and turbulent kinetic energy (TKE, shown in  $\log_{10}$  scale) close to the wind-turbine HH of 150 m, and the freestream planetary boundary layer height (PBLH) in the centroid of the lease-area cluster. (A) Results from the simulations of the control layouts, where wind turbines are installed with the mean separation of 7.7 times the wind-turbine rotor diameter. The installed capacity density for these control simulations is approximately  $4.34 \text{ MWkm}^{-2}$ .

(C) Results from the simulations of the half-density layouts, where the density of wind turbines is reduced to half that used in the control layout and represents the lowest densities used in European offshore wind farms. The associated installed capacity density is  $\sim 2.2 \text{ MWkm}^{-2}$ .

(B and D) Scatterplots of the normalized wake extent (NWE) for each combined WS, PBLH, and TKE class derived directly from the WRF-Fitch output versus those predicted from the regression models.

(B) Results for an installed capacity density of  $4.34 \text{ MWkm}^{-2}$  (i.e., the control simulations) where the regression model has the form,  $NWE = 3.52 - 0.093 \times WS - 0.73 \times \log_{10}(TKE) - 6.3 \times 10^{-4} \times PBLH$ .

(D) Results for an installed capacity density of  $\sim 2.2 \text{ MWkm}^{-2}$  (i.e., the half-density simulations) where the regression model has the form,  $NWE = 3.00 - 0.056 \times WS - 0.57 \times \log_{10}(TKE) - 11 \times 10^{-4} \times PBLH$ .

SW4-10 (1988-07-04), SW10-16 (1986-03-26), SW16-25 (1981-04-04) or northeasterly flow, NE4-10 (2012-11-17), velocity deficits above 5% fully encompass all of the mid-Atlantic LA clusters (LAs 9–13) indicating substantial array-array interactions, despite separation distances of up to  $\sim 23 \text{ km}$  (Figure 6).

The SW4-10 flow scenario is observed for 12.5% of hours (Table 1) and is associated with the largest systemwide wake losses, and hence the smallest CFs (Table 1; Figure 4A). The 5-day simulation period starting 1988-07-04 has a freestream modal wind direction of  $\sim 210^\circ$ , median WS of  $6.3 \text{ ms}^{-1}$ , and TKE below  $0.01 \text{ m}^2\text{s}^{-1}$  in LA 8. Mean CFs for LAs 1–7 for this flow scenario are particularly small (Figure 4B) due to low freestream WSs and a clear deep array wake effect. Fewer than 6% of wind turbines, all of which are located on the edge of the array, exhibit power production above 10% of rated power. Mean CFs for LAs 9–13 are also low for this flow scenario (14%) (Figure 4B), and the contour enclosing mean velocity deficits above 5% ( $v_d \leq -0.05$ ) over the mid-Atlantic LA cluster for this flow scenario extends

over a 210-km distance aligned along a south-southwest to north-northeast axis (Figure 6).

This variability in wake extents and CFs between the flow scenarios emphasizes the importance of simulating a wide array of atmospheric conditions and affirms the scenario construction used herein encompasses examples of maximum and minimum wake intensity and extent (Table 1). The composite overlay of areas with mean velocity deficits of over 5% (i.e.,  $v_d \leq -0.05$ ) under one or more of the flow scenarios (Figure 6L) provides important guidance for the selection of future LAs in order to avoid places with substantial wind shadowing from existing lease areas.

These thorough analyses of the power production and wake behavior across the different LA clusters along the U.S. east coast and their dependence on wind turbine layout and prevailing meteorology provides context that is critical to developing a generalized model for wind-farm wake extents that is presented in the next section.

### A generalized model of wind farm wake extent

As illustrated in the previous discussion, the time or distance downstream required for a wind turbine wake to be eroded due to mixing with surrounding, higher-momentum air, is determined by the original intensity of the wake and the mixing state of the atmosphere. The wake intensity is, in large part, dictated by the freestream WS and the wind turbine thrust coefficient (Figure 1E). The mixing state of the atmosphere and ability to transfer higher-momentum air into the wake is determined by the ambient TKE and the planetary boundary layer height. Accordingly, the mean normalized spatial extent of wakes from each LA cluster scales primarily according to both mean freestream TKE and WS at HH (Figure 4C). Large, NWEs are most evident at low WSs and low TKE (Figure 4C). Conversely, for mean TKE above  $0.5 \text{ m}^2\text{s}^{-2}$ , the NWE is almost uniformly less than twice the area of the LA clusters (Figure 4C). A weaker but still important third control on wake extent is the planetary boundary layer height (Figure 7A).

Under the hypothesis that wind-farm intensity, areal extent, and recovery are largely controlled by three variables—freestream WS, TKE, and planetary boundary layer height—a generalized model of NWE is derived. The predictand is the NWE, i.e., the area covered by a mean velocity deficit [ $v_d] \leq -0.05$ ). The predictors are freestream WS, TKE, and planetary boundary layer height (PBLH) for the center of each LA cluster from the domain in which no wind turbine effects are simulated. Two models are derived (see details in methods). The first uses model output from simulations of the control layout that employ a wind turbine spacing equal to that agreed for some of the LAs and that typifies the European offshore wind energy industry (ICD of  $4.34 \text{ MWkm}^{-2}$ ). The second model uses output from half-density layouts where the wind turbines are installed over the same area but with greater separation leading to an ICD of approximately  $2.2 \text{ MWkm}^{-2}$ . The NWE model for the control layouts has the following form:

$$NWE = 3.52 - 0.093 \times WS - 0.73 \times \log_{10}(TKE) - 6.3 \times 10^{-4} \times PBLH \quad (\text{Equation 1})$$

All of the coefficients are statistically different from zero at a confidence level of 99% and variance explanation ( $R^2$ ), adjusted for the number of predictors,<sup>45</sup> is 0.72 (Figure 7).

The form of this linear model (Equation 1) indicates that the areal extent of the wake from a large offshore wind farm exhibits a statistically significant negative dependence on freestream WS close to the wind turbine HH, with larger wake generation



at lower WSs. There is also a negative dependence on the base-10 logarithm of turbulence intensity ( $\log_{10}[\text{TKE}]$ ) at wind turbine HH. Weaker ambient turbulence leads both to slower wake recovery and to larger wake extent. Both findings are consistent with analyses of operational data from offshore wind farms that have indicated below average power production, and larger wake effects, under moderate WSs and low turbulence intensity.<sup>15</sup> The model also indicates evidence of a negative dependence of NWE on freestream PBLH at the center of each LA cluster. For very large wind turbine arrays wake recovery is largely dictated by the rate at which momentum can be transferred from aloft. Mixing of high-momentum air from the free troposphere across the temperature inversion that typifies the top of the boundary layer into the boundary layer is very slow. Thus, under low PBLH the volume of air from which momentum can be extracted to recover the wake is smaller than under higher PBLH.

Using the half-density layout, the coefficients in the linear model are of the same sign for each of the predictors:

$$\text{NWE} = 3.00 - 0.056 \times \text{WS} - 0.57 \times \log_{10}(\text{TKE}) - 11 \times 10^{-4} \times \text{PBLH} \quad (\text{Equation 2})$$

Again, all of the coefficients are statistically different from zero at a confidence level of 99% and variance explanation ( $R^2$ ), adjusted for the number of predictors,<sup>45</sup> is 0.70 (Figure 7).

The high variance explanation for Equations 1 and 2 indicate that these models are relatively good representations of the model output on which they are based. Further, there are robust relationships between the areal extent of a wake generated by very large offshore wind farms and the freestream WS and TKE near the wind turbine HH and the freestream PBLH. Consistent with expectations, for the same freestream WS, turbulence intensity, and PBLH the area covered by a wake from each wind farm is smaller for wind farms that have lower ICD, or greater wind turbine spacing. For example, for a WS of  $7 \text{ ms}^{-1}$ , TKE of  $0.001 \text{ ms}^{-2}$  and a PBLH of 500 m, the area covered by a 5% velocity deficit will be an average of 4.74 times the areal footprint of the wind farm if the wind turbines are installed with a spacing equal to that of current offshore wind farms in Europe. Conversely, for the half density of wind turbine deployments, the areal extent of the wind shadow is estimated to be 3.78 the area of the offshore wind farm.

In addition to demonstrating the functional dependence of wake extent on key meteorological drivers, these equations could provisionally be used with output from WRF simulations of other global regions to provide first-order estimates of likely wind shadows from proposed offshore wind farms. Naturally, caution should be used in extrapolating to atmospheric conditions beyond those sampled in this analysis and/or to scales of wind deployments dissimilar to those addressed here. Further, it is important to note that other modeling approaches are available to describe wind turbine and wind-farm wakes,<sup>46,47</sup> and different wind-farm parameterizations for use within the WRF model.<sup>43</sup> No assessment can currently be made regarding how results presented herein may differ from those generated using other modeling frameworks.

## DISCUSSION

Expansion of offshore wind is a key component of global efforts to reduce the carbon intensity of the energy sector. Deeper understanding of the atmospheric physics of large wind farms is critical to optimal, cost-effective exploitation of the substantial offshore wind resource. Our research addresses this need and is unique in several

regards. First, we present a computationally efficient and robust method to derive representative power production and wake projections for large offshore wind farms. Second, we demonstrate the approach and the concept of NWEs by applying our method to offshore wind LAs along that U.S. east coast. Last, we quantify the sensitivity of power production and wake-induced power losses to both wind-farm ICD and prevailing meteorology for a wide range of meteorological conditions that prevail offshore.

Our results indicate that power production of 116 TWh/year and mean CFs of  $\sim 50\%$  can be achieved from the 15 U.S. east coast offshore wind energy LAs by employing 15-MW wind turbines at the anticipated spacing of 1.85 km (Table 1; Figure 4). CFs calculated for all three wind turbine layouts we considered meet or exceed those of currently operating offshore wind farms in Europe. They are consistent with, and indeed slightly higher than, those from an analogous WRF modeling study for projected installed wind energy capacity in 2050 for the German Bight region of the North Sea<sup>6</sup> (Figure 5). However, for wind turbine layouts similar to those from smaller offshore wind farms in Europe, a substantial fraction of these wind turbines will operate in wakes from upstream turbines and wind farms. These wake effects will reduce power production by over one-third (Figure 6; Table 1). There is clear evidence for substantial array-array interactions (i.e., power losses at downwind wind farms caused by wind turbines operating upwind) even for LAs separated by 23 km. These results emphasize the critical importance of evaluating potential wake losses from upstream wind farms as the BOEM moves forward with tendering additional LAs along the U.S. east coast.<sup>36</sup>

Using a low estimate of revenues from electricity production of \$62 per MWh there are clear and substantial potential financial benefits from improved array layouts and careful siting of new wind turbine developments to reduce wake-induced power losses and increase CFs. At this scale of development (28.8 GW), a 1% increase in the CF would increase electricity output by about 2.5 TWh per year, leading to additional annual revenues of over US\$150 million. Introduction of maritime corridors in the wind turbine layouts decreases estimated annual electrical-power production from 116 to 99 TWh/year. Thus, a reduction of total IC by 16.5% yields a reduction in projected power production of 14.7% because the increase in wind turbine spacing reduces wake-induced power losses and increases the efficiency of power production from the wind turbines. To provide an economic assessment of the maritime corridors scenario, we assume an installation cost of US\$ 3 million per MW (the average of those projected for the U.S.<sup>14</sup> and realized in Germany<sup>13</sup>) and a power purchase price of US\$ 62 per MWh of electricity produced (the average bid prices for European offshore wind farms<sup>13</sup>). Excluding any resulting additional cabling costs, introduction of the maritime corridors will decrease initial investment costs by  $\sim$ US\$ 14.3 billion but will also lower annual revenues by  $\sim$ US\$ 1.06 billion. Thus, the ultimate system-wide benefits of introducing maritime corridors and/or using higher or lower ICD merits detailed analyses, including all internal and external costs and benefits.

Projected power production, wake extent, and intensity are a nonlinear function of prevailing meteorology, e.g., wind resource and turbulence intensity (Figures 4C and 7), wind turbine layouts, e.g., ICD and areal extent (Figures 5 and 7), and model assumptions (e.g., wind-farm parameterization).<sup>26,48,49</sup> The statistical models developed here show the extent of wakes from large offshore wind farms can be explained by three atmospheric variables that are commonly available from meteorological models and/or can be measured using existing *in situ* and remote sensing technologies. The areal extent of disturbed flow normalized to the area of the wind farm that generates the wake is maximized under conditions of low turbulence intensity,

moderate Ws, and low boundary layer heights (Figure 7). Thus, offshore wind farms are most likely to experience lower power production due to the presence of upstream wind farms under relatively low Ws and when warmer air moves over a colder sea. Under these conditions, the lower atmosphere will become stably stratified resulting in low ambient turbulence and low boundary layer heights.

Given the scale of the financial investment and the critical importance of offshore wind energy to the zero-carbon-emissions economy, further work is warranted. This should include a diversity of wind turbine layouts, inclusion of alternative windfarm parameterizations and additional atmospheric flow scenarios to ensure optimal design of individual offshore wind farms and management of the large-scale global expansion of offshore wind energy.

## EXPERIMENTAL PROCEDURES

### Resource availability

#### Lead contact

Requests for further information should be directed to the lead contact, Sara C. Pryor (s.c.pryor@cornell.edu).

#### Materials availability

No materials were used in this study.

#### Data and code availability

Source code for WRF v3.8.1 including the wind-farm parameterization patch is available from [http://www2.mmm.ucar.edu/wrf/users/download/get\\_sources.html](http://www2.mmm.ucar.edu/wrf/users/download/get_sources.html). ERA5 data are available from <https://climate.copernicus.eu/climate-reanalysis>. Shapefiles of the lease areas are available from the BOEM at; <https://www.boem.gov/renewable-energy/mapping-and-data/renewable-energy-gis-data>. The population density in the contiguous U.S. according to the 2010 census is available from; <https://www.census.gov/data/tables/time-series/demo/popest/2010s-state-total.html>. Output from the WRF simulations presented in figures and analyses herein is available for download from ZENODO (10.5281/zenodo.5137547) access to the full suite of WRF output are available via the DoE tape archive. Output from simulations of the control layouts is available from: [https://portal.nersc.gov/archive/home/projects/m2645/www/public\\_data\\_NY\\_lease\\_fitc\\_full\\_density](https://portal.nersc.gov/archive/home/projects/m2645/www/public_data_NY_lease_fitc_full_density). Output from simulations of the layouts with maritime corridors is available from: [https://portal.nersc.gov/archive/home/projects/m2645/www/public\\_data\\_NY\\_lease\\_fitc\\_recovery\\_corridors](https://portal.nersc.gov/archive/home/projects/m2645/www/public_data_NY_lease_fitc_recovery_corridors). Output from simulations of the half-density layouts is available from: [https://portal.nersc.gov/archive/home/projects/m2645/www/public\\_data\\_NY\\_lease\\_fitc\\_half\\_density](https://portal.nersc.gov/archive/home/projects/m2645/www/public_data_NY_lease_fitc_half_density). MATLAB is a proprietary software program developed and available for purchase from MathWorks. MATLAB code used to perform the analyses is available for download from ZENODO (10.5281/zenodo.5137547).

## Methods

### Selecting the flow scenarios

The simulation and analysis framework presented here is designed to optimally quantify wake impacts on power production while reducing the computational cost and redundancy inherent in long-term continuous simulations. It further avoids limitations associated with use of idealized flow scenarios or individual case studies. The scenario approach ensures timely production of actionable information to those responsible for progressing development of offshore resources at the lowest LCoE. Details of the computational approach and costs are given in [supplemental information](#).

The ERA5 reanalysis<sup>50</sup> is used to derive representative flow scenarios and the initial and lateral boundary conditions (LBC) for simulations with the WRF model. The ERA5 reanalysis model ingests an unprecedented suite of assimilated *in situ* and remote sensing observations.<sup>50</sup> ERA5 exhibits relatively high fidelity for 100-m wind speeds<sup>40,51–53</sup> and has been used as LBC in a range of WRF-based regional simulations including those performed for the New European Wind Atlas.<sup>54</sup> The periods for which WRF simulations are performed are selected based on analyses of WS and direction at 100 m a.g.l. for 1979–2018 from the ERA5 grid cell (30 × 30 km) containing the center of the New York LA (LA 8, Figures 1A and 1B). They are selected to represent commonly occurring flow conditions of relevance to power production and wake generation from wind turbines. Accordingly, the flow scenarios focus on the following WS classes; 4–10 ms<sup>-1</sup> (high thrust coefficients causing relatively large wake magnitudes, Figure 1E), 10–16 ms<sup>-1</sup> (moderate thrust coefficients and wakes) and 16–25 ms<sup>-1</sup> (low thrust coefficients with small wake magnitude). The wind directions (WD) are also clustered into physically meaningful groups that represent differentiable modes of over-water fetch to the offshore LAs (Figure 2). Four directional classes are defined: 270°–360°, 180°–270°, 0°–90° and 90°–180° (listed in decreasing frequency). These directional classes represent flow that has a relatively short fetch over water to LA 8 (of the order tens rather than hundreds of km) for the two west sectors (SW: 180–270°, NW: 270–360°) versus those for the two easterly sectors (NE: 0–90°, SE: 90–180°) with hundreds to thousands of km of over-water fetch (Figures 1A and 1B). Ten combined WS and direction classes are required to capture 75% of the total 40 years of hourly observations. The flow scenarios are described using the nomenclature; WDWS, where WD is NE, SE, SW or NW, and WS is 4–10, 10–16 or 16–25.

Once the flow scenarios are identified, the 40 year record of hourly ERA5 derived WSs and directions at 100 m over the center of LA 8 is scanned to identify 5 day periods with the maximum number of hours that conform to each flow scenario (Table 1). Variation in atmospheric stability, turbulence intensity and PBLH offshore is dominated by the seasonal timescale due to the low frequency variability in sea surface temperatures.<sup>55</sup> Thus, in selecting the 5-day periods to represent the flow scenarios consideration is also given to ensuring the seasonal representation (Figure 2E). For the most frequent flow scenario (NW4-10), two cases; one in later autumn and one in summer are selected. Hence, 11 5-day periods are selected for the WRF model simulations (Table 1).

### Simulation settings

Simulations are performed with WRF v3.8.1 and use the Fitch wind-farm parameterization.<sup>38</sup> This parameterization works such that every wind turbine in a grid cell contributes to estimated power production (in watts) as a function of the incident WS and the wind-turbine power curve (Figure 1E). Each wind turbine also induces wakes by applying a local drag force that reduces WSs and adds TKE to all model vertical levels that intersect the turbine rotor. Drag applied and TKE introduced are functions of the thrust coefficient (Figure 1E) and thus are determined by the incident WS and wind-turbine specifications.<sup>38</sup> Simulations performed here employ a modified version of the Fitch parameterization corrected for an earlier coding error that prevented advection of wind turbine induced TKE and that employs an updated algorithm for wind turbine added TKE.<sup>37</sup> Key physics setting are as in previous research<sup>2</sup> and shown in supplemental information. Each simulation employs a 6-h spin up and then runs for 5 days. All variables presented herein are output at 10-min intervals.

Wind resources and wind turbine wake effects are a function of model resolution.<sup>26,48</sup> Power density estimates from mesoscale models with a 10-km grid spacing

can be 50% lower than those from higher-resolution modeling.<sup>48</sup> Here, four simulation domains are employed (Figure 1A). The outer domain comprises 150 × 150 grid cells with a grid resolution of 16.67 km (d01). This is nested down to the middle domain (d02) comprising 250 × 250 grid cells resolved at 5.56 km. Two inner domains of 340 × 361 grid cells resolved using a 1.85 km resolution are run sequentially. The first (d03) is operated without the action of wind turbines to provide a freestream WS. A second identical innermost domain (d04) is run with the wind-farm parameterization turned on. The resolution used for d03 and d04 is selected to match the expected wind-turbine separation of 1.85 km.

There are 57 layers in the vertical, 20 levels at which WSs are output are below 370 m and 14 are within the rotor plane. The ninth level has a mean height of 143 m and is taken as equivalent to that at the nominal wind turbine HH = 150 m (Figure 1D).

As of early 2021 wind-turbine selections and locations for the different U.S. offshore LAs are not available. Thus, simulations are performed for three plausible wind-farm layouts. The control employs a wind-turbine spacing of 1.85 km. For the IEA 15 MW reference turbine used herein has a HH ~ 150 m and a rotor diameter (D) ~ 240 m.<sup>12</sup> Thus, the spacing between wind turbine of 1.85 km is equal to a spacing of 7.7D. It is equal to the average wind-turbine spacing from operating wind farms in Europe. In this set of simulations all LAs are fully covered by a total of 1922 wind turbines (Figure 3). The mean wind turbine ICD for these control simulations is 4.34 MWkm<sup>-2</sup>. Two sets of sensitivity simulations are also performed for a subset of atmospheric flow conditions. In the corridor simulations, a maritime corridor is inserted by removing the sixth north-south “column” of wind turbines in each wind-turbine cluster, reducing the number of wind turbines to 1,604 (Figure 3). Such corridors have been proposed to accommodate shipping safety considerations and enable fishing,<sup>56</sup> and may also mitigate wildlife impacts.<sup>57</sup> In the half-density sensitivity simulations, the density of wind turbines in each LA is halved reducing the total number of wind turbines to 968. The resulting ICD (~2.1 MWkm<sup>-2</sup>) is at the lower end of current-generation European offshore wind farms.

### Statistical methods

Power production reported here derives directly from the WRF wind-farm parameterization and is determined by the WS across the rotor plane and the wind-turbine power curve (Figure 1E).

Wind regimes in the LA clusters are compared by fitting time series of modeled free-stream WS at the nominal wind-turbine HH of 150 m from the centroids of each LA cluster to a two-parameter Weibull distribution:

$$p(WS) = 1 - \exp \left[ - \left( \frac{WS}{A} \right)^k \right] \quad (\text{Equation 3})$$

where the two parameters in this probability distribution are the scale parameter, A (units of ms<sup>-1</sup>) that describes the peak in the WS distribution and shape parameter, k, that describes the dispersion around that peak. These parameters are fitted using maximum likelihood methods.<sup>45</sup>

The wake intensity and spatial extent is characterized using the mean fractional velocity deficit ( $v_d$ ) that describes the difference in WS due to the action of wind turbines. The mean  $v_d$  in each grid cell is computed using all output from each 5-day simulation (i.e., after the 6-h spin-up period is concluded) as:

$$v_d = \frac{1}{n} \sum_{i=1}^{i=n} \left[ \frac{WS_{WT(x,y,i)} - WS_{NoWT(x,y,i)}}{WS_{NoWT(x,y,i)}} \right] \quad (\text{Equation 4})$$

The fractional velocity deficit is calculated using wind speeds at the wind-turbine HH using output from simulation domain d04 with the action of wind turbines included ( $WS_{WT}$ ) and output from simulation domain d03 where no wind turbines are included ( $WS_{NoWT}$ ).  $v_d$  is the mean of normalized difference in WS in each grid cell ( $x, y$ ) at each of the 720 10-min timesteps in each 5-day period ( $i = 1$  to  $n = 720$ ). A two-sample t-test with a threshold  $p$  value of 0.01 is applied to assign statistical significance to the mean pairwise differences in WS. Results are corrected for multiplicity by ranking the  $p$  values from each grid cell (where  $j = 1$  is allocated to the smallest  $p$  value and  $kk$  is the total number of grid cells) and then selecting as statistically significant only those for which the following condition is realized<sup>45</sup>:

$$p_j \leq \frac{j}{kk} p \quad (\text{Equation 5})$$

The concept of NWE is introduced to characterize the region of disturbed flow generated by a wind farm that is colloquially referred to as the “wind shadow.” NWEs are calculated for each LA cluster in each 5-day simulation as the area covered by a mean  $v_d \leq -0.05$  ( $Area_{v_d \leq -0.05}$ ) divided by the spatial extent of the LA cluster (i.e., group of adjacent LAs,  $Area_{LAcluster}$ ) that generates the wake:

$$NWE = \frac{Area_{v_d \leq -0.05}}{Area_{LAcluster}} \quad (\text{Equation 6})$$

The difference in NWE ( $\Delta NWE$ ) from each LA cluster in simulations with the control layout and the half-density layout is given by:

$$\Delta NWE = \frac{NWE_{control} - NWE_{half}}{NWE_{control}} \quad (\text{Equation 7})$$

Statistical models are constructed that describe the NWE, (i.e., the area covered by a 5% velocity deficit relative to the freestream WS normalized by the areal extent of the wind-turbine deployment) as a function of prevailing meteorology. Separate models are developed using output from the control layout simulations and using output from the half-density wind-farm layouts. In these analyses the NWE from each cluster of LAs is computed for each 10-min period along with the freestream WS,  $\log_{10}(\text{TKE})$  and PBLH at the center of that LA cluster. To build stable regression models output from each LA cluster and each 10-min time stamp are first composited into combined classes of wind speed, turbulence and planetary boundary layer heights using seven WS classes (4–7, 7–10, 10–13, 13–16, 16–19, 19–22, 22–25  $\text{ms}^{-1}$ ), five  $\log_{10}(\text{TKE})$  classes ( $5 \times 10^{-5}$  to  $5 \times 10^{-4}$ ,  $5 \times 10^{-4}$  to  $5 \times 10^{-3}$ ,  $5 \times 10^{-3}$  to  $5 \times 10^{-2}$ ,  $5 \times 10^{-2}$  to  $5 \times 10^{-1}$ ,  $5 \times 10^{-1}$  to  $5 \text{ m}^2\text{s}^{-2}$ ) and six PBLH classes (0–400, 400–800, 800–1,200, 1,200–1,600, 1,600–2,000, 2,000–2,400 m). The calculations are performed separately for each LA cluster (Figure 7) and then combined for the model generation. For each combined class of wind speed, turbulent kinetic energy and planetary boundary layer heights that has > 4 members, mean values of NWE, WS,  $\log_{10}(\text{TKE})$  and PBLH are computed. The resulting regression equations describe NWE as a function of these predictors (see Figure 7). The regression coefficients are deemed statistically significant if they differ from zero at the 99% confidence level and the goodness of fit is evaluated using the  $R^2$  value adjusted for the number of predictors.<sup>45</sup>

An estimate of wake-induced power production loss is made by computing the maximum possible power production in each 10-min period if each wind turbine experienced undisturbed flow. This estimate is derived by applying the IEA reference turbine power curve (Figure 1E) to freestream WSs from the third



simulation domain (d03) at a model height of  $\sim 150$  m in each grid cell where a wind turbine is present in simulation domain d04. The difference between the power derived using the wind-farm parameterization and this maximum possible power from the freestream WS is the wake loss:

$$wakeuploss = \frac{\sum_{i=1}^{i=n} \left( \sum_{y=y_1}^{y=y_2} \sum_{x=x_1}^{x=x_2} PC \left( WS \left( x_{NO_{WT}}, y_{NO_{WT}}, i \right) \right) \right) - \sum_{i=1}^{i=n} \left( \sum_{y=y_1}^{y=y_2} \sum_{x=x_1}^{x=x_2} P_{Fitch} \left( x_{WT}, y_{WT}, i \right) \right)}{n}$$

(Equation 8)

where  $i$  denotes the time stamps and ranges from 1 to  $n$ , where  $n = 720$  for 10-min output over 5 days.  $PC$  is the power production as a function of  $WS$  computed from the power curve for the IEA 15 MW reference wind turbine (Figure 1E).  $P_{Fitch}$  is the power production from those same grid cells in simulation domain d04 computed by the modified Fitch scheme. The grid cells considered  $y_1:y_2$  and  $x_1:x_2$  are those that contain wind turbines in d04 for the control simulation.

## SUPPLEMENTAL INFORMATION

Supplemental information can be found online at <https://doi.org/10.1016/j.joule.2021.09.002>.

## ACKNOWLEDGMENTS

The US Department of Energy Office of Science (DE-SC0016605), the US Department of Energy Office of Energy Efficiency and Renewable Energy, and New York State Energy Research and Development Authority via the National Offshore Wind Research and Development consortium (147505) funded this research. This research was enabled by computational resources supported by the U.S. National Science Foundation via the Extreme Science and Engineering Discovery Environment (XSEDE) (award TG-ATM170024) and ACI-1541215, and those of the National Energy Research Scientific Computing Center, a DOE Office of Science User Facility supported by the Office of Science of the U.S. Department of Energy under contract no. DE-AC02-05CH11231. The comments from four reviewers are acknowledged.

## AUTHOR CONTRIBUTIONS

S.C.P. and R.J.B. conceived the original concept and obtained the funding for the research. S.C.P. conducted all analyses presented here and drafted the manuscript and all figures. R.J.B. and S.C.P. designed the wind-turbine scenarios employed. R.J.B. designed the flow scenarios. T.J.S. performed the WRF simulations. S.C.P. and R.J.B. addressed review comments.

## DECLARATION OF INTERESTS

The authors declare no competing interests.

Received: February 19, 2021

Revised: June 7, 2021

Accepted: September 8, 2021

Published: September 30, 2021

## REFERENCES

1. Pryor, S.C., Barthelmie, R.J., Bukovsky, M.S., Leung, L.R., and Sakaguchi, K. (2020). Climate change impacts on wind power generation. *Nat. Rev. Earth Environ.* 1, 627–643. <https://doi.org/10.1038/s43017-020-0101-7>.
2. Pryor, S.C., Barthelmie, R.J., and Shepherd, T.J. (2020). 20% of US electricity from wind will have limited impacts on system efficiency and regional climate. *Sci. Rep.* 10, 541. <https://doi.org/10.1038/s41598-019-57371-1>.
3. Jacobson, M.Z., Delucchi, M.A., Bauer, Z.A.F., Goodman, S.C., Chapman, W.E., Cameron, M.A., Bozonnat, C., Chobadi, L., Clonts, H.A., Enevoldsen, P., et al. (2017). 100% clean and renewable wind, water, and

- sunlight all-sector energy roadmaps for 139 countries of the world. *Joule* 1, 108–121. <https://doi.org/10.1016/j.joule.2017.07.005>.
4. He, G., Lin, J., Sifuentes, F., Liu, X., Abhyankar, N., and Phadke, A. (2020). Rapid cost decrease of renewables and storage accelerates the decarbonization of China's power system. *Nat. Commun.* 11, 2486. <https://doi.org/10.1038/s41467-020-16184-x>.
  5. HM Government. (2020). Energy white paper. Powering our net zero future. <https://www.gov.uk/government/publications/energy-white-paper-powering-our-net-zero-future>.
  6. Engiewende, Agora, and Verkehrswende, Agora; Technical University of Denmark; max-planck-Institute for Biogeochemistry (2020). Making the most of offshore wind: re-evaluating the potential of offshore wind in the German North Sea. <https://www.agora-energiewende.de/en/publications/making-the-most-of-offshore-wind/>.
  7. Musial, W., Heimiller, D., Beiter, P., Scott, G., and Draxl, C. (2016). Offshore wind energy resource assessment for the United States, p. 88, Technical report NREL/TP-5000-66599. <https://www.nrel.gov/docs/fy16osti/66599.pdf> 2016.
  8. EIA (2020). Electric power annual 2019 (Energy Information Administration). <https://www.eia.gov/electricity/annual/pdf/epa.pdf>.
  9. BOEM (2020). Coastal Virginia offshore wind project (CVOW) (United States Department of the Interior, Bureau of Ocean Energy Management). <https://www.boem.gov/renewable-energy/state-activities/coastal-virginia-offshore-wind-project-cvow>.
  10. Barthelmie, R.J., Dantuono, K.E., Renner, E.J., Letson, F.L., and Pryor, S.C. (2021). Extreme wind and waves in U.S. east coast offshore wind energy lease areas. *Energies* 14, 1053. <https://doi.org/10.3390/en14041053>.
  11. Jorgensen, B.H., Holtinnen, H., D'ahlgard, K., Rosenfeldt Jakobson, K., and Marti, I. (2020). IEA Wind TCP Annual Report 2019 (International Energy Agency).
  12. Gaertner, E., Rinker, J., Sethuraman, L., Zahle, F., Anderson, B., Barter, G.E., Abbas, N.J., Meng, F., Bortolotti, P., and Skrzypinski, W. (2020). IEA wind TCP Task 37: definition of the IEA 15-megawatt offshore reference wind turbine (National Renewable Energy Laboratory(NREL)). <https://www.osti.gov/biblio/1603478>.
  13. Jansen, M., Staffell, I., Kitzing, L., Quoilin, S., Wiggelinkhuizen, E., Bulder, B., Riepin, I., and Müsgens, F. (2020). Offshore wind competitiveness in mature markets without subsidy. *Nat. Energy* 5, 614–622. <https://doi.org/10.1038/s41560-020-0661-2>.
  14. Stehly, T., Beiter, P., and Duffy, P. (2020). 2019 cost of wind energy review (National Renewable Energy Laboratory). <https://www.nrel.gov/docs/fy21osti/78471.pdf>.
  15. Barthelmie, R.J., Hansen, K.S., and Pryor, S.C. (2013). Meteorological controls on wind turbine wakes. *Proc. IEEE* 101, 1010–1019. <https://doi.org/10.1109/JPROC.2012.2204029>.
  16. Barthelmie, R.J., and Jensen, L.E. (2010). Evaluation of wind farm efficiency and wind turbine wakes at the Nysted offshore wind farm. *Wind Energy* 13, 573–586. <https://doi.org/10.1002/we.408>.
  17. Thomsen, K., and Sørensen, P. (1999). Fatigue loads for wind turbines operating in wakes. *J. Wind Eng. Ind. Aerodyn.* 80, 121–136. [https://doi.org/10.1016/S0167-6105\(98\)00194-9](https://doi.org/10.1016/S0167-6105(98)00194-9).
  18. Veers, P., Dykes, K., Lantz, E., Barth, S., Bottasso, C.L., Carlson, O., Clifton, A., Green, J., Green, P., Holtinen, H., et al. (2019). Grand challenges in the science of wind energy. *Science* 366, eaau2027. <https://doi.org/10.1126/science.aau2027>.
  19. Lundquist, J.K., DuVivier, K.K., Kaffine, D., and Tomaszewski, J.M. (2019). Costs and consequences of wind turbine wake effects arising from uncoordinated wind energy development. *Nat. Energy* 4, 26–34. <https://doi.org/10.1038/s41560-018-0281-2>.
  20. Miller, L.M., Brunzell, N.A., Mechem, D.B., Gans, F., Monaghan, A.J., Vautard, R., Keith, D.W., and Kleidon, A. (2015). Two methods for estimating limits to large-scale wind power generation. *Proc. Natl. Acad. Sci. USA* 112, 11169–11174. <https://doi.org/10.1073/pnas.1408251112>.
  21. Miller, L.M., and Keith, D.W. (2018). Observation-based solar and wind power capacity factors and power densities. *Environ. Res. Lett.* 13, 104008. <https://doi.org/10.1088/1748-9326/aae102>.
  22. Miller, L.M., and Keith, D.W. (2019). Corrigendum: observation-based solar and wind power capacity factors and power densities (2018 *Environ. Res. Lett.* 13 104008). *Environ. Research Letters* 14, 079501. <https://doi.org/10.1088/1748-9326/aaf9cf>.
  23. Hasager, C.B., Vincent, P., Badger, J., Badger, M., Di Bella, A., Peña, A., Husson, R., and Volker, P.J. (2015). Using satellite SAR to characterize the wind flow around offshore wind farms. *Energies* 8, 5413–5439. <https://doi.org/10.3390/en8065413>.
  24. Platis, A., Siedersleben, S.K., Bange, J., Lampert, A., Bärfuss, K., Hankers, R., Cañadillas, B., Foreman, R., Schulz-Stellenfleth, J., Djath, B., et al. (2018). First in situ evidence of wakes in the far field behind offshore wind farms. *Sci. Rep.* 8, 2163. <https://doi.org/10.1038/s41598-018-20389-y>.
  25. Barthelmie, R.J., Pryor, S.C., Frandsen, S.T., Hansen, K.S., Schepers, J.G., Rados, K., Schlez, W., Neubert, A., Jensen, L.E., and Neckelmann, S. (2010). Quantifying the impact of wind turbine wakes on power output at offshore wind farms. *J. Atmos. Oceanic Technol.* 27, 1302–1317. <https://doi.org/10.1175/2010JTECHA1398.1>.
  26. Pryor, S.C., Shepherd, T.J., Volker, P.J.H., Hahmann, A.N., and Barthelmie, R.J. (2020). "Wind theft" from onshore wind turbine arrays: sensitivity to wind farm parameterization and resolution. *J. Appl. Meteorol. Climatol.* 59, 153–174. <https://doi.org/10.1175/JAMC-D-19-0235.1>.
  27. Wind Europe. (2020). Offshore Wind in Europe key trends and statistics (wind Europe). <https://windeurope.org/wp-content/uploads/files/about-wind/statistics/WindEurope-Annual-Offshore-Statistics-2019.pdf>.
  28. Mytilinou, V., and Kolios, A.J. (2019). Techno-economic optimisation of offshore wind farms based on life cycle cost analysis on the UK. *Renew. Energy* 132, 439–454. <https://doi.org/10.1016/j.renene.2018.07.146>.
  29. Bosch, J., Staffell, I., and Hawkes, A.D. (2019). Global levelised cost of electricity from offshore wind. *Energy* 189, 116357. <https://doi.org/10.1016/j.energy.2019.116357>.
  30. Deutsche WindGuard. (2018). Capacity densities of European offshore wind farms. <https://www.msp-platform.eu/practices/capacity-densities-european-offshore-wind-farms>.
  31. Enevoldsen, P., and Jacobson, M.Z. (2021). Data investigation of installed and output power densities of onshore and offshore wind turbines worldwide. *Energy Sustain. Dev.* 60, 40–51. <https://doi.org/10.1016/j.esd.2020.11.004>.
  32. Wisser, R., Rand, J., Seel, J., Beiter, P., Baker, E., Lantz, E., and Gilman, P. (2021). Expert elicitation survey predicts 37% to 49% declines in wind energy costs by 2050. *Nat. Energy* 6, 555–565.
  33. Nygaard, N.G. (2014). Wakes in very large wind farms and the effect of neighbouring wind farms. *J. Phys.: Conf. Ser.* 524, 012162. <https://doi.org/10.1088/1742-6596/524/1/012162>.
  34. Schneemann, J., Rott, A., Dörenkämper, M., Steinfeld, G., and Kühn, M. (2020). Cluster wakes impact on a far-distant offshore wind farm's power. *Wind Energy. Sci.* 5, 29–49. <https://doi.org/10.5194/wes-5-29-2020>.
  35. Lee, J.C.Y., and Fields, M.J. (2021). An overview of wind-energy-production prediction bias, losses, and uncertainties. *Wind Energy. Sci.* 6, 311–365. <https://doi.org/10.5194/wes-6-311-2021>.
  36. Boutwell, S. (2019). The path forward for offshore wind leasing on the outer continental shelf (Bureau of Ocean Energy Management), June 11, 2019. <https://www.boem.gov/newsroom/notes-stakeholders/message-boems-acting-director-path-forward-offshore-wind-leasing-outer>.
  37. Archer, C.L., Wu, S., Ma, Y., and Jiménez, P.A. (2020). Two corrections for turbulent kinetic energy generated by wind farms in the WRF model. *Mon. Weather Rev.* 148, 4823–4835. <https://doi.org/10.1175/MWR-D-20-0097.1>.
  38. Fitch, A.C., Olson, J.B., Lundquist, J.K., Dudhia, J., Gupta, A.K., Michalakes, J., and Barstad, I. (2012). Local and mesoscale impacts of wind farms as parameterized in a mesoscale NWP model. *Mon. Weather Rev.* 140, 3017–3038. <https://doi.org/10.1175/MWR-D-11-00352.1>.
  39. Tammelin, B., Vihma, T., Atlaskin, E., Badger, J., Fortelius, C., Gregow, H., Hörttanainen, M., Hyvönen, R., Kilpinen, J., Latikka, J., et al. (2013). Production of the Finnish wind atlas. *Wind Energy* 16, 19–35. <https://doi.org/10.1002/we.517>.
  40. Pryor, S.C., Letson, F.W., and Barthelmie, R.J. (2020). Variability in wind energy generation across the contiguous United States. *J. Appl.*

- Meteorol. Climatol. 59, 2021–2039. <https://doi.org/10.1175/JAMC-D-20-0162.1>.
41. Wind Europe. (2020). Wind Energy in Europe in 2019: Trends and Statistics. <https://windeurope.org/wp-content/uploads/files/about-wind/statistics/WindEurope-Annual-Statistics-2019.pdf>.
42. Ahsbahs, T., Maclaurin, G., Draxl, C., Jackson, C.R., Monaldo, F., and Badger, M. (2020). US East Coast synthetic aperture radar wind atlas for offshore wind energy. *Wind Energ. Sci.* 5, 1191–1210. <https://doi.org/10.5194/wes-5-1191-2020>.
43. Volker, P.J.H., Badger, J., Hahmann, A.N., and Ott, S. (2015). The explicit wake parametrisation V1.0: a wind farm parametrisation in the mesoscale model WRF. *Geosci. Model Dev.* 8, 3715–3731. <https://doi.org/10.5194/gmd-8-3715-2015>.
44. Judge, F., McAuliffe, F.D., Sperstad, I.B., Chester, R., Flannery, B., Lynch, K., and Murphy, J. (2019). A lifecycle financial analysis model for offshore wind farms. *Renew. Sustain. Energy Rev.* 103, 370–383. <https://doi.org/10.1016/j.rser.2018.12.045>.
45. Wilks, D.S. (2011). *Statistical Methods in the Atmospheric Sciences* (Academic Press).
46. Sharma, V., Cortina, G., Margairaz, F., Parlange, M.B., and Calaf, M. (2018). Evolution of flow characteristics through finite-sized wind farms and influence of turbine arrangement. *Renew. Energy* 115, 1196–1208. <https://doi.org/10.1016/j.renene.2017.08.075>.
47. Wu, K.L., and Porté-Agel, F. (2017). Flow adjustment inside and around large finite-size wind farms. *Energies* 10, 2164. <https://doi.org/10.3390/en10122164>.
48. Badger, J., and Volker, P.J.H. (2017). Efficient large-scale wind turbine deployment can meet global electricity generation needs. *Proc. Natl. Acad. Sci. USA* 114, E8945. <https://doi.org/10.1073/pnas.1708350114>.
49. Volker, P.J.H., Hahmann, A.N., Badger, J., and Jørgensen, H.E. (2017). Prospects for generating electricity by large onshore and offshore wind farms. *Environ. Res. Lett.* 12, 034022. <https://doi.org/10.1088/1748-9326/aa5d86>.
50. Hersbach, H., Bell, B., Berrisford, P., Hirahara, S., Horányi, A., Muñoz-Sabater, J., Nicolas, J., Peubey, C., Radu, R., Schepers, D., et al. (2020). The ERA5 global reanalysis. *QJR Meteorol. Soc.* 146, 1999–2049. <https://doi.org/10.1002/qj.3803>.
51. Kalverla, P.C., Holtslag, A.A.M., Ronda, R.J., and Steeneveld, G.J. (2020). Quality of wind characteristics in recent wind atlases over the North Sea. *QJR Meteorol. Soc.* 146, 1498–1515. <https://doi.org/10.1002/qj.3748>.
52. Ramon, J., Lledó, L., Torralba, V., Soret, A., and Doblas-Reyes, F.J. (2019). What global reanalysis best represents near-surface winds? *QJR Meteorol. Soc.* 145, 3236–3251. <https://doi.org/10.1002/qj.3616>.
53. Jourdier, B. (2020). Evaluation of ERA5, MERRA-2, COSMO-REA6, NEWA and AROME to simulate wind power production over France. *Adv. Sci. Res.* 17, 63–77. <https://doi.org/10.5194/asr-17-63-2020>.
54. Hahmann, A.N., Sile, T., Witha, B., Davis, N.N., Dörenkämper, M., Ezber, Y., García-Bustamante, E., González-Rouco, J.F., Navarro, J., Olsen, B.T., and Söderberg, S. (2020). The making of the new European wind atlas – part 1: model sensitivity. *Geosci. Model Dev.* 13, 5053–5078. <https://doi.org/10.5194/gmd-13-5053-2020>.
55. Barthelmie, R.J., Grisogono, B., and Pryor, S.C. (1996). Observations and simulations of diurnal cycles of near-surface wind speeds over land and sea. *J. Geophys. Res.* 101, 21327–21337. 337. <https://doi.org/10.1029/96JD01520>.
56. Mehdi, R.A., Schröder-Hinrichs, J.U., van Overloop, J., Nilsson, H., and Pålsson, J. (2018). Improving the coexistence of offshore wind farms and shipping: an international comparison of navigational risk assessment processes. *WMU J. Marit. Affairs* 17, 397–434. <https://doi.org/10.1007/s13437-018-0149-0>.
57. Petruny, L.M., Wright, A.J., and Smith, C.E. (2014). Getting it right for the North Atlantic right whale (*Eubalaena glacialis*): a last opportunity for effective marine spatial planning? *Mar. Pollut. Bull.* 85, 24–32. <https://doi.org/10.1016/j.marpolbul.2014.06.004>.



# Mesoscale modelling of North Sea wind resources with COSMO-CLM: model evaluation and impact assessment of future wind farm characteristics on cluster-scale wake losses

Ruben Borgers<sup>1</sup>, Marieke Dirksen<sup>2</sup>, Ine L. Wijnant<sup>3</sup>, Andrew Stepek<sup>3</sup>, Ad Stoffelen<sup>3</sup>, Naveed Akhtar<sup>4</sup>, Jérôme Neiryneck<sup>1</sup>, Jonas Van de Walle<sup>1</sup>, Johan Meyers<sup>5</sup>, and Nicole P. M. van Lipzig<sup>1</sup>

<sup>1</sup>Department of Earth and Environmental Sciences, KU Leuven, Leuven, Belgium

<sup>2</sup>Department of Geoscience and Remote Sensing, Delft University of Technology, Delft, the Netherlands

<sup>3</sup>Royal Netherlands Meteorological Institute (KNMI), De Bilt, the Netherlands

<sup>4</sup>Institute of Coastal Systems – Analysis and Modeling, Helmholtz-Zentrum Hereon, Geesthacht, Germany

<sup>5</sup>Department of Mechanical Engineering, KU Leuven, Leuven, Belgium

**Correspondence:** Ruben Borgers [redacted]@kuleuven.be)

Received: 27 March 2023 – Discussion started: 6 April 2023

Revised: 14 December 2023 – Accepted: 30 January 2024 – Published: 20 March 2024

**Abstract.** As many coastal regions experience a rapid increase in offshore wind farm installations, inter-farm distances become smaller, with a tendency to install larger turbines at high capacity densities. It is, however, not clear how the wake losses in wind farm clusters depend on the characteristics and spacing of the individual wind farms. Here, we quantify this based on multiple COSMO-CLM simulations, each of which assumes a different, spatially invariant combination of the turbine type and capacity density in a projected, future wind farm layout in the North Sea. An evaluation of the modelled wind climate with mast and lidar data for the period 2008–2020 indicates that the frequency distributions of wind speed and wind direction at turbine hub height are skillfully modelled and the seasonal and inter-annual variations in wind speed are represented well. The wind farm simulations indicate that for a typical capacity density and for SW winds, inter-farm wakes can reduce the capacity factor at the inflow edge of wind farms from 59 % to between 54 % and 30 % depending on the proximity, size and number of the upwind farms. The efficiency losses due to intra- and inter-farm wakes become larger with increasing capacity density as the layout-integrated, annual capacity factor varies between 51.8 % and 38.2 % over the considered range of 3.5 to 10 MW km<sup>-2</sup>. Also, the simulated efficiency of the wind farm layout is greatly impacted by switching from 5 MW turbines to next-generation, 15 MW turbines, as the annual energy production increases by over 27 % at the same capacity density. In conclusion, our results show that the wake losses in future wind farm clusters are highly sensitive to the inter-farm distances and the capacity densities of the individual wind farms and that the evolution of turbine technology plays a crucial role in offsetting these wake losses.

## 1 Introduction

The global capacity of offshore wind technologies has increased more than 10-fold over the previous decade as part of the urgent transition to low-emission energy systems (IPCC, 2022). In 2021, the unprecedented commissioning of over 17 GW of offshore wind capacity pushed the cumulative, global capacity past 50 GW (Musial et al., 2022). In Europe, hosting more than half of that global offshore capacity, annual growth rates are expected to surpass 4 GW per year in 2023 (Komusanac et al., 2021). At the same time, the size and capacity of individual turbines are increasing, with a global average rating of 7.4 MW (8.5 MW in Europe) in 2021 compared to 3.3 MW in 2011 (Komusanac et al., 2021; Musial et al., 2022). As wind turbines offshore are organized in arrays, the total efficiency is impacted by turbine-to-turbine wake effects which strongly depend on the inter-turbine spacing and the size of the wind farm (e.g. Meyers and Meneveau, 2012; Stevens et al., 2016; Antonini and Caldeira, 2021). Currently, limited space and the urgent decarbonization of electricity systems lead to the installation and planning of very dense wind farms (capacity density  $> 10 \text{ MW km}^{-2}$ ) and exceptionally large wind farms (capacity  $> 1 \text{ GW}$ ) that are strongly impacted by these turbine interactions (Borrmann et al., 2018; Komusanac et al., 2020; EMODnet, 2022). On top of that, hotspots such as the North Sea are becoming more densely built (Matthijssen et al., 2018), which amplifies the risk of inter-farm interference through far-field wind farm wakes. These can extend several tens of kilometres (Platis et al., 2018; Schneemann et al., 2020) and can lead to considerable reductions in the wind resource (e.g. Lundquist et al., 2019; Akhtar et al., 2021; Munters et al., 2022). These developments raise questions on the magnitude of intra- and inter-farm wake losses in a future, densely clustered wind farm layout including large wind farms. Mesoscale models have been applied to illustrate the strongly reduced efficiency of very large wind farms (e.g. Volker et al., 2017; Antonini and Caldeira, 2021; Pryor et al., 2021) and how this depends on the turbine spacing (Volker et al., 2017), but also how wind farms can significantly alter the energy yield of neighbouring wind farms (e.g. Akhtar et al., 2021; Fischereit et al., 2022b). In this study, we aim to complement the existing work by quantifying how the long-term effect of wake losses in a hypothetical, future North Sea wind farm layout depends on the characteristics of the individual wind farms and on the inter-farm distances. Concretely, this is done based on a set of continuous simulations for one representative wind year, with each simulation including a different but spatially invariant combination of the turbine type and capacity density for the wind farms in a projected, future wind farm layout. Although the WRF model is the most commonly used mesoscale model for wind energy applications (Fischereit et al., 2022a), it is important to involve several mesoscale models to determine whether signals are robust, especially

when going to climatological timescales. In this study, we make use of the regional climate model COSMO-CLM, which has previously been applied for mesoscale wind farm simulations (Chatterjee et al., 2016; Akhtar et al., 2021, 2022) and also for the modelling of wind and wind resources of the past (e.g. Reyers et al., 2015; Geyer et al., 2015; Li et al., 2016) and future (e.g. Nolan et al., 2014; Santos et al., 2015; Reyers et al., 2016). The quality of mesoscale wind farm simulations relies heavily on the accurate simulation of the background wind climate, which is why these models are typically evaluated with in situ, lidar and/or satellite data (e.g. Hahmann et al., 2015; van Stratum et al., 2022; Dirksen et al., 2022). The COSMO-CLM model has been shown to skilfully reproduce winds from LES (Chatterjee et al., 2016) and measurements by offshore masts (Geyer et al., 2015; Akhtar et al., 2021). However, these evaluations have only considered a limited number of datasets and time periods. Therefore, an additional objective of this study is to extend the evaluation of COSMO-CLM based on a large set of multi-year, spatially distributed mast and wind lidar data and a satellite product covering most of the North Sea. With the focus on the wind resource, the evaluation includes metrics of power production derived from the modelled and measured wind speed data.

## 2 Data and methods

### 2.1 Model description

The development of the regional climate model COSMO-CLM (COSMO version 5.0, CLM version 15) is a joint effort between the Consortium for Small-scale MOdelling (COSMO) and the Climate Limited-area Modelling community (CLM-Community) (Rockel et al., 2008). The Runge–Kutta dynamical core solves the non-hydrostatic, compressible hydro-thermodynamical equations on a rotated latitude–longitude grid (Doms and Baldauf, 2013). Several coordinate systems are available in the vertical dimension, of which we used the height-based, terrain-following coordinate with grid stretching. Additional physical processes were represented with available parametrizations: for subgrid-scale turbulence the standard choice was adopted, which is the one-dimensional diagnostic closure scheme (level 2.5) which is based on a prognostic TKE equation after Mellor and Yamada (1982) as described in Raschendorfer (2001). Surface fluxes were also parametrized and are coupled to the included multi-layer soil model, TERRA-ML. In addition, parametrizations for grid-scale clouds and precipitation, moist convection, and radiative processes were included (Doms et al., 2013). An extensive description of the model system is available in the documentation (e.g. Doms and Baldauf, 2013).

The simulation domain covered a large fraction of the North Sea with a horizontal grid spacing of  $0.025^\circ$  ( $\sim 2.8 \text{ km}$ ) (Fig. 1). In the vertical dimension, 61 levels were



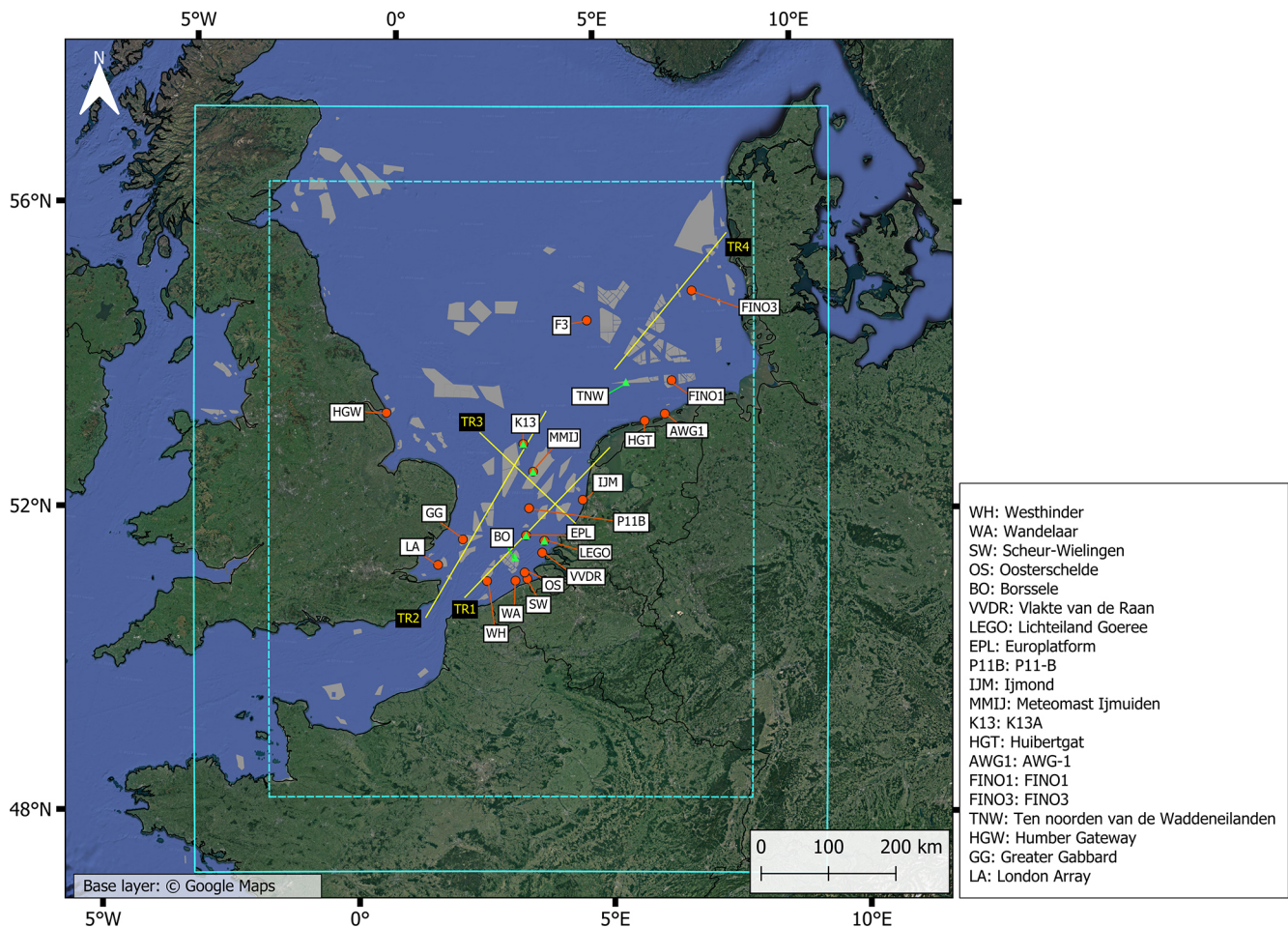


**Figure 1.** Map of the study area showing the simulation domain (cyan, solid line) and the evaluation domain (cyan, dashed line). The locations of the in situ measurement stations (orange dots) and lidar stations (green triangles) that are used for the model evaluation are also indicated, in addition to the hypothetical future wind farm layout (grey polygons) and the four analysis transects TR1–TR4 (yellow lines) used for the wind farm simulations. Created using QGIS3.4.

used up to an elevation of 22 km with a spacing of approximately 20 m near the surface and 30 m at turbine hub height. The relaxation zone at the lateral boundaries was set to a width of 40 km, whereas the spin-up zone was considered an additional 73 km wide, in agreement with the recommendations of Matte et al. (2017). The remaining inner part of the simulation domain was considered for the evaluation and analysis (Fig. 1). The ERA5 reanalysis (Hersbach et al., 2020) was used as forcing at the boundaries with updates every hour. No additional nesting stages were used, in line with results from Brisson et al. (2015). At the meso- $\gamma$  scale, the model resolution partly allows the explicit development of deep convection so that only shallow convection was parametrized according to the scheme of Tiedtke (1989). Switching of the deep convection parametrization on this resolution has previously been shown not to degrade COSMO simulations (Vergara-Temprado et al., 2020). In COSMO5.0, the TKE advection term in the prognostic equation is only

included for the experimental, LES-type turbulence schemes. With the focus on wind farm wake development in the second part of this study, we implemented the TKE advection term for the standard turbulence scheme in COSMO5.0 based on version 5.01.

Specific to this study, we also employed the Fitch wind farm parametrization (WFP; Fitch et al., 2012), which has been implemented in COSMO5-CLM15 (Chatterjee et al., 2016; Akhtar and Chatterjee, 2020). This additional module represents the wind farm forcing on the atmosphere as a sink of kinetic energy and a source of TKE. Although it has been suggested to reduce the TKE coefficient in the parametrization based on a comparison with large eddy simulations (LES) (Archer et al., 2020), the original value was retained in this study, as other studies did not find that this leads to better performance (Siedersleben et al., 2020; Larsén and Fischereit, 2021). Several other wind farm parametrizations exist (Fischereit et al., 2022a), and it has been shown



that the modelled wind speed deficits inside and behind a wind farm can vary substantially from the Fitch WFP (Ali et al., 2023). However, validation of the Fitch WFP with offshore masts, lidars and airborne measurements in the wake of a wind farm has shown very good performance for HARMONIE-AROME as wind speed biases are strongly reduced (van Stratum et al., 2022; Dirksen et al., 2022). This good performance has also been determined in WRF by comparing to offshore masts (Garcia-Santiago et al., 2022) and in COSMO-CLM by comparing to LES (Chatterjee et al., 2016) and airborne measurements (Akhtar et al., 2021). Wind speed reductions inside of a wind farm have also been shown to agree well with airborne measurements (Ali et al., 2023), mast measurements (Dirksen et al., 2022) and RANS simulations (Fischereit et al., 2022c). Moreover, comparisons with other WFP schemes show that Fitch generally outperforms these other schemes, both inside a wind farm and in the farm wake (Fischereit et al., 2022c; Ali et al., 2023). For a detailed overview of the performance validation of this parametrization, we refer to the review of Fischereit et al. (2022a).

## 2.2 Evaluation run

To evaluate the model performance, a simulation was performed for a period of 13 years (2008–2020). Data from in situ, lidar and satellite measurements over the North Sea are abundant in both space and time for this period. Additionally, the length of the simulation ensures that a large variation in wind conditions, as described in e.g. Geyer et al. (2015) and Ronda et al. (2017), is sampled. The wind farm parametrization was excluded in this simulation because a time-static wind farm layout cannot represent the rapidly growing wind farm layout over this time period and most observations were representative for wind-farm-free conditions. Hence, only the undisturbed wind climate was evaluated, and the observations were filtered accordingly, which will be discussed in more detail in Sect. 2.4.1. The instantaneous wind field around hub height was written to output at a 10 min frequency following the standard for wind energy assessments (Menezes et al., 2020).

## 2.3 Wind farm simulations

The projected future wind farm layout used in the wind farm simulations was constructed from the EMODnet wind farm dataset (EMODnet, 2022) and GIS data from the Royal Belgian Institute for Natural Sciences (Vigin, 2022) (Fig. 1). Next to the operational wind farms today, this layout incorporates the concessions that are in different stages of the construction process, zones for which consent has been authorized and also large development zones. Because the wind farm parametrization assumes that turbines within a single grid cell never have any wake interactions, no additional information is required on the layout of the turbines in each wind farm. The turbines were assumed constantly op-

erational, unless the wind speed was below the cut-in wind speed or above the cut-out wind speed. Considering the computational cost of these experiments, the time span was limited to one representative year in terms of the North Sea wind field. This year was determined in a procedure based on the one outlined in Tammelin et al. (2013). We used 31 years of hourly, hub-height wind fields from the ERA5 reanalysis (1990–2020) to compute a metric  $R$  for the representativeness per year and per grid cell:

$$R_{i,j,y} = \frac{S1_{i,j,y}}{\sigma_{S1}} + \frac{S2_{i,j,y}}{\sigma_{S2}} + \frac{S3_{i,j,y}}{\sigma_{S3}}, \quad (1)$$

where the indices  $i$ ,  $j$  and  $y$  refers to a specific grid cell and year. These  $R$  values were computed per year for each North Sea grid cell between 51 and 55.5° latitude. Higher values of  $R$  correspond to more representative years. The different scores (S1–S3) are based on the agreement between single-year and the long-term (31 year) histograms as computed by the Perkins skill score:

$$PSS(H_1, H_2) = \sum_{b=1}^n \text{MIN}\left(F_{H_1}^b, F_{H_2}^b\right), \quad (2)$$

where  $H_1$  and  $H_2$  represent the first and second histogram and  $F^b$  represents the normalized frequency for bin  $b$ . The PSS represents the fraction of overlap between the two histograms, so that a PSS of 1 (or 100 %) represents complete overlap. For one-dimensional histograms, this metric is connected to the Earth mover's distance (EMD) metric, which in contrast represents the area of mismatch between two histograms (Rabin et al., 2008). S1 is the PSS between a wind speed histogram for a single-year and the multi-year wind speed histogram, using a bin width of 0.5 m s<sup>-1</sup>. S2 is the same as S1 but for wind direction, using a bin width of 30°. Finally, S3 represents the mean PSS between the single- and multi-year wind speed distributions over 12 wind direction sectors. The scores (S1–S3) are standardized by the standard deviation to give each term in the sum equal weight. Summation of  $R$  over all grid cells then yields a representativeness for a specific year. The different scores and the final score per year are summarized in Figs. S1 and S2 in the Supplement, respectively. Based on this procedure, the year 2016 was selected for the simulations, as the representativeness is high overall for this year (Fig. S1). In addition, the representativeness is especially high for wind direction (Fig. S2), which is particularly important for the study of inter-farm wake interactions.

Five simulations were performed, consisting of one simulation without wind farms (NOWF) and four simulations using a fixed wind farm layout with the same turbine type and capacity density for all wind farms (Table 1). Based on the number of turbines, the total capacity and the surface area of operational wind farms in the North Sea, a median turbine capacity of 4.85 MW and a representative capacity density of 8.1 MW km<sup>-2</sup> were determined. The 5 MW refer-

**Table 1.** Summary of the turbine type and capacity density used in the different wind farm model simulations.

Identifier	Turbine type	Capacity density (MW km <sup>-2</sup> )
NOWF	–	–
NREL8.1	NREL 5 MW	8.1
IEA3.5	IEA 15 MW	3.5
IEA8.1	IEA 15 MW	8.1
IEA10.0	IEA 15 MW	10

ence wind turbine of the National Renewable Energy Laboratory (NREL) (Jonkman et al., 2009)) with a hub height of 90 m and a rotor diameter of 126 m was therefore used in conjunction with the aforementioned capacity density in one of the wind farm simulations (NREL8.1). Three additional cases were simulated in which the NREL 5 MW was replaced by the 15 MW reference wind turbine of the International Energy Agency (IEA) (Gaertner et al., 2020) with a hub height of 150 m and a rotor diameter of 240 m, as 15 MW turbines are expected to reach the market in a few years and are now being selected for upcoming projects (Bento and Fontes, 2019; Shields et al., 2021). The power curves of these three turbines are available in Fig. S3. The three cases with 15 MW turbines were simulated with a different wind farm capacity density.

- *IEA3.5: low capacity density in which the inter-turbine distance is 10 rotor diameters.* This turbine spacing is larger than is found in most offshore wind farms today and corresponds to a lower cost per unit energy production as the impact of turbine wakes is reduced and is most relevant in regions where offshore space is relatively abundant, such as for the United Kingdom or Denmark (Borrmann et al., 2018).
- *IEA8.1: the same capacity density as for the NREL8.1 scenario.*
- *IEA10.0: high capacity density with a larger revenue per unit area but also increased wake-related losses.* This corresponds to a capacity density for planned projects in regions where the available space is limited, such as Belgium, the Netherlands and Germany (Borrmann et al., 2018).

Based on the different simulations, the impact of the turbine type and capacity density on the wake losses was assessed. In addition, the roles of wind farm size and inter-farm distance in these wake losses were investigated based on the large variation in these properties over the wind farm layout. The different simulations were compared along the transects indicated on Fig. 1, which correspond to dominant but also strongly disturbed wind directions, i.e. directions along which the wind farms are densely clustered. For this analysis, only winds in a sector of 30° around the transect

orientation (SW to NE for TR1, TR2 and TR4 and NW to SE for TR3) were selected based on the centre grid cell on the transect. The data selection based on the wind direction reduced the dataset to approximately 14 % of the total for transects TR1, TR2 and TR4 and to 8.1 % for TR3. Additionally, this transect analysis was extended to three stability classes based on the bulk Richardson number ( $R_B$ ), a metric for the dynamic stability, which will be discussed in more detail in Sect. 2.5.3.

## 2.4 Measurement data

### 2.4.1 In situ masts

Wind measurements of 19 in situ stations (Fig. 1) were obtained from the KNMI data platform, Meetnet Vlaamse Banken, the Marine Data Exchange, the FINO data platform and the TNO wind energy data platform (Table A1). Of these 19 stations, 6 were actual meteorological masts with measuring devices at multiple altitudes. The remaining stations correspond to coastal measurement poles and instrumentation mounted on oil, gas or light platforms and provide information at a single altitude. Average wind speed and wind direction are available at 10 min intervals. A timeline of the data availability is summarized for each station in Fig. S4. For most stations, corrections were applied to the measurements of the boom- or platform-mounted anemometers and wind vanes in order to account for flow distortions by the mast or other mounting infrastructure. These corrections were performed by the data providers for the stations FINO1 and FINO3 (Westerhellweg et al., 2012; Leiding et al., 2016), MMIJ (Werkhoven and Verhoef, 2012), WH and WA. For the remaining stations with multiple anemometers per height level, we avoided using measurements in the wake of the mast or other infrastructure by selecting the measurement with the highest 10 min average wind speed. A possible drawback of this approach is that the measured wind speed is overestimated in the case of lateral speed-up effects (Leiding et al., 2016). If wind direction was provided with respect to magnetic north, a magnetic-to-true north correction was applied according to the location and timing of the dataset. Finally, because no wind farm parametrization was included in the evaluation run, measurements potentially taken in the wake of wind farms were omitted from the dataset by filtering out either a specific time range or a directional sector. These dataset corrections are summarized in Table S1 in the Supplement. A station-to-farm distance threshold of 50 km was chosen to perform these corrections, as it is expected that the impact of wind farm wakes on the long-term wind speed statistics becomes relatively unimportant at this distance (Schneemann et al., 2020; Dirksen et al., 2022). The total uncertainty on the wind speed measurements is a combination of the uncertainties of calibration, mounting (including flow obstruction by the mast), data acquisition and the local site conditions. This total uncertainty can vary signifi-

cantly between the stations. For the class 0.9A anemometers at station MMIJ the total uncertainty was estimated at 1.5 % for the top anemometer and 1.9 % for the boom-mounted anemometers (Duncan et al., 2019). For the top anemometers of the other meteorological masts, which have a comparable class number as for MMIJ (Friis Pedersen et al., 2006), we applied the same value of 1.5 % as the uncertainty estimate. As the boom-mounted anemometers at the FINO stations were also mast-corrected prior to use, we adopted the same value of 1.9 %. The mounting uncertainty for boom anemometers at stations GG, LA and HGW is expected to be larger because we only performed a simple correction. Assuming an additional 2 % uncertainty on the mast correction, this leads to a total uncertainty of 3.7 %. For the remaining stations, we assumed a calibration uncertainty of 1.5 % (Coquilla et al., 2007), an operational uncertainty of 0.8 % (Friis Pedersen et al., 2006) and an augmented 2 % uncertainty on the data acquisition due to limited information on acquisition and post-processing. For AWG1, P11B and WH a mounting uncertainty of 5 % was estimated due to presence of lateral flow obstructions. For the other stations, where the device is mounted on the top of a platform or platform-mounted mast, a mounting uncertainty of 2 % was assumed following Verkaik (2001).

#### 2.4.2 Wind lidar

In addition to the cup anemometers, measurements from six wind lidars were used for the evaluation (Fig. 1). These lidars use light beam scanning technology to derive vertical profiles of wind speed and direction at regular height intervals and allow evaluation of the wind field above the typical 90 m top of meteorological masts. As for the in situ measurements, wind speed and direction are provided as 10 min averages. The data were obtained from the Dutch services TNO wind energy and Rijksdienst voor Ondernemend Nederland (RVO). The lidars were installed during the pre-construction stages of offshore wind farm development (Table A2). The LEGO, MMIJ, K13 and EPL lidars are installed on the same platforms as the cup anemometers (Table A1). The BO and TNW lidars are floating lidars and are mounted on a Fugro SEA-WATCH buoy. Estimates of the uncertainty are from Wouters and Verhoef (2019a, b, c) for LEGO, EPL and K13; from Poveda and Wouters (2015) for MMIJ; and from the report by Dhirendra (2014) for the floating lidars BO and TNW.

#### 2.4.3 ASCAT

The Advanced SCATterometer (ASCAT) sensor on the European MetOp satellites uses radar technology to determine the near-surface wind speed and direction over the sea (Gellsthorpe et al., 2000; Figa-Saldaña et al., 2002). Although the ASCAT product only provides information on the surface wind, it complements the in situ and lidar data as it covers most of the North Sea basin. For this study, we considered

the L3-reprocessed ascending and descending passes of the MetOp-A satellite from the website of the Copernicus Marine Service (CMEMS). The satellite was operational for the complete 13 years of this simulation. Specifically, the variant on a 12.5 km grid with a horizontal grid spacing of 25 km was used, which has been validated against buoy measurements (Verhoef and Stoffelen, 2009). The long-term instrumental stability is estimated to be below  $0.1 \text{ m s}^{-1}$  for this product, whereas the climatological uncertainty is  $\pm 0.1 \text{ m s}^{-1}$ , with some anomalies of  $+1 \text{ m s}^{-1}$  at the Dutch coast. The datasets for both passes together provide roughly one instantaneous measurement per day for most of the North Sea that we consider (4500 samples in total). Only close to the coasts is data coverage much lower (100–3000 samples), which is a well-known issue with remotely sensed winds related to contamination with land signal (Bourassa et al., 2019).

### 2.5 Evaluation approach

#### 2.5.1 Model collocation with in situ and lidar

Over a 10 min period, the wind travels over a distance comparable to the edge length of a  $0.025^\circ$  grid cell. Because the model wind components represent smoothed grid box averages, the 10 min time averages of the observations were directly compared to instantaneous values of the grid cell in which the station is located. In the case of gaps in the time series of the in situ and lidar data, the corresponding time steps were also eliminated from the model grid point time series. The model wind speed data were interpolated to the measurement heights using the wind profile power law:

$$V_s = V(h_m) \cdot \left( \frac{h_s}{h_m} \right)^\alpha, \quad (3)$$

where  $V_s$  is the wind speed at sensor height,  $V(h_m)$  is the wind speed at the first model level below sensor height and  $\alpha$  is the shear coefficient which is computed as

$$\alpha = \frac{\ln(V(h_{m+1})/V(h_m))}{\ln(h_{m+1}/h_m)}, \quad (4)$$

where  $m+1$  denotes the first model level above sensor height. In contrast to the wind speed, the model wind direction at sensor height was computed after linear interpolation of the horizontal wind components of the model levels just above and below sensor height. The Zephir 300S lidar has a well-known  $180^\circ$  ambiguity that can occur in the wind direction time series as it relies on a sonic anemometer just above the lidar to determine the sign of the wind vector. In the case of low wind speeds and/or flow obstructions, it is possible that the incorrect sign is determined and the lidar's wind direction is  $180^\circ$  off (Knoop et al., 2021). We corrected this  $180^\circ$  error by adding or subtracting  $180^\circ$  if the wind direction in the measurements differs more than  $90^\circ$  from the modelled wind direction ( $\sim 2\%$  occurrence) after Dirksen et al. (2022).

### 2.5.2 Model collocation with ASCAT and triple collocation

For the comparison with ASCAT, the model surface winds were regridded to the 12.5 km grid of the measurements with first-order conservative remapping. This ensures that all the source grid cells contained within a target grid cell have similar weight in the regridding, in agreement with the ASCAT winds being computed from the signal of this complete area. Afterwards, the measurement time series of each ASCAT grid cell was matched by a model time series for that same grid cell by linear interpolation in time.

Additionally, a comparison between the model, ASCAT and in situ data was conducted at stations WH, EPL and MMIJ. These stations were selected because the location is far enough from the coast to ensure sufficient data points in the ASCAT data and the measurement height is close to 10 m, which reduces any vertical extrapolation errors to 10 m in the in situ data. This extrapolation was done using the power law with a constant shear coefficient of 0.11. The in situ data were then also linearly interpolated to the ASCAT measurement times, and all datasets were limited to the timings where both ASCAT and in situ measurements are available. Finally, the grid cells in which the stations are located were selected from the model and ASCAT datasets for the comparison.

### 2.5.3 Stability classification

The comparison between COSMO-CLM and the measurements in terms of wind speed was further extended to different classes of atmospheric, dynamic stability because the stability strongly determines the wind conditions over the North Sea (Stull, 1988; Sathe et al., 2011) and also determines the atmospheric response to a wind farm forcing (Platis et al., 2021). This stability classification was done based on the bulk Richardson number ( $R_B$ ), which is computed as

$$R_B = \frac{\frac{g}{\theta_v} \frac{\Delta\theta_v}{\Delta z}}{\left(\frac{\Delta u}{\Delta z}\right)^2 + \left(\frac{\Delta v}{\Delta z}\right)^2}, \quad (5)$$

where  $g$  corresponds to the gravitational constant,  $\theta_v$  is the virtual potential temperature,  $z$  is height, and  $u$  and  $v$  are the zonal and meridional wind speed components, respectively. The overbar over the virtual potential temperature denotes that it is averaged over the four model layers between 50 and 150 m height. Finally, the gradients in  $u$ ,  $v$  and  $\theta_v$  were determined by averaging the gradients between each of the subsequent layers between 50 and 150 m. Based on the ( $R_B$ ), we can identify three distinct dynamic stability regimes (Grachev et al., 2013; Dirksen et al., 2022).

- *Unstable*:  $R_B < 0$ . This is the case when the temperature gradient is negative, which corresponds to an unstable thermal stratification.

- *Weakly stable*:  $0 \leq R_B \leq 0.25$ . This is the case when the temperature gradient is positive, but the temperature effect is weak compared to the vertical wind shear. In this case, the wind-shear-generated turbulence is relatively strong compared to the buoyant damping.
- *Stable*:  $R_B > 0.25$ . This is the case when the temperature gradient is positive and strong compared to the vertical shear. In this case, the wind-shear-generated turbulence is strongly damped, and this region of the ABL can be considered dynamically stable.

Gradients were calculated based on potential temperature instead of virtual potential temperature as an analysis of the driving data showed minimal variations of specific humidity over the considered height range. A comparison of the modelled temperature gradients with measured temperature gradients at station MMIJ between 90 and 21 m a.m.s.l. shows a good correspondence in the long-term temperature gradient probability distribution, indicating sufficient model skill for this subdivision into stability classes (Fig. S5). Because vertical profiles of pressure and temperature are generally not available over the range of the meteorological masts or wind lidar scanning ranges, the stability criterion can only be computed for the model. Based on a good temporal correlation between the temperature gradients of COSMO-CLM and measurement mast MMIJ (Pearson correlation coefficient = 0.85), the time steps matched to a stability class for the model grid cell nearest to each measurement location were also matched to that stability class for the measurement data.

### 2.5.4 Evaluation metrics

We compared the magnitudes of the mean wind speed difference and the observational uncertainty to identify any model bias: an exceedance of the observational uncertainty at a measurement station was used as the threshold for the presence of a model bias at that location. In addition, the PSS (Sect. 2.3) was employed as a metric to express the agreement in the shape of two histograms of either wind speed or wind direction.

Because the relationship between wind speed and wind turbine power production is non-linear, we also evaluated differences between COSMO-CLM and the observations in terms of the capacity factor, which is given by

$$CF = 100 \frac{\sum_{i=1}^n P(V_i)}{nP(V_r)} [\%], \quad (6)$$

where  $V_i$  is the hub-height wind speed at some instance  $i$  in the time series;  $V_r$  is the rated wind speed; and  $P$  is the generated power, which is a turbine-specific function of the wind speed. So, the capacity factor is the ratio between the power production of a specific turbine based on a wind speed time



series and the theoretical, maximum power production over that same period, i.e. for a turbine continuously operating at full capacity. This is an idealized notion of the capacity factor as it concerns an isolated turbine which constantly operates according to the power curve. For these calculations, we considered the power curve of the NREL 5 MW reference wind turbine, with a hub height of 90 m, for the meteorological masts with the top anemometer below 100 m and the power curve of the DTU 10 MW reference wind turbine (Bak et al., 2013), with a hub height of 119 m, for FINO1, FINO3 and the wind lidars (Fig. S3). An uncertainty range on the capacity factor based on the observed wind speeds was determined based on the uncertainty on the wind speed measurements: the observed wind speed distribution was shifted linearly by the product of the uncertainty and the mean wind speed after which upper and lower bounds on the capacity factor were computed. As the capacity factor is a percentage, absolute differences are also a percentage, so to avoid confusion it is always explicitly stated whether absolute or relative differences in the capacity factor are considered.

### 3 Results and discussion

#### 3.1 Model evaluation

This subsection covers the model performance evaluation. First, the general evaluation based on all validation sources and the complete height range (10 to 290 m) is described. This is followed by a more detailed performance analysis at turbine hub height ( $\sim 100$  m), and finally the evaluation is extended to the different atmospheric stability classes.

The difference in the long-term mean wind speed between the in situ and lidar stations varies with height (Fig. 2). Below 90 m, the difference is generally negative (model underestimates the mean) and exceeds the measurement uncertainty range, indicating a model bias to lower wind speeds. However, the magnitude of the bias generally drops with increasing altitude over the considered height range, albeit with some exceptions (MMIJ, TNW). At measurement heights at or above 90 m, the difference is generally smaller and falls within the uncertainty range of the measurements. The gradient with height persists and the difference is positive above 130 m at the locations of the wind lidars. Although differences over height are substantial, there is no robust indication of regional differences in the ability of COSMO-CLM to model the climatological mean wind speed. The same figure but with relative differences is included in the Supplement (Fig. S6).

The mean difference between COSMO-CLM and the ASCAT data is between  $-0.5$  and  $0.5 \text{ m s}^{-1}$  for most grid cells (Fig. 3). For approximately 45 % of the grid cells the mean difference is within the ASCAT climatological uncertainty of  $\pm 0.1 \text{ m s}^{-1}$ . These grid cells are generally located farther from the coast and correspond to the regions without in situ measurements, which is an indication of good model

performance in this region. The model underestimation near the surface that was identified against the in situ data in the southern North Sea is much smaller than the differences compared to ASCAT in this region (cf. Figs. 2 and 3). A three-way comparison with three in situ stations shows that the mean differences against the in situ data exceed the in situ measurement uncertainty for both COSMO-CLM and ASCAT (Fig. 3). Whereas COSMO-CLM generally underestimates the mean near-surface wind speed, ASCAT overestimates it with a larger magnitude, which explains the differences in PSS values. The PSS values are similar when both COSMO-CLM and ASCAT are corrected for the systematic bias with respect to the in situ data, which indicates that both perform similarly in approximating the distribution shape of the in situ data.

The distributions of wind speed near 100 m height match well with the meteorological masts and lidar stations in most cases (Fig. 4), leading to a PSS generally above 95 %. The associated absolute differences in the idealized capacity factor are within the uncertainty based on the wind speed measurements for 4 out of 10 stations. For FINO1, K13, MMIJ and HGW the differences are outside the uncertainty range, but the deviations from the lower bound of the uncertainty range are less than 1 %, while the deviations are higher for the GG and LA masts. For K13 and HGW the capacity factor difference exceeds the capacity factor uncertainty, whereas the mean wind speed difference is within the wind speed uncertainty, which can be linked to the non-linear relationship between wind speed and power production.

Although the inter-annual variability of the annual mean hub-height wind speed is typically around  $1 \text{ m s}^{-1}$ , the corresponding variability in the wind speed bias between the model and the measurements is typically around  $0.1 \text{ m s}^{-1}$  or 10 % of that value (Table 2). The corresponding overlap between the single-year histograms generally does not vary more than 2 % over the years. Hence, the agreement in distribution location and shape between COSMO-CLM and the measurements remains consistent over consecutive years, regardless of the inter-annual variability in the wind conditions.

The intra-annual cycle in the wind speed distribution is also well represented by the model (Fig. 5). The gradual seasonal variation from higher (winter) to lower (summer) median wind speeds is accurately reproduced in addition to the variation in distribution width ( $Q_{25}$ – $Q_{75}$  range) and more extreme conditions ( $Q_5$  and  $Q_{95}$ ). Moreover, in extreme months the model also succeeds in modelling the wind speed distribution as can be deduced from Fig. 5b at station TNW for February 2020, albeit with a heavier right tail and consequently more winds above the cut-out wind speed.

Evaluation of the long-term wind direction histograms near turbine hub height (using a bin width of  $20^\circ$ ) shows an overlap of 95 % or more in most cases (Table 3) with the magnitude of the bias generally below  $4^\circ$ . A reason for the stronger deviation at FINO3 and EPL has not been identified. Because the considered measurements vary sub-

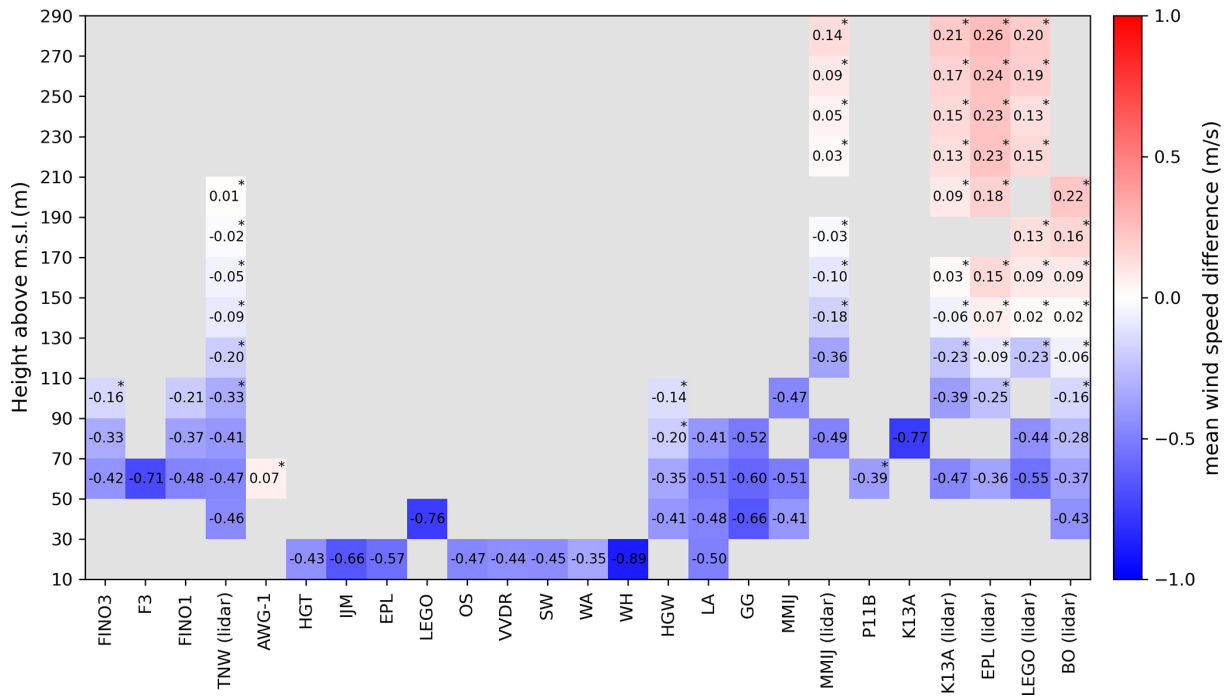


**Figure 2.** Wind speed bias ( $\text{m s}^{-1}$ ) for the complete time span of each measurement dataset. This concerns measurements between 10 and 290 m a.m.s.l. The vertical range is subdivided into 20 m intervals for readability. The presence of an asterisk indicates that the bias is within the measurement uncertainty. Stations are clustered per region. The considered time periods for each measurement dataset can be found in Tables A1 and A2.

**Table 2.** Inter-annual range of the mean wind speed and of the agreement between the model and observations, as expressed by the minimum/maximum annual mean difference and the minimum/maximum annual PSS for the different years in the measurement period.

Station	Period (NR years)	Annual mean ( $\text{m s}^{-1}$ )		Mean difference ( $\text{m s}^{-1}$ )		PSS (%)	
		MAX	MIN	MAX	MIN	MAX	MIN
FINO3 (107 m)	2010–2013 (4)	11.2	9.5	-0.11	-0.22	98	97
MMIJ (92 m)	2012–2015 (4)	10.3	9.8	-0.44	-0.50	96	94
K13 lidar (115 m)	2018–2020 (3)	10.4	9.9	-0.2	-0.28	97	97
LEGO lidar (115 m)	2015–2020 (6)	11.1	9.2	-0.18	-0.28	97	95
LA (82 m)	2008–2010 (3)	9.5	8.6	-0.32	-0.47	95	93

stantially in measurement height, i.e. from 62 m a.m.s.l. up to 120 m a.m.s.l., this comparison indicates consistency of the good performance with height. The variations of the wind speed statistics with the wind direction are also captured by the model (Fig. S7). This accurate reproduction of the wind direction distributions and the direction-dependent wind speed distributions is encouraging for the application to wind farm modelling as wind farm shapes are tailored to the regional wind climate.

The general differences in mean wind speed profiles for the three stability classes agree well between the model and the measurements (Fig. 6): winds are strongest under weakly stable conditions and weakest under stable conditions, with the wind speeds under unstable conditions falling in between.

The agreement between the profiles of the model and the measurements differs between the stability classes: under stable conditions the shear in the model is too strong between 40 and 200 m, leading to a negative model bias below 160 m for EPL and LEGO and below 180 m for K13 and TNW. Around 100 m, the respective underestimations are at least  $-0.3$  and  $-0.6 \text{ m s}^{-1}$ . Such an underestimation under stable conditions is not uncommon for climate models (Wijnant et al., 2014; Sheridan et al., 2021). For weakly stable conditions, there is not a clear bias around 100 m, but the deviations below 90 m and above 150 m are outside of the observational uncertainty. The small vertical gradient under unstable conditions is represented well by the model with only small deviations that are well within the measurement



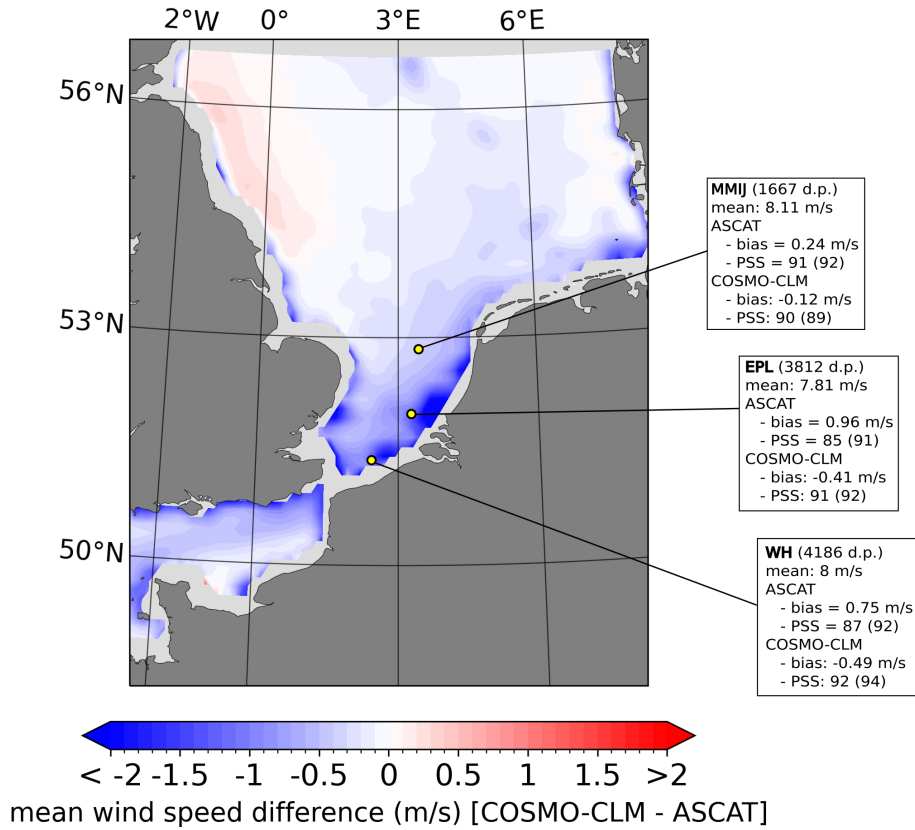


**Figure 3.** Difference in long-term mean wind speed between COSMO-CLM and ASCAT. Yellow dots indicate the measurement stations for triple collocation. The text boxes summarize the mean 10m wind speed for three in situ stations and the agreement of ASCAT and COSMO-CLM in terms of the mean difference and the PSS. The PSS values between brackets are after elimination of the mean difference between the two histograms to remove the effect of distribution location.

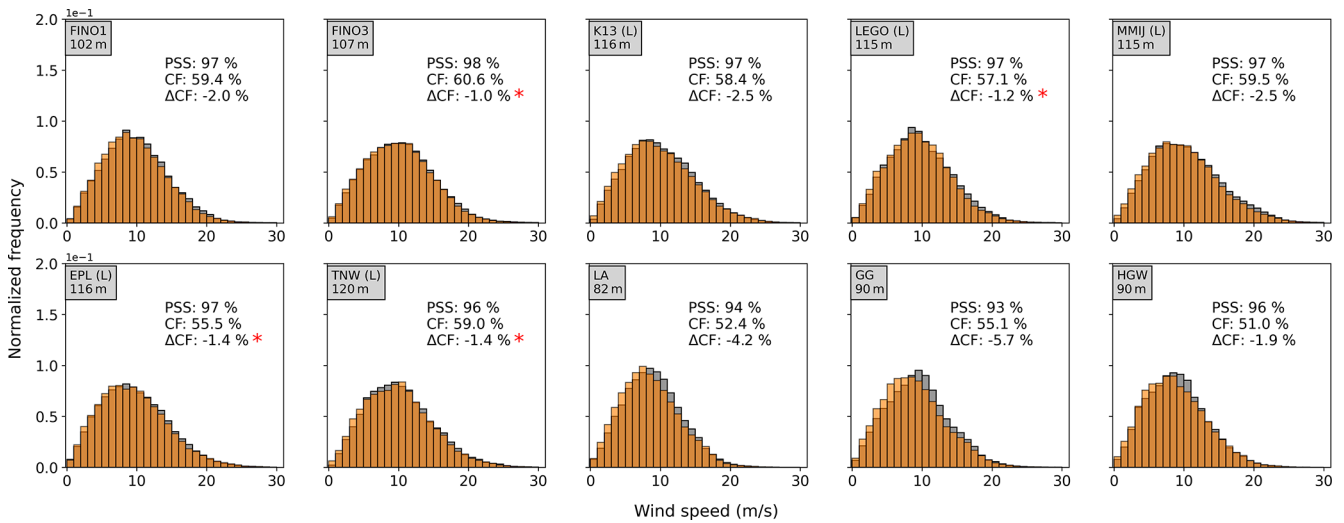


**Figure 4.** Histograms of the collocated wind speed datasets. Orange: overlap between the histograms; light orange: only COSMO-CLM; grey: only the measurements. In addition, the associated PSS, the capacity factor based on the measured wind speeds and the absolute difference in capacity factor between the model and the measurements are indicated. The presence of a red asterisk indicates that the capacity factor difference falls within the uncertainty on the capacity factor for the measurements.

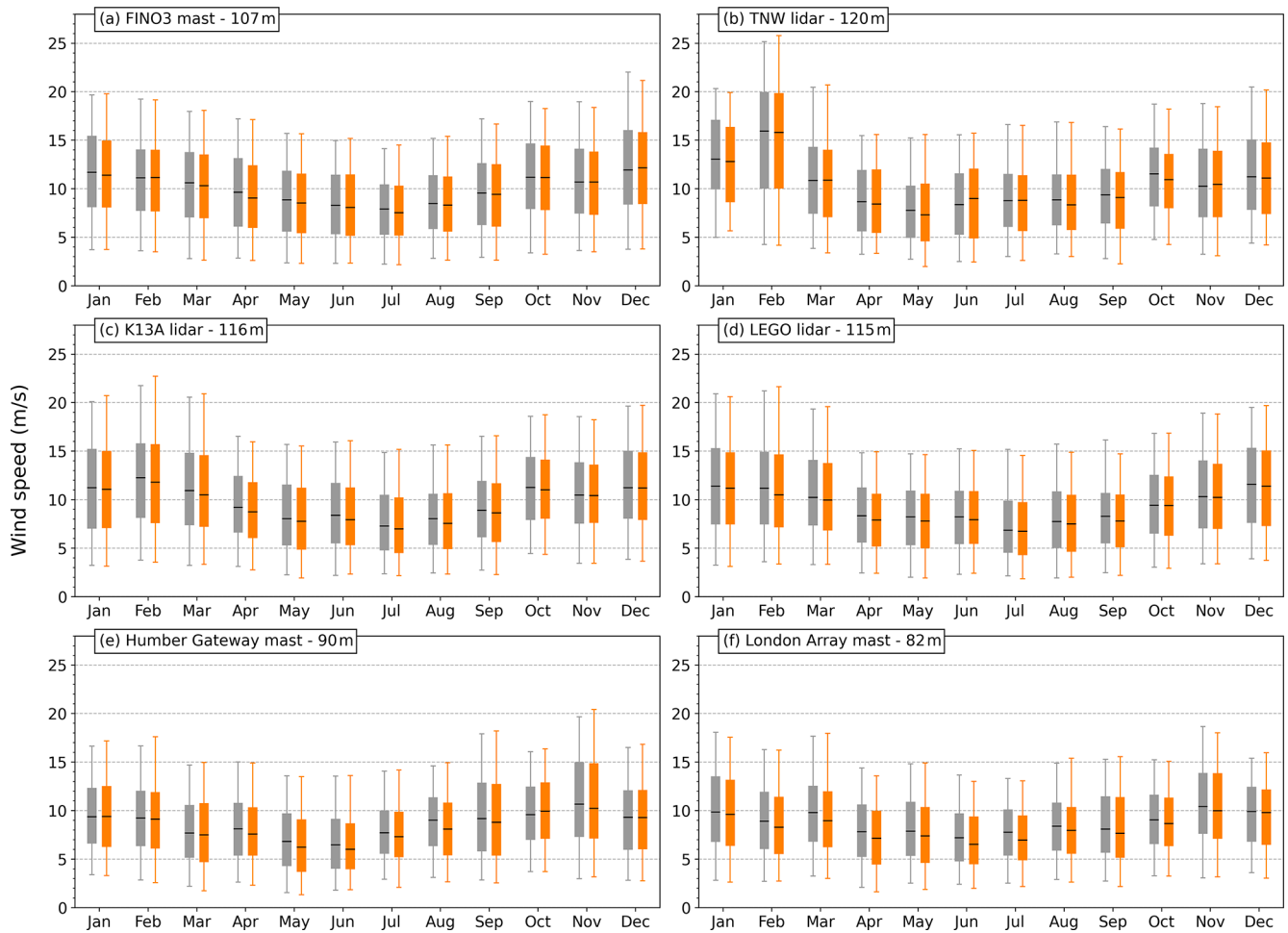


**Figure 5.** Boxplots representing the multi-year wind speed distribution per month for the observations (grey) and the model (orange). Shown for the three masts and three lidar stations at turbine hub height. The box corresponds to the  $Q_{25}$ – $Q_{50}$ – $Q_{75}$  wind speeds. The lower and upper whiskers are the  $Q_5$  and the  $Q_{95}$  percentiles, respectively.

**Table 3.** Bias in the wind direction (model – observations) and the Perkins skill score between the histograms of wind direction (bin width = 20°).

Station	Bias (°)	PSS (%)
FINO3 (101 m)	–8.0	96
FINO1 (91 m)	1.9	95
TNW lidar (120 m)	–4.0	97
K13A lidar (116 m)	–2.2	97
MMIJ lidar (115 m)	1.0	96
EPL lidar (116 m)	8.7	93
LEGO lidar (115 m)	0.7	96
London Array (78 m)	–1.9	96
Humber Gateway (86 m)	2.3	96
Greater Gabbard (62 m)	–3.5	97

uncertainty over the complete height range. The hub-height wind speed distributions as reflected in the boxplot mainly differ in distribution location, with the strongest differences under stable conditions. Corresponding capacity factor values were calculated with lower and upper uncertainty bounds for the observations (Fig. S8). Under stable conditions, the deviations between the model and observations exceed the uncertainty range, so the absolute model underestimation of the capacity factor is at least 2.5 %. For unstable and weakly stable conditions, the deviations are within the uncertainty range.

### 3.2 Impact of wind farm characteristics on cluster-scale wake losses

This subsection covers the results of the wind farm simulations. First, the impact of the NREL8.1 base scenario on the wind climate and wind resource is described, also under different atmospheric stability conditions. Afterwards, the dif-

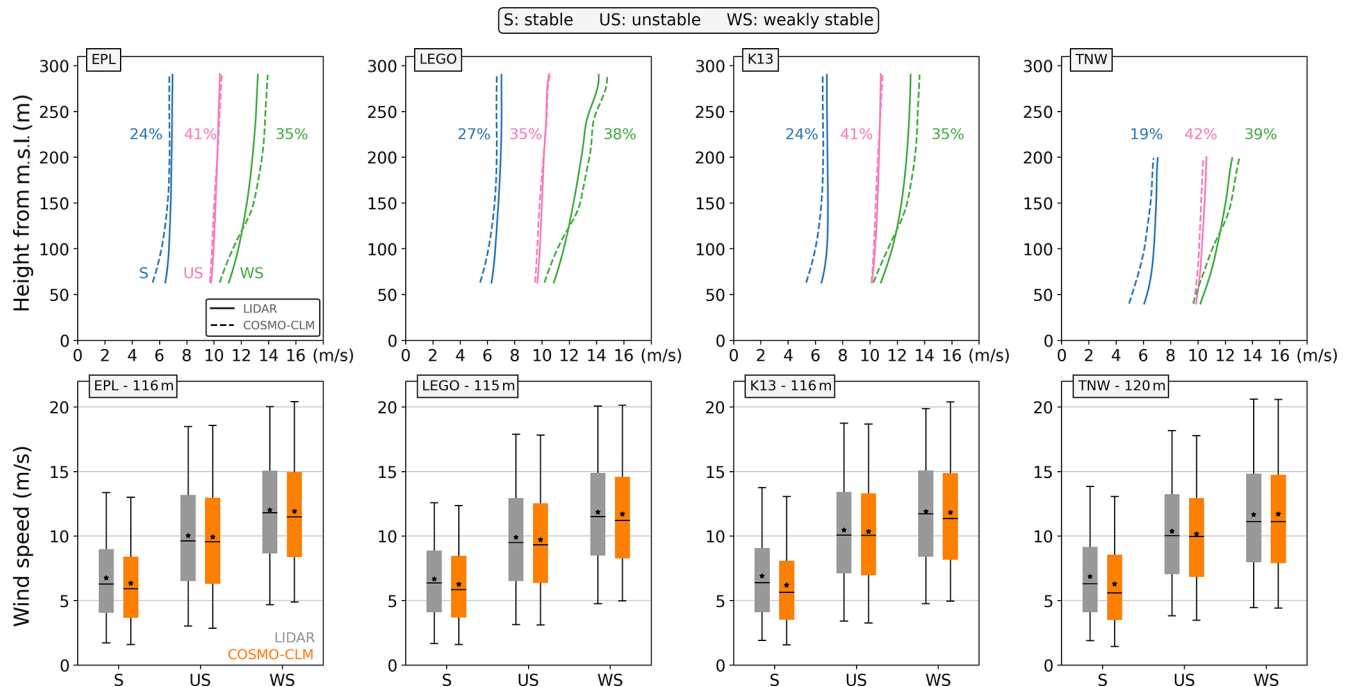


**Figure 6.** Model evaluation for different stability classes. Top row: vertical profiles of the mean wind speed per stability class for four lidar stations (full line) and the corresponding model output (dashed line). The stability classes are stable (blue), unstable (pink) and weakly stable (green). The indicated percentages are the relative frequency of the different stability classes at hub height. Bottom row: boxplots of the hub-height wind speeds per stability class for the same four lidar stations (grey) and the corresponding model output (orange). The box corresponds to the  $Q_{25}$ – $Q_{50}$ – $Q_{75}$  wind speeds. The asterisk indicates the mean, and the lower and upper whiskers are the  $Q_5$  and the  $Q_{95}$  percentiles, respectively.

ferent wind farm scenarios are compared in terms of cluster-scale wake effects and efficiency of power production.

The modelled mean wind speed at 90 m for 2016 varies from  $7.5 \text{ m s}^{-1}$  at the coast up to  $10 \text{ m s}^{-1}$  in the open North Sea (Fig. 7). The associated capacity factor varies between 45 % and 60 %, and the simulated pattern agrees well with earlier, multi-decadal estimates over the North Sea (Geyer et al., 2015). Stability separation shows that the capacity factors are generally largest under weakly stable conditions and can reach 75 % in the open North Sea. For stable conditions, capacity factors are considerably lower but also prone to the bias discussed in Sect. 3.1. The bottom row of Fig. 7 visualizes the impact of the projected, future wind farm layout if they were all occupied with NREL 5 MW turbines at  $8.1 \text{ MW km}^{-2}$ . Without subdividing for stability, the absolute reductions of the full-year capacity factor in the immediate vicinity of farms located in dense clusters are around 15 %, with cumulative contributions from multiple wind farms. The magnitude of the long-term resource reductions is similar to what other studies have identified in terms of closely spaced wind farms (Akhtar et al., 2021; Fischereit et al., 2022b). Very close to the larger farms, larger values can be found even when the farms are isolated. The absolute and relative changes in the capacity factor vary over the stability classes. Absolute capacity factor reductions are typically the small-

est for stable conditions, but these are the largest in relative terms as capacity factors are small themselves. In weakly stable conditions, absolute capacity factor reductions are much higher, as these exceed 13 % over large zones within and outside the wind farm clusters and 5 % more than 20 km from wind farm clusters and larger wind farms.

The impact of the atmospheric stability on the wind-farm-induced reduction in hub-height wind speed can be analysed in more detail along the four analysis transects (Fig. 8). For TR1, TR2 and TR4, the data are dominated by weakly stable conditions ( $\sim 65\%$ ) compared to unstable ( $\sim 19\%$ ) and stable ( $\sim 16\%$ ) conditions, whereas for TR3 unstable conditions are more prevalent ( $\sim 59\%$ ) compared to stable ( $\sim 29\%$ ) and weakly stable ( $\sim 12\%$ ) conditions. The relative reductions at the end of wind farms typically exceed 20 % for all stability classes, but reductions are generally smaller for unstable conditions than for stable and weakly stable conditions. However, the transects do not show a significantly slower wind farm wake recovery for stable conditions, as has been found based on observations (Cañadillas et al., 2020; Platis et al., 2021). The presented transect analysis also differs strongly from such studies in that it considers time averages of different wind speeds and covers a very large extent with the stability and wind direction criterion only evaluated at the centre of the transects. Added to that,

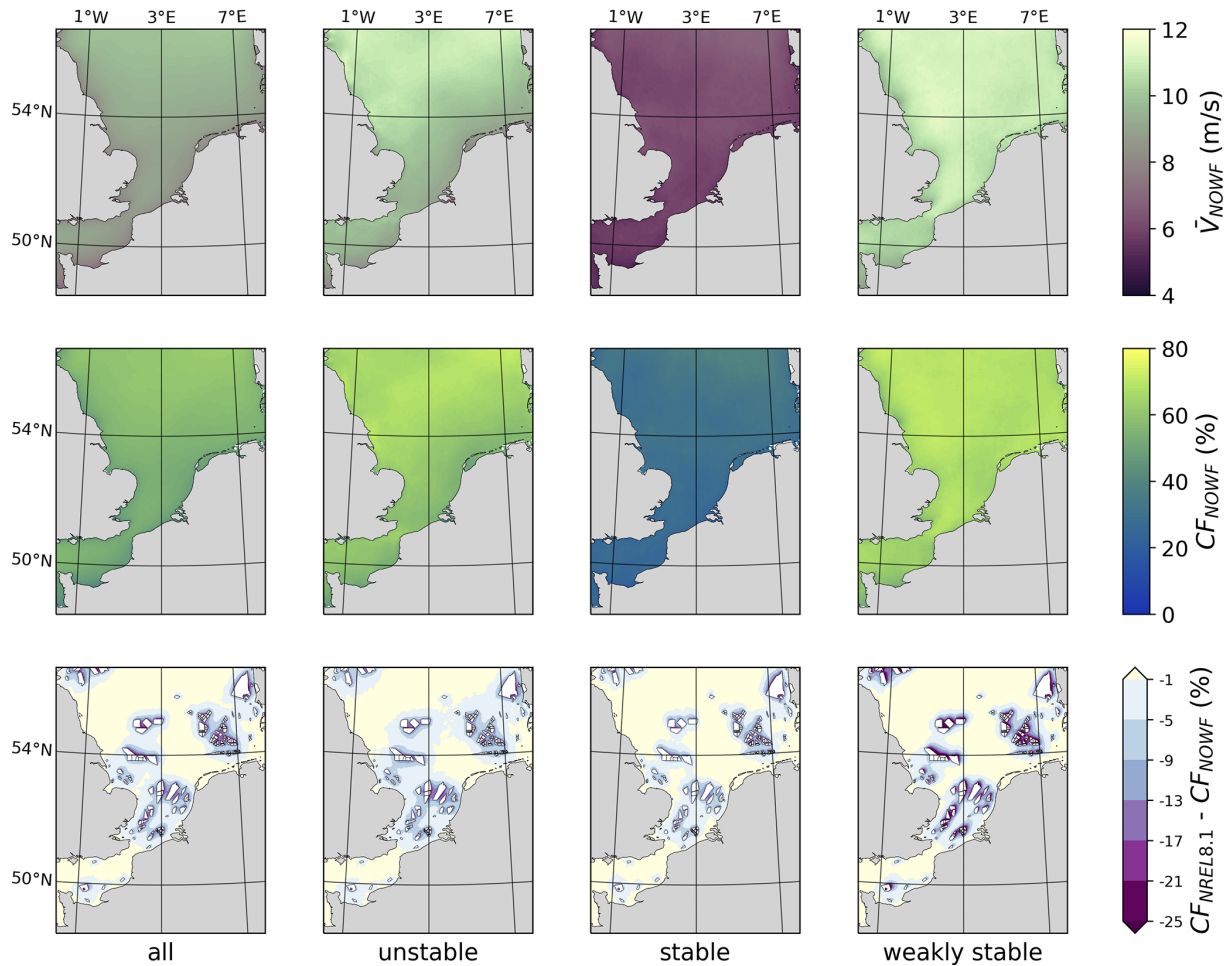


**Figure 7.** Maps of the modelled North Sea wind climatology at 90 m a.m.s.l., the corresponding wind resource in terms of the capacity factor, and the resource deficit under the NREL8.1 scenario for the complete year and for the three stability classes. Top: maps of the yearly mean wind speed ( $\text{m s}^{-1}$ ) under the NOWF scenario. Middle: capacity factor under the NOWF scenario (%). Bottom: absolute capacity factor deficit for the NREL8.1 scenario (%). White polygons represent wind farm locations. Capacity factor computations are based on the power curve of the NREL 5 MW wind turbine.

modifications of dynamic stability by wind farms, which has previously been modelled with LES (Porté-Agel et al., 2014; Lu and Porté-Agel, 2015), could be strongly enhanced by the large, non-existent wind farms used in this study. The associated capacity factor profiles show that the relative impact on the wind resource is large for all stability classes (Fig. S9). The forcing by large wind farms and clusters can lead to a halving of the capacity factor for all stability classes in some transect sections. The relative impact on the capacity factor values is much larger than for the mean wind speed, due to the non-linearity of the turbine power curves (Fig. S3).

The wind farm capacity density used in the different wind farm simulations strongly determines the mean wind speed profile along these transects (Fig. 9). In each case, zones of densely clustered farms ( $< 20$  km apart) are characterized by the strongest reductions and a limited farm wake recovery that is typically less than half of the maximum deficit at the

previous wind farm. The scenario with IEA 15 MW turbines at  $3.5 \text{ MW km}^{-2}$  is characterized by the smallest reductions, which are typically within  $1.5 \text{ m s}^{-1}$  at the upwind side of wind farms. For higher capacity densities, these upwind edge reductions are often more than twice as large and can exceed  $3 \text{ m s}^{-1}$  under very dense clustering. Only for recovery distances of 30–60 km, the IEA8.1 and IEA10.0 scenarios converge to within  $0.5 \text{ m s}^{-1}$  of the IEA3.5 scenario. Furthermore, the impact of wind farm size on the intensity of the reduction can be assessed by focusing on the first wind farm in each transect: the larger wind farms of TR1, TR3 and TR4 have an along-transect farm length between 24 and 31 km, while this is only 9 km for the one in TR2. The associated reductions at the downwind edge of the wind farms are approximately twice as large for TR1, TR3 and TR4 than for TR2.

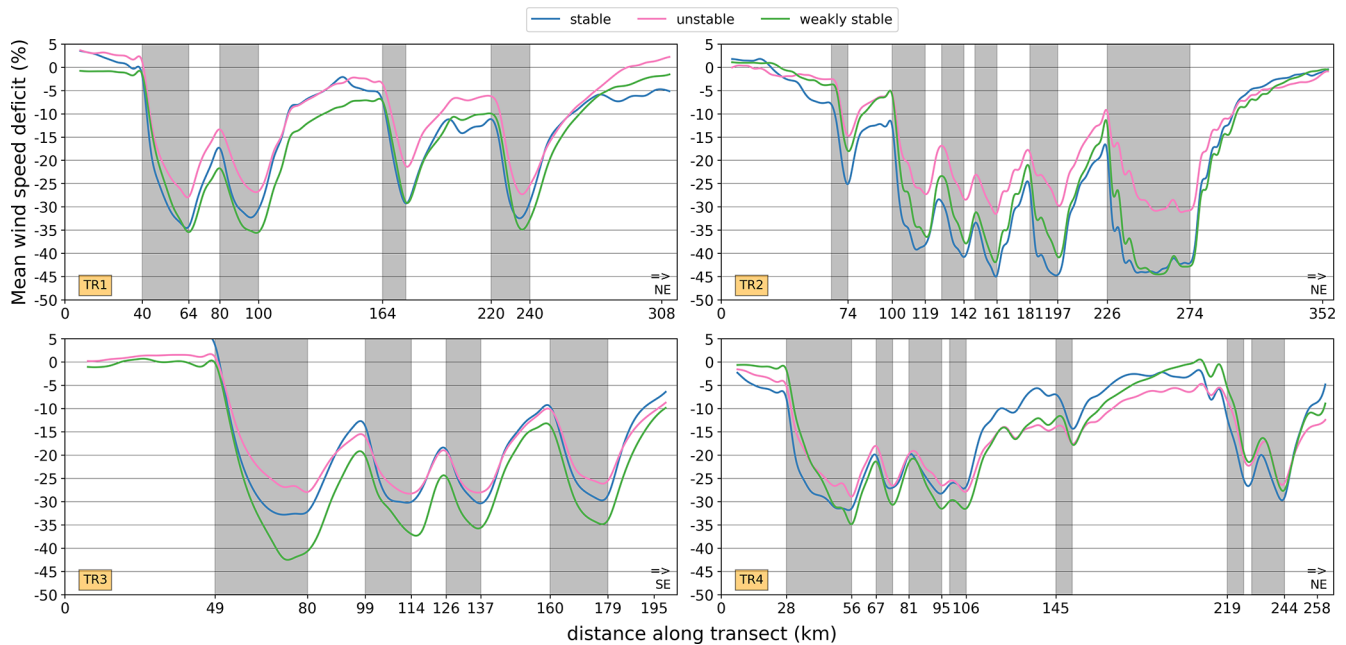


**Figure 8.** Relative deficit of the along-transect mean wind speed (%) at 90 m a.m.s.l. for the four transects indicated on Fig. 1. This concerns the NREL8.1 scenario, subdivided in the three dynamic stability classes: unstable (pink), weakly stable (green) and stable (blue) according to the  $R_B$ . Wind data are only considered when the wind direction deviates within  $\pm 15^\circ$  from the transect orientation (W to E) at the middle grid cell of each transect. Grey shadings represent wind farm locations.

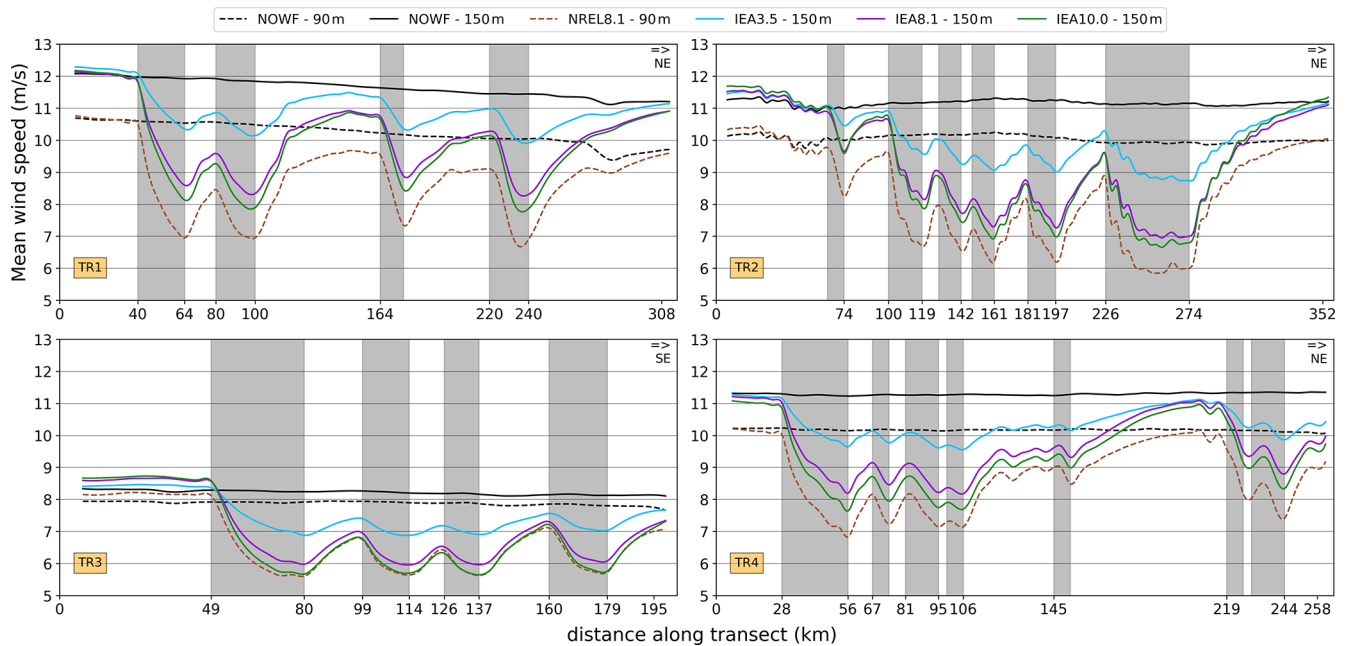


**Figure 9.** Transects of the mean wind speed at turbine hub height for the different wind farm scenarios. These transects correspond to the four lines in Fig. 1. Wind data are only considered when the wind direction deviates within  $\pm 15^\circ$  from the transect orientation (W to E) at the middle grid cell of each transect. Grey shadings represent wind farm locations.



When converting the wind speed information of the NOWF scenario into capacity factors, the transect averages are  $\sim 58\%$  for TR1, TR2 and TR4 and  $\sim 38\%$  for TR3 when considering the hub height and power curve of the NREL 5 MW turbine. For the IEA 15 MW turbine, these increase to  $\sim 66\%$  and  $\sim 46\%$ , respectively. Figure 10 shows that the associated, absolute reductions in these capacity factor follow the general patterns established for the mean wind speed. In each transect, the IEA3.5 scenario is characterized by the smallest deficits at the upwind edge of wind farms, typically around 10% with larger values in dense clusters. For higher capacity densities, the upwind edge reductions reach 25% to 30% for closely spaced wind farms. The intensity of these upwind edge reductions is strongly dependent on the degree of upwind clustering and the sizes of the upwind farms. For the scenarios with higher capacity densities, the superposition of the high momentum sink on the already intense farm wake deficit eventually results in much lower wind farm efficiencies for these scenarios. For the SW–NE-oriented transects, the impact of the turbine type becomes apparent: for the 90 m turbines in the NREL8.1 scenario, the absolute deficits over the wind farms exceed those of the IEA8.1 scenario, which translates to a much stronger reduction in relative terms as the unaltered (NOWF) capacity factors for the 5 MW turbines are lower than for the 15 MW turbines.

The wind farm layout in the IEA8.1 scenario is significantly more efficient than for the NREL8.1 scenario, as reflected in the layout-integrated capacity factor and full load hours in the evaluation domain (Table 4). As a consequence, the integrated AEP is 27.4% higher in the former. This difference is partly due to the rated wind speed being  $0.8\text{ m s}^{-1}$  lower for the 15 MW turbines so that the rated section of the power curve is more wide (Fig. S2). Added to that, taller turbines can take advantage of the wind speed gradient with height, which leads to a larger fraction of wind speeds in the rated regime and a reduced fraction in the steep part of the power curve. To disentangle both effects, the 90 m wind speed data of the NREL8.1 scenario were fed to the 15 MW power curve, which resulted in an AEP of 539 TW h. This implies that approximately 40% of the increase in AEP can be attributed to the lower rated wind speed and approximately 60% to the wind speed gradient with height. Combining 15 MW turbines with a low capacity density of  $3.5\text{ MW km}^{-2}$  only reduces the integrated capacity factor from 64.2% in the NOWF scenario to 51.8%, as a consequence of limited intra- and inter-farm wake impacts, in agreement with Meyers and Meneveau (2012) and Gupta and Baidya Roy (2021). From IEA3.5 to IEA8.1, the capacity density increases by 131%, whereas the AEP only increases by 82%. From IEA8.1 to IEA10.0, these increases are 23.4% and 13.1%, respectively. This efficiency degradation when moving to larger capacity densities can be recognized in a reduced capacity factor and a reduction in the full load hours (FLH): compared to IEA3.5, the IEA10.0 capacity factor is reduced from 51.8% to 38.2% and the FLH is reduced

**Table 4.** Annual energy and power metrics integrated over all wind farms in the evaluation domain. CF: layout-integrated capacity factor. FLH: full load hours for the complete layout. AEP: annual energy production for the complete layout. The calculations are based on the wind speed data of the wind farm grid cells. The capacity factors for the NOWF simulation correspond to efficiency in absence of intra- and inter-farm wakes.

Experiment	Turbine	Total capacity (GW)	CF (%)	FLH (h)	AEP (TW h)
NOWF	NREL 5 MW	–	56.1	–	–
NOWF	IEA 15 MW	–	64.2	–	–
NREL8.1	NREL 5 MW	191	32.7	2549	488
IEA3.5	IEA 15 MW	83	51.8	4136	342
IEA8.1	IEA 15 MW	191	41.4	3252	622
IEA10.0	IEA 15 MW	236	38.2	2981	704

by approximately 1150 h. This follows from the increased wake losses that are further exacerbated by the densely clustered layout and the presence of several large wind farms that are typically characterized by very low power densities (Volker et al., 2017).

#### 4 Conclusions

We have used the regional climate model COSMO-CLM to quantify the dependence of long-term, cluster-scale wake losses on the turbine type, capacity density, wind farm spacing and wind farm size for a hypothetical future wind farm layout. First, the model skill in simulating the wind climate was evaluated in a comparison with in situ, lidar and satellite data, which revealed the following.

- The differences between the measured and modelled, long-term mean wind speed at turbine hub height ( $\sim 100\text{ m}$ ) are generally within the measurement uncertainty. This is also the case for differences at higher altitudes (up to 290 m), but closer to the surface COSMO-CLM underestimates the mean wind speed ( $\sim -0.5\text{ m s}^{-1}$ ). Under stable stratification ( $\sim 25\%$ ), the model underestimates the long-term mean wind speed at turbine height but not under weakly stable and unstable stratification ( $\sim 75\%$ ).
- The agreement between the measured and modelled, long-term wind speed histograms is high, with a PSS above 95% in most cases. The theoretical capacity factors derived from these histograms agree well overall, but small underestimations ( $\sim 1\%–5\%$ ) are present at some locations.
- The agreement with the wind speed measurements is consistent over the different years of the simulation period as inter-annual variations in the mean wind speed



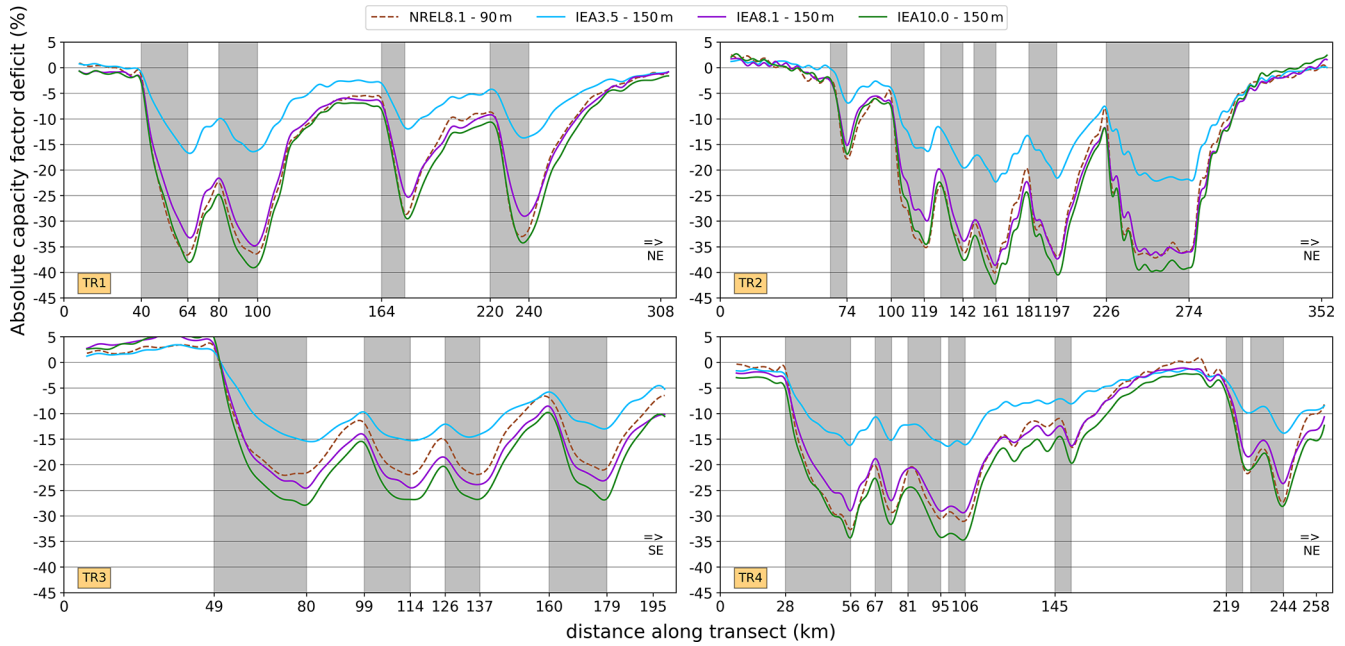


**Figure 10.** Transects of the absolute capacity factor deficit at hub height for the different wind farm scenarios. These transects correspond to the four lines in Fig. 1. Wind data are only considered when the wind direction deviates within  $\pm 15^\circ$  from the transect orientation (W to E) at the middle grid cell of each transect. Grey shadings represent wind farm locations.

difference and the PSS are small. The seasonal variability in the shape and location of the wind speed distribution is also captured by COSMO-CLM.

- Multi-year histograms of wind direction also agree well, with again a PSS above 95 % in most cases. The variation of the wind speed histograms over 12 directional bins ( $30^\circ$ ) is also adequately captured in the model. This encourages the application of COSMO-CLM to wind farm modelling as wind farm shapes are adapted to the regional wind climate.

As deviations mainly occur under stable conditions, a stability-dependent bias correction could be considered for future applications in addition to continuous efforts to improve the model. Overall, this evaluation emphasizes the value of having a large set of wind measurements available in regions for offshore wind farm development, as it allows a benchmarking of mesoscale models over the region of interest.

The application of the model to a hypothetical, future wind farm layout indicates that the creation of dense wind farm clusters is accompanied by an alteration of the surrounding wind climate and significant farm-to-farm wake interactions. The impact of these interactions depends heavily on the turbine type, the capacity density, the inter-farm spacing and the size of the wind farms. In this study, the comparison of two turbine types (NREL 5 MW and IEA 15 MW) and three capacity densities ( $3.5$ ,  $8.1$  and  $10 \text{ MW km}^{-2}$ ) show the following.

- For a capacity density of  $8.1 \text{ MW km}^{-2}$ , the layout-integrated AEP is  $\sim 27 \%$  larger for a layout of 15 MW turbines than for 5 MW turbines. This difference is linked to the layout-integrated capacity factor being considerably larger when using taller, 15 MW turbines because of the increase in the wind resource with height (60 %) and a lower rated wind speed (40 %). The use of 15 MW turbines compensates for  $\sim 37 \%$  of the wake losses recorded in the NREL8.1 simulation.
- Under dominant wind directions with dense wind farm clustering, the wind resource is strongly reduced due to inter-farm wakes. Assuming 15 MW turbines, the absolute reductions in the capacity factor at the upwind edge of wind farms range from 3 % to 17 % for a capacity density of  $3.5 \text{ MW km}^{-2}$  depending on the degree of clustering and the size of the upwind farms. For a capacity density of  $8.1 \text{ MW km}^{-2}$  this ranges from 5 % to 30 % and for  $10 \text{ MW km}^{-2}$  from 5 % to 33 %.
- Assuming a projected, future wind farm layout with 15 MW turbines, increases in the capacity density of the wind farms lead to strong efficiency reductions. The layout-integrated capacity factor reduces from 51.8 % for a  $3.5 \text{ MW km}^{-2}$  capacity density to 38.2 % for a  $10 \text{ MW km}^{-2}$  capacity density, due to the intensification of intra- and inter-farm wake losses.
- Wind farm wake effects play an important role for all considered atmospheric stability classes, even if the im-

fact is a bit smaller for unstable conditions. Under strongly waked wind directions, the low capacity factors (20%–30%) under stable conditions ( $R_B > 0.25$ ) can be further reduced to well below 10%, thereby nearly completely halting the production of some of the simulated wind farms. Although these results are possibly impacted by the negative model bias that was found for stable stratification, it is expected that this large impact under stable conditions still holds.

Whereas comparisons between wind farm parametrizations have shown large variations in terms of modelled wind speed deficits inside and behind wind farms (Ali et al., 2023), validation efforts in several mesoscale models have indicated a very good performance of the Fitch WFP (Fischereit et al., 2022c; van Stratum et al., 2022; Ali et al., 2023). Nonetheless, the use of other WFP schemes might significantly alter the magnitudes presented here, more so due to the large clusters and large wind farms included in the considered layout, which can even lead to wake losses for background wind speeds well above rated. Hence, further benchmarking studies of WFPs for a range of atmospheric conditions and validation data could help in further reducing this WFP-related uncertainty. An additional complication here is that this study includes wind farms of non-existent sizes for which validations simply do not exist.

Even if the mesoscale wind farm parametrization approach has limitations, these modelling studies provide valuable information for the efficient deployment and operation of offshore wind infrastructure, more so because mesoscale models can consider the climatic variability of wake effects, for large regions. This study demonstrates the potential of this modelling approach to explore a large variety of wind farm characteristics and layouts in a climatic context, which can aid in a more efficient expansion of the offshore infrastructure.

## Appendix A

**Table A1.** Description of the in situ measurement stations.  $S$ : wind speed ( $\text{m}^{-1}$ );  $D$ : wind from direction ( $^{\circ}$ ). The superscripts a, b and c link measurement heights to measurement devices in the next column.  $1 \times$ ,  $2 \times$  and  $3 \times$  refers to one, two, or three anemometers and/or wind vanes at one measurement height. Source acronyms: KDP, Royal Netherlands Meteorological Institute (KNMI) data platform; MNVB, Meetnet Vlaamse Banken; MDE, the Marine Data Exchange; FINO, Forschungsplattformen in Nord- und Ostsee; TNO, Nederlandse Organisatie voor Toegepast-natuurwetenschappelijk Onderzoek.

Name (abbreviation)	Location	Heights (m a.m.s.l.)	Measured variables	Period	Uncertainty (%)	Source
Westhinder (WH)	platform	26	$2 \times S, D$	2008–2020	5.6	MNVB
Wandelaar (WA)	measuring pole	26	$2 \times S, 1 \times D$	2013–2020	3.3	MNVB
Scheur-Wielingen (SW)	measuring pole	25	$1 \times S, D$	2010–2020	3.3	MNVB
Oosterschelde (OS)	measuring pole	17		2008–Jun 2019	3.3	KDP
Vlakte van de Raan (VVDR)	measuring pole	17		Sep 2009–Jun 2019	3.3	KDP
Lichteiland Goeree (LEGO)	platform	38	$2 \times S, D$	2008–2020	3.3	KDP
Europlatform (EPL)	platform	29	$2 \times S, D$	2008–2020	3.3	KDP
Ijmond (IJM)	measuring pole	17		2008–Jun 2019	3.3	KDP
P11-B (P11B)	mast on platform	51	$2 \times S, D$	2010–2020	5.6	KDP
Meteomast IJmuiden (MMIJ)	meteorological mast	27, 58 <sup>a</sup> , 92 <sup>b</sup>	$a : 3 \times S, D, b : 2 \times S$	Nov 2011–Mar 2016	$a : 1.9; b : 1.5$	TNO
K13A (K13)	mast on platform	74	$2 \times S, D$	2008–2019	3.3	KDP
F3N (F3)	mast on platform	60	$2 \times S, D$	2010–Dec 2019	3.3	KDP
Huibertgat (HGT)	measuring pole	18		2008–Jun 2019	3.3	KDP
AWG-1 (AWG1)	mast on platform	60	$2 \times S, D$	Sep 2009–2020	5.6	KDP
FINO1 (FINO1)	meteorological mast	51, 71, 91 <sup>a</sup> , 102 <sup>b</sup>	$a : 1 \times S, D; b : 1 \times S$	2008–Jul 2009	$a : 1.9; b : 1.5$	FINO
FINO3 (FINO3)	meteorological mast	50, 70, 90, 100 <sup>a</sup> , 107 <sup>b</sup>	$a : 3 \times S, D; b : 1 \times S$	2009–Oct 2014	$a : 1.9; b : 1.5$	FINO
Humber Gateway (HGW)	meteorological mast	34, 52, 70, 88 <sup>a</sup> , 68 <sup>b</sup> , 90 <sup>c</sup>	$a : 2 \times S; b : 1 \times D; c : 1 \times S$	Oct 2009–Jul 2011	$a : 3.7; c : 1.5$	MDE
Greater Gabbard (GG)	meteorological mast	42, 52, 72, 82 <sup>a</sup> , 62 <sup>b</sup> , 88 <sup>c</sup>	$a : 2 \times S; b : 2 \times D; c : 1 \times S$	2008–2010	$a : 3.7; c : 1.5$	MDE
London Array (LA)	meteorological mast	20, 32, 57 <sup>a</sup> , 29, 78 <sup>b</sup> , 82 <sup>c</sup>	$a : 2 \times S; b : 1 \times D; c : 1 \times S$	2008–2010	$a : 3.7; c : 1.5$	MDE

**Table A2.** Description of the lidar measurement stations. Source acronyms: RVO, Rijksdienst voor Ondernemend Nederland; TNO, Nederlandse Organisatie voor Toegepast-natuurwetenschappelijk Onderzoek.

Name (abbreviation)	Type	Location	Heights (m a.m.s.l.)	Period	Uncertainty (%)	Source
Borssele 1 (BO)	Zephyr 300S	buoy	40:20:200	Jun 2015–Feb 2017	3.3–3.4	RVO
Lichteiland Goeree (LEGO)	Leosphere Windcube	platform	90:25:290 and 63	Nov 2014–2020	2.6–3.3	TNO
Europlatform (EPL)	Zephyr 300S	platform	91:25:291 and 63	May 2016–2020	2.9–3.5	TNO
Meteomast IJmuiden (MMIJ)	Zephyr 300S	platform	90:25:290	Nov 2011–Mar 2016	2.5–3.1	TNO
K13A (K13)	Zephyr 300S	platform	91:25:291 and 63	2018–2020	2.7–3.2	TNO
TNVD Waddeneilanden A (TNW)	Zephyr 300S	buoy	40:20:200	Sep 2019–2020	3.3–3.4	RVO

**Code and data availability.** The code and data used to generate Figs. 3–10 can be retrieved as one dataset at <https://doi.org/10.5281/zenodo.8348700> (Borgers, 2023). The ERA5 reanalysis data used to identify representative wind years were downloaded via the Copernicus Climate Change Service (C3S) Climate Data Store (CDS) and can be found at <https://doi.org/10.24381/cds.adbb2d47> (Hersbach et al., 2022). The ASCAT data were retrieved from the Copernicus Marine Service via <https://doi.org/10.48670/moi-00183> (Copernicus Marine Service, 2022). The in situ measurements of the KNMI can be retrieved from their data platform, at <https://dataplatfom.knmi.nl/group/wind> (Koninklijk Nederlands Meteorologisch Instituut, 2022). For the in situ data at the Belgian coast, data are accessible via the website of

the Belgian coastal measurement network, at <https://meetnetvlaamsebanken.be/> (Meetnet Vlaamse Banken, 2022). Mast data at the coast of the United Kingdom are available via the website of the Marine Data Exchange, at <https://www.marinedataexchange.co.uk/> (The Crown Estate, 2022). For the German Bight, the data are available at the website of the FINO data platform, <http://fino.bsh.de/> (Das Bundesamt für Seeschifffahrt und Hydrographie, 2022). Data from the IJmuiden meteorological mast and from the platform-mounted wind lidars can be found at the TNO data cloud website <https://nimbus.windopzee.net/> (Nederlandse Organisatie voor toegepast-natuurwetenschappelijk onderzoek, 2022). Finally, the data from the buoy-mounted lidars can be found

at <https://offshorewind.rvo.nl/> (Rijksdienst voor Ondernemend Nederland, 2022).

**Supplement.** The supplement related to this article is available online at: <https://doi.org/10.5194/wes-9-697-2024-supplement>.

**Author contributions.** RB contributed to the conceptualization, data curation, formal analysis, investigation, methodology, project administration, software, validation, visualization and writing (original draft, review and editing). MD contributed to the data curation, resources, methodology and writing (review and editing). IW, ASt and ASto contributed to the resources, methodology and writing (review and editing). NA contributed to the methodology, software and writing (review and editing). JN and JvW contributed to the methodology and writing (review and editing). JM contributed to the conceptualization, funding acquisition, methodology, project administration, supervision and writing (review and editing). NPMvL contributed to the conceptualization, funding acquisition, investigation, methodology, project administration, resources, supervision, visualization and writing (original draft, review and editing).

**Competing interests.** At least one of the (co-)authors is a member of the editorial board of *Wind Energy Science*. The peer-review process was guided by an independent editor, and the authors also have no other competing interests to declare.

**Disclaimer.** Publisher's note: Copernicus Publications remains neutral with regard to jurisdictional claims made in the text, published maps, institutional affiliations, or any other geographical representation in this paper. While Copernicus Publications makes every effort to include appropriate place names, the final responsibility lies with the authors.

**Acknowledgements.** The computational resources and services in this work were provided by the VSC (Flemish Supercomputer Center), funded by the Research Foundation Flanders (FWO) and the Flemish government department EWI.

The authors further acknowledge the COSMO-CLM community for support in the modelling efforts in this study. EUMETSAT OSI-SAF, in which Ad Stoffelen is involved, is also acknowledged. Naveed Akhtar also acknowledges the support from the German Federal Ministry of Education and Research (BMBF) under project CoastalFutures (03F0911A), a project of the DAM Research Mission sustainMare – Protection and Sustainable Use of Marine Areas.

The authors further thank the Royal Netherlands Meteorological Institute (KNMI), the Meetnet Vlaamse Banken, the German Federal Maritime and Hydrographic Agency (BSH), and the Marine Data Exchange (MDE) for the in situ wind measurements, metadata and additional data handling support. The Energieonderzoek Centrum Nederland (ECN) and the Nederlandse Organisatie voor toegepast-natuurwetenschappelijk onderzoek (TNO) are also thanked for the mast and lidar measurements at IJmuiden and lidar measurements at Lichteiland Goeree, Europlatform, and K13A,

and Rijksdienst voor Ondernemend Nederland (RVO) is thanked for the lidar data of Borssele and Ten Noorden van de Waddeneilanden. Finally, Copernicus and the Copernicus Marine Service are acknowledged for the ERA5 reanalysis and MetOp-A ASCAT measurements.

**Financial support.** This research has been supported by the project FREEWIND, funded by the Energy Transition Fund of the Belgian Federal Public Service for Economy, SMEs, and Energy (FOD Economie, K.M.O., Middenstand en Energie).

**Review statement.** This paper was edited by Julie Lundquist and reviewed by Andrea Hahmann, David Schultz, and Pablo Ouro.

## References

- Akhtar, N. and Chatterjee, F.: Wind farm parametrization in COSMO5.0\_c1m15, World Data Center for Climate (WDCC) at DKRZ, <https://doi.org/10.35089/WDC/WindFarmPCOSMO5.0c1m15>, 2020.
- Akhtar, N., Geyer, B., Rockel, B., Sommer, P. S., and Schrum, C.: Accelerating deployment of offshore wind energy alter wind climate and reduce future power generation potentials, *Sci. Rep.*, 11, 11826, <https://doi.org/10.1038/s41598-021-91283-3>, 2021.
- Akhtar, N., Geyer, B., and Schrum, C.: Impacts of accelerating deployment of offshore windfarms on near-surface climate, *Sci. Rep.*, 12, 18307, <https://doi.org/10.1038/s41598-022-22868-9>, 2022.
- Ali, K., Schultz, D. M., Revell, A., Stallard, T., and Ouro, P.: Assessment of Five Wind-Farm Parameterizations in the Weather Research and Forecasting Model: A Case Study of Wind Farms in the North Sea, *Mon. Weather Rev.*, 151, 2333–2359, <https://doi.org/10.1175/MWR-D-23-0006.1>, 2023.
- Antonini, E. G. and Caldeira, K.: Spatial constraints in large-scale expansion of wind power plants, *P. Natl. Acad. Sci. USA*, 118, e2103875118, <https://doi.org/10.1073/pnas.2103875118>, 2021.
- Archer, C. L., Wu, S., Ma, Y., and Jiménez, P. A.: Two corrections for turbulent kinetic energy generated by wind farms in the WRF model, *Mon. Weather Rev.*, 148, 4823–4835, <https://doi.org/10.1175/MWR-D-20-0097.1>, 2020.
- Bak, C., Zahle, F., Bitsche, R., Kim, T., Yde, A., Henriksen, L. C., Hansen, M. H., Blasques, J. P. A. A., Gaunaa, M., and Natarajan, A.: The DTU 10-MW reference wind turbine, in: Danish wind power research 2013, <https://orbit.dtu.dk/en/publications/the-dtu-10-mw-reference-wind-turbine> (last access: 6 May 2022), 2013.
- Bento, N. and Fontes, M.: Emergence of floating offshore wind energy: Technology and industry, *Renew. Sustain. Energ. Rev.*, 99, 66–82, <https://doi.org/10.1016/j.rser.2018.09.035>, 2019.
- Borgers, R.: Mesoscale modelling of North Sea wind resources with COSMO-CLM: model evaluation and impact assessment of future wind farm characteristics on cluster-scale wake losses, Zenodo [data set], <https://doi.org/10.5281/zenodo.8348700>, 2023.
- Borrmann, R., Knud, R., Wallasch, A.-K., and Lüers, S.: Capacity densities of European offshore wind

- farms, Tech. rep., no. SP18004A1, Deutsche WindGuard GmbH, Varel, Germany, <https://vasab.org/document/capacity-densities-of-european-offshore-wind-farms/> (last access: 2 February 2022), 2018.
- Bourassa, M. A., Meissner, T., Cerovecki, I., Chang, P. S., Dong, X., De Chiara, G., Donlon, C., Dukhovskoy, D. S., Elya, J., Fore, A., et al.: Remotely sensed winds and wind stresses for marine forecasting and ocean modeling, *Front. Mar. Sci.*, 6, 443, <https://doi.org/10.3389/fmars.2019.00443>, 2019.
- Brisson, E., Demuzere, M., and Van Lipzig, N.: Modelling strategies for performing convection-permitting climate simulations, *Meteorol. Z.*, 25, 149–163, <https://doi.org/10.1127/metz/2015/0598>, 2015.
- Cañadillas, B., Foreman, R., Barth, V., Siedersleben, S., Lampert, A., Platis, A., Djath, B., Schulz-Stellenfleth, J., Bange, J., Emeis, S., and Neumann, T.: Offshore wind farm wake recovery: Airborne measurements and its representation in engineering models, *Wind Energy*, 23, 1249–1265, 2020.
- Chatterjee, F., Allaerts, D., Blahak, U., Meyers, J., and van Lipzig, N.: Evaluation of a wind-farm parametrization in a regional climate model using large eddy simulations, *Q. J. Roy. Meteorol. Soc.*, 142, 3152–3161, <https://doi.org/10.1002/qj.2896>, 2016.
- Copernicus Marine Service: Global Ocean Daily Gridded Reprocessed L3 Sea Surface Winds from Scatterometer, Copernicus Marine Service [data set], <https://doi.org/10.48670/moi-00183>, 2022.
- Coquilla, R. V., Obermeier, J., and White, B. R.: Calibration procedures and uncertainty in wind power anemometers, *Wind Eng.*, 31, 303–316, <https://doi.org/10.1260/030952407783418720>, 2007.
- Das Bundesamt für Seeschifffahrt und Hydrographie: FINO database, <http://fino.bsh.de/> (last access: 10 January 2022), 2022.
- Dhirendra, D.: Uncertainty Assessment Fugro OCEANOR SEAWATCH Wind LiDAR Buoy at RWE Meteomast IJmuiden, Tech. rep., ECOFYS, <https://offshorewind.rvo.nl/file/download/45051422> (last access: 15 February 2022), 2014.
- Dirksen, M., Wijnant, I., Siebesma, P., Baas, P., and Natalie, T.: Validation of wind farm parameterisation in Weather Forecast Model HARMONIE-AROME – Analysis of 2019, Tech. rep., WINS50 report, TU Delft, [https://www.wins50.nl/downloads/dirksen\\_et\\_al\\_validationreport.pdf](https://www.wins50.nl/downloads/dirksen_et_al_validationreport.pdf) (last access: 1 September 2022), 2022.
- Doms, G. and Baldauf, M.: A description of the nonhydrostatic regional COSMO-Model Part I: dynamics and numerics, Tech. rep., COSMO documentation, Deutscher Wetterdienst, [https://doi.org/10.5676/DWD\\_pub/nwv/cosmo-doc\\_5.00\\_I](https://doi.org/10.5676/DWD_pub/nwv/cosmo-doc_5.00_I), 2013.
- Doms, G., Förstner, J., Heise, E., Herzog, H.-J., Mironov, D., Raschendorfer, M., Reinhardt, T., Ritter, B., Schrodin, R., Schulz, J.-P., and Vogel, P.: A description of the nonhydrostatic regional COSMO-Model Part II: physical parametrization, Tech. rep., COSMO documentation, Deutscher Wetterdienst, [https://doi.org/10.5676/DWD\\_pub/nwv/cosmo-doc\\_5.00\\_II](https://doi.org/10.5676/DWD_pub/nwv/cosmo-doc_5.00_II), 2013.
- Duncan, J., Wijnant, I., and Knoop, S.: DOWA validation against offshore mast and LiDAR measurements, Tech. rep., TNO report 2019 R10062, KNMI – Royal Netherlands Meteorological Institute, <https://www.dutchoffshorewindatlas.nl/binaries/dowa/> (last access: 1 September 2021), 2019.
- EMODnet: Wind Farms (Polygons), EMODnet Human Activities [data set], <https://emodnet.ec.europa.eu/en/human-activities#humanactivities-data-products> (last access: 21 January 2022), 2022.
- Figa-Saldaña, J., Wilson, J. J., Attema, E., Gelsthorpe, R., Drinkwater, M. R., and Stoffelen, A.: The advanced scatterometer (ASCAT) on the meteorological operational (MetOp) platform: A follow on for European wind scatterometers, *Can. J. Remote Sens.*, 28, 404–412, <https://doi.org/10.5589/m02-035>, 2002.
- Fischereit, J., Brown, R., Larsén, X. G., Badger, J., and Hawkes, G.: Review of mesoscale wind-farm parametrizations and their applications, *Bound.-Lay. Meteorol.*, 182, 175–224, <https://doi.org/10.1007/s10546-021-00652-y>, 2022a.
- Fischereit, J., Larsén, X. G., and Hahmann, A. N.: Climatic Impacts of Wind-Wave-Wake Interactions in Offshore Wind Farms, *Front. Energ. Res.*, 10, 881459, <https://doi.org/10.3389/fenrg.2022.881459>, 2022b.
- Fischereit, J., Schaldemose Hansen, K., Larsén, X. G., van der Laan, M. P., Réthoré, P.-E., and Murcia Leon, J. P.: Comparing and validating intra-farm and farm-to-farm wakes across different mesoscale and high-resolution wake models, *Wind Energ. Sci.*, 7, 1069–1091, <https://doi.org/10.5194/wes-7-1069-2022>, 2022c.
- Fitch, A. C., Olson, J. B., Lundquist, J. K., Dudhia, J., Gupta, A. K., Michalakes, J., and Barstad, I.: Local and mesoscale impacts of wind farms as parameterized in a mesoscale NWP model, *Mon. Weather Rev.*, 140, 3017–3038, <https://doi.org/10.1175/MWR-D-11-00352.1>, 2012.
- Friis Pedersen, T., Dahlberg, J.-Å., and Busche, P.: ACCUWIND – Classification of five cup anemometers according to IEC 61400-12-1, no. 1556(EN) in Denmark, Forskningscenter Risoe, Risoe-R, ISBN 87-550-3516-7, 2006.
- Gaertner, E., Rinker, J., Sethuraman, L., Zahle, F., Anderson, B., Barter, G. E., Abbas, N. J., Meng, F., Bortolotti, P., Skrzypinski, W., Scott, G., Feil, R., Bredmose, H., Dykes, K., Shields, M., Allen, C., and Viselli, A.: IEA wind TCP task 37: definition of the IEA 15-megawatt offshore reference wind turbine, Tech. rep., no. NREL/TP-5000-75698, NREL – National Renewable Energy Lab., Golden, CO, USA, <https://doi.org/10.2172/1603478>, 2020.
- García-Santiago, O. M., Badger, J., Hahmann, A. N., and da Costa, G. L.: Evaluation of two mesoscale wind farm parametrizations with offshore tall masts, *J. Phys.: Conf. Ser.*, 2265, 022038, <https://doi.org/10.1088/1742-6596/2265/2/022038>, 2022.
- Gelsthorpe, R., Schied, E., and Wilson, J.: ASCAT-Metop’s advanced scatterometer, *ESA Bulletin*, 102, 19–27, 2000.
- Geyer, B., Weisse, R., Bisling, P., and Winterfeldt, J.: Climatology of North Sea wind energy derived from a model hindcast for 1958–2012, *J. Wind Eng. Indust. Aerodynam.*, 147, 18–29, <https://doi.org/10.1016/j.jweia.2015.09.005>, 2015.
- Grachev, A. A., Andreas, E. L., Fairall, C. W., Guest, P. S., and Persson, P. O. G.: The critical Richardson number and limits of applicability of local similarity theory in the stable boundary layer, *Bound.-Lay. Meteorol.*, 147, 51–82, <https://doi.org/10.1007/s10546-012-9771-0>, 2013.
- Gupta, T. and Baidya Roy, S.: Recovery processes in a large offshore wind farm, *Wind Energ. Sci.*, 6, 1089–1106, <https://doi.org/10.5194/wes-6-1089-2021>, 2021.
- Hahmann, A. N., Vincent, C. L., Peña, A., Lange, J., and Hasager, C. B.: Wind climate estimation using WRF model output:



- method and model sensitivities over the sea, *Int. J. Climatol.*, 35, 3422–3439, <https://doi.org/10.1002/joc.4217>, 2015.
- Hersbach, H., Bell, B., Berrisford, P., Hirahara, S., Horányi, A., Muñoz-Sabater, J., Nicolas, J., Peubey, C., Radu, R., Schepers, D., Simmons, A., Soci, C., Abdalla, S., Abellan, X., Balsamo, G., Bechtold, P., Biavati, G., Bidlot, J., Bonavita, M., De Chiara, G., Dahlgren, P., Dee, D., Diamantakis, M., Dragani, R., Flemming, J., Forbes, R., Fuentes, M., Geer, A., Haimberger, L., Healy, S., Hogan, R. J., Hólm, E., Janisková, M., Keeley, S., Laloyaux, P., Lopez, P., Lupu, C., Radnoti, G., de Rosnay, P., Rozum, I., Vamborg, F., Villaume, S., and Thépaut, J.-N.: The ERA5 global reanalysis, *Q. J. Roy. Meteorol. Soci.*, 146, 1999–2049, <https://doi.org/10.1002/qj.3803>, 2020.
- Hersbach, H., Bell, B., Berrisford, P., Hirahara, S., Horányi, A., Muñoz-Sabater, J., Nicolas, J., Peubey, C., Radu, R., Schepers, D., Simmons, A., Soci, C., Abdalla, S., Abellan, X., Balsamo, G., Bechtold, P., Biavati, G., Bidlot, J., Bonavita, M., De Chiara, G., Dahlgren, P., Dee, D., Diamantakis, M., Dragani, R., Flemming, J., Forbes, R., Fuentes, M., Geer, A., Haimberger, L., Healy, S., Hogan, R. J., Hólm, E., Janisková, M., Keeley, S., Laloyaux, P., Lopez, P., Lupu, C., Radnoti, G., de Rosnay, P., Rozum, I., Vamborg, F., Villaume, S., and Thépaut, J.-N.: ERA5 monthly averaged data on single levels from 1940 to present, Copernicus Climate Change Service (C3S) Climate Data Store (CDS) [data set], <https://doi.org/10.24381/cds.adbb2d47>, 2022.
- IPCC: Summary for Policymakers, in: *Climate Change 2022: Mitigation of Climate Change, Contribution of Working Group III to the Sixth Assessment Report of the Intergovernmental Panel on Climate Change*, edited by: Shukla, P., Skea, J., Slade, R., Xue, P., Misra, S., Chatterjee, A., Prasad, A., Van Diemen, R., Mallick, M., Sumner, S., Klose, S., Hayashi, H., Tada, T., Yamamoto, T., Hiraishi, T., Ishii, K., Sugita, M., Inada, M., Morita, T., Takemura, T., and Miwa, K., Cambridge University Press, Cambridge, UK and New York, NY, USA, <https://doi.org/10.1017/9781009157926.001>, 2022.
- Jonkman, J., Butterfield, S., Musial, W., and Scott, G.: Definition of a 5-MW reference wind turbine for offshore system development, Tech. rep., no. NREL/TP-500-38060, NREL – National Renewable Energy Lab., Golden, CO, USA, <https://doi.org/10.2172/947422>, 2009.
- Knoop, S., Bosveld, F. C., de Haij, M. J., and Apituley, A.: A 2-year intercomparison of continuous-wave focusing wind lidar and tall mast wind measurements at Cabauw, *Atmos. Meas. Tech.*, 14, 2219–2235, <https://doi.org/10.5194/amt-14-2219-2021>, 2021.
- Komusanac, I., Brindley, G., Fraile, D., and Ramirez, L.: Wind energy in Europe: 2020 Statistics and the outlook for 2021–2025, Tech. rep., WindEurope, Brussels, Belgium, <https://windeurope.org/intelligence-platform/product/wind-energy-in-europe-2020-statistics-and-the-outlook-for-2021> (last access: 10 January 2022), 2020.
- Komusanac, I., Brindley, G., Fraile, D., and Ramirez, L.: Wind energy in Europe: 2021 Statistics and the outlook for 2022–2026, Tech. rep., WindEurope, Brussels, Belgium, <https://windeurope.org/intelligence-platform/product/wind-energy-in-europe-2021-statistics-and-the-outlook-for-2022> (last access: 10 January 2022), 2021.
- Koninklijk Nederlands Meteorologisch Instituut: KNMI data platform, <https://dataplatform.knmi.nl/group/wind> (last access: 25 February 2022), 2022.
- Larsén, X. G. and Fischereit, J.: A case study of wind farm effects using two wake parameterizations in the Weather Research and Forecasting (WRF) model (V3. 7.1) in the presence of low-level jets, *Geosci. Model Dev.*, 14, 3141–3158, <https://doi.org/10.5194/gmd-14-3141-2021>, 2021.
- Leiding, T., Tinz, B., Gates, L., Rosenhagen, G., Herklotz, K., and Senet, C.: Standardisierung und vergleichende Analyse der meteorologischen FINO-Messdaten (FINO123): Forschungsvorhaben FINO-Wind: Abschlussbericht: 12/2012–04/2016, Deutscher Wetterdienst, [https://www.dwd.de/DE/klimaumwelt/klimaforschung/klimaueberwachung/finowind/finodoku/abschlussbericht\\_pdf.pdf?\\_\\_blob=publicationFile&v=3](https://www.dwd.de/DE/klimaumwelt/klimaforschung/klimaueberwachung/finowind/finodoku/abschlussbericht_pdf.pdf?__blob=publicationFile&v=3) (last access: 1 October 2021), 2016.
- Li, D., Geyer, B., and Bisling, P.: A model-based climatology analysis of wind power resources at 100-m height over the Bohai Sea and the Yellow Sea, *Appl. Energy*, 179, 575–589, <https://doi.org/10.1016/j.apenergy.2016.07.010>, 2016.
- Lu, H. and Porté-Agel, F.: On the impact of wind farms on a convective atmospheric boundary layer, *Bound.-Lay. Meteorol.*, 157, 81–96, 2015.
- Lundquist, J. K., DuVivier, K. K., Kaffine, D., and Tomaszewski, J. M.: Costs and consequences of wind turbine wake effects arising from uncoordinated wind energy development, *Nat. Energy*, 4, 26–34, <https://doi.org/10.1038/s41560-018-0281-2>, 2019.
- Matte, D., Laprise, R., Thériault, J. M., and Lucas-Picher, P.: Spatial spin-up of fine scales in a regional climate model simulation driven by low-resolution boundary conditions, *Clim. Dynam.*, 49, 563–574, 2017.
- Matthijssen, J., Dammers, E., and Elzenga, H.: De toekomst van de Noordzee: de Noordzee in 2030 en 2050: een scenariostudie, Planbureau voor de Leefomgeving, <https://www.pbl.nl/sites/default/files/downloads/pbl-2018-toekomst-van-de-noordzee-2728.pdf> (last access: 1 July 2021), 2018.
- Meetnet Vlaamse Banken: Data of the Flemish Banks Monitoring Network, <https://meetnetvlaamsebanken.be/Download/Welcome> (last access: 25 February 2022), 2022.
- Mellor, G. L. and Yamada, T.: Development of a turbulence closure model for geophysical fluid problems, *Rev. Geophys.*, 20, 851–875, <https://doi.org/10.1029/RG020i004p00851>, 1982.
- Menezes, D., Mendes, M., Almeida, J. A., and Farinha, T.: Wind farm and resource datasets: A comprehensive survey and overview, *Energies*, 13, 4702, <https://doi.org/10.3390/en13184702>, 2020.
- Meyers, J. and Meneveau, C.: Optimal turbine spacing in fully developed wind farm boundary layers, *Wind Energy*, 15, 305–317, <https://doi.org/10.1002/we.469>, 2012.
- Munters, W., Adiloglu, B., Buckingham, S., and van Beeck, J.: Wake impact of constructing a new offshore wind farm zone on an existing downwind cluster: a case study of the Belgian Princess Elisabeth zone using FLORIS, *J. Phys.: Conf. Ser.*, 2265, 022049, <https://doi.org/10.1088/1742-6596/2265/2/022049>, 2022.
- Musial, W., Spitsen, P., Duffy, P., Beiter, P., Marquis, M., Hammond, R., and Shields, M.: Offshore Wind Market Report: 2022 Edition, Tech. rep., no. NREL/TP-5000-83544, NREL – National Renewable Energy Lab., Golden, CO, USA, <https://doi.org/10.2172/1883382>, 2022.



- Nederlandse Organisatie voor toegepast-natuurwetenschappelijk onderzoek: Nimbus, <https://nimbus.windopzee.net/> (last access: 15 February 2022), 2022.
- Nolan, P., Lynch, P., and Sweeney, C.: Simulating the future wind energy resource of Ireland using the COSMO-CLM model, *Wind Energy*, 17, 19–37, <https://doi.org/10.1002/we.1554>, 2014.
- Platis, A., Siedersleben, S. K., Bange, J., Lampert, A., Bärfuss, K., Hankers, R., Cañadillas, B., Foreman, R., Schulz-Stellenfleth, J., Djath, B., Neumann, T., and Emeis, S.: First in situ evidence of wakes in the far field behind offshore wind farms, *Sci. Rep.*, 8, 2163, <https://doi.org/10.1038/s41598-018-20389-y>, 2018.
- Platis, A., Hundhausen, M., Lampert, A., Emeis, S., and Bange, J.: The role of atmospheric stability and turbulence in offshore wind-farm wakes in the German bight, *Bound.-Lay. Meteorol.*, 182, 441–469, <https://doi.org/10.1007/s10546-021-00668-4>, 2021.
- Porté-Agel, F., Lu, H., and Wu, Y.-T.: Interaction between large wind farms and the atmospheric boundary layer, *Procedia Iutam*, 10, 307–318, 2014.
- Poveda, J. M. and Wouters, D. A. J.: Wind measurements at meteorological mast IJmuiden, Tech. rep., eCN-E-14-058, ECN, <https://publicaties.ecn.nl/PdfFetch.aspx?nr=ECN-E-14-058> (last access: 19 January 2022), 2015.
- Pryor, S. C., Barthelmie, R. J., and Shepherd, T. J.: Wind power production from very large offshore wind farms, *Joule*, 5, 2663–2686, <https://doi.org/10.1016/j.joule.2021.09.002>, 2021.
- Rabin, J., Delon, J., and Gousseau, Y.: Circular Earth Mover’s Distance for the comparison of local features, in: 2008 19th International Conference on Pattern Recognition, 8–11 December 2008, Tampa, USA, <https://doi.org/10.1109/ICPR.2008.4761372>, 2008.
- Raschendorfer, M.: The new turbulence parameterization of LM, Tech. rep., COSMO newsletter, Deutscher Wetterdienst, [http://www.cosmo-model.org/content/model/documentation/newsLetters/newsLetter01/newsLetter\\_01.pdf](http://www.cosmo-model.org/content/model/documentation/newsLetters/newsLetter01/newsLetter_01.pdf) (last access: 22 May 2021), 2001.
- Reyers, M., Pinto, J. G., and Moemken, J.: Statistical–dynamical downscaling for wind energy potentials: evaluation and applications to decadal hindcasts and climate change projections, *Int. J. Climatol.*, 35, 229–244, <https://doi.org/10.1002/joc.3975>, 2015.
- Reyers, M., Moemken, J., and Pinto, J. G.: Future changes of wind energy potentials over Europe in a large CMIP5 multi-model ensemble, *Int. J. Climatol.*, 36, 783–796, <https://doi.org/10.1002/joc.4382>, 2016.
- Rijksdienst voor Ondernemend Nederland: Offshorewind RVO, <https://offshorewind.rvo.nl/> (last access: 15 February 2022), 2022.
- Rockel, B., Will, A., and Hense, A.: The regional climate model COSMO-CLM (CCLM), *Meteorol. Z.*, 17, 347–348, <https://doi.org/10.1127/0941-2948/2008/0309>, 2008.
- Ronda, R., Wijnant, I., and Stepek, A.: Inter-annual wind speed variability on the North Sea, Tech. rep., TR-360, KNMI – Royal Netherlands Meteorological Institute, <https://cdn.knmi.nl/knmi/pdf/bibliotheek/knmi/TR/TR360.pdf> (last access: 5 April 2021), 2017.
- Santos, J., Rochinha, C., Liberato, M., Reyers, M., and Pinto, J.: Projected changes in wind energy potentials over Iberia, *Renew. Energy*, 75, 68–80, <https://doi.org/10.1016/j.renene.2014.09.026>, 2015.
- Sathe, A., Gryning, S.-E., and Peña, A.: Comparison of the atmospheric stability and wind profiles at two wind farm sites over a long marine fetch in the North Sea, *Wind Energy*, 14, 767–780, <https://doi.org/10.1002/we.456>, 2011.
- Schneemann, J., Rott, A., Dörenkämper, M., Steinfeld, G., and Kühn, M.: Cluster wakes impact on a far-distant offshore wind farm’s power, *Wind Energ. Sci.*, 5, 29–49, <https://doi.org/10.5194/wes-5-29-2020>, 2020.
- Sheridan, L. M., Krishnamurthy, R., and Gaudet, B. J.: Assessment of model hub height wind speed performance using DOE lidar buoy data, Tech. rep., pNNL-30840, PNNL – Pacific Northwest National Lab., Richland, WA, USA, <https://doi.org/10.2172/1779495>, 2021.
- Shields, M., Beiter, P., Nunemaker, J., Cooperman, A., and Duffy, P.: Impacts of turbine and plant up sizing on the levelized cost of energy for offshore wind, *Appl. Energy*, 298, 117189, <https://doi.org/10.1016/j.apenergy.2021.117189>, 2021.
- Siedersleben, S. K., Platis, A., Lundquist, J. K., Djath, B., Lampert, A., Bärfuss, K., Cañadillas, B., Schulz-Stellenfleth, J., Bange, J., Neumann, T., and Emeis, S.: Turbulent kinetic energy over large offshore wind farms observed and simulated by the mesoscale model WRF (3.8.1), *Geosci. Model Dev.*, 13, 249–268, <https://doi.org/10.5194/gmd-13-249-2020>, 2020.
- Stevens, R. J., Gayme, D. F., and Meneveau, C.: Effects of turbine spacing on the power output of extended wind-farms, *Wind Energy*, 19, 359–370, <https://doi.org/10.1002/we.1835>, 2016.
- Stull, R. B.: An introduction to boundary layer meteorology, in: vol. 13, Springer Science & Business Media, <https://doi.org/10.1007/978-94-009-3027-8>, 1988.
- Tammelin, B., Vihma, T., Atlaskin, E., Badger, J., Fortelius, C., Gregow, H., Horttanainen, M., Hyvönen, R., Kilpinen, J., Latikka, J., Ljungberg, K., Mortensen, N. G., Niemelä, S., Ruosteenoja, K., Salonen, K., Suomi, I., and Venäläinen, A.: Production of the Finnish wind atlas, *Wind Energy*, 16, 19–35, <https://doi.org/10.1002/we.517>, 2013.
- The Crown Estate: Marine Data Exchange, <https://www.marinedataexchange.co.uk> (last access: 22 March 2022), 2022.
- Tiedtke, M.: A comprehensive mass flux scheme for cumulus parameterization in large-scale models, *Monthly weather review*, 117, 1779–1800, [https://doi.org/10.1175/1520-0493\(1989\)117<1779:ACMFSF>2.0.CO;2](https://doi.org/10.1175/1520-0493(1989)117<1779:ACMFSF>2.0.CO;2), 1989.
- van Stratum, B., Theeuwes, N., Barkmeijer, J., van Ulft, B., and Wijnant, I.: A One-Year-Long Evaluation of a Wind-Farm Parameterization in HARMONIE-AROME, *J. Adv. Model. Earth Syst.*, 14, e2021MS002947, <https://doi.org/10.1029/2021MS002947>, 2022.
- Vergara-Temprado, J., Ban, N., Panosetti, D., Schlemmer, L., and Schär, C.: Climate models permit convection at much coarser resolutions than previously considered, *J. Climate*, 33, 1915–1933, <https://doi.org/10.1175/JCLI-D-19-0286.1>, 2020.
- Verhoef, A. and Stoffelen, A.: Validation of ASCAT 12.5-km winds, Tech. rep., reference: SAF/OSI/CDOP/KNMI/TEC/RP/147, [https://knmi-scatterometer-website-prd.s3-eu-west-1.amazonaws.com/publications/validation\\_of\\_ascat\\_12.5km\\_winds\\_1.3.pdf](https://knmi-scatterometer-website-prd.s3-eu-west-1.amazonaws.com/publications/validation_of_ascat_12.5km_winds_1.3.pdf) (last access: 6 May 2021), 2009.
- Verkaik, J.: Documentatie Windmetingen In Nederland (in Dutch), Tech. rep., KNMI – Royal Netherlands Meteorological Institute – klimatologische dienst, <https://www.knmi.nl/windmetingen>, 2015.

- [//www.researchgate.net/publication/266441846\\_Documentatie\\_Windmetingen\\_In\\_Nederland](https://www.researchgate.net/publication/266441846_Documentatie_Windmetingen_In_Nederland) (last access: 6 June 2021), 2001.
- Vigin, L.: shapefiles of the Belgian and Dunkirk offshore zones, RBINS – Royal Belgian Institute of Natural Science, <https://www.bmdc.be/NODC/index.xhtml> (last access: 19 January 2022), 2022.
- Volker, P. J., Hahmann, A. N., Badger, J., and Jørgensen, H. E.: Prospects for generating electricity by large onshore and offshore wind farms, *Environ. Res. Lett.*, 12, 034022, <https://doi.org/10.1088/1748-9326/aa5d86>, 2017.
- Werkhoven, E. and Verhoef, J.: Offshore Meteorological Mast IJmuiden – Abstract of Instrumentation Report, Tech. rep., ECN-Wind Memo-12-010, Ministry of Economic Affairs, Agriculture and Innovation of The Netherlands, <https://offshorewind-measurements.tno.nl/> (last access: 26 March 2022), 2012.
- Westerhellweg, A., Neumann, T., and Riedel, V.: FINO1 mast correction, Vol. 21, DEWI-Magazin, 2012.
- Wijnant, I., van den Brink, H., and Stepek, A.: North Sea wind climatology Part 1: a review of existing wind atlases, Tech. rep., technical report TR-342, KNMI – Royal Netherlands Meteorological Institute, <https://cdn.knmi.nl/knmi/pdf/bibliotheek/knmipubTR/TR342.pdf> (last access: 30 March 2021), 2014.
- Wouters, D. and Verhoef, J.: Verification of Leosphere Windcube WLS7-577 at ECN part of TNO LiDAR Calibration Facility, for offshore measurements at Lichteiland Goeree, Tech. rep., TNO 2019 R10398, ECN, <https://offshorewind-measurements.tno.nl/> (last access: 21 May 2021), 2019a.
- Wouters, D. and Verhoef, J.: Verification of ZephIR 300 unit 315 at ECN part of TNO LiDAR Calibration Facility, for offshore measurements at Euro Platform, Tech. rep., TNO 2018 R10762, ECN, <https://offshorewind-measurements.tno.nl/> (last access: 21 May 2021), 2019b.
- Wouters, D. and Verhoef, J.: Verification of ZephIR 300 unit 563 at ECN part of TNO LiDAR Calibration Facility, for offshore measurements at K13-A production platform, Tech. rep., TNO 2018 R10850, ECN, <https://offshorewind-measurements.tno.nl/> (last access: 21 May 2021), 2019c.



OPEN

## Accelerating deployment of offshore wind energy alter wind climate and reduce future power generation potentials

Naveed Akhtar<sup>✉</sup>, Beate Geyer, Burkhardt Rockel, Philipp S. Sommer & Corinna Schrum

The European Union has set ambitious CO<sub>2</sub> reduction targets, stimulating renewable energy production and accelerating deployment of offshore wind energy in northern European waters, mainly the North Sea. With increasing size and clustering, offshore wind farms (OWFs) wake effects, which alter wind conditions and decrease the power generation efficiency of wind farms downwind become more important. We use a high-resolution regional climate model with implemented wind farm parameterizations to explore offshore wind energy production limits in the North Sea. We simulate near future wind farm scenarios considering existing and planned OWFs in the North Sea and assess power generation losses and wind variations due to wind farm wake. The annual mean wind speed deficit within a wind farm can reach 2–2.5 ms<sup>-1</sup> depending on the wind farm geometry. The mean deficit, which decreases with distance, can extend 35–40 km downwind during prevailing southwesterly winds. Wind speed deficits are highest during spring (mainly March–April) and lowest during November–December. The large-size of wind farms and their proximity affect not only the performance of its downwind turbines but also that of neighboring downwind farms, reducing the capacity factor by 20% or more, which increases energy production costs and economic losses. We conclude that wind energy can be a limited resource in the North Sea. The limits and potentials for optimization need to be considered in climate mitigation strategies and cross-national optimization of offshore energy production plans are inevitable.

The increasing demand for carbon-neutral energy production has fostered the rapidly increasing deployment of offshore wind farms (OWFs). The construction of OWFs is generally 1.5–2 times more expensive than onshore wind farms<sup>1</sup>. Additionally, their maintenance/repair, power network, and obtaining observational data for optimization are more challenging and costlier<sup>2</sup>. Although OWFs are more expensive in construction and maintenance than onshore wind farms, these costs are offset to some extent by the higher capacity factor (CF) of OWFs due to the strength of offshore wind resources<sup>3</sup>. About 10 km off the coast, sea surface winds are generally 25% higher than onshore winds. These high offshore wind resources can be utilized 2–3 times longer to generate electricity than onshore wind farms in the same period of time<sup>4,5</sup>. Europe's total installed OWF capacity reached 22 GW in 2019; of that capacity, 77% is installed in the North Sea<sup>6</sup>. As part of the ambitious plans of the EU to reach climate neutrality a significant increase to 450 GW total offshore wind energy capacity is intended by 2050<sup>7</sup>. About 47% (212 GW) of these will be installed in the North Sea at an annual consenting rate of 8.8 GW per year during the 2020s<sup>8</sup>. This implies that the North Sea forms one of the worldwide hotspots of OWF development. Figure 1 shows the planning status of OWFs in the North Sea by 2019<sup>9</sup>. These massive developments are motivated by the strong and reliable wind resources in the North Sea at shallow water depths.

Wind farms are usually clustered around transmission lines to minimize deployment and operating costs. Hence, in addition to the quality of wind resources also the transmission lines determine whether a location is optimal for a wind farm. Despite the considerable availability of wind resources, evidence suggests that wake effects, which manifest as a downwind reduction in wind speed, can undermine the potential of cost-efficient wind energy production<sup>10–12</sup>. The efficiency limits that can arise from clustering and the overall regional saturation might limit the offshore wind energy production. These important questions at regional and longer times scales remain yet unassessed and need detailed scientific analysis for an efficient climate mitigation strategy.

Institute of Coastal Systems-Analysis and Modeling, Helmholtz-Zentrum Hereon, Geesthacht, Germany. ✉email: [redacted]@hereon.de

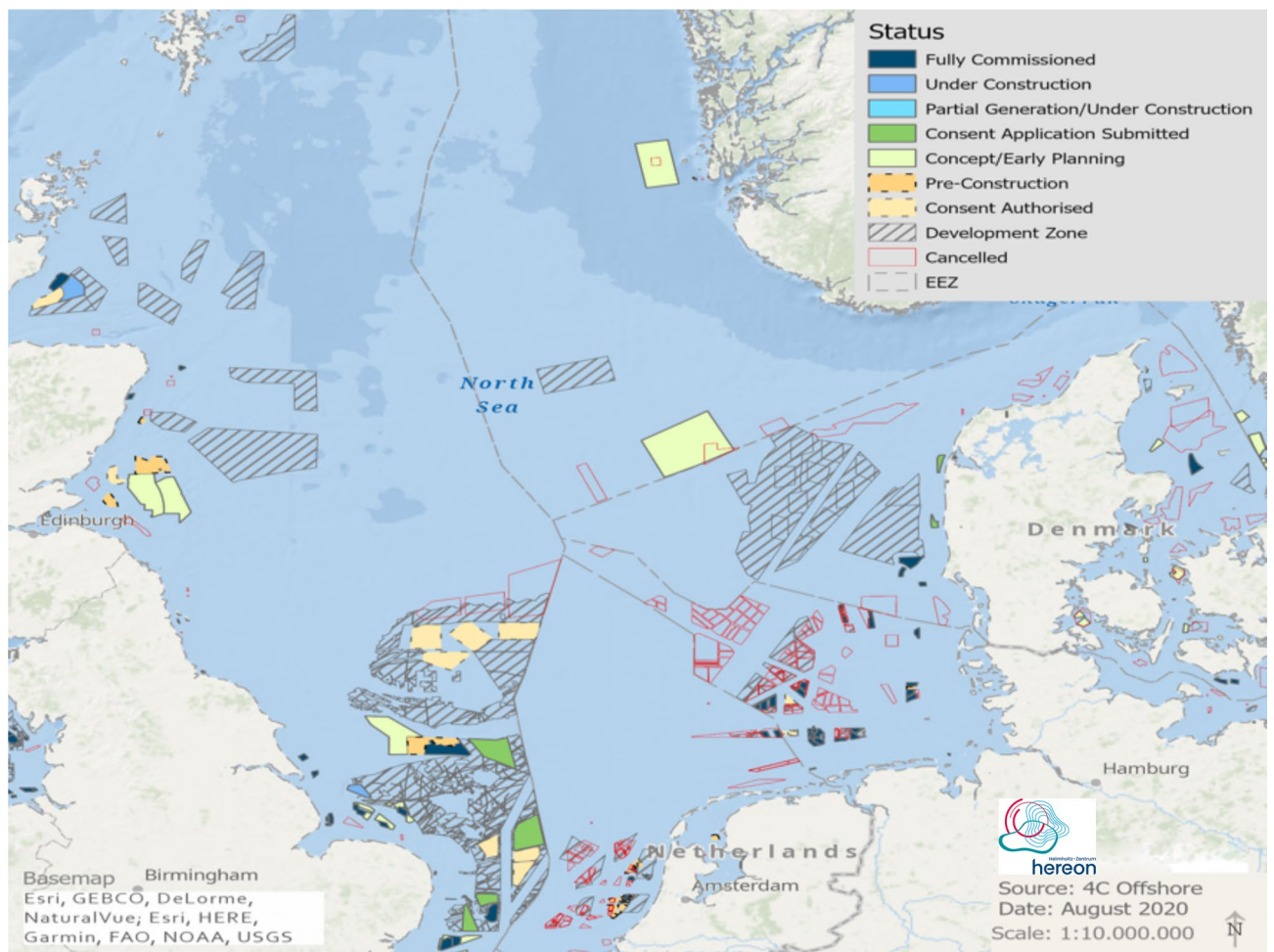


**Figure 1.** Distribution of OWFs in the North Sea (4c Offshore. <https://www.4coffshore.com/windfarms/>, 2019). Colors indicate the planning status of the OWFs by 2019. This map was created by Ulrike Kleeberg with ArcGIS Pro 10.7 (ESRI Inc. ArcGIS Pro 10.7, 2019).

Additionally, in order to develop the OWFs efficiently and accurately, a comprehensive evaluation of the wind resources is required.

Wind turbines extract kinetic energy (KE) from the atmosphere and convert part of that energy into electric power. The remaining part of the energy is converted into turbulent kinetic energy (TKE); that generates wakes (downwind wind speed deficits)<sup>13–17</sup>. Airborne observations show that TKE is significantly increasing (factor of 10–20) above the wind farms<sup>17</sup>. These observations also show that wind farm wakes can extend up to 50–70 km under stable atmospheric conditions<sup>18</sup>. These wakes further impact the efficiency of downwind wind farms through changes in the temperature and turbulence in the boundary layer<sup>19</sup>. At a given wind speed, colder and denser air masses provide more energy than warmer and lighter air masses. Moreover, atmospheric turbulence additionally reduces the energy output and increases the load on wind farm structures and equipment<sup>19</sup>. Observational evidence shows that wakes can increase the temperature by 0.5 °C and humidity by 0.5 g per kilogram at hub height, even as far as 60 km downwind of wind farms<sup>20</sup>. Case studies related to wake dynamics have largely been limited to single wind turbines<sup>21,22</sup> and/or individual wind farms<sup>23–26</sup>. Only a few studies have analyzed the wake effects caused by neighboring wind farms<sup>11,25,27</sup>. In a recent study<sup>11</sup>, the authors highlighted the economic losses suffered by onshore downwind wind farms due to the wake effects of upwind wind farms. Estimates of the wake effects on power production and environmental changes have been limited to short timescales (on the order of a few days or to a specific year<sup>28</sup>) and only one or two wind farms. The aforementioned studies emphasize the need to better understand the physical and economic interactions of large wind farms with complex clustered layouts (such as those planned in the North Sea) to ensure the efficient utilization of wind energy resources.

Building on process understanding of case studies, we assess for the first time the wake effect on the power production of both existing and planned large OWFs on a regional scale for the North Sea over a period of 10 years. It allows us to take into account the natural variability in wind climate, as inter-annual variability plays an important role in wind energy<sup>29</sup>. We perform two high-resolution numerical scenario simulations for a multi-year simulation period, one considering existing and currently planned OWFs in the North Sea and one for the undisturbed atmosphere. For the future scenario simulation, we apply a generic wind farm parameterization considering energy extraction and turbulence effects using a standard wind farm configuration, which we validate



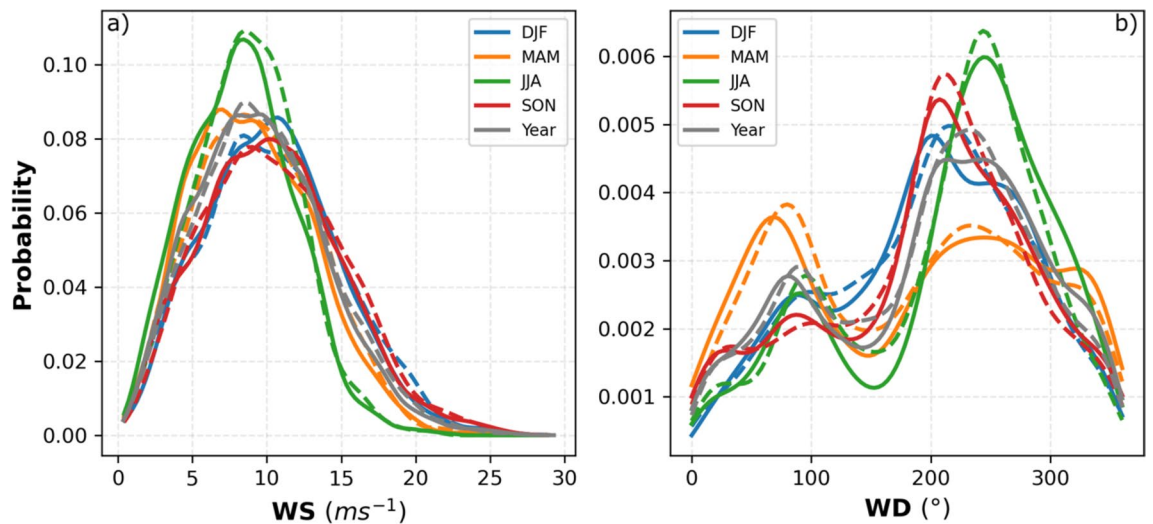


**Figure 2.** Annual and seasonal probability density functions calculated using the hourly (a) wind speed and (b) wind direction data at FINO1 (6.5875°E and 54.01472°N) at a height of 90 m in the period 2008–2009. Dashed lines result from measurements, while solid lines are from COSMO-CLM simulation. Gray lines indicate data for the entire period whereas colors indicate the different seasons as given in the legend.

against earlier published high-resolution observations<sup>30</sup> to ensure the realism of the scenario simulation. Mean wind changes will be analyzed and efficiency loss in offshore energy production will be estimated in terms of the Capacity Factor (CF) deficiency. Given the ongoing development of OWFs in the North Sea, our study highlights the urgent need to consider feedbacks between existing and planned OWFs to assess physical and economic impacts to optimize planning and to assess the limits and environmental impacts of industrial offshore energy production. To the best of our knowledge, this is the first study to estimate the wind speed deficits due to OWF production at a basin-wide scale covering a multi-year period and to investigate the effect of these deficits on the CF of wind farms. Furthermore, in this study, we evaluated the wind farm parameterization for real case simulations against the observations.

### Experimental design

All existing and planned OWFs by 2015<sup>31</sup> in the North Sea area (see Fig. SI 1, the latest planning status is shown in Fig. 1) are considered for the scenario simulations. We focus on the Central and Southern North Sea where OWFs are planned close to each other. The scenario simulations are carried out for a multi-year period from 2008 to 2017, to account for a range of different weather conditions to assess the impact of large-scale OWF development on the production potential of wind farms. For the numerical simulations, we use the high-resolution Consortium for Small-Scale Modeling (COSMO)-CLimate Mode (CLM) regional climate model (RCM)<sup>32</sup> both without and with a wind farm parameterization. An existing wind farm parameterization<sup>15,16,33,34</sup> for a standard turbine size has been implemented into COSMO-CLM to include the effects of wind farms; these RCM simulations provide us with high-resolution spatiotemporal estimates of the wind speed over wind farm areas. A CF model<sup>35</sup> has been used to assess the average energy production of wind farms based on wind speed. Several factors can influence the CF, such as the wake effect, turbine efficiency, and offshore distance<sup>36</sup>. For the inter-comparison of scenario simulations, we consider the impact of wakes on the CF, to illustrate the potential impact of feedbacks between wind farm deployment and regional atmospheric conditions. Hereafter, “CCLM\_WF” and “CCLM” refer to the COSMO-CLM simulations with and without a wind farm parameterization, respectively.

### Verification of the simulated wind fields and OWFs wakes

**Comparison with the point observations of wind fields.** To verify the realism of our scenario simulation, a detailed validation against published data<sup>30,37</sup> was performed. The simulated wind characteristics over the North Sea can be directly evaluated using data from the research platforms<sup>37</sup> FINO1 (6.5875°E, 54.01472°N) and FINO3 (7.158333°E, 55.195°N) starting in 2004 and 2009, respectively. The high quality of the mast-corrected measurement data allows for a detailed analysis of both the wind speed and the wind direction. Here we compared the FINO1 and FINO3 measurements with CCLM simulations for the period 2008–2009 and 2009–2014 respectively to avoid the effects of the OWF Alpha Ventus and DanTysk on the mast measurements<sup>38</sup>. The annual and seasonal probability density functions (PDFs) derived from hourly values of the wind speed and wind direction are in good agreement with the FINO1 data (Fig. 2). The annual and seasonal biases, root mean square error (RMSE), correlation coefficients, and Perkins’ score (PS)<sup>39</sup> calculated between the CCLM simulation results and observations (FINO1 and FINO3) are presented in Tables 1 and 2. Compared with the FINO1 data, the CCLM winds show small, mostly negative biases of 0.27 ms<sup>-1</sup> with simulated wind speeds that are lower than the observed wind speeds. During the spring and summer season model bias become stronger, along with higher RMSE values (Table 1). The autumn correlations of 0.87 are slightly higher than those in the other seasons. The PS of the yearly mean simulated wind speed is 0.95, with the highest values during winter (0.92) and the



	Bias		RMSE		CORR		PS	
	WS (ms <sup>-1</sup> )	WD (°)	WS (ms <sup>-1</sup> )	WD (°)	WS	WD	WS	WD
Yearly	-0.27	3.07	2.81	70.11	0.79	0.71	0.95	0.92
DFJ	-0.08	1.44	3.41	64.61	0.73	0.71	0.92	0.88
MAM	-0.34	1.21	2.54	76.53	0.82	0.72	0.85	0.77
JJA	0.40	8.08	2.73	72.18	0.72	0.67	0.79	0.80
SON	-0.25	1.40	2.49	65.89	0.87	0.73	0.91	0.87

**Table 1.** Yearly and seasonal mean wind speed and wind direction bias (CCLM – FINO1), root mean square error (RMSE), correlation (CORR), and Perkin's score (PS) of CCLM compared with FINO1 in the period 2008–2009.

	Bias		RMSE		CORR		PS	
	WS (ms <sup>-1</sup> )	WD (°)	WS (ms <sup>-1</sup> )	WD (°)	WS	WD	WS	WD
Yearly	-0.39	-6.34	2.59	67.01	0.85	0.75	0.95	0.93
DFJ	-0.54	-7.95	2.60	55.91	0.87	0.81	0.92	0.88
MAM	-0.40	-9.12	2.55	70.32	0.84	0.77	0.73	0.80
JJA	-0.30	-0.45	2.72	79.92	0.75	0.63	0.62	0.78
SON	-0.37	-7.99	2.50	58.11	0.85	0.79	0.81	0.89

**Table 2.** Yearly and seasonal mean wind speed and wind direction bias (CCLM – FINO3), root mean square error (RMSE), correlation (CORR), and Perkin's score (PS) of CCLM compared with FINO3 in the period 2009–2014.

lowest values during summer (0.79). The simulated CCLM wind direction PDFs are also well represented; the prevailing southwesterly (200°–280°) wind directions are effectively captured (Fig. 2). On average, the CCLM-simulated wind directions show a positive bias of 3.07°, a small counterclockwise shift with an RMSE of 70.11° and a correlation coefficient of 0.71 (Table 1). Again, the simulated summer values show larger deviations from the observations with a bias of 8.08° and an RMSE of 72.18°; in addition, the correlation coefficient is lower than those in the other seasons. The simulated wind direction shows the highest PS during winter (0.88) and the lowest PS during spring (0.77) with a yearly value of 0.92. The simulated wind direction relative to FINO3 shows a negative bias of -6.34°, an RMSE of 67.01°, a correlation coefficient of 0.75, and a PS of 0.93 (Table 2). Studies show that the existing wind farms in the North Sea are already affecting the wind field reaching FINO1 and FINO3<sup>38</sup>. A comparison of the wind speed and direction between CCLM\_WF and FINO1 shows that the construction of planned wind farms will further affect their measurements in the future (Fig. SI 2). The annual and seasonal probability density functions (PDFs) derived from hourly values of the wind speed and wind direction are also in good agreement with the FINO3 data (Table 2 and Fig. SI 3).

**Wake effects in case studies: evaluation of CCLM.** For the sake of completeness, CCLM\_WF has been evaluated against airborne campaign data<sup>18</sup> to illustrate the ability of CCLM\_WF to simulate upwind flow and the spatial extent of wakes generated by wind farms. Here, we choose two different cases. In the first case, we evaluate the wake extent of the Amrumbank West wind farm; in the second case, we evaluated the wind speed deficit over the two Godewind farms. Only operational wind farms at the measurement times are considered in these simulations. Figure SI 4 shows the model domain and the wind farm locations.

*Case 10 September 2016.* A detailed comparison is performed for the wakes observed downwind of the Amrumbank West, Meerwind SüdOst, and Nordsee Ost wind farms with model simulations. The wake was measured during an aircraft campaign on 10 September 2016 between 0800 to 1100 UTC using five flight legs of 5 km, 15 km, 25 km, 35 km, and 45 km downwind of the Amrumbank West wind farm<sup>18,30</sup>. Stable atmospheric conditions and a wake extent of at least 45 km were measured. The installed turbines in Amrumbank West have a 90 m hub height and 120 m rotor diameter<sup>12</sup>. For this experiment, we employ only those wind farms which were existing at the time of measurements (see Fig. SI 4).

The simulated spatial extent of the wake agrees well with the measurement. Figure 3 shows the wake extents simulated in CCLM\_WF (interpolated on the aircraft track) and airborne observations (see Fig. SI 5a for a complete snapshot of the wind speed field simulated in CCLM\_WF and its difference from the observation). Both the observations and the simulations show a wake extending more than 45 km downwind of the wind farm. The simulation shows that the wake reached down to the Butendiek wind farm, located 50 km downwind of the Amrumbank West wind farm. However, the simulated wind direction is slightly rotated counterclockwise. Similar to the width of the wind farms, the wake width is approximately 12 km at the beginning, which expands and weakens as the distance increases from the generating wind farm. The transect of the simulated and observed wind speeds through the first flight leg of 5 km downwind of the wind farm shows that the simulated-observed

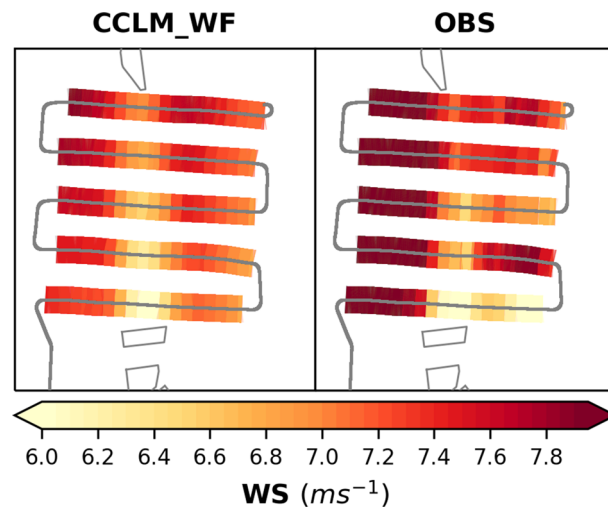


**Figure 3.** Wind speed at 90 m hub height (a) simulated in CCLM\_WF and (b) observed by aircraft measurements. The aircraft track (gray lines) shown here ranged from 0820 to 0924 UTC on 10 September 2016. The model simulations show the wind speed at 0900 UTC.

differences are smaller inside the wake than outside (Fig. SI 5b). In general, the model slightly underestimates the wind speed compared to the observations.

*Case 14 October 2017.* In the chosen case, we evaluate the wind speed at a height of 250 m over Godewind farms 1 and 2 with aircraft observations. The installed turbines in these wind farms have a 110 m hub height and 153 m diameter<sup>18</sup>. For this experiment, we employ the wind farm location data as in Fig. SI 4; however, we used the turbine dimensions as installed in Godewind farms.

Figure 4 shows the wind speeds at 1500 UTC on 14 October 2017 over the Godewind farms simulated in CCLM\_WF (interpolated on the aircraft track) and observed wind speeds (see Fig. SI 6a for a complete snapshot of the wind speed field simulated in CCLM\_WF and its difference from the observation). Stable atmospheric conditions were observed at the times of the measurements<sup>18</sup>. An observed speed-up around the wind farms is well reproduced in the simulations. The simulated wind speeds agree better with the observations inside the wake than outside (Fig. SI 6b).

Due to the relatively coarse horizontal resolution of RCMs (1–2 km), the effects of individual wind turbines (with a rotor span of 120 or 153 m) cannot be fully resolved. Therefore, the simulated wake effects of the wind turbine can be underestimated, and thus, the wake effects of wind farms can be underestimated. In the present wind farm parameterization<sup>16</sup>, the power produced by the wind turbine depends on the wind speed in the grid cell at the model level interacting with the rotor. The wind turbine removes momentum from the rotor-interacting layers to produce the power that leads to wind speed deficits in downwind grid cells.

The evaluation results show that COSMO-CLM with a wind farm parameterization realistically reproduces the effects of wind farms. The spatiotemporal variability of the wake effects and their impact on the CF of the wind farms at 90 m hub height are analyzed for the period 2008–2017 in the following sections.

### Wake effect on wind speed and turbulent kinetic energy

Our simulations show that the development of massive clustered OWFs significantly impacts the wind climate and efficiency of renewable energy production on a regional scale. The reduction in the annual mean wind speed reaches up to 2–2.5  $\text{ms}^{-1}$  during prevailing southwesterly (200°–280°) winds, and that in the seasonal mean reaches more than 3  $\text{ms}^{-1}$  (see Fig. 5 and Figs. SI 2 and SI 8).

The wind speed in the North Sea exhibits strong spatial and temporal variability. At 90 m hub height, the wind speed varies seasonally, with a minimum of approximately 7–8.5  $\text{ms}^{-1}$  in summer and a maximum of 10–11.5  $\text{ms}^{-1}$  in winter (Fig. SI 7). The presence of a wind farm impacts the boundary layer flow over the wind farm and its vicinity by extracting KE from the mean flow and generating TKE. The highest wind speed deficit in the annual mean is about –18%, and the increase in TKE is nearly a factor of 4 over the wind farm itself (Fig. 6). These changes in wind speed and TKE extend vertically to a height of approximately 500 m (about 350 m above the turbine height). A deficit/raise of about 1  $\text{ms}^{-1}$ /0.6  $\text{m}^2 \text{s}^{-2}$  in wind speed/TKE extends to a height of approximately 200 m. The maximum change in wind speed and TKE found in the atmospheric levels between the hub (90 m) and tip height (153 m) of the wind turbines. The change in the wind speed and TKE above the turbine height is consistent with the previous studies<sup>16,40,41</sup>. The wind speed deficits are higher during spring (–22%) and summer (–20.8%) than during the other seasons (see also Fig. SI 8), the reason for which is explained later in this section. The increase in the TKE is found higher during winter (factor of 3.2) and autumn (factor of 3.8). The addition TKE source in the wind farm parameterization improves the representation of mixing and wind speed deficit during stable conditions<sup>17</sup>. The change in wind speed and TKE increases the boundary layer height<sup>16</sup>.

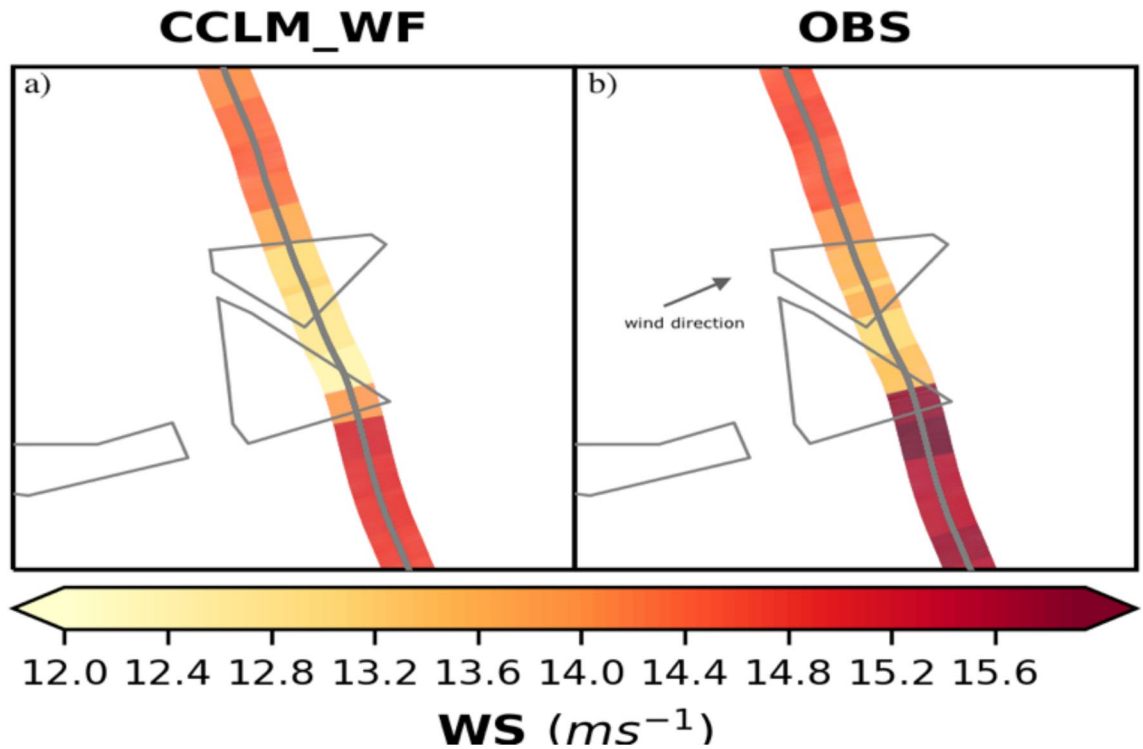


**Figure 4.** Wind speed at a height of 250 m (a) simulated in CCLM\_WF and (b) observed by aircraft measurements. The aircraft track shown here ranged from 1445 to 1500 UTC on 14 October 2017. Arrow indicates the wind direction. The model simulations show the wind speed at 1500 UTC.

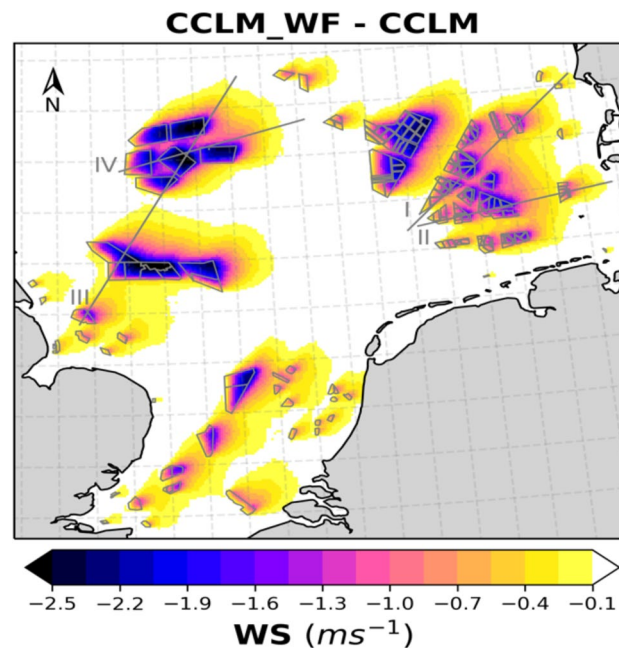


**Figure 5.** Annual mean wind speed deficits (CCLM\_WF – CCLM) outside and inside the wind farms for the prevailing wind directions of  $200^{\circ}$ – $280^{\circ}$  at hub height (90 m) in the period 2008–2017. Numbered gray lines indicate the transects used for calculations of Fig. 8 and Fig. SI 6 and SI 7. This figure was created with Matplotlib (Hunter, J. D., Matplotlib: a 2D graphics environment. Computing in Science and Engineering 9, 2007) and Cartopy (Met office, Cartopy: a cartographic python library with a matplotlib interface. Exeter, Devon, <https://scitools.org.uk/cartopy>, 2015).

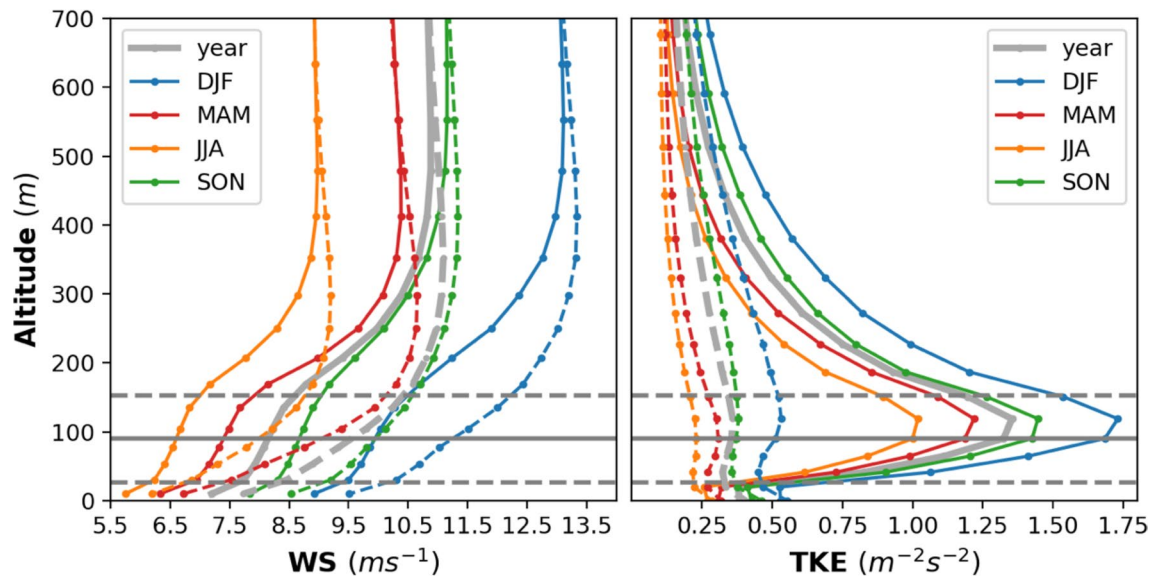


**Figure 6.** Annual and seasonal mean vertical profiles of the wind speed (left) and turbulent kinetic energy (right) simulated by CCLM (broken dotted lines) and CCLM\_WF (solid dotted line) over the wind farm areas in the period 2008–2017. Solid circles indicate the model levels. The horizontal solid gray line indicates the hub height (90 m) of the turbine whereas dotted gray lines indicate lower (27 m) and upper (153 m) tip of the rotor.

Wakes, i.e., downwind reductions in wind speed, exhibit significant spatial variability inside and outside wind farms (Fig. 5). The wind speed deficit inside a wind farm increases with increasing distance from the upstream edge, reaching a maximum of 2–2.5  $\text{ms}^{-1}$ . In an idealized numerical study, a maximum reduction of approximately 16% in the wind speed and increase in TKE by nearly a factor of 7 was estimated at hub height over a  $10 \times 10$  km wind farm<sup>16</sup>. Here we used a realistic climate set up to study a scenario with clustered and large-scale wind farms and found larger mean wind speed deficits of approximately 18–20% of the annual mean wind. In our case, the increase in the mean TKE within the wind farm is almost a factor of 3 less than that reported (factor of 7) in the idealized study<sup>16</sup>. This could be due to the reason that mean values of TKE over a longer period 2008–2017 are shown here.

The wind farm induced boundary layer mixing, air friction, turbulence and weaken stratification effects within and above the rotor area that reach about 600 m. The maximum differences are found in the layers between the hub and tip height of the turbine. The reduction in the wind speed extends highest during spring when the atmospheric conditions are generally stable. The increase in TKE leads to the mixing of more momentum from aloft<sup>15,24</sup>. This mechanism is more pronounced during winter and autumn when atmospheric conditions are generally unstable in the North Sea. The strength of the TKE depends on the difference between the power coefficient and thrust coefficients which varies with the wind speed.

The wakes forming downwind extend over large distances and influence the wind climate at surrounding wind farms. The wake extends varies, it depends on wind speed and atmospheric stratification and might extend up to 70 km downwind<sup>11,18,20</sup>. On average wakes extend ca 40–45 km downwind (Fig. SI 8).

### Implications for the CF

The downwind speed reduction results in a significant decrease in the efficiency of energy production here illustrated in terms of the CF. The wake induced decrease in CF up to 22% in the annual mean and up to 26% for the seasonal mean with the highest values at the downwind edge within the wind farms during southwesterly wind directions (see Fig. 7 and Figs. SI 4 and SI 5). Outside of the wind farms, these values decrease as the distance from the wind farms is increasing. A decrease of about 1% has been noted at a distance of 35–40 km in annual means during southwesterly wind directions. The highest drops are observed for the large wind farms in the German Bight and the UK's Dogger Bank for southwesterly wind directions (Fig. 7).

Without the wind farms, the annual mean CF for all wind directions varies spatially in the North Sea from 50 to 62%, with higher values during winter (65–70%) and lower values in summer (37–50%, Fig. SI 9). These values are strongly reduced in the areas where the large-size wind farms are clustered. The mean wind speed deficits and CF losses for all wind directions show that the wake effect extends more towards the northeast than in the other wind directions, indicating the dominance of southwesterly winds (Fig. SI 8 and Fig. SI 10).

A more specific analysis of the implications of large wind farm clusters and extremely large farms for the efficiency of neighboring farms and clusters in the area of the German Bight and the Dogger Bank (Fig. SI 1) highlights substantial CF losses. Figure 8 shows the annual and seasonal mean wind speed deficits and CF losses through the wind farms on two of the transects (gray lines I and III) shown in Fig. 5 in the case of prevailing winds in the German Bight and the UK's Dogger Bank. The wind farms in both of these areas are large and are located spatially close to each other. These transects show the strong horizontal influences of the wind farms together with the reductions in the wind speed and CF. Mean CF and wind speed show characteristic patterns



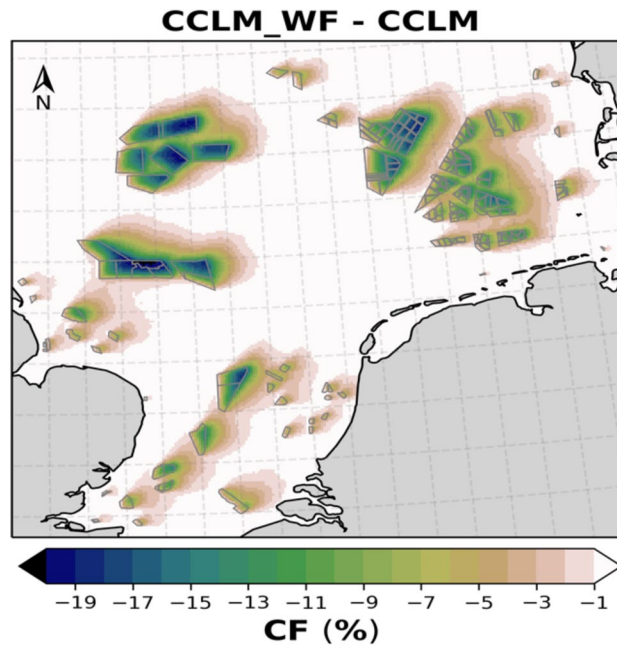


**Figure 7.** Annual mean losses in the capacity factor CF (CCLM\_WF – CCLM) out- and inside of the wind farms (gray lines) for the prevailing wind directions of 200°–280° at hub height (90 m) in the period 2008–2017. This figure was created with Matplotlib (Hunter, J. D., Matplotlib: a 2D graphics environment. Computing in Science and Engineering 9, 2007) and Cartopy (Met office, Cartopy: a cartographic python library with a matplotlib interface. Exeter, Devon, <https://scitools.org.uk/cartopy>, 2015).

along transects crossing several wind farms (Fig. 8). The wind speed deficit, being higher towards the downwind wind farm edge, leads to an annual reduction of up to 25% in the CF of downwind wind turbines inside wind farms; outside these wind farms, the CF losses reach up to 20% depending on the size of the farm and distance away from it. For example, as shown in Fig. 8a, wind farm 2, which is 7 km from wind farm 1, suffers a mean wind speed deficit of 1–1.5  $\text{ms}^{-1}$ . This reduces the CF of upwind turbines by 10–15% and that of downwind turbines by 15–20% in wind farm 2. Then, the wakes generated by wind farm 2 extend up to wind farm 3 (25 km away) with a deficit of 0.5–0.8  $\text{ms}^{-1}$  and CF losses of 5–8%. The wake effect of wind farm 4 reaches up to 30 km. The wind speed between wind farms 1 and 2 recovers approximately 45% in 5 km. However, the recovery of the wind speed in the following wind farms is slow due to the accumulated effects. Similarly, as shown in Fig. 8b, the wake effect reaches approximately 33 km between wind farms 2 and 3 and approximately 28 km beyond wind farm 5. The wake generated by the wind farm 4 reduces the CF of wind farm 5 (17 km away) up to 12%. Due to the short distance between wind farms 3 and 4 (about 5 km), wind farm 4 receives about 1.5–2  $\text{ms}^{-1}$  less wind speed which is equivalent to CF losses of 12–16%, during prevailing southwesterly winds. The transects of lines II and IV are shown in Fig. SI 11. The most productive wind turbines/farms are those located on the grid-cells at upwind edge/farms of the wind farms where the wind flow is uninterrupted<sup>25</sup>.

The wake effect can substantially influence the economic potential of wind power generation within a cluster, in large farms, and in neighboring farms located at a distance within the wake. Annual mean wind speed deficits of 1–1.5  $\text{ms}^{-1}$  and CF deficits of wind farms in the vicinity of large downwind clusters are frequent, within clusters, the reduction is even stronger and amounts up to a seasonal mean wind speed reduction of more than 3  $\text{ms}^{-1}$  or a seasonal CF reduction of up to 25% (Fig. 8). Average wakes extend up to 40 km for the largest wind farms and clusters.

The highest wind speed deficits occur during the spring season which leads to the highest CF losses in these seasons. On a monthly timescale, the highest wind speed deficits are simulated in March and April, whereas the lowest deficits are simulated in November and December (see Fig. SI 12). The seasonal variations in wind speed deficits are related to the relatively stronger winds (see Fig. SI 12) and weaker stratification<sup>42</sup> during the autumn and winter seasons compared to the spring seasons. During spring, the atmospheric conditions are more stable than the other seasons which leads to longer wakes<sup>18,42–44</sup>. It implies that the most productive season is winter when the wind speed is higher and the stratification not stable.

## Discussion and conclusions

The results show that the wind fields simulated by the regional climate model COSMO-CLM are in good agreement with the mast measurement stations FINO1 and FINO3 in the North Sea. It also indicates that the deployment of large wind farms near the mast measurement stations will affect their measurements. The COSMO-CLM model with the wind farm parametrization<sup>15</sup> simulated the wake generated by the wind farms reasonably well. Despite the differences in the upwind wind speed, the length and width of the wake were simulated quite well.



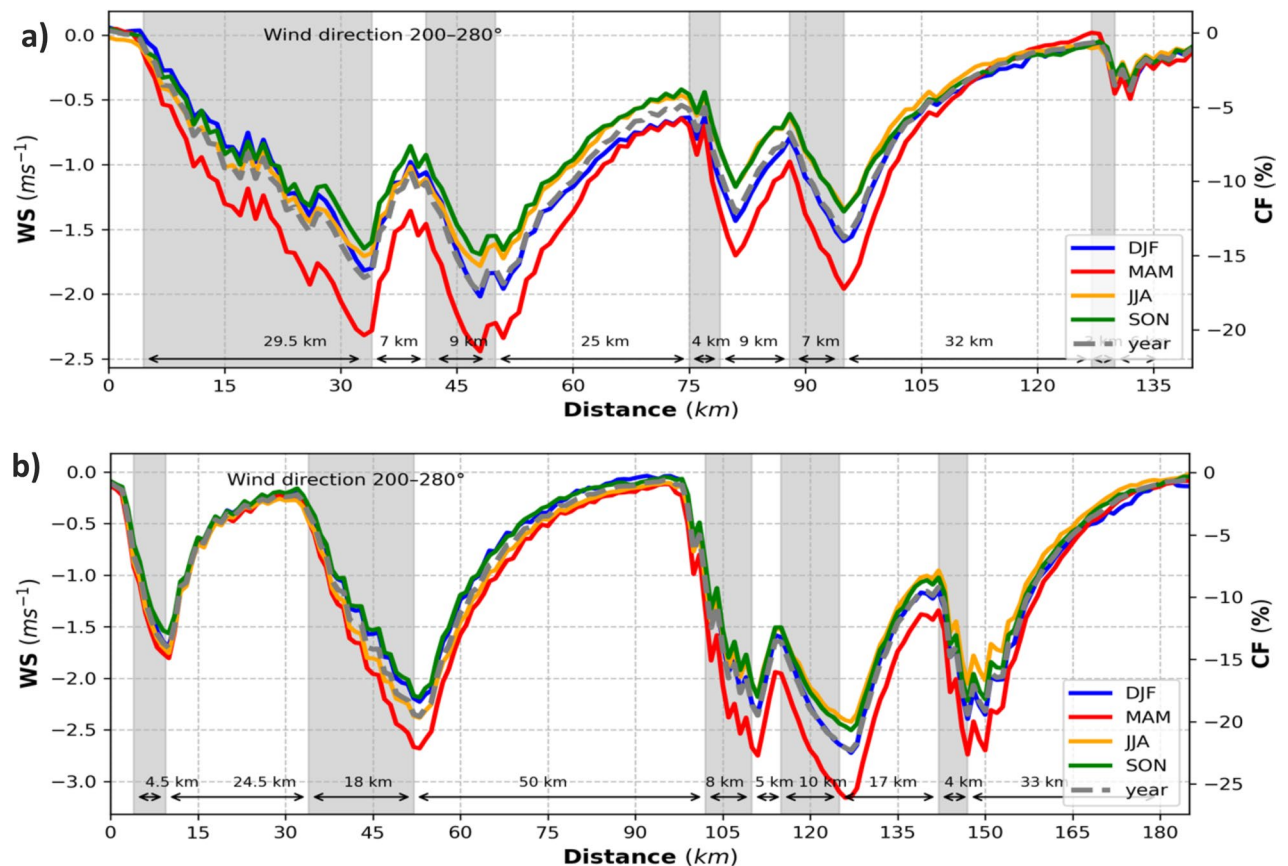


**Figure 8.** (a) Transects of the seasonal (colored, see legend) and yearly mean (dashed gray) wind speed deficits (left axis;  $\text{CCLM\_WF} - \text{CCLM}$ ) and capacity factor losses (right axis;  $\text{CCLM\_WF} - \text{CCLM}$ ) for the prevailing wind directions of  $200^{\circ}$ – $280^{\circ}$  in the period 2008–2017 at hub height (90 m) taken at transect I (German Bight, Fig. 5) latitude  $54.2^{\circ}$ – $55.6^{\circ}$ N and longitude  $5.45^{\circ}$ E– $8.0^{\circ}$ E. Gray sectors indicate the wind farm positions. Arrows and attached numbers give the distances between the edges of the wind farms. (b) As of (a) but for transect III (Dogger Bank, Fig. 5) latitude  $54.4^{\circ}$ – $55.8^{\circ}$ N and longitude  $0.8^{\circ}$ E– $3.15^{\circ}$ E.

Our results show that clusters of large wind farms, such as the farms planned for the near future in the UK's Dogger Bank and the German Bight, have the potential to substantially modify the atmospheric dynamics and lead to local mean wind speed reductions extending as far as more than 40 km downwind from the farm. Depending on the size of the wind farm, generally, the annual mean wind speed deficit can reach  $2$ – $2.5 \text{ ms}^{-1}$  which is equivalent to the power loss of  $1$ – $2 \text{ MW}^{45}$ . These results are consistent with the previous studies<sup>15,46,47</sup>. These authors studied the consequences of wind farms in case studies and short-term simulations. Our results show that the previously identified effects accumulate and influence the mean wind pattern. We identified a trade-off in the clustering of offshore wind farms. Clustering supports reduced energy production costs due to reduced infrastructure investments, but these advantages can be offset by wakes effects and the consequent reduction of CF. Our results emphasize that wind energy in the North Sea can be considered a limited resource. With the current plans to install offshore wind energy farms in the North Sea locally resource exploitation limits are reached. Better planning and optimization of locations are required that consider the development of wind wakes under realistic multi-year atmospheric conditions.

It is important to note that for our idealized study we used an average size (90 m hub height and 126 m rotor diameter) of turbines for existing wind farms. The rapidly increasing size and power generation of wind turbines<sup>48</sup> can intensify the wake effects vertically and horizontally. Moreover, wind farm installations in the North Sea are further accelerating and the here identified limits of power generation will become more important.

Southwesterly winds are predominant in the North Sea<sup>49</sup> (Fig. 2 and Fig. SI 3), and wake effects and their implications for power generation are therefore of particular importance for efficient energy production and production costs. During prevailing southwesterly winds, the power production of a downwind wind farm on the northeastern side is generally undermined by the wind farms located upwind.

Under stably stratified atmospheric conditions, weak vertical momentum mixing strengthens the wake effect<sup>11,15,18,20</sup>, and observational evidence shows that the wake can extend up to  $50$ – $70 \text{ km}$  under such atmospheric conditions<sup>30</sup>. Such individual cases are also well reproduced in the model simulations. These findings suggest that CF losses can be greater than the mean values shown herein and last longer under stable atmospheric conditions. Additionally, this study shows the annual and seasonal mean values calculated using hourly values during the period 2008–2017 to illustrate the mean wake effect on the CF using multi-year weather conditions

under all atmospheric conditions. This shows that the wind speed and CF deficits are highest during spring (mainly March–April) and lowest during November–December. The proximity of large wind farms affects the production of downwind wind turbines and wind farms, reducing the CF by more than 20–25%.

Already now, offshore renewable energy production in the North Sea shows substantial impacts on the atmospheric conditions therein, and these effects will continue to increase in the future. The evidence indicates that OWFs can impact marine animals and can raise environmental and climate concerns<sup>2,50,51</sup>. Since wind is one of the main factors modulating ecosystem productivity and ecosystem structure, OWFs have the potential to develop into dominant ecosystem drivers and need to be considered for ecosystem management and fisheries assessment. Therefore, an optimization strategy based on both national and international considerations is required to minimize economic losses and to assess the limits and environmental impacts of industrial offshore energy production. Furthermore, atmospheric wakes can induce ocean responses by modifying the sea surface roughness, atmospheric stability, and heat fluxes, and hence have the potential to influence local climate that requires further investigation<sup>32,52,53</sup>.

## Methods

**Numerical model setup.** In this study, we employ the regional climate model COSMO-CLM<sup>32</sup> with a wind farm parameterization<sup>15,33,34</sup> to consider the wind farm impacts on local atmospheric dynamics and the spatial–temporal pattern of wind speed deficits for a near-future wind farm scenario in the North Sea (see Fig. SI 1). COSMO-CLM uses a horizontal atmospheric grid mesh size of 0.02° (~2 km; 396 × 436 grid cells) and 62 vertical levels. In our configuration, COSMO-CLM uses a time step of 12 s with a third-order Runge–Kutta numerical integration scheme. The physics options include a cloud microphysics scheme, a delta-two-stream scheme for shortwave and longwave radiation, and a one-dimensional prognostic TKE advection scheme for the vertical turbulent diffusion parameterization<sup>54</sup>. The roughness length over the sea is computed on the basis of the Charnock formula<sup>54</sup>. The initial and lateral boundary conditions for the wind, sea surface temperature and other meteorological variables are taken from a CoastDat3 simulation<sup>29</sup>, which provides hourly data at a horizontal resolution of 0.11° (~11 km). The CoastDat3 atmospheric simulation was driven by European Centre for Medium-Range Weather Forecast (ECMWF) ERA-Interim reanalysis data in 6 hourly intervals at a horizontal resolution of 0.703°<sup>55</sup>.

To include wind farm effects, a wind farm parameterization for mesoscale numerical weather prediction models is implemented into COSMO-CLM<sup>56</sup>. This parameterization represents wind turbines as a momentum sink for the mean flow that converts KE into electric energy and TKE. The parameterization uses the velocity in each grid to estimate the average effect of the wind turbines within that grid. In our configuration, we use five vertical levels within the rotor area. The wind turbine extracts KE from the mean flow of each layer intersecting the rotor area. The amount of extracted KE depends on the wind speed, thrust, power coefficients, air density, and the density of the wind turbines in the considered grid<sup>45</sup> (see Fig. SI 13). A fraction of the extracted KE is converted into electric power by the turbine, whereas the remaining part of KE is converted into TKE. Here, we use the thrust and power coefficients as a function of wind speed derived from the theoretical National Renewable Energy Laboratory (NREL) 5 MW reference wind turbine for offshore system development<sup>45</sup>. These coefficients are close to those of real wind turbines, as the NREL 5 MW turbine data were derived from the REPower 5 MW offshore wind turbine. The wind turbine is hallmarked by a cut-in wind speed of 3 ms<sup>-1</sup>, a rated power speed of 12 ms<sup>-1</sup>, and a cut-out speed of 25 ms<sup>-1</sup>. In this study, we used the 90 m hub height and a 126 m rotor diameter with a rated power of 5.3 MW. The chosen turbine size falls within the range of existing wind farms by 2017 (Table SI 3). For a more detailed description of the wind farm parameterization and its implementation, we refer the readers to the previous studies<sup>15,33,34</sup>.

**Capacity factor (CF).** Because of the high variability of wind, low, medium, and high wind speeds alternate frequently, and wind turbines cannot operate continuously at the rated power. Therefore, the CF is commonly used to calculate the average energy production of a wind turbine. In turn, the CF is used for the economic assessment of a project, optimum turbine site matching, and the ranking of potential sites<sup>35</sup>. Several generic models are available in the literature to represent the ascending segment of the power curve between the cut-in and rated speeds (Fig. SI 13) independent of the power coefficients, which are unique to every turbine and difficult to generalize. These generic models use the cut-in, rated, and cut-out speeds to estimate the ascending segment of the power curve without information on the turbine output. We use a polynomial generic model<sup>35</sup> to estimate the CF using a Weibull probability density function based on hourly wind speed values and three speeds, namely, the cut-in (3 ms<sup>-1</sup>), rated (12 ms<sup>-1</sup>), and cut-out (25 ms<sup>-1</sup>), of the performance curve shown in Fig. SI 13.

## Data availability

The model COSMO-CLM\_WF and COSMO-CLM datasets supporting the results can be downloaded via CERA-DKRZ<sup>57,58</sup> and the COSMO-CLM namelists are available from the authors upon request. The COSMO-CLM simulations employ the community-wide publicly available (<http://www.clm-community.eu>) COSMO-CLM code. In situ airborne observational data were accessed via PANGAEA<sup>30</sup> and the FINO data were obtained via <https://www.fino-offshore.de/en/> and <http://fino.bsh.de>.

Received: 31 January 2021; Accepted: 24 May 2021  
Published online: 03 June 2021

## References

- Zheng, C. W., Li, C. Y., Pan, J., Liu, M. Y. & Xia, L. L. An overview of global ocean wind energy resource evaluations. *Renew. Sustain. Energy Rev.* **53**, 1240–1251 (2016).
- Leung, D. Y. C. & Yang, Y. Wind energy development and its environmental impact: A review. *Renew. Sustain. Energy Rev.* **16**, 1031e9 (2012).
- Junfeng, L., Pengfei, S. & Hu, G. China Wind Power Outlook 2010 (2010).
- Tambke, J., Lange, M., Focken, U., Wolff, J. O. & Bye, J. A. T. Forecasting offshore wind speeds above the North Sea. *Wind Energy* **8**, 3–16 (2005).
- Wang, J., Qin, S., Jin, S. & Wu, J. Estimation methods review and analysis of offshore extreme wind speeds and wind energy resources. *Renew. Sustain. Energy Rev.* **42**, 313–322 (2015).
- WindEurope. Offshore wind in Europe: Key trends and statistics 2019 (2019).
- The European Green Deal. Communication from the commission to the European parliament, the European council, the council, the European economic and social committee and the committee of the regions (2019).
- WindEurope. Our Energy Our Future: How offshore wind will help Europe go carbon-neutral (2019).
- 4c Offshore. <https://www.4c offshore.com/windfarms/>. (2019).
- Hasager, C. B. *et al.* Wind farm wake: The 2016 Horns Rev photo case. *Energies* **10**, 317 (2017).
- Lundquist, J. K., DuVivier, K. K., Kaffine, D. & Tomaszewski, J. M. Costs and consequences of wind turbine wake effects arising from uncoordinated wind energy development. *Nat. Energy* **4**, 26–34 (2019).
- Siedersleben, S. K. *et al.* Evaluation of a wind farm parametrization for mesoscale atmospheric flow models with aircraft measurements. *Meteorol. Z.* **27**, 401–415 (2018).
- Rhodes, M. E. & Lundquist, J. K. The effect of wind-turbine wakes on summertime US midwest atmospheric wind profiles as observed with ground-based Doppler Lidar. *Bound.-Layer Meteorol.* **149**, 85–103 (2013).
- Djath, B., Schulz-Stellenfleth, J. & Cañadillas, B. Impact of atmospheric stability on X-band and C-band synthetic aperture radar imagery of offshore windpark wakes. *J. Renew. Sustain. Energy* **10**, 043301 (2018).
- Fitch, A. C., Olson, J. B. & Lundquist, J. K. Parameterization of wind farms in climate models. *J. Clim.* **26**, 6439–6458 (2013).
- Fitch, A. C. *et al.* Local and mesoscale impacts of wind farms as parameterized in a mesoscale NWP model. *Mon. Weather Rev.* **140**, 3017–3038 (2012).
- Siedersleben, S. K. *et al.* Turbulent kinetic energy over large offshore wind farms observed and simulated by the mesoscale model WRF (3.8.1). *Geosci. Model Dev.* **13**, 249–268 (2020).
- Platis, A. *et al.* First in situ evidence of wakes in the far field behind offshore wind farms. *Sci. Rep.* **8**, 1–10 (2018).
- Irena. Renewable energy technologies: Cost analysis series. *Green Energy Technol.* **1** (2012).
- Siedersleben, S. K. *et al.* Micrometeorological impacts of offshore wind farms as seen in observations and simulations. *Environ. Res. Lett.* **13**, 124012 (2018).
- Smalikho, I. N. *et al.* Lidar investigation of atmosphere effect on a wind turbine wake. *J. Atmos. Ocean. Technol.* **30**, 2554–2570 (2013).
- Churchfield, M. J., Lee, S., Michalakes, J. & Moriarty, P. J. A numerical study of the effects of atmospheric and wake turbulence on wind turbine dynamics. *J. Turbul.* **13**, 1–32 (2012).
- Aitken, M. L., Kosović, B., Mirocha, J. D. & Lundquist, J. K. Large eddy simulation of wind turbine wake dynamics in the stable boundary layer using the Weather Research and Forecasting Model. *J. Renew. Sustain. Energy* **6**, 033137 (2014).
- Calaf, M., Meneveau, C. & Meyers, J. Large eddy simulation study of fully developed wind-turbine array boundary layers. *Phys. Fluids* **22**, 015110 (2010).
- Nygaard, N. G. Wakes in very large wind farms and the effect of neighbouring wind farms. *J. Phys. Conf. Ser.* **524**, 012162 (2014).
- Nygaard, N. G. & Christian Newcombe, A. Wake behind an offshore wind farm observed with dual-Doppler radars. *J. Phys. Conf. Ser.* **1037**, 032020 (2018).
- Nygaard, N. G. & Hansen, S. D. Wake effects between two neighbouring wind farms. *J. Phys. Conf. Ser.* **753**, 032020 (2016).
- Badger, J. *et al.* Making the most of offshore wind: Re-evaluating the potential of offshore wind in the German North Sea. Study commissioned by Agora Energiewende and Agora Verkehrswende, 1–84 (2020).
- Geyer, B., Weisse, R., Bisling, P. & Winterfeldt, J. Climatology of North Sea wind energy derived from a model hindcast for 1958–2012. *J. Wind Eng. Ind. Aerodyn.* **147**, 18–29 (2015).
- Bärfuss, K. *et al.* In-situ airborne measurements of atmospheric and sea surface parameters related to offshore wind parks in the German Bight. PANGAEA <https://doi.org/10.1594/PANGAEA.902845> (2019).
- EWEA. The European offshore wind industry key 2015 trends and statistics. ... *Documents/Publications/Reports/Statistics/ ... 31* (2015). <https://doi.org/10.1109/CCA.1997.627749>.
- Rockel, B., Will, A. & Hense, A. The regional climate model COSMO-CLM (CCLM). *Meteorol. Z.* **17**, 347–348 (2008).
- Chatterjee, F., Allaerts, D., Blahak, U., Meyers, J. & van Lipzig, N. P. M. Evaluation of a wind-farm parametrization in a regional climate model using large eddy simulations. *Q. J. R. Meteorol. Soc.* **142**, 3152–3161 (2016).
- Blahak, U., Goretzki, B. & Meis, J. A simple parameterization of drag forces induced by large wind farms for numerical weather prediction models. *European Wind Energy Conference and Exhibition 2010, EWEC 2010* **6**, 4577–4585 (2010).
- Albadi, M. H. & El-Saadany, E. F. Optimum turbine-site matching. *Energy* **35**, 3593–3602 (2010).
- Dean, N. Performance factors. *Nat. Energy* **5**, 5 (2020).
- Leiding, T. *et al.* Standardisierung und vergleichende Analyse der meteorologischen FINO-Messdaten (FINO123) (2016).
- Westerhellweg, A., Cañadillas, B., Kinder, F. & Neumann, T. Wake measurements at alpha ventus—Dependency on stability and turbulence intensity. *J. Phys. Conf. Ser.* **555**, 012106 (2014).
- Perkins, S. E., Pitman, A. J., Holbrook, N. J. & McAneney, J. Evaluation of the AR4 climate models' simulated daily maximum temperature, minimum temperature, and precipitation over Australia using probability density functions. *J. Clim.* **20**, 4356–4376 (2007).
- Lu, H. & Porté-Agel, F. Large-eddy simulation of a very large wind farm in a stable atmospheric boundary layer. *Phys. Fluids* **23**, 065101 (2011).
- Chamorro, L. P. & Porté-Agel, F. A wind-tunnel investigation of wind-turbine wakes: Boundary-Layer turbulence effects. *Bound. Layer Meteorol.* **132**, 129–149 (2009).
- Djath, B. & Schulz-Stellenfleth, J. Wind speed deficits downstream offshore wind parks—A new automatised estimation technique based on satellite synthetic aperture radar data. *Meteorol. Z.* **28**, 499–515 (2019).
- Emeis, S. A simple analytical wind park model considering atmospheric stability. *Wind Energy* **13**, 459–469 (2010).
- Christiansen, M. B. & Hasager, C. B. Wake effects of large offshore wind farms identified from satellite SAR. *Remote Sens. Environ.* **98**, 251–268 (2005).
- Jonkman, J., Butterfield, S., Musial, W. & Scott, G. Definition of a 5-MW reference wind turbine for offshore system development. *United States* <https://doi.org/10.2172/947422> (2009).
- Abkar, M. & Porté-Agel, F. Influence of atmospheric stability on wind-turbine wakes: A large-eddy simulation study. *Phys. Fluids* **27**, 035104 (2015).
- Allaerts, D. Large-eddy simulation of wind farms in conventionally neutral and stable atmospheric boundary layers (2016).

48. IEA. Offshore Wind Outlook 2019. *World Energy Outlook* <https://doi.org/10.1787/caf32f3b-en> (2019).
49. Siegmund, F. & Schrum, C. Decadal changes in the wind forcing over the North Sea. *Clim. Res.* **18**, 39–45 (2001).
50. Saidur, R., Rahim, N. A., Islam, M. R. & Solangi, K. H. Environmental impact of wind energy. *Renew. Sustain. Energy Rev.* **15**, 2423–2430 (2011).
51. Tabassum, A., Premalatha, M., Abbasi, T. & Abbasi, S. A. Wind energy: Increasing deployment, rising environmental concerns. *Renew. Sustain. Energy Rev.* **31**, 270–288 (2014).
52. Boettcher, M., Hoffmann, P., Lenhart, H. J., Heinke Schlunzen, K. & Schoetter, R. Influence of large offshore wind farms on North German climate. *Meteorol. Z.* **24**, 465–480 (2015).
53. Platis, A. *et al.* Long-range modifications of the wind field by offshore wind parks—Results of the project WIPAFF. *Meteorol. Z.* <https://doi.org/10.1127/metz/2020/1023> (2020).
54. Doms, G., Schättler, U. & Baldauf, M. *A Description of the Nonhydrostatic Regional COSMO Model. DWD COSMO V5.4.* <http://www.cosmo-model.org> (2011).
55. Dee, D. P. *et al.* The ERA-Interim reanalysis: Configuration and performance of the data assimilation system. *Q. J. R. Meteorol. Soc.* **137**, 553–597 (2011).
56. Akhtar, N. & Chatterjee, F. Wind farm parametrization in COSMO5.0\_clm15 (2020) doi:<https://doi.org/10.35089/WDCC/WindFarmPCOSMO5.0clm15>.
57. Akhtar, N. coastDat-3\_COSMO-CLM\_HR\_WF. *World Data Center for Climate (WDCC) at DKRZ.* [http://cera-www.dkrz.de/WDCC/ui/Compact.jsp?acronym=DKRZ\\_LTA\\_302\\_ds00001](http://cera-www.dkrz.de/WDCC/ui/Compact.jsp?acronym=DKRZ_LTA_302_ds00001) (2020).
58. Akhtar, N. coastDat-3\_COSMO-CLM\_HR. *World Data Center for Climate (WDCC) at DKRZ.* [http://cera-www.dkrz.de/WDCC/ui/Compact.jsp?acronym=DKRZ\\_LTA\\_302\\_ds00002](http://cera-www.dkrz.de/WDCC/ui/Compact.jsp?acronym=DKRZ_LTA_302_ds00002) (2020).

## Acknowledgements

The study is initiated and funded by the Initiative and Networking Fund of the Helmholtz Association through the project “Advanced Earth System Modelling Capacity (ESM)”. The authors would like to acknowledge the German Climate Computing Center (DKRZ) for providing computational resources, the Federal Ministry for Economic Affairs and Energy (BMWi) and the Federal Agency for Shipping and Sea for the FINO data, and Wind Park Far Field (WIPAFF) project for providing first in situ airborne atmospheric observational data of the offshore wind farms. The authors also acknowledge F. Chatterjee for helping with the implementation of the wind farm parameterization in COSMO-CLM. The authors thank Johannes Schulz-Stellenfleth for fruitful discussion and suggestions and Ulrike Kleeberg for contributing Fig. 1. We thank the CLM Community for their assistance and collaboration.

## Author contributions

N.A. and B.R. implemented the wind farm parameterization in COSMO-CLM. N.A. designed the atmospheric simulations. B.G. provided the forcing data. N.A. and P.S. analyzed the data. B.G. wrote the FINO validation section. C.S. and B.R. initiated and supervised the work. N.A. wrote the original draft. All authors contributed to writing, reviewing, and editing the manuscript.

## Funding

Open Access funding enabled and organized by Projekt DEAL.

## Competing interests

The authors declare no competing interests.

## Additional information

**Supplementary Information** The online version contains supplementary material available at <https://doi.org/10.1038/s41598-021-91283-3>.

**Correspondence** and requests for materials should be addressed to N.A.

**Reprints and permissions information** is available at [www.nature.com/reprints](http://www.nature.com/reprints).

**Publisher’s note** Springer Nature remains neutral with regard to jurisdictional claims in published maps and institutional affiliations.



**Open Access** This article is licensed under a Creative Commons Attribution 4.0 International License, which permits use, sharing, adaptation, distribution and reproduction in any medium or format, as long as you give appropriate credit to the original author(s) and the source, provide a link to the Creative Commons licence, and indicate if changes were made. The images or other third party material in this article are included in the article’s Creative Commons licence, unless indicated otherwise in a credit line to the material. If material is not included in the article’s Creative Commons licence and your intended use is not permitted by statutory regulation or exceeds the permitted use, you will need to obtain permission directly from the copyright holder. To view a copy of this licence, visit <http://creativecommons.org/licenses/by/4.0/>.

© The Author(s) 2021, corrected publication 2021





# Seasonal variability of wake impacts on US mid-Atlantic offshore wind plant power production

David Rosencrans<sup>1,2</sup>, Julie K. Lundquist<sup>1,2,3</sup>, Mike Optis<sup>2,4</sup>, Alex Rybchuk<sup>2</sup>, Nicola Bodini<sup>2</sup>, and Michael Rossol<sup>2</sup>

<sup>1</sup>Department of Atmospheric and Oceanic Sciences, University of Colorado, Boulder, CO 80303, USA

<sup>2</sup>National Renewable Energy Laboratory, Golden, CO 80401, USA

<sup>3</sup>Renewable and Sustainable Energy Institute, Boulder, CO 80303, USA

<sup>4</sup>Veer Renewables, Courtenay, V9N 9B4, Canada

**Correspondence:** David Rosencrans [REDACTED]@colorado.edu)

Received: 7 April 2023 – Discussion started: 4 May 2023

Revised: 23 January 2024 – Accepted: 1 February 2024 – Published: 14 March 2024

**Abstract.** The mid-Atlantic will experience rapid wind plant development due to its promising wind resource located near large population centers. Wind turbines and wind plants create wakes, or regions of reduced wind speed, that may negatively affect downwind turbines and plants. We evaluate wake variability and annual energy production with the first yearlong modeling assessment using the Weather Research and Forecasting model, deploying 12 MW turbines across the domain at a density of  $3.14 \text{ MW km}^{-2}$ , matching the planned density of  $3 \text{ MW km}^{-2}$ . Using a series of simulations with no wind plants, one wind plant, and complete build-out of lease areas, we calculate wake effects and distinguish the effect of wakes generated internally within one plant from those generated externally between plants. We also provide a first step towards uncertainty quantification by testing the amount of added turbulence kinetic energy (TKE) by 0 % and 100 %. We provide a sensitivity analysis by additionally comparing 25 % and 50 % for a short case study period. The strongest wakes, propagating 55 km, occur in summertime stable stratification, just when New England's grid demand peaks in summer. The seasonal variability of wakes in this offshore region is much stronger than the diurnal variability of wakes. Overall, yearlong simulated wake impacts reduce power output by a range between 38.2 % and 34.1 % (for 0 %–100 % added TKE). Internal wakes cause greater yearlong power losses, from 29.2 % to 25.7 %, compared to external wakes, from 14.7 % to 13.4 %. The overall impact is different from the linear sum of internal wakes and external wakes due to non-linear processes. Additional simulations quantify wake uncertainty by modifying the added amount of turbulent kinetic energy from wind turbines, introducing power output variability of 3.8 %. Finally, we compare annual energy production to New England grid demand and find that the lease areas can supply 58.8 % to 61.2 % of annual load. We note that the results of this assessment are not intended to make nor are they suitable to make commercial judgments about specific wind projects.

## 1 Introduction

The US offshore wind industry is flourishing, with a target capacity of 30 GW by 2030 (FACT SHEET, 2023). New England features the highest population density in the United States and commensurate utility usage, making offshore wind an attractive regional electricity source. A total of 27 active lease areas now span the mid-Atlantic Outer Continental Shelf (OCS). The OCS features low turbulence

(Bodini et al., 2019) and fast winds, with 100 m winds averaging  $10 \text{ m s}^{-1}$  (Musial et al., 2016). Consequently, large wind plants will be constructed to harness the ample wind resource.

Meteorological conditions and construction challenges constrain siting options for large wind plants. Because the average wind direction is southwesterly (Bodini et al., 2019), a southwest-to-northeast wind plant orientation mitigates ex-



ternal waking from neighboring plants. Further, preserving efficient vessel transit, upholding common fishery practices, and prioritizing safe Coast Guard search-and-rescue operations necessitate  $1 \times 1$  nm corridors (W.F. Baird & Associates, 2019). Considering these constraints, wind plants will be densely packed into clusters.

Densely packed clusters produce wakes that adversely affect downwind turbines (Nygaard, 2014; Platis et al., 2018; Lundquist et al., 2019; Schneemann et al., 2020). Wakes are plumes downwind of turbines with slower wind speeds and increased turbulence. Mid-Atlantic wakes induced by large wind plants could impose wind speed deficits up to  $2 \text{ m s}^{-1}$  (Pryor et al., 2021; Golbazi et al., 2022). Wind speed deficits can be replenished by wake recovery in which turbulence entrains momentum from aloft into the waked zone (Stevens et al., 2016; Gupta and Baidya Roy, 2021). However, stably stratified conditions suppress mixing for wake recovery (Fitch et al., 2013; Vanderwende et al., 2016; Porté-Agel et al., 2020). Under certain conditions, mid-Atlantic wakes could propagate 100 km or more (Pryor et al., 2021; Golbazi et al., 2022; Stoelinga et al., 2022).

Wake characteristics have been evaluated using physics-based models of varying complexity. High-fidelity methods include computational fluid dynamics models solving Reynolds-averaged Navier–Stokes equations (Antonini et al., 2020); large-eddy simulations resolving the turbine rotor as an actuator disk (Mirocha et al., 2014; Aitken et al., 2014; Shapiro et al., 2019; Arthur et al., 2020); and mesoscale models parameterizing a hub-height momentum sink, sometimes including a turbulence source (Fitch et al., 2013; Volker et al., 2015; Archer et al., 2020; Gupta and Baidya Roy, 2021), as reviewed by Fischereit et al. (2022). Pryor et al. (2021) characterized mid-Atlantic wake impacts using mesoscale modeling of 55 simulation days. They examined modified wind plant layouts of 15 MW turbines under different flow scenarios, considering power densities between 2.1 and  $4.34 \text{ MW km}^{-2}$ . Stoelinga et al. (2022) estimated wake impacts using 15 MW turbines and 16 simulation days under typical southwesterly flow. Golbazi et al. (2022) considered summertime wakes with three scales of turbines to consider surface impacts. Finally, Rybchuk et al. (2022) addressed the sensitivity to wake characteristics under idealized conditions by varying planetary boundary layer (PBL) schemes.

In this work, we assess intra-plant and inter-plant wakes throughout the mid-Atlantic OCS using a yearlong mesoscale modeling study. The results of this assessment are not intended to make nor are they suitable to make commercial judgments about specific wind projects. The simulations use the Weather Research and Forecasting (WRF) model version 4.2.1 (Skamarock et al., 2019). One set of simulations runs with no wind farms (NWF) as a control, validated with lidar measurements, while the others use the Fitch wind farm parameterization (WFP) (Fitch et al., 2012, with updates described by Archer et al., 2020) to incorporate turbine effects. Our simulations incorporate 12 MW turbines and a

power density of  $3.14 \text{ MW km}^{-2}$ . Simulations employ different wind plant layouts, including one representative lease area alone (ONE) within the Rhode Island–Massachusetts (RIMA) block, all lease areas (LA), and the lease areas plus the call areas (CA), to assess different waking scenarios (Table 1). WFP simulations run separately by added turbulent kinetic energy (TKE) amount, including 0% added TKE (TKE\_0) and 100% added TKE (TKE\_100) to quantify the full range of uncertainty. NWF, ONE, and LA simulations run from 1 September 2019 to 1 September 2020 to capture a full year with available lidar measurement data. Due to computational costs, CA simulations focus on the summertime stable period from 1 September to 31 October 2019 and 1 July to 31 August 2020 (Table 1). This time period highlights wake impacts during months with presumed frequent stable stratification and high electricity demands (Livingston and Lundquist, 2020) as a worst-case scenario.

The remainder of this article is structured as follows. Section 2 introduces the model setup and configuration, model validation, and the analysis methods. Section 3 discusses variability in stratification, wakes, and power production. Section 4 concludes the work and offers recommendations for future work.

## 2 Methods

### 2.1 WRF modeling setup

We assess the effects of wakes and power production across the mid-Atlantic OCS using numerical weather prediction simulations with WRF version 4.2.1 and the WFP (Fitch et al., 2012). Version 4.2.1 allows for modifying the amount of TKE produced by wind turbines and ensures turbulence advection (Archer et al., 2020). Two nested domains comprise 6 and 2 km horizontal resolutions (Pronk et al., 2022; Xia et al., 2022; Bodini et al., 2023; Redfern et al., 2023), respectively, and the inner nest begins 20 grid cells into the parent domain (Fig. 1). This same domain and period of study have been used to explore interactions between power production and sea breezes (Xia et al., 2022). Fine vertical resolution (10 m) near the surface stretches aloft, with 17 levels within the lowest 200 m as recommended by Tomaszewski and Lundquist (2020). We choose an 18 s time step in the outer domain, 54 vertical levels, a 5000 Pa top, simple diffusion, and damping 6000 m below the model top to prevent gravity wave reflection. Hourly 30 km initial and boundary conditions are provided by the European Centre for Medium-Range Weather Forecasts (ECMWF) fifth-generation reanalysis (ERA5) data set (Hersbach et al., 2020). Sea surface temperature is provided by the UK Met Office Operational Sea Surface Temperature and Sea Ice Analysis (OSTIA) data set (Donlon et al., 2012). We choose the Noah land surface model (Niu et al., 2011), the Mellor–Yamada–Nakanishi and Niino level 2.5 PBL and surface layer (Nakanishi and Niino, 2006), new Thompson microphysics (Thompson et al.,

**Table 1.** Summary of WRF simulations.

Simulation type	Abbreviation	Turbine type	Period	Added TKE amount	No. of turbines
No wind farms	NWF	n/a	Sep 2019–Sep 2020	n/a	0
One wind farm only	ONE	12 MW	Sep 2019–Sep 2020	0 % and 100 %	177
Lease areas	LA	12 MW	Sep 2019–Sep 2020	0 % and 100 %	1418
Call areas	CA	12 MW	Sep 2019–Nov 2019 Jul 2020–Sep 2020	100 %	3219

n/a: not applicable

2008), and the rapid radiative transfer model longwave and shortwave radiative transfer (Iacono et al., 2008) schemes. The Kain–Fritsch cumulus scheme parameterizes cloud microphysics in the outer domain only (Kain, 2004).

### 2.2 Wind turbine layouts

Wind turbines are sited within lease areas offshore of the US East Coast (Fig. 1) as defined by the Bureau of Ocean Energy Management (Bureau of Ocean Energy Management, 2023). Following realistic deployment strategies, we site individual turbines 1 nm, or 8.6 rotor diameters, apart and an additional 0.5 nm from lease area boundaries (W.F. Baird & Associates, 2019; Beiter et al., 2020; Walter Musial, personal communication, September 2020). This layout provides a power density of 3.14 MW km<sup>-2</sup>. Lower power densities in US waters reflect wake concerns in Europe and the need to increase turbine spacing for wake replenishment. Areas that had already been approved for development are denoted as the lease areas. Areas where competitive interest was yet to be determined are denoted as the call areas. Both lease areas and call areas are filled to spatial capacity with turbines (Fig. 1), recognizing renewable energy targets (218th Legislature, 2018).

### 2.3 Wind turbine characteristics

For our simulations, we parameterize 12 MW turbines which are scaled by Beiter et al. (2020) from a 15 MW reference turbine with a 138 m hub height and 215 m rotor diameter. The power and thrust coefficient curves were held constant from the 15 MW machine. The rotor diameter was scaled to maintain a specific power of 332 W m<sup>-2</sup>, which is the same as the reference 15 MW turbine. Then, the hub height was determined such that a 30 m gap was maintained between the lower bound of the rotor tip and the sea surface. No power is produced in region 1 of the power curve, from 0 m s<sup>-1</sup> to cut-in wind speed (3 m s<sup>-1</sup>). In region 2 of the power curve, power production increases between cut-in wind speed and rated speed (11 m s<sup>-1</sup>). In region 3, between rated and cut-out wind speed (30 m s<sup>-1</sup>), an increase in wind speed no longer yields additional power production (Beiter et al., 2020) (Fig. 2a).

### 2.4 Wind farm parameterization

We use the WFP (Fitch et al., 2012) to incorporate the effects of wind turbines on the 2 km grid. Horizontal wind speed reduction from turbine drag (Eq. 1), power production (Eq. 2), and turbulence generation (Fitch et al., 2012; Archer et al., 2020) (Eq. 3) are calculated in the WFP from the following:

$$\frac{\delta|V|_{ijk}}{\delta t} = -\frac{N_{ij}C_T(|V|_{ijk})|V|_{ijk}^2A_{ijk}}{2(z_{k+1} - z_k)}, \tag{1}$$

$$\frac{\delta P_{ijk}}{\delta t} = \frac{N_{ij}C_P(|V|_{ijk})|V|_{ijk}^3A_{ijk}}{2(z_{k+1} - z_k)}, \tag{2}$$

$$\frac{\delta TKE_{ijk}}{\delta t} = \frac{N_{ij}C_{TKE}(|V|_{ijk})|V|_{ijk}^3A_{ijk}}{2(z_{k+1} - z_k)}, \tag{3}$$

where *i*, *j*, and *k* represent Cartesian model coordinates; *C<sub>T</sub>*(*|V|<sub>ijk</sub>*) is the wind-speed-dependent thrust coefficient; *|V|* is the wind speed at turbine hub height; *ρ* is the air density; *A<sub>ijk</sub>* is the rotor-swept area; *N<sub>ij</sub>* is the number density of turbines in grid cell *ij*; *C<sub>P</sub>*(*|V|<sub>ijk</sub>*) is the wind-speed-dependent power coefficient; *z<sub>k</sub>* is the height of vertical model level *k*; and *C<sub>TKE</sub>* is the fraction of energy converted to TKE (Fitch et al., 2012). These values are calculated at each model level, as the use of a rotor-equivalent wind speed generally exerts a minor effect (Redfern et al., 2019).

The thrust and power coefficients (*C<sub>T</sub>* and *C<sub>P</sub>*, respectively) vary with wind speed as defined by wind turbine manufacturers (Fig. 2b). The thrust coefficient *C<sub>T</sub>* is the non-dimensionalized thrust force exerted by wind on the rotor-swept plane (Burton et al., 2011).

The power coefficient, *C<sub>P</sub>*, governs the fraction of rotor kinetic energy converted into electrical power. This conversion is not perfectly efficient due to electrical and mechanical losses (Fitch et al., 2012; Archer et al., 2020). The leftover fraction of energy (Eq. 4) from the difference between *C<sub>T</sub>* and *C<sub>P</sub>* is transformed into turbulence, *C<sub>TKE</sub>*.

$$C_{TKE} = C_T - C_P \tag{4}$$

Because electromechanical losses are not represented by the WFP, all leftover energy converts to TKE, so the TKE may be overestimated (Fitch et al., 2012; Archer et al., 2020). Some

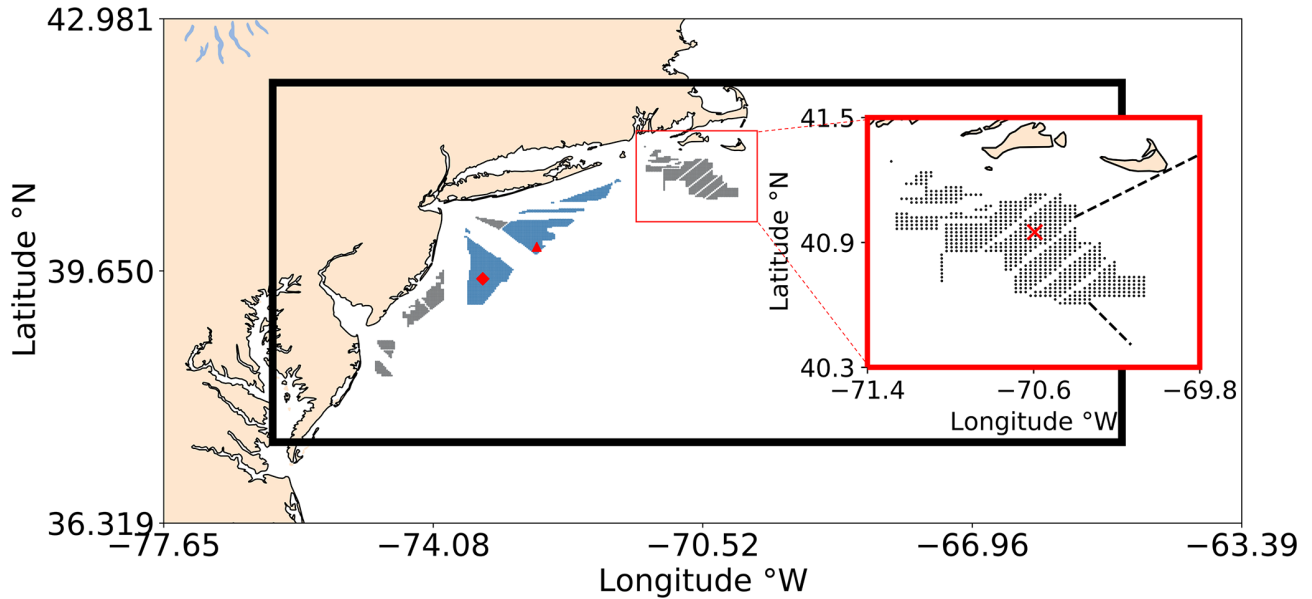


**Figure 1.** Simulation Domain 1 includes the entire region, and Simulation Domain 2 is outlined by the black rectangle. Each dot represents a wind turbine. Wind energy lease areas are shown in gray and call areas in blue. The red square zooms in on the Rhode Island–Massachusetts block of lease areas. The E05 (triangle) and E06 (diamond) floating lidars are shown in red. Atmospheric stratification is assessed at the red X. Wake propagation distances are assessed along the dashed black lines.

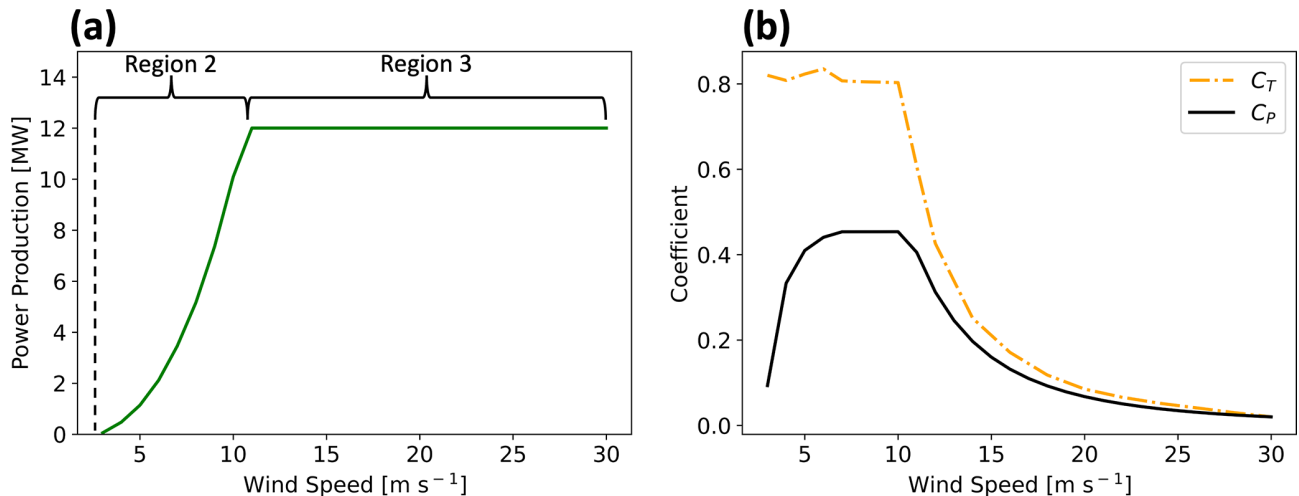


**Figure 2.** Characteristics of the 12 MW scaled turbine used herein. (a) The power curve and (b) curves showing the thrust coefficients ( $C_T$ ; dashed orange) and the power coefficients ( $C_P$ ; solid black) with wind speed across the x axis.

researchers suggest this TKE term is unnecessary (Volker et al., 2015), although comparisons to large-eddy simulations (Vanderwende et al., 2016) and observations (Siedersleben et al., 2020) suggest the turbine-produced TKE is critical to include. Any overestimation of TKE would enhance turbulent mixing, thereby exaggerating turbulent transport of momentum that causes wake recovery and overestimating power production. Therefore, Archer et al. (2020) propose reducing  $C_{TKE}$  to 25%. For these simulations, we bound this uncer-

tainty by carrying out simulations with 100% and 0% added TKE (Fig. A1). TKE advection is turned on.

### 2.5 Observations

We compared the NWF simulation to observations of offshore wind profiles. Two buoy-mounted meteorological ocean observing systems, denoted E05 and E06, are located within the Hudson North and Hudson South call areas of the New York Bight (Fig. 3). Each buoy system samples line-of-

sight boundary layer wind speed and wind direction using the ZephIR ZX300M light detection and ranging (lidar) instrument. The lidars are mounted 2 m above the sea surface and take measurements at 20 m intervals up to 200 m, providing 10 min averages of wind speed and direction, which the New York State Energy Research and Development Authority (NYSERDA) has made publicly available (DNV, 2019). We use floating lidar data to validate simulations for 1 September 2019 to 1 September 2020.

## 2.6 Stability classification

Different methods can be used to identify stratification, or atmospheric stability. Stable stratification can occur in coastal regions when warm air advects over a cooler sea surface, thereby suppressing buoyancy and turbulent mixing. Likewise, unstable stratification can occur when cool air advects over a warmer sea surface. Some observations suggest more frequent unstable stratification, based on the Obukhov length (Archer et al., 2016). The sign of the Obukhov length depends on the sign of heat flux and can be a useful metric for determining stability conditions. Other observations suggest that minimal turbulence and strong veer can be characteristic of stable conditions (Bodini et al., 2019). Wind veer increases in stable stratification as the influence of buoyant-turbulence-induced friction decreases. Thus, winds turn to approach quasi-geostrophic flow at a quicker rate, which can be further exaggerated by the presence of a low-level jet.

We calculate the Obukhov length (Monin and Obukhov, 1954) ( $L$ ), representative of the height at which buoyant production of turbulence first dominates mechanical shear production of turbulence:

$$L = -\frac{u_*^3 \overline{\theta_v}}{\kappa g \overline{w'\theta'_v}}, \quad (5)$$

where  $u_*$  is the friction velocity (UST from WRF output),  $\theta_v$  is the virtual potential temperature,  $\kappa$  is the von Karman constant of 0.4,  $g$  is gravitational acceleration, and  $\overline{w'\theta'_v}$  is the vertical turbulent heat flux (HFX from WRF output). Lengths between 0 and  $-500$  m are characterized as unstable stratification, and lengths between 0 and 500 m are categorized as stable stratification (Muñoz-Esparza et al., 2012). Lengths approaching negative or positive infinity are neutral. Each timestamp from the NWF run is assigned a stability for the 1 September 2019 to 1 September 2020 period at a grid point centered on the RIMA block (Fig. 1).

## 2.7 Model validation

We validate the NWF model by comparing wind speed estimated by the turbine-free simulations with observations from E05 and E06 lidars. Model output is obtained from the grid cells containing the lidars in 20 m intervals from 60 to 200 m following Pronk et al. (2022). Wind speeds and directions

are compared using a suite of metrics recommended by Opatis et al. (2020) for wind resource assessment, including the correlation coefficient ( $r$ ), centered root-mean-square error (cRMSE), and bias:

$$r = \frac{\sum_i^N (V_{W_i} - \overline{V_W})(V_{L_i} - \overline{V_L})}{N \sigma_W \sigma_L}, \quad (6)$$

$$\text{cRMSE} = \sqrt{\frac{\sum_i^N ((V_{W_i} - \overline{V_W}) - (V_{L_i} - \overline{V_L}))^2}{N}}, \quad (7)$$

$$\text{Bias} = \frac{\sum_i^N (V_{W_i} - V_{L_i})}{N}, \quad (8)$$

where  $V$  is the wind speed,  $N$  is the total number of values,  $\sigma$  is the standard deviation, and subscripts “W” and “L” indicate WRF and lidar, respectively. Earth mover’s distance (EMD), or the Wasserstein metric, is calculated with a SciPy function (Virtanen et al., 2020) as in other wind resource evaluations (Hahmann et al., 2020). Each of these metrics provides different insights into the performance of the model. For instance, the correlation coefficient illuminates how well the model captures the timing of weather systems and diurnal variability. EMD emphasizes the difference between distributions but not the timing. Bias captures the difference between measured and modeled values. Finally, cRMSE describes the random component of error.

The circularity of wind direction must be accounted for in statistical calculations. For example, computing the average between  $359$  and  $1^\circ$ , using a typical arithmetic mean, would result in  $180^\circ$ . However, the mean wind direction between those two values should be  $360^\circ$ . The SciPy (Virtanen et al., 2020) and Astropy (Price-Whelan et al., 2022) Python packages offer convenient functions which allow the user to calculate statistics for a circular variable by passing in the lower and upper bounds, in this case 0 and  $360^\circ$ . We calculate the mean and standard deviation of wind direction using the SciPy circmean and circstd functions, respectively, and the correlation coefficient using the Astropy circcorrcoef function. The cRMSE for wind direction is then calculated following

$$\text{cRMSE} = \sqrt{\text{circmean}(180^\circ - |(D_{W_i} - \overline{D_W}) - (D_{L_i} - \overline{D_L})| - 180^\circ)^2}, \quad (9)$$

where  $D$  is wind direction, and  $\overline{D}$  is the circular mean of wind direction. Bias is calculated similarly to Eq. (8), except that differences between NWF and lidar values that are less than  $-180^\circ$  have  $360^\circ$  added and differences greater than  $180^\circ$  have  $360^\circ$  subtracted:

$$x = \begin{cases} x + 360^\circ & \text{for } x < -180^\circ \\ x - 360^\circ & \text{for } x > 180^\circ \end{cases}, \quad (10)$$

where  $x$  is the  $(D_{WRF_i} - D_{Lidar_i})$  difference.

Time stamps in which the lidar returns NaN values are removed from WRF data sets during comparison (Table 2). Doing so removes 8.1 % of wind speed data at 140 m at E05,



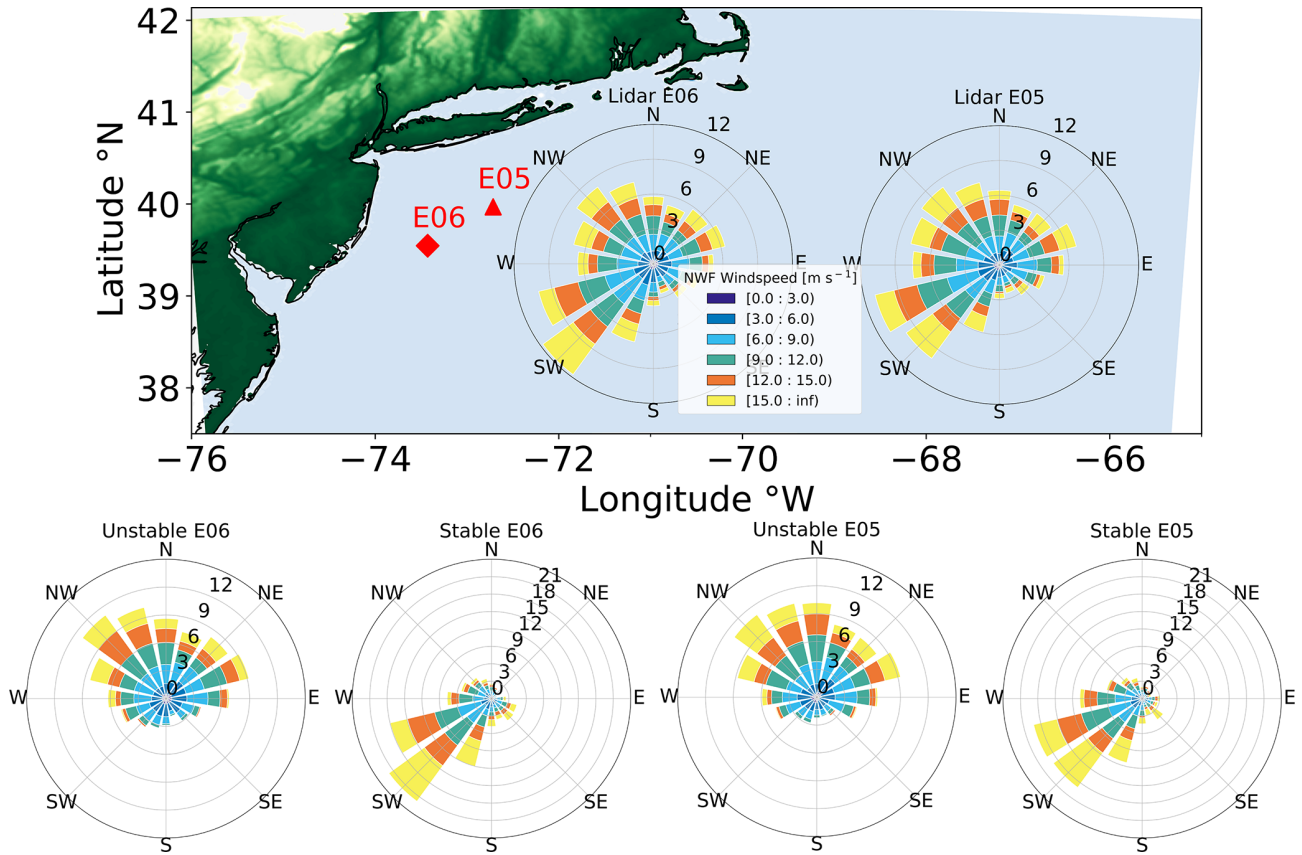


**Figure 3.** Hub-height wind roses for the NYSEDA Hudson North (E05) and Hudson South (E06) floating lidars during the 1 September 2019 to 1 September 2020 period. The location of E06 is shown as the red diamond and E05 as the red triangle. The bottom row shows wind roses segregated by atmospheric stratification.

**Table 2.** Percentage of data removed at 140 m due to not-a-number (NaN) values.

	Unstable	Stable	Neutral
E05	1.35 %	6.44 %	0.33 %
E06	3.64 %	9.48 %	0.62 %

made up by 1.22 %, 5.76 %, and 1.13 % in unstable, stable, and neutral stratification, respectively. Similarly, 13.7 % of wind speed data are removed at E06 and are made up by 3.20 %, 9.38 %, and 1.15 % in unstable, stable, and neutral stratification, respectively. An  $r^2$  value of 1 indicates a perfect correlation between NWF and lidar values. A value of 0 for cRMSE indicates that all values, with model bias removed, lie on the 1 : 1 regression line. A cRMSE value greater than 0 indicates the distance of residual points from the regression line. Negative biases indicate an underestimation from WRF, while positive biases indicate overestimation. A value of 0 for EMD indicates that probability density functions from each data source are equivalent. A positive

EMD indicates that the NWF wind speed distribution must shift towards lower values to match the lidar distribution.

NWF wind speed profiles are compared with lidar observations for the 1 September 2019 to 1 September 2020 period to assess model skill (Fig. 4). Note that Pronk et al. (2022) provide validation metrics against the E05 lidar profile during the same period of study and find similar results. Negative biases (Eq. 8) increase in magnitude with height between 0 and  $-0.5 \text{ m s}^{-1}$  (Fig. 4a), showing the model underestimates the wind speed. Strengths of variation (Eq. 6) among WRF output and the lidars range between 0.82 and 0.86 (Fig. 4b). Centered RMSE (Eq. 7) increases with height around  $2 \text{ m s}^{-1}$  (Fig. 4c). Finally, EMD values originate around  $0.2 \text{ m s}^{-1}$  at 60 m and increase with height (Fig. 4d). Comparing lidars E05 and E06, WRF performs better at E06 with a smaller bias by  $0.04 \text{ m s}^{-1}$ , lower cRMSE by  $0.08 \text{ m s}^{-1}$ , better correlation by 0.003, and smaller EMD by  $0.05 \text{ m s}^{-1}$ .

We further assess the NWF performance, partitioned by stability conditions. In unstable stratification, WRF wind speeds have a negative bias that gradually increases in magnitude with height from  $-0.5 \text{ m s}^{-1}$  at 60 m (Fig. 5a). In sta-



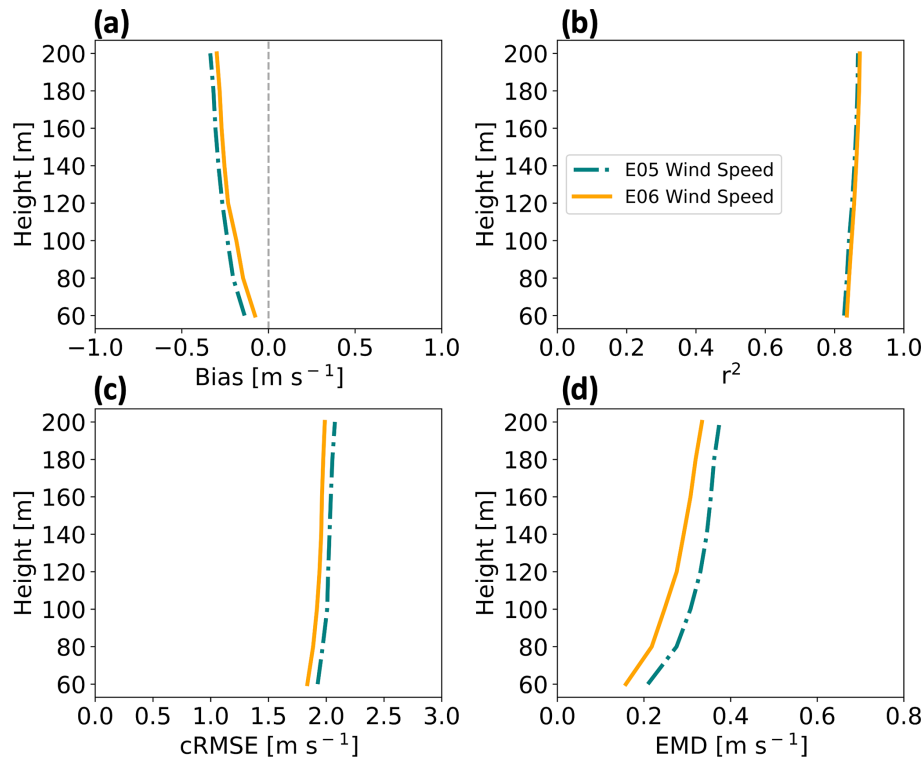


**Figure 4.** Vertical profiles for wind speed comparative metrics at the E05 (teal) and E06 (orange) lidars from 1 September 2019 to 1 September 2020. Shown are (a) bias, (b) correlation, (c) cRMSE, and (d) EMD.

ble conditions, WRF overestimates wind speeds by roughly  $0.4 \text{ m s}^{-1}$  at 60 m with biases approaching  $0.0 \text{ m s}^{-1}$  further aloft (Fig. 5a). In neutral conditions, WRF overestimates wind speeds by up to  $0.3 \text{ m s}^{-1}$  near the surface and underestimates wind speeds further aloft. Comparing between mean E05 and E06 profiles, WRF performs better at the E06 lidar location by  $0.08 \text{ m s}^{-1}$  in unstable conditions,  $0.04 \text{ m s}^{-1}$  in stable conditions, and  $0.1 \text{ m s}^{-1}$  in neutral conditions.

NWF and lidar wind speeds correlate well. Correlation remains the largest in unstable conditions for all heights (Fig. 5b). The worst strength of relationship occurs in stable stratification, although there is improvement aloft, and by 160 m, correlation between stable and neutral conditions is largely equivalent (Fig. 5b). On average, WRF performance between lidar locations is the same in unstable and stable conditions and better at E06 by 0.02 in neutral conditions.

Centered RMSE profiles change with stratification. In unstable conditions, cRMSE increases somewhat with height originating from greater than  $1.5 \text{ m s}^{-1}$  at 60 m (Fig. 5c). In stable stratification, the cRMSE profile begins at roughly  $2.3 \text{ m s}^{-1}$  at 60 m and increases with height. In neutral conditions, cRMSE increases with height from around  $2 \text{ m s}^{-1}$ . As before, WRF performs better at E06. On average, cRMSE is lower at E06 by  $0.1 \text{ m s}^{-1}$  in unstable conditions, by a negligible amount in stable conditions, and by  $0.1 \text{ m s}^{-1}$  in neutral conditions.

Earth mover's distance has more variability with height. It is the largest in unstable stratification, increasing with height from roughly  $0.5 \text{ m s}^{-1}$  at 60 m (Fig. 5d). In stable conditions, EMD decreases with height and originates at around  $0.35 \text{ m s}^{-1}$  at 60 m. In neutral stratification, EMD decreases with height from about  $0.2 \text{ m s}^{-1}$ . On average, WRF performs better at E06 by  $0.07 \text{ m s}^{-1}$  in unstable conditions, by  $0.04 \text{ m s}^{-1}$  in stable conditions, and by  $0.06 \text{ m s}^{-1}$  in neutral conditions.

Next, we show metrics to compare WRF output wind direction profiles with lidar measurements. Bias is negative, or counterclockwise, at both E05 and E06 lidar locations. NWF output resolves wind directions better at E06 with a mean bias of  $-7.8^\circ$  with height as compared to  $-11.1^\circ$  at E05 (Fig. 6a). Correlation coefficients at both locations are strong, at 0.83 and 0.82 for E06 and E05, respectively (Fig. 6b). Mean cRMSE (Eq. 9) is similar between lidar locations, at  $5.9$  and  $6.2^\circ$  for E06 and E05, respectively (Fig. 6c). Finally, EMD is lower at E06, increasing with height with an average of  $3.3^\circ$  (Fig. 6d). EMD is larger at E05, increasing with height with an average of  $4.8^\circ$  (Fig. 6d). Overall, WRF performs better at E06 with lower absolute bias by  $3.3^\circ$ , lower RMSE by  $0.3^\circ$ , higher correlation by  $0.01$ , and lower EMD by  $1.48^\circ$ .

We use the same metrics to validate WRF against lidar-reported wind directions by stratification and begin with bias

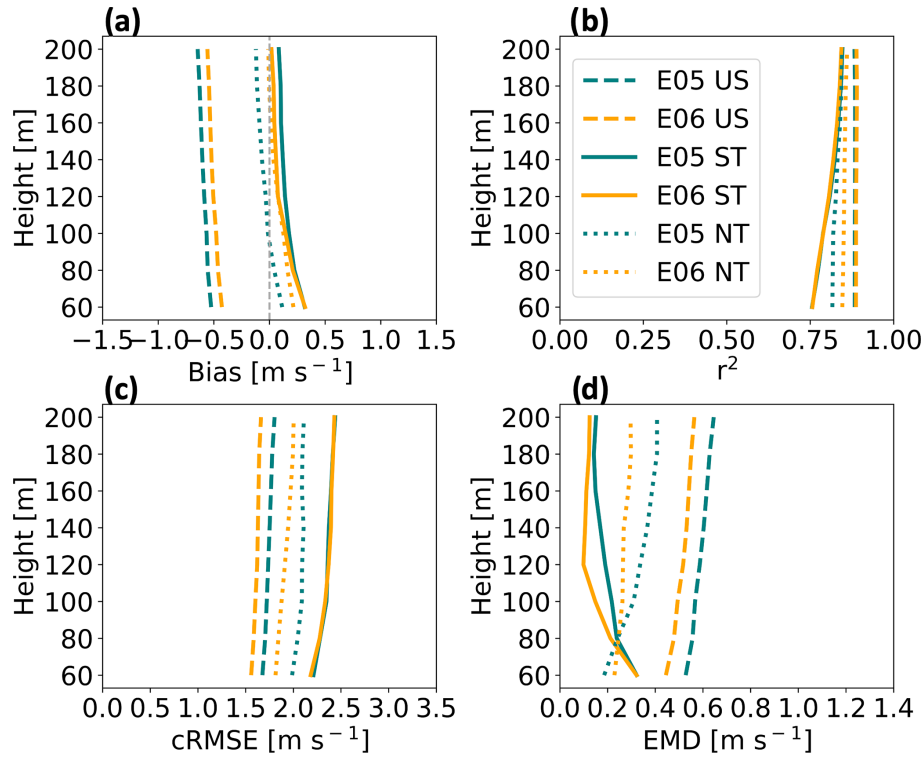


**Figure 5.** Vertical profiles for wind speed comparative metrics at the E05 (teal) and E06 (orange) lidar locations subset by stratification (US – unstable, ST – stable, NT – neutral) from 1 September 2019 to 1 September 2020. Shown are (a) bias, (b) correlation, (c) cRMSE, and (d) EMD.

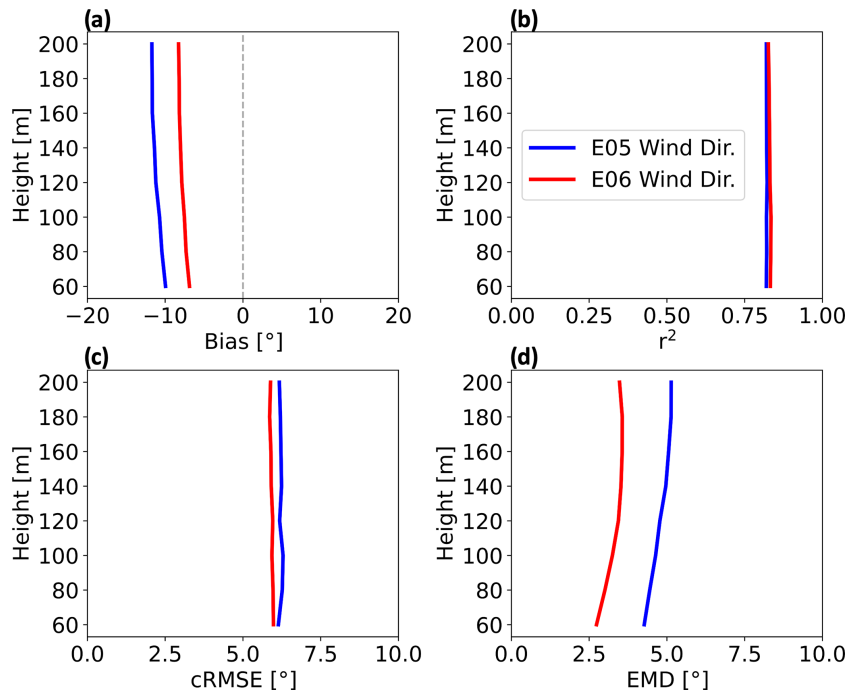


**Figure 6.** Vertical profiles for wind direction comparative metrics at the E05 (blue) and E06 (red) lidar locations from 1 September 2019 to 1 September 2020. Shown are (a) bias, (b) correlation, (c) cRMSE, and (d) EMD.

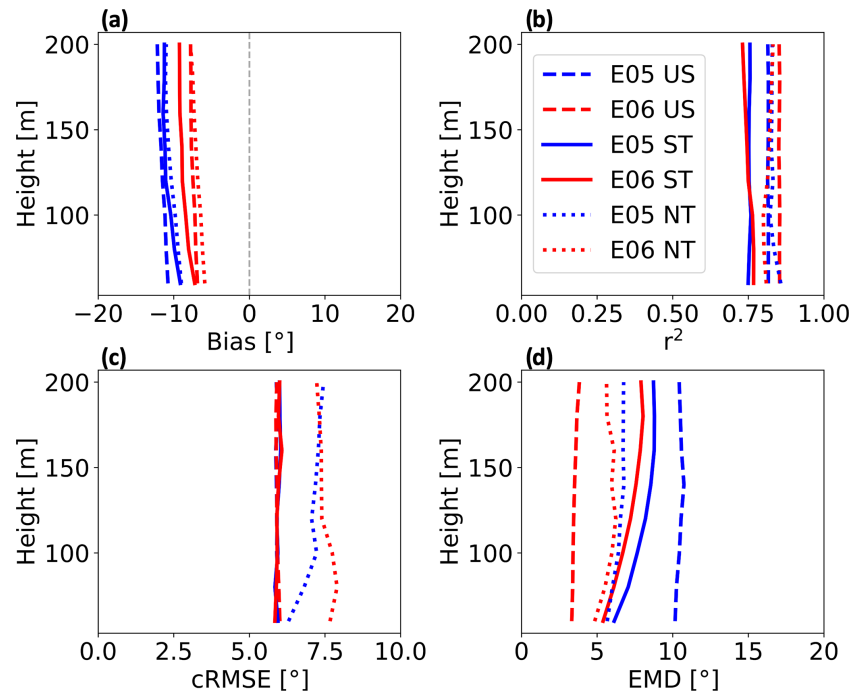


**Figure 7.** Vertical profiles for wind direction comparative metrics at the E05 (blue) and E06 (red) lidar locations subset by stratification (US – unstable, ST – stable, NT – neutral) from 1 September 2019 to 1 September 2020. Shown are (a) bias, (b) correlation, (c) cRMSE, and (d) EMD.

(Fig. 7a). In unstable conditions, mean biases are  $-7.4^\circ$  at E06 and  $-11.5^\circ$  at E05. In stable stratification, bias profiles are more similar between lidar locations, reaching  $-8.6^\circ$  at E06 and  $-10.7^\circ$  at E05. Bias is the smallest in neutral conditions at both locations, with mean values of  $-6.8^\circ$  at E06 and  $-10.2^\circ$  at E05. Overall, WRF performs better at the E06 lidar location by  $4.1^\circ$  in unstable conditions and by  $2.0^\circ$  in stable conditions and better at the E05 lidar location by  $3.4^\circ$  in neutral conditions.

The correlation between WRF-derived lidar-measured wind directions is strong in all stability conditions at both lidar locations (Fig. 7b). The strength of relation in unstable conditions is 0.85 at E06 and 0.81 at E05. In stable conditions, the mean correlation is 0.75 at both E06 and E05. In neutral conditions, the strengths of relation are 0.81 at E06 and 0.83 at E05. Overall, WRF performs better at E06 by  $0.03^\circ$  in unstable conditions and by  $0.003^\circ$  in stable conditions and better at E05 by  $0.01^\circ$  in neutral conditions.

Profiles for cRMSE are similar in unstable and stable conditions, with worse performance in neutral conditions (Fig. 7c). In both unstable and stable conditions, mean cRMSE is  $5.9^\circ$  at both E05 and E06. In neutral conditions, mean cRMSE is  $7.5^\circ$  at E06 and  $7.0^\circ$  at E05. WRF performs the same at both lidar locations in unstable and stable conditions and is better at E05 by  $0.4^\circ$  in neutral conditions.

Large variability exists for EMD between lidar locations in WRF (Fig. 7d). Unstable stratification features the largest spread between lidar locations, with EMD values of  $3.5^\circ$  at

E06 and  $10.4^\circ$  at E05. In stable conditions, EMD is  $7.0^\circ$  at E06 and  $7.9^\circ$  at E05. In neutral stratification, mean EMD values are  $5.7^\circ$  at E06 and  $6.4^\circ$  at E05. On average, WRF performs the best at the E06 lidar location:  $6.9^\circ$  in unstable conditions,  $0.8^\circ$  in stable conditions, and  $0.7^\circ$  in neutral conditions.

Wind speed time series are collected and averaged for the full yearlong period from the grid cells housing lidars E05 and E06 in NWF and from the lidar measurements. The shear exponent is calculated as

$$a = \frac{\log(V_2) - \log(V_1)}{\log(z_2) - \log(z_1)}, \quad (11)$$

where  $V_1$  and  $V_2$  are the mean wind speeds at heights  $z_1$  and  $z_2$ , respectively. We hold  $V_1$  and  $z_1$  constant at a reference height of 60 m and substitute  $V_2$  and  $z_2$  with values from 80 to 200 m at 20 m intervals.

Wind speed shear exponents (Eq. 11) differ between NWF and the lidar measurements. The average exponents from lidars E05 and E06 are 0.117 and 0.122, respectively, and are in good agreement with the annual average of 0.12 for both measured and modeled results in the mid-Atlantic (Viselli et al., 2018). The average exponents from WRF at grid cells housing E05 and E06 are 0.099 and 0.106, respectively. NWF-derived exponents correctly capture a decrease with height and lower coefficients at the E05 lidar. However, the exponents are smaller than those calculated from lidar measurements by  $-0.018$  and  $-0.016$  at E05 and E06, respec-

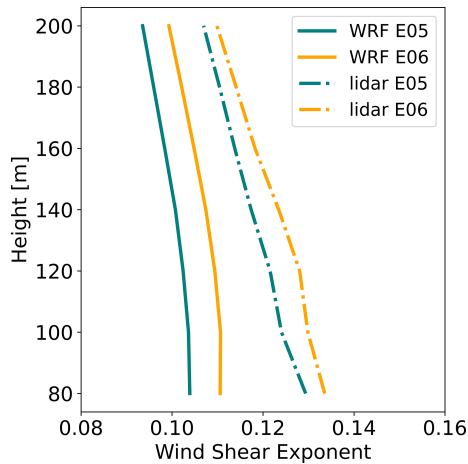


**Figure 8.** Mean wind speed shear exponent by height from NWF (solid) and from lidar measurements (dashed) from 1 September 2019 to 1 September 2020. E05 is shown in blue, and E06 is shown in orange.

tively. Smaller exponents in NWF may result from overestimated mixing or misrepresentation of wave-induced roughness.

We calculate profiles of the Perkins skill score (PSS) (Perkins et al., 2007) between NWF and lidar wind speeds. Wind speeds are considered at 20 m height intervals from 20 to 200 m. Each wind speed time series is subset by all time stamps with unstable, stable, and neutral stratification. After subsetting, time stamps where lidar observations return NaN are removed from both lidar and NWF time series. At each height, the probability distribution functions of wind speeds are binned at  $0.2 \text{ m s}^{-1}$  intervals and normalized such that the frequencies add to unity. The minimum frequency between modeled and observed values for each bin is stored, and the resulting stored values are summed to calculate the following score:

$$\text{PSS} = \sum_{i=1}^n \min(C_W(z), C_L(z)), \quad (12)$$

where  $n$  is the number of bins,  $C$  is the count of normalized values in a bin, and  $z$  is the height. A PSS of 1.0 suggests perfect overlap of the two distributions.

Profiles of PSS (Eq. 12) between NWF and lidar observations of wind speed vary by location and stratification. Performance is generally best in unstable conditions at both E05 and E06 lidar locations with a mean value of 0.93. Performance is the second best in stable conditions, starting around 0.90 at the surface and increasing to 0.93 at 120 m at E05. At E06 in stable conditions, PSS reaches a maximum value of 0.93 at 100 m. Neutral conditions exhibit worse PSS and larger spread by location. At E05, PSS minimizes at 0.85 at 160 m and maximizes around 0.88 at 60 m. At E06, PSS scores minimize at 0.87 at 80 m and maximize at 0.89 at 140 m.

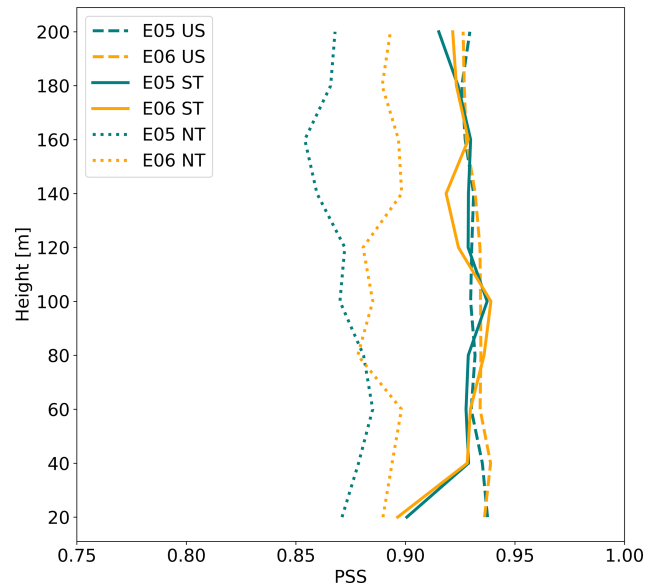


**Figure 9.** Vertical profiles of the Perkins skill score by stratification at the E05 (teal) and E06 (orange) lidars subset by stratification (US – unstable, ST – stable, NT – neutral).

## 2.8 Wake identification

The wake delineates the region downwind of turbines with a velocity deficit and turbulence enhancement. We identify the wind speed wake deficit by subtracting NWF wind speeds from WFP wind speeds at the hub height. Averaging across all times during the 1 September 2019 to 1 September 2020 period identifies the overall mean wake wind speed. Because wakes typically propagate to the northeast during stable conditions (Fig. 3), we calculate the propagation distance of wakes along a line extending northeast of the RIMA block (Fig. 1) and report the distance along the line where wake wind speeds reach a threshold. In unstable conditions the prevailing wind direction is northwesterly (Fig. 3), so we assess the wake propagation distance to the southeast instead. The threshold of  $-0.5 \text{ m s}^{-1}$  is chosen following Golbazi et al. (2022) and Rybchuk et al. (2022). Finally, we define the areal extent of wakes as the area with a wind speed deficit less than  $-0.5 \text{ m s}^{-1}$ .

## 2.9 Grid balancing

We compare model output energy production to New England grid demand. Demand data are provided hourly (NEISO, 2019). For comparison, we compute hourly averages of WFP power production from each set of simulations. We compare those averages to the national energy supply by acquiring the total from the U.S. Energy Information Administration (EIA, 2023).

### 2.10 Power variability

Assessing power variability is essential for addressing temporally changing grid demands. We assess the differences in electricity generation for each deployment scenario by separately collecting power output from grid cells containing wind turbines from ONE, LA, and CA simulations. Power is summed across grid cells containing turbines and averaged at 1, 7, and 30 d intervals for comparison. We address seasonal and diurnal variability by further separating and averaging power production totals at each time step into bins by month and hour of day. Power losses from the total, internal, and external wake effects are calculated from the following:

$$\text{Loss}_{\text{tot}} = 100\% - \left( \frac{P_{\text{LA,CA}}}{P_{\text{NWF}}} \right) \times 100\%, \quad (13)$$

$$\text{Loss}_{\text{int}} = 100\% - \left( \frac{P_{\text{ONE}}}{P_{\text{NWF}}} \right) \times 100\%, \quad (14)$$

$$\text{Loss}_{\text{ext}} = 100\% - \left( \frac{P_{\text{LA,CA}}}{P_{\text{ONE}}} \right) \times 100\%, \quad (15)$$

$$\text{Loss}_{\text{ext}} = \text{Loss}_{\text{tot}} - \text{Loss}_{\text{int}}, \quad (16)$$

where  $P_{\text{LA,CA}}$  is the power production at ONE grid cells in the presence of wakes by either the LA or the CA,  $P_{\text{ONE}}$  is the power production in the presence of internal wakes from ONE, and  $P_{\text{NWF}}$  is the power production from coupling hub-height wind speeds to the power curve. These methods are performed separately by added TKE amount. We note that the upwind conditions change in a LA or CA scenario due to external wakes, which can modify the internal losses in the numerator of Eq. (15). Thus, we provide an alternative method for calculating the external power losses as the difference between the total losses and the internal losses in Eq. (16).

Cluster-induced power deficits at ONE occur due to external wakes from the upwind lease and call areas. Power output from ONE, LA, and CA simulations are averaged in hourly windows at grid cells containing ONE turbines to reduce the effects of numerical noise (Appendix F). The resulting power averages from LA and CA simulations are divided by the averages from ONE at each time stamp. The hour of day and month of year categorize each time stamp, and percentages are placed into bins accordingly. Within each bin the percentages are averaged. Only power production totals greater than 9.9 MW are considered when calculating power losses. This threshold represents the power production total when all turbines within ONE begin operating at the cut-in wind speed. For reference, the total power production for ONE at rated power is 2124 MW. This method is repeated separately for TKE\_0 and TKE\_100 runs.

Individual wind turbines generate internal wakes within the ONE plant that adversely affect power production. To quantify internal wake effects at ONE, we collect NWF wind speeds at the hub height in each cell containing ONE turbines. Wind speeds are convolved with the power curve and

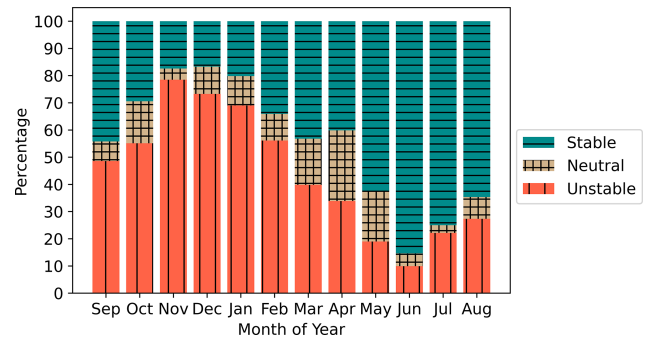


**Figure 10.** Stability classification using the Obukhov length for the 1 September 2019 to 1 September 2020 period at the RIMA block from NWF. The tan crosshatch represents neutral stratification, teal horizontal lines are stable stratification, and red vertical lines are unstable stratification.

scaled by the number of turbines per cell at  $0.01 \text{ m s}^{-1}$  intervals. This method returns the amount of power that ONE would produce in the absence of wakes. Hourly power averages are obtained from both NWF and ONE runs and considered only if power production exceeds 9.9 MW. ONE power totals are divided by the NWF power estimations from the power curve. Again, each time stamp is categorized by hour of day and month of year, and percentages are binned for averaging. These steps are repeated for both TKE\_0 and TKE\_100 runs.

## 3 Results

### 3.1 Year-round NWF stratification

The predominance of NWF stability conditions changes throughout the year (Figs. 10, 11) as assessed using the Obukhov length (Eq. 5) centered on the RIMA block.

The winter features predominant unstable stratification, whereas the summer features frequent stable stratification (Bodini et al., 2019; Optis et al., 2020) (Figs. 10, 11). The strong stability in summer is caused by nearby surface-heated air advecting over the colder OCS. These dynamics reverse during winter when cold air from land advects over warmer water. Overall, stratification is most frequently unstable during November and stable during June. April features the greatest percentage of neutral conditions as the spring-time transition from cooler to warmer air reduces the air-sea temperature gradient. The same pattern occurs elsewhere throughout the OCS because diurnal variability in stratification is weaker than the seasonal cycle (Fig. 11). The mean unstable, stable, and neutral percentages of occurrence at the RIMA block are 44.3 %, 44.4 %, and 11.2 %, respectively, for the 1 September 2019 to 1 September 2020 period. Stability calculations from the model grid cells that house lidars E05 and E06 reveal similar results (Fig. B1). However,  $L$  may not always represent conditions aloft (Fig. C1).



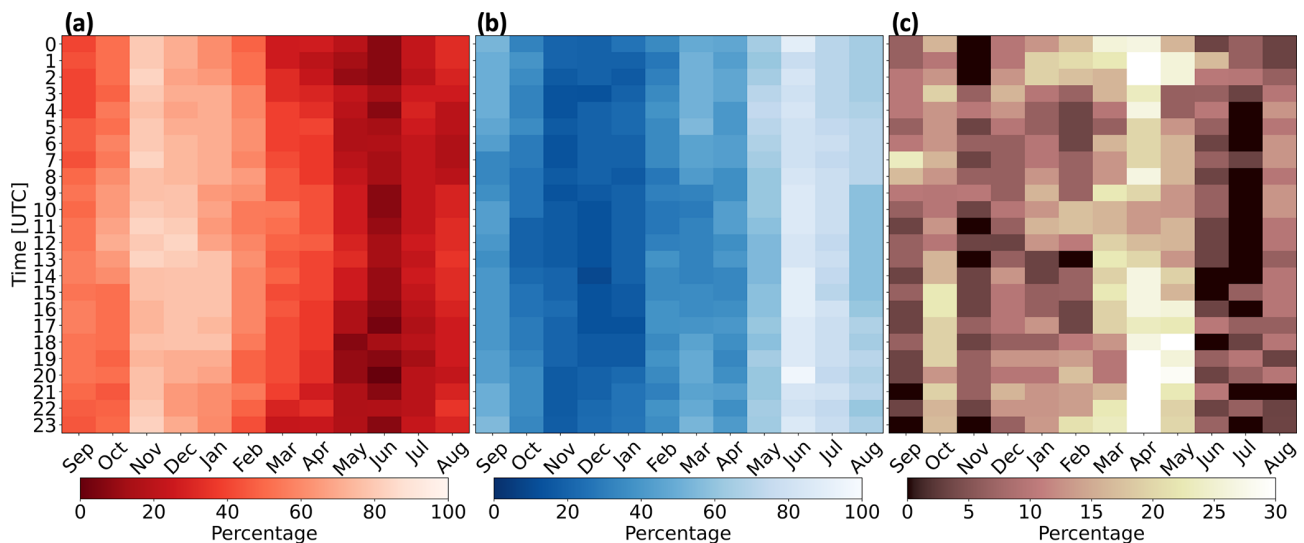


**Figure 11.** Percentages of occurrence for (a) unstable stratification, (b) stable stratification, and (c) neutral stratification from 1 September 2019 to 1 September 2020.

### 3.2 Wake variability

Here, we categorize wakes by the maximum wind speed deficit in space, the spatial extent, and the downwind propagation distance. While wakes remain relatively unchanged between TKE\_0 and TKE\_100, they drastically vary by stratification. The maximum average wake wind speed deficit occurs within the wind plant areas and intensifies from  $-1.5$  to  $-2.8$   $\text{m s}^{-1}$ , moving from unstable to stable conditions for TKE\_100 (Fig. 12a, c). Normalized with mean NWF hub-height wind speeds of  $9.2$   $\text{m s}^{-1}$  (unstable) and  $11.2$   $\text{m s}^{-1}$  (stable), the corresponding mean wind speed deficits are 16 % and 25 %. Similarly, the maximum average wind speed deficit intensifies from  $-1.8$  to  $-3.1$   $\text{m s}^{-1}$ , a normalized reduction of 19 % and 27 %, moving from unstable to stable at TKE\_0 (Fig. 12b, d). Thus, reducing TKE from 100 % to 0 % has a smaller impact on wake strength than increasing stability.

The areal extent of wakes changes by stability and added TKE. Wake deficits stronger than the  $-0.5$   $\text{m s}^{-1}$  cutoff in unstable stratification at TKE\_100 (Fig. 12a) cover a total area of  $7208$   $\text{km}^2$  and represent the best-case scenario where wakes impact the smallest area. In stable stratification at TKE\_100 (Fig. 12c), wakes cover a larger area of  $15948$   $\text{km}^2$ , or 2.2 times larger. A similar increase occurs using TKE\_0, although areal coverage of the wake is larger due to weaker turbulence-induced wind speed replenishment from aloft. At TKE\_0 in unstable conditions (Fig. 12b), wakes stronger than  $-0.5$   $\text{m s}^{-1}$  cover an area of  $7780$   $\text{km}^2$ . In stable stratification, the area increases to  $15636$   $\text{km}^2$  (Fig. 12d), a factor of 2. The spatial extent of strong wakes spreading furthest throughout the region, representing the worst-case scenario, occurs in stable conditions

at TKE\_100. Wakes interact between immediate wind plant neighbors for all scenarios.

Stratification exerts a stronger effect on wake propagation distance than TKE does. For instance, wakes extending 3.7 km downwind in unstable conditions reach 55.4 km in stable conditions at TKE\_100 (Fig. 12a, c), similar to the estimate of 50 km from Golbazi et al. (2022). Likewise, wake deficits reaching 5.9 km downwind in unstable stratification reach 55.4 km downwind in stable stratification at TKE\_0 (Fig. 12b, d). The same pattern exists for CA wakes (Fig. D1). Overall, altering the added TKE amount has a small impact on the propagation distance of wakes relative to stratification, and combining stable stratification with TKE\_0 results in the strongest wakes.

Yearly averaged wakes show similar trends with TKE and stability (Table 4). The maximum wake strength intensifies from  $-2.2$  to  $-2.5$   $\text{m s}^{-1}$  moving from TKE\_100 to TKE\_0 (Fig. 12e, f). Reducing TKE also increases the spatial coverage of wakes from  $13040$   $\text{km}^2$  using TKE\_100 (Fig. 12e) to  $13268$   $\text{km}^2$  using TKE\_0 (Fig. 12f). Downwind propagation distances remain similar over the yearlong period with wakes reaching 43.4 km at TKE\_100 and 41.3 km at TKE\_0.

Reduced TKE limits turbulence-induced momentum transport from aloft, thereby increasing wake strength. Counterintuitively, longer-lasting wakes in TKE\_100 develop from a larger reduction in momentum from wake recovery above the turbines (Fitch et al., 2012; Siedersleben et al., 2020), leaving less momentum available for replenishment downwind.

**Table 3.** Wake wind speed reduction by stratification and TKE amount.

	Unstable TKE_100	Stable TKE_100	Unstable TKE_0	Stable TKE_0
Wind speed deficit	$-1.5 \text{ m s}^{-1}$	$-2.8 \text{ m s}^{-1}$	$-1.8 \text{ m s}^{-1}$	$-3.1 \text{ m s}^{-1}$
Normalized deficit	16 %	25 %	19 %	27 %

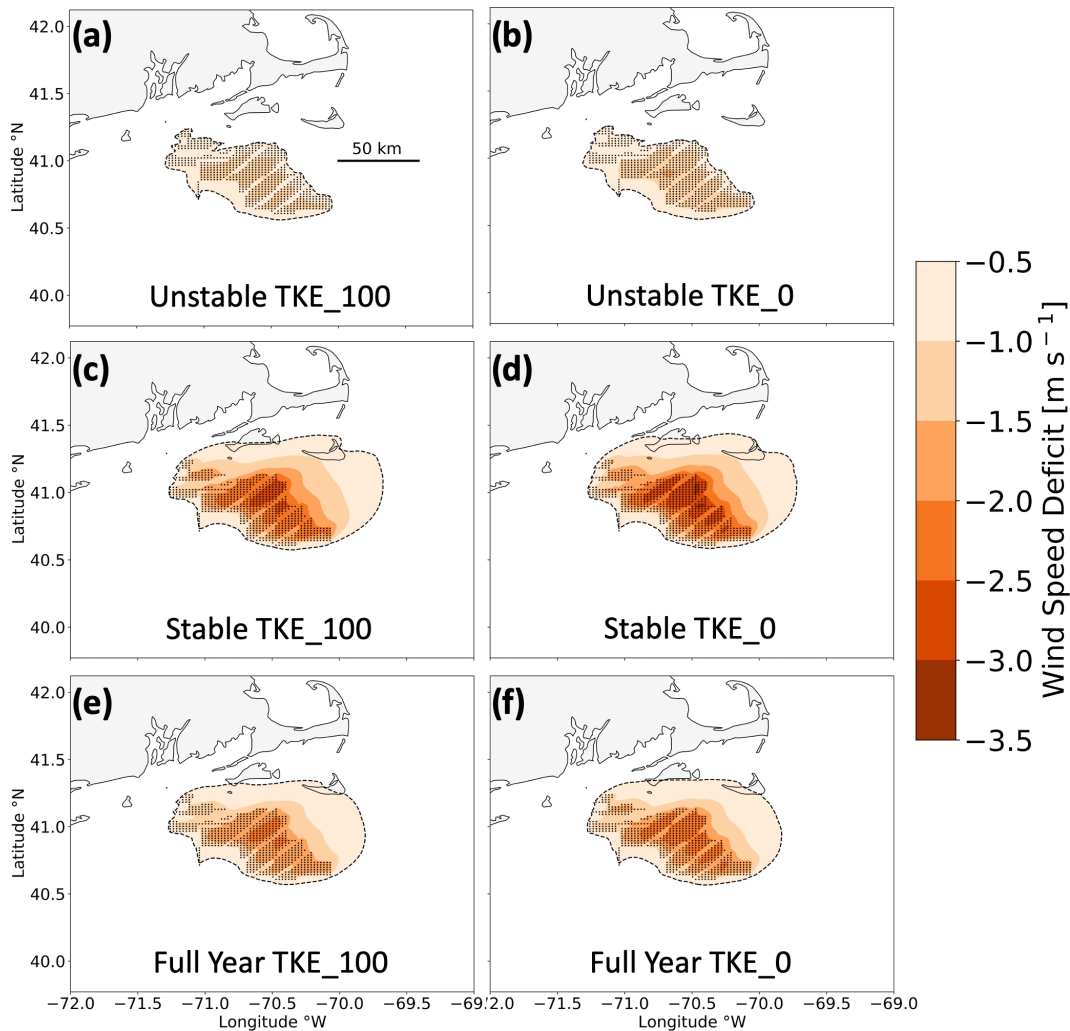


**Figure 12.** Average wake wind speeds among the lease areas during (a, b) unstable stratification, (c, d) stable stratification, and (e, f) the full 1 September 2019 to 1 September 2020 period. Wakes are simulated with 100 % added TKE (a, c, e) or 0 % added TKE (b, d, f). Wind speed deficits are shown by the colored contouring, and turbines are shown as the black dots. The  $-0.5 \text{ m s}^{-1}$  threshold is outlined by the dashed black line.

### 3.3 Power deficits

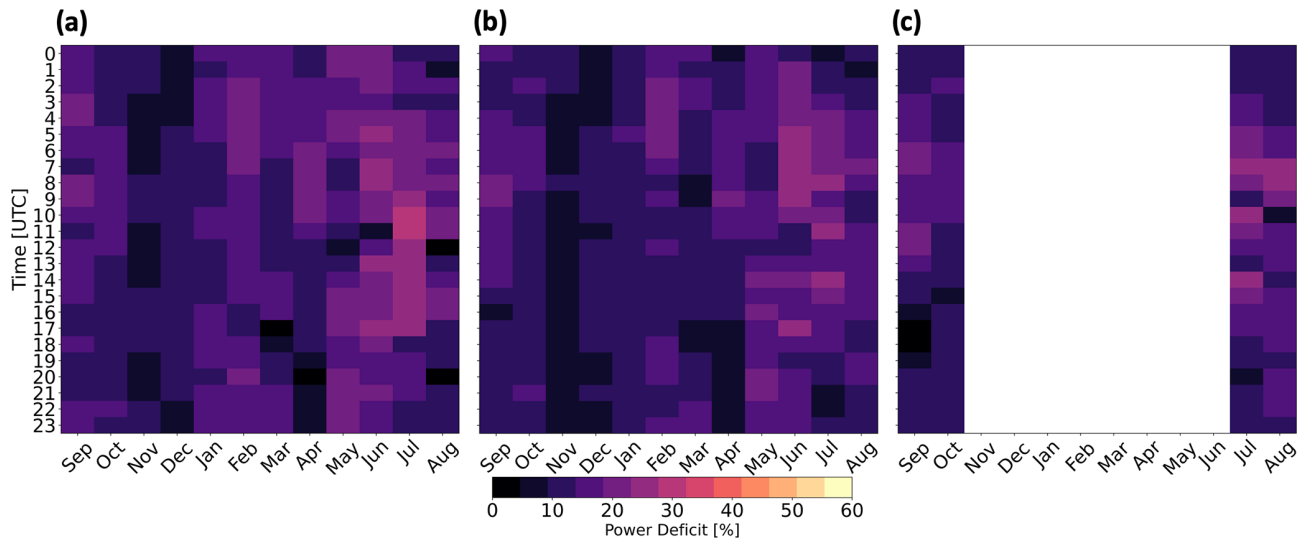
#### 3.3.1 External wake losses

ONE experiences power deficits due to external wakes from the LA and the CA. Considering external wakes from the LA at TKE\_0 (Eq. 15), the average yearlong power deficit at ONE is 14.7 % (Fig. 13a) and increases to 15.7 % considering only the 4 stable CA months. When ONE is waked by the LA at TKE\_100, the average yearlong power deficit

reduces to 13.4 % (Fig. 13b) because increased turbulence supports faster replenishment. During the 4 months only, the deficit is 14.4 %. When incorporating wakes from the CA (at TKE\_100), the mean ONE power deficit (over 4 months) is 14.3 % (Fig. 13c). By calculating the external power losses as the difference between total and internal losses (Eq. 16) instead, the deficits are 8.97 % and 8.43 % for the LA at TKE\_0 and TKE\_100, respectively. However, power losses vary as

**Table 4.** The wake wind speed deficit, spatial extent, and downwind propagation distance by added TKE amount.

	Wind speed deficit	Spatial extent	Propagation distance
TKE_100	$-2.2 \text{ m s}^{-1}$	13 040 km <sup>2</sup>	43.4 km
TKE_0	$-2.5 \text{ m s}^{-1}$	13 268 km <sup>2</sup>	41.3 km

**Figure 13.** The power deficit at ONE when waked by (a) the LA at TKE\_0, (b) the LA at TKE\_100, and (c) the CA at TKE\_100. The white space reflects the simulation period. The color bar is broad to facilitate comparison with losses in Fig. 14.

larger reductions from external wakes occur during summer, whereas smaller reductions occur during winter.

External wake-induced losses vary both diurnally and seasonally. Larger power deficits occur more often during summer due to stable stratification (Figs. 10, 11a). Smaller power deficits occur during winter (Fig. 13), with faster winds that exceed rated wind speed and unstable conditions that erode wakes faster. Larger power deficits correspond with stable stratification in June and July. Conversely, smaller power deficits occur with unstable stratification throughout November and December. These patterns occur because colder air advects over warmer water in winter, which causes unstable conditions that erode wakes faster. Conversely, warmer air advects over colder water during the summer, inducing stable conditions that limit turbulent wake recovery. While wake-induced losses vary somewhat across the diurnal cycle, there is no discernible pattern. The ocean's large heat capacity suppresses daytime heating, which limits changes in stratification and, by extension, the magnitude of changes in wake losses.

### 3.3.2 Internal wake losses

Internal power deficits (Eq. 14) at ONE are at least 25 % stronger than externally induced power deficits but experience similar variability with stability and TKE amount (Fig. 14). Internal wakening induces weaker deficits during

winter and stronger deficits during summer. As with external wakes, a clear diurnal pattern fails to emerge. Yearlong internal wakes from TKE\_0 and TKE\_100 induce power losses of 29.2 % and 25.7 %, respectively. During the 4 stable months only, the deficits increase to 36.9 % and 32.9 %, respectively. Using different PBL schemes with similar turbine spacing under steady-state idealized conditions, Rybchuk et al. (2022) find similar internal losses to capacity factor, up to 31.6 %.

The average yearlong power deficits (Eq. 13) at ONE considering internal wakes and external wakes from the LA range between 38.2 % (TKE\_0) and 34.1 % (TKE\_100). These results concur with wake-induced losses found by Pryor et al. (2021) of 35.3 % among the LA, based on 11 periods of different flow scenarios spanning 5 d. Observations of wake-induced power losses have large variability over the year, ranging from as low as 5 % to as high as 40 % (Lee and Fields, 2021). Overall, external wakes produce yearly averaged power losses of 14.1 %, whereas internal wakes induce larger losses of 27.4 %. Thus, we stress the importance of resolving region-specific and time-varying wakes for accurate energy prediction estimates.

### 3.4 Annual energy production

Predictions of energy supply are critical for planning, operations, and diversification of renewables. Without internal

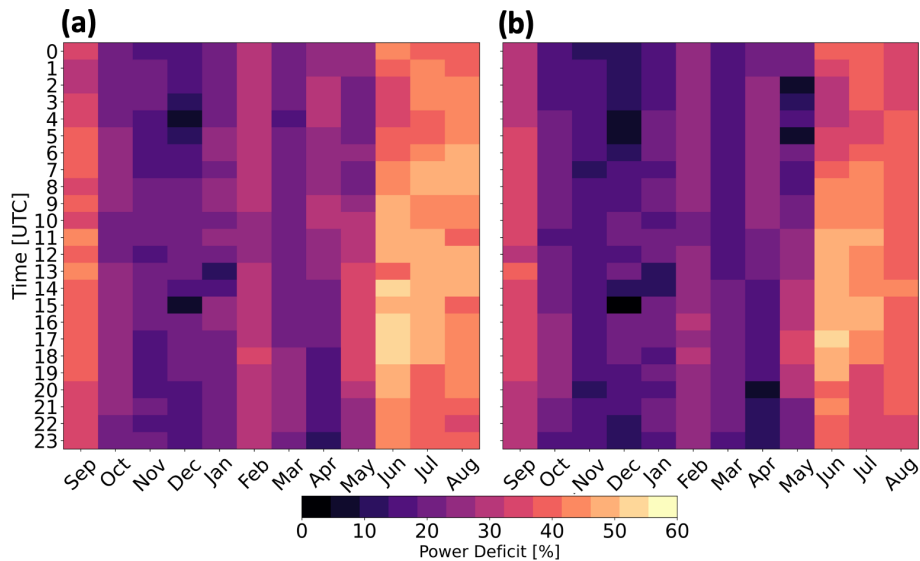


**Figure 14.** The percentage of power loss at ONE from internal wakes at (a) TKE<sub>0</sub> and (b) TKE<sub>100</sub>.

or external wake effects, ONE would produce 11.61 TW h and meet 10.02 % of New England’s average demand. Annual energy production (AEP) from ONE, considering just internal wakes, reduces to 9.19 TW h (TKE<sub>0</sub>) or 9.55 TW h (TKE<sub>100</sub>), which could meet 7.94 % to 8.24 % of New England’s demand. Including both internal and external wakes from the LA, ONE would produce 8.19 TW h (TKE<sub>0</sub>) or 8.65 TW h (TKE<sub>100</sub>), meeting 7.07 % to 7.47 % of demand.

Increasing the number of wind turbines increases the demand fulfilled; AEP from the LA is 68.12 TW h (TKE<sub>0</sub>) or 70.9 TW h (TKE<sub>100</sub>), supplying 58.82 % to 61.22 % of New England’s demand. On an hourly basis, the LAs fulfill demand only 24.6 % (TKE<sub>0</sub>) and 26.5 % (TKE<sub>100</sub>) of the time, highlighting the necessity for resolving accurate wake losses across the OCS. Previous work (Livingston and Lundquist, 2020) assuming a constant 20 % wake loss, shown here to be underestimated, has suggested that 2000 turbines of 10 MW could meet New England’s demand 37 % of the time. All in all, the LA, with 1418 turbines of 12 MW, supplies 68 and 71 TW h yr<sup>-1</sup>, or 1.72 % (TKE<sub>0</sub>) to 1.65 % (TKE<sub>100</sub>) of the nation’s energy supply.

### 3.5 Power variability by TKE amount

#### 3.5.1 Temporal power variability

While differences in wake strength between TKE amounts alter power production, wind speed exerts a larger influence. Maximum power is produced during spring with the least amount of power produced during summer (Fig. 15a) for both TKE<sub>0</sub> and TKE<sub>100</sub> because spring features faster wind speeds (Fig. 15b). Power production responds to hub-height wind speeds (Fig. 15) more than stability conditions (Figs. 10, 11). Reduced power production during summer

may be problematic as New England’s top-10 utility demand days since 1997 have all occurred in July or August (NEISO, 2023).

Total power production varies slightly between TKE<sub>100</sub> and TKE<sub>0</sub>. Due to weaker replenishment within the rotor-swept area, TKE<sub>0</sub> wakes are stronger, so TKE<sub>0</sub> produces less total power than TKE<sub>100</sub> (Fig. 15a). Over the year, TKE<sub>0</sub> runs produce 96.2 % (ONE) and 96.1 % (LA) of the power of TKE<sub>100</sub>. This difference does not arise from extreme outliers, as TKE<sub>0</sub> runs produce less power more frequently, at 71.3 % (ONE) or 81.2 % (LA) of the time.

#### 3.5.2 Power variability by wind speed

Differences in power production (TKE<sub>100</sub> – TKE<sub>0</sub>) vary by NWF hub-height wind speed (Fig. 16). These differences are small at slow wind speeds because little momentum is available for wake recovery and at faster wind speeds within region 3 of the power curve (11–30 m s<sup>-1</sup>) where wind speed changes do not affect power production (Fig. 2a). Differences in wind speed within region 3 should have no effect on power production and are caused by numerical noise propagating through wind plant areas (Fig. F1). The largest differences in power production occur in region 2 and around rated wind speed where the power curve is steep (Figs. 2a, 16). Additionally, large differences in power production can occur in specific meteorological conditions such as frontal propagation.

Comparison of power production between TKE amounts by other meteorological variables lacked significant trends. For example, we additionally analyzed differences in power production by wind direction, following the hypothesis that northerly wind directions could transport more turbulence offshore because land has a higher roughness length than the

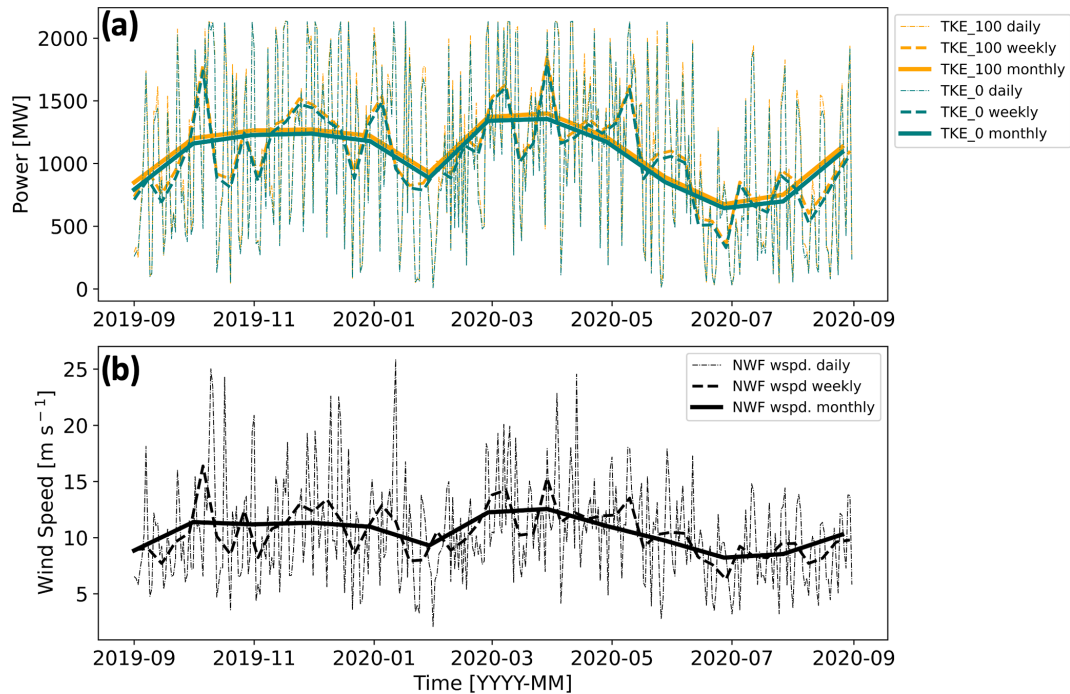


**Figure 15.** (a) Total power production at ONE by TKE amount. TKE\_100 power output is shown in orange and TKE\_0 output in teal. (b) Hub-height NWF wind speed at a point centered on the RIMA block. The dotted lines represent the daily average, dashed lines the 7 d average, and solid lines the 30 d average.

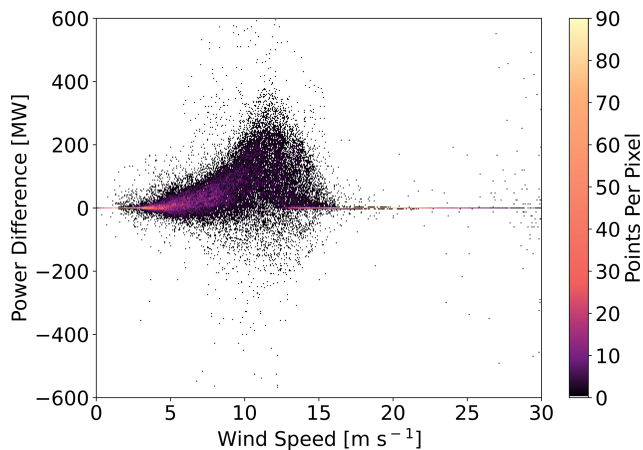


**Figure 16.** The difference in power production (TKE\_100-TKE\_0) at ONE as a function of wind speed. The colored contouring depicts the density of scattered points per pixel. Wind speeds are obtained every 10 m from a point centered on ONE at hub height.

ocean. TKE\_100 runs may harness this mechanical turbulence more for wake replenishment. Analysis of differences in power production by PBL height also failed to show significant patterns. We assumed that higher PBL heights indicated a greater reservoir of turbulence from which TKE\_100 runs could replenish the wake, resulting in greater power production. Further analysis concluded by comparing power dif-

ferences with the aforementioned variables' rates of change. However, we reached the same conclusions, as higher densities of scattered points existed around frequently occurring conditions such as southwesterly wind directions.

Wake strength varies spatiotemporally between TKE\_0 and TKE\_100 runs. While the mean difference in wind speed at hub height between TKE\_100 and TKE\_0 runs indicates that TKE\_0 produces stronger wakes, this averaging may obscure the actual spatiotemporal variability. For example, a wind plant may have greater TKE\_100 wake wind speeds, while its nearby neighbor has greater TKE\_0 wake wind speeds at the same point in time. Additionally, a specific wind plant may not consistently produce stronger wakes under one TKE setting. A wind plant may fluctuate between producing stronger wakes in TKE\_100 runs and TKE\_0 runs throughout time. This finding suggests that other boundary layer dynamics play a role in wake strength, and the variability of power production must be explored.

We note that wind speed and numerical noise are not the only contributors to power differences. One case study analysis shows that TKE\_0 and TKE\_100 separately produce more power within respective 99th percentiles over a short period of time in September (Fig. 17c). Investigation reveals that a cold front propagated through the ONE wind plant from the northwest to the southeast during this period. The cold front is identified by a lenticular band of upward vertical motion at the frontal head followed by turbulent vertical



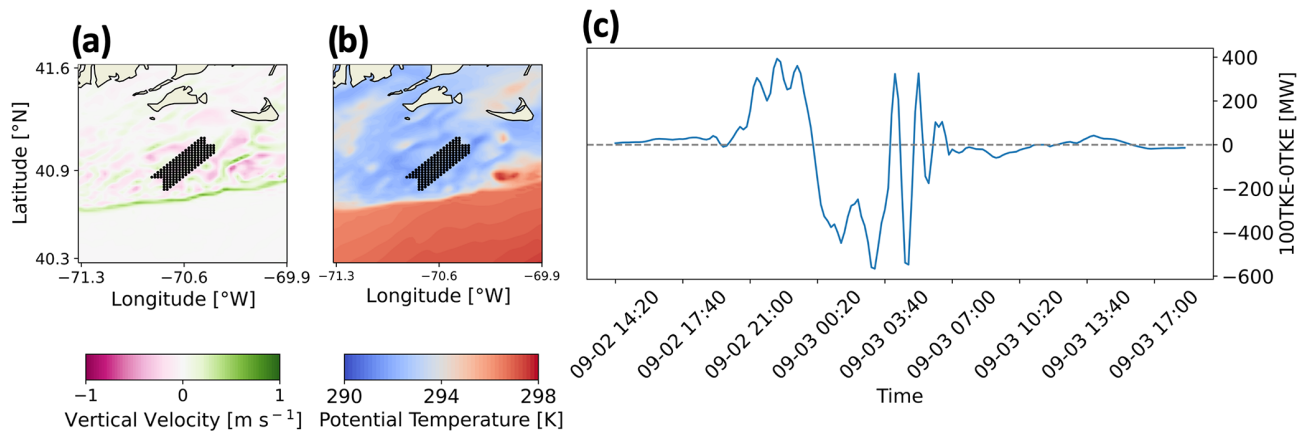


**Figure 17.** Propagation of a cold front through the ONE wind plant. (a) NWF vertical wind speed is shown as the colored contour with upward vertical velocities in greens and downward vertical velocities in purples. (b) NWF potential temperature is shown with lower temperatures in blues and higher temperatures in reds. In both (a) and (b), the black dots indicate wind turbine locations in ONE TKE\_0 and TKE\_100. (c) The difference in power production between TKE\_100 and TKE\_0 is shown in MW, with positive values indicating that TKE\_100 produces more power.

motion (Fig. 17a) in addition to advection of lower potential temperatures (Fig. 17c). As the cold front approaches, more power is produced by the TKE\_100 simulation and is within the 99th percentile. When the frontal head first interacts with Vineyard Wind, more power is produced by the TKE\_0 simulation and is within the 99th percentile. Conversely, TKE\_100 produces more power following the frontal head. Frontal propagation can induce Kelvin–Helmholtz instabilities, the turbulence of which may aid wake recovery by vertically mixing momentum (Jiang, 2021). Increased turbulence in the TKE\_100 simulation can harness more downward vertical transport of momentum from Kelvin–Helmholtz instabilities aft of the frontal head, increase wake replenishment, and produce more power.

#### 4 Conclusions

This modeling study assesses the variability of wake effects across the mid-Atlantic OCS based on yearlong simulations, including a first step towards uncertainty quantification and approaches for distinguishing internal and external wake effects. In addition to a simulation without wind plants (NWF), validated by comparison to floating lidar observations, three wind plant layouts are explored, including a representative wind plant alone (ONE), all lease areas (LA), and the lease areas plus the call areas (CA). Modifying the added TKE amount (TKE\_0 or TKE\_100) by turbines provides uncertainty quantification in power production estimates.

The OCS is characterized by more frequent unstable stratification during winter and stable stratification during summer (Bodini et al., 2019; Optis et al., 2020; Debnath et al., 2021). In stable conditions, wakes are stronger and propagate further downwind, (Fitch et al., 2013; Vanderwende et al., 2016; Porté-Agel et al., 2020). In the worst-case sce-

nario where downwind wake recovery diminishes during stable stratification, mean wakes propagate 55 km downwind. While wakes may not reach downwind clusters on average, inter-cluster wakening occurs intermittently. While TKE\_0 produces stronger wakes than TKE\_100, the downwind propagation distances do not differ.

Reduced wake wind speeds, as compared to the NWF simulation, affect power production. Yearly averaged wake losses induce power deficits at ONE from 38.2 % (TKE\_0) to 34.1 % (TKE\_100). This deficit comprises both internal and external wakening. External wakes induce yearly averaged power losses of 14.7 % (TKE\_0) or 13.4 % (TKE\_100), whereas wakes from the CA induce similar losses of 14.3 % over 4 months. Using an alternative method, external wakes induce losses of 8.97 % and 8.43 % for the LA at TKE\_0 and TKE\_100, respectively. Internal wakes at ONE promote larger power losses of 29.2 % (TKE\_0) or 25.7 % (TKE\_100). Wake-induced power losses vary seasonally with smaller diurnal variability. Larger power deficits occur during summer, where frequent stable conditions limit wake erosion. Although upwind clusters may generate strong external wakes among the LA, wind plant orientation with respect to prevailing winds can reduce adverse impacts from nearby neighbors. Ample distance for replenishment of external wakes by the CA moderates the negative effects. Internal wake losses remain larger due to shorter distances with limited wake recovery. Both external and internal wake-induced losses grow in summer stably stratified conditions. These losses similarly increase in strength for TKE\_0 simulations from inhibited recovery.

Resolving precise wake losses and AEP are crucial for stakeholders and grid operators. In the absence of wakes, ONE could supply 10.02 % of New England’s demand. Operating alone, ONE’s supply reduces to 7.94 % (TKE\_0) or

8.24 % (TKE<sub>100</sub>). Adding external wakes from the LA, ONE's annual supply lessens to 7.07 % (TKE<sub>0</sub>) or 7.47 % (TKE<sub>100</sub>). Although wakes are stronger among the LA, the greater number of turbines can meet 58.82 % (TKE<sub>0</sub>) and 61.22 % (TKE<sub>100</sub>) of New England's demand, or roughly 1.72 % and 1.65 % of national demand. However, the LA only satisfies demand about 25 % of the time on an hourly basis. Overall, spring features maximum power production with the fastest hub-height wind speeds. Wind speeds are slower in summer, reducing power production during July and August, which have featured New England's top-10 utility demand days since 1997 (NEISO, 2023).

Variable TKE amounts marginally impact power generation. TKE<sub>0</sub> simulations average 3.8 % less production than TKE<sub>100</sub> throughout the year, as reduced turbulence in TKE<sub>0</sub> limits momentum transport into the waked zone. Although differences in power production are small, both simulations exhibit large variability at short temporal periods. Improving WFP accuracy by accounting for wind shear throughout the rotor-swept region (Redfern et al., 2019) and dynamic air density may increase the variability in power production further (Wu et al., 2022). Further, different sizes of turbines may be installed in some of these regions, and the size of the turbine can influence the impacts of the turbine (Golbazi et al., 2022).

Future wind resource assessments may neglect differences between TKE<sub>0</sub> and TKE<sub>100</sub> because the power production offset is minor, although we identify a strong outlier during a frontal passage when differences in power production between TKE<sub>100</sub> and TKE<sub>0</sub> are large. While power production differences are minor, effects on other atmospheric variables may be more significant (Fig. A1). Variability may be influenced by other meteorological conditions. Successive analyses should consider yearlong CA simulations to identify the full range of external wake impacts. Although we infer that the effects of CA wakes on ONE are small relative to LA wakes, yearlong estimates may show otherwise. Notably, we find that internal wakes have larger impacts on power production than those generated externally.

## Appendix A

To assess the sensitivity of simulations to the amount of parameterized TKE, we conducted a set of 2 d test runs from 11 to 13 July 2017. This time period was chosen for its predominance of southwesterly winds, which represent typical conditions across the OCS, and for the availability of Air–Sea Interaction Tower lidar observations for wind profile validation of the NWF simulations. Test runs consist of 0 % (TKE<sub>0</sub>), 25 % (TKE<sub>25</sub>), 50 % (TKE<sub>50</sub>), and 100 % (TKE<sub>100</sub>) added TKE with the WFP.

Hub-height wind speeds vary by simulation type and added TKE amount (Fig. A1a). Mean WFP wind speeds are always slower than NWF wind speeds due to the momen-

tum sink introduced by wind turbines, by  $2.9 \text{ m s}^{-1}$ . Larger variations between wind speeds (Fig. A1a) correspond with larger spreads in power output by TKE amount (Fig. A1c). The sequencing of power production driven by TKE amount remains consistent, namely that the differences progress from TKE<sub>0</sub> to TKE<sub>25</sub>, TKE<sub>50</sub>, TKE<sub>75</sub>, and TKE<sub>100</sub>. Because power production totals for TKE<sub>25</sub> and TKE<sub>50</sub> are typically bounded by the totals for TKE<sub>0</sub> and TKE<sub>100</sub>, production simulations incorporate TKE<sub>0</sub> and TKE<sub>100</sub> only to account for the full range of uncertainty throughout a full yearlong period from 1 September 2019 to 1 September 2020.

Although subtle, several important meteorological quantities from the model grid cell at the center of the RIMA block vary by the added TKE amount. For example, wind speeds are slower on 12 July between 12:00 and 16:00 UTC (Fig. A1a). The wind speed reduction during this time period causes a corresponding decrease in turbulent transport of moisture. The mean difference in moisture fluxes throughout the full period between TKE<sub>100</sub> and TKE<sub>0</sub> is  $2.84 \times 10^{-6} \text{ kg m}^{-2} \text{ s}^{-1}$  (Fig. A1b). Note that the surface moisture flux remains negative throughout the period. While maritime moisture profiles typically exhibit a decrease in concentration with height, corresponding with a positive flux, mixing from the turbines reduces the near-surface concentration and reverses the gradient.

Heat flux exhibits large variability. The mean difference in heat flux throughout the full period between TKE<sub>100</sub> and TKE<sub>0</sub> is  $3.61 \text{ W m}^{-2}$  (Fig. A1d). The wind speed decrease between 12:00 and 16:00 UTC reduces surface stresses and turbulent transport of heat. The reduction in heat flux during this time period causes 2 m temperatures to decrease and exhibit less variability by TKE amount, with a mean difference of 0.26 K between TKE<sub>100</sub> and TKE<sub>0</sub> (Fig. A1f).

The reduction in turbulent mixing lowers the PBL, regardless of TKE amount, to shallow heights between 30 to 80 m at 13:00 UTC (Fig. A1e). The near-surface PBL height suppresses the small variations in turbulent mixing across test runs and causes fluxes to equalize. PBL heights differ the most by added TKE amount and may result from changes in weighting between two separate height determination methods present in the MYNN physics driver (Fig. A1c).

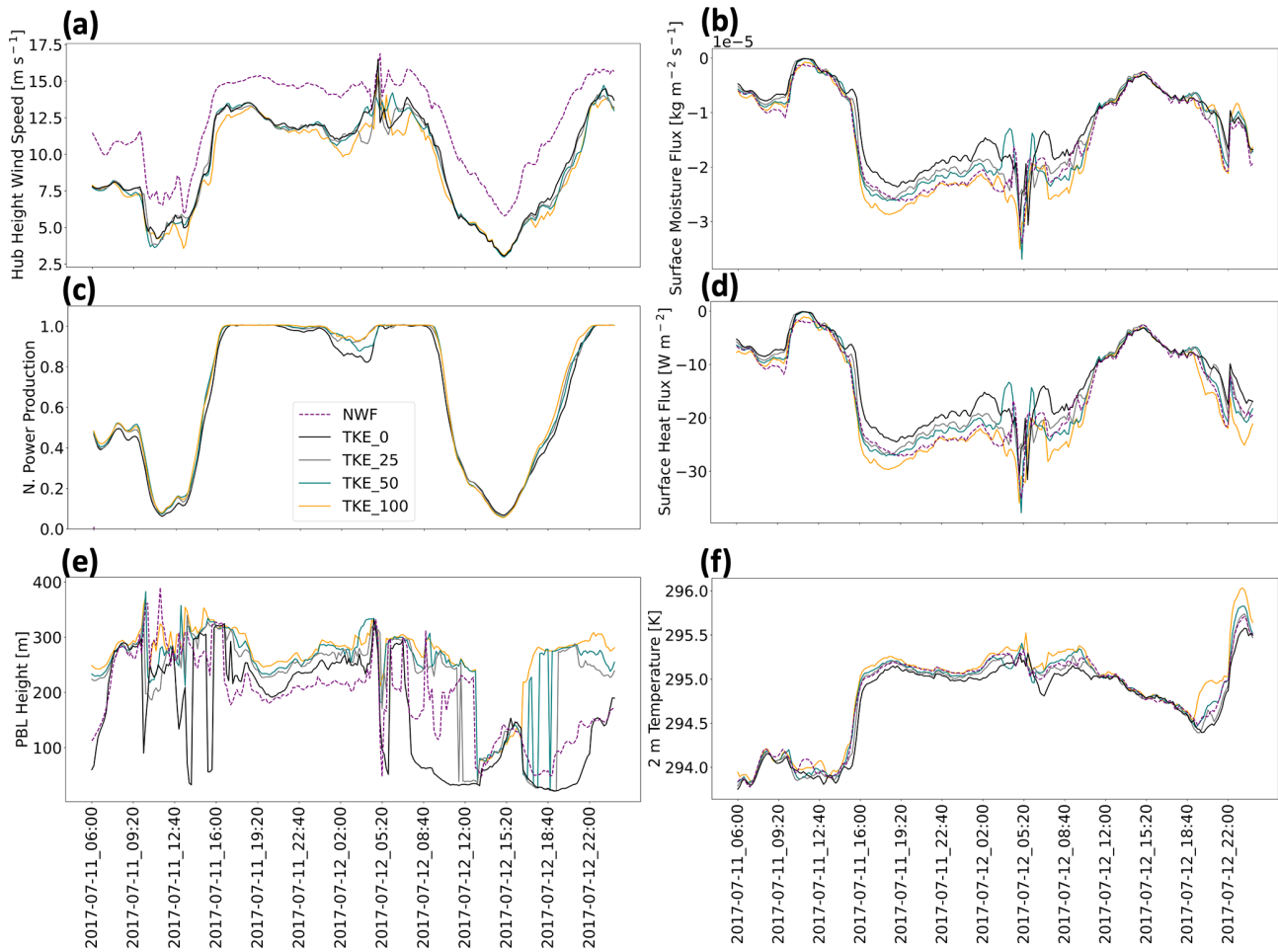


**Figure A1.** The effects of modifying the amount of turbulent kinetic energy (TKE) during test runs. Panels show (a) hub-height wind speed, (b) surface moisture flux, (c) normalized power production, (d) surface heat flux, (e) planetary boundary layer (PBL) height, and (f) 2 m temperature. Values are collected from a point centered on the RIMA block. Power production is the sum of all cells containing wind turbines. TKE\_100 is shown in orange, TKE\_50 in blue, TKE\_25 in gray, TKE\_0 in black, and NWF in purple dashes.

## Appendix B

Stratification at the E05 and E06 lidars (Fig. B1) exhibits similar seasonal variability to the RIMA block (Fig. 10). The winter months feature predominant unstable stratification caused by cold air advecting over a warm sea surface. In the spring and early summer, stratification transitions to more common stable conditions as warm air advects over a cooler sea surface. Stratification is most commonly unstable in November and stable in May.

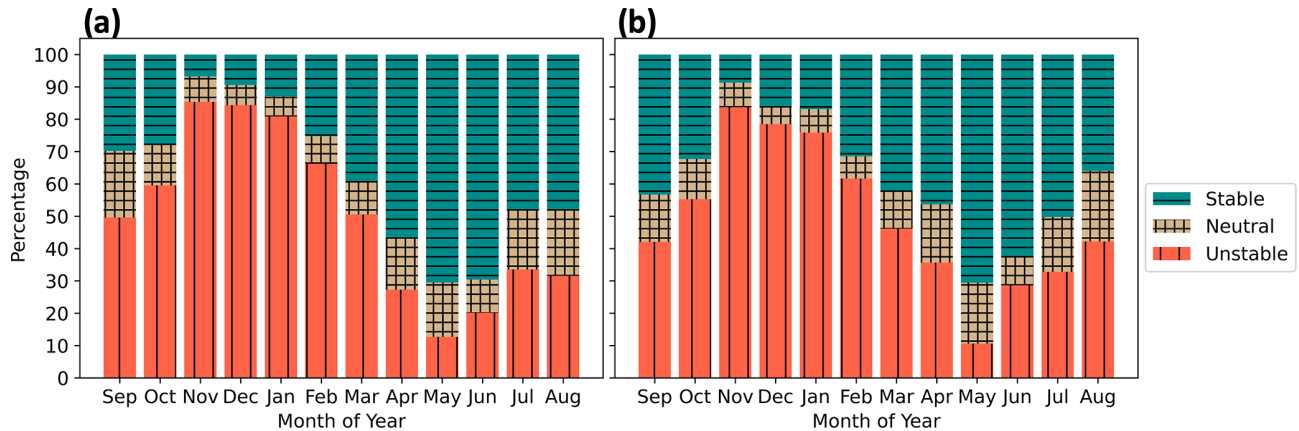


**Figure B1.** Stability classification using the Obukhov length for the 1 September 2019 to 1 September 2020 period at the (a) E05 and (b) E06 lidars from NWF. The tan crosshatches are neutral stratification, blue horizontal bars are stable stratification, and red vertical bars are unstable stratification.

## Appendix C

Surface estimates of  $L$  may not represent stability aloft (Fig. C1) and may overestimate unstable conditions. When considering monthly averaged potential temperature profiles through the rotor layer, only November and December appear unstably stratified. While September and October appear predominantly unstable based on surface estimates, potential temperature gradients within the rotor-swept area suggest slightly stable conditions, supporting inferences that offshore conditions are stable during late summer. Therefore, our limited set of CA simulations focus on 1 September to 31 October 2019 and 1 July to 31 August 2020 for its presumed abundance of stable stratification.

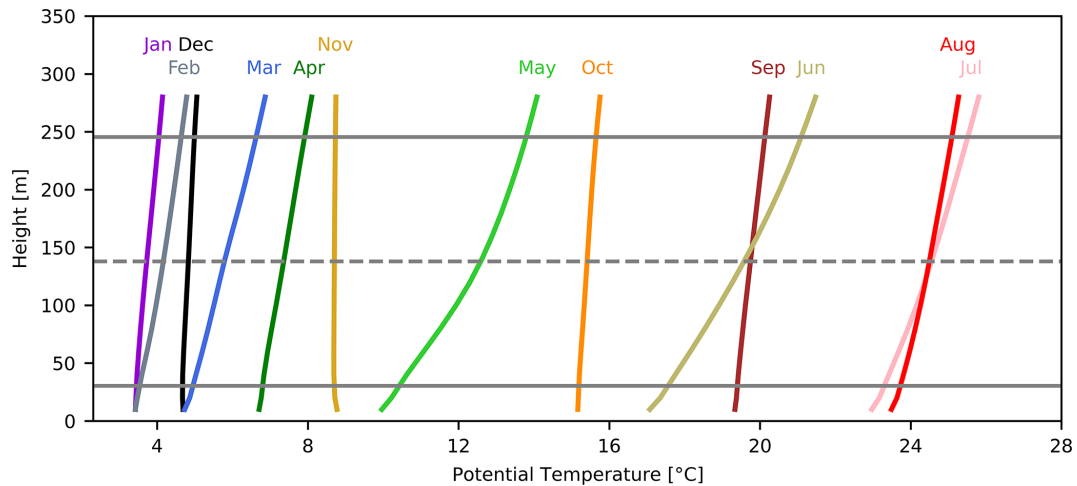


**Figure C1.** Monthly averaged WRF-simulated potential temperature profiles at a point centered on the RIMA block. Horizontal gray lines indicate the levels of the hub height (dashed) and the rotor-swept area (solid).



## Appendix D

Wakes in the simulations with CA show similar dependence on stratification (Fig. D1). Note that we simulate the CA for 4 months only (1 September to 31 October 2019 and 1 July to 31 August 2020) at one TKE level only (TKE<sub>100</sub>) due to computational costs. The maximum wake strength intensifies from  $-1.6$  to  $-3.2$   $\text{m s}^{-1}$  moving from unstable to stable stratification (Fig. D1b, c).

Wake propagation distance for the call area simulation is also affected by stratification. During the 4 months considered, unstable, stable, and neutral conditions occur 38.2 %, 53.4 %, and 8.3 % of the time, respectively. As such, there is essentially an even split between the percentage of occurrence of unstable and stable conditions. In unstable conditions, wakes from the two southernmost lease areas fail to reach neighboring downwind clusters on average, and no wakes stronger than this threshold reach the RIMA block (Fig. D1e). In stable stratification, wakes from each cluster reach downwind clusters, including the RIMA block (Fig. D1f). Averaged over all 4 months, wakes between LA and the CA along the New Jersey and New York bights affect each other, but no wakes reach the RIMA block. Wakes may still interact with downwind plants at individual times and affect power production.

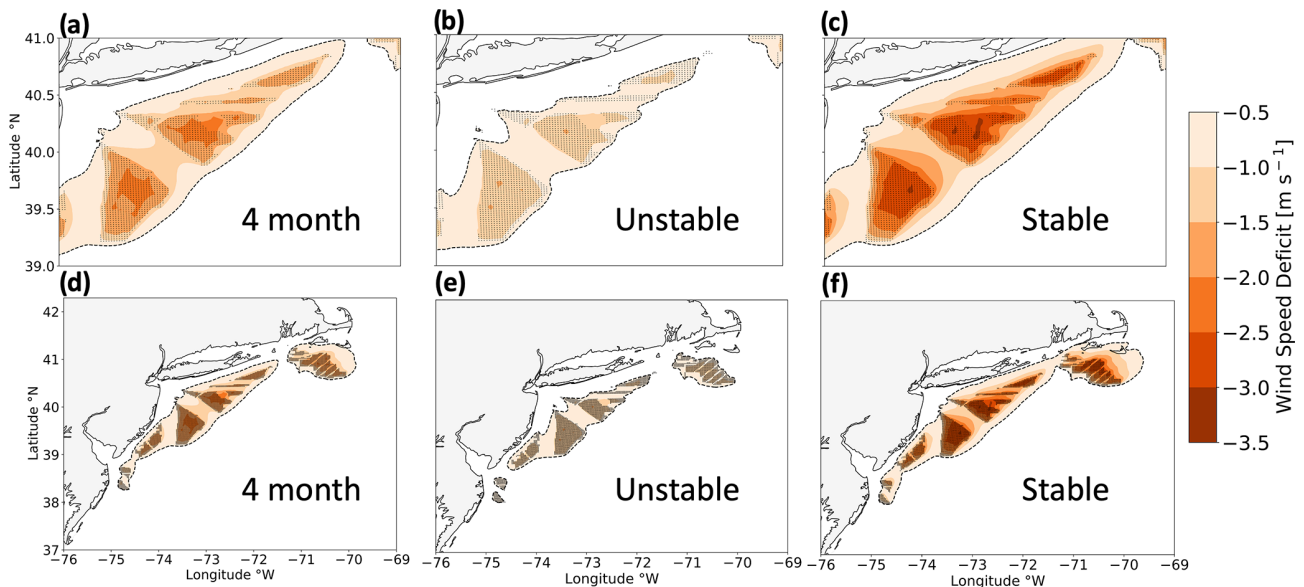


**Figure D1.** Average wake wind speed deficits among the call areas (a, d) for the combined 4-month period, 1 September to 31 October 2019 and 1 July to 31 August 2020, (b, e) during unstable stratification and (c, f) during stable stratification. All panels show 100 % added TKE. Wake wind speed deficits are shown by the colored contour, and turbines are shown as black dots. The upper row is zoomed in to increase granularity.

## Appendix E

Here, we characterize the (WFP-NWF) TKE differences by maximum value and by spatial extent. The maximum average TKE additions remain similar by stratification at TKE<sub>100</sub>, reaching 1.00, 1.01, and  $1.00 \text{ m}^2 \text{ s}^{-2}$  during unstable conditions, stable conditions, and the full year, respectively (Fig. E1a, c, e). The amount of added TKE is not homogeneous across the wind plants in TKE<sub>100</sub>, as the greatest contributions occur in grid cells containing more wind turbines. Some TKE is introduced in TKE<sub>0</sub> due to wind speed shear, although the amounts are over an order of magnitude smaller. The maximum average TKE amounts for TKE<sub>0</sub> are 0.05, 0.03, and  $0.03 \text{ m}^2 \text{ s}^{-2}$  during unstable conditions, stable conditions, and the full year, respectively. Being purely shear induced, regions experiencing the most TKE in TKE<sub>0</sub> correspond more with the maximum wake wind speed deficits (Fig. 12b, d, f).

We further characterize added TKE amounts by their spatial extent. We report the area encompassed by added TKE amounts greater than a threshold of  $0.005 \text{ m}^2 \text{ s}^{-2}$  because a cutoff of  $0 \text{ m}^2 \text{ s}^{-2}$  includes noise throughout the domain (Fig. F1), and the spatial extent is not realistic. In TKE<sub>100</sub>, the spatial extents are 10 724, 10 064, and  $9608 \text{ km}^2$  in unstable stratification, stable stratification, and for the full year, respectively (Fig. E1a, c, e). In TKE<sub>0</sub>, the spatial extents are 13 888, 10 724, and  $11\,332 \text{ km}^2$  in unstable stratification, stable stratification, and for the full year, respectively (Fig. E1b, d, f).

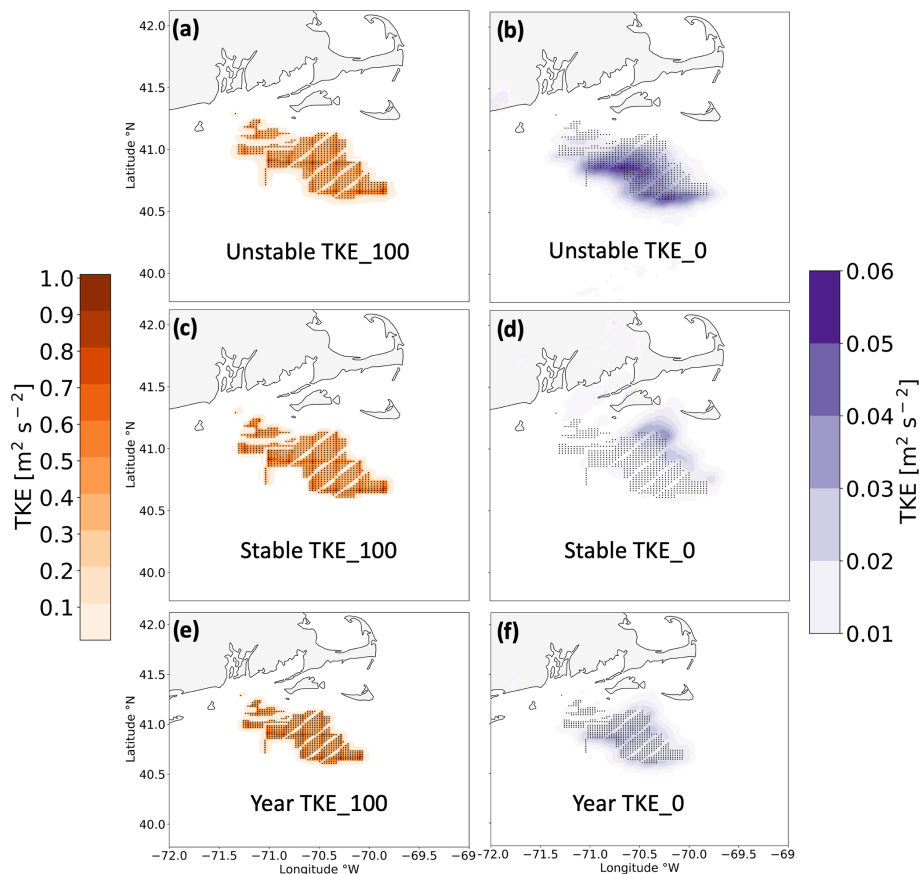


**Figure E1.** Average hub-height (WFP-NWF) TKE difference among the lease areas during (a, b) unstable stratification, (c, d) stable stratification, and (e, f) the full 1 September 2019 to 1 September 2020 period. Panels show 100 % added TKE (a, c, e) or 0 % added TKE (b, d, f). The TKE amount is shown by the colored contouring, and turbines are shown as the black dots.

## Appendix F

Results can show evidence of numerical noise, which emerges when simulations incorporate the WFP (Ancell et al., 2018; Lauridsen and Ancell, 2018). In our simulations, these brief periods of numerical noise emerge and decay, often coincident with precipitation. While we expect differences in wake wind speed immediately downwind of power plants, it is unlikely that these differences could advect to the southeast corner of the domain, roughly 600 km southeast of the RIMA block (Fig. F1a). If this numerical noise occurred in grid cells with turbines, then this noise would introduce error in power estimations.

We explored several approaches to mitigate the numerical noise, none of which succeeded. First, we increased the floating-point accuracy of numerical calculations by enabling double precision in WRF. Double precision limits the growth of rounding error to smaller magnitudes (Ancell et al., 2018). This attempt aimed to confine perturbations to smaller orders of magnitude that take longer periods of time to become substantial. To prevent “runaway” error growth after long periods of time, we submit simulation restarts each month.

In observing a spatial correlation of numerical noise with convective precipitation during test runs, we reran test simulations with a more complex microphysics scheme. The Thompson microphysics scheme, used throughout, is double moment with respect to cloud ice only. We substituted the Morrison microphysics scheme, which is fully double moment with respect to cloud droplets and rain, cloud ice, snow, and graupel (Morrison et al., 2009). The use of Morrison microphysics did not improve numerical noise, so its computational cost could not be justified.

Next, we introduced a filter for shortwave numerical noise by prohibiting upgradient diffusion. Doing so requires setting the parameter `diff_6th_opt` to 2 in the namelist, as certain combinations of advection and diffusion orders are conducive to mitigating noise around heavy precipitation (Kusaka et al., 2005). While Kusaka et al. (2005) found the combination of fifth-order advection and sixth-order diffusion to perform best, we had previously attempted this combination because default advection in WRF is fifth order. Thus, we attempted the next best recommendation – combining sixth-order advection and diffusion. Again, this combination did not improve results.

We made a final attempt at noise reduction by running an ensemble of three members using a stochastic kinetic energy backscatter scheme. Ensemble members contain seeds with variable time steps that randomly inject kinetic energy into grid cells (Berner, 2013). These stochastic supplements replenish the kinetic energy sink from unresolvable subgrid-scale processes. We followed recommendations to perturb the stream function and potential temperature backscatter rates by  $1 \times 10^{-5}$  and  $1 \times 10^{-6}$ , respectively. Again, while subtle differences emerged between the simulations, little improvement was found.

We saw little improvement from the aforementioned pre-processing efforts. Given this lack of improvement and a need to conserve computational resources, we employed averaging during postprocessing to alleviate the effects of noise. Modifying averaging periods impacts the range of numerical noise in the wind speed field (Fig. F1b). Noise occurring in grid cells containing turbines could undermine power estimation accuracy, and we observed noise occurring in the southeastern portion of the domain. Subtraction of wind speeds between simulations with variable TKE amounts should only show differences within the wake, and such differences are a result of noise. Averaging periods provide greater relief. While 2 and 4 h averaging periods deliver the best results, these temporal scales can hide important diurnal variability. Conversely, a 30 min averaging period can improve results, but local extrema occasionally reach magnitudes similar to the magnitudes of the raw noise. Thus, hourly averaging can mitigate noise without masking important variability. As a final note, other researchers have benefitted by employing grid nudging within this domain above the PBL (Maryam Golbazi, personal communication, September 2022).

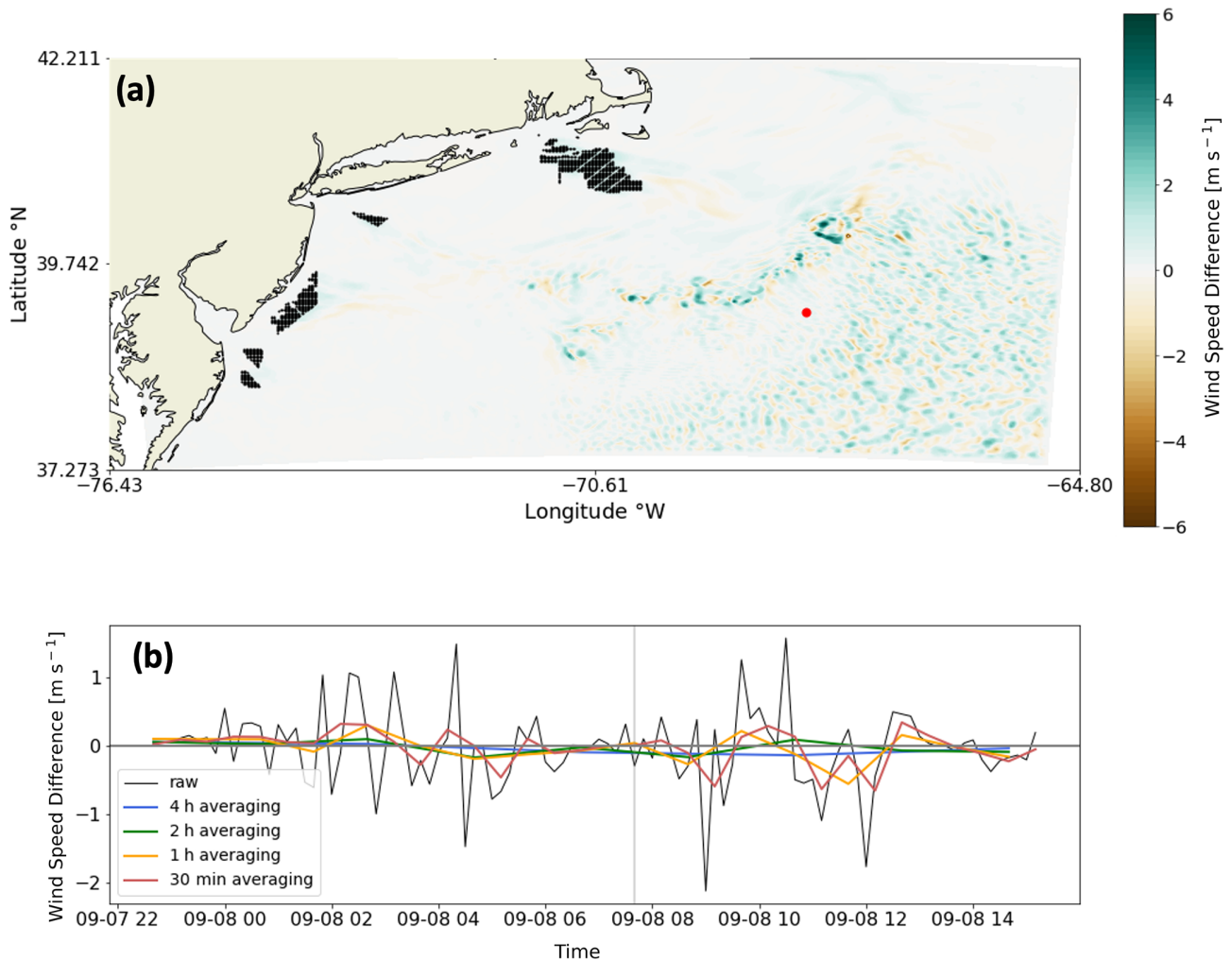


**Figure F1.** (a) The wind speed difference between TKE\_100 and TKE\_0 at the hub height from LA runs. Wind turbines are shown as black dots. The blue contouring indicates TKE\_100 produced faster wind speeds and vice versa. (b) Wind speeds obtained at the red circle in (a) are shown as a time series. The raw difference in wind speeds and averaging periods are shown as different line colors in the time series. The vertical gray line shows the time stamp of the map.

**Code and data availability.** The data and files that support this work are publicly available. The ERA5 boundary conditions can be downloaded from the ECMWF Climate Data Store at <https://doi.org/10.24381/cds.bd0915c6> (Hersbach et al., 2023). Shapefiles including the bounding extents of the lease and call areas are available at <https://www.boem.gov/renewable-energy/mapping-and-data/renewable-energy-gis-data> (Bureau of Ocean Energy Management, 2023). Individual turbine coordinates and their power and thrust curves are provided at <https://doi.org/10.5281/zenodo.7374283> (Rosencrans, 2022). WRF namelists for NWF and WFP simulations can be obtained at <https://doi.org/10.5281/zenodo.7374239> (Rosencrans, 2021). The simulation output data will be available in HDF5 format at <https://doi.org/10.25984/1821404> (National Renewable Energy Laboratory, 2020).

**Author contributions.** Conceptualization: JKL and MO. Methodology: DR, JKL, and MO. Software: DR, AR, and MR. Validation: DR. Formal analysis: DR. Investigation: DR and JKL. Resources: MO and NB. Writing (original draft): DR and JKL. Writing (review and editing): all co-authors. Visualization: DR. Supervision: JKL, MO, and NB. Project administration: MO and NB. Funding acquisition: MO and NB.

**Competing interests.** At least one of the (co-)authors is a member of the editorial board of *Wind Energy Science*. The peer-review process was guided by an independent editor. Furthermore, Mike Optis co-authored the submitted manuscript while he was an employee of the National Renewable Energy Laboratory. He has since founded Veer Renewables, which recently released a wind modeling product, WakeMap, which is based on a similar numerical weather prediction modeling framework as the one described in this paper. Data from WakeMap are sold to wind energy stakeholders for profit. Public content on WakeMap include a website (<https://veer.eco/wakemap/>, last access: 18 March 2023), a white paper ([https://veer.eco/wp-content/uploads/2023/02/WakeMap\\_White\\_Paper\\_Veer\\_Renewables.pdf](https://veer.eco/wp-content/uploads/2023/02/WakeMap_White_Paper_Veer_Renewables.pdf), last access: 18 March 2023), and several LinkedIn posts promoting WakeMap. Mike Optis is the founder and president of Veer Renewables, a for-profit consulting company. Mike Optis is a shareholder of Veer Renewables and owns 92 % of its stock.

**Disclaimer.** The views expressed in the article do not necessarily represent the views of the DOE or the U.S. Government. The U.S. Government and the publisher, by accepting the article for publication, acknowledge that the U.S. Government retains a nonexclusive, paid-up, irrevocable, worldwide license to publish or reproduce the published form of this work, or allow others to do so, for U.S. Government purposes. Neither NYSERDA nor OceanTech Services/DNV have reviewed the information contained herein and the opinions in this report do not necessarily reflect those of any of these parties.

**Publisher's note:** Copernicus Publications remains neutral with regard to jurisdictional claims made in the text, published maps, institutional affiliations, or any other geographical represen-

tation in this paper. While Copernicus Publications makes every effort to include appropriate place names, the final responsibility lies with the authors.

**Acknowledgements.** This work was supported by an agreement with NREL under APUP UGA-0-41026-125. This work was authored (in part) by the National Renewable Energy Laboratory, operated by the Alliance for Sustainable Energy, LLC, for the US Department of Energy (DOE) under contract no. DE-AC36-08GO28308. A portion of computation used the Blanca condo computing resource at the University of Colorado Boulder. Blanca is jointly funded by computing users and the University of Colorado Boulder. A portion of computation used the Summit supercomputer, which is supported by the National Science Foundation (awards ACI-1532235 and ACI-1532236), the University of Colorado Boulder, and Colorado State University. The Summit supercomputer is a joint effort of the University of Colorado Boulder and Colorado State University. A portion of this research was performed using computational resources sponsored by the DOE's Office of Energy Efficiency and Renewable Energy and located at NREL.

**Financial support.** Funding was provided by the US Department of Energy's Office of Energy Efficiency and Renewable Energy and the Wind Energy Technologies Office and by the National Offshore Wind Research and Development Consortium (grant no. CRD-19-16351).

**Review statement.** This paper was edited by Andrea Hahmann and reviewed by three anonymous referees.

## References

- 218th Legislature: NJ Renewable Portfolio Standards, [https://pub.njleg.gov/bills/2018/A4000/3723\\_I1.PDF](https://pub.njleg.gov/bills/2018/A4000/3723_I1.PDF) (last access: 10 August 2022), 2018.
- Aitken, M. L., Kosoviae, B., Mirocha, J. D., and Lundquist, J. K.: Large eddy simulation of wind turbine wake dynamics in the stable boundary layer using the Weather Research and Forecasting Model, *J. Renew. Sustain. Ener.*, 6, 033137, <https://doi.org/10.1063/1.4885111>, 2014.
- Ancell, B. C., Bogusz, A., Lauridsen, M. J., and Nauert, C. J.: Seeding Chaos: The Dire Consequences of Numerical Noise in NWP Perturbation Experiments, *B. Am. Meteorol. Soc.*, 99, 615–628, <https://doi.org/10.1175/BAMS-D-17-0129.1>, 2018.
- Antonini, E. G. A., Romero, D. A., and Amon, C. H.: Optimal design of wind farms in complex terrains using computational fluid dynamics and adjoint methods, *Appl. Energ.*, 261, 114426, <https://doi.org/10.1016/j.apenergy.2019.114426>, 2020.
- Archer, C. L., Colle, B. A., Veron, D. L., Veron, F., and Sienkiewicz, M. J.: On the predominance of unstable atmospheric conditions in the marine boundary layer offshore of the U.S. northeastern coast, *J. Geophys. Res.-Atmos.*, 121, 8869–8885, <https://doi.org/10.1002/2016JD024896>, 2016.
- Archer, C. L., Wu, S., Ma, Y., and Jiménez, P. A.: Two Corrections for Turbulent Kinetic Energy Generated by Wind Farms



- in the WRF Model, *Mon. Weather Rev.*, 148, 4823–4835, <https://doi.org/10.1175/MWR-D-20-0097.1>, 2020.
- Arthur, R. S., Mirocha, J. D., Marjanovic, N., Hirth, B. D., Schroeder, J. L., Wharton, S., and Chow, F. K.: Multi-Scale Simulation of Wind Farm Performance during a Frontal Passage, *Atmosphere*, 11, 245, <https://doi.org/10.3390/atmos11030245>, 2020.
- Beiter, P., Musial, W., Duffy, P., Cooperman, A., Shields, M., Heimiller, D., and Optis, M.: The Cost of Floating Offshore Wind Energy in California Between 2019 and 2032, NREL/TP-5000-77384, <https://doi.org/10.2172/1710181>, 2020.
- Berner, J.: WRF Implementation Details and Version history of a Stochastic Kinetic-Energy Backscatter Scheme (SKEBS), National Center for Atmospheric Research Tech. Note, [https://www2.mmm.ucar.edu/wrf/users/docs/skebs\\_in\\_wrf.pdf](https://www2.mmm.ucar.edu/wrf/users/docs/skebs_in_wrf.pdf) (last access: 22 July 2023), 2013.
- Bodini, N., Lundquist, J. K., and Kirincich, A.: U.S. East Coast Lidar Measurements Show Offshore Wind Turbines Will Encounter Very Low Atmospheric Turbulence, *Geophys. Res. Lett.*, 46, 5582–5591, <https://doi.org/10.1029/2019GL082636>, 2019.
- Bodini, N., Optis, M., Redfern, S., Rosencrans, D., Rybchuk, A., Lundquist, J. K., Pronk, V., Castagneri, S., Purkayastha, A., Draxl, C., Krishnamurthy, R., Young, E., Roberts, B., Rosenlieb, E., and Musial, W.: The 2023 National Offshore Wind data set (NOW-23), *Earth Syst. Sci. Data Discuss.* [preprint], <https://doi.org/10.5194/essd-2023-490>, in review, 2023.
- Bureau of Ocean Energy Management: Renewable Energy GIS Data, Bureau of Ocean Energy Management [data set], <https://www.boem.gov/renewable-energy/mapping-and-data/renewable-energy-gis-data>, last access: 4 April 2023.
- Burton, T., Jenkins, N., Sharpe, D., and Bossanyi, E.: *Wind Energy Handbook*, John Wiley & Sons, 784 pp., 2011.
- Debnath, M., Doubrawa, P., Optis, M., Hawbecker, P., and Bodini, N.: Extreme wind shear events in US offshore wind energy areas and the role of induced stratification, *Wind Energ. Sci.*, 6, 1043–1059, <https://doi.org/10.5194/wes-6-1043-2021>, 2021.
- DNV: NYSEDA Floating LiDAR Buoy Data, Resource Panorama Public Data [data set], <https://oswbuoysny.resourcepanorama.dnv.com/download/f67d14ad-07ab-4652-16d2-08d71f257da1> (last access: 6 July 2021), 2019.
- Donlon, C. J., Martin, M., Stark, J., Roberts-Jones, J., Fiedler, E., and Wimmer, W.: The Operational Sea Surface Temperature and Sea Ice Analysis (OSTIA) system, *Remote Sens. Environ.*, 116, 140–158, <https://doi.org/10.1016/j.rse.2010.10.017>, 2012.
- EIA: Frequently Asked Questions (FAQs) – U.S. Energy Information Administration (EIA), <https://www.eia.gov/tools/faqs/faq.php> (last access: 4 April 2023), 2023.
- FACT SHEET: Biden Administration Jumpstarts Offshore Wind Energy Projects to Create Jobs, <https://www.whitehouse.gov/briefing-room/statements-releases/2021/03/29/fact-sheet-biden-administration-jumpstarts-offshore-wind-energy-projects-to-create-jobs/>, last access: 4 April 2023.
- Fischer, J., Brown, R., Larsén, X. G., Badger, J., and Hawkes, G.: Review of Mesoscale Wind-Farm Parametrizations and Their Applications, *Bound.-Lay. Meteorol.*, 182, 175–224, <https://doi.org/10.1007/s10546-021-00652-y>, 2022.
- Fitch, A. C., Olson, J. B., Lundquist, J. K., Dudhia, J., Gupta, A. K., Michalakes, J., and Barstad, I.: Local and Mesoscale Impacts of Wind Farms as Parameterized in a Mesoscale NWP Model, *Mon. Weather Rev.*, 140, 3017–3038, <https://doi.org/10.1175/MWR-D-11-00352.1>, 2012.
- Fitch, A. C., Lundquist, J. K., and Olson, J. B.: Mesoscale Influences of Wind Farms throughout a Diurnal Cycle, *Mon. Weather Rev.*, 141, 2173–2198, <https://doi.org/10.1175/MWR-D-12-00185.1>, 2013.
- Golbazi, M., Archer, C. L., and Alessandrini, S.: Surface impacts of large offshore wind farms, *Environ. Res. Lett.*, 17, 064021, <https://doi.org/10.1088/1748-9326/ac6e49>, 2022.
- Gupta, T. and Baidya Roy, S.: Recovery processes in a large offshore wind farm, *Wind Energ. Sci.*, 6, 1089–1106, <https://doi.org/10.5194/wes-6-1089-2021>, 2021.
- Hahmann, A. N., Sile, T., Witha, B., Davis, N. N., Dörenkämper, M., Ezber, Y., García-Bustamante, E., González-Rouco, J. F., Navarro, J., Olsen, B. T., and Söderberg, S.: The making of the New European Wind Atlas – Part 1: Model sensitivity, *Geosci. Model Dev.*, 13, 5053–5078, <https://doi.org/10.5194/gmd-13-5053-2020>, 2020.
- Hersbach, H., Bell, B., Berrisford, P., Hirahara, S., Horányi, A., Muñoz-Sabater, J., Nicolas, J., Peubey, C., Radu, R., Schepers, D., Simmons, A., Soci, C., Abdalla, S., Abellan, X., Balsamo, G., Bechtold, P., Biavati, G., Bidlot, J., Bonavita, M., De Chiara, G., Dahlgren, P., Dee, D., Diamantakis, M., Dragani, R., Flemming, J., Forbes, R., Fuentes, M., Geer, A., Haimberger, L., Healy, S., Hogan, R. J., Hólm, E., Janisková, M., Keeley, S., Laloyaux, P., Lopez, P., Lupu, C., Radnoti, G., de Rosnay, P., Rozum, I., Vamborg, F., Villaume, S., and Thépaut, J.-N.: The ERA5 global reanalysis, *Q. J. Roy. Meteor. Soc.*, 146, 1999–2049, <https://doi.org/10.1002/qj.3803>, 2020.
- Hersbach, H., Bell, B., Berrisford, P., Biavati, G., Horányi, A., Muñoz Sabater, J., Nicolas, J., Peubey, C., Radu, R., Rozum, I., Schepers, D., Simmons, A., Soci, C., Dee, D., and Thépaut, J.-N.: ERA5 hourly data on pressure levels from 1940 to present, Copernicus Climate Change Service (C3S) Climate Data Store (CDS) [data set], <https://doi.org/10.24381/cds.bd0915c6>, 2023.
- Iacono, M. J., Delamere, J. S., Mlawer, E. J., Shephard, M. W., Clough, S. A., and Collins, W. D.: Radiative forcing by long-lived greenhouse gases: Calculations with the AER radiative transfer models, *J. Geophys. Res.-Atmos.*, 113, D13103, <https://doi.org/10.1029/2008JD009944>, 2008.
- Jiang, Q.: Impact of Elevated Kelvin-Helmholtz Billows on the Atmospheric Boundary Layer, *J. Atmos. Sci.*, 1, 3983–3999, <https://doi.org/10.1175/JAS-D-21-0062.1>, 2021.
- Kain, J. S.: The Kain-Fritsch Convective Parameterization: An Update, *J. Appl. Meteorol. Clim.*, 43, 170–181, [https://doi.org/10.1175/1520-0450\(2004\)043<0170:TKCPAU>2.0.CO;2](https://doi.org/10.1175/1520-0450(2004)043<0170:TKCPAU>2.0.CO;2), 2004.
- Kusaka, H., Crook, A., Kniviel, J. C., and Dudhia, J.: Sensitivity of the WRF Model to Advection and Diffusion Schemes for Simulation of Heavy Rainfall along the Baiu Front, *SOLA*, 1, 177–180, <https://doi.org/10.2151/sola.2005-046>, 2005.
- Lauridsen, M. J. and Ancell, B. C.: Nonlocal Inadvertent Weather Modification Associated with Wind Farms in the Central United States, *Adv. Meteorol.*, 2018, e2469683, <https://doi.org/10.1155/2018/2469683>, 2018.
- Lee, J. C. Y. and Fields, M. J.: An overview of wind-energy-production prediction bias, losses, and uncertainties, *Wind En-*

- erg. Sci., 6, 311–365, <https://doi.org/10.5194/wes-6-311-2021>, 2021.
- Livingston, H. G. and Lundquist, J. K.: How many offshore wind turbines does New England need?, *Meteorol. Appl.*, 27, e1969, <https://doi.org/10.1002/met.1969>, 2020.
- Lundquist, J. K., DuVivier, K. K., Kaffine, D., and Tomaszewski, J. M.: Costs and consequences of wind turbine wake effects arising from uncoordinated wind energy development, *Nature Energy*, 4, 26–34, <https://doi.org/10.1038/s41560-018-0281-2>, 2019.
- Mirocha, J. D., Kosovic, B., Aitken, M. L., and Lundquist, J. K.: Implementation of a generalized actuator disk wind turbine model into the weather research and forecasting model for large-eddy simulation applications, *J. Renew. Sustain. Ener.*, 6, 013104, <https://doi.org/10.1063/1.4861061>, 2014.
- Monin, A. S. and Obukhov, A. M.: Basic laws of turbulent mixing in the surface layer of the atmosphere, *Tr. Akad. Nauk SSSR Geophys. Inst.*, 24, 30, [https://gibbs.science/efd/handouts/monin\\_obukhov\\_1954.pdf](https://gibbs.science/efd/handouts/monin_obukhov_1954.pdf) (last access: 28 November 2022), 1954.
- Morrison, H., Thompson, G., and Tatarskii, V.: Impact of Cloud Microphysics on the Development of Trailing Stratiform Precipitation in a Simulated Squall Line: Comparison of One- and Two-Moment Schemes, *Mon. Weather Rev.*, 137, 991–1007, <https://doi.org/10.1175/2008MWR2556.1>, 2009.
- Muñoz-Esparza, D., Cañadillas, B., Neumann, T., and van Beeck, J.: Turbulent fluxes, stability and shear in the offshore environment: Mesoscale modelling and field observations at FINO1, *J. Renew. Sustain. Ener.*, 4, 063136, <https://doi.org/10.1063/1.4769201>, 2012.
- Musial, W., Heimiller, D., Beiter, P., Scott, G., and Draxl, C.: 2016 Offshore Wind Energy Resource Assessment for the United States, NREL/TP-5000-66599, <https://doi.org/10.2172/1324533>, 2016.
- Nakanishi, M. and Niino, H.: An Improved Mellor–Yamada Level-3 Model: Its Numerical Stability and Application to a Regional Prediction of Advection Fog, *Bound.-Lay. Meteorol.*, 119, 397–407, <https://doi.org/10.1007/s10546-005-9030-8>, 2006.
- National Renewable Energy Laboratory: 2023 National Offshore Wind data set (NOW-23), National Renewable Energy Laboratory [data set], <https://doi.org/10.25984/1821404>, 2020.
- NEISO: Energy, Load, and Demand Reports, ISO New England [data set], <https://www.iso-ne.com/isoexpress/web/reports/load-and-demand/-/tree/dmnd-rt-hourly-sys> (last access: 24 October 2022), 2019.
- NEISO: Reliable Electricity. Competitive Prices. Clean-Energy Transition, <https://www.iso-ne.com> (last access: 10 January 2023), 2023.
- Niu, G.-Y., Yang, Z.-L., Mitchell, K. E., Chen, F., Ek, M. B., Barlage, M., Kumar, A., Manning, K., Niyogi, D., Rosero, E., Tewari, M., and Xia, Y.: The community Noah land surface model with multiparameterization options (Noah-MP): 1. Model description and evaluation with local-scale measurements, *J. Geophys. Res.-Atmos.*, 116, D12110, <https://doi.org/10.1029/2010JD015139>, 2011.
- Nygaard, N. G.: Wakes in very large wind farms and the effect of neighbouring wind farms, *J. Phys. Conf. Ser.*, 524, 012162, <https://doi.org/10.1088/1742-6596/524/1/012162>, 2014.
- Optis, M., Bodini, N., Debnath, M., and Doubrawa, P.: Best Practices for the Validation of U.S. Offshore Wind Resource Models, National Renewable Energy Lab. (NREL), Golden, CO (United States), NREL/TP-5000-78375, <https://doi.org/10.2172/1755697>, 2020.
- Perkins, S. E., Pitman, A. J., Holbrook, N. J., and McAneney, J.: Evaluation of the AR4 Climate Models' Simulated Daily Maximum Temperature, Minimum Temperature, and Precipitation over Australia Using Probability Density Functions, *J. Climate*, 20, 4356–4376, <https://doi.org/10.1175/JCLI4253.1>, 2007.
- Platis, A., Siedersleben, S. K., Bange, J., Lampert, A., Bärfuss, K., Hankers, R., Cañadillas, B., Foreman, R., Schulz-Stellenfleth, J., Djath, B., Neumann, T., and Emeis, S.: First in situ evidence of wakes in the far field behind offshore wind farms, *Sci. Rep.*, 8, 2163, <https://doi.org/10.1038/s41598-018-20389-y>, 2018.
- Porté-Agel, F., Bastankhah, M., and Shamsoddin, S.: Wind-Turbine and Wind-Farm Flows: A Review, *Bound.-Lay. Meteorol.*, 174, 1–59, <https://doi.org/10.1007/s10546-019-00473-0>, 2020.
- Price-Whelan, A. M., Lim, P. L., Earl, N., Starkman, N., Bradley, L., Shupe, D. L., Patil, A. A., Corrales, L., Bresseur, C. E., Nöthe, M., Donath, A., Tollerud, E., Morris, B. M., Ginsburg, A., Vaher, E., Weaver, B. A., Tocknell, J., Jamieson, W., Kerkwijk, M. H. van, Robitaille, T. P., Merry, B., Bachetti, M., Günther, H. M., Authors, P., Aldcroft, T. L., Alvarado-Montes, J. A., Archibald, A. M., Bódi, A., Bapat, S., Barentsen, G., Bazán, J., Biswas, M., Boquien, M., Burke, D. J., Cara, D., Cara, M., Conroy, K. E., Conseil, S., Craig, M. W., Cross, R. M., Cruz, K. L., D'Eugenio, F., Dencheva, N., Devillepoix, H. A. R., Dietrich, J. P., Eigenbrot, A. D., Erben, T., Ferreira, L., Foreman-Mackey, D., Fox, R., Freij, N., Garg, S., Geda, R., Glatly, L., Gondhalekar, Y., Gordon, K. D., Grant, D., Greenfield, P., Groener, A. M., Guest, S., Gurovich, S., Handberg, R., Hart, A., Hatfield-Dodds, Z., Homeier, D., Hosseinzadeh, G., Jenness, T., Jones, C. K., Joseph, P., Kalmbach, J. B., Karamahmetoglu, E., Kaluszyński, M., Kelley, M. S. P., Kern, N., Kerzendorf, W. E., Koch, E. W., Kulumani, S., Lee, A., Ly, C., Ma, Z., MacBride, C., Maljaars, J. M., Muna, D., Murphy, N. A., Norman, H., O'Steen, R., Oman, K. A., Pacifici, C., Pascual, S., Pascual-Granado, J., Patil, R. R., Perren, G. I., Pickering, T. E., Rastogi, T., Roulston, B. R., Ryan, D. F., Rykoff, E. S., Sabater, J., Sakurikar, P., Salgado, J., Sanghi, A., Saunders, N., Savchenko, V., Schwardt, L., Seifert-Eckert, M., Shih, A. Y., Jain, A. S., Shukla, G., Sick, J., Simpson, C., Singanamalla, S., Singer, L. P., Singhal, J., Sinha, M., Sipócz, B. M., Spittler, L. R., Stansby, D., Streicher, O., Šumak, J., Swinbank, J. D., Taranu, D. S., Tewary, N., Tremblay, G. R., de Val-Borro, M., Kooten, S. J. V., Vasović, Z., Verma, S., Cardoso, J. V. de M., Williams, P. K. G., Wilson, T. J., Winkel, B., Wood-Vasey, W. M., Xue, R., Yoachim, P., Zhang, C., and Zonca, A.: The Astropy Project: Sustaining and Growing a Community-oriented Open-source Project and the Latest Major Release (v5.0) of the Core Package, *Astrophys. J.*, 935, 167, <https://doi.org/10.3847/1538-4357/ac7c74>, 2022.
- Pronk, V., Bodini, N., Optis, M., Lundquist, J. K., Moriarty, P., Draxl, C., Purkayastha, A., and Young, E.: Can reanalysis products outperform mesoscale numerical weather prediction models in modeling the wind resource in simple terrain?, *Wind Energ. Sci.*, 7, 487–504, <https://doi.org/10.5194/wes-7-487-2022>, 2022.
- Pryor, S. C., Barthelmie, R. J., and Shepherd, T. J.: Wind power production from very large offshore wind farms, *Joule*, 5, 2663–2686, <https://doi.org/10.1016/j.joule.2021.09.002>, 2021.

- Redfern, S., Olson, J. B., Lundquist, J. K., and Clack, C. T. M.: Incorporation of the Rotor-Equivalent Wind Speed into the Weather Research and Forecasting Model's Wind Farm Parameterization, *Mon. Weather Rev.*, 147, 1029–1046, <https://doi.org/10.1175/MWR-D-18-0194.1>, 2019.
- Redfern, S., Optis, M., Xia, G., and Draxl, C.: Offshore wind energy forecasting sensitivity to sea surface temperature input in the Mid-Atlantic, *Wind Energ. Sci.*, 8, 1–23, <https://doi.org/10.5194/wes-8-1-2023>, 2023.
- Rosencrans, D.: mid-Atlantic\_namelists, Zenodo [code], <https://doi.org/10.5281/zenodo.7374239>, 2021.
- Rosencrans, D.: mid-Atlantic\_turbines, Zenodo [code], <https://doi.org/10.5281/zenodo.7374283>, 2022.
- Rybachuk, A., Juliano, T. W., Lundquist, J. K., Rosencrans, D., Bodini, N., and Optis, M.: The sensitivity of the Fitch wind farm parameterization to a three-dimensional planetary boundary layer scheme, *Wind Energ. Sci.*, 7, 2085–2098, <https://doi.org/10.5194/wes-7-2085-2022>, 2022.
- Schneemann, J., Rott, A., Dörenkämper, M., Steinfeld, G., and Kühn, M.: Cluster wakes impact on a far-distant offshore wind farm's power, *Wind Energ. Sci.*, 5, 29–49, <https://doi.org/10.5194/wes-5-29-2020>, 2020.
- Shapiro, C. R., Gayme, D. F., and Meneveau, C.: Filtered actuator disks: Theory and application to wind turbine models in large eddy simulation, *Wind Energy*, 22, 1414–1420, <https://doi.org/10.1002/we.2376>, 2019.
- Siedersleben, S. K., Platis, A., Lundquist, J. K., Djath, B., Lampert, A., Bärfuss, K., Cañadillas, B., Schulz-Stellenfleth, J., Bange, J., Neumann, T., and Emeis, S.: Turbulent kinetic energy over large offshore wind farms observed and simulated by the mesoscale model WRF (3.8.1), *Geosci. Model Dev.*, 13, 249–268, <https://doi.org/10.5194/gmd-13-249-2020>, 2020.
- Skamarock, W. C., Klemp, J. B., Dudhia, J., Gill, D. O., Liu, Z., Berner, J., Wang, W., Powers, J. G., Duda, M. G., and Barker, D. M.: A description of the advanced research WRF model version 4, NCAR/TN-556+ STR, <https://doi.org/10.5065/1dfh-6p97>, 2019.
- Stevens, R. J. A. M., Gayme, D. F., and Meneveau, C.: Effects of turbine spacing on the power output of extended wind-farms, *Wind Energy*, 19, 359–370, <https://doi.org/10.1002/we.1835>, 2016.
- Stoelinga, M., Sanchez-Gomez, M., Poulos, G. S., and Crescenti, J.: Estimating Long-Range External Wake Losses in Energy Yield and Operational Performance Assessments Using the WRF Wind Farm Parameterization, 20, <https://arcvera.com/wp-content/uploads/2022/08/ArcVera-White-Paper-Estimating-Long-Range-External-Wake-Losses-WRF-WFP-1.0.pdf> (last access: 2 January 2022), 2022.
- Thompson, G., Field, P. R., Rasmussen, R. M., and Hall, W. D.: Explicit Forecasts of Winter Precipitation Using an Improved Bulk Microphysics Scheme. Part II: Implementation of a New Snow Parameterization, *Mon. Weather Rev.*, 136, 5095–5115, <https://doi.org/10.1175/2008MWR2387.1>, 2008.
- Tomaszewski, J. M. and Lundquist, J. K.: Simulated wind farm wake sensitivity to configuration choices in the Weather Research and Forecasting model version 3.8.1, *Geosci. Model Dev.*, 13, 2645–2662, <https://doi.org/10.5194/gmd-13-2645-2020>, 2020.
- Vanderwende, B. J., Kosovix, B., Lundquist, J. K., and Mirocha, J. D.: Simulating effects of a wind-turbine array using LES and RANS, *J. Adv. Model. Earth Sy.*, 8, 1376–1390, <https://doi.org/10.1002/2016MS000652>, 2016.
- Virtanen, P., Gommers, R., Oliphant, T. E., Haberland, M., Reddy, T., Cournapeau, D., Burovski, E., Peterson, P., Weckesser, W., Bright, J., van der Walt, S. J., Brett, M., Wilson, J., Millman, K. J., Mayorov, N., Nelson, A. R. J., Jones, E., Kern, R., Larson, E., Carey, C. J., Polat, Y., Feng, Y., Moore, E. W., VanderPlas, J., Laxalde, D., Perktold, J., Cimrman, R., Henriksen, I., Quintero, E. A., Harris, C. R., Archibald, A. M., Ribeiro, A. H., Pedregosa, F., and van Mulbregt, P.: SciPy 1.0: fundamental algorithms for scientific computing in Python, *Nat. Methods*, 17, 261–272, <https://doi.org/10.1038/s41592-019-0686-2>, 2020.
- Viselli, A., Faessler, N., and Filippelli, M.: Analysis of Wind Speed Shear and Turbulence LiDAR Measurements to Support Offshore Wind in the Northeast United States, ASME 2018 1st International Offshore Wind Technical Conference, <https://doi.org/10.1115/iowtc2018-1003>, 2018.
- Volker, P. J. H., Badger, J., Hahmann, A. N., and Ott, S.: The Explicit Wake Parametrisation V1.0: a wind farm parametrisation in the mesoscale model WRF, *Geosci. Model Dev.*, 8, 3715–3731, <https://doi.org/10.5194/gmd-8-3715-2015>, 2015.
- W.F. Baird & Associates: Vessel Navigation Through the Proposed Rhode Island/Massachusetts and Massachusetts Wind Energy Areas, <https://static1.squarespace.com/static/5a2eae32be42d64ed467f9d1/t/5dd3d3e476d4226b2a83db25/1574163438896/Proposed+1x1+layout+from+RI-MA+Leaseholders+1+Nov+19+%281%29.pdf> (last access: 5 April 2022), 2019.
- Wu, C., Luo, K., Wang, Q., and Fan, J.: A refined wind farm parameterization for the weather research and forecasting model, *Appl. Energ.*, 306, 118082, <https://doi.org/10.1016/j.apenergy.2021.118082>, 2022.
- Xia, G., Draxl, C., Optis, M., and Redfern, S.: Detecting and characterizing simulated sea breezes over the US northeastern coast with implications for offshore wind energy, *Wind Energ. Sci.*, 7, 815–829, <https://doi.org/10.5194/wes-7-815-2022>, 2022.

Article

## Using Satellite SAR to Characterize the Wind Flow around Offshore Wind Farms

Charlotte Bay Hasager <sup>1,\*</sup>, Pauline Vincent <sup>2,†</sup>, Jake Badger <sup>1,†</sup>, Merete Badger <sup>1,†</sup>,  
Alessandro Di Bella <sup>1,†</sup>, Alfredo Peña <sup>1,†</sup>, Romain Husson <sup>2,†</sup> and Patrick J. H. Volker <sup>1,†</sup>

<sup>1</sup> Technical University of Denmark, Wind Energy Department, Frederiksborgvej 399, Roskilde 4000, Denmark; E-Mails: [REDACTED]@dtu.dk (J.B.); [REDACTED]@dtu.dk (M.B.); [REDACTED]@dtu.dk (A.D.B.); [REDACTED]@dtu.dk (A.P.); [REDACTED]@dtu.dk (P.J.H.V.)

<sup>2</sup> Collecte Localisation Satellites, Avenue La Pérouse, Bâtiment le Ponant, Plouzané 29280, France; E-Mails: [REDACTED]@cls.fr (P.V.); [REDACTED]@cls.fr (R.H.)

† These authors contributed equally to this work.

\* Author to whom correspondence should be addressed; E-Mail: [REDACTED]@dtu.dk; Tel.: +[REDACTED] Fax: +[REDACTED].

Academic Editors: Vincenzo Dovi and Antonella Battaglini

Received: 16 April 2015 / Accepted: 1 June 2015 / Published: 5 June 2015

---

**Abstract:** Offshore wind farm cluster effects between neighboring wind farms increase rapidly with the large-scale deployment of offshore wind turbines. The wind farm wakes observed from Synthetic Aperture Radar (SAR) are sometimes visible and atmospheric and wake models are here shown to convincingly reproduce the observed very long wind farm wakes. The present study mainly focuses on wind farm wake climatology based on Envisat ASAR. The available SAR data archive covering the large offshore wind farms at Horns Rev has been used for geo-located wind farm wake studies. However, the results are difficult to interpret due to mainly three issues: the limited number of samples per wind directional sector, the coastal wind speed gradient, and oceanic bathymetry effects in the SAR retrievals. A new methodology is developed and presented. This method overcomes effectively the first issue and in most cases, but not always, the second. In the new method all wind field maps are rotated such that the wind is always coming from the same relative direction. By applying the new method to the SAR wind maps, mesoscale and microscale model wake aggregated wind-fields results are compared. The SAR-based findings strongly support the model results at Horns Rev 1.

**Keywords:** wind farm wake; offshore; satellite; SAR; remote sensing

---

## 1. Introduction

In the Northern European Seas offshore wind farms are planned as clusters. The wind farm wake from one wind farm thus has the potential to influence the power production at neighboring wind farms. The expected wake loss due to wind farm cluster effects is investigated in the present study. The wind farm wake cluster effects are strongly dependent upon the atmospheric conditions. These vary spatially and temporally. One remote sensing method for observing ocean surface winds is satellite Synthetic Aperture Radar (SAR). The advantage of SAR is that a large area is observed and several wind farms are covered. The derived wind map from SAR provides a snapshot of the wind field during a few seconds at the time of acquisition.

In the satellite SAR data archives covering the North Sea, thousands of wind turbines are visible as white dots in calm conditions. For low wind speed the backscatter signal over the ocean is low and the images appear dark while hard targets such as wind turbines and ships provide high backscatter and the objects appear very bright. During windy conditions wind farm wakes are sometimes visible as dark elongated areas downwind of a wind farm while the surrounding seas appear brighter. This is a result of the differences in wind speed with reduced winds downwind of large operating wind farms. The intensity of backscatter of microwave electromagnetic radiation from the ocean surface is a non-linear function of the wind speed over the ocean. The physical relationship is due to the capillary and short gravity waves formed at the ocean surface by the wind. For higher wind speeds the backscatter is higher.

Previous wind farm wake studies based on SAR from ERS-1/-2, Envisat, RADARSAT-1/-2, TerraSAR-X and airborne SAR show great variability in wind farm wakes [1–4]. This reflects the natural variability in atmospheric conditions at the micro- and mesoscale. Wind farm wakes are often not clearly visible in the SAR archive data. This may be explained by wind turbines out of operation or presence of oceanic features, e.g., bathymetry, currents, surfactants. However, the great variability in the wind field is most likely a major cause.

In order to show that wind farm wakes are detectable from SAR, we present in this study one case based on RADARSAT-2 ScanSAR Wide. This scene is a good example where ideal conditions for wake analysis occur and the coverage is just right for capturing 10 large offshore wind farms located in the southern North Sea. We compare the instantaneous SAR-based wind farm wakes to micro- and mesoscale wake model results.

For the rest of our SAR wind archive, we wish to find out if wakes can be detected even if they are not so clearly visible. We first use a simple method which has some disadvantages. Next we apply the aggregated method to overcome some of these disadvantages.

This is the first time that a suitable number of SAR scenes covering several large operating wind farms have become available [5]. The present study focuses on the wind farm wake climatology using many overlapping SAR scenes. The wide-swath-mode (WSM) products from the Advanced SAR (ASAR) on-board Envisat are selected. This data source is sampled routinely so there are many more samples but with less spatial detail (original resolution 150 m) than those used in previous studies



(of the order 5 to 30 m spatial resolution) where the data are rare and infrequent and only sampled upon request [1–4]. It is questionable whether wake effects can be detected from Envisat ASAR WSM data as we cannot always visually see the wind farm wakes. However, we hypothesize that the combination of many satellite samples will show an aggregated effect of the wind farm wakes on the mean wind climate in the area. The SAR-based wind farm wake climatology results therefore can be used to validate wake model results. The wind farm wake climatology can be modelled by micro- and mesoscale models but perfect agreement cannot be expected between SAR and wake model results. This is due to the different nature of data with SAR based on the sea surface while wake models operate around wind turbine hub-height.

The main topic of the study is on the potential of using SAR for characterization of wind flow around offshore wind farms. Our mission is to find out how to best utilize SAR for wake mapping. Three modes of investigation are considered: (1) Wind flow observed at 10 offshore farms with wind farm wakes concurrent in one SAR scene; (2) Wind flow observed at two wind farms concurrent and wind farm wakes average value based on 7 to 30 SAR scenes; (3) Wind flow observed at one wind farm at a time and the aggregated wind farm wake based on 100 to 800 SAR scenes. Basic information on the three modes of investigation is listed in Table 1. The advantages and limitations of each investigation mode in regard to wind farm wake model comparison are provided. Selected wake model results are presented as demonstration for each of the modes. Presenting the three modes in such an order clearly shows the evolution of wake studies using SAR.

**Table 1.** SAR source, number of wind farms covered in the method, number of SAR scenes used in each method for wake identification based on no averaging, geo-located SAR wind field averaging and rotated SAR wind field averaging. The spatial resolution of the wind fields are given. The Section in this paper where each mode is presented is also indicated.

Satellite Data	Number of Wind Farms	Number of SAR Scenes	Averaging	Analysis Type	Resolution (km)	Section
RADARSAT-2	10	1	None	Qualitative	1	3
Envisat ASAR	2	7–30	Geo-located	Quantitative	1	4
Envisat ASAR	1	100–800	Rotated	Quantitative	1	5

The structure of the paper includes in Section 2 a description of the study site, satellite data and the two wake models used. In Section 3 the results from the case study based on RADARSAT-2 and the results from two wake models are presented and discussed. Section 4 presents the Envisat SAR-based wind farm wake climatology based on simple averaging of the wind fields at Horns Rev 1 and 2 wind farms and comparison to results from one wake model. Section 5 gives introduction to the new methodology developed in which the wind field maps are rotated such that the wind is always coming from the same relative direction. The Envisat SAR-based results from the new methodology as well as wake model results from two models are presented and Envisat SAR-based results from four other wind farms are presented. In Section 6 is the discussion of results. Conclusions are given in Section 7.

## 2. Study Site, Satellite SAR and Wake Modelling

### 2.1. Study Site

Wind flow around the wind farms in the southern part of the North Sea is investigated. The wind farms studied are listed in Table 2 and the location of most of the wind farms is shown in Figure 1. Those not shown in Figure 1 are the Alpha ventus wind farm located in the German North Sea and Horns Rev 1 and 2 located in the Danish North Sea. The information in Table 2 includes the year of start of operation and key data on the wind turbines and area covered.

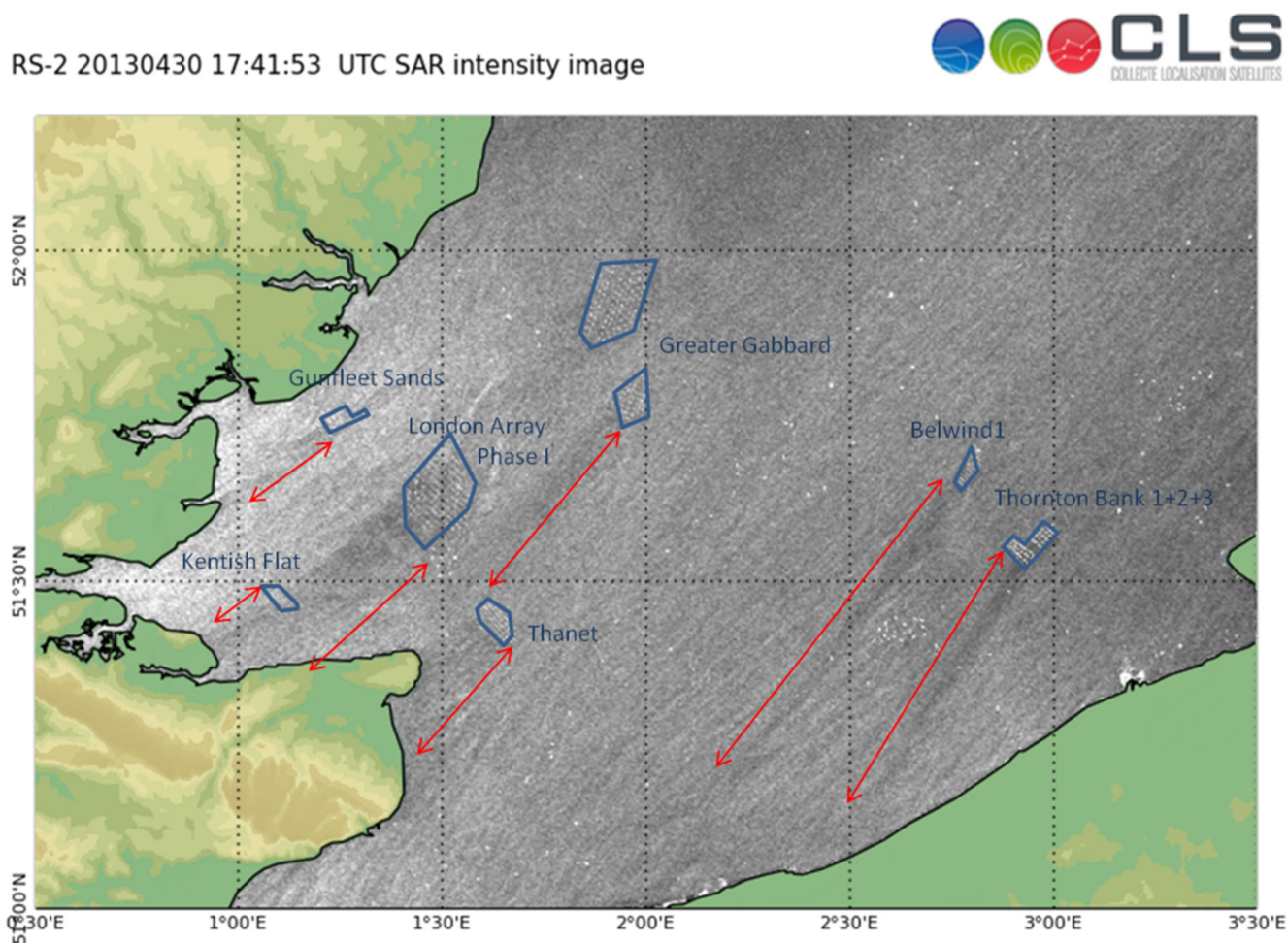


**Figure 1.** RADARSAT-2 intensity map of the southern North Sea observed 30 April 2013 at 17:41 UTC. The blue lines outline wind farms and the red arrows the wind farm wake.

**Table 2.** Wind farm info: Country, start year of operation, approximated latitude and longitude, number and size of turbines, wind park capacity and area covered.

Wind Farm	Nationality	Year	Latitude (°)	Longitude (°)	Number of Turbines	Turbine Size (MW)	Park (MW)	Area (km <sup>2</sup> )
Alpha ventus	Germany	2009	54.010	6.606	12	5	60	4
Belwind 1	Belgium	2010	51.670	2.802	55	3	165	13
Greater Gabbard	United Kingdom	2012	51.883	1.935	140	3.6	504	146
Gunfleet Sands 1 + 2I	United Kingdom	2010	51.730	1.229	48	3.6	172.8	16
Horns Rev 1	Denmark	2002	55.486	7.840	80	2.0	160	21
Horns Rev 2	Denmark	2009	55.600	7.582	91	2.3	209.3	33
Kentish Flats	United Kingdom	2005	51.460	1.093	30	3	90	10
London Array Phase 1	United Kingdom	2012	51.626	1.495	175	3.6	630	100
Thanet	United Kingdom	2010	51.430	1.633	100	3	300	35
Thornton Bank 1	Belgium	2009	51.544	2.938	6	6	30	1
Thornton Bank 2	Belgium	2012	51.556	2.969	30	6.15	184.5	12
Thornton Bank 3	Belgium	2013	51.540	2.921	18	6.15	110.7	7

## 2.2. Satellite SAR

SAR data from RADARSAT-2 and Envisat ASAR WSM are used. From RADARSAT-2 only one scene is investigated. It is ScanSAR Wide in VV polarization. The wind field retrieval requires input information about the wind direction. From the RADARSAT-2 image the wake direction has been estimated as  $40^\circ$  and using this input for wind direction, wind speed has been retrieved using CMOD-IFR2 [6]. It is the equivalent neutral wind (ENW) at the height 10 m. The calculated wind speed is presented in Figure 2a. The original ScanSAR Wide product has spatial resolution 100 m. The spatial resolution is reduced to approx. 1 km in connection with the processing of wind fields. This is performed to eliminate effects of random noise and long-period waves.

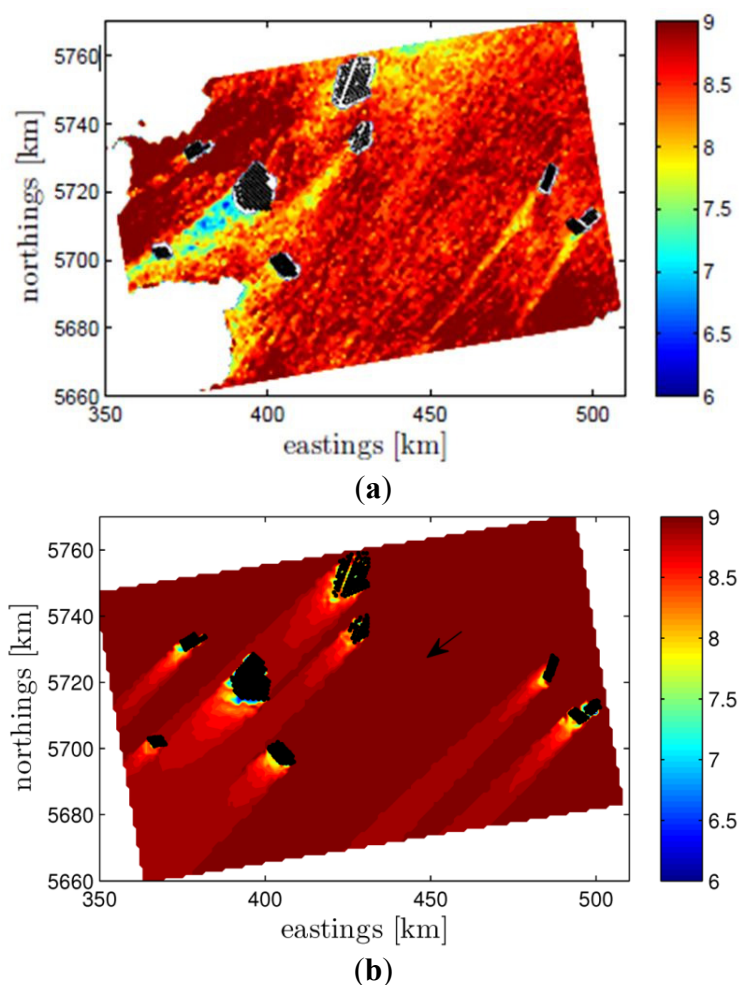


**Figure 2.** (a) Satellite 10-m SAR wind retrieval observed 30 April 2013 at 17:41 UTC and (b) modified PARK wake results at 70 m for the wind farms in the UK and Belgium. The wind direction used for the modeling is indicated with the black arrow.

The Envisat ASAR data were processed to wind fields as part of the project NORSEWInD [5]. The wind field retrieval gives the ENW at the height 10 m. For processing of large image archives, it is desirable to use wind direction information from an atmospheric model. In this case the wind directions were obtained from the European Centre for Medium-Range Weather Forecasts (ECMWF) model and interpolated spatially to match the higher resolution of the satellite data. Further details about the

SAR-wind processing chain, which was setup by Collecte Localisation Satellites (CLS), are given in [5]. The original WSM product has spatial resolution 150 m. The spatial resolution is to approx. 1 km in the wind field.

### 2.3. Wake Modelling with PARK and WRF

A modified version of the PARK wake model [7], also implemented in the Wind Atlas Analysis and Application Program (WAsP) [8], is here used for wake calculations. The main difference between this modified version and that in WAsP is that the former does not take into account the effects of the “ground reflecting back wakes” and so it only takes into account the shading rotors both directly upstream and sideways. The PARK wake model is based on the wake deficit suggested by [9], who derived a mass-conservation-like equation for the velocity immediately before a turbine  $u_2$ , which is affected by a wake:

$$u_2 = u_1 \left[ 1 - \frac{a}{\left(1 + \frac{k_w x}{r_r}\right)^2} \right] \quad (1)$$

where  $u_1$  is the upstream wind speed,  $a$  the induction factor which is a function of the thrust coefficient ( $C_t$ ),  $k_w$  the wake decay coefficient,  $x$  the downstream distance and  $r_r$  the turbine’s rotor radius. The square of the total wake deficit is estimated as the sum of the square of all contributing wake deficits. We implemented the model in a Matlab script. This allows us to compute wake deficits at any given point. The wake model can be compared to satellite derived wind maps which contains information over a large area. We use  $k_w = 0.03$  for the wake computations.

The Weather Research and Forecasting (WRF) mesoscale model [10] is also used for wake modelling. The advantage of WRF is that the dynamic synoptic flow is considered. The computational cost is much higher than that for the PARK model though.

Mesoscale models have been developed to simulate the atmosphere flow over areas on the order of hundreds of kilometers. Due to their low horizontal resolution unresolved processes, such as turbulence and turbine induced wakes have to be parametrized. In common wind farm parametrisations [11–16] the local turbine interaction is not accounted for, instead the wind speed reduction within the wind farm is obtained from the interaction between the turbine containing grid-cells. The Explicit Wake Parametrisation (EWP) is used for the parametrization of wind farms [16]. In this approach a grid-cell averaged deceleration is applied, which accounts for the unresolved wake expansion with the turbine containing grid-cell. Turbulence Kinetic Energy (TKE) is provided by the Planetary Boundary Layer (PBL) scheme from a changed vertical shear in horizontal velocity in the wake. The EWP scheme is independent of the PBL scheme, although, a second order scheme is recommended.

We use WRF V3.4 with the selected mesoscale model physics parametrizations: PBL [17] (MYNN 2.5), convection [18] (Domain I and II), micro-physics [19], long-wave radiation [20], shortwave radiation [21], land-surface [22] and Nudging of U and V in the outer domain (outside PBL). The number of grid cells in the innermost domain were 427 times 304 in the  $x$  and  $y$  direction, with a 2 km grid-spacing. We used [16] for the wind farm parametrization.



The model outer domain is driven by ERA-Interim reanalysis data [23] and two nests are inside. The horizontal resolution for the three domains is 18 km, 6 km and 2 km, respectively. The inner nest is run twice, without and with the wind farm parametrization. The number of vertical layers is set to 60. The second mass level is at around 12 m above sea level and it is used for the comparison to the satellite images.

### 3. Case Study Based on RADARSAT-2

The case study is based on the RADARSAT-2 scene from 30th April 2013 at 17:41 UTC (selected from around 30 images with visible wakes). Figure 1 shows the backscatter intensity map. The wind is from the northeast and the map shows elongated long dark areas downwind of most of the wind farms. These are the wind farm wakes. The approximate extent of the individual wind farm wakes is outlined in the image. The longest is at Belwind around 55 km long while at Thornton Bank it is 45 km, London Array 15 km and Thanet 14 km. At Kentish Flat the wind farm wake is only 10 km long but it is probably passing over the coast and inland in the UK. This cannot be mapped from SAR. It should be noticed that all wakes are very straight and with similar direction. In the intensity map the wind turbines can be seen as small regularly spaced white dots while numerous ships can be noted in irregular spatial pattern. Some large ships show higher backscatter than the turbines.

The retrieved wind speed map is shown in Figure 2a. The wind speed in the northern part of the map is slightly lower than in the southern part. Yet the synoptic flow appears to be fairly homogenous across the entire area. Coastal speed up is seen particular near the UK and Belgium coastlines. The wind speed varies around  $8.5\text{--}9.5\text{ m}\cdot\text{s}^{-1}$  in areas not affected by wind farms while the wind farm wake regions show lower wind speed around  $7\text{--}8\text{ m}\cdot\text{s}^{-1}$  dependent upon location. The wake at London Array is very wide and it appears to influence Kentish Flat at this time. The wake at London Array has a large wake deficit with much lower wind speeds in the wake than in the upwind free stream region. Wake meandering is not pronounced.

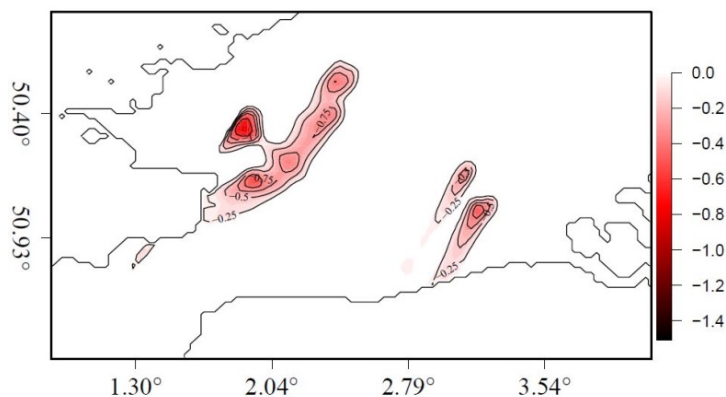
The case illustrates a rather unique situation. Firstly because we observe wakes in the satellite image for all wind farms distributed in a large area of the North Sea (all farms in the area show clear speed deficits). Secondly the wind speed and wind the direction do not seem to largely change over such an extended area. Therefore we are able to simulate with the PARK wake model all wind farms at the same time (assuming the same background inflow conditions for all of them). The background wind speed is about  $9\text{ m}\cdot\text{s}^{-1}$  and direction  $40^\circ$ . We use these two values at 70 m as inflow conditions for the wake modeling.

Figure 2a shows the SAR wind retrieval at 10 m, where most of the variability seems to come from the wake deficits downstream the wind farms, and the wake model results at 70 m in Figure 2b. In this case, we do not extrapolate the satellite background conditions up to 70 m or extrapolate downwards the model results to 10 m as we assume the same wind speed at around hub height when performing the wake simulations. The comparison is only qualitative.

Interestingly, the speed deficits seem to be rather well reproduced by the wake model, extending in most cases nearly as long as the wakes observed in the SAR image.

The WRF wake model with the EWP wind farm scheme is also used for simulation. We include only London Array, Greater Gabbard, Thanet, Belwind1 and Thornton Bank which are the largest wind farms.

The domain is rotated around  $10^\circ$  at the wind farm location. The simulation is from the 24 April to 1 May 2013. The velocity deficit at 10 m at 30 April 2013 at 18:00 UTC is shown in Figure 3. We have chosen to plot the velocity deficit since due to the gradients in the background velocity the wake is not visible in the velocity field from the wind farm simulation.



**Figure 3.** WRF wake model results on velocity deficit in  $\text{m}\cdot\text{s}^{-1}$  at 10 m AMSL at 30 April 2013 at 18:00 UTC at the wind farms London Array, Greater Gabbard, Thanet, Belwind 1 and Thornton Bank.

The WRF modelled wakes at the UK wind farms are oriented slightly more towards the eastern direction than the satellite wakes. The orientations differ by around  $10^\circ$ . For the Belgian wind farms we find that the wakes are well aligned in the SAR and WRF results. Regarding the wake extension behind the wind farms we find for the London Array short wakes both in SAR and WRF while the wakes at the Thanet and Greater Gabbard wind farms are considerably longer both in SAR and WRF. However WRF shows even longer wakes than SAR for Greater Gabbard and Thanet. The extension of wakes at the Belgian wind farms compare well in SAR and WRF.

From WRF it is found that the synoptic conditions two hours before 18:00 UTC show intensified pressure gradients, leading to increased wind speeds near the English coast from  $4 \text{ m}\cdot\text{s}^{-1}$  to higher winds in the order of  $10 \text{ m}\cdot\text{s}^{-1}$ . The Greater Gabbard and Thanet wind farms experienced high wind speeds for two hours at 18:00 UTC. The wind speeds started to increase at the London Array only shortly before 18:00 UTC. It might be that the increasing model wind speeds are for some hours out of phase, which would explain the longer wakes behind Greater Gabbard and Thanet wind farms in WRF compared to SAR.

In summary, the wind farm wakes from several wind farms are visually compared between SAR and WRF simulations of the velocity deficit obtained without wind farm and with wind farms using the EWP scheme. The wind farm wake directions and extension of wake are found to compare well despite that mesoscale features, such as that resulting from unsteady flow conditions, are noted in the wind farm wakes in the WRF simulation. We cannot expect the WRF simulations to match the observed velocity and wind direction in SAR satellite data perfectly. The PARK model results do not include unsteady flow but even so the PARK model results have overall good agreement to SAR. This can in part be attributed to the rather unique atmospheric conditions at the time of this SAR acquisition. The results for single events only can be used qualitatively. For a quantitative comparison statistics over longer periods are needed.

#### 4. Wind Farm Wake Climatology Geo-Located Wind Maps

The case in Section 3 was selected based on clear visual observation of wind farm wakes at several wind farms within one satellite SAR image. However, we would like to study the behavior of the wind farm wake in a climatological fashion and investigate whether this can be performed using our Envisat ASAR WSM data set. We select to study the Horns Rev 1 and 2 wind farms for which we have 356 SAR scenes in total for the period of dual wind farm operation from September 2009 to the termination of the Envisat mission in March 2012.

As the wake behavior is highly dependent on the inflow wind conditions, in particular the wind direction, we perform the study for 12 directional sectors based on the ECMWF model wind direction used to retrieve the SAR winds. The SAR scenes are first binned according to the wind directions extracted for a single point near the two wind farms. The data set is then filtered such that only scenes with wind speeds in the range  $4\text{--}14\text{ m}\cdot\text{s}^{-1}$  at the same point are included (total of 241). This is the range where wind farm wakes are expected to be most detectable. At lower wind speeds, the turbines are not operating and at higher wind speeds, wind penetration through the wind farms is expected. For each directional bin, we extract the inflow conditions from a point upstream of the wind farms for every SAR scene in the bin. The reference points are located on two circles circumscribing the wind farms Horns Rev 1 and Horns Rev 2 with radii of 7.5 km and 10 km, respectively, as shown in Figure 4. To get representative inflow conditions, the satellite winds are extracted within a radius of 10 km for Horns Rev 2 and a radius of 7.5 km for Horns Rev 1 wind farm.

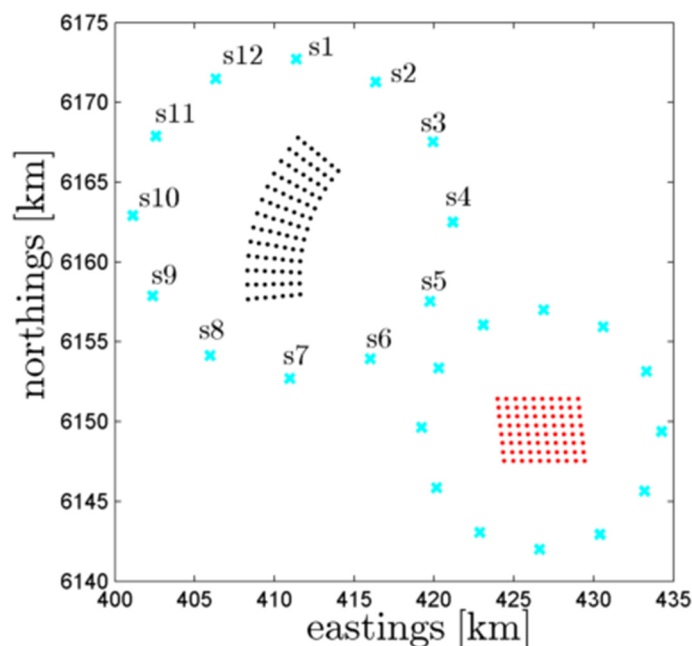


**Figure 4.** Horns Rev 1 and 2 wind farms in red and black markers, respectively. The locations of the points where the inflow conditions are extracted per sector (cyan markers) is also illustrated.

We perform simulations using the modified PARK model at all positions on the satellite grid and for all the inflow conditions per sector. The point around the wind farms where we extract the inflow conditions is selected based on the sector analyzed, e.g., we use the point north of Horns Rev 2 when

performing simulations for Sector 1. In the following subsections we perform qualitative comparisons of the 10 m wind speed SAR retrievals with the results of the wake model per sector at the same height. Both results (wind speed maps) show the average wind speed per sector. We choose to show results for Sector 2 and 3 in Figure 5 because the coastal wind speed gradient and wind farm wakes can be seen in these results even though relatively few data are available. Table 3 shows the number of samples per sector. The inflow wind speed for Sector 2 and Sector 3 is  $8.52$  and  $8.25$   $\text{m}\cdot\text{s}^{-1}$  in average with a standard deviation of  $3.50$  and  $2.55$   $\text{m}\cdot\text{s}^{-1}$ , respectively (these are the values at 70 m height). This means that simulations are performed for a rather wide range of wind speeds. These two examples have several overlapping images and several features can be noted such as the coastal wind speed gradient and wind farm wake.

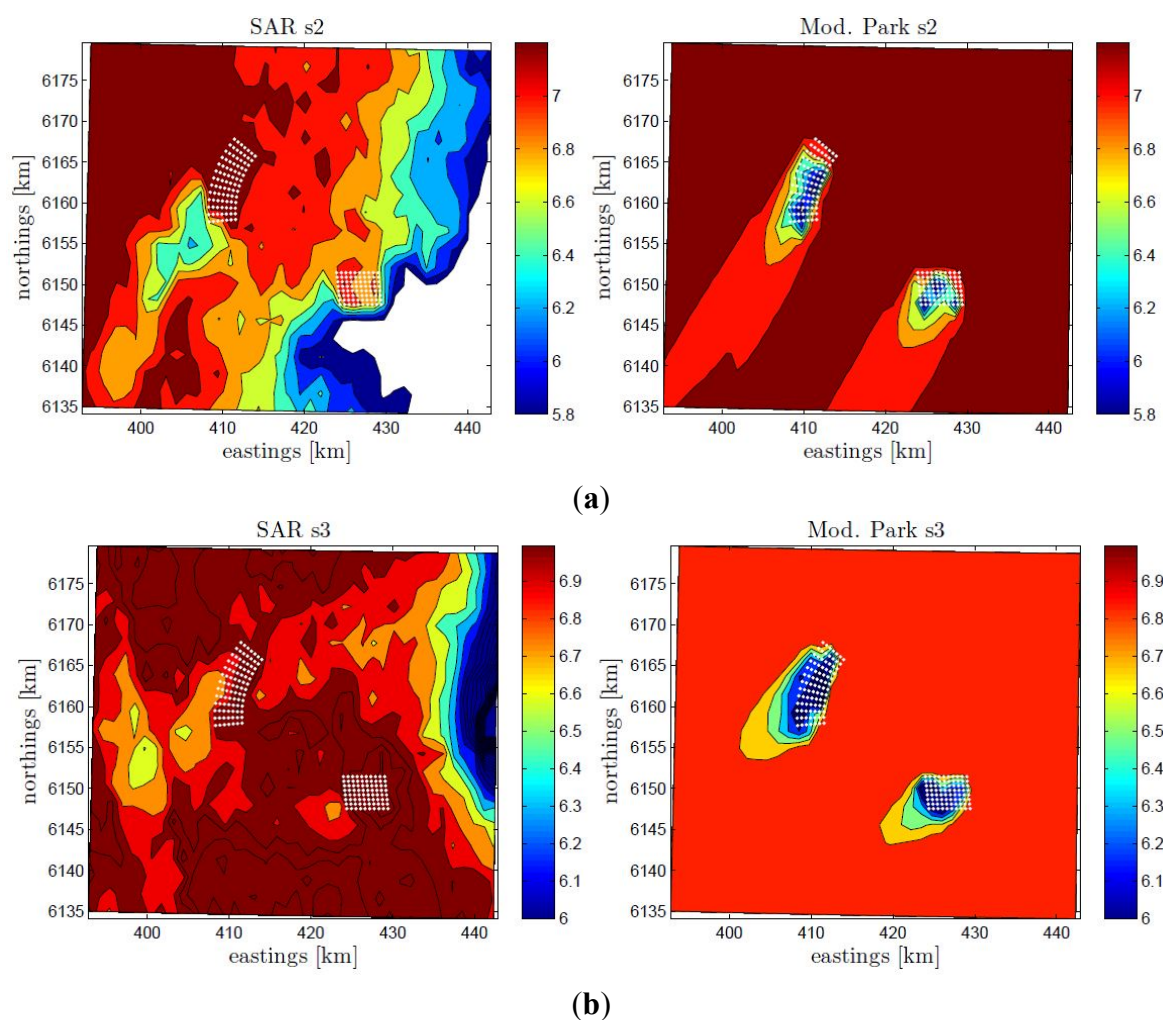


**Figure 5.** Average wind speed based on satellite SAR (left) and modified PARG wake model results (right) at 10 m height for the Horns Rev wind farm area for winds from Sector 2 (a) and Sector 3 (b). The color bar indicates wind speed in  $\text{m}\cdot\text{s}^{-1}$ .

**Table 3.** Number of Envisat ASAR samples available per wind directional bin at Horns Rev.

Sector	1	2	3	4	5	6	7	8	9	10	11	12	Total
Samples	13	7	12	16	24	21	22	28	22	30	20	26	241

For Sector 2 there are seven available SAR images for the analysis and the average wind speed is  $7.2 \text{ m}\cdot\text{s}^{-1}$ . It is surprising we do not observe wakes from the Horns Rev 1 wind farm (Figure 5a). This might be simply because of the high horizontal wind speed gradient approaching the coast, which is located east of Horns Rev 1. There is a clear wake spreading towards the southwest direction of the Horns Rev 2 wind farm. The PARK model results show clear wakes spreading southwest of both wind farms.

For Sector 3 twelve SAR images are available for the analysis (west of Horns Rev 2 the number is reduced to 10) with an average wind speed of  $7.0 \text{ m}\cdot\text{s}^{-1}$ . This case shows agreement in terms of the location of the areas where wakes are observed in both the SAR and the PARK wake model at both wind farms (Figure 5b).

The number of samples per sector varies from 7 to 30 within the 12 sectors. The overall agreement between SAR and the wake model is variable. For some sectors (1 and 7) the bathymetry effect at Horns Rev appears to be particularly strong as previously noted by [1]. This results in the lack of wake effects in the mean wind speed maps from SAR due to the interaction of bathymetry and currents, which sometimes leaves a detectable “imprint” at the sea surface. This effect is most visible when winds blow directly from the north or south at Horns Rev (not shown here).

Another reason for the difficulties to systematically observe wakes of offshore wind farms from satellite-derived wind products are inhomogeneous flow. Although the ocean surface is rather homogenous, e.g., when compared to the land surface, the effects of the horizontal wind variability diminish those of the wakes. In the particular case of the Horns Rev area, there is a systematic wind speed gradient near the coast also obstructing the observation of wakes, particularly for easterly and westerly winds. These effects are not taken into account in the PARK modeling. The coastal gradient in wind speed is noticeable in the SAR images in Figure 5.

Finally it can be noted that the distribution of wind maps into direction sectors is performed with some uncertainty. The model wind directions used to drive the SAR wind speed retrieval are not always accurate. The accuracy of the wind direction input could be improved through implementation of higher-resolution regional model simulations, e.g., from WRF. Another option is to detect the wind direction directly from wake signatures whenever they are visible in the images. The distribution of satellite scenes into the 12 sectors is based on information extracted at a single point. Local turning of the wind is possible but not accounted for in the analysis. Each directional bin is  $30^\circ$  wide thus the peak wake directions are expected to vary within this and it will diffuse the observed aggregated wake features. Due to the nature of the SAR images (specifically its number) and due to other phenomena causing spatial variability in the wind speed (like coastal gradients and mesoscale phenomena), it seems not suitable to perform the SAR wake analysis per sectors this wide.

## 5. Wind Farm Wake Climatology Based on Rotation of Wind Maps

In this section a new approach to analyze SAR-derived wind farm wakes in a climatological way is presented. The method aligns (rotates) all SAR wind field samples such that the wind farm wakes are overlapping before the wake deficit is calculated. This increases the number of samples considerably compared to the method presented in Section 3. Furthermore the  $30^\circ$  wind direction bins used previously give diffuse results whereas in the new method wind directions alignment at  $1^\circ$  resolution is used.



The new method is based on extracting wind speeds along points inscribed by circles centered on the wind farm under analysis. While the method was developed for analysis of wakes in SAR scenes, here it is also applied to the WRF simulations as a way to validate the mesoscale simulated wakes.

### 5.1. Description of the Method

For each SAR scene (or WRF simulated wind field) the wind speeds as a function of compass direction  $\theta$  are extracted along 3 concentric circles centered on the wind farm. The radii depend on the wind farm in question, and are given in Table 3.

Figure 6 gives an example of the circles centered on the Horns Rev 2 wind farm. The wind fields are based on SAR data (1 km). It can be difficult to determine a wake by eye. For each SAR scene the wind speeds along these 3 circles are extracted and stored as  $U_i(\theta_j)$ , where  $U_i$  is the wind speed for circle  $i$  where  $i = 1, 2, 3$  and  $\theta_j$  is the compass direction relative to the center of the wind farm.  $\theta_j$  steps through values from 0 to 359° with a 1 degree increment. The number of scenes used for the analysis depends on the wind farm under examination. The number is given in Table 4. The WRF model is run for all SAR scenes from Horns Rev 1 and 2, and results are extracted in a similar way from the WRF simulation results as for the SAR wind fields. The SAR results are valid at 10 m AMSL while WRF model results are available at 14 m AMSL.

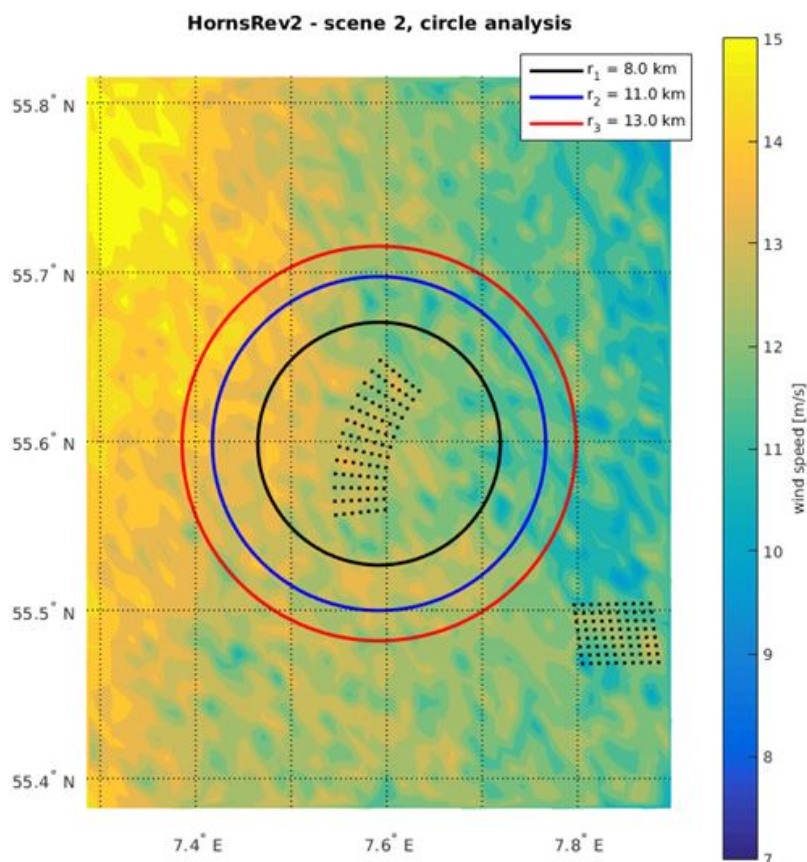


**Figure 6.** Example of the circles centered on Horn Rev 2 wind farm. The radii are 8, 11 and 3 km.

**Table 4.** The radii of the three concentric circles for the different wind farms and the number of Envisat ASAR scenes used for the analysis.

Wind Farm	$r_1$ (km)	$r_2$ (km)	$r_3$ (km)	$N_{scenes}$
Alpha ventus	5	10	15	245
Belwind1	6	11	15	97
Gunfleet Sands 1 + 2	4	5	6	153
Horns Rev 1	6	10	13	835
Horns Rev 2	8	12	15	303
Thanet	7	9	11	128

First the sum of wind speeds is calculated:

$$S_i^N(\theta_j) = \frac{1}{N_{scene}} \sum_{k=1}^{N_{scene}} (U_i(\theta_j))_k \quad (2)$$

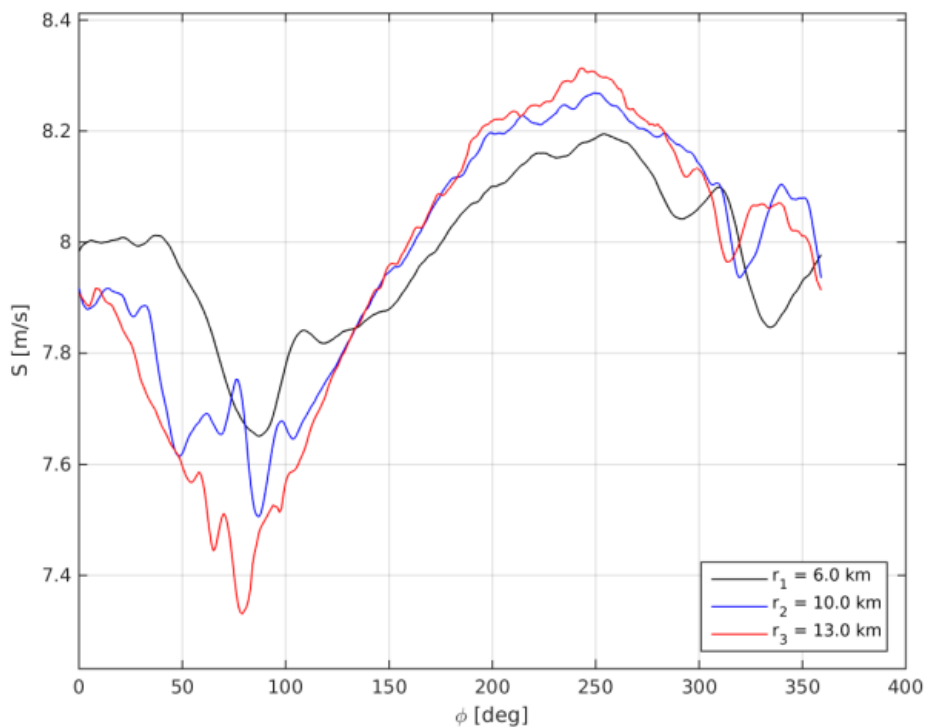
where  $k$  is the scene number, and  $N_{scene}$  is the total number of scenes. Figure 7a shows  $S^N$  plotted against  $\theta$ , for the Horns Rev 1 wind farm. We see from this plot how the mean wind speed depends on  $\theta$ . This can be explained in terms of the gradient of the mean wind in the vicinity of the coastline. We call this the coastal gradient. Similar results of  $S^N$  based on WRF are shown in Figure 7b. The coastal gradient in wind speed at Horns Rev 1 shows lowest values around  $80^\circ$ – $110^\circ$  (east), where the inscribed circles are closest to the coastline, and highest around  $250^\circ$  (west), where the inscribed circles are furthest from the coastline both in SAR and WRF. SAR shows a direction closer to  $80^\circ$  while WRF shows a direction closer to  $110^\circ$ . It is expected that there is an east-west gradient at Horns Rev as reported in [24]. For the eastern sector SAR shows higher wind speed values at the inner radius (6 km) and progressively lower values at outer radii (10 and 13 km) (nearer to the coastline). For the western sector SAR shows slightly higher wind speed at outer radii (further from the coastline).

WRF shows a similar pattern as SAR for the western sector but shows a reverse order in the wind speed at the eastern sector at different radii. This most likely is due to the simulated wake effects of Horns Rev 2 influencing the results at the 13 km radius around  $260^\circ$ – $350^\circ$ . This is supported by examining the results from using WRF without simulating the wind farms, shown in Figure 8. In this plot a very much cleaner signature of the coastal gradient is seen. The next step is to rotate the direction frame of reference for each SAR scene by using each scene's reported wind direction,  $\theta_k$ , to give a new direction reference,  $\varphi$ . In the new direction reference frame for each scene  $\varphi = 0^\circ$  is aligned in the upwind direction and thus one may expect that the wake direction is in the region of  $\varphi = 180^\circ$ . Now we can determine the wind speeds on the inscribed circles as a function of  $\varphi_j$  instead of  $\theta_j$  by using:

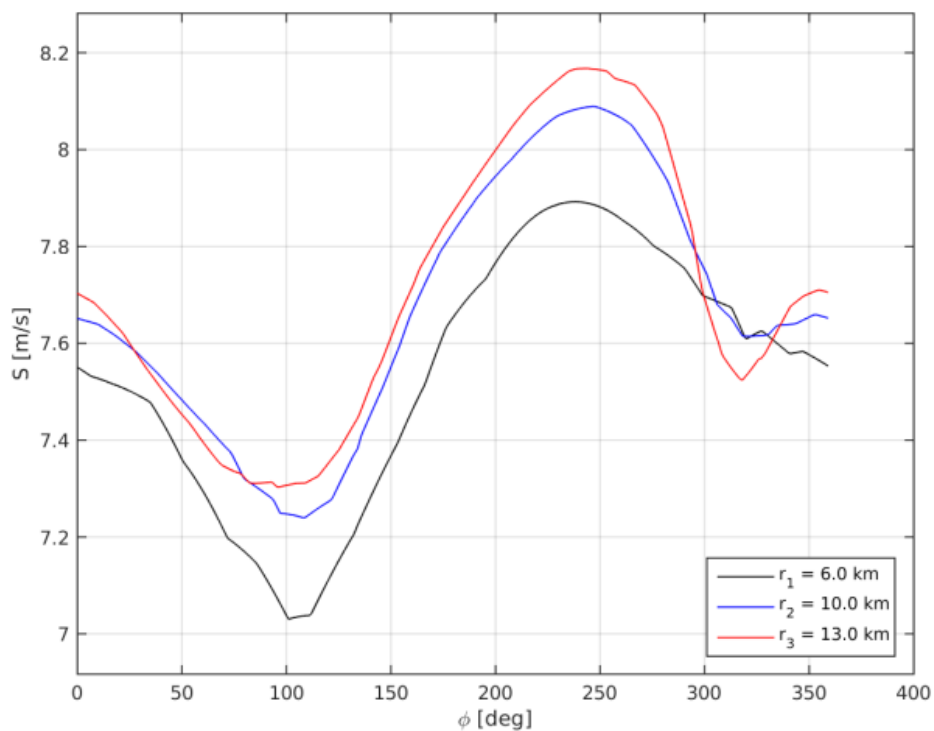
$$\varphi_j = \theta_j - \theta_k \quad (3)$$

The sum of wind speeds for all scenes is now calculated with respect to the new direction frame, *i.e.*:

$$S_i^R(\varphi_j) = \frac{1}{N_{scene}} \sum_{k=1}^{N_{scene}} (U_i(\varphi_j))_k \quad (4)$$



(a)



(b)

**Figure 7.** Horns Rev 1 wind speed summations without rotation (mean wind speed gradient) (*S*) based on SAR (a) and WRF (b).

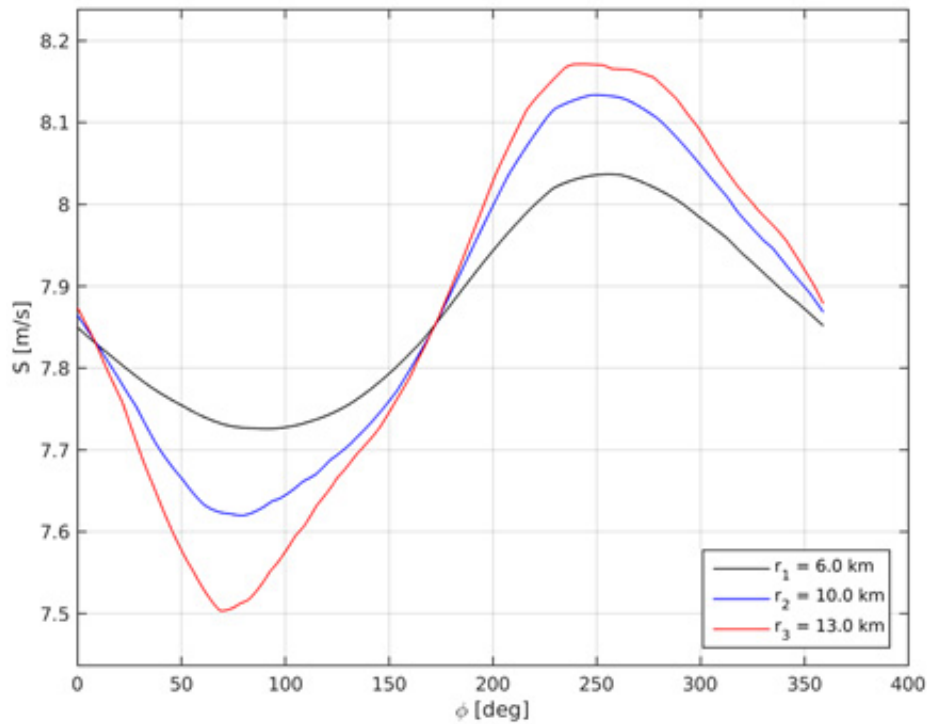


**Figure 8.** Horns Rev 1 wind speed summations without rotation ( $S$ ) based on WRF without wind farms, so showing only the coastal wind speed gradient.

Figure 9a shows  $S^R$  plotted against  $\phi$ , for the Horns Rev 1 wind farm. The corresponding results of  $S^R$  based on WRF simulations are shown in Figure 9b. Please note that the differences between the top and bottom panels are due to the individual rotation of each scene prior to averaging and not the result of a single rotation by one angle. The similarity in form between SAR and WRF for the rotated maps ( $S_{rot}$ ) is very good with low wind speeds showing at all radii at around  $\phi = 180^\circ$ . The inner radius shows more wake effect than outer radii. The SAR derived results are less smooth than those from WRF because the SAR scenes capture variability at smaller scales, due to the heterogeneity of the wind field, than is modelled by WRF.

To further reveal the wind farm wake from the heterogeneous wind field around the wind farm a method to calculate a wake wind speed deficit is employed. It is based on calculating a local perturbation of the wind speed on each SAR scene based on the side lobe wind speeds. The side lobe wind speeds are used at the directions  $\phi + \Delta\phi_i$  and  $\phi - \Delta\phi_i$ . For the smallest radius  $\Delta\phi_1 = 90^\circ$ , this means that the side lobe wind speed is from the left and right of the wind farm, at a distance of  $r_1$  from the farm center. For the other radii, the side lobes have the same distance,  $r_1$ , from the line aligned with the wind direction and passing through the center of the wind farm, thus:

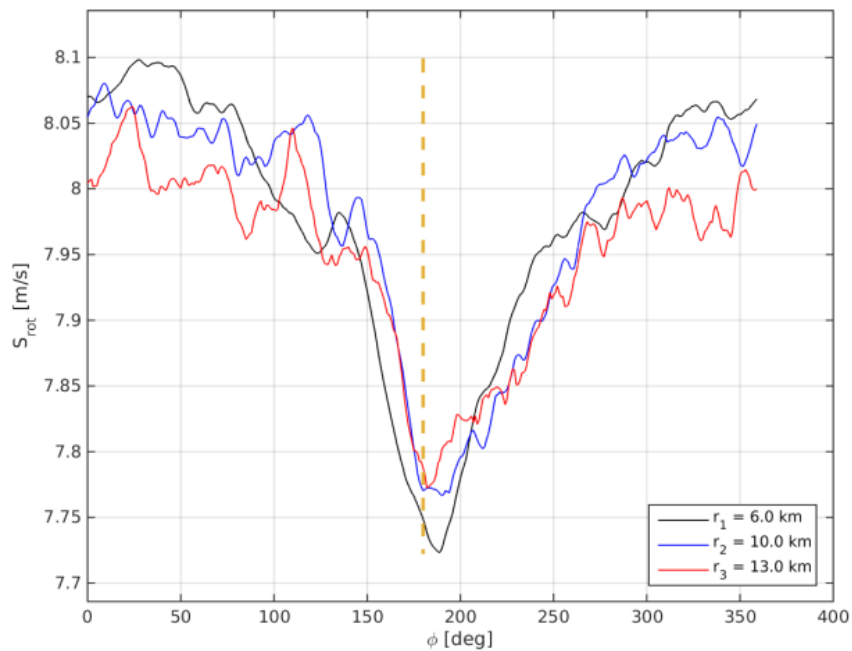
$$\Delta\phi_i = \arcsin\left(\frac{r_1}{r_i}\right) \tag{5}$$

The wake wind speed deficit is defined by:

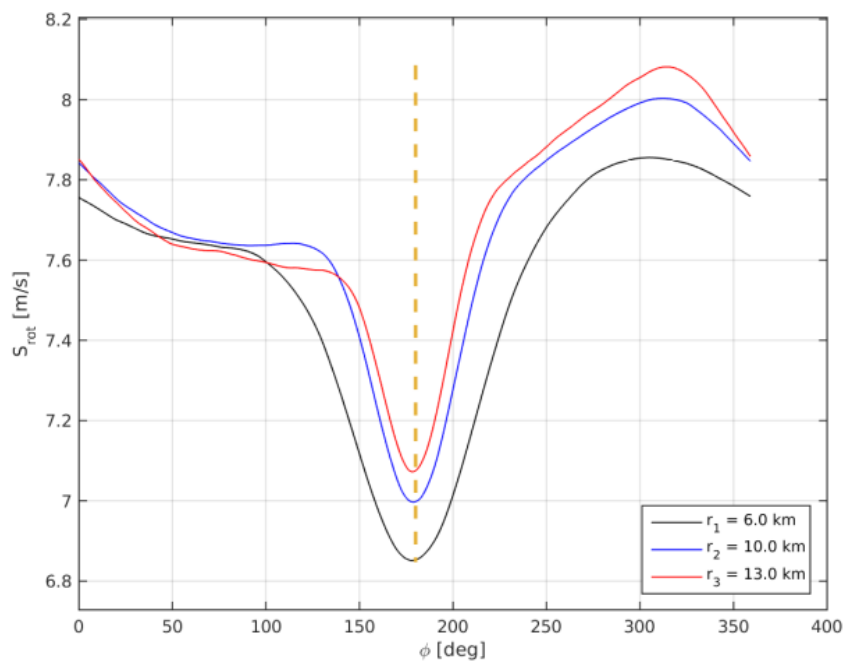
$$U_i^D = U_i(\phi_j) - \frac{1}{2}(U_i(\phi_j + \Delta\phi_i) + U_i(\phi_j - \Delta\phi_i)) \tag{6}$$

and the wake wind speed deficit summation is:

$$S_i^D(\varphi_j) = \frac{1}{N_{scene}} \sum_{k=1}^{N_{scene}} (U_i^D(\varphi_j))_k \tag{7}$$



(a)



(b)

**Figure 9.** Horns Rev 1 wind speed summations with rotation ( $S_{rot}$ ) based on SAR (a) and WRF (b).

Figure 10 shows  $S^D$  plotted *versus*  $\varphi$  for the Horn Rev 1 wind farm for SAR and WRF. In Figure 10 the wake wind speed deficit results based on SAR wind fields and WRF simulations both show the deepest wake at the inner radius and gradual recovery at the outer radii. Both SAR and WRF results show a speed up along the sides of the wake. This shows most clearly at the inner radius but is also noted



at the outer radii. The SAR results on wake deficit compares well to the WRF results at Horns Rev 1, however the magnitude of the SAR derived wake is weaker compared to the WRF wakes. It should be noted that the WRF simulations here are one embodiment of WRF simulations and that broader variability in WRF-generated wakes would be generated by other choices of PBL schemes, vertical resolution and approach for representing the wind farm effect.

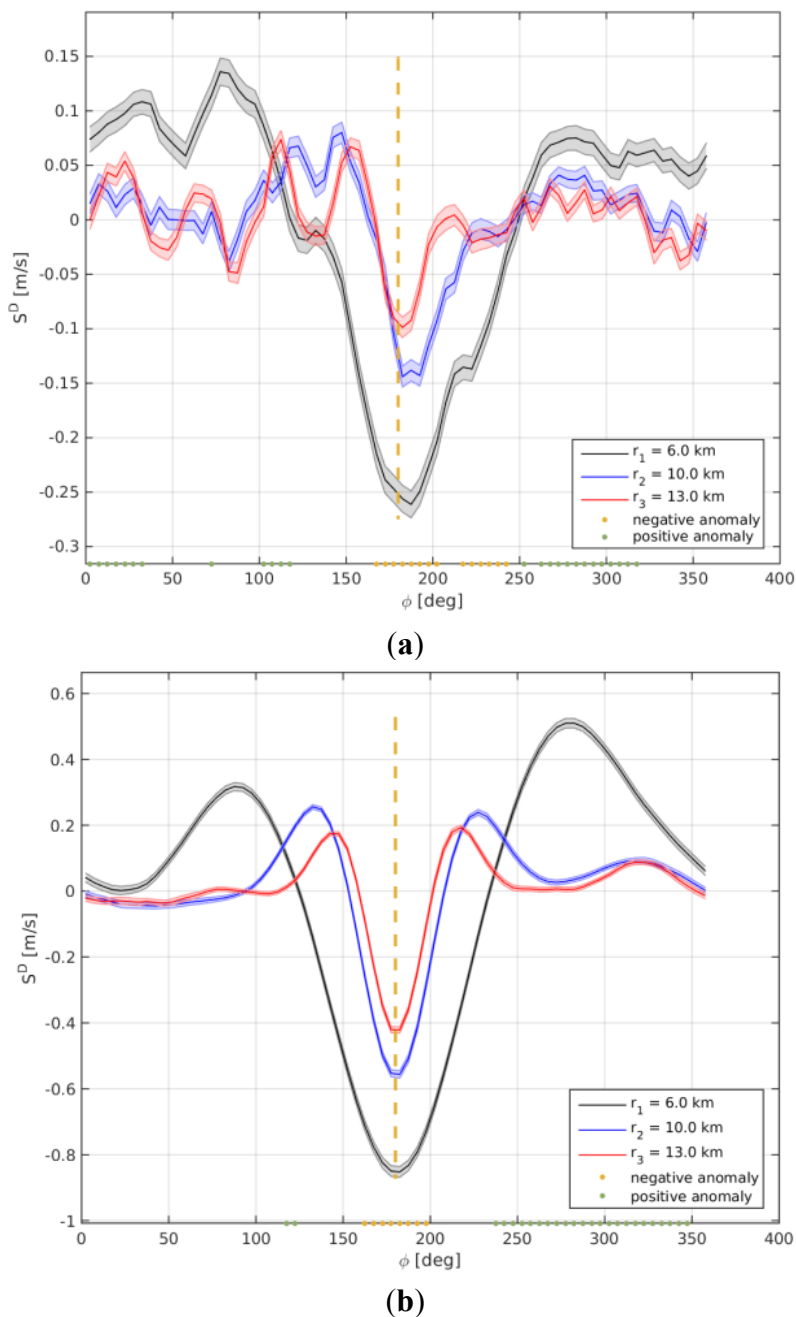
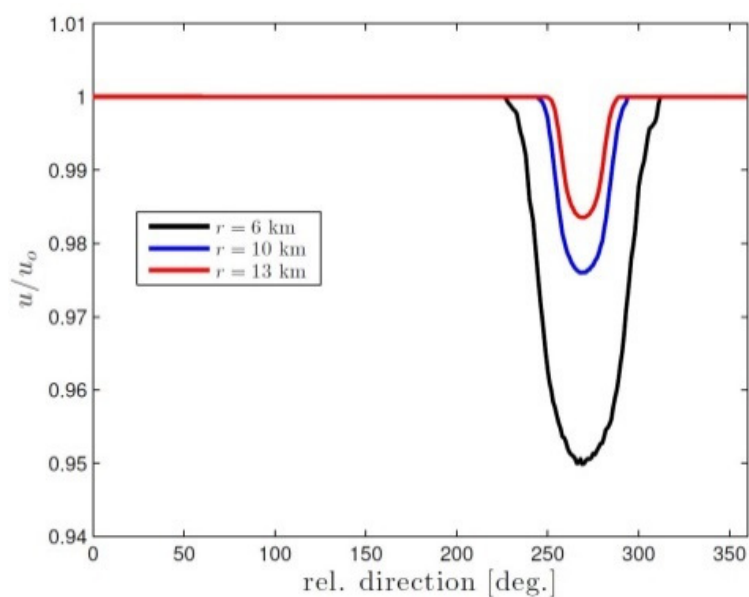


**Figure 10.** Horns Rev 1 wake wind speed deficit ( $S^D$ ) based on SAR (a) and WRF (b). The shaded areas in SAR indicate the standard error.

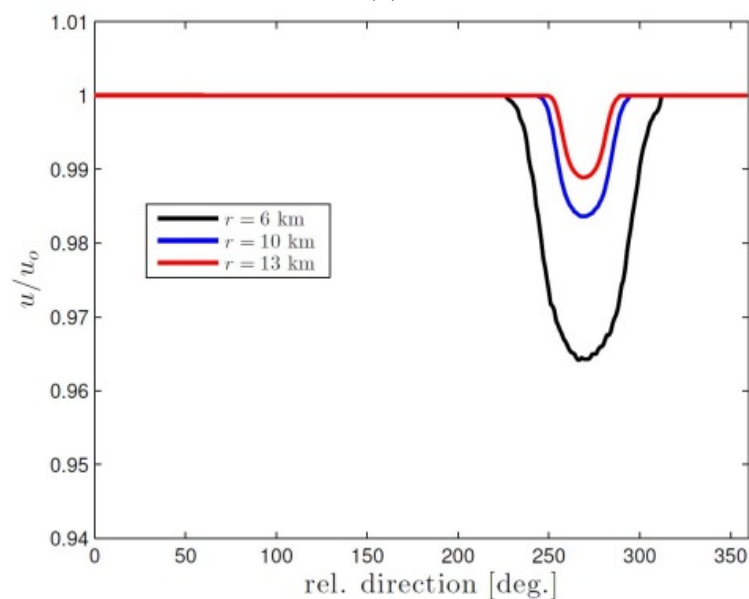
### 5.2. PARK Model Results

The PARK model is used to simulate 855 cases (a few more cases than used above but the results are expected to be comparable) at Horns Rev 1. The SAR wind time series at 10 m is used as input,

the winds are extrapolated to 70 m and the wake is modeled at that height and finally the winds are extrapolated downwards to 10 m again. The extrapolation is done using the logarithmic wind profile assuming a constant roughness length of 0.0002 m. The results are presented at 10 m. Three wake decay coefficients are used. The three wake decay coefficients are: 0.03, 0.04 and 0.05. The wake decay coefficient 0.04 is often used offshore while the lower and higher values are used in case of more stable or unstable cases. The results are rotated and averaged and the results are shown in Figure 11. The coastal gradient is not accounted for in the PARK model results. In case the coastal gradient should be added in the PARK model this could either be from SAR or from WRF, but it has not been attempted in the current study. The results are comparable to the wake wind speed deficit ( $S^D$ ) results.



(a)



(b)

Figure 11. Cont.

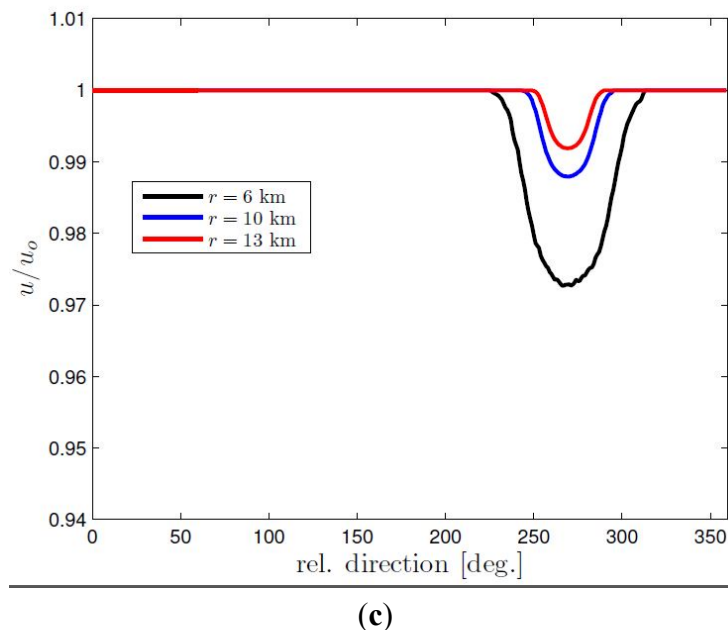


**Figure 11.** Wake results from the modified PARK model at Horns Rev 1 using wake decay coefficients (a) 0.03; (b) 0.04 and (c) 0.05.

Figure 11 shows the systematic variation in wake with deeper wakes at the inner radius and progressively weaker wakes further from the wind farm. The wake decay coefficient of 0.03 gives much deeper wakes than for the higher wake decay coefficients, in particular for the inner radius. The shape of the wake compares well to Figure 10 from SAR and WRF.

### 5.3. Horns Rev 2 Results

Horns Rev 2 is located further offshore than Horns Rev 1 thus similar directional but lower wind speed gradients are expected. The mean wind speed gradient results based on SAR and WRF for Horns Rev 2 are presented in Figure 12a,b. The coastal wind speed gradient observations in SAR at Horns Rev 2 (Figure 12a) show a very peaked and significant minimum around  $110^\circ$  corresponding to the direction of Horns Rev 1. The feature (drop of around  $0.2 \text{ m}\cdot\text{s}^{-1}$ ) is observed at all radii (8, 11 and 13 km) and is most pronounced at the outer radius. This narrow fine-scale feature is only fully observed in SAR. SAR resolves features at smaller spatial scales than the WRF simulations presented here. This minimum value might be related to the wind farm wake from Horns Rev 1. Interestingly WRF shows a broad minimum with a shift in direction between radii from  $100^\circ$  at the 8 km radius to  $110^\circ$  at the 10 km radius and  $120^\circ$  at the 13 km radius (Figure 12b). Thus the WRF simulation may in fact here capture a blend of coastal gradient and wind farm wake from Horns Rev 1. At the western sector SAR shows a peaked maximum around  $250^\circ$  and similar wind speeds at all three radii while WRF shows flatter maximum and slightly higher winds at outer radii.

Figure 12c,d shows the rotated maps ( $S_{\text{rot}}$ ) for Horns Rev 2. For SAR a minimum around  $180^\circ$  at 8 km radius is observed while at 10 km and 13 km the minima are around  $250^\circ$  and  $110^\circ$ , respectively. Only at 8 km do the WRF simulations agree with the SAR observations. The three radii at Horns Rev 2 are each located 2 km further from the wind farm center than the results for Horns Rev 1. This was necessary because the Horns Rev 2 wind farm is larger than the Horns Rev 1 wind farm. This however

means that the wind alignment between inflow conditions and the deepest wind farm wake potentially deviate relatively more at Horns Rev 2 than Horns Rev 1.

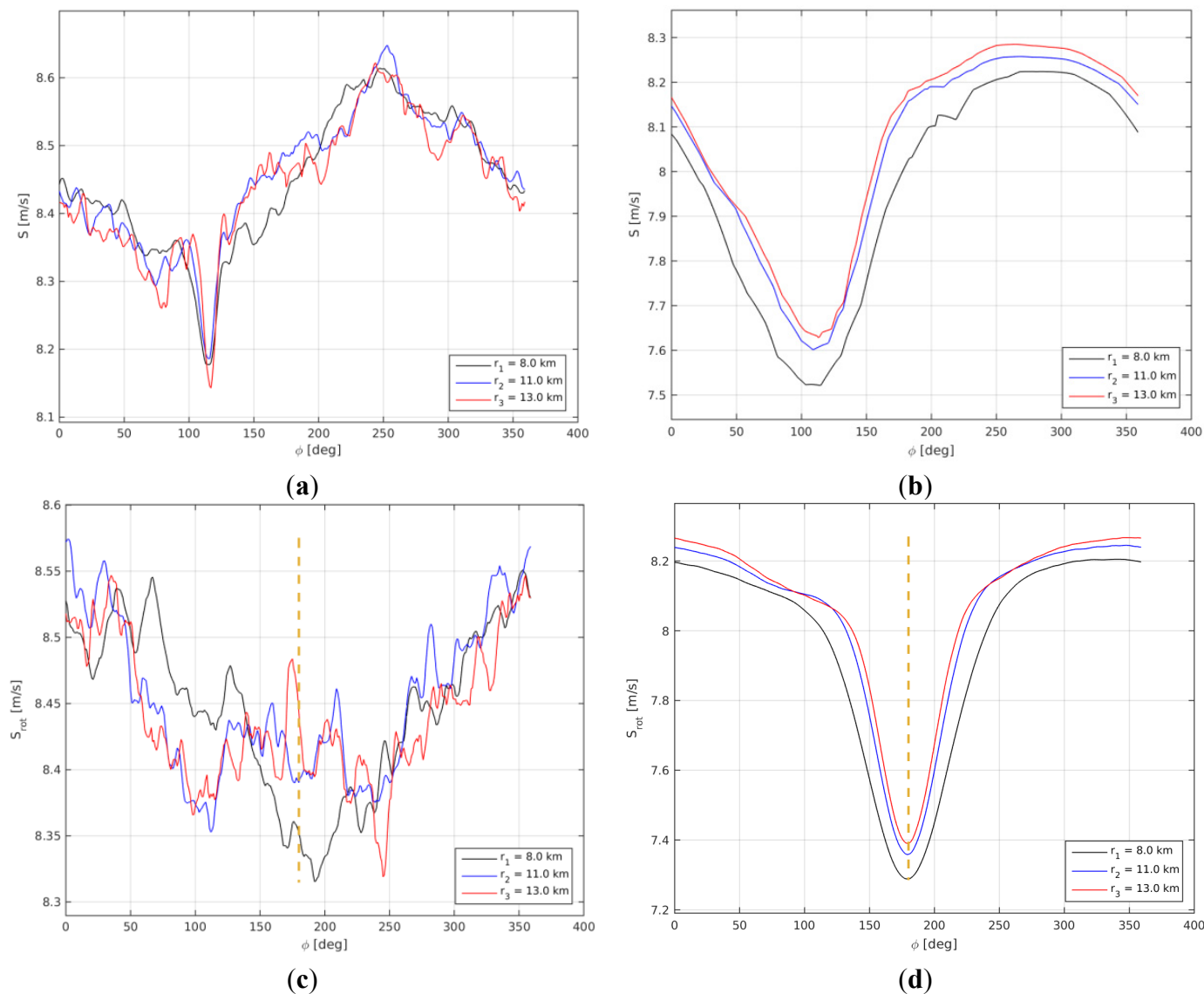


**Figure 12.** Results for Horns Rev 2. (a) wind speed summations without rotation (mean wind speed gradient) ( $S$ ) based on SAR; (b) WRF; (c) wind speed summations with rotation ( $S_{rot}$ ) based on SAR; (d) WRF.

Figure 13 shows the wake wind speed deficit ( $S^D$ ) results from SAR and WRF. The results at the inner radius compare well even though the SAR results show a broader wake than WRF. Speed up in the side lobe winds are noticed both in SAR and WRF at the inner radii and no residual wind speed gradient is noted. At the middle and outer radii WRF shows gradual decrease in the wake winds speed deficit and speed up at the sides while the SAR results are difficult to interpret. In SAR the minimum wake wind speed deficit is not observed around  $180^\circ$  but around  $100^\circ$  and  $250^\circ$ . The analysis appears not to work so well in this case, in part due to the significant minimum around  $110^\circ$  in Figure 12a. This feature may possibly be the wake feature of Horn Rev 1, which acts to contaminate the analysis, as this feature can be as strong as the Horn Rev 2 wake itself.

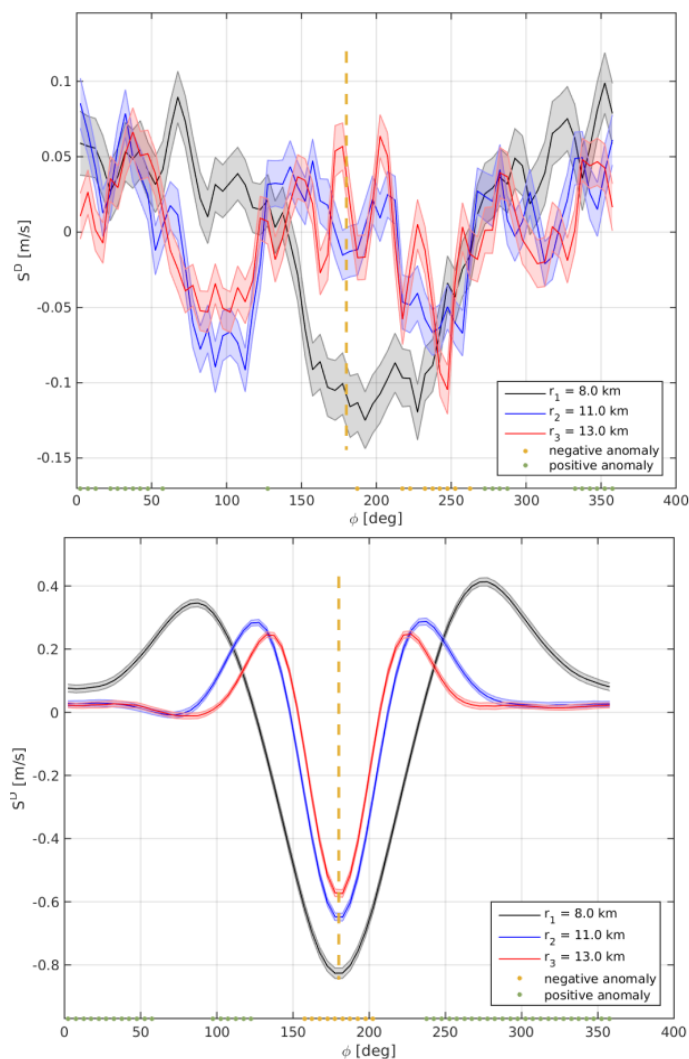


**Figure 13.** Similar to Figure 10 but for Horns Rev 2.

#### 5.4. SAR-Based Results for Six Wind Farms

Based on the available Envisat ASAR wind field archive we find it interesting to compare the observed aggregated wind farm wakes at four other wind farms in the southern North Sea using the new methodology of rotation of the wind maps. The results of the wake wind speed deficit ( $S^D$ ) are shown in Figure 14 together with the results from Horns Rev 1 and Horns Rev 2 already discussed.

It is the results for the average of the three radii (see Table 4) for each wind farm that is shown. Figure 14 shows results for six wind farms. It is noted that Gunfleet Sands 1 + 2 show the deepest wake wind speed deficit. The side lobe speed-up effects are clear. A residual wind speed gradient is not noted. For the wind speed summation ( $S$ ) (not shown) there is a weaker signature of a climatological wind speed gradient across the wind farm compared to other wind farms, this may be because the radii used are smaller.



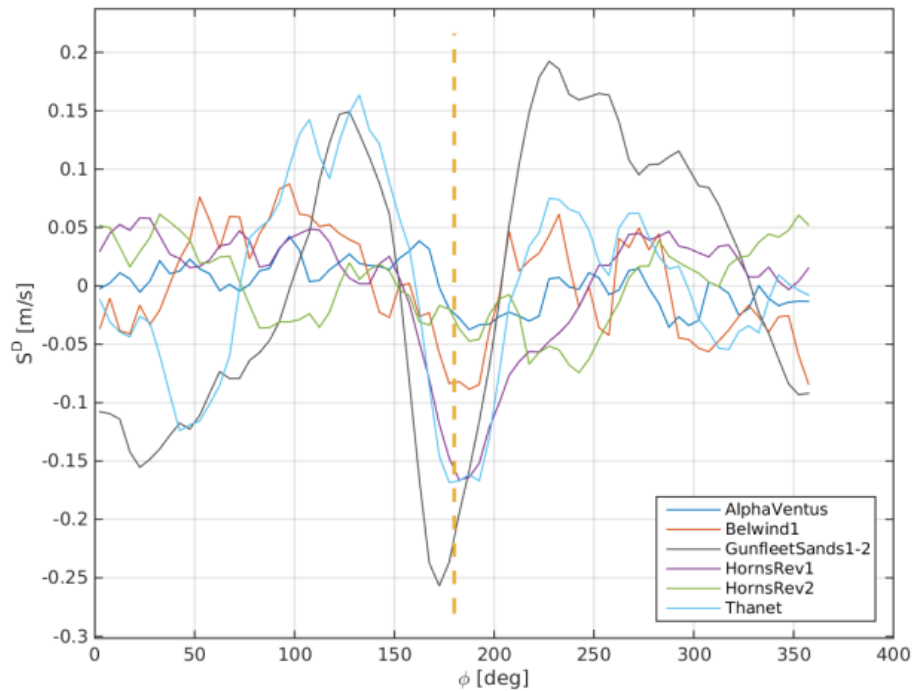


**Figure 14.** SAR-based wind farm wake observed at six wind farms, Alpha ventus, Belwind 1, Gunfleet Sands 1 + 2, Horns Rev 1, Horns Rev 2 and Thanet, showing the wake wind speed deficit ( $S^D$ ).

At the Thanet wind farm, the wake wind speed deficit results show very clear wake at around  $180^\circ$  and side lobe speed-up effects. A residual of the coastal wind speed gradient is noted. There is a feature at  $50^\circ$  with lower winds that would need further investigation.

At the Belwind 1 wind farm the wake wind speed deficit is clear but not as pronounced as for the Gunfleet Sands 1 + 2, Thanet and Horns Rev 1 results. Weak side lobe effects are observed at Belwind 1. A residual of coastal wind speed gradient is not noted in the wake wind speed deficit despite that strong coastal gradient mean wind speed gradient is found in the coastal gradient plot ( $S$ ) (not shown).

Finally, at the Alpha ventus wind farm, the smallest wind farm in terms of installed capacity and area, there is observed wake wind speed deficit at around  $180^\circ$ . The wind farm wake is not as pronounced as for the larger wind farms investigated. This is expected due to the size of the wind farm. The coastal gradient is not observed in the result but is noted in the coastal wind speed gradient ( $S$ ) (not shown).

## 6. Discussion

The very long wind farm wakes observed in the RADARSAT-2 scene have in qualitative terms successfully been modeled both by the PARK and WRF model at several wind farms in the southern North Sea. The comparison is qualitative due the different nature of data. The SAR-based results are near-instantaneous observations of the sea surface while wake model results are time-averaged results with best representation of the conditions at around hub-height. Thus we focus on the apparent wind farm wake direction and the length of the wakes in this comparison instead of the wake deficit at any given location. The SAR image has the advantage of clear visible wake features. Thus the retrieved wind field can be used to evaluate the wake model results in qualitative terms.

We are interested in developing more robust SAR-based wind farm wake data representation for the evaluation of wake models. Therefore the climatology of wind farm wake is necessary. The Envisat ASAR data of wind fields enable us to study the wind farm wake at Horns Rev 1 and 2 with the data set divided into 12 wind directional bins. The results are compared to the PARK model. Occasionally good agreement is found but due to strong coastal wind speed gradients, bathymetry effects and too few samples firm conclusions cannot be drawn.

The new method, in which the wind field maps are rotated, overcomes two of the main issues when trying to isolate the wind farm effect of the wake on the wind fields: the low number of samples and the coastal gradient. The first advantage is that the inflow wind is aligned (rotated) with  $1^\circ$  bins instead of  $30^\circ$  bins. This gives more certainty that the deepest wind farm wake are overlapping in the aggregated results. With the inflow wind speed used to normalize the winds in the wake, the wake are clearly seen but at the same time a residual of the coastal gradient is often noted, e.g., at Horns Rev 1. The clearest wind farm wake results are typically obtained using the side lobe winds for normalization, the wake wind speed deficit method ( $S^D$ ). This is not too surprising as the coastal wind speed gradients at most wind farms are significant and the circles used around the large offshore wind farms need to be at some distance. Therefore any inhomogeneity in the flow, most importantly the coastal gradient, but in fact also meandering and other atmospheric features gain importance. Also in [2] the nearby parallel transects winds along the wind farm wake were optimal for normalization, rather than the inflow winds upwind of the wind farm.

The number of samples at Horns Rev 2 is 303 while at Horns Rev 1 it is 835. So the lower number of samples at Horns Rev 2 could be one reason for the lesser clarity in data at this site when compared to Horns Rev 1. Also the influence of the Horns Rev 1 wind farm wake may hinder full interpretation at Horns Rev 2 in particular at radii far from the Horns Rev 2 wind farm. Finally it should be mentioned that the Horns Rev 1 wind farm has a geometric shape (turbine lay-out) more convenient for the proposed new methodology of analysis than that of the Horns Rev 2 wind farm. We assume that all wind turbines are in operation at all times a characteristic which may not be fulfilled.

The SAR-based aggregated wind farm wake data compare well both to the WRF simulations and the PARK model results. It is the first time that assessment of the wind farm wake climatology has been attempted based on SAR (to our knowledge) and the results are promising. The main importance of the establishment of SAR-based wake wind speed aggregated results is for the validation of wind farm wake models in the far-field wake region where other observations are extremely limited. In the future more wind farms will operate offshore thus cluster-scale wind farm wake therefore become an even more important focus area. It is suggested to continue this type of research using new SAR data from the Sentinel-1 mission.

## 7. Conclusions

The case study based on a RADARSAR-2 scene is a unique situation with fairly homogeneous flow across the southern North Sea. The observed wind farm wakes are visible in the SAR scene and thus appealing for demonstration. Both WRF and PARK reproduce the observed very long wind farm wakes convincingly regarding their direction and extent. SAR archive renders possible climatology studies.

The available Envisat ASAR data archive at Horns Rev is the most comprehensive. It has therefore been used for geo-located wind farm wake climatology studies. However the results are only occasionally clear for interpretation due to the limited number of samples per 30° sectors, the coastal wind speed gradient and oceanic bathymetry effects in SAR at Horns Rev.

The key results are based on a new methodology of rotating wind maps. By applying the new methodology to SAR-based wind fields, mesoscale model WRF and microscale model PARK results comparable aggregated wind farm wake results are obtained. The SAR-based findings strongly support the model results at Horns Rev 1. The new methodology increases the number of samples, aligns the wind direction of inflow much more accurately (1° bins) and in most cases but not always overcome the coastal wind gradient. The most convincing results are obtained for the wind wake deficit results in which the side lobe winds are used for normalization.

### Acknowledgments

Support from the European Energy Research Alliance-Design Tools for Offshore wind farm Clusters (EERA DTOC) project FP7-ENERGY-2011-1/n 282797 and satellite images from RADARSAT-2 from Data and Products © MacDonald, Dettewiler and Associates Ltd and Envisat ASAR data from the European Space Agency are acknowledged. We are thankful to the Northern Seas Wind Index Database (NORSEWIND) project for the Envisat ASAR wind field archive processed by Alexis Mouche.

### Author Contributions

Charlotte Bay Hasager coordinated the main theme of this paper and wrote the manuscript. Pauline Vincent and Romain Husson processed the RADARSAT-2 scene, identified the wind farm wakes and retrieved the wind speed. Jake Badger and Alessandro Di Bella developed the new methodology of rotating the wind maps for aggregated wake results and Alessandro Di Bella programmed and applied the methodology on Envisat ASAR wind fields and WRF model results and produced the graphics. Merete Badger prepared the Envisat ASAR wind field archive and extracted all information for the wake research. Alfredo Peña programmed the PARK model in Matlab and produced results and graphics. Patrick Volker set up the WRF model and produced the results used for wake comparison. All authors discussed the research results and commented on the manuscript. All the authors read and approved the final manuscript.

### Conflicts of Interest

The authors declare no conflict of interest.

### References

1. Christiansen, M.B.; Hasager, C.B. Wake effects of large offshore wind farms identified from satellite SAR. *Remote Sens. Environ.* **2005**, *98*, 251–268.
2. Christiansen, M.B.; Hasager, C.B. Using airborne and satellite SAR for wake mapping offshore. *Wind Energy* **2006**, *9*, 437–455.

3. Li, X.; Lehner, S. Observation of TerraSAR-X for Studies on Offshore Wind Turbine Wake in near and Far Fields. *IEEE* **2013**, *5*, 1757–1768.
4. Hasager, C.B.; Vincent, P.; Husson, R.; Mouche, A.; Badger, M.; Peña, A.; Volker, P.; Badger, J.; Di Bella, A.; Palomares, A.; *et al.* Comparing satellite SAR and wind farm wake models. *J. Phys. Conf. Ser.* **2015**, *625*, in press.
5. Hasager, C.B.; Mouche, A.; Badger, M.; Bingöl, F.; Karagali, I.; Driessenaar, T.; Stoffelen, A.; Peña, A.; Longépé, N. Offshore wind climatology based on synergetic use of Envisat ASAR, ASCAT and QuikSCAT. *Remote Sens. Environ.* **2015**, *156*, 247–263.
6. Quilfen, Y.; Chapron, B.; Elfouhaily, T.; Katsaros, K.; Tournadre, J. Observation of tropical cyclones by high-resolution scatterometry. *J. Geophys. Res.* **1998**, *103*, 7767–7786.
7. Katic, I.; Højstrup, J.; Jensen, N.O. A simple model for cluster efficiency. In Proceedings of the European Wind Energy Association Conference & Exhibition, Rome, Italy, 7–9 October 1986.
8. Mortensen, N.G.; Heathfield, D.N.; Myllerup, L.; Landberg, L.; Rathmann, O. *Getting Started with WAsP 9*; Tech. Rep. Risø-I-2571(EN); Risø National Laboratory: Roskilde, Denmark, 2007.
9. Jensen, N.O. *A Note on Wind Generator Interaction*; Tech. Rep. Risø-M-2411(EN); Risø National Laboratory: Roskilde, Denmark, 1983.
10. Skamarock, W.C.; Klemp, J.B.; Dudhia, J.; Gill, D.O.; Barker, D.M.; Duda, M.; Huang, X.Y.; Wang, W.; Powers, J.G. A description of the advanced research WRF version 3. *Tech. Rep.* **2008**, doi:10.5065/D68S4MVH.
11. Adams, A.S.; Keith, D.W. A wind farm parametrization for WRF. Available online: [http://www2.mmm.ucar.edu/wrf/users/workshops/WS2007/abstracts/5-5\\_Adams.pdf](http://www2.mmm.ucar.edu/wrf/users/workshops/WS2007/abstracts/5-5_Adams.pdf) (accessed on 2 June 2015).
12. Baidya Roy, S. Simulating impacts of wind farms on local hydrometeorology. *J. Wind Eng. Ind. Aerodyn.* **2011**, *99*, 491–498.
13. Blahak, U.; Goretzki, B.; Meis, J. A simple parametrisation of drag forces induced by large wind farms for numerical weather prediction models. In Proceedings of the European Wind Energy Conference & Exhibition 2010 (EWEC), Warsaw, Poland, 20–23 April 2010.
14. Jacobson, M.Z.; Archer, C.L. Saturation wind power potential and its implications for wind energy. *Proc. Natl. Acad. Sci. USA* **2012**, *109*, 15679–15684.
15. Fitch, A.; Olson, J.; Lundquist, J.; Dudhia, J.; Gupta, A.; Michalakes, J.; Barstad, I. Local and mesoscale impacts of wind farms as parameterized in a mesoscale NWP model. *Mon. Weather Rev.* **2012**, *140*, 3017–3038.
16. Volker, P.J.H.; Badger, J.; Hahmann, A.H.; Ott, S. The Explicit Wake Parametrisation V1.0: A wind farm parametrisation in the mesoscale model WRF. *GMDD* **2015**, *8*, 3481–3522.
17. Nakanishi, M.; Niino, H. Development of an improved turbulence closure model for the atmospheric boundary layer. *J. Meteorol. Soc. Jpn.* **2009**, *87*, 895–912.
18. Kain, J.S. The Kain-Fritsch convective parameterization: An update. *J. Appl. Meteorol. Climatol.* **2004**, *43*, 170–181.
19. Thompson, G.; Field, P.R.; Rasmussen, M.; Hall, W.D. Explicit forecasts of winter precipitation using an improved bulk micro- physics scheme. Part II: Implementation of a new snow parameterization. *Mon. Weather Rev.* **2008**, *136*, 5095–5115.

20. Mlaver, E.J.; Taubman, S.J.; Brown, P.D.; Iacono, M.J.; Clough, S.A. Radiative transfer for inhomogeneous atmosphere: RRTM, a validated corrected-k model for the long wave. *J. Geophys. Res.* **1997**, *102*, 16663–16682.
21. Dudhia, J. Numerical study of convection observed during the wind monsoon experiment using a mesoscale two-dimensional model. *J. Atmo. Sci.* **1989**, *46*, 3077–3107.
22. Chen, F.; Dudhia, J. Coupling an advanced land surface-hydrology model with the Penn State-NCAR MM5 modeling system. Part I: Model implementation and sensitivity. *Mon. Weather Rev.* **2001**, *129*, 569–585.
23. Uppala, S.M.; Kallberg, P.W.; Simmons, A.J.; Andrae, U.; Bechtold, V.; Fiorino, M.; Gibson, J.K.; Haseler, J.; Hernandez, A.; Kelly, G.A.; *et al.* The ERA-40 re-analysis. *Quart. J. R. Meteorol. Soc.* **2005**, *131*, doi:10.1256/qj.04.176.
24. Barthelmie, R.J.; Badger, J.; Pryor, S.C.; Hasager, C.B.; Christiansen, M.B.; Jørgensen, B.H. Offshore coastal wind speed gradients: Issues for the design and development of large offshore windfarms. *Wind Eng.* **2007**, *31*, 369–382.

© 2015 by the authors; licensee MDPI, Basel, Switzerland. This article is an open access article distributed under the terms and conditions of the Creative Commons Attribution license (<http://creativecommons.org/licenses/by/4.0/>).



# SCIENTIFIC REPORTS



OPEN

## First *in situ* evidence of wakes in the far field behind offshore wind farms

Andreas Platis<sup>1</sup>, Simon K. Siedersleben<sup>2</sup>, Jens Bange<sup>1</sup>, Astrid Lampert<sup>3</sup>, Konrad Bärfuss<sup>3</sup>, Rudolf Hankers<sup>3</sup>, Beatriz Cañadillas<sup>4</sup>, Richard Foreman<sup>4</sup>, Johannes Schulz-Stellenfleth<sup>5</sup>, Bughsin Djath<sup>5</sup>, Thomas Neumann<sup>4</sup> & Stefan Emeis<sup>1</sup> 

Received: 3 May 2017


Accepted: 15 January 2018

Published online: 01 February 2018

More than 12 GW of offshore wind turbines are currently in operation in European waters. To optimise the use of the marine areas, wind farms are typically clustered in units of several hundred turbines. Understanding wakes of wind farms, which is the region of momentum and energy deficit downwind, is important for optimising the wind farm layouts and operation to minimize costs. While in most weather situations (unstable atmospheric stratification), the wakes of wind turbines are only a local effect within the wind farm, satellite imagery reveals wind-farm wakes to be several tens of kilometres in length under certain conditions (stable atmospheric stratification), which is also predicted by numerical models. The first direct *in situ* measurements of the existence and shape of large wind farm wakes by a specially equipped research aircraft in 2016 and 2017 confirm wake lengths of more than tens of kilometres under stable atmospheric conditions, with maximum wind speed deficits of 40%, and enhanced turbulence. These measurements were the first step in a large research project to describe and understand the physics of large offshore wakes using direct measurements, together with the assessment of satellite imagery and models.

Offshore wind farms contribute a considerable fraction to the production of renewable electrical energy. In 2015, 12 GW of offshore wind-energy capacity was successfully installed in Europe<sup>1</sup>. In Germany offshore capacity is expected to reach 7.8 GW by 2020<sup>2</sup>. In Europe, it is expected to reach 73 GW by 2030<sup>3</sup>. A significant number of these new installations will be in the North and Baltic Seas<sup>4,5</sup>.

For an optimal use of the marine areas<sup>6</sup>, wind farms are constructed at favourable locations and in clusters (see Fig. 1). As wind farms are built to extract considerable kinetic energy from the atmosphere, a downwind wake region is formed, characterised by a reduced mean wind speed and, additionally, an enhanced level of turbulence. Most research in this area focuses on wakes behind single turbines, and on the wake interaction from a larger number of turbines within one and the same wind farm<sup>7</sup>. Only some experimental and recent numerical studies consider the wakes of entire wind farms and the impact of wakes on neighbouring downwind wind farms on a larger spatial scale<sup>6,8–22</sup>. The spatial extension of wakes from offshore wind farms is not understood to the extent that the length of a wake may be predicted based on all influencing parameters, such as wind-farm characteristics, atmospheric conditions, and sea state<sup>23</sup>. The most efficient mechanism for wake recovery is the vertical transfer of momentum from higher atmospheric layers downwards<sup>24</sup>, implying atmospheric turbulence to be the decisive parameter governing wake recovery<sup>16,25,26</sup>. Atmospheric turbulence is primarily produced from vertical wind speed gradients (mechanical turbulence) and thermal convection (thermal turbulence). Over rough land surfaces, both mechanical and thermal turbulence are abundant and wakes are usually short (at maximum a few kilometres in length). Much less turbulence is produced at sea, because of the small surface friction and weak temperature gradients, since the response of the ocean to solar radiation is slow. The wakes from wind farms over the sea are, therefore, expected to extend further downwind than over land, especially under a stably stratified flow, which inhibits thermally produced turbulence<sup>5,27</sup>. Since offshore wind farms are located close to the coastline (i.e. a distance less than 100 km to the coast), warm air from land may flow over the colder sea to generate stable stratification, especially during spring and summer. While not yet verified by direct *in situ* measurements, analytical<sup>20,24,28</sup> and numerical flow models<sup>13,22,29,30</sup> predict the length of far wakes up to 100 km in

<sup>1</sup>University of Tuebingen, ZAG, Environmental Physics, 72074, Tuebingen, Germany. <sup>2</sup>Karlsruhe Institute of Technology (KIT), Institute of Meteorology and Climate Research (IMK-IFU), 82467, Garmisch-Partenkirchen, Germany. <sup>3</sup>Technische Universität Braunschweig, Institute of Flight Guidance, 38108, Braunschweig, Germany. <sup>4</sup>UL DEWI - UL International GmbH, 26382, Wilhelmshaven, Germany. <sup>5</sup>Helmholtz-Zentrum Geesthacht (HZG), Institute of Coastal Research, 21502, Geesthacht, Germany. Correspondence and requests for materials should be addressed to A.P. (email: @uni-tuebingen.de)

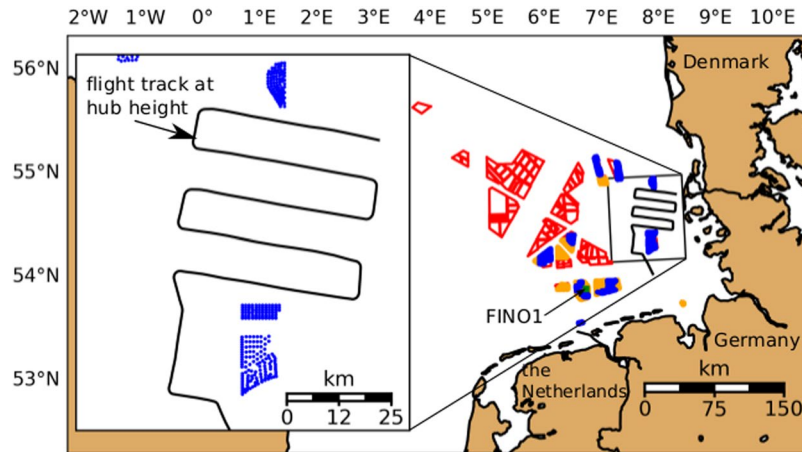


**Figure 1.** Distribution of offshore wind farms in the German Bight. Blue regions are farms currently in operation and orange regions are those wind farms that are under construction or have been approved (as of 2017). Red polygons indicate farms with a submitted application (as of 2016). The plot on the left side indicates the flight track of Flight 7 on September 10, 2016. The blue dots represent the location of the individual wind turbines.

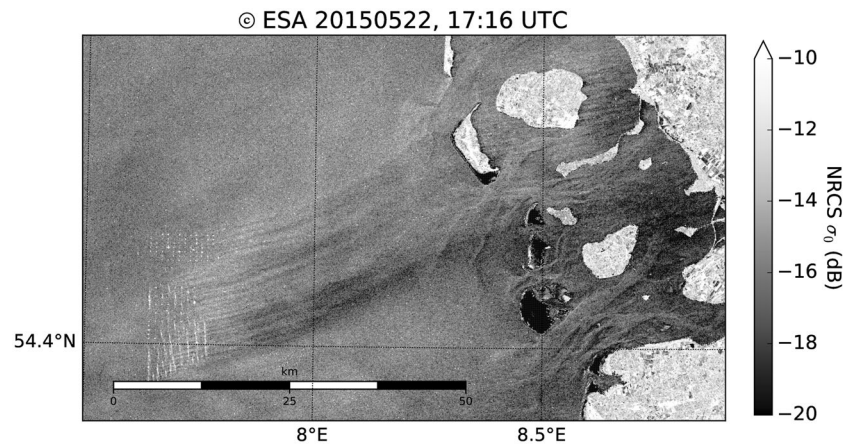


**Figure 2.** Example of a SENTINEL-1A satellite SAR image (Copernicus Sentinel data [2015]) acquired over the North Frisian Coast in the German Bight on May 22, 2015 at 17:16 UTC with westerly winds created by Matplotlib<sup>37</sup>. The white dots on the lower left are radar signatures from windfarm turbines of the three wind parks Amrumbank West, Nordsee Ost and Meerwind Süd/Ost. A wake of reduced wind speed generated by the wind turbines is indicated by darker streaks downwind of the wind farms.

stable stratification. Further, satellite images from synthetic aperture radar (SAR) suggest the existence of wake lengths of several tens of kilometres (Fig. 2) under stable atmospheric conditions, i.e., in the absence of thermally produced turbulence<sup>31,32</sup>. However, such images are rare as the repeat cycle of the satellite is about 11–12 days and lack some observational verification in addition.

Verification of numerical and analytical models and SAR is difficult because *in situ* measurements of offshore wind-farm wakes only exist in the near field, directly behind single turbines and wind farms<sup>22,33,34</sup>. In fact, *in situ* measurements of far-field wakes at hub height on a larger scale behind whole offshore wind farms are not currently available. The German research project WIPAFF (WInd Park Far Field)<sup>35</sup> has performed the first aircraft measurements of the far wakes of wind farm clusters in the North Sea. We summarise the first measurements here and compare them with numerical simulations of the Weather Research and Forecasting model (WRF)<sup>36</sup>.

## Methods

Table 1 gives an overview of all 41 measurement flights performed during the WIPAFF project with the Dornier DO 128 aircraft (Fig. 3) in 2016 and 2017 over the German Bight. The starting points of all flights were Wilhelmshaven, Borkum or Husum airport. The aircraft airspeed during the measurements was  $66 \text{ m s}^{-1}$ .

**Meteorological data.** The wind vector measurement is performed by measuring the flow speed and flow angles at the aircraft nose with a multi-hole flow probe (Figs 3 and 4), as well as the aircraft's motion and orientation in the geodetic coordinate system with an inertial measurement unit (IMU) and the ground speed vector

Flight code	Date (dd. mm. yyyy)	Start Time (UTC)	End Time (UTC)	WS ( $\text{m s}^{-1}$ )	Wind dir ( $^{\circ}$ )	Wake length (km)	Atmospheric stratification
September							
Flight 1	06.09.2016	14:13	17:20	7	190	25	stable
Flight 2	07.09.2016	09:25	13:00	4	210	20	stable
Flight 3	07.09.2016	10:00	14:00	4	190	at least 10	stable
Flight 4	08.09.2016	10:38	14:25	8	120	at least 40	stable
Flight 5	09.09.2016	10:54	14:50	6	240	at least 45	stable
Flight 6	09.09.2016	15:43	19:17	6	250	at least 5	unstable
<b>Flight 7</b>	<b>10.09.2016</b>	<b>07:30</b>	<b>11:30</b>	<b>7</b>	<b>190</b>	<b>45</b>	<b>stable</b>
Flight 8	10.09.2016	12:05	16:00	4	190	at least 20	stable
March–April							
Flight 1	30.03.2017	15:57	19:02	15	240	70	stable
Flight 2	31.03.2017	15:36	19:00	13	180	50	stable
Flight 3	05.04.2017	15:42	16:34	14	310	10	neutral
Flight 4	06.04.2017	15:29	18:22	8	310	at least 10	unstable
Flight 5	09.04.2017	12:36	16:07	7	220	at least 50	stable
Flight 6	09.04.2017	16:32	20:12	4	200	n.a.	stable
Flight 7	11.04.2017	11:25	15:10	8	300	5	unstable
Flight 8	11.04.2017	16:12	20:04	8	240–280	25	neutral
Flight 9	13.04.2017	13:35	17:39	16	290	10	neutral
May–June							
Flight 1	17.05.2017	12:35	16:28	8	110	n.a.	stable
Flight 2	17.05.2017	17:16	21:22	12	120	55	stable
Flight 3	23.05.2017	15:42	16:34	5	250	at least 25	stable
Flight 4	23.05.2017	13:18	17:15	11	310	at least 35	neutral
Flight 5	24.05.2017	07:40	11:34	8	300	n.a.	unstable
Flight 6	24.05.2017	12:13	16:11	9	270	5	unstable
Flight 7	27.05.2017	09:57	13:58	10	150	at least 50	stable
Flight 8	27.05.2017	14:39	18:36	12	140	55	stable
Flight 9	31.05.2017	09:58	13:46	8	290	2	unstable
Flight 10	31.05.2017	15:00	18:50	9	290	0	unstable
Flight 11	01.06.2017	08:55	12:54	6	300	0	unstable
Flight 12	02.06.2017	08:55	12:40	4	170	at least 15	stable
August							
Flight 1	08.08.2017	10:35	14:35	9	80	at least 35	stable
Flight 2	08.08.2017	15:06	19:07	14	80	at least 55	stable
Flight 3	09.08.2017	10:34	14:37	15	210	n.a.	unstable
Flight 4	09.08.2017	15:09	19:05	13	240	n.a.	unstable
Flight 5	10.08.2017	12:49	16:54	5	330	n.a.	unstable
Flight 6	14.08.2017	12:08	16:07	8	150	at least 35	neutral
Flight 7	14.08.2017	16:40	20:31	7	120	50	stable
Flight 8	15.08.2017	09:22	13:15	8	180	30	stable
Flight 9	17.08.2017	08:06	12:10	12	160	40	stable
October							
Flight 1	14.10.2017	14:59	18:40	15	260	n.a.	stable
Flight 2	15.10.2017	09:05	13:09	14	200	n.a.	unstable
Flight 3	15.10.2017	13:52	17:50	13	190	at least 25	stable

**Table 1.** Full list of all measurement flights conducted within the WIPAFF project. Wake length: Assessed wake distance with a wind speed deficit with more than  $0.1 \text{ m s}^{-1}$  compared to the undisturbed flow. Wake lengths measured during a flight pattern that did not cover the full extent of the wake are indicated with “at least”. Some flights focused on the processes above wind farms, hence, no data is available describing the length of the wakes, for such flights the wake length is not available (n. a.). Atmospheric stratification: Estimation of the atmospheric stability by analysing the airborne measured potential temperature vertical profiles between near surface (30 m) and hub height (100 m), which were flown close to the wind farm. WS means wind speed. Bold text marks the investigated flight in this study.



**Figure 3.** The research aircraft Dornier DO-128 of the Technische Universität Braunschweig.

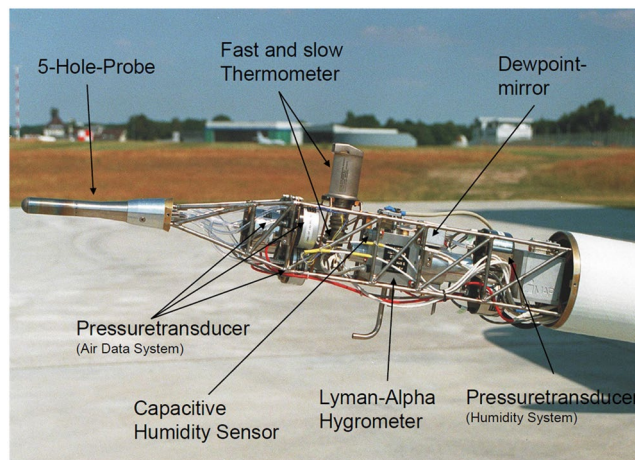


**Figure 4.** Instrumentation of the nose boom of the DO-128.

with a combination of IMU and GPS. More details on the aircraft's sensor system can be found in<sup>38–40</sup>. The total duration of a measurement flight lasted 2 to 4 h, and the main downwind flight pattern lasted about 1 h as shown in Fig. 1. The data acquisition rate is 100 Hz. Given the information of these sensors, the wind speed can be calculated as

$$\mathbf{u} = \mathbf{v}_{\text{gs}} + \mathbf{M}(\mathbf{v}_{\text{tas}} + \boldsymbol{\Omega} \times \mathbf{s}), \quad (1)$$

where  $\mathbf{u}$  is the wind speed vector,  $\mathbf{v}_{\text{gs}}$  is the ground speed vector,  $\mathbf{v}_{\text{tag}}$  is the airspeed vector,  $\mathbf{M}$  is the rotation matrix from the aircraft's fixed coordinate system with respect to the geodetic coordinate system, and  $\mathbf{s}$  is the lever arm between the IMU and the flow probe. The rate of angular rotation vector  $\boldsymbol{\Omega}$  contains the angular velocities of the aircraft fixed coordinate system relative to the geodetic coordinate system, and is among the primary output data of the IMU. A detailed description of the airborne wind speed measurement, including an error estimation, can be found in<sup>33</sup> and<sup>41</sup>.

The turbulent kinetic energy, TKE is calculated by

$$\text{TKE} = \frac{1}{2}(\sigma_u^2 + \sigma_v^2 + \sigma_w^2) \quad (2)$$

with  $\sigma_u$  representing the fluctuations of the wind vector component  $u$ ,  $\sigma_v$  of the component  $v$  and  $\sigma_w$  of  $w$ .

For example,  $\sigma_u$  is computed as

$$\sigma_u^2 = \frac{1}{N-1} \sum_{n=1}^N (u(n) - \bar{u})^2, \quad (3)$$

where  $N$  is the number of data points within the moving data window and  $\bar{u}$  denotes the average of  $u$  within the window. To study the variability of the wind speed field and TKE, it is necessary to determine a suitable horizontal length scale over which to compute the mean wind speed and the fluctuation  $\sigma$  of the wind components within



sub-legs (data windows) along a flight leg. The method is the so-called moving-average method. Given a series of values (the total data point along one flight leg) and a fixed subset size (sub-legs), the first element of the moving average is obtained by taking the average of the initial fixed subset of the time series. The subset is then modified by a forward shift, so that the first value of the series is excluded, while including the next value following the original subset in the series to create a new subset of numbers for averaging. The process is repeated over the entire data series.

However, sub-legs not exceeding the largest eddies in size insufficiently sample the dynamic wind field, causing a systematic error by systematically under- or overestimating the turbulent wind and its standard deviation<sup>42</sup>. This sampling error can be estimated by the expression stated in<sup>43</sup> and<sup>44</sup> representing the absolute systematic statistical uncertainty of the standard deviation  $\sigma_u$  related to a single flight leg on which  $\sigma_u$  was calculated,

$$\Delta\sigma_u = 2 \frac{L_u}{P_l} \cdot \sigma_u, \quad (4)$$

where  $L_u$  is the integral length scale<sup>45</sup> of  $u$  and  $P_l$  the averaging length. The  $L_u$  can be explained as the correlation time, i.e. the persistence or memory of the turbulent flow<sup>46</sup>. The integral time scale  $I_u$  for the wind speed  $u$  is

$$I_u = \int_0^{\tau_1} d\tau \frac{u'(t+\tau) \cdot u'(t)}{u'^2} = \int_0^{\tau_1} d\tau \frac{\text{Cov}_u(\tau)}{\sigma_u^2}, \quad (5)$$

where  $\text{Cov}_u$  represents the covariance of  $u$ , and is calculated by integration from zero lag to the first zero crossing at  $\tau_1$ <sup>47</sup>. The transformation into the  $L_u$  is carried out by multiplication of the  $I_u$  by the aircraft's ground speed, assuming that Taylor's hypothesis of frozen turbulence is valid<sup>45</sup>. For example, the integral length scale for the wind speed  $u$  for Flight 7 is about 90 m. To obtain an error of less than 10% of  $\sigma_u$ , the window length should be at least 1800 m according to Eq. 4. We have defined windows of 2-km width using unweighted means, sequentially shifted through the leg by increments of 0.66 m for a sampling rate of 100 Hz and an aircraft ground speed of 66 m s<sup>-1</sup>. As  $\sigma_u$  is about 0.1 m s<sup>-1</sup> for Flight 7, the error for the measured wind speed  $u$  is 1%.

**Scanning lidar.** We recorded sea surface measurements using a scanning LiDAR-system supported by a navigation grade IMU for registering the measurement points. The effective pulse rate of 22 kHz theoretically provides spatial-point densities of one per metre along, and five per metre perpendicular to, the flight direction for an effective overall measurement rate of about 4.5 kHz. In addition to spatial information, the calibrated echo amplitude is used to compute the reflectance relative to a perpendicular white target at the same distance.

Data have been calculated as the average relative reflectance over 2 s. Fewer measurement points were received within the wake because of the smoother sea surface. In the averaged data set, this resulted in a generally higher reflectance inside the wake caused by more specular reflections.

**Numerical model WRF.** We conducted numerical simulations with the Weather Research and Forecasting Model WRF (Version 3.7.1)<sup>36</sup> using three nested domains with grid size of 15 km, 5 km and 1.7 km. The nesting allows feedback between the nested domains with an update frequency of 20 s for the second domain and 60 s for the first domain. All model domains have 50 vertical levels with a spacing of approximately 40 m at the rotor area. The model top is at 100 hPa (=16 km). The initial and lateral boundary conditions are defined by the European Centre for Medium-Range Weather Forecasts (ECMWF) model operational analysis data at 6-h intervals. The ECMWF data has a grid size of 0.1 degrees (i.e. similar to the grid size of the first domain). The model is initialised at 12 UTC, 9 September 2016 (i.e. 19 h before the first measurements) and integrated for 36 h.

The following parametrizations are used for all domains: The Noah land surface model<sup>48</sup>, the WRF double-moment 6-class cloud microphysics scheme (WDM6<sup>49</sup>), the Rapid Radiative Transfer Model for the GCM scheme for short- and longwave radiation<sup>50</sup> and the Mellor-Yamada-Nakanishi-Niino boundary-layer parametrization<sup>51</sup>. The ocean surface roughness is determined by a modified Charnock relation<sup>52</sup>. In contrast to the two innermost domains, the outermost domain uses the Kain-Fritsch cumulus parametrization scheme<sup>53</sup>.

**Wind farm parameterization.** The grid size of the numerical model WRF is too large to capture the effect of a single wind farm explicitly. Therefore, we use the wind farm parametrization of Fitch *et al.*<sup>13</sup>, which acts as a momentum sink for the mean flow and as a source of turbulence at the height of the rotor. The wind turbines at the wind farms Amrumbank West (AW), Windpark Meerwind Süd/Ost (WM) and Nordsee Ost (OWPN) have a hub height ranging from 90 m to 95 m and a diameter of 120 m up to 126 m. Therefore, the rotor area of the wind turbines intersects with three model levels. The effects of the wind turbine towers on the atmosphere are neglected.

A wind turbine extracts kinetic energy from the atmosphere, with the total extracted fraction from the atmosphere described by the thrust coefficient  $C_T$ . Only a fraction of the extracted kinetic energy is converted into electrical energy as quantified by the power coefficient  $C_p$ . The difference between  $C_T$  and  $C_p$  stems from electrical and mechanical losses, and the production of non-productive drag. By neglecting the electrically and mechanically induced losses and assuming that all non-productive drag is converted into electrical energy, the difference  $C_T - C_p$  describes the amount of kinetic energy that is extracted from the mean flow and then converted into turbulent kinetic energy<sup>13</sup>.

The coefficients  $C_T$  and  $C_p$  are a function of wind speed and depend on the type of turbine<sup>13</sup>. The three wind farms of interest (AW, WM, OWPN) have two different wind turbine types: At AW and WM, Siemens SWT 3.6–120 offshore turbines are installed whereas at OWPN, Senvion 6.2 wind turbines are used, with nominal powers of 3.6 MW and 6.2 MW, respectively. Since  $C_T$  and  $C_p$  for these turbines are unavailable to the public, we adapt coefficients from the wind turbine Siemens SWT 3.6–120 onshore, as these are available online (see <http://>



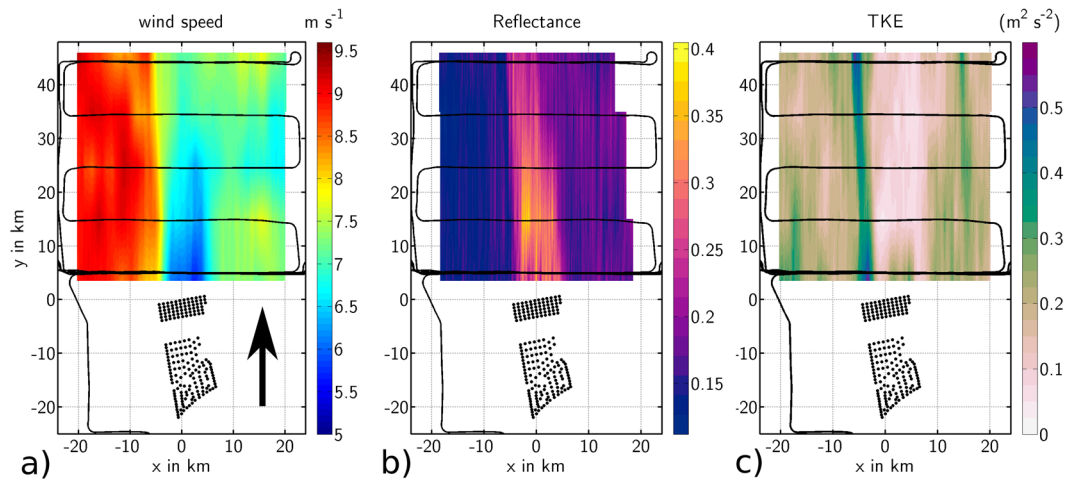


**Figure 5.** (a) Wind speed measurements at hub height (90 m) from the DO 128 flight on September 10, 2016 08:30–09:30 UTC (Flight 7). The wind speed measured along the flight track (black lines) is linearly interpolated perpendicular to the mean wind direction (south 190, indicated by the black arrow). Black dots mark the position of the wind turbines of the wind farms Amrumbank West, Nordsee Ost and Meerwind Süd/Ost. The geographical GPS-coordinates are converted into a Cartesian coordinate system aligned with the mean wind direction (190) for a better comprehension of the orientation and length of the wake. (b) As in Fig. 5a), but for the dimensionless reflectance of the sea surface. A higher reflectance may be interpreted as a lower wind speed near the ocean surface. (c) As in Fig. 5a), but for the TKE.

[www.wind-turbine-models.com/turbines/646-siemens-swt-3.6-120-onshore](http://www.wind-turbine-models.com/turbines/646-siemens-swt-3.6-120-onshore)). The model underestimates the wind at hub height by up to  $1 \text{ m s}^{-1}$ . Furthermore, the parametrisation of Fitch *et al.*<sup>13</sup> neglects the dependence of the power and thrust coefficients on the stability of the atmosphere. Therefore, the power and thrust coefficients chosen in the present study are only a suitable first approximation.

**Measurements of wind-farm wakes in the far field.** *In situ* observations from fixed platforms like FINO 1 are available, but do not provide the spatial sampling required to study the three-dimensional structure of wakes. The institutes involved in the WIPAFF project were aware of these shortcomings in currently available data sources. Therefore, we collected *in situ* data with the research aircraft Dornier DO-128 belonging to the Technische Universität Braunschweig, Germany. Measurement flights delivered wind speed and direction, turbulence, temperature, humidity, surface-temperature and sea-state data at high resolution (sampling frequency 100 Hz), similarly to campaigns documented in<sup>38,39</sup>. A laser scanner was also integrated into the research aircraft to determine sea-surface properties.

We performed 41 measurement flights between September 2016 and October 2017 downwind of wind farm clusters, such as Amrumbank West and Godewind located in the German Bight (Table 1). We discuss the results of Flight 7 on September 10, 2016 here as a typical example for the wake extent during moderate wind speeds of  $7\text{--}10 \text{ m s}^{-1}$  and under stable conditions. Throughout the September 2016 campaign, a dominant high-pressure system was located over Central and Eastern Europe, resulting in the advection of warm sub-tropical air over the German Bight from the south. The warm air over the colder water during the campaign resulted in stable atmospheric stratification (i.e. no thermal turbulence and, therefore, the prevention of convective motion), which is favourable for the generation of long wakes. By vertical profiling of the lower atmosphere with the aircraft, we observed stable conditions over the sea during the September 2016 campaign during 7 flights, where wakes over the whole flight range up to 45 km were detected. In total we detected wakes with a length of at least 10 km during 27 cases, the longest wake length was 70 km (see Table 1). The flight pattern of Flight 7 on September 10 shown in Fig. 5a)–c) measured both the undisturbed air flow and the wake dispersion downwind from the wind farm cluster Amrumbank West, Nordsee Ost and Meerwind Süd/Ost with 90% of the wind turbines running. Several flight legs of 40 km length positioned perpendicular to the mean wind direction and staggered (5, 15, 25, 35, 45 km) behind the wind farm captured both the wake and the adjacent undisturbed air flow at hub height (90 m) of the wind turbines.

Wind speed measurements from Flight 7 are shown in Fig. 5a), where data recorded from individual legs are linearly interpolated, and displayed as coloured contours. Behind the wind farm, a zone of reduced wind speed extended to at least 45 km, with a wind speed deficit up to  $3 \text{ m s}^{-1}$  at 5 km downwind and about  $1 \text{ m s}^{-1}$  at 45 km behind the wind farm resulting in a maximum wind speed deficit of 40%. In this manuscript we refer to wind speed deficit as the difference between the flow within the wake and the undisturbed flow outside of the wake on the western side along each flight leg (where the maximum wind speed was measured) instead of using the wind speed measured upstream of the wind farms as a reference. This definition is necessary because of two reasons. First, the wind speed has a gradient from East to West. Therefore, it would be difficult to define an upstream wind speed. Secondly, the upstream wind speed decreased during field experiment. Hence, using the upstream measured wind speed as reference would lead to an underestimation of the wind speed reduction. The wind

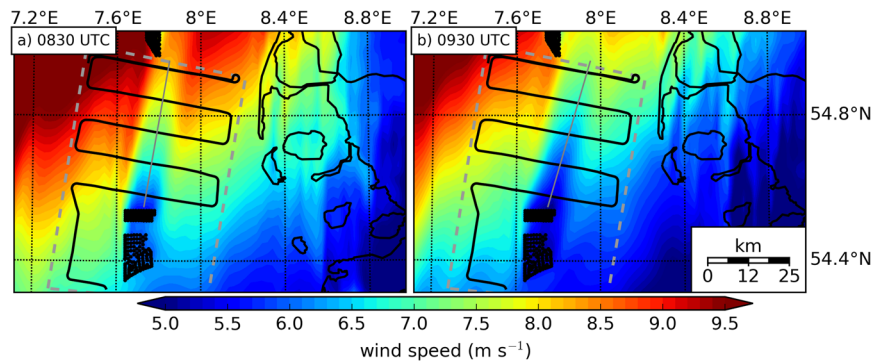


**Figure 6.** (a) WRF model simulation of the wind field at hub height (90 m) for 10 September 2016 08:30 UTC. (b) WRF model simulation for 09:30 UTC on the same day. The flight pattern over the German Bight is marked by the black line, the measurement flight domain according to Fig. 5(a)–(c) by grey dashed line, German and Danish coast by black lines and wind turbines by black dots. Grey line indicates a cross-section of the wind speed, which is displayed in Fig. 7. The figures were generated with Matplotlib<sup>37</sup>.

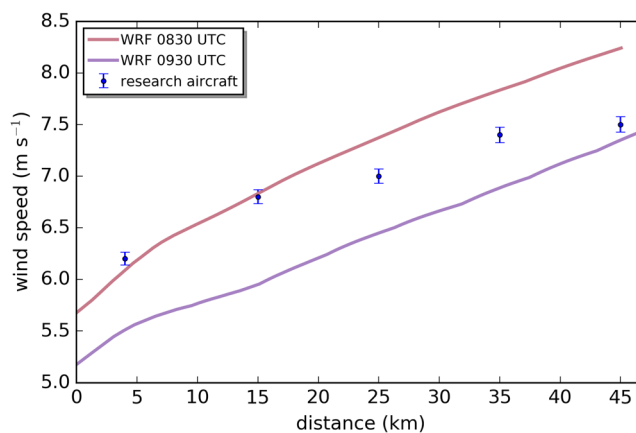


**Figure 7.** Cross-section along the wake as marked in Fig. 6 of the WRF simulations at 08:30 UTC (red) and 09:30 UTC (purple) and the *in situ* data (blue). Error bars indicate the estimated wind measurement error as explained in Section Meteorological data.

speed deficit in the wake is aligned along the mean wind direction. The wake sector has the width of the wind farm (10 km) for the closest flight legs (at 5 km and 10 km downwind) and no pronounced spreading out can be detected with increasing distance from the wind farm.

A lower wind speed results in a smoother water surface. The smoothness of the water surface was measured by laser reflectance aboard the aircraft using the downwards-looking laser scanner (Sect. Methods). The scattering of the signal transmitted by the laser is less diffuse for smoother water, hence, the probability of a specular reflection in the direction of the sensor is higher. This effect of increased reflectance at low wind speeds is well known from microwave radar altimeter studies<sup>54</sup>, which we use to help visualise the far wake and relate to SAR images. As shown in Fig. 5(b), we measured a higher reflectance by a factor of four inside the wake than in the neighbouring region, indicating lower wind speeds in the wake during Flight 7. *In situ* wind speed measurements (Fig. 5a) and laser reflectance (Fig. 5b) both show a wake throughout the whole scanning area of 45 km downwind of the wind farm. Furthermore, Fig. 5(a) and (b) display a horizontal wind speed reduction from west to east (i.e. perpendicular to the mean wind direction) caused by the higher surface friction along the coast, east of the flight path.

**Turbulence in the far wake.** The degree of atmospheric turbulence impacts the efficiency and fatigue loading of a wind turbine<sup>55</sup>. A typical parameter to describe turbulence is the turbulent kinetic energy (TKE) described in Sect. Methods. Measurements of TKE reveal a far downwind dispersion of the turbulence produced by the wind farm and as a result of the mixing of the wake with the undisturbed flow (Fig. 5c). A slender wake of TKE with a width less than 5 km is aligned with the western edge of the wind farm. A stronger horizontal wind speed gradient exists between the decelerated wind field in the wake and undisturbed wind field to the west. The eastern edge of the wake is much less pronounced as a result of the lower wind speeds along the coast. Inside the wake less turbulence is produced due to a lower wind speed than in the undisturbed flow outside the wake, thus TKE is smaller. Moreover, the eastern boundary of the cluster of wind farms is more irregular compared with the western edge (see Fig. 5c). The TKE of  $0.5 \text{ m}^2 \text{ s}^{-2}$  in the wake sector is about five times that in the undisturbed air flow and decays slowly after 10 km to about  $0.3 \text{ m}^2 \text{ s}^{-2}$ . An elevated level of TKE remains at even 45 km downwind

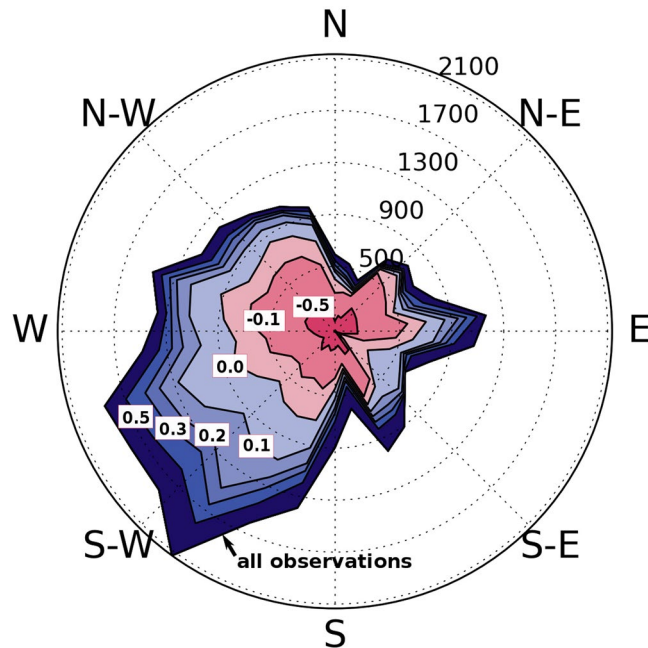


**Figure 8.** Stability wind rose indicating the frequency (number of 10-min intervals per 12° wind direction sector) of atmospheric stability. Lines are labelled in terms of the stability measure  $z/L$ , where  $z$  is the height above ground, and  $L$  is the Monin-Obukhov length. Blue and red shading indicates stable and unstable stratification, respectively. The higher the value the stronger the stability. Data are from the FINO 1 offshore platform in the North Sea for the whole year of 2005 at a height of 60 m above the sea surface. Data is available from <http://fino.bsh.de/>. Only data with wind speeds between the cut-in ( $5 \text{ m s}^{-1}$ ) and cut-off ( $25 \text{ m s}^{-1}$ ) wind speed have been considered.

of the wind farm. Within the eastern part of the wake, the TKE remains lower (below  $0.1 \text{ m}^2 \text{ s}^{-2}$ ) than in the undisturbed flow ( $0.1\text{--}0.25 \text{ m}^2 \text{ s}^{-2}$ ) at least 45 km downwind on account of the lower wind speeds and reduced horizontal wind shear.

**Comparison with model simulations.** We performed numerical simulations of the wake using the wind farm parametrisation of Fitch *et al.*<sup>13</sup> within the Weather Research and Forecasting Model for a grid size of 1.6 km. Operational analysis data from the European Centre for Medium-Range Weather Forecasts (ECMWF) provided the initial and lateral boundary conditions. The model results (Fig. 6) have been obtained for two times at the beginning of the measurement pattern and at the end.

The model simulations reveal a similar structure and orientation of the far wake for the 10 September 2016 as observed by the airborne data (Fig. 6), with a wind speed of about  $6 \text{ m s}^{-1}$  at the first flight leg 5 km downwind (08:30 UTC) and  $7.3 \text{ m s}^{-1}$  at the last flight leg (09:30 UTC) 45 km downwind (Fig. 7). However, the observations indicate higher wind speeds within the wake than the simulations (Fig. 7). This finding is consistent with the wind speed observations taken upwind of the wind farm where the model is underestimating the wind speed. Consequently, the wind speed within the wake has to be lower than the *in situ* data, otherwise the wind farm parameterization would underestimate the wind speed deficit induced by the wind farm.

The wind speed averaged over the measurement domain during the flight decreases from approximately  $7 \text{ m s}^{-1}$  (08:30 UTC) to  $5 \text{ m s}^{-1}$  (09:30 UTC), which is consistent with flight measurements. The attenuated wind field along the coast observable in the simulations matches well with *in situ* observations (Fig. 5a).

## Discussion

As expected from the results of remote sensing observations, numerical and analytical studies<sup>13,20,22,24,28,30–32,56,57</sup>, the wind speed deficits downwind of offshore wind farms tend to be larger in stable than in unstable conditions, and the lengths of wakes are longer. Likewise, our aircraft measurements show strong indications for longer wakes for all flights under stable situations, whereas wakes were not observed far away from the farms during unstable conditions (see Table 1). These first airborne *in situ* results fortify assumptions from the previous studies. A further detailed analysis of the stratification and wake length will be presented in a future work, as an exact stability analysis is very complex and must be done for each single flight, which is beyond the scope of this paper.

The question now is how often do stable conditions occur, and are stable conditions coupled to certain wind directions? Fig. 8 displays a stability wind rose (32,736 10-min mean values for the relevant wind speed range of  $5 \text{ m s}^{-1}$  to  $25 \text{ m s}^{-1}$ ) from the offshore research platform FINO 1<sup>58</sup> located in the German Bight to the north of the island of Borkum (see Fig. 1) for the whole of the year 2005. While 20% of all values exceed a moderate stability of  $z/L = 0.2$ , 10% of all values still exceed a stability of  $z/L = 0.5$ .

Figure 8 also demonstrates a correlation between the wind direction and atmospheric stratification, which is typical for mid-latitudes on the northern hemisphere<sup>59</sup>, resulting from the alternating warm and cold sectors of the eastward moving cyclones at this latitude. Stable situations are most likely found for south-west wind directions, from which we can infer that this is the most likely direction producing long wakes in the North Sea. Further, the predominant wind directions in the North Sea are west and south-west wind directions as 42% of all values in Fig. 8 come from the 90 sector from south to west, meaning we expect stable situations from this predominant sector about 5% of the time. For wind farms located several tens of kilometres downwind of neighbouring wind farms along the main wind direction, the productivity of the downwind farms may be reduced during periods with stable stratification.

Our airborne observations provide the first *in situ* confirmation of the existence of far wakes extending at least 45 km downwind from wind farms, confirming the ability of numerical simulations and SAR satellite images in capturing the spatial structure of wind-farm wakes. Further analysis for different atmospheric conditions are foreseen to provide a clearer quantitative relationship between wind speed, turbulence intensity, atmospheric stability and wake length.

## References

- Colmenar-Santos, A., Perera-Perez, J. & Borge-Diez, D. *et al.* Offshore wind energy: A review of the current status, challenges and future development in Spain. *Renew. Sustain. Energy Rev.* **64**, 1–18 (2016).
- Neddernann, B., Realistic, T. N. Scenario for the Offshore Wind Power Development in Germany. *DEWI Mag.* **47** (2015).
- van Hoof, J. Unlocking Europe's offshore wind potential. *PwC Nederlande* **March 2017**, 40 (2017).
- GWEC. Global wind report, annual market update 2013. *Global Wind Energy Council* 80pp (2013).
- Dörenkämper, M., Optis, M., Monahan, A. & Steinfeld, G. On the offshore advection of boundary-layer structures and the influence on offshore wind conditions. *Boundary-Layer Meteorol.* **155**, 459–482 (2015).
- Nygaard, N. G. & Hansen, S. D. Wake effects between two neighbouring wind farms. *J. Physics: Conf. Ser.* **753**, 032020 (2016).
- Martinez-Tossas, L. A., Churchfield, M. J. & Meneveau, C. Large eddy simulation of wind turbine wakes: detailed comparisons of two codes focusing on effects of numerics and subgrid modeling. *J. Physics: Conf. Ser.* **625**, 012024 (2015).
- Jensen, L. E., Mørch, C., Sørensen, P. & Svendsen, K. Wake measurements from the Horns Rev wind farm European Wind Energy Conference. *European wind energy conference* **9** (2004).
- Frandsen, S. *et al.* The shadow effect of large wind farms: measurements, data analysis and modelling. *Report from Risø National Laboratory for Sustainable Energy–Risø-R1615 (EN)* (2007).
- Baidya Roy, S. & Traiteur, J. J. Impacts of wind farms on surface air temperatures. *Proc. Natl. Acad. Sci.* **107**, 17899–17904 (2010).
- Fiedler, B. & Bukovsky, M. The effect of a giant wind farm on precipitation in a regional climate model. *Environ. Res. Lett.* **6**, 045101 (2011).
- Zhou, L. *et al.* Impacts of wind farms on land surface temperature. *Nat. Clim. Chang.* **2**, 539–543 (2012).
- Fitch, A. C. *et al.* Local and mesoscale impacts of wind farms as parameterized in a mesoscale NWP model. *Mon. Weather. Rev.* **140**, 3017–3038 (2012).
- Barthelmie, R. *et al.* Offshore wind turbine wakes measured by SODAR. *J. Atmospheric Ocean. Technol.* **20**, 466–477 (2003).
- Fitch, A. C., Lundquist, J. K. & Olson, J. B. Mesoscale influences of wind farms throughout a diurnal cycle. *Mon. Weather. Rev.* **141**, 2173–2198 (2013).
- Prospathopoulos, J. & Chaviaropoulos, P. Numerical simulation of offshore wind farm clusters. In *European Wind Energy Association, Conference proceedings* (2013).
- Vautard, R. *et al.* Regional climate model simulations indicate limited climatic impacts by operational and planned European wind farms. *Nat. communications* **5** (2014).
- Wolken-Möhlmann, G., Gottschall, J. & Lange, B. First verification test and wake measurement results using a ship-lidar system. *Energy Procedia* **53**, 146–155 (2014).
- Jiménez, P. A., Navarro, J., Palomares, A. M. & Dudhia, J. Mesoscale modeling of offshore wind turbine wakes at the wind farm resolving scale: a composite-based analysis with the Weather Research and Forecasting model over Horns Rev. *Wind. Energy* **18**, 559–566 (2015).
- Hasager, C. B. *et al.* Using satellite SAR to characterize the wind flow around offshore wind farms. *Energies* **8**, 5413–5439 (2015).
- Lu, H. & Porté-Agel, F. On the impact of wind farms on a convective atmospheric boundary layer. *Boundary-Layer Meteorol.* **157**, 81–96 (2015).
- Volker, P., Badger, J., Hahmann, A. N. & Ott, S. The Explicit Wake Parametrisationv1. 0: a wind farm parametrisation in the mesoscale model WRF. *Geosci. Model. Dev.* **8**, 3715–3731 (2015).
- Troldborg, N. *et al.* Numerical simulations of wake interaction between two wind turbines at various inflow conditions. *Wind. Energy* **14**, 859–876 (2011).
- Emeis, S. A simple analytical wind park model considering atmospheric stability. *Wind. Energy* **13**, 459–469 (2010).
- Hansen, K. S., Barthelmie, R. J., Jensen, L. E. & Sommer, A. The impact of turbulence intensity and atmospheric stability on power deficits due to wind turbine wakes at Horns Rev wind farm. *Wind. Energy* **15**, 183–196 (2012).
- Wu, Y.-T. & Porté-Agel, F. Atmospheric turbulence effects on wind-turbine wakes: An LES study. *Energies* **5**, 5340–5362 (2012).
- Smedman, A.-S., Bergström, H. & Grisogono, B. Evolution of stable internal boundary layers over a cold sea. *J. Geophys. Res. Ocean.* **102**, 1091–1099 (1997).
- Emeis, S. *Wind energy meteorology: atmospheric physics for wind power generation*. Springer Science & Business Media (2012).
- Vermeer, L., Sørensen, J. N. & Crespo, A. Wind turbine wake aerodynamics. *Prog. aerospace sciences* **39**, 467–510 (2003).
- Fiedler, B. & Adams, A. A subgrid parameterization for wind turbines in weather prediction models with an application to wind resource limits. *Advances in Meteorology* **2014** (2014).
- Christiansen, M. B. & Hasager, C. B. Wake effects of large offshore wind farms identified from satellite SAR. *Remote. Sens. Environ.* **98**, 251–268 (2005).
- Li, X. & Lehner, S. Observation of TerraSAR-X for studies on offshore wind turbine wake in near and far fields. *IEEE J. Sel. Top. Appl. Earth Obs. Remote. Sens.* **6**, 1757–1768 (2013).
- Wildmann, N., Hofsaß, M., Weimer, F., Joos, A. & Bange, J. MASC—a small remotely piloted aircraft (RPA) for wind energy research. *Adv. Sci. Res.* **11**, 55–61 (2014).
- Jacobsen, S., Lehner, S., Hieronimus, J., Schneemann, J. & Kühn, M. Joint offshore wind field monitoring with spaceborne SAR and platform-based Doppler LIDAR measurements. *The Int. Arch. Photogramm. Remote. Sens. Spatial Inf. Sci.* **40**, 959 (2015).
- Emeis, S. *et al.* Exploring the wakes of large offshore wind farms. *J. Physics: Conf. Ser.* **753**, 092014 (2016).
- Skamarock, W. C. *et al.* A description of the advanced research WRF version 2. Tech. Rep., National Center For Atmospheric Research Boulder Co Mesoscale and Microscale Meteorology Div (2005).
- Hunter, J. D. Matplotlib: A 2D graphics environment. *Comput. In Sci. & Eng.* **9**, 90–95 (2007).



38. Bange, J. & Spieß, T. Airborne measurements in the early-morning shallow convective boundary layer. In *17th Symposium on Boundary Layers and Turbulence* 11 pp. (Amer. Meteorol. Soc., San Diego, CA, USA, 2006).
39. Bange, J., Zittel, P., Spieß, T., Uhlenbrock, J. & Beyrich, F. A new method for the determination of area-averaged turbulent surface fluxes from low-level flights using inverse models. *Bound.-Layer Meteorol.* **119**, 527–561 (2006).
40. Corsmeier, U., Hankers, R. & Wieser, A. Airborne turbulence measurements in the lower troposphere onboard the research aircraft Dornier 128-6, D-IBUF. *Meteorol. Zeitschrift* **10**, 315–329 (2001).
41. van den Kroonenberg, A. C., Martin, T., Buschmann, M., Bange, J. & Vörsmann, P. Measuring the wind vector using the autonomous Mini Aerial VehicleM<sup>2</sup>AV. *J. Atmos. Ocean. Technol.* **25**, 1969–1982 (2008).
42. Grossmann, S., Lohse, D., Lvov, V. & Procaccia, I. Finite size corrections to scaling in high Reynolds number turbulence. *Phys. review letters* **73**, 432 (1994).
43. Mann, J. & Lenschow, D. H. Errors in airborne flux measurements. *J. Geophys. Res. Atmospheres (1984–2012)* **99**, 14519–14526 (1994).
44. Lenschow, D., Mann, J. & Kristensen, L. How long is long enough when measuring fluxes and other turbulence statistics? *J. Atmospheric Ocean. Technol.* **11**, 661–673 (1994).
45. van den Kroonenberg, A., Martin, S., Beyrich, F. & Bange, J. Spatially-averaged temperature structure parameter over a heterogeneous surface measured by an unmanned aerial vehicle. *Boundary-Layer Meteorol.* **142**, 55–77 (2012).
46. Kaimal, J. C. & Finnigan, J. J. *Atmospheric boundary layer flows: their structure and measurement* (Oxford University Press, 1994).
47. Lenschow, D. H. & Stankov, B. B. Length scales in the convective boundary layer. *J. Atmos. Sci.* **43**, 1198–1209 (1986).
48. Chen, F. & Dudhia, J. Coupling an Advanced Land Surface-Hydrology Model with the Penn State-NCAR MM5 Modeling System. Part I: Model Implementation and Sensitivity. *MWR* **129**, 569–585 (2001).
49. Lim, K.-S. S. & Hong, S.-Y. Development of an Effective Double-Moment Cloud Microphysics Scheme with Prognostic Cloud Condensation Nuclei (CCN) for Weather and Climate Models. *Mon. Wea. Rev.* **138**, 1587–1612 (2010).
50. Iacono, M. J. *et al.* Radiative forcing by long-lived greenhouse gases: Calculations with the AER radiative transfer models. *J. Geophys. Res.* **113** (2008).
51. Nakanishi, M. & Niino, H. An Improved Mellor–Yamada Level-3 Model with Condensation Physics: Its Design and Verification. *Bound.-Layer Meteorol.* **112**, 1–31. <https://doi.org/10.1023/B:BOUN.0000020164.04146.98> (2004).
52. Fairall, C., Bradley, E. F., Hare, J., Grachev, A. & Edson, J. Bulk parameterization of air-sea fluxes: Updates and verification for the COARE algorithm. *J. climate* **16**, 571–591 (2003).
53. Kain, J. S. The Kain-Fritsch Convective Parameterization: An Update. *J. Atmos. Sci.* **43**, 170–181 (2004).
54. Chelton, D. B. & Wentz, F. J. Further development of an improved altimeter wind speed algorithm. *J. Geophys. Res. Ocean.* **91**, 14250–14260 (1986).
55. Lee, S., Churchfield, M., Moriarty, P., Jonkman, J. & Michalakes, J. Atmospheric and wake turbulence impacts on wind turbine fatigue loadings. In *50th AIAA Aerospace Sciences Meeting including the New Horizons Forum and Aerospace Exposition*, 540 (2012).
56. Barthelmie, R., Frandsen, S., Rethore, P. & Jensen, L. Analysis of atmospheric impacts on the development of wind turbine wakes at the Nysted wind farm. In *European Offshore Wind Conference*, vol. 6 (2007).
57. Türk, M. & Emeis, S. The dependence of offshore turbulence intensity on wind speed. *J. Wind. Eng. Ind. Aerodyn.* **98**, 466–471 (2010).
58. Türk, M., Grigutsch, K. & Emeis, S. The wind profile above the Sea- Investigations basing on four years of FINO 1 data. *DEWI Mag* **33**, 12–16 (2008).
59. Coelingh, J., Van Wijk, A. & Holtslag, A. Analysis of wind speed observations over the North Sea. *J. Wind. Eng. Ind. Aerodyn.* **61**, 51–69 (1996).

## Acknowledgements

The authors would like to thank the additional crew of the WIPAFF campaign, Per Schachtebeck, Thomas Feuerle, Helmut Schulz and Thomas Rausch, for their support. The project WIPAFF is funded by the German Federal Ministry for Economic Affairs and Energy (Bundesministerium für Wirtschaft und Energie) on the basis of a decision by the German Bundestag grant number: FKZ 0325783. TerraSAR-X data were kindly provided by the German Aerospace Center (DLR) in the framework of the WIPAFF\_TSX AO for scientific use. We thank the European Space Agency (ESA) for making SENTINEL-1 data available.

## Author Contributions

Andreas Platis contributed by writing the manuscript, analysing the data and conducting the measurement campaign. Astrid Lampert, Konrad Bärfuss, Rolf Hankers and Jens Bange contributed by organising and conducting the measurement campaign, data analysis and discussion. Simon Siedersleben performed the numerical simulations with the WRF model and contributed Figs 1, 6 and 7, Bughsin Djath and Johannes Schulz-Stellenfleth provided analysis of TerraSAR-X and SENTINEL-1 SAR data. Beatriz Canadillas contributed with FINO 1 data analysis and discussions. Richard Foreman took care of the overall structure of the paper and helped with the English language. Tom Neumann and Stefan Emeis had organised the WIPAFF project as a whole and contributed to the Introduction and Discussion, and Stefan Emeis made the analysis displayed in Fig. 8.

## Additional Information

**Competing Interests:** The authors declare that they have no competing interests.

**Publisher's note:** Springer Nature remains neutral with regard to jurisdictional claims in published maps and institutional affiliations.



**Open Access** This article is licensed under a Creative Commons Attribution 4.0 International License, which permits use, sharing, adaptation, distribution and reproduction in any medium or format, as long as you give appropriate credit to the original author(s) and the source, provide a link to the Creative Commons license, and indicate if changes were made. The images or other third party material in this article are included in the article's Creative Commons license, unless indicated otherwise in a credit line to the material. If material is not included in the article's Creative Commons license and your intended use is not permitted by statutory regulation or exceeds the permitted use, you will need to obtain permission directly from the copyright holder. To view a copy of this license, visit <http://creativecommons.org/licenses/by/4.0/>.

© The Author(s) 2018



# Long-range modifications of the wind field by offshore wind parks – results of the project WIPAFF

ANDREAS PLATIS<sup>1\*</sup>, JENS BANGE<sup>1</sup>, KONRAD BÄRFUSS<sup>3</sup>, BEATRIZ CAÑADILLAS<sup>4</sup>, MARIE HUNDHAUSEN<sup>1</sup>, BUGHSIN DJATH<sup>5</sup>, ASTRID LAMPERT<sup>3</sup>, JOHANNES SCHULZ-STELLENFLETH<sup>5</sup>, SIMON SIEDERSLEBEN<sup>2</sup>, THOMAS NEUMANN<sup>4</sup> and STEFAN EMEIS<sup>2</sup>

<sup>1</sup>University of Tuebingen, ZAG, Environmental Physics, Tübingen, Germany

<sup>2</sup>Karlsruhe Institute of Technology – Institute of Meteorology and Climate Research – Atmospheric Environmental Research, Garmisch-Partenkirchen, Germany

<sup>3</sup>Technische Universität Braunschweig, Institute of Flight Guidance, Braunschweig, Germany

<sup>4</sup>UL International GmbH, Oldenburg, Germany

<sup>5</sup>Helmholtz-Zentrum Geesthacht Zentrum für Material- und Küstenforschung GmbH, Geesthacht, Germany

(Manuscript received December 18, 2019; in revised form March 5, 2020; accepted March 6, 2020)

## Abstract

This publication synthesizes the results of the WIPAFF (WInd Park Far Fields) project. WIPAFF focused on the far field of large offshore wind park wakes (more than 5 km downstream of the wind parks) located in the German North Sea. The research project combined *in situ* aircraft and remote sensing measurements, satellite SAR data analysis and model simulations to enable a holistic coverage of the downstream wakes. The *in situ* measurements recorded on-board the research aircraft DO-128 and remote sensing by laser scanner and SAR prove that wakes of more than 50 kilometers exist under certain atmospheric conditions. Turbulence occurs at the lateral boundaries of the wakes, due to shear between the reduced wind speed inside the wake and the undisturbed flow. The results also reveal that the atmospheric stability plays a major role in the evolution of wakes and can increase the wake length significantly by a factor of three or more. On the basis of the observations existing mesoscale and industrial models were validated and updated. The airborne measurement data is available at PANGAEA/ESSD.

**Keywords:** WIPAFF, wind energy, offshore, wakes, marine boundary layer

## 1 Introduction

Wind park wakes have found increasing interest in recent years, when industry and authorities have started to plan wind parks closer together for good reasons (e.g. nature conservation, bundling of grid access, public acceptance), especially in offshore regions. As wind parks are built to extract kinetic energy from the atmosphere, downwind wake regions form behind turbines and wind parks, characterised by reduced mean wind speed and enhanced levels of turbulence (LISSAMAN, 1979). Both effects downgrade the conditions for downstream turbines and wind parks and are thus relevant for the expected power output from and the endurance of the installations. However, a deeper understanding of the physics of atmospheric flow in wind park wakes is needed to obtain better operational forecasts of wind energy production or scenario simulations (VEERS *et al.*, 2019; ROHRIG *et al.*, 2019).

We distinguish here between the near wake of wind parks (a few hundreds of metres to a few kilometres behind the parks) where the effects of single turbines are

clearly discernible, and the far wake (about five kilometres and more behind the parks) where the wakes of the single turbines have merged into a more or less uniform park wake (e.g. LI and LEHNER, 2013a). Most research on wakes so far has focused on near wakes behind single turbines and on wake interactions from a larger number of turbines within one and the same wind park (e.g., MARTÍNEZ-TOSSAS *et al.*, 2015; TRABUCCHI *et al.*, 2015). Only some experimental and recent numerical studies consider the wakes of entire wind parks and the impact of far wakes on neighbouring downwind wind parks on a larger spatial scale (e.g., CHAVIAROPOULOS, 2013; NYGAARD and HANSEN, 2016; SCHNEEMANN *et al.*, 2019).

The impact of far wakes from offshore wind parks on the regional climate has only been addressed in isolated studies (e.g., BOETTCHER *et al.*, 2015) with hardly any definite conclusions. Recent studies for onshore wind parks found similar effects of the impact PRYOR *et al.*, 2018. Wind park far wakes are of particular interest for offshore installations, because turbulence intensity – which is the main driver for wake dissipation – is much lower over the ocean than over land. Therefore, wakes behind offshore wind turbines and wind parks are expected to be much longer than behind onshore wind turbines and parks (see e.g., BARTHELMIE *et al.*, 2007; PORTÉ-AGEL *et al.*, 2020). Analytical studies (EMEIS,

\*Corresponding author: Andreas Platis, University of Tuebingen, ZAG, Environmental Physics, 72074 Tübingen, Germany, e-mail: andreas.platis@uni-tuebingen.de

2010; EMEIS, 2018; PORTÉ-AGEL et al., 2020) as well as numerical simulations (e.g. FITCH et al., 2012) have predicted these prolonged wind park wakes as well. Wake lengths up to about 100 km were found in these simulations (FITCH et al., 2012). Observational evidence of such long wakes has been available only indirectly so far from the evaluation of satellite data (CHRISTIANSEN and HASAGER, 2005).

*In situ* measurements of the far wakes were missing before the initiation of the research project WIPAFF (WInd PARK Far Fields), the main results of which are reported here. WIPAFF has been funded by the German Federal Ministry for Economic Affairs and Energy and ran from November 2015 to April 2019. The main goal of WIPAFF (EMEIS et al., 2016) was – for the first time – to perform a large number of *in situ* measurements from aircraft operations at hub height behind wind parks in the German Bight (North Sea), to evaluate further SAR images and to update and validate existing mesoscale and industrial models on the basis of the observations. First results from WIPAFF aircraft operations have been reported by PLATIS et al. (2018).

This publication is designed to give an integrative overview on the results of WIPAFF. Results from the evaluations of the different measurement and modelling efforts in the project (see EMEIS et al., 2016; DJATH et al., 2018; PLATIS et al., 2018; SIEDERSLEBEN et al., 2018b; SIEDERSLEBEN et al., 2018a; SIEDERSLEBEN et al., 2020; LAMPERT et al., 2020; PLATIS et al., in review; DJATH and SCHULZ-STELLENFLETH, 2020; CAÑADILLAS et al., 2020) are put into a common perspective. The airborne data set of the WIPAFF project is accessible to the community via the PANGAEA database (BÄRFUSS et al., 2019; LAMPERT et al., 2020). Section 2 gives the initial hypotheses of the project and Section 3 briefly reviews methods and their state of the art at the beginning of the project. The main results of WIPAFF are summarized in Section 4. Section 5 concludes the study and prepares an outlook to further necessary research.

## 2 The WIPAFF project's initial hypotheses

Wind turbines generate rotating wake vortices in which wind speed, turbulence intensity and turbulent fluxes are modified compared to the undisturbed flow. In a wind park with many wind turbines arranged in a tight grid, these single wakes are considered to superimpose each other (MARTÍNEZ-TOSSAS et al., 2015; TRABUCCHI et al., 2015). For the successful planning of further offshore parks, it is therefore crucial to identify the parameters that affect the wake development. There have been some model approaches of varying complexity that simulate these wake processes (FRANDSEN, 1992; EMEIS and FRANDSEN, 1993; VERMEER et al., 2003; EMEIS, 2010; FITCH et al., 2012; FIEDLER and ADAMS, 2014; VOLKER et al., 2015). A validation, however, of these models has not yet been available so far due to the lack of large offshore wind parks. With the installation of the first large

wind park cluster in the German Bight in the recent decade, this has become possible now. The WIPAFF project aimed to understand the wake development in the lee of wind parks, the corresponding decay dynamics and the size and impact of the wakes downstream of entire offshore wind parks by considering all influencing parameters. In the following, we address the four initial hypotheses of the WIPAFF project.

### 2.1 Hypothesis 1: Wake appearance is related to atmospheric stability

The most efficient mechanism for wake recovery is the vertical transfer of momentum from higher atmospheric layers downwards by atmospheric turbulence (EMEIS, 2010; ABKAR and PORTÉ-AGEL, 2015a; et al., 2015a; EMEIS, 2018). Because of the small surface friction and weak temperature gradients over the sea, much less mechanical turbulence is produced compared to onshore sites (SMEDMAN et al., 1997; et al., 2015b) and, hence, longer wakes are expected. For this reason, surface roughness and atmospheric stability are regarded to be the decisive parameters governing the generation of turbulence and thus the wake recovery (BARTHELMIE et al., 2009; BARTHELMIE and JENSEN, 2010; HANSEN et al., 2012; WU and PORTÉ-AGEL, 2012; CHAVIARPOULOS, 2013).

Wakes of several tens of kilometres were expected to be especially pronounced at offshore locations during stable conditions (HANSEN et al., 2012). This presumption of the existence of far wakes was supported by observational hints of long reaching wakes on satellite images of the sea surface from synthetic aperture radar (SAR, Figure 2). In stable stratifications, long wakes with a length exceeding 20 km have been assessed from synthetic aperture radar data (CHRISTIANSEN and HASAGER, 2005; LI and LEHNER, 2013a).

In addition to the fact that stability may play a very important role in the generation of far wakes, studies such as FRANDSEN et al. (2006); PORTÉ-AGEL et al. (2014); PORTÉ-AGEL et al. (2013); BARTHELMIE et al. (2009) showed that the wake intensity within the wind park depends crucially on the wind direction and the park layout. A larger initial wind speed deficit is observed when the wind direction is parallel to the turbine rows and the turbines are aligned. This larger initial wind speed deficit was expected to cause longer wakes according to EMEIS (2010).

### 2.2 Hypothesis 2: Wakes are associated with increased turbulence

Besides the reduction of the wind speed in the wake, turbulent effects, such as high turbulent kinetic energy (TKE) and increased momentum flux were expected. The degree of atmospheric turbulence impacts the efficiency and fatigue loading of a wind turbine (LEE et al., 2012). Two factors were considered responsible for the

production of turbulence. Firstly, the rotating wake vortices by the wind turbines and secondly, the production of turbulence as a result of the mixing of the wake and its decelerated wind field with the undisturbed flow. So far, mesoscale numerical models parameterize wind turbines as elevated moment sinks, and some of them as a source of TKE (BLAHAK et al., 2010; FITCH et al., 2012; ABKAR and PORTÉ-AGEL, 2015b; VOLKER et al., 2015). In large-eddy simulation (LES) studies and wind-tunnel experiments, these effects were determined at a distance of almost 20 times the wind turbine rotor diameter  $d$  ( $20d$ ) (WU and PORTÉ-AGEL, 2012). However, a validation with *in situ* measurement data has not yet been carried out, except in VOLKER et al. (2015) who used tower measurements collected during neutral conditions to evaluate the wind parks parameterizations of FITCH et al. (2012) and VOLKER et al. (2015).

### 2.3 Hypothesis 3: Wakes have the potential to impact other wind parks downstream

For an optimal use of the marine areas, wind parks are constructed at favourable locations and in clusters in order to minimize the expense of grid connections and due to other constraints like military zones, pipelines, and nature preserves. However, the close proximity can undermine power production in other wind parks downstream, due to wakes from upwind wind parks, causing an economic loss (KAFFINE and WORLEY, 2010; NYGAARD, 2014; NYGAARD and HANSEN, 2016; BODINI et al., 2017; LUNDQUIST et al., 2019). Simple analytical models and first studies confirmed that especially during thermally stable stratification wakes have an impact on downwind wind parks reducing their efficiency.

### 2.4 Hypothesis 4: Wakes impact local climate

Large wind farm impose an obstacle in a flat environment, which decelerate the flow locally associated with a flow-around and overflow effects. As a result, the turbulent fluxes and heat in the atmospheric boundary layer (ABL) may change.

It was already known that onshore wind parks can impact the near surface temperature, and the turbulent fluxes of sensible heat, CO<sub>2</sub>, and water vapour (latent heat) (e.g. ROY and TRAITÉUR, 2010; ZHOU et al., 2012; RAJEWSKI et al., 2013; RAJEWSKI et al., 2014; ARMSTRONG et al., 2016). For example, ZHOU et al. (2012) observed a warming of 0.5 K in the vicinity of onshore wind parks, especially during nocturnal stable conditions. But only a few studies have investigated the potential effect of offshore wind parks on the marine boundary layer (MBL). These studies were motivated by visible cloud effects as they were seen in photos taken at a wind park at the coast of Denmark (EMEIS, 2010; HASAGER et al., 2013; HASAGER et al., 2017), indicating fog formation and dispersion due to enhanced mixing and adiabatic cooling downwind of wind parks. Associated with

enhanced mixing, FOREMAN et al. (2017) reported a decreased sensible heat flux downwind of a small offshore wind park during stable conditions in the German Bight by using eddy-covariance measurements of heat and humidity fluxes at the research platforms FINO1 mast.

Also numerical simulations have indicated a change in air temperature and humidity in the downwind direction of offshore wind parks. VAUTARD et al. (2014) identified increased temperatures in the area of offshore wind parks in their simulations, whereby WANG and PRINN (2011) reported a potential cooling effect in the vicinity of offshore wind parks due to an increased latent heat flux. These thermal effects were not investigated by field measurements, so far. Therefore, in the framework of the WIPAFF project, their spatial extent was investigated together with the possibility that larger wind parks may have an influence on the local climate.

## 3 Methods used in the WIPAFF project

### 3.1 Airborne Data

Airborne *in situ* data were collected with the research aircraft Dornier DO-128 operated by the Technische Universität Braunschweig, Germany. 41 measurement flights over the German Bight during the WIPAFF project during 2016 and 2017 delivered (in general at a sampling frequency of 100 Hz) 3D wind vector, temperature, humidity, and sea surface-temperature. A detailed explanation of the used measurement instruments and the aircraft can be found in CORSMIEIER et al. (2001); PLATIS et al. (2018); LAMPERT et al. (2020). The starting points of the flights were Wilhelmshaven, Borkum or Husum airport, respectively. A typical flight pattern to capture the wakes is displayed in Figure 1 is the so-called "meander pattern", with several flight legs at hub height (at about 100 m above sea level) positioned downstream of the wind-park cluster. The data is freely available from BÄRFUSS et al. (2019) and further explained in LAMPERT et al. (2020).

Besides the meteorological *in situ* data, a downward-looking scanning lidar system measuring the distance aboard the research aircraft recorded the sea-surface state for deriving the shape and distribution of the sea waves, and for characterizing the far-field wakes.

### 3.2 Satellite information for retrieving surface properties

Active microwave radar sensors such as Synthetic Aperture Radar (SAR) are powerful instruments for sunlight and weather independent measurements of the ocean surface roughness at high spatial resolution. The capability of SAR to provide information on offshore windpark wakes has been amply demonstrated (CHRISTIANSEN and HASAGER, 2005; LI and LEHNER, 2013a; DJATH et al., 2018). Far field wake effects of more than 10 km downstream of offshore wind parks have for the

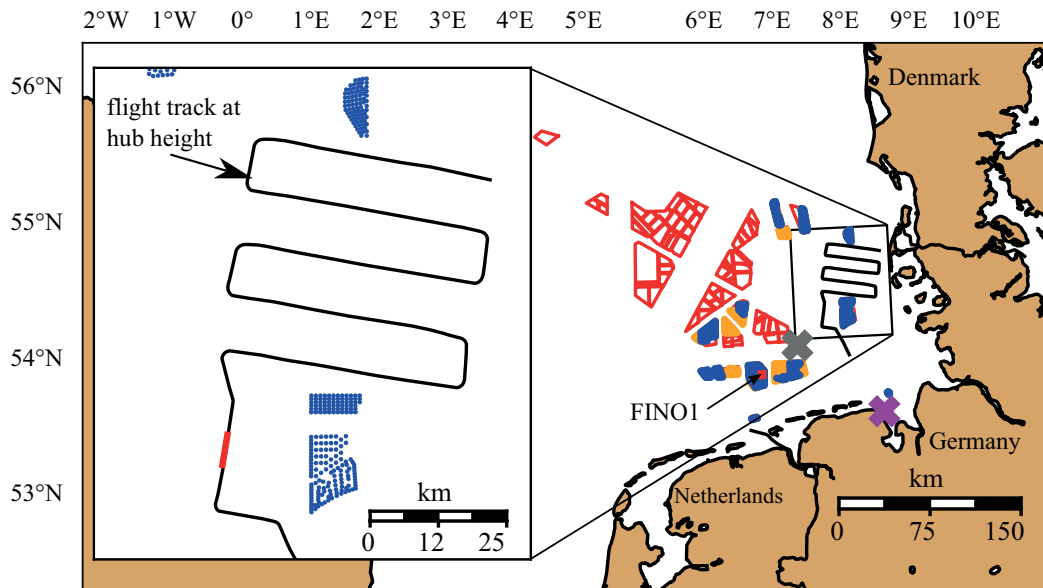


**Figure 1:** Distribution of offshore wind parks in the German Bight as of December 2017. Blue regions are parks currently in operation, red indicate parks still in the approval process. Orange regions are those wind parks that are under construction. The red line within the close-up indicates the area where typically the vertical profiles were flown to capture the atmospheric stratification in close vicinity to the wind farm. The map is adapted from data of the German Federal Maritime and Hydrographic Agency (BSH) and adapted from [PLATIS et al., 2018](#). The magenta and grey colored crosses show locations of climb flights as indicated in Figure 16.

first time become evident based on the analysis of SAR images ([CHRISTIANSEN and HASAGER, 2005](#); [LIN et al., 2008](#); [LI and LEHNER, 2013b](#)). In the WIPAFF project, SAR revealed changes of surface properties downwind of wind parks, expanding the airborne observations to a scale beyond 100 km.

SAR measures near surface wind fields in an indirect way through the small scale roughness of the sea surface. The wind influences the sea surface by generating cm-scale roughness, which is captured by active microwave sensors due to the Bragg-scattering principle. Low image intensities thus indicate areas of reduced wind speed.

Sentinel-1A (launched in 2014) and Sentinel-1B (launched in 2016) are twin satellites that provide SAR data in the German Bight on a regular basis. They were launched into a sun-synchronous orbit and operate at C-band (5.405 GHz) at vertical receive and transmit polarization (VV). Each satellite has an exact repeat cycle of 12 days for the same imaging geometry (i.e., incidence angles and area covered are identical), but can provide data for a particular spot at one or two day intervals, if different imaging geometries are acceptable. Thus, the combination of both satellites provide an image every 6 days with identical geometry. The estimation of wind speeds from SAR requires the radiometric calibration of the SAR raw data and the inversion of a so called geophysical model function (GMF) ([HERSBACH et al., 2007](#); [VERHOEF et al., 2008](#)). Wind direction information can be retrieved either from SAR image structures or alternatively external sources (e.g., atmospheric models) are used.

Wind speed deficits were estimated from SAR using a technique proposed in [CHRISTIANSEN and HASAGER \(2005\)](#) and a new filter approach described in [DJATH and SCHULZ-STELLENFLETH \(2020\)](#). The overall challenge in this application is the estimation of the undisturbed background wind speed, which is not available at the exact location of the wake. The use of wind speeds in neighbouring areas as a proxy leads to certain errors, which depend on spectral properties of the background wind field and which are discussed in more detail in [DJATH and SCHULZ-STELLENFLETH \(2020\)](#).

A spectral analysis of wind fields in the German Bight was conducted as follows. SAR scenes from both satellites were collected for the period September 2016 to December 2017. The occurrence of wakes around the wind park Amrumbank West was analysed (Figure 1). Only the scenes that included the entire Amrumbank West were considered and overall, 177 scenes were collected. Wave-number spectra were then computed from the SAR derived 10 m-wind speed maps. Wind field data were classified considering the stability conditions based on the thermal stratification from FINO1 data. Wind fields associated with stable conditions (STA) and unstable conditions (NOSTA) were considered. A 2D spectral analysis was applied to a square box of 320×320 grid points (with a grid spacing of 300 m, i.e. spatial resolution) aside the wind turbines (see blue box in Figure 2). Using this area, a wavelength range between 0.6 km and 100 km is covered. A 2D Fast Fourier Transform (FFT) was applied to the SAR derived wind fields after the mean was removed. The resulting 2D wavenumber spectrum was scaled in



such a way, that integration of the entire spectral domain equalled the total variance of the wind field. As the wavenumber and directional dependency were also analysed, the spectra were interpolated from the original 2D Cartesian grid to a polar grid. The 1D spectrum was then computed by integrating over all directions.

Besides the observational data, different (numerical) model types were used to investigate the far field of offshore wind parks.

### 3.3 Mesoscale model and wind-park parameterizations (WPPs)

All mesoscale numerical simulations were performed with the Weather Research and Forecasting Model WRF (version 3.8.1). We used the wind park parameterization of FITCH *et al.* (2012) to simulate the wakes of offshore wind parks in the German Bight. Wind park parameterizations (WPPs) allow one to simulate the impact of several wind parks on the marine boundary layer due their low computational costs. Nowadays, offshore wind parks cover an area on the order of 100 km<sup>2</sup> and the corresponding wakes exceed 50 km downwind (Figure 2). Consequently, large offshore wind parks affect a large area, hence, high resolution large-eddy simulations covering the wake area and the corresponding wind park are computationally too expensive to estimate the economic potential loss of planned offshore wind parks or the regional climate impact of wind parks. For such purposes, WPPs are a suitable tool.

The wind park parameterization of FITCH *et al.* (2012) extracts momentum from the mean flow at the rotor area and adds TKE at rotor height. In contrast, others (e.g. JACOBSON and ARCHER, 2012; e.g. VOLKER *et al.*, 2015) do not add any TKE as they assume that the TKE develops due the resolved shear. However, both approaches simulate wakes of offshore wind parks with a length exceeding 50 km during neutral conditions (VOLKER *et al.*, 2015).

Evaluation studies testing the performance of WPPs for offshore wind parks during stable conditions are rare. HASAGER *et al.* (2015) compared SAR retrieved wind speed to mesoscale simulations. VOLKER *et al.* (2015) tested their WPP and that of FITCH *et al.* (2012) with real case data using idealized simulations. However, all these evaluation studies were either based on remote sensing data allowing only an evaluation of the wind speed 10 m above mean sea level (msl) or on idealized simulations omitting moisture effects and assuming a stationary inflow. Therefore, studies investigating the performance of WPPs for real case simulations are necessary.

### 3.4 Analytical model

Analytical wind park models for the assessment of wakes can be constructed in two ways. These models are either bottom-up models which are based on overlays of several single-turbine wakes (the description of which

dates back to JENSEN, 1983) or they are top-down models which consider wind parks as a whole, e.g., as an additional surface roughness, as an additional momentum sink or as a gravity wave generator in association with a temperature inversion aloft at the top of the boundary layer (for the latter idea see SMITH, 2010), which modifies the mean flow above wind parks (NEWMAN, 1977; BOSSANYI *et al.*, 1980; FRANSEN, 1992). Such models have analytical solutions which make them attractive, although they necessarily contain considerable simplifications. Nevertheless, they can be used for first-order approximations in wind park design. Furthermore, a significant advantage of top-down models that they implicitly include the ‘deep array’ effects (BARTHELMIE and JENSEN, 2010). Wind turbines in a large array influence the flow in the atmosphere above the wind farm (CHAMORRO and PORTE-AGEL, 2011). It has been proposed that this prevents the entrainment of momentum from the air above the wind farm, restricting the wake recovery (NYGAARD, 2014).

The analytical wind park model of EMEIS (2010) is an extension of earlier ideas documented in FRANSEN (1992) and EMEIS and FRANSEN (1993). An updated version which additionally includes the turbulence generated by the turbines in the wind park itself is documented with all equations in Chapter 6 of EMEIS (2018). The basic idea of this model is that the overall momentum consumption of the turbines in very large wind parks, which is proportional to the drag coefficient of the turbines and the wind speed at hub height, can only be compensated for by a turbulent momentum flux from above. This leads to an analytical equation for the reduced horizontal wind speed at hub height in the interior of large wind parks. In the wake behind such large wind parks the wind speed at hub height can only recover again due to a turbulent momentum flux from above. This leads to an exponential function for the wind speed recovery at hub height in the wake. The length of the wake is arbitrarily defined as the distance behind the wind park where the wind speed has recovered to more than 95 % of the undisturbed value ahead of the wind park. We note that the decay coefficient used here is not the wake decay coefficient (WDC) used in the quadratic decay function of JENSEN (1983). In this analytical model the wind speed reduction at hub height within a large wind park is given as a function of the areal density of turbines in the park, (sea) surface roughness, turbine-induced turbulence and the thermal stability of the atmospheric boundary layer. The wake length in the analytical model depends on the reduced wind speed right after the wind park and the latter three parameters mentioned before. The park layout, i.e., the spatial arrangement of turbines within a wind park, is not covered by this analytical model.

### 3.5 Engineering models

Engineering models are widely used in the wind energy industry due to their low computational costs and ease



of use to account for wind park wakes. Direct wakes of each individual turbine are simulated with the ‘modified PARK’ model (KATIC et al., 1987). Alternatively, the ‘Eddy Viscosity’ model AINSLIE (1988) could be used. Experience shows that the differences between the two models are particularly relevant in the first kilometers behind the wake-generating turbine. Since in the WIPAFF context, however, the effects beyond 10 km on the lee side of the wind park are particularly relevant, the ‘modified PARK’ model is used here due to the significantly shorter computing time.

In large (offshore) wind parks, the turbines cannot be regarded as independent of the free wind field. Rather, they extract momentum from the wind and therefore act like an area with increased roughness. This results in the formation of an internal boundary layer (IBL) with reduced wind speed behind each turbine. The exact shape of the IBL and the resulting wind speed reduction depends on the orientation of the wind park layout relative to the wind direction (DNV-GL, 2013a).

Both (the ‘modified PARK’ model combined with an IBL) together allow a reasonable simulation of the wake in offshore wind parks and wind park clusters and are often used in this combination for the determination of wind park yields. Importantly, as the individual turbine wake and IBL models have been developed assuming neutral conditions, stratification needs to be explicitly accounted for by tuning the parameters of these models to match the observations (PEÑA and RATHMANN, 2014) and to get an accurate estimation of energy production.

## 4 Results

In the following the four hypotheses described in Section 2 are tested.

### 4.1 On hypothesis 1: Wake Appearance

#### 4.1.1 Appearance of wakes from SAR and airborne data

28 out of the total 41 flights during the WIPAFF project included a flight strategy which allowed for the determination of wakes behind wind parks. For 12 out of the 28 flights, the wake length, defined as the distance to 95 % recovery of the wind field, exceeded the length of the flight meander pattern and for two flights the wake length was observed to be shorter than the downwind distance of the first measured leg. The observed wakes within the WIPAFF campaigns range from nearly 0 km in unstable atmospheric conditions to over 65 km in atmospheric stable conditions (see for further results and discussion Section 4.1.2). The flow inside the wakes was reduced up to 43 % compared to the undisturbed flow, two examples are shown in Figure 4 and 10a).

In addition to the airborne observations, wakes were identified by the analysed surface roughness and backscatter signal (Normalized Radar Cross Section –

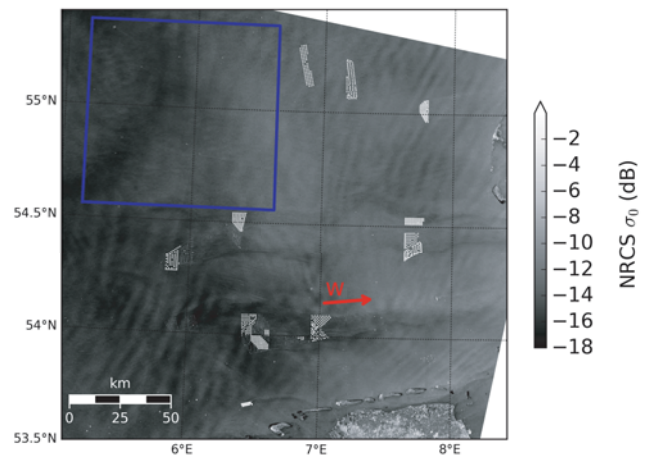


**Figure 2:** NRCS from Sentinel-1A acquired on 27 May 2019 at 05:49 UTC (Copernicus Sentinel data [2019]). Dark streaks in East-West direction behind the wind parks represent atmospheric wakes. Strong atmospheric related NRCS modulation are also found in North-South direction. The blue box was used for the estimation of 2D wavenumber wind spectra. The red arrow indicates the wind direction.

NRCS) from SAR Sentinel – 1A and 1B observations, e.g. Figure 2. The images exhibit darker streaks downwind of wind parks and brighter features at the edges of the wakes, which indicate that surface roughness is reduced downstream of wind parks, and increased along the edges of the wind parks. An example of recent Sentinel-1A SAR image on 27 May 2019 in Figure 2 shows the wakes through the east-west oriented dark streaks behind the wind parks and are in line with the wind direction coming from West. The wind direction is given by the German weather service (DWD) that provides hourly weather data. The wake behind individual wind parks are longer than 30 km. Statistical analysis from SAR data and atmospheric stability by DJATH et al., 2018 showed wakes longer than 50 km and also revealed that the wakes are longer for stable conditions. Overall, from the total 177 collected scenes between 2016 and 2017, 38 % of them show wakes downstream of offshore wind parks. The case with missing wakes on SAR could be related to either strong atmospheric instability or the fact that the wind farms are not in operation.

#### 4.1.2 Longer wakes during stable stratification

Experimental observations by SAR and aircraft indicated that the wake length depends on the stability of the surrounding atmospheric flow. Therefore, a detailed correlation analysis was performed in order to quantify the effect of different stability definitions on the wake length.

A layer is considered as stable, when vertical motion is suppressed, and as unstable or convective, when vertical motion is enhanced (STULL, 2012). By theory and as outlined in EMEIS et al. (2016), it is typical over the ocean for the northern hemisphere in the temperate west-wind belts that warm sector winds most fre-

quently come from the south-west and thus are followed by rather stable conditions, whereas cold-sector winds come from the north-west and predominantly bring convective conditions. For the German Bight, long term studies conducted during recent years support these assumptions (WESTERHELLWEG et al., 2010; SATHE, 2010; MUÑOZ-ESPARZA et al., 2012; EMEIS et al., 2016).

A common stability parameter is the static stability or lapse rate  $\gamma$ , which takes solely buoyancy into account. The lapse rate is defined by the derivation of the virtual potential temperature  $\theta_v$  with respect to the vertical coordinate  $z$ , and can be approximated by the temperature difference  $\Delta\theta_v$  between two levels separated by height difference  $\Delta z$ :

$$\gamma = \frac{d\theta_v}{dz} \approx \frac{\Delta\theta_v}{\Delta z} \quad (4.1)$$

Thus,  $\gamma$  is negative during convective conditions and positive for stable cases.

Common parameters that express dynamic stability, considering both buoyancy and shear, are the Obukhov length and the bulk Richardson number (STULL, 2012; MUÑOZ-ESPARZA et al., 2012). Moreover, there are measures of the magnitude of turbulence, not considering any thermal stratification at all. Most common in ABL science is the turbulence kinetic energy (TKE) per volume and unit mass

$$k = \frac{1}{2} \cdot (\overline{u'^2} + \overline{v'^2} + \overline{w'^2}) \quad (4.2)$$

taking the turbulent part of the wind speed components into account.

We used SAR and flight data in the WIPAFF project to investigate the correlation between stability and wake length.

In a first step SAR scenes taken over the offshore windpark Alpha Ventus were analysed and wake lengths were estimated using the technique described in CHRISTIANSEN and HASAGER (2005). This technique consists of estimating the velocity deficit from two parallel transects defined such that one transect encloses the wake area and the second transect is defined outside the wake, which is characterised as freestream conditions. The length at which the wind speed inside the wake has recovered to the freestream characterizes the maximum length of the wake. The scenes were collocated with estimates of the vertical gradient of potential temperature obtained from the nearby FINO-1 platform. The vertical gradient is based on the measurement of the hourly sea surface temperature at FINO1 and the air temperature at 50 m height. The resulting scatter plot is shown in Figure 3. One has to emphasize that this analysis only includes measurements during the early period (2011–2015), where the Alpha Ventus windpark was not affected by neighbouring wind farms, like it is today. One can clearly see a relationship between increasing atmospheric stabilities and growing lengths of the offshore wind farm wake. More details are given in DJATH et al. (2018).

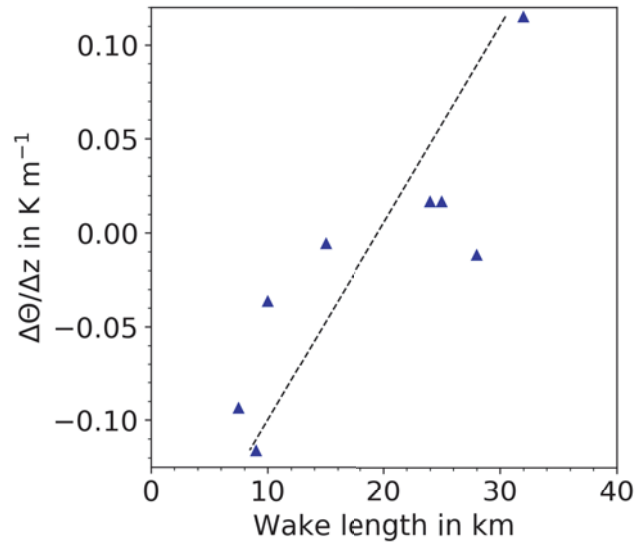


**Figure 3:** Scatterplot of SAR derived wake lengths versus atmospheric lapse rate  $\gamma = \frac{\Delta\theta_v}{\Delta z}$  derived from FINO-1 data (adapted from DJATH et al. (2018)).

The second data source for the determination of the stability were the airborne measurements. We used the vertical profiles obtained during the WIPAFF measurement flights close to the wind parks as marked in Figure 1 for the stability estimation. Further, to examine the relationship between wake expansion and stability, the wake length obtained from flight data (e.g Figure 4) was compared to the stability parameters such as  $L$ ,  $Ri_B$ , and  $\gamma$ . However, a general statement is difficult. Most promising results were achieved using  $\gamma$  (Figure 5a), using a height interval  $\Delta z$  from the uppermost position of the wind turbine blade tip (at 150 m agl for the Amrumbank West wind park AW, for instance) to the lowest position (at 30 m agl for AW). Thus, the height interval covers the entire rotor area, as this was assumed to be the most representative height interval with respect to the wake origin.

Looking at the distinct wind park clusters (Figure 5), the correlation between wake length and stronger stability, as observed for the wind parks GO (Godewind) and AW, can be approximated by two different exponential functions. This is an indication that there are more parameters that govern the wake length, in addition to stability – possibly also the wind-park architecture as considered in the analytical model. Moreover, strong stability coincides with the absence of short wakes. In addition, there is a correlation between higher wind speed deficit with more stable atmospheric conditions (not shown), while small wind deficits occur during more convective conditions.

Using the airborne data set of the WIPAFF project, a distinct correlation between the wake length and the other stability parameters  $L$  and  $Ri_B$  (not shown) was not apparent. Summing up, the correlation analysis for wake length and stability exhibits large uncertainty and data scatter. A major problem is the exact determination

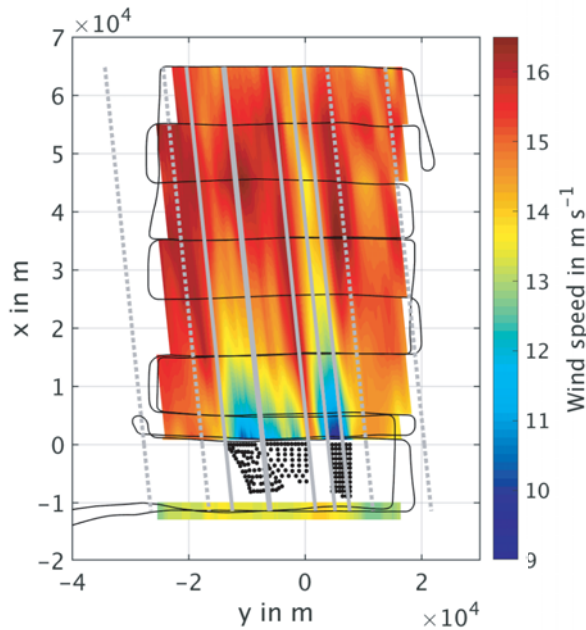


**Figure 4:** Contour plot of the interpolated wind field, measured during Flight 31 on 08 August, 2017, including the indication of the undisturbed wind field (grey dashed lines) and the wake boundaries (grey solid lines). The black line refers to the flight track (so-called “meander pattern”), black dots indicate the wind turbines of the wind park cluster Amrumbank West, Nordsee Ost and Meerwind Süd/Ost. The mean wind direction is from the east. The top of the map is oriented towards the west. Adapted from [PLATIS et al. \(in review\)](#).

of stability. A variation of e.g. the height interval for the lapse rate  $\gamma$  or the occurrence of an inversion below the hub height (cf. Section 4.1.3) changes the results significantly. A more detailed analysis will be shown in a following study.

#### 4.1.3 Vertical Structure of wakes

The vertical structure of the atmospheric boundary layer approaching the wind park has a decisive impact on the wake forming. Especially the occurrence of temperature inversions is important. The aircraft data documented several cases where the inversion was either below, at the rotor area of the turbines, or above ([SIEDERSLEBEN et al., 2018b](#)). In each of these cases a different behaviour of the wake could be observed. The main challenge with inversions near to or at hub height is that the thermal stratification of the atmospheric boundary layer and the respective level of turbulence are different below and above the inversion. This makes it very difficult to assign a specific thermal stratification to an observed wake development. An inversion below the rotor area decouples the wake development from the state of the sea surface. An inversion above the rotor area prevents the wake from spreading into higher parts of the boundary layer. Inversions are quite common above the North Sea, especially if the flow comes from land upstream. Internal boundaries form when the flow transits across the shoreline from land to water (see, e.g., [SMEDMAN et al., 1997](#)).

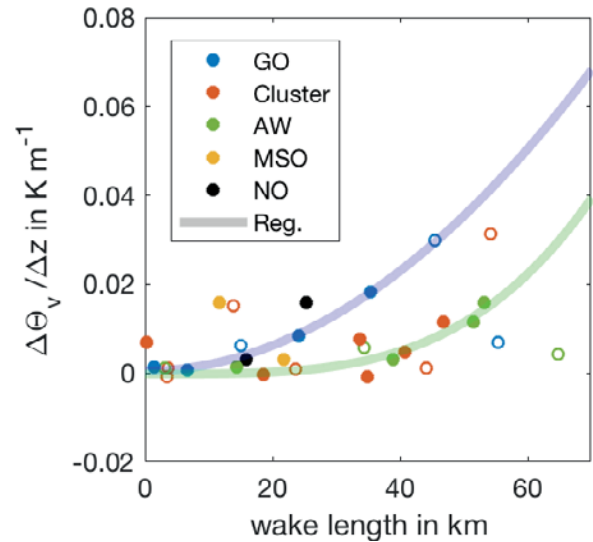


**Figure 5:** Scatter plots of the wake length versus lapse rate  $\gamma = \frac{\Delta\Theta_v}{\Delta z}$  obtained from the flight measurement. The according wind park is colour coded. Wakes were measured downstream of the wind parks Amrumbank West (AW), Nordsee Ost (NO), Meerwind Süd/Ost (MSO), Godewind (GO). Cluster implies that only one single wake was identified downstream of the wind park cluster consisting of the wind parks AW, NO and MSO. The regression lines (Reg.) are color coded with respect to the color of the respective wind farm cluster. The regression line is plotted is blue for the wind farm GO green and for the AW. In the case the wake length exceeds the coverage of the flown meander pattern (cf. Figure 4), the non-filled marker is used for the minimum measured wake length.

Given the distance of the North Sea wind parks from the coast the top of this internal boundary layer is very often found in the height range of the rotor area ([LAMPERT et al., 2020](#)). There are not only newly-formed inversions at the top of internal boundary layers but also inversions advected from the land upstream where they had formed due to radiative cooling in the nocturnal boundary layer. If these cold near-surface layers are advected over warmer sea water, the layer underneath the inversion can be turned into a neutral or even slightly unstable layer while the stratification above the inversion remains more or less unchanged. The propagation conditions for wind park wakes may be further complicated by jet-like wind maxima at the top or just above the internal boundary layer (see, e.g. [SMEDMAN et al., 1996](#)). The variety of different vertical profiles of potential temperature and wind speed from 26 aircraft operations in WIPAFF is documented in [SIEDERSLEBEN et al. \(2018b\)](#); [LAMPERT et al. \(2020\)](#) while a case study from one flight is presented in [SIEDERSLEBEN et al. \(2018a\)](#). It is not only the propagation of the wake which is determined by the vertical structure of the air approaching the wind parks but the vertical structure also determines whether the air at hub height behind the wind park is warmer or cooler than before. Figure 6 shows a schematic of this dependence. An inversion in the upper part or just above the rotor area associated with turbulent vertical



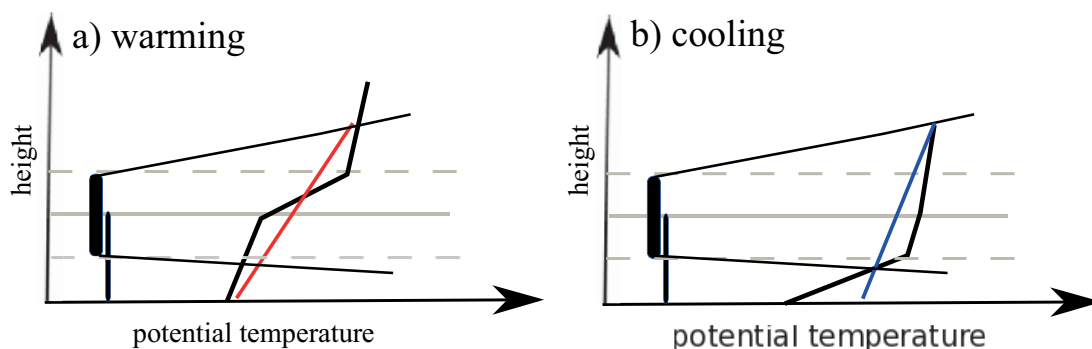


**Figure 6:** Schematic of stability-dependent temperature change at hub height in wind park wakes (left: warming, right: cooling). Bold vertical line: rotor disk, cone-like structure: wake, black vertical profile: initial temperature profile, red and blue curves: temperature profiles modified by the wake. (From [SIEDERSLEBEN et al., 2018b](#))

mixing within the wake results in a warming of the air at that height. In contrast, an inversion in the lower part or just below the rotor area results in a cooling of the air at that height. In a constantly stable boundary layer without inversions turbulent mixing within the wake will lead to warming below hub height and cooling above hub height. This warming below hub height is similar to satellite observations of nocturnal surface warming behind onshore wind turbines (see, e.g. [XIA et al., 2017](#) and references therein). Nevertheless, the observed temperature changes are merely a vertical re-distribution of heat by the additional turbulence in the wake.

#### 4.1.4 Wakes covered by mesoscale and industrial models

The numerous observations of wakes allowed the evaluation of wake simulations. Within the WIPAFF project, two kind of simulations were evaluated. First of all, mesoscale simulations using WRF and the wind park parameterization of [FITCH et al. \(2012\)](#) were compared against the airborne observations. Secondly, we tested the ability of commonly used industrial models to capture wakes of large offshore wind parks during stable conditions. In this overview paper we focus on observations covering simulations of a wake event observed on 10 September 2016 during atmospheric stable conditions and moderate wind speed of around  $8.5 \text{ m s}^{-1}$ .

The WRF simulations captured the horizontal dimensions of the wake but overestimated the vertical extent ([SIEDERSLEBEN et al., 2018a](#)). The wake observed on 10 September 2016 extended more than 45 km downwind of the wind park Amrumbank West, agreeing with the simulations [PLATIS et al., 2018](#). However, the vertical extent of the wake was overestimated in the simulations. For example, a wind deficit in the order of 5%–10% was observed 5 km downwind of the last turbines of Amrumbank West at 200 m above MSL. In contrast, a wind deficit on the order of 20% and 15% was simulated (not shown).

The simulated wind speed upwind of the wind parks was  $1.5 \text{ m s}^{-1}$ – $2 \text{ m s}^{-1}$  too low [SIEDERSLEBEN et al., 2018a](#). Consequently, the wind speed within the wake of

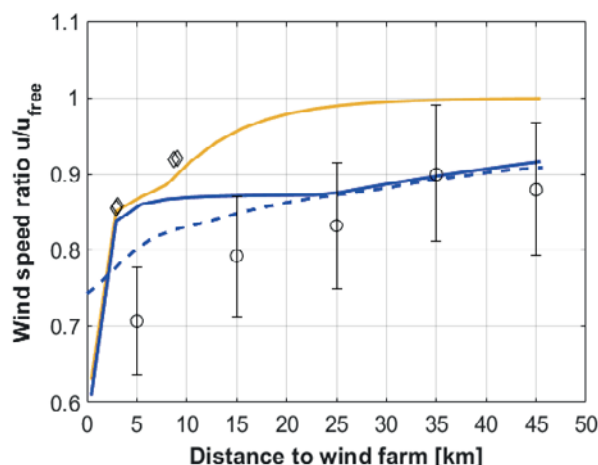


**Figure 7:** Wind speed reduction relative to free wind speed (10 m/s) in the wake of the wind park cluster Amrumbank/North Sea Ost/Meerwind on 10 September 2016. Shown are the flight data (black dots with error bars), the WRF simulation (blue dashed line), as well as two wake simulated with WindFarmer: default settings (orange solid line) and adjusted settings (blue solid line) the diamonds correspond to the original measurements used to calibrate the default WindFarmer set-up [DNV-GL, 2013b](#).

the simulations was underestimated as well (Figure 7). Aircraft vertical profiles of the atmosphere obtained by climb flights revealed that the simulated stratification of the atmosphere was too unstable at the transition area from land to open ocean. Therefore, we suggest that the overestimated vertical extent of the simulated wake is rooted in a wrongly simulated stratification of the atmosphere.

To compare the WRF simulation and the industrial model (WindFarmer Version 5.2.11 was used within the project) with the flight measurements, a methodology similar to that described in [CAÑADILLAS et al. \(2020\)](#) was used to extract the minimum value of the wind speed along the wake centerline. Layouts and turbine types were chosen identical to those used in the WRF simulation. In WindFarmer, the model options “modified PARK” and “IBL” (internal boundary layer) were selected. This combination is based on the best repre-

sensation of the park effects in offshore wind parks and clusters to determine park yields. While the wind speed deficit in the modified PARK and Eddy Viscosity models decreases with increasing turbine spacing, this is not the case in the IBL implementation, which is of course unphysical. The recovery of the wind velocity deficit from the IBL model was therefore realized by an additional function (so-called “wake recovery function”). Downstream of the wind farm, the wind speed recovery is modelled explicitly as a power function [DNV-GL, 2013a](#)

$$U_R(x) = 1 - \left(1 - \frac{U}{U_\infty}\right) 0.5^{\left(\frac{x-x_{\text{start}}}{x_{50\%}}\right)}, \quad (4.3)$$

where  $x_{\text{start}}$  is the downstream distance specifying the start of the power function, and  $x_{50\%}$  is the location where the wind speed recovery  $U_R$  has recovered to half its initial value.

The standard parameterization of the wake recovery function starts at  $x_{\text{start}} = 60D$  ( $D$  is the rotor diameter; here  $D = 120$  m) behind the turbine and after another  $x_{50\%} = 40D$  has reduced half of the wind speed deficit. These values were derived by WindFarmer from mast measurements at the lee side of the Danish wind parks “Horns Rev” and “Nysted”. With this parameterization the wake curve (orange solid line) is obtained by [DNV-GL, 2013b](#), which is shown in Figure 7. Apparently the wind speed recovers much faster with this parameterization than measured by the research aircraft on 10 September 2016.

A more detailed analysis shows that the measuring masts at “Horns Rev” and “Nysted” are each installed east of the parks, so that the park wake there can only be determined with westerly winds. It is known from stability studies conducted at the offshore mast FINO1 that neutral to stable stability conditions dominate in westerly winds ([EMEIS et al., 2016](#)). Probably the parameters for the wake recovery function in WindFarmer were determined on the basis of neutral to unstable stratifications. By contrast, neutral to slightly stable conditions prevailed on 10 September 2016.

It is known from the observations in WIPAFF ([CAÑADILLAS et al., 2020](#)) and from the analytical wake model of Section 4.1.5, that considerably larger wake lengths result with stable atmospheric stratification compared to neutral and unstable stratification. This supports the assumption that the wake length differences between the measurements and the standard parameterization in WindFarmer are mainly due to an incorrect accounting of stability effects in the default set-up of Wind Farmer. However, the measurements can be well reproduced by a different parameterization (start of wake recovery at  $200D$ , 50% recovery after another  $200D$ ) for distances beyond 22 km from the wind park cluster (Figure 7). For further discussions, please refer to [CAÑADILLAS et al. \(2020\)](#).

#### 4.1.5 Wake Decay Formula

Besides the numerical models, a simple analytical model approach to determine the wake length and wind speed recovery was validated based on the flight data collected during WIPAFF [PLATIS et al., in review](#). The analysis of several different case studies (Figure 8) suggests that the recovery in terms of the wind speed ratio (wake wind speed to undisturbed wind speed at hub height) can be characterized by an exponential function as expected from the analytical model described in [EMEIS \(2010\)](#); [EMEIS \(2018\)](#).

The advantage of the model is that the spatial behavior of the reduced wind speed  $u_r(x)$  in the wake at the downstream distance  $x$  is described in a single equation. It solely depends on the initial wind speed deficit  $u_{r0}$  directly downstream of the wind farm and the wake recovery rate  $\alpha$ .

$$u_r(x) = u_f + (u_{r0} - u_f) \exp(-\alpha x) \quad (4.4)$$

where  $u_f$  is the undisturbed (free) wind speed (outside the wake) at hub height. The wake recovery rate  $\alpha$  is

$$\alpha = \frac{K_m}{(\Delta z)^2}, \quad (4.5)$$

where  $K_m$  is the momentum exchange coefficient. The height  $z = h + \Delta z$  describes the height where the undisturbed wind speed is reached above the wind farm.

By testing the analytical model against the airborne data set, we showed in [PLATIS et al. \(in review\)](#); [CAÑADILLAS et al. \(2020\)](#) that the analytical model performs very well as a first-order approximation. This strengthens the hypothesis that the vertical downward momentum flux is the dominating factor for the wake recovery. Best agreement of the exponential wake recovery curve with the observations was achieved for the case study for Flight 31 (Figure 4). The wind data was extracted based on the method described in [PLATIS et al. \(in review\)](#) and plotted in Figure 8, showing the relative wind speeds between the wind speed in the wake and the undisturbed speed behind several wind farms during which stable and homogeneous conditions prevailed. Further results are discussed in detail in [PLATIS et al. \(in review\)](#); [CAÑADILLAS et al. \(2020\)](#).

A drawback of the analytical model is the determination of the separation height between the hub height and the undisturbed flow above the wind park which must be specified in order to determine the decay coefficient in the exponential wake recovery relation as already noted by [PEÑA and RATHMANN \(2014\)](#). It is also expected, that  $\Delta z$  might not be constant along the wake. Further, the impact of the park layout on the intensity and length of the wake is only covered by the analytical model through the initial deficit. Apart from that, the decay coefficient in the analytical model does not depend on the turbine-induced turbulence left over from the wind park, but only on the upstream conditions. As expected by [PORTÉ-AGEL et al. \(2020\)](#) a modification of



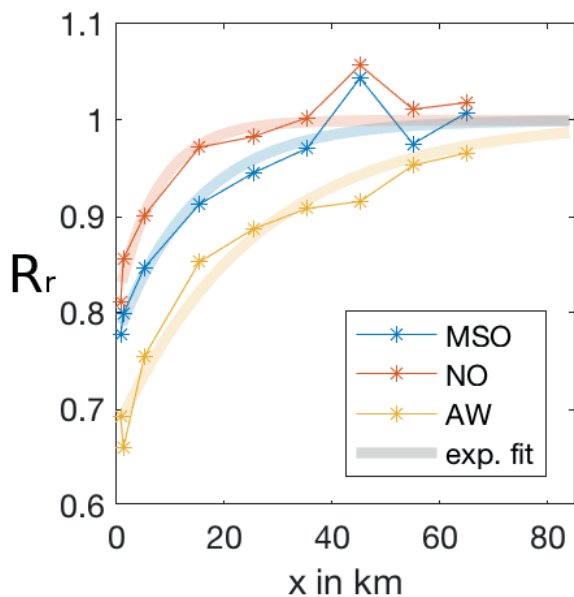


**Figure 8:** Wind speed ratio  $R_r = \frac{u_r}{u_{im}}$  between the wind speed inside ( $u_r$ ) and outside the wake ( $u_{im}$ ) of flight 31 on August 8, 2017. Dots indicate the measured ratios  $R_r = \frac{u_r}{u_{im}}$  and the line the exponential fit according to the analytical model. Blue indicates the wind speed analysis in the wake downstream of the wind farm Meerwind Süd/Ost (MSO), red Nordsee Ost (NO) and yellow Amrumbank West (AW). Adapted from [PLATIS et al. \(in review\)](#)

the atmospheric stability (e.g.  $u_*$ ) by forming a farm-induced internal boundary layer (IBL) is likely and has to be considered in further editions of this model.

#### 4.1.6 Wakes change the sea surface

Wakes downstream wind parks are visually detectable on SAR images and usually characterized by dark streaks in line with wind direction (Figure 2). However, some images show brighter areas (increase of NRCS and thus wind speed) within the first 10 km downstream the wind parks. An example of an increase of NRCS downstream of the wind park is shown on Figure 9 acquired on 18 June, 2017 at 05:48 UTC during stable stratification (air temperature is 16 °C, while SST is 15.4 °C). This leads to an inferred increase of wind speed in Figure 9b, which is an unusual behavior. The mechanism of this behaviour is unknown. Nevertheless, a theoretical model was proposed in [DJATH et al. \(2018\)](#), which tried to explain this atypical observation by an increased downward momentum flux associated with increased turbulence generated by the wind park. Indeed, the turbulence, which is generated mechanically by the wind turbines, leads to an increase of friction velocity and radar cross section. The turbulence slowly dissipates downstream and after some distance the downward momentum flux is not effective any more. Mechanisms of this kind can be expected to be most effective in atmospheric stable stratification with strong vertical wind speed gradients. The SAR observations are confirmed by airborne laser scanner observations: Within the wake,

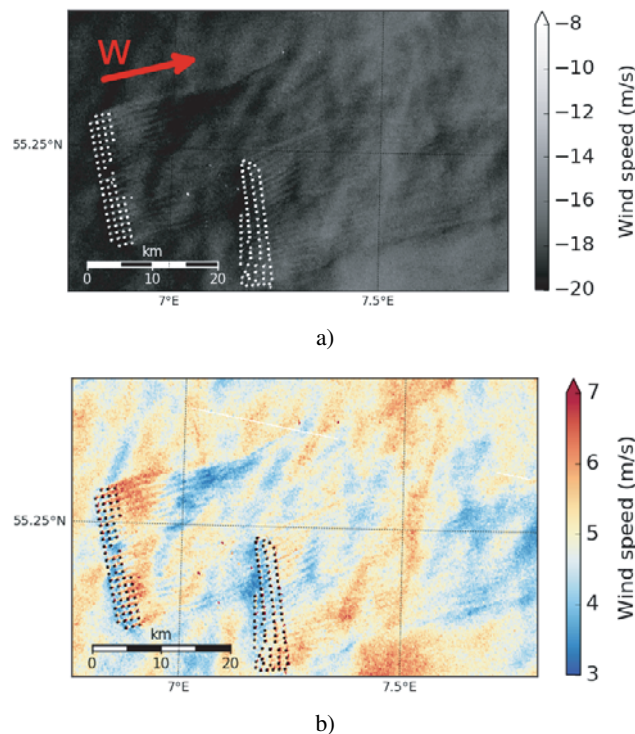


**Figure 9:** Normalised radar cross section (a) associated with sea surface roughness as derived from a Sentinel-1B image acquired on 18 June 2017 at 05:48 UTC (Copernicus Sentinel data [2007]) and derived near surface wind speed (b) showing an increase of NRCS and wind speed within the first 10 km downstream Sandbank (wind park on the left) and DanTysk (wind park on the right) wind parks. The red arrow indicates the wind direction.

the reflectance is significantly enhanced (Figure 10c). An explanation is the flatter surface, which reflects back more energy of individual laser pulses, as they are only little scattered. Further, the number of returned pulses is reduced. A smoother surface reflects the laser pulses more directed, reducing the probability of receiving a reflected laser pulse.

## 4.2 On hypothesis 2: Wakes and increased turbulence

### 4.2.1 Turbulence in the wake

The reduction of the wind speed by wind turbines leads to an area of low wind speed which can generate large horizontal shear at the boundary between the undisturbed wind field and the wake. For flights perpendicular to the wake at hub height, the measurements show strongly enhanced turbulence parameters at the edges of the wakes. For pronounced far-reaching wakes, the turbulent kinetic energy (TKE) at the edges of the wake is still at the same level several 10 km behind the wind park (Figure 10b). During the airborne measurements, the enhanced aircraft vibrations during entering and leaving the wake were noticeable to the crew. Turbulence was found to be particularly enhanced for high wind speed gradients between the wake and the undisturbed flow

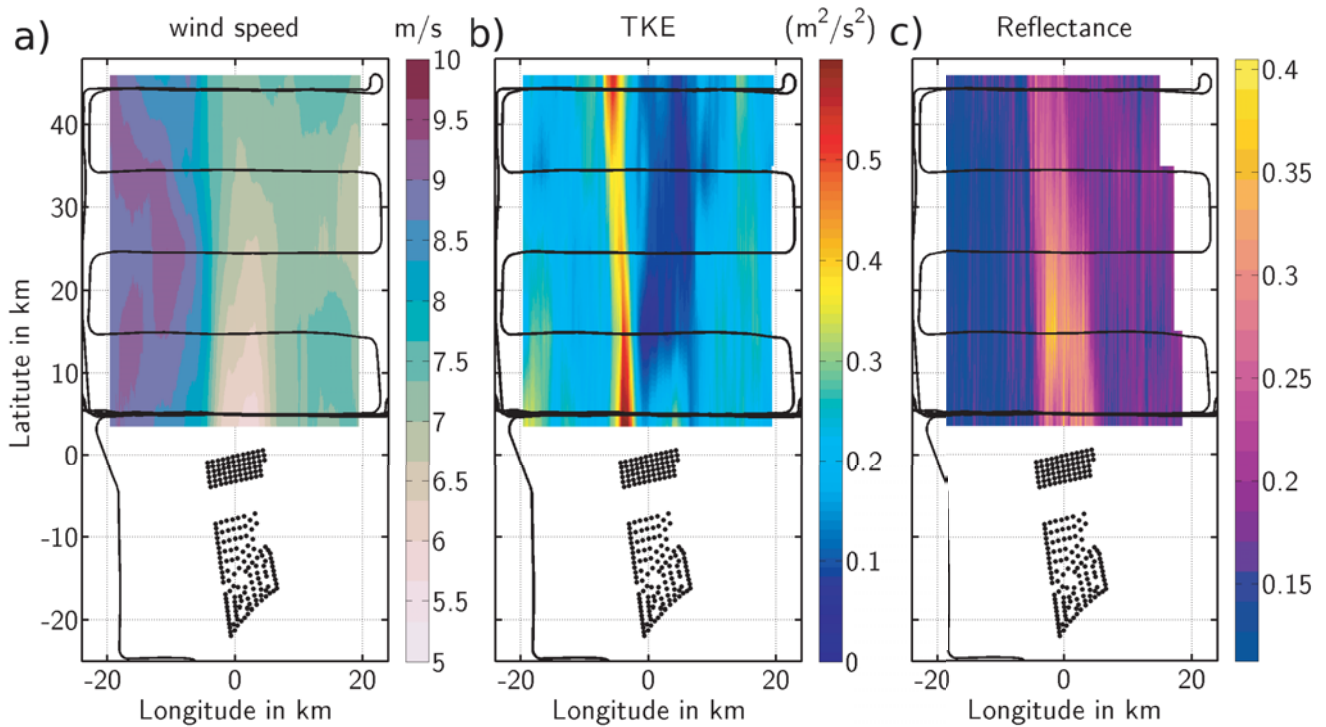


**Figure 10:** Measurements of wind speed (a), turbulent kinetic energy (b) and surface reflectance (c) downwind of the wind parks Amrumbank West, Nordsee Ost and Meerwind Süd/Ost. The measurement flight took place on 10 September 2016. Adapted from [PLATIS et al. \(2018\)](#).

(Figure 10a, b), and for denser wind park geometries. In contrast, within the wake, turbulent kinetic energy is reduced even compared to the undisturbed flow (Figure 10b).

As any change in wind field at the turbine level affects also the sea surface, SAR is capable of detecting the horizontal shear on the edge of the wake through the roughness as well. Figure 9a shows an example of the roughness by the indication of the Normalized Radar Cross Section (NRCS), obtained by Sentinel-1A on June 18, 2017 at 05:48 UTC during stable conditions (air temperature at 50 m was 16 °C and 15.4 °C for the sea surface temperature). Strong increases of NRCS and friction velocity can be seen at the boundaries of wakes downstream wind parks at the northern edge of the two wind parks.

Similarly, the derived wind speed at 10 m altitude (Figure 9b) using the geophysical model function CMOD5N GMF ([HERSBACH et al., 2007](#); [VERHOEF et al., 2008](#)) tuned for C-band displays an increase of amplitude at the edge. These features can be explained by the considerable horizontal shear that exists between the wind field inside the wake and outside the wake. This shear leads to an increase in turbulence, which is also captured in numerical model simulations ([ABKAR and PORTÉ-AGEL, 2015a](#)). The higher turbulence levels at the boundaries of wakes have also been confirmed by airborne lidar surface roughness measurements ([PLATIS et al., 2018](#)), see Figure 10. This turbulence then causes an increase in the downward momentum flux, which can

explain a growth of the friction velocity and hence the radar cross section. This effect can be expected to be particularly effective in stable situations with strong vertical wind speed gradients. These are actually the conditions where wakes are most visible on SAR images. A semi-empirical model to describe the effect of increased downward momentum flux associated with turbulence on surface roughness measured by SAR is given in [DJATH et al. \(2018\)](#).

#### 4.2.2 TKE above the wind park

The mixing above offshore wind parks determines the wake recovery as pointed out in [EMEIS \(2010\)](#). Consequently, mesoscale WPPs should represent the enhanced mixing above offshore wind parks to capture the correct wake extent. In [SIEDERSLEBEN et al. \(2020\)](#) we presented three aircraft case studies, where the TKE above the wind parks Godewind and neighbouring wind parks Nordsee Ost and Meerwind Süd/Ost was measured and compared to mesoscale simulations.

The most important ingredient for capturing the TKE above offshore wind parks with WPPs are correctly simulated upwind conditions. The WPP of [FITCH et al. \(2012\)](#) captured the enhanced TKE above the wind parks Godewind 1, 2 during onshore winds. In contrast, the model overestimated the TKE above the wind parks during offshore winds. By the use of vertical profiles taken by the aircraft close to the coast, we showed that the boundary layer parameterization (MYNN 2.5, [NAKANISHI and NIINO, 2004](#)) was not able to represent the

transition from land to open ocean close to the coast in case of offshore winds. Hence, we suggest the deviation of the simulated and observed TKE above offshore wind parks is largely rooted in the deviation of the simulated and observed upwind conditions. These results agree with the findings in [SIEDERSLEBEN et al. \(2018a\)](#) (Section 4.1.4) where the overestimated extent of the wake was related to deviations between the simulated and observed stratification of the atmosphere.

We recommend using the TKE source of the WPP of [FITCH et al. \(2012\)](#) for offshore wind park simulations during stable conditions, especially for simulations having a horizontal grid coarser or equal to 5 km. For example, simulations with a horizontal grid size of 16 km did not capture the enhanced mixing over the wind parks although the WPP of [FITCH et al. \(2012\)](#) adds additional TKE to the model to account for the not resolved shear within the simulations.

The WPP of [FITCH et al. \(2012\)](#) adds too much TKE at the upwind side of a wind park. During two case studies it was observed that TKE above the wind parks increased with the path of the air through the wind park resulting in a higher TKE at the downwind side of a wind park than on the upwind side. In contrast, the WPP simulated the highest TKE at the upwind side of the wind park associated with the highest wind speeds and wind park density at the front row turbines. On the other hand, the wind speed deficit is underestimated with a disabled TKE source. Therefore, we suggest to use the TKE source for stable conditions ([SIEDERSLEBEN et al., 2020](#)) although the TKE at the upwind side of the wind park might be overestimated.

#### 4.2.3 Wave-number spectrum vs. stability

Wave-number spectra were computed from the 10 m-wind speed derived from the SAR dataset taking into account the stability conditions based on the thermal stratification from the FINO1 data. The spectral analysis is performed for the period September 2016 to May 2017 and considered stable and unstable stratification cases. The results for all stability cases are shown in Figure 11. Each spectrum represents the average over the considered period. Although their spectral forms appear to be different at high wavenumber, the shapes look quite similar in general at low wavenumber. The slope is quite close to the  $k^{-5/3}$  power law ([POND et al., 1966](#); [KAIMAL et al., 1972](#); [NICHOLLS and READINGS, 1981](#); [CHIN et al., 1998](#); [WIKLE et al., 1999](#); [CHO et al., 1999b](#); [CHO et al., 1999a](#); [HÖGSTRÖM et al., 2002](#); [TULLOCH and SMITH, 2009](#); [XU et al., 2011](#)).

The change in stability does not affect the spectral slope in general, but rather modifies the amplitude of spectral power. The spectral power for unstable conditions (green curve in Figure 11) is indeed higher than the spectral power of stable conditions (black in Figure 11). This analysis is in agreement with the previous works ([KAIMAL et al., 1972](#); [NICHOLLS and READINGS, 1981](#); [DJATH and SCHULZ-STELLENFLETH, 2020](#)).

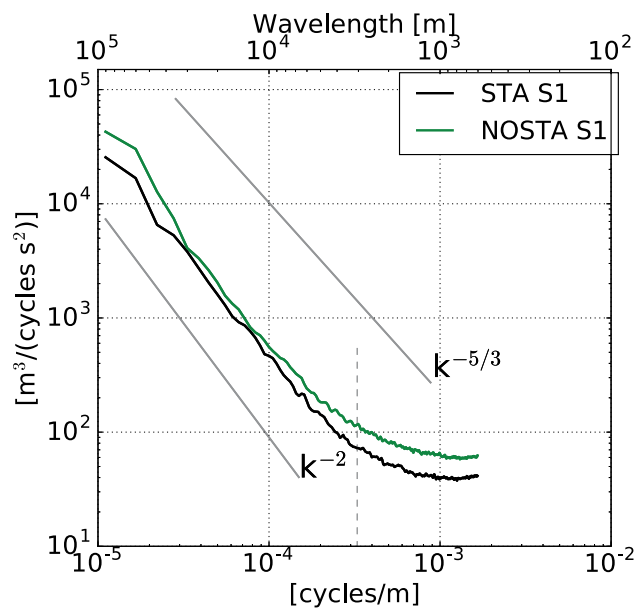


**Figure 11:** Wavenumber spectra computed from near-surface wind fields derived from Copernicus Sentinel-1 data. “STA” stands for stable cases (black curve) and “NOSTA” for unstable cases (green curve).

The high spectral power associated with the unstable stratification confirms that the unstable flows are more turbulent than stable flows. Within the wind park wake context, the generation of turbulence increases mixing and therefore dampens the wake, which lead to having no or short wakes during unstable conditions, while long wakes are pronounced for stable stratification ([CHRISTIANSEN and HASAGER, 2005](#); [DJATH et al., 2018](#)).

#### 4.2.4 Anisotropy spectra aligned wind direction

2D wind spectra were also computed from the mean normalised wind speed (Figure 12). As the stable atmospheric boundary layers are favorable conditions, where wakes are most pronounced, the spectrum is estimated by averaging over the spectra of SAR derived wind fields for stable cases as derived from FINO1. The spectrum is oriented with the wind direction along the horizontal axis. It is interesting to note, that the isolines are bunched in the wind direction, at least for wave lengths shorter than about 10 km. This is equivalent to the occurrence of wind field structures, which are aligned in wind direction. For instance, the atmospheric boundary rolls are aligned with wind direction and are used to estimate the wind direction on SAR images ([KOCH, 2004](#)).

### 4.3 On hypothesis 3: Impact on other wind parks downstream

The impact of far wakes on the environment and on other wind parks depends on the wake length and on the shape of the wind speed recovery within the wakes. In [CAÑADILLAS et al. \(2020\)](#) data from 11 flight measurements collected within the wakes at several downstream



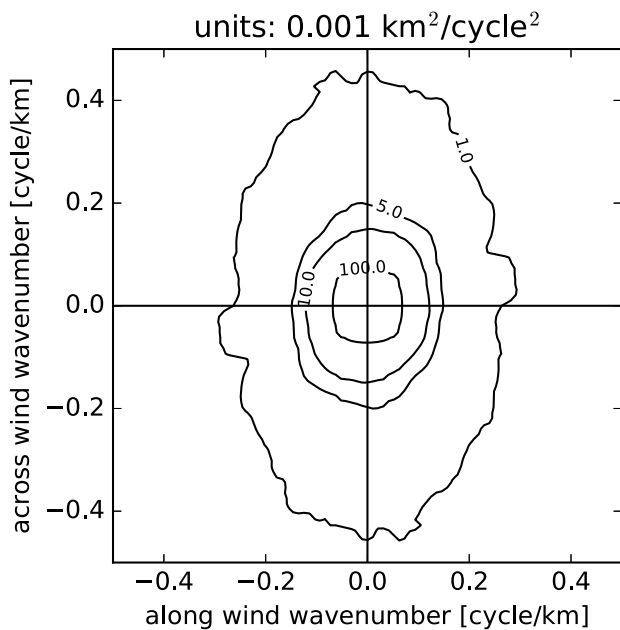


**Figure 12:** Mean 2D wind modulation spectrum estimated from SAR derived normalised wind field spectra.

distances of two offshore wind park clusters were analyzed.

A method was developed to extract the wake recovery function of each measurement flight and a median value was computed for each stable and neutral/unstable atmospheric conditions group. It allowed to calibrate the engineering model WindFarmer used in WIPAFF project. For further details please refer to CAÑADILLAS et al. (2020).

The findings from this study support the results in Section 4.1.1–4.1.2 that stable stratifications is associated with significantly longer wakes characterized by a slower wind speed recovery compared to unstable conditions. The results show that the average wake length under stable conditions exceeds 50 km, while under neutral/unstable conditions, the wake length typically extends to 15 km similar to the results presented in Section 4.1.2. The default settings of the engineering model WindFarmer have to be modified to account for a slower wind speed recovery in stable stratification, as the observed length of wakes under these conditions highly exceeds the wake length arising from the default settings (see Figure 7).

The examination of the effect of the modified recovery on the park efficiency of an isolated downstream wind farm cluster reveals that, for distances > 30 km, the calculated reduction of the wind park efficiency does not exceed 0.5 %. This is considered to be a lower limit of the actual economic effect, as distances between most wind park clusters in the German exclusive economic zone (EEZ) and other offshore regions are < 30 km. However, modelling wakes at distances < 30 km downstream requires modification of not only the stability behaviour of the wind speed recovery, but also of the direct wake and IBL models.

### 4.3.1 Influence of park architecture

The effect of wind park architecture was estimated when distinct wakes were visible downstream of single wind parks within the same atmospheric conditions. As presented in PLATIS et al., in review this was the case for the Flights 25, 30 and 31 within the WIPAFF project. Here, a distinct example is shown in Figure 4 for the case study Flight 31. The wakes of the two adjacent parks Meerwind Süd/Ost (MSO) and Nordsee Ost (NO) are similar in their length (15 to 21 km). However, they differ in the initial wind speed deficit, i.e. 29 % for MSO and 19 % for NO. The wake of the very dense wind park AW is significantly longer at 38 km with initial wind deficit of 28 %. Other case studies showed similar observations in PLATIS et al., in review. As a consequence, it can be concluded that a clear influence of the park layout is evident and longer wakes appeared with a denser alignment of wind turbines in contrast to a low-density wind park. Therefore, to minimize the impact of downstream installations a less narrow alignment of the wind turbines could be considered in future offshore wind park planning.

### 4.4 On hypothesis 4: Impact of wind-park wakes on local climate and surface fluxes

Given the warming and cooling in the rotor layer associated with the enhanced vertical mixing at the rotor area (Section 4.1.3) the question arises whether wind parks can alter local climate.

A change in local climate would be equal to a change in the energy budget of the atmosphere. According to TRENBERTH et al. (2001) and PORTER et al. (2011) a change in the energy budget of the atmosphere is associated with a change in radiation budget and/or in the turbulent surface fluxes. Hence, it is relevant whether the temperature and moisture changes at hub height as investigated in SIEDERSLEBEN et al. (2018b) are associated with temperature and moisture changes at the surface that in turn could enhance the turbulent fluxes at the surface resulting in a change of the energy budget of the atmosphere. Temperature and moisture changes were well observed on 10 September 2016, hence, we investigated the potential impact of all planned and existing offshore wind parks in the German Bight on the turbulent surface fluxes (i.e. sensible and latent heat flux) by the use of WRF simulations. The locations of the planned wind parks follow plans of the Bundesamts für Seeschifffahrt und Hydrographie (BSH) published in 2015 (Figure 13). Although such a numerical simulation can not give an answer on whether offshore wind farms have an impact on the local climate or not, we can still determine the maximal impact of offshore wind farms on the boundary layer by simulating a day, that was characterised by large wakes in the German Bight. Based on these results further studies should be conducted, investigating the impact of offshore wind farms on the local climate.

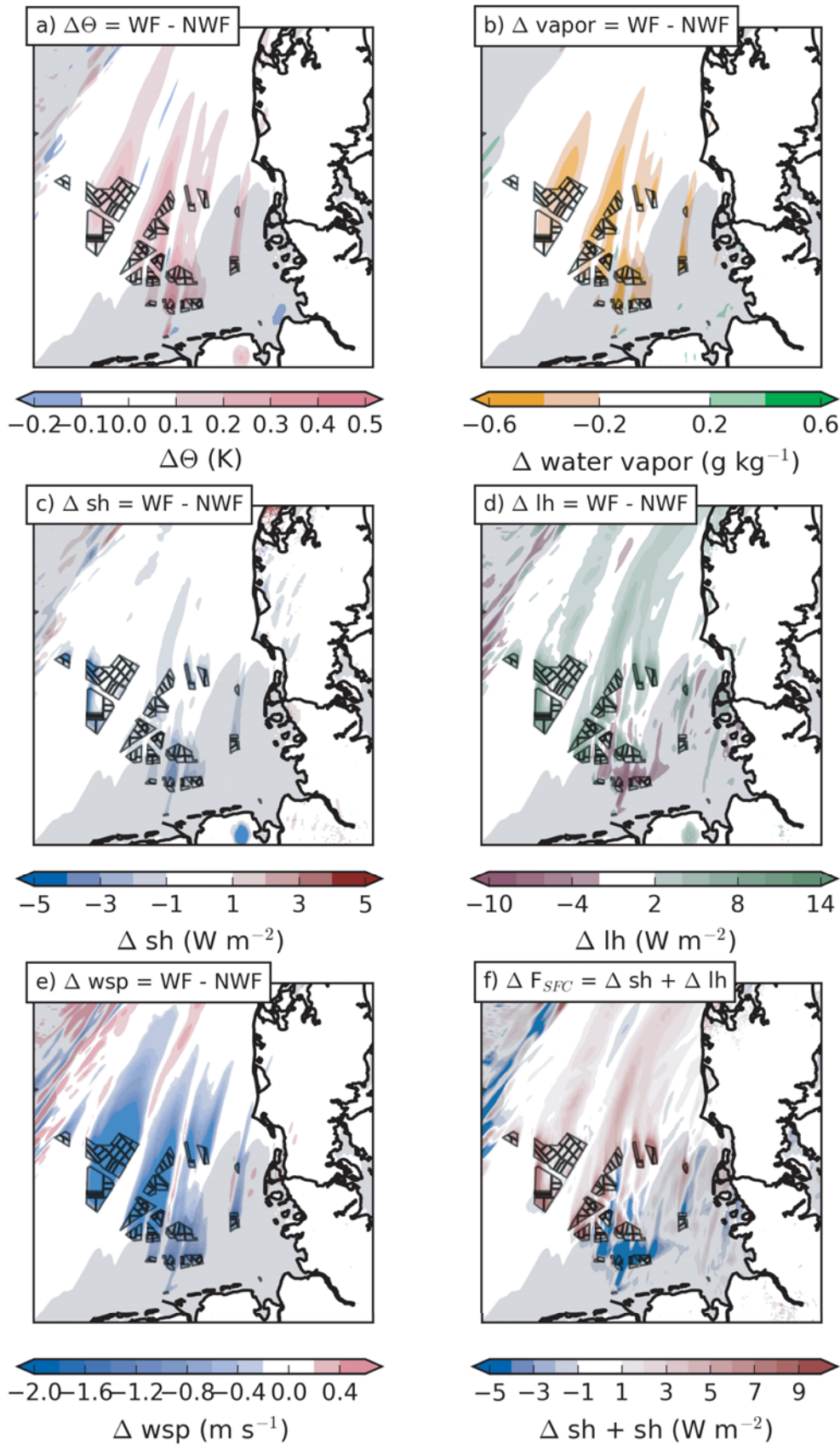


**Figure 13:** The impact of all potentially planned offshore wind parks at the North Sea for the meteorological situation 10 September 2016 averaged from 08:00 UTC to 09:00 UTC. Shown is the difference at hub height of (a) potential temperature, (b) water vapor mixing ratio and (e) wind speed between a simulation with wind parks (WF) and a simulation with no wind parks (NWF). The resulting changes of sensible heat flux (sh) and latent heat flux (lh) are shown in (c) and (d). The sum of differences in sensible and latent heat flux is shown in (f). The gray shading depicts areas where the SST is higher than the air temperature. Taken from [SIEDERSLEBEN \(2019\)](#).



Although some wind parks in the simulations are much bigger than already existing wind parks in the German Bight, the impact on temperature and water vapor at hub height is not larger than observed on 10 September 2016 (Figure 13a–b). For example, the simulations suggest a warming and a drying at hub height in the order of 0.5 K and  $0.5 \text{ g kg}^{-1}$  downwind of the large offshore wind park cluster located in the west of the domain. For comparison, the already existing wind parks around Amrumbank West cause a similar warming signal at hub height.

The warming induced by the wind parks in the rotor area is partly associated with a decreased sensible heat flux at the surface (Figure 13c). Two different processes drive the reduction of the sensible heat flux rooted in the different temperature gradients between the SST and the lowest model level located at 17 m AMSL (Figure 14). On 10 September 2016 we encountered areas with a lower air temperature than SST (i.e. gray shaded area in Figure 13, SIEDERSLEBEN, 2019). During non-waked conditions the sensible heat flux is orientated towards the atmosphere in these regions, resulting in a warming of the lower atmosphere (Figure 14a). According to aircraft measurements recorded on 10 September 2016, the warming induced by the wind turbines was also effective at 60 m AMSL (see Figure 4a in SIEDERSLEBEN et al., 2018b). The simulations indicate that the warming at the rotor area even spread down to the ocean's surface. Consequently, a higher surface temperature results in a reduction of the temperature gradient between air temperature and SST that in turn weakens the sensible heat flux towards the atmosphere as it is schematically sketched in Figure 14a). In contrast, the sensible heat flux is orientated towards the ocean in case of a lower SST than air temperature (*not* gray shaded area in Figure 13) during non-waked conditions. However, a warming at the ocean's surface results in an increased temperature gradient between air temperature and SST, resulting in an larger sensible heat flux pointing towards the ocean (Figure 14b). Therefore, the net effect of the warming at the surface is an increased sensible heat flux towards the ocean (Figure 14b). However, the changes in the sensible heat flux are not larger than  $3 \text{ W m}^{-2}$ .

The impact of offshore wind parks on the latent heat flux is determined by the temperature gradient between SST and the temperature at the lowest model level (Figure 13d). In areas with a higher SST than air temperature the simulated latent heat flux is decreased. In contrast, the latent heat flux is increased in areas with a higher air temperature than SST. As humidity usually has a strong vertical gradient in the marine boundary layer (decreasing with height), the latent heat flux is pointing upward regardless of the temperature gradient. Obviously, the dryer air within the wakes of larger offshore wind parks enhances the vertical moisture gradient, that in turn should enhance the latent heat flux towards the atmosphere. However, this is only true for areas with a higher air temperature than SST (Figure 13d). In contrast, in regions with a lower SST than air temperature,

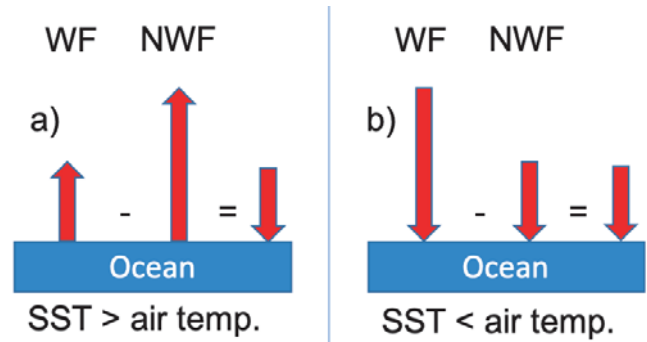


**Figure 14:** Schematic sketch of impact of offshore wind parks on the sensible heat flux in case of (a) a SST higher than the air temperature and (b) vice versa. WF is a wind park simulation with the wind farm parameterization turned on, while NWF has the parameterization switched off. Taken from SIEDERSLEBEN (2019).

we observe a decreased latent heat flux (purple contours in Figure 13e), although the latent heat flux is supposed to increased due to dryer air within the wake. Hence, we suggest, that the weakening of the temperature gradient between SST and air temperature mainly drives the changes in the latent heat flux.

The overall change in the surface fluxes is driven by the changes in the latent heat flux (Figure 13f), in case of inversions close to the rotor height. As the impact on 10 September 2016 on the latent heat flux is almost twice as much than the changes in the sensible heat flux the net impact on the surface fluxes is dominated by the changes in latent heat flux. As the changes in the latent heat flux are determined by the temperature gradient between the lowest model level and SST, so is the overall impact: A cooling effect is present in areas with a higher air temperature than SST and vice versa. However, we only observed a change in the latent heat flux associated with the existence of an inversion close to rotor height SIEDERSLEBEN et al., 2018b. Hence, the latent heat flux only dominates the overall impact in case of an inversion close to the rotor area otherwise only the sensible heat flux is affected.

The effects discussed above were observed in six of our flights, nevertheless for a sound climatology reliable conclusion, further studies are mandatory.

## 5 Conclusion/Outlook

A unique dataset from airborne *in situ* data, remote sensing by laser scanner and SAR gained during the WIPAFF project proves that wakes up to several tens of kilometers exist downstream of offshore wind farms. The wind speed deficits in the wakes and their length tend to be larger in stable than in unstable conditions. The results show that the average wake lengths under stable conditions exceed 50 km, while under neutral/unstable conditions, the wake length amounts to 15 km or less. Data also indicates that a denser wind park layout increases the wake length additionally due

to a higher initial wind speed deficit. Turbulence occurs at the edges of the wakes due to shear between the reduced wind speed inside the wake and the undisturbed flow. The intensity depends on the strength of the wind speed gradient and is further enhanced for denser wind park geometries. In contrast, within the wake, turbulent kinetic energy is reduced even compared to the undisturbed flow.

The observational data of the WIPAFF project was further compared to industrial, analytical and mesoscale models. The respective models show in general a good correlation with the measured wake lengths, nevertheless, they also show deficiencies:

- As a first order approximation the analytical model seems to work well, however it has to be optimized to be able to account for the park layout and turbine turbine-induced turbulence left over from the wind park. This has to be improved in the future.
- The engineering model WindFarmer underestimates the wake length during stable conditions when using the default settings. Therefore, default settings of the engineering model WindFarmer have been modified to account for a slower wind speed recovery in stable stratification (CAÑADILLAS et al., 2020).
- The mesoscale WRF model enables the simulation of a complete area like the German Bight. However, the results of the simulations show that the WRF model is highly sensitive to the upwind conditions. During offshore winds (advecting warm air over the ocean) strong inversions developed at rotor height that are challenging for a mesoscale model. Hence, the up-stream wind speed was sometimes underestimated due to a wrongly predicted stratification in the model.

To accomplish accurate predictions of the wind energy production by numerical models, further effects have to be taken into account, e.g. the blockage effects of wind parks or how the state of the operation of wind parks influences the wakes, which requires the analysis of operational data. As such data was not available in the WIPAFF project, this is a topic of future research and implementation in numerical models.

Besides the wake effects, the influence of offshore wind parks on the marine boundary layer was investigated by using the airborne observations and the WRF model. The impact on the marine boundary layer depends on several parameters. First of all, wind parks can cause a warming or a cooling at hub height during stable conditions as discussed in Section 4.1.3. However, the inversion can also be located such that a cooling at the ocean's surface takes place, although we only presented here a warming case. Secondly, only in case of a pronounced inversion close to hub height we simulated and observed a change in the water vapor mixing ratio corresponding to changes in latent heat flux. Thirdly, the net impact on the latent heat flux was determined by the temperature gradient between SST and the ambient air temperature.

Several potential impacts of offshore wind parks on the marine boundary layer were not discussed in this study i.e the formation of clouds. HUANG and HALL (2015) and BOETTCHER et al. (2015) showed that large offshore wind park could have an influence on the cloud cover. Consequently, wind parks could have an influence on the radiation budget as well. These aspects were not presented as we could not identify a clear impact of offshore wind parks on the cloud cover or any radiation budget due to lacking equipment.

Given the high sensitivity of the simulated impacts of offshore wind farms, studies making general statements about the impacts of offshore wind farms based on numerical climate or mesoscale models should be carefully examined. As discussed above, simulated impact on the local climate is extremely sensible to the simulated stability in the lowest 200 m of the marine boundary layer. Within the WIPAFF project we showed that mesoscale simulations were lacking to represent the stable boundary layer during offshore winds close to the coast, although most wind parks are in the transition area from coast to open sea and their impact is largest during stable conditions (SIEDERSLEBEN et al., 2018b).

The above documented results may have several consequences.

## 5.1 Wind direction-based layout of wind parks

Analysis of data from FINO1 for the year 2005 shows a clear correlation between wind direction and atmospheric stratification in the North Sea (EMEIS et al., 2016). Stable situations are coupled to the main wind direction (South-West). This direction-stability correlation is assumed to be typical for the two temperate latitude west-wind belts on both hemispheres of the globe, because it is caused by the usual sequence of warm sector winds having a poleward component followed by cold sector winds having an equatorward component in eastward moving low-pressure systems. The WIPAFF results clearly documented the dependence of the wake intensity and wake length on atmospheric stratification. Therefore, it could be advisable that wind park layout and park cluster layout take this dependence into account. Figure 15 shows a possible array of wind parks in the German Bight which reflects this correlation. Distances between single turbines within wind parks and between entire parks are larger along the most frequent direction of stably stratified flow (from Southwest to Northeast) and they are shorter along the perpendicular direction of unstably stratified flow.

## 5.2 Additional measurement requirements and stability measures for the marine BL

For future estimations of wind park power output and for improving analyses of offshore wind park wakes, a crucial parameter was found to be profiles of temperature and the stability parameter. Temperature inversions occur at different altitudes above, below and within the rotor area. A near-surface, predominantly convective layer

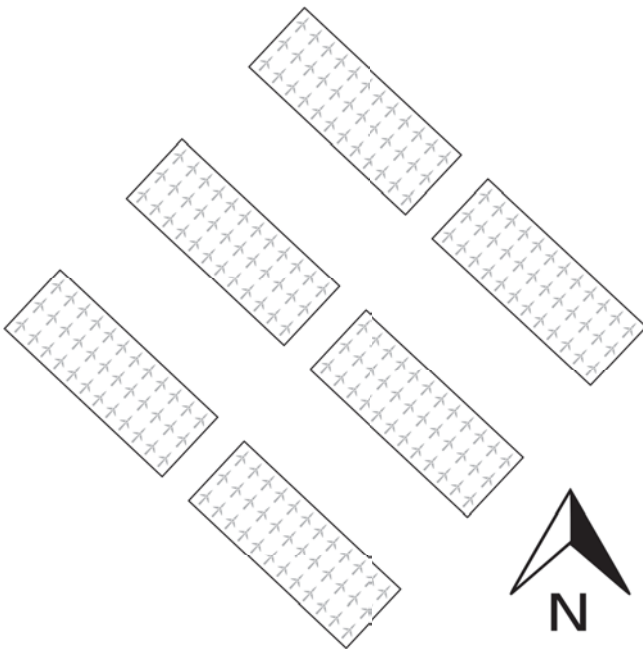


**Figure 15:** Schematic of stability-dependent wind park layout in the German Bight. Crosses denote single wind turbines and boxes indicate wind parks. North is towards the top. (Adapted from [EMEIS et al., 2016](#))

may be present and an inversion with more stable conditions may be found aloft. Therefore, a simple approach for defining stability, e.g. the temperature difference between the sea surface and the atmosphere at one particular altitude, is not suitable for describing stability conditions and wake development. In addition, other stability parameters are partly inconsistent with each other. Therefore, defining stability measures for the marine boundary layers which can be representative for atmospheric stability for an offshore wind park and the evolution of wind park wakes is a very crucial task for the future.

Moreover, the representation of temperature profiles in numerical simulations and the deduced stability need higher accuracy and improvement. The comparison of the airborne observations and WRF simulations show potential for improving the representation of coastal effects, where temperature profiles develop from the coast to the wind parks. For example, from the simulations of 15 October 2017 two profiles are compared to the simulations, one close to the coast, one further offshore (Figure 16). Close to the coast the simulation and observation show an inversion. However, the inversion of the simulation is located above the rotor area, whereby the inversion in the observations is located within the rotor area. Further offshore, the performance of the model improves slightly. Nevertheless, the height of the inversion is still overestimated by 150 m. The numerical simulations where performed with the setup as described in [SIEDERSLEBEN et al. \(2018a\)](#). As the development of the stability for the flow above the coast strongly influences the wake extent, an improvement of the simulations is

required for correctly representing the inflow conditions reaching the wind park. The availability of additional measurements of temperature profiles at a coastal and at an offshore locations could serve as reference and would contribute to a better understanding of the processes in the atmospheric boundary layer and the interaction with wind parks and lead to improvement of numerical simulations.

### 5.3 Impact on cloud development

On three out of 41 measurement flights, the formation of small patches of clouds directly above the wind park was observed. The cloud patches were transported downwind. No such clouds were observed in the lee and next to the wind park. Cloud formation was observed on days with relative humidity close to saturation, and slightly stable conditions. The documentation of the clouds was attempted by photographing. However, the image quality was hampered by other cloud layers above. The sensors on board were not suitable for systematic analyses of the phenomenon and its importance. This should be addressed in future research in combination with the analysis of downward heat and humidity fluxes above wind parks.

### 5.4 Future SAR data evaluation

About one third of the SAR scenes with visible wake structures show increased radar cross section values for roughly the first 10 km of the wake downstream the wind park. There are several approaches to explain this phenomenon, which seems to be a paradox at first sight. One possible explanation proposed in [DJATH et al. \(2018\)](#) is based on the hypothesis of increased downward momentum fluxes caused by turbulence introduced by the wind turbines. Making this assumption, SAR data would provide very valuable information on the advection and dissipation of turbulence in the vicinity of offshore wind parks. However, observational evidence is missing to confirm or refute this or a number of other possible mechanisms to explain the effect. Measurements are a challenge in this context, because the sea surface roughness measured by the radar is strongly dependent on the detailed structure of the atmospheric boundary layer close to the water. New measurement technologies and sampling approaches are currently investigated to obtain more information on this important region. These activities are not only of high value to improve our understanding of the atmospheric processes around offshore wind parks, but are of more general relevance in the context of atmosphere/ocean interaction, which is a field of intense research worldwide.

A topic that is directly related to the phenomenon just described, is the derivation of wind speed information above the sea surface from microwave radar data. Radar measurements have a direct physical connection to the friction velocity at the surface, but wind speeds at higher levels depend on the stability conditions in



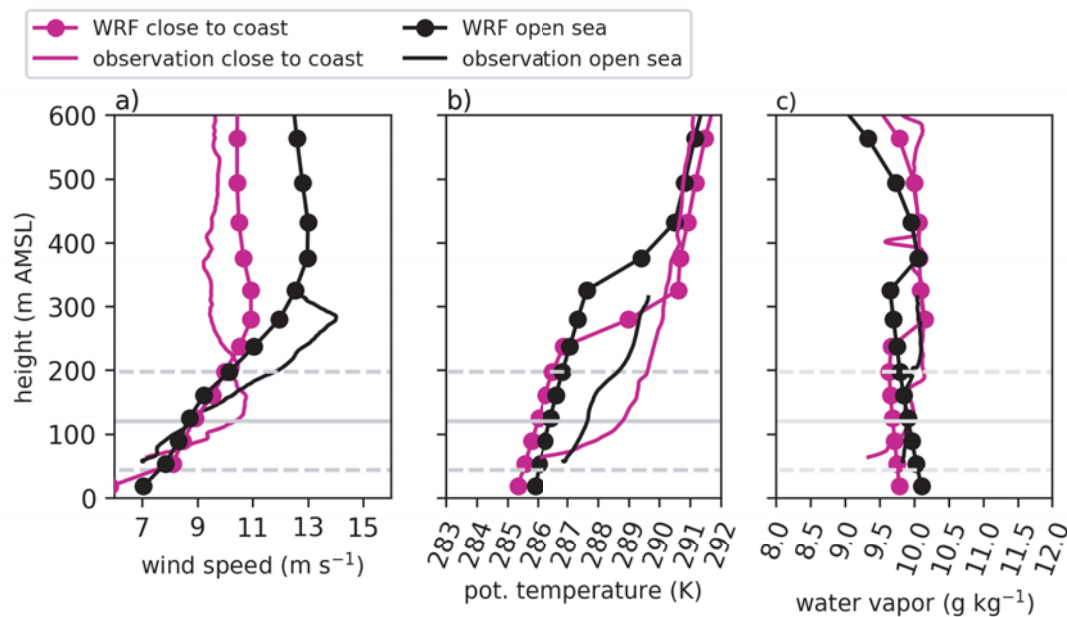


**Figure 16:** Vertical profiles of wind speed (a), potential temperature (b) and water vapour mixing ratio (c) obtained by probing the atmosphere with the research aircraft on 15 October 2017 close to the coast (magenta solid lines) and further offshore (black solid lines). The corresponding locations of the vertical profiles are shown in detail in Figure 1. The interpolated WRF data along the climb flights is shown with the solid lines having the circles on top, whereby each circle represents a vertical level of the simulation.

the boundary layer, which are usually not well known. The empirical functions used for SAR wind speed retrieval so far were usually derived based on observation data sets taken in the open ocean, making very simplifying assumptions about the conditions in the atmosphere. This is another area of research, where more sophisticated measurements of the atmospheric boundary layer in near coastal areas could help to optimise the exploitation of SAR information for offshore wind park applications. This issue is also related to the more general question about the optimal integration of satellite, *in situ* and model data to provide efficient information products to the offshore wind park community.

## Acknowledgments

The authors thank the aircraft crew of the WIPAFF campaign, RUDOLF HANKERS, THOMAS FEUERLE, MARK BITTER and HELMUT SCHULZ from the Technische Universität Braunschweig for their great support. The project WIPAFF is funded by the German Federal Ministry for Economic Affairs and Energy (Bundesministerium für Wirtschaft und Energie) on the basis of a decision by the German Bundestag under grant number: FKZ 0325783.

## References

ABKAR, M., F. PORTÉ-AGEL, 2015a: Influence of atmospheric stability on wind-turbine wakes: A large-eddy simulation study. – *Phys. Fluids* **27**, 035104.

ABKAR, M., F. PORTÉ-AGEL, 2015b: A new wind-farm parameterization for large-scale atmospheric models. – *J. Renew. Sustain. Energy* **7**, 013121.

AINSLIE, J., 1988: Calculating the flow field in the wake of wind turbines. – *J. Wind Engin. Indust. Aerodyn.* **27**, 213–224, DOI: [10.1016/0167-6105\(88\)90037-2](https://doi.org/10.1016/0167-6105(88)90037-2).

ARMSTRONG, A., R.R. BURTON, S.E. LEE, S. MOBBS, N. OSTLE, V. SMITH, S. WALDRON, J. WHITAKER, 2016: Ground-level climate at a peatland wind farm in Scotland is affected by wind turbine operation. – *Env. Res. Lett.* **11**, 044024.

BÄRFUSS, K., R. HANKERS, M. BITTER, T. FEUERLE, H. SCHULZ, T. RAUSCH, A. PLATIS, J. BANGE, A. LAMPERT, 2019: In-situ airborne measurements of atmospheric and sea surface parameters related to offshore wind parks in the German Bight. – PANGAEA, published online. DOI: [10.1594/PANGAEA.902845](https://doi.org/10.1594/PANGAEA.902845).

BARTHELMIE, R., S. FRANDBEN, P. RETHORE, L. JENSEN, 2007: Analysis of atmospheric impacts on the development of wind turbine wakes at the Nysted wind farm. – In: *European Offshore Wind Conference*, volume **6**.

BARTHELMIE, R.J., L. JENSEN, 2010: Evaluation of wind farm efficiency and wind turbine wakes at the Nysted offshore wind farm. – *Wind Energy* **13**, 573–586.

BARTHELMIE, R.J., K. HANSEN, S.T. FRANDBEN, O. RATHMANN, J. SCHEPERS, W. SCHLEZ, J. PHILLIPS, K. RADOS, A. ZERVOS, E. POLITIS, OTHERS, 2009: Modelling and measuring flow and wind turbine wakes in large wind farms offshore. – *Wind Energy* **12**, 431–444.

BLAHAK, U., B. GORETZKI, J. MEIS, 2010: A simple parameterization of drag forces induced by large wind farms for numerical weather prediction models. – In: *Proceedings of the European Wind Energy Conference & Exhibition*.

BODINI, N., D. ZARDI, J.K. LUNDQUIST, 2017: Three-dimensional structure of wind turbine wakes as measured by scanning lidar. – *Atmos. Measur. Techn.* **10**, 2881–2896.

- BOETTCHER, M., P. HOFFMANN, H.J. LENHART, H. SCHLÜNZEN, R. SCHOETTER, 2015: Influence of large offshore wind farms on north german climate. – *Meteorol. Z.* **24**, 465–480.
- BOSSANYI, E., G. WHITTLE, P. DUNN, N. LIPMAN, P. MUSGROVE, C. MACLEAN, 1980: The efficiency of wind turbine clusters. – In: 3rd International symposium on wind energy systems, 401–416.
- CAÑADILLAS, B., R. FOREMAN, V. BARTH, A. PLATIS, S.K. SIEDERSLEBEN, J. BANGE, A. LAMPERT, K. BÄRFUSS, R. HANKERS, J. SCHULZ-STELLENFLETH, B. DJATH, S. EMEIS, T. NEUMANN, 2020: Offshore wind farm wake recovery: Airborne measurements and its representation in engineering models. – *Wind Energy*, published online. DOI: [10.1002/we.2484](https://doi.org/10.1002/we.2484).
- CHAMORRO, L.P., F. PORTE-AGEL, 2011: Turbulent flow inside and above a wind farm: a wind-tunnel study. – *Energies* **4**, 1916–1936.
- CHIN, T.M., R.F. MILLIFF, W.G. LARGE, 1998: Basin-scale, high-wavenumber sea surface wind fields from a multiresolution analysis of scatterometer data. – *J. Atmos. Oceanic Technol.* **15**, 741–763.
- CHO, J.Y., R.E. NEWELL, J.D. BARRICK, 1999a: Horizontal wavenumber spectra of winds, temperature, and trace gases during the pacific exploratory missions: 2. gravity waves, quasi-two-dimensional turbulence, and vortical modes. – *J. Geophys. Res.* **104**, 16297–16308.
- CHO, J.Y.N., Y. ZHU, R.E. NEWELL, B.E. ANDERSON, J.D. BARRICK, G.L. GREGORY, G.W. SACHSE, M.A. CARROLL, G.M. ALBERCOOK, 1999b: Horizontal wavenumber spectra of winds, temperature, and trace gases during the Pacific Exploratory Missions: 1. Climatology. – *J. Geophys. Res. Atmos.* **104**, 5697–5716.
- CHRISTIANSEN, M.B., C.B. HASAGER, 2005: Wake effects of large offshore wind farms identified from satellite SAR. – *Remote Sens. Env.* **98**, 251–268.
- CORSMEIER, U., R. HANKERS, A. WIESER, 2001: Airborne turbulence measurements in the lower troposphere onboard the research aircraft dornier 128-6, D-IBUF. – *Meteorol. Z.* **10**, 315–329.
- DJATH, B., J. SCHULZ-STELLENFLETH, 2020: Wind speed deficits downstream offshore wind parks – a new automatised estimation technique based on satellite synthetic aperture radar data. – *Meteorol. Z.* **28**, 499–515. DOI: [10.1127/metz/2019/0992](https://doi.org/10.1127/metz/2019/0992).
- DJATH, B., J. SCHULZ-STELLENFLETH, B. CAÑADILLAS, 2018: Impact of atmospheric stability on X-band and C-band synthetic aperture radar imagery of offshore windpark wakes. – *J. Renew. Sustain. Energy* **10**, 043301.
- DNV-GL, 2013a: WindFarmer v.5.2 theory manual. – Technical report, Garrad Hassan and Partners, Ltd.
- DNV-GL, 2013b: WindFarmer v.5.2 validation report. – Technical report, Garrad Hassan and Partners, Ltd.
- DÖRENKÄMPER, M., B. WITHA, G. STEINFELD, D. HEINEMANN, M. KÜHN, 2015a: The impact of stable atmospheric boundary layers on wind-turbine wakes within offshore wind farms. – *J. Wind Engineer. Indust. Aerodyn.* **144**, 146–153.
- DÖRENKÄMPER, M., M. OPTIS, A. MONAHAN, G. STEINFELD, 2015b: On the offshore advection of boundary-layer structures and the influence on offshore wind conditions. – *Bound.-Layer Meteor.* **155**, 459–482.
- EMEIS, S., 2010: A simple analytical wind park model considering atmospheric stability. – *Wind Energy* **13**, 459–469.
- EMEIS, S., 2018: Wind energy meteorology: atmospheric physics for wind power generation. – Springer, 255 + XXVI pp.
- EMEIS, S., S. FRANDBSEN, 1993: Reduction of horizontal wind speed in a boundary layer with obstacles. – *Bound.-Layer Meteorol.* **64**, 297–305.
- EMEIS, S., S. SIEDERSLEBEN, A. LAMPERT, A. PLATIS, J. BANGE, B. DJATH, J. SCHULZ-STELLENFLETH, T. NEUMANN, 2016: Exploring the wakes of large offshore wind farms. – *J. Phys. Conference Series* **753**, 092014.
- FIEDLER, B., A. ADAMS, 2014: A subgrid parameterization for wind turbines in weather prediction models with an application to wind resource limits. – *Adv. Meteor.* **2014**, 696202. DOI: [10.1155/2014/696202](https://doi.org/10.1155/2014/696202).
- FITCH, A.C., J.B. OLSON, J.K. LUNDQUIST, J. DUDHIA, A.K. GUPTA, J. MICHALAKES, I. BARSTAD, 2012: Local and mesoscale impacts of wind farms as parameterized in a meso-scale NWP model. – *Mon. Wea. Rev.* **140**, 3017–3038.
- FOREMAN, R., B. CAÑADILLAS, T. NEUMANN, S. EMEIS, 2017: Measurements of heat and humidity fluxes in the wake of offshore wind turbines. – *J. Renew. Sustain. Energy* **9**, 053304.
- FRANDBSEN, S., 1992: On the wind speed reduction in the center of large clusters of wind turbines. – *J. Wind Engin. Indust. Aerodyn.* **39**, 251–265.
- FRANDBSEN, S., R. BARTHELMIE, S. PRYOR, O. RATHMANN, S. LARSEN, J. HØJSTRUP, M. THØGERSEN, 2006: Analytical modelling of wind speed deficit in large offshore wind farms. – *Wind Energy* **9**, 39–53.
- HANSEN, K.S., R.J. BARTHELMIE, L.E. JENSEN, A. SOMMER, 2012: The impact of turbulence intensity and atmospheric stability on power deficits due to wind turbine wakes at horns rev wind farm. – *Wind Energy* **15**, 183–196.
- HASAGER, C., L. RASMUSSEN, A. PEÑA, L. JENSEN, P.E. RÉTHORÉ, 2013: Wind farm wake: The Horns Rev photo case. – *Energies* **6**, 696–716.
- HASAGER, C., N. NYGAARD, P. VOLKER, I. KARAGALI, S. ANDERSEN, J. BADGER, 2017: Wind farm wake: The 2016 Horns Rev photo case. – *Energies* **10**, 317.
- HASAGER, C.B., P. VINCENT, J. BADGER, M. BADGER, A. DI BELLA, A. PEÑA, R. HUSSON, P.J. VOLKER, 2015: Using Satellite SAR to Characterize the Wind Flow Around Offshore Wind Farms. – *Energies* **8**, 5413–5439, DOI: [10.3390/en8065413](https://doi.org/10.3390/en8065413).
- HERSBACH, H., A. STOFFELEN, S. DE HAAN, 2007: An improved C-band scatterometer ocean geophysical model function: CMOD5. – *J. Geophys. Res. Oceans* **112**, published online. DOI: [10.1029/2006JC003743](https://doi.org/10.1029/2006JC003743).
- HÖGSTRÖM, U., J. HUNT, A.S. SMEDMAN, 2002: Theory and measurements for turbulence spectra and variances in the atmospheric neutral surface layer. – *Bound.-Layer Meteor.* **103**, 101–124.
- HUANG, H.Y., A. HALL, 2015: OFFSHORE WIND DEVELOPMENT IMPACTS ON MARINE ATMOSPHERIC ENVIRONMENT. – Available online at <http://www.energy.ca.gov/2016publications/CEC-500-2016-023/CEC-500-2016-023.pdf>.
- JACOBSON, M.Z., C.L. ARCHER, 2012: Saturation wind power potential and its implications for wind energy. – *Proc of the Natl Acad of Sci USA* **109**, 15679–15684.
- JENSEN, N.O., 1983: A note on wind generator interaction. – Risø National Laboratory Roskilde.
- KAFFINE, D.T., C.M. WORLEY, 2010: The windy commons? – *Env. Res. Econom.* **47**, 151–172.
- KAIMAL, J.C., J.C. WYNGAARD, Y. IZUMI, O.R. COTÉ, 1972: Spectral characteristics of surface-layer turbulence. – *Quart. J. Roy. Meteor. Soc.* **98**, 563–589.
- KATIC, I., J. HØJSTRUP, N. JENSEN, 1987: A simple model for cluster efficiency. – In: W. PALZ and E. SESTO (Eds.): EWEC'86. – Proceedings. Vol. 1, 407–410.
- KOCH, W., 2004: Directional Analysis of SAR images aiming at wind direction. – *IEEE Transactions on Geoscience and Remote Sensing* **42**, 702–710.



- LAMPERT, A., K.B. BÄRFUSS, A. PLATIS, S.K. SIEDERSLEBEN, B. DJATH, B. CAÑADILLAS, R. HANKERS, M. BITTER, T. FEUERLE, H. SCHULZ, T. RAUSCH, M. ANGERMANN, A. SCHWITHAL, J. BANGE, J. SCHULZ-STELLENFLETH, T. NEUMANN, S. EMEIS, 2020: In-situ airborne measurements of atmospheric and sea surface parameters related to offshore wind parks in the German Bight. – *Earth Sys. Sci. Data*, **12**, 935–946.
- LEE, S., M. CHURCHFIELD, P. MORIARTY, J. JONKMAN, J. MICHALAKES, 2012: Atmospheric and wake turbulence impacts on wind turbine fatigue loadings. – In: 50th AIAA Aerospace Sciences Meeting including the New Horizons Forum and Aerospace Exposition, 540.
- LI, X., S. LEHNER, 2013a: Observation of TerraSAR-X for studies on offshore wind turbine wake in near and far fields. – *IEEE Journal of Selected Topics in Applied Earth Observations and Remote Sensing* **6**, 1757–1768.
- LI, X.M., S. LEHNER, 2013b: Algorithm for sea surface wind retrieval from terrasarsar-x and tandem-x data. – *IEEE Transactions on Geoscience and Remote Sensing* **52**, 2928–2939.
- LIN, H., Q. XU, Q. ZHENG, 2008: An overview on sar measurements of sea surface wind. – *Prog. Natural Sci.* **18**, 913–919.
- LISSAMAN, P., 1979: Energy effectiveness of arbitrary arrays of wind turbines. – *J. Energy* **3**, 323–328.
- LUNDQUIST, J., K. DU VIVIER, D. KAFFINE, J. TOMASZEWSKI, 2019: Costs and consequences of wind turbine wake effects arising from uncoordinated wind energy development. – *Nature Energy* **4**, 26–34.
- MARTÍNEZ-TOSSAS, L.A., M.J. CHURCHFIELD, C. MENEVEAU, 2015: Large eddy simulation of wind turbine wakes: detailed comparisons of two codes focusing on effects of numerics and subgrid modeling. – *J. Phys. Conference Series* **625**, 012024.
- MUÑOZ-ESPARZA, D., B. CAÑADILLAS, T. NEUMANN, J. VAN BEECK, 2012: Turbulent fluxes, stability and shear in the offshore environment: Mesoscale modelling and field observations at fino1. – *J. Renew. Sustain Energy* **4**, 063136.
- NAKANISHI, M., H. NIINO, 2004: An improved mellor–yamada level-3 model with condensation physics: Its design and verification. – *Bound.-layer Meteor.* **112**, 1–31.
- NEWMAN, B., 1977: The spacing of wind turbines in large arrays. – *Energy conversion* **16**, 169–171.
- NICHOLLS, S., C.J. READINGS, 1981: Spectral characteristics of surface layer turbulence over the sea. – *Quart. J. Roy. Meteor. Soc.* **107**, 591–614.
- NYGAARD, N.G., 2014: Wakes in very large wind farms and the effect of neighbouring wind farms. – *J. Phys. Conference Series* **524**, 012162.
- NYGAARD, N.G., S.D. HANSEN, 2016: Wake effects between two neighbouring wind farms. – *J. Phys. Conference Series* **753**, 032020. DOI: [10.1088/1742-6596/753/3/032020](https://doi.org/10.1088/1742-6596/753/3/032020).
- PEÑA, A., O. RATHMANN, 2014: Atmospheric stability-dependent infinite wind-farm models and the wake-decay coefficient. – *Wind Energy* **17**, 1269–1285, DOI: [10.1002/we.1632](https://doi.org/10.1002/we.1632).
- PEÑA, A., O. RATHMANN, 2014: Atmospheric stability-dependent infinite wind-farm models and the wake-decay coefficient. – *Wind Energy* **17**, 1269–1285.
- PLATIS, A., S.K. SIEDERSLEBEN, J. BANGE, A. LAMPERT, K. BÄRFUSS, R. HANKERS, B. CAÑADILLAS, R. FOREMAN, J. SCHULZ-STELLENFLETH, B. DJATH, OTHERS, 2018: First in situ evidence of wakes in the far field behind offshore wind farms. – *Scientific reports* **8**, 2163.
- PLATIS, A., M. HUNDHAUSEN, S.K. SIEDERSLEBEN, A. LAMPERT, K. BÄRFUSS, J. SCHULZ-STELLENFLETH, B. DJATH, S. EMEIS, T. NEUMANN, B. CAÑADILLAS, J. BANGE, in review: Evaluation of a simple analytical model for offshore wind farm wake recovery by in-situ data and WRF simulations. – *Wind Energy*, in review.
- POND, S., S. SMITH, P. HAMBLIN, R. BURLING, 1966: Spectra of velocity and temperature fluctuations in the atmospheric boundary layer over the sea. – *J. Atmos. Sci.* **23**, 376–386.
- PORTÉ-AGEL, F., Y.T. WU, C.H. CHEN, 2013: A numerical study of the effects of wind direction on turbine wakes and power losses in a large wind farm. – *Energies* **6**, 5297–5313.
- PORTÉ-AGEL, F., H. LU, Y.T. WU, 2014: Interaction between large wind farms and the atmospheric boundary layer. – *Procedia Iutam* **10**, 307–318.
- PORTÉ-AGEL, F., M. BASTANKHAH, S. SHAMSODDIN, 2020: Wind-turbine and wind-farm flows: A review. – *Bound.-Layer Meteor.* **174**, 1–59.
- PORTER, D.F., J.J. CASSANO, M.C. SERREZE, 2011: Analysis of the Arctic atmospheric energy budget in WRF: A comparison with reanalyses and satellite observations. – *J. Geophysical Res. Atmos.* **116**, published online. DOI: [10.1029/2011JD016622](https://doi.org/10.1029/2011JD016622).
- PROSPATHOPOULOS, J., P. CHAVIAROPOULOS, 2013: Numerical simulation of offshore wind farm clusters. – In: European Wind Energy Association, Conference proceedings.
- PRYOR, S., R. BARTHELMIE, A. HAHMANN, T. SHEPHERD, P. VOLKER, 2018: Downstream effects from contemporary wind turbine deployments. – *J. Phys. Conference Series* **1037**, 072010. IOP Publishing.
- RAJEWSKI, D.A., E.S. TAKLE, J.K. LUNDQUIST, S. ONCLEY, J.H. PRUEGER, T.W. HORST, M.E. RHODES, R. PFEIFFER, J.L. HATFIELD, K.K. SPOTH, OTHERS, 2013: Crop wind energy experiment (CWEX): observations of surface-layer, boundary layer, and mesoscale interactions with a wind farm. – *Bull. Amer. Meteor. Soc.* **94**, 655–672.
- RAJEWSKI, D.A., E.S. TAKLE, J.K. LUNDQUIST, J.H. PRUEGER, R.L. PFEIFFER, J.L. HATFIELD, K.K. SPOTH, R.K. DOORENBOS, 2014: Changes in fluxes of heat, H<sub>2</sub>O, and CO<sub>2</sub> caused by a large wind farm. – *Agricult. Forest Meteor.* **194**, 175–187.
- ROHRIG, K., V. BERKHOUT, D. CALLIES, M. DURSTEWITZ, S. FAULSTICH, B. HAHN, M. JUNG, L. PAUSCHER, A. SEIBEL, M. SHAN, OTHERS, 2019: Powering the 21st century by wind energy-options, facts, figures. – *Appl. Phys. Rev.* **6**, 031303.
- ROY, S.B., J.J. TRAITTEUR, 2010: Impacts of wind farms on surface air temperatures. – *Proceedings of the National Academy of Sciences* **107**, 17899–17904.
- SATHE, A., 2010: Atmospheric stability and wind profile climatology over the north Sea-Case study at Egmond aan Zee. – *Proceedings of the conference torque*, 1–10.
- SCHNEEMANN, J., A. ROTT, M. DÖRENKÄMPER, G. STEINFELD, M. KÜHN, 2019: Cluster wakes impact on a far distant offshore wind farm’s power. – *Wind Energy Sci. Discuss.*, published online. DOI: [10.5194/wes-2019-39](https://doi.org/10.5194/wes-2019-39).
- SIEDERSLEBEN, S.K., 2019: Numerical analysis of offshore wind farm wakes and their impact on the marine boundary layer. – PhD thesis, Universität zu Köln.
- SIEDERSLEBEN, S.K., A. PLATIS, J.K. LUNDQUIST, A. LAMPERT, K. BÄRFUSS, B. CAÑADILLAS, B. DJATH, J. SCHULZ-STELLENFLETH, J. BANGE, T. NEUMANN, OTHERS, 2018a: Evaluation of a wind farm parametrization for mesoscale atmospheric flow models with aircraft measurements. – *Meteorol. Z.* **27**, 401–415.
- SIEDERSLEBEN, S.K., J.K. LUNDQUIST, A. PLATIS, J. BANGE, K. BÄRFUSS, A. LAMPERT, B. CAÑADILLAS, T. NEUMANN, S. EMEIS, 2018b: Micrometeorological impacts of offshore wind farms as seen in observations and simulations. – *Env. Res. Lett.*, published online, <https://iopscience.iop.org/article/10.1088/1748-9326/a6ea0b/pdf>.
- SIEDERSLEBEN, S.K., A. PLATIS, J.K. LUNDQUIST, B. DJATH, A. LAMPERT, K. BÄRFUSS, B. CAÑADILLAS, J. SCHULZ-

- STELLENFLETH, J. BANGE, T. NEUMANN, S. EMEIS, 2020: Turbulent kinetic energy over large offshore wind farms observed and simulated by the mesoscale model WRF (3.8.1). – *Geosci. Model Develop.* **13**, 249–268, DOI: [10.5194/gmd-13-249-2020](https://doi.org/10.5194/gmd-13-249-2020).
- SMEDMAN, A.S., U. HÖGSTRÖM, H. BERGSTRÖM, 1996: Low level jets – a decisive factor for off-shore wind energy siting in the baltic sea. – *Wind Engineering* **20**, 137–147.
- SMEDMAN, A.S., H. BERGSTRÖM, B. GRISOGONO, 1997: Evolution of stable internal boundary layers over a cold sea. – *J. Geophys. Res. Oceans* **102**, 1091–1099.
- SMITH, R.B., 2010: Gravity wave effects on wind farm efficiency. – *Wind Energy* **13**, 449–458.
- STULL, R.B., 2012: An introduction to boundary layer meteorology, volume 13. – Springer Science & Business Media.
- TRABUCCHI, D., G. STEINFELD, D. BASTINE, J.J. TRUJILLO, J. SCHNEEMANN, M. KÜHN, 2015: Study of wake meandering by means of fixed point lidar measurements: Spectral analysis of line-of-sight wind component. – *J. Phys. Conference Series* **625**, 012016.
- TRENBERTH, K.E., J.M. CARON, D.P. STEPANIAK, 2001: The atmospheric energy budget and implications for surface fluxes and ocean heat transports. – *Climate Dyn.* **17**, 259–276, DOI: [10.1007/PL00007927](https://doi.org/10.1007/PL00007927).
- TULLOCH, R., K.S. SMITH, 2009: Quasigeostrophic turbulence with explicit surface dynamics: Application to the atmospheric energy spectrum. – *J. Atmos. Sci.* **66**, 450–467.
- VAUTARD, R., F. THAIS, I. TOBIN, F.M. BRÉON, J.G.D. DE LAVERGNE, A. COLETTE, P. YIOU, P.M. RUTI, 2014: Regional climate model simulations indicate limited climatic impacts by operational and planned european wind farms. – *Nature communications* **5**, 3196.
- VEERS, P., K. DYKES, E. LANTZ, S. BARTH, C.L. BOTTASSO, O. CARLSON, A. CLIFTON, J. GREEN, P. GREEN, H. HOLTINEN, OTHERS, 2019: Grand challenges in the science of wind energy. – *Science* **366**, eaau2027, DOI: [10.1126/science.aau2027](https://doi.org/10.1126/science.aau2027).
- VERHOEF, A., M. PORTABELLA, A. STOFFELEN, H. HERSBACH, 2008: CMOD5. n-the CMOD5 GMF for neutral winds. – Technical Report SAF/OSI/CDOP/KNMI/TEC/TN/3, 165, KNMI, De Bilt, Netherlands.
- VERMEER, L., J.N. SØRENSEN, A. CRESPO, 2003: Wind turbine wake aerodynamics. – *Prog. Aerospace Sci.* **39**, 467–510.
- VOLKER, P., J. BADGER, A.N. HAHMANN, S. OTT, 2015: The Explicit Wake Parametrisation v1.0: A wind farm parametrisation in the mesoscale model WRF. – *Geosci. Model Develop.* **8**, 3715–3731.
- WANG, C., R.G. PRINN, 2011: Potential climatic impacts and reliability of large-scale offshore wind farms. – *Env. Res. Lett.* **6**, 025101.
- WESTERHELLWEG, A., B. CANADILLAS, A. BEEKEN, T. NEUMANN, 2010: One year of LiDAR measurements at FINO1-platform: Comparison and verification to met-mast data. – In: 10th German Wind Energy Conference, Bremen, 18–19.
- WIKLE, C.K., R.F. MILLIFF, W.G. LARGE, 1999: Surface wind variability on spatial scales from 1 to 1000 km observed during TOGA COARE. – *J. Atmos. Sci.* **56**, 2222–2231.
- WU, Y.T., F. PORTÉ-AGEL, 2012: Atmospheric turbulence effects on wind-turbine wakes: An LES study. – *Energies* **5**, 5340–5362.
- XIA, G., M.C. CERVARICH, S.B. ROY, L. ZHOU, J.R. MINDER, P.A. JIMENEZ, J.M. FREEDMAN, 2017: Simulating impacts of real-world wind farms on land surface temperature using the WRF model: Validation with observations. – *Mon. Wea. Rev.* **145**, 4813–4836.
- XU, Y., L.L. FU, R. TULLOCH, 2011: The global characteristics of the wavenumber spectrum of ocean surface wind. – *J. Phys. Oceanography* **41**, 1576–1582.
- ZHOU, L., Y. TIAN, S.B. ROY, C. THORNCROFT, L.F. BOSART, Y. HU, 2012: Impacts of wind farms on land surface temperature. – *Nature Climate Change* **2**, 539.



# Offshore wind farm cluster wakes as observed by long-range-scanning wind lidar measurements and mesoscale modeling

Beatriz Cañadillas<sup>1,2</sup>, Maximilian Beckenbauer<sup>1</sup>, Juan J. Trujillo<sup>2</sup>, Martin Dörenkämper<sup>3</sup>, Richard Foreman<sup>2</sup>, Thomas Neumann<sup>2</sup>, and Astrid Lampert<sup>1</sup>

<sup>1</sup>Institute of Flight Guidance, Technische Universität Braunschweig, Braunschweig, Germany

<sup>2</sup>Renewables, UL International GmbH, Oldenburg, Germany

<sup>3</sup>Fraunhofer Institute for Wind Energy Systems, Oldenburg, Germany

**Correspondence:** Beatriz Cañadillas [redacted]@tu-braunschweig.de, [redacted]@ul.com)

Received: 21 December 2021 – Discussion started: 18 January 2022

Revised: 25 May 2022 – Accepted: 2 June 2022 – Published: 20 June 2022

**Abstract.** As part of the ongoing X-Wakes research project, a 5-month wake-measurement campaign was conducted using a scanning lidar installed amongst a cluster of offshore wind farms in the German Bight. The main objectives of this study are (1) to demonstrate the performance of such a system and thus quantify cluster wake effects reliably and (2) to obtain experimental data to validate the cluster wake effect simulated by the flow models involved in the project. Due to the lack of free wind flow for the wake flow directions, wind speeds obtained from a mesoscale model (without any wind farm parameterization) for the same time period were used as a reference to estimate the wind speed deficit caused by the wind farm wakes under different wind directions and atmospheric stabilities. For wind farm waked wind directions, the lidar data show that the wind speed is reduced up to 30 % at a wind speed of about  $10 \text{ m s}^{-1}$ , depending on atmospheric stability and distance to the wind farm. For illustrating the spatial extent of cluster wakes, an airborne dataset obtained during the scanning wind lidar campaign is used and compared with the mesoscale model with wind farm parameterization and the scanning lidar. A comparison with the results of the model with a wind farm parameterization and the scanning lidar data reveals a relatively good agreement in neutral and unstable conditions (within about 2 % for the wind speed), whereas in stable conditions the largest discrepancies between the model and measurements are found. The comparative multi-sensor and model approach proves to be an efficient way to analyze the complex flow situation in a modern offshore wind cluster, where phenomena at different length scales and timescales need to be addressed.

## 1 Introduction

Offshore wind energy, i.e., the use of wind farms built offshore or on the continental shelf to harvest wind energy for electricity generation, is playing an important role in achieving a low-carbon future of economic prosperity. In 2020, 6.1 GW was commissioned worldwide. The total offshore wind capacity has now passed 35 GW, representing 4.8 % of the total global cumulative wind capacity. In particular, Germany represents a 22 % contribution (7.8 GW) of the total installed power (Lee and Zhao, 2021). In the North Sea,

the available offshore area for wind energy is becoming increasingly scarce. In order to contribute to the planned target of 30 GW by 2030 (long-term goal recently approved by the German government) and to make wind energy extraction economically profitable, wind farms need to be installed relatively close to each other. While this may be beneficial in terms of infrastructure sharing, it may also be detrimental to the overall energy extraction due to the influence of the wakes generated by the upstream wind farms.

Therefore, knowledge of the prevailing wind conditions is one of the crucial parts not only in the first phase of a po-

tential offshore wind farm to accurately assess the wind resource, but also during the operation phase of the wind farm. Although numerical simulations and the detailed analysis of experiments in wind tunnels can provide good insight into the actual conditions, high-quality in situ measurements in a real environment are essential.

As the size of offshore wind farms increases and they are grouped into larger arrays, also called clusters, wake effects take on greater importance, not only affecting the surrounding wind conditions but also reducing the efficiency of power generation for downstream wind farms. In the North Sea, for example, the large size of wind farms and their proximity affect not only the performance of single downstream turbines but also that of whole neighboring downstream farms (Cañadillas et al., 2020; Ahsbahs et al., 2020), which may reduce the capacity factor by approximately 20 % or more as suggested by Akhtar et al. (2021). The effect of atmospheric stability on the extension of the wakes behind wind farms has been intensively studied in recent years through a number of analytical and experimental studies (Christiansen and Hasager, 2005; Emeis, 2010, 2018; Djath et al., 2018; Ahsbahs et al., 2018; Nygaard and Newcombe, 2018; Cañadillas et al., 2020; Ahsbahs et al., 2020; Platis et al., 2020), as well as numerical investigations (Patrick et al., 2014; Siedersleben et al., 2018b). For instance, Cañadillas et al. (2020) analyzed data from a series of flights collected within the wakes at several downstream distances of two offshore wind farm clusters located in the North Sea during different atmospheric stability conditions. They found that stable stratification leads to significantly longer wakes with a slower wind speed recovery compared to unstable conditions. Their results reveal that the average wake length (defined as the downstream distance where the wind speed has recovered to 95 % of the free-stream wind speed) under stable conditions exceeds 50 km, while under neutral/unstable conditions, the wake length amounts to around 15 km.

The analysis of wind farm cluster wake interaction is a complex task, as different interacting processes on multiple scales have to be taken into account. On the one hand, these effects depend on climatological and seasonal changes, and on the other hand, the wind farms extend over very large areas, experiencing natural spatial gradients with regard to the wind conditions. This makes it necessary to find new long-term wind speed measurements of the incoming wind, important not only for wind farms already installed but also for future wind farms to be installed in the vicinity of a cluster (Neumann et al., 2020).

Due to the high spatial and temporal resolution, long-range-scanning Doppler wind lidars (also lidar, light detection and ranging) have gained importance in the wind energy industry for a variety of applications, such as wind resource assessment (Neumann et al., 2020), wind turbine and wind farm wake studies (Schneemann et al., 2020), and power performance testing (Rettenmeier et al., 2014; Gómez Arranz and Courtney, 2021). Especially in the offshore sector, tradi-

tional masts are associated with a high cost and long approval processes. In contrast, scanning wind lidars are cheaper, very flexible in terms of the scan set-up and the installation (for instance, on a wind turbine transition piece), and easily accessible for system maintenance during the maintenance routines of wind farms. In the past, most studies, using scanning Doppler lidar, have been limited to investigations of the spatial wake characteristics of isolated wind turbines (Wang and Barthelmie, 2015; Bastine et al., 2015; Bingöl et al., 2010; Käsler et al., 2010) or individual wind farms (Smalikho et al., 2013; Aitken et al., 2014; Iungo and Porté-Agel, 2014; Herges et al., 2017; Krishnamurthy et al., 2017; Zhan et al., 2020), such as the velocity deficit, the single wake extent (length and width) of a wake, and wake meandering (Trujillo et al., 2010; Krishnamurthy et al., 2017) under various atmospheric conditions. More recently, lidars have also been used to study the wind speed reduction upstream of a wind farm, the so-called blockage effect (Schneemann et al., 2021). Only a few studies have focused on the effects of cluster wind farm wakes on the wind speed (Schneemann et al., 2020), the value of the scanning lidar measurements for validating wind farm parameterizations in mesoscale models (Goit et al., 2020) or simple wake engineering models used for wind farm optimization and energy yield estimation (e.g., Brower and Robinson, 2012).

Mesoscale models are capable of resolving effects that are relevant on these large scales using wind farm parameterizations developed to account for the wind speed reduction and turbulence increase downstream of wind farms (Fitch et al., 2012; Volker et al., 2015). A validation of simulations with airborne in situ data (Lampert et al., 2020) has been one of the aims of the projects WIPAFF (Wind Park Far Field) and X-Wakes (Interaction of the wake of large offshore wind farms and wind farm clusters with the marine atmospheric boundary layer) (Siedersleben et al., 2018b, a, 2020), and the airborne datasets have been used as reference for the validation of simulations and parameterizations (Akhtar et al., 2021; Larsén and Fischereit, 2021). In this study, in order to determine the wake effects of interacting wind farms, data from different measurement locations and methods are combined with the aim of obtaining a comprehensive picture of the wind situation in the region of an offshore wind farm cluster.

This paper is structured as follows. Section 2 provides an overview of the locations and datasets used, including a thorough description of the scanning lidar set-up, airborne measurements and mesoscale simulations. Section 3.1 presents a direct comparison of the lidar data with high-resolution airborne data in the vicinity of the measurement location; visualization of the aircraft measurements and a mesoscale model data give an example of the spatial extent of wind farm cluster wakes. Section 3.2 shows the influence of upstream wind farms by comparing the scanning lidar data with mesoscale simulations without the wind farm parameterization (to estimate the wind speed deficit) and with consideration of the



wind farm wake (to compare the model output with the in situ scanning data). After a brief discussion of the study, the conclusions are presented in Sects. 4 and 5 respectively, where the potential of the scanning wind lidar for validating wind farm parameterizations in numerical simulations is highlighted.

## 2 Site and methods

A field campaign using a scanning Doppler lidar was conducted at the western edge of the wind farm Gode Wind 1 in the German Bight (see Fig. 1) for a period of 5 months, from May to September 2020. Additionally, data from the Dornier 128 D-IBUF research aircraft of the Technische Universität (TU) Braunschweig are used for a single flight to extend the range of the available wind speed measurements upstream, around and within the wind farm cluster wakes. Due to the lack of a free wind reference (without any flow disturbance generated by the wind farms), high-resolution mesoscale model data from the Weather Research and Forecasting model (without the wind farm parameterization, hereafter WRF) were used to assess the wind speed deficit due to the presence of wind farms surrounding the lidar measurement location. Moreover, the scanning wind lidar dataset is used to evaluate the WRF model outputs considering wind farm wakes with the wind farm parameterization of Fitch (Fitch et al., 2012), hereafter referred to as the WRF-WF set-up.

Starting from the location of the scanning lidar measurements, five different sectors were defined for the subdivision of the measurement data into different wind direction regions. Figure 1 shows a map of the study area in the German Bight with the defined wind direction sectors. The individual regions are labeled R1 to R5.

A detailed description of the measurement methods can be found in the following sections. For the classification into the five different regions according to the wind direction, the actual position of the profile measurements at a distance of 1.5 km west of the scanning lidar device was used. From here, the positions of the outermost wind turbines of each wind farm cluster were used to limit the area as presented in Table 1. The regions R2 (south of the lidar location) and R5 (northwest) are not influenced by upstream wind farms. Region R1 (east) is influenced by the wind farms Gode Wind 1 and 2. Region R3 is influenced by the wind farm Nordsee One and region R4 by the wind farm cluster N-2 composed of the wind farms Trianel Borkum, Merkur, alpha ventus, and Borkum Riffgrund 1 and 2 (see Table 2 for a summary of the key characteristics of the wind farms surrounding the scanning lidar measurements).

After dividing the measurements into different regions based on wind direction, the lidar data have been further divided into subsets of atmospheric stability, which is expected

**Table 1.** Ranges of the individual wind sectors (regions) and distances based on the measurement location of the scanning lidar system.

Region	Sector boundaries [°]	Distance to lidar meas. point [km]
R1	[24, 170]	1.5
R2	[170, 186]	(free wind)
R3	[186, 235]	8
R4	[235, 277]	20
R5	[277, 24]	(free wind)

to strongly affect the wind speed downstream due to the presence of far-field wind farm wakes (Cañadillas et al., 2020).

In this study, we use the static atmospheric stability, which only takes into account buoyancy effects and is characterized through the lapse rate ( $\gamma$ ) based on the temperature gradient at two different altitudes, sea surface temperature (SST) and air temperature at the height of the transition piece (23.3 m) corrected for air pressure and density effects to obtain the virtual potential temperature ( $\theta_v$ ) gradient,

$$\gamma = \frac{d\theta_v}{dz} \approx \frac{\Delta\theta_v}{\Delta z}, \quad (1)$$

with  $z$  the measurement height. Negative values of the virtual potential temperature gradient  $\gamma$ , or lapse rate, represent an unstable stratification of the atmosphere; positive values represent a stable stratification; and values around zero represent a neutral stratification. The stability classes were chosen as follows:

- $\gamma < -0.04$ : unstable stratification,
- $-0.04 \geq \gamma \geq 0.04$ : near-neutral stratification,
- $\gamma > 0.04$ : stable stratification.

A thorough discussion of different parameters used to characterize stability and the influence on wakes is provided by Platis et al. (2021), who use similar values to classify atmospheric stability based on lapse rate. Ideally, it would be optimal to measure the air temperature at hub height or above, but due to the lack of measurements and considering that the air temperature measurements at the nacelle are highly biased due to the rotor effect, we consider our estimation to be suitable as a first-order approximation for the framework of this study.

### 2.1 Scanning wind lidar

Wind data were recorded with a long-range-scanning Doppler wind lidar system of the type Streamline XR manufactured by Halo Photonics, UK (METEK-GmbH, 2021). The lidar system emits short laser pulses into the atmosphere and detects the radiation backscattered by aerosols



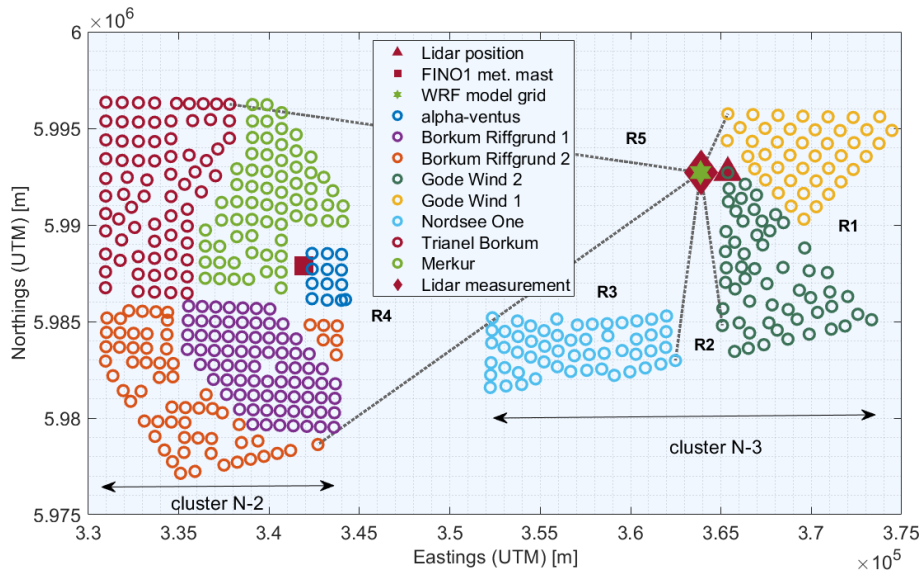


**Figure 1.** Location of the scanning lidar between the wind farm clusters showing the five sectors (from R1 to R5) into which the data are grouped for the analysis (dashed black lines). The individual wind turbines are represented by circles, and each individual wind farm is shown in a different color. The location of the meteorological mast FINO1 is also indicated (red square). The WRF model grid point investigated in this study is marked with a green star. Lidar system and lidar profile measurement locations are marked with a red triangle and a red diamond, respectively. Coordinates refer to UTM WGS84, zone 32.

**Table 2.** Properties of the wind farms (as of May 2020) surrounding the scanning lidar measurement. The cluster name is defined by the German Federal Hydrographic Agency BSH, wind turbine (WT) type within the wind farms, WT rated power ( $P_{\text{rated}}$ ), their rotor diameter ( $D$ ), hub height ( $h$ ) for LAT (lowest astronomical tide) and the number of wind turbines (No. of WTs).

Cluster	Wind farm	WT type	$P_{\text{rated}}$ [MW]	$D$ [m]	$h$ [m]	No. of WTs
N-3	Gode Wind 1 and 2	Siemens	6	154	110	55/42
N-3	Nordsee One	Senvion	6.2	126	90	54
N-2	Alpha ventus	Senvion/Adwen	5	126/116	92/90	6/6
N-2	Borkum Riffgrund 1 and 2	Siemens/Vestas	4	120/154	83	78/56
N-2	Trianel Wind Farm Borkum 1 and 2	Adwen/Senvion	5, 6.3	116/164	87/111	40/32
N-2	Merkur	GE	6	150	102	66

through optical heterodyning. This makes it possible to determine both the intensity of the backscattered radiation and its Doppler shift in the line-of-sight (LOS) direction, which is proportional to its radial wind speed, also called LOS wind speed.

The lidar system (see Fig. 2) was installed on the transition piece (TP) of the northernmost wind turbine (K01) of the wind farm Gode Wind 1, at a height of approximately 23.3 m LAT (lowest astronomical tide) and positioned on a metal support structure for a clear view in the azimuthal range  $[160^\circ, 20^\circ]$  over the railing to the west. In addition to the scanning lidar device, other sensors for collecting thermodynamic data (namely air temperature and humidity, pressure, precipitation, and water surface temperature) were installed. The purpose of these measurements was to characterize the atmospheric stability regime with the method previously described. The thermometer and hygrometer were mounted on

a 50 cm long boom at a height of 22.5 m LAT, and the barometer was located in the control cabinet 50 cm below. The infrared sensor for measuring the SST was located on the railing of the TP and consists of a pair of sensors, with one sensor pointed towards the sea surface and the other towards the sky, which allows the temperature measurements to be corrected for the effects of background radiation (refer to Fröhmann et al., 2018, for further details).

The lidar system, with a maximum range of 10 km, was set up with a gate length of 120 m. The sampling rate of the back-scattered signal of 50 MHz gives a spatial resolution of 3 m along the LOS. Furthermore, the accumulation rate can be reduced so that the highest beam sampling rate is 10 Hz. The laser beam is directed by a scanner with an arrangement of mirrors with 2 degrees of freedom, allowing scanning in all directions. The positioning of the scanner at the top of the lidar container box enables scanning of the sky above and a

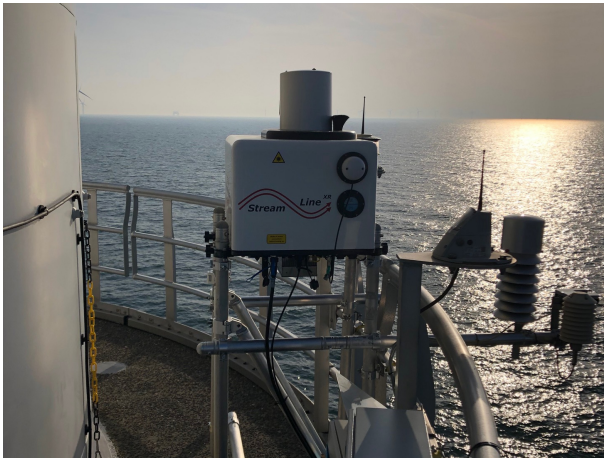


**Figure 2.** Long-range-scanning lidar and additional measurement systems (on the right side) on the TP of one of the northernmost wind turbines (K01) at the wind farm Gode Wind 1.

**Table 3.** Overview of scanning lidar set-up during the measurement campaign.

Parameter	Value
Target distance [m]	1500
Target heights [m]	40, 80, 120, 160, 200
Elevation angles [°]	0.64, 2.17, 3.70, 5.22, 6.77
Azimuth sectors [°]	$230^\circ \pm 7.5^\circ$ and $300^\circ \pm 7.5^\circ$
Scan duration [s]	75
Scan speed [° s <sup>-1</sup> ]	3.17
Accumulation time [s]	0.6
Range gate length [m]	120

reduced area below the horizontal, without interference with itself.

The lidar performed plan position indicator (PPI) scans (at five elevations) with continuous scanner movement in two azimuthal sectors of 15° width upstream of the wind turbine K01. An overview of the lidar set-up is given in Table 3.

The set-up enabled the measurement of the wind profile in the vicinity of the wind farm Gode Wind 1 (approximately 1.5 km west of the wind turbine K01). To derive vertical profiles, we generate a so-called partial velocity azimuth display (VAD) plot at several altitudes using a sinusoidal function fitted to radial velocity data (Werner, 2005), which is represented as a function of azimuth. Then the results are calculated in terms of the Cartesian velocity components ( $u$ ,  $v$ ,  $w$ ), and finally the wind speed and direction are derived. The classical approach relies on four radial velocities measured at constant elevation and in four quadrants in the azimuth around the lidar. In our approach, we rely on several radial velocities measured continuously on a limited area in azimuth and constant elevation to avoid measurements influenced by the wake of the wind farms Gode Wind 1 and 2. The

general sketch of the approach in Fig. 3a shows how data are selected for the VAD plot near a target point and for several heights (panel b). After selecting data for an altitude, a check is made to see if the data meet a minimum carrier-to-noise ratio (CNR), and then a sine function is fitted using random sampling consensus (RANSAC) (Fischler and Bolles, 1981). This last method is used to avoid the remaining outliers and to increase the robustness of the fitting procedure.

As the lidar was positioned west of Gode Wind 1, the scanning was performed to the western side, targeting five heights above LAT, namely at 40, 80, 120, 160 and 200 m. In this free sector, we followed the scanning trajectory shown in Fig. 4a and with the scanner set-up shown in Table 3. In Fig. 4b, an example of the VAD results for the wind speed and wind direction for 1500 m and a height of 120 m is shown. In practice, every time a scan is finished, i.e., every 75 s (see key scanning parameters in Table 3), a VAD is performed and wind speed and wind direction at all five heights are stored. Finally, these data are averaged over 10 min.

An important point to consider when measuring wind with a lidar system is the orientation of the system. Orientation errors in the scanning lidar affect the exact position at which the wind is interrogated by the laser beam. Three angles are used to fully define the orientation of the lidar in three-dimensional space, namely bearing, tilt and roll. The further the distance to the lidar, the larger the error in positioning is, due to errors in one of these angles. It is therefore necessary to determine these angles at very high accuracy in order to reduce and properly quantify the positioning uncertainty. While the offset in the azimuthal direction between the geographic north and the lidar's north mark can be determined with a compass, this is very inaccurate for the site installation because the turbine structure affects the magnetic field around the lidar. A better option is to use the lidar itself and neighboring turbines of which their position is known ("hard targeting"). In this study, we target turbines of the neighboring wind farm Nordsee One at distances between 8 and 10 km and identified them by their very high backscattered signal with an accuracy of at least 0.1°. In addition, the system is equipped with an internal inclinometer, which is used to quantify tilt and roll. However, the manufacturer does not provide calibration information for this sensor. Furthermore, due to the high relevance of these angles, it is desirable, if not mandatory, to perform an on-site assessment of mounting errors and inclinometer performance. For this purpose, we apply the so-called sea surface leveling (SSL) proposed by Rott et al. (2022) during the commissioning of the lidar system at the offshore site. In this procedure, the sea surface is used as a reference to assess the orientation of the lidar system relative to the horizontal plane. Mainly, the scanning lidar, which is installed several meters above the sea, is set to perform a scan with constant downward elevation and constant azimuth velocity. In this set-up, the backscattered lidar signal describes the surface of a cone that extinguishes by absorption as it enters the water. The geometric analysis of

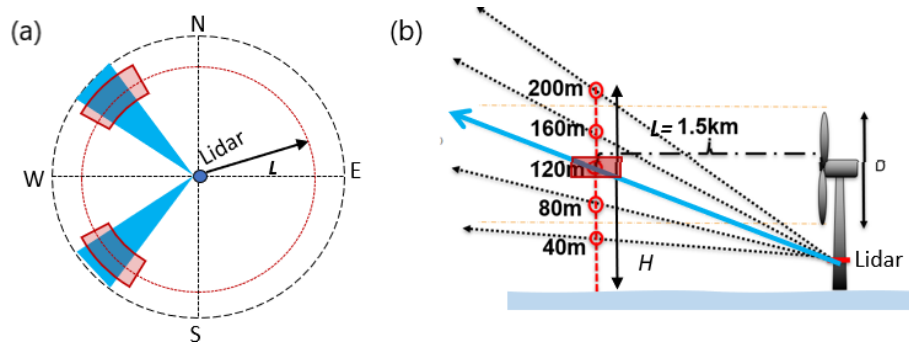


**Figure 3.** (a) Sketch of scanning for partial VAD. Shaded areas in blue represent areas where the wind is interrogated continuously. Areas in red represent the volumes where data for VAD are selected. (b) Sketch of the vertical profile of the wind speed and wind direction at the five target heights selected in this campaign, where  $L$  is the distance from the lidar system to the measurement location.

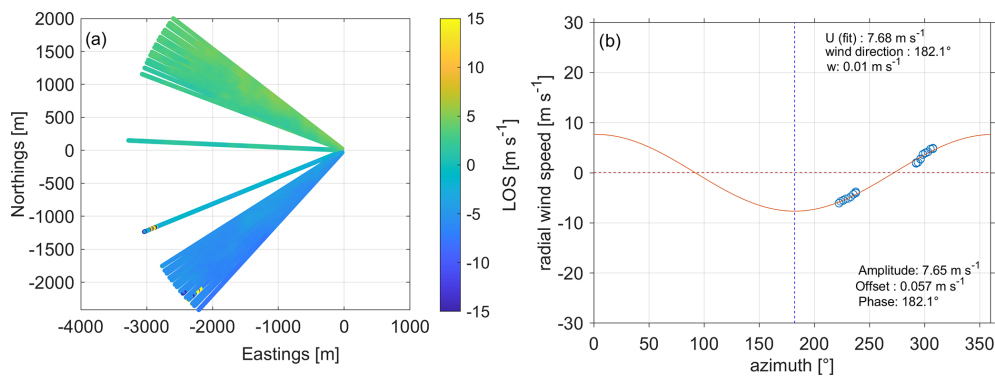


**Figure 4.** (a) Example of the top view of the radial wind speed ( $u_r$ ) for a single full scan taking approximately 75 s on 29 August 2020. Eastings and northings are given in meters and relative to the lidar position. (b) Example of VAD data selected from the scan in (a) for a distance of  $1500\text{ m} \pm 150\text{ m}$  and a height of  $120\text{ m} \pm 5\text{ m}$ . The bottom legend shows results for the radial wind speed fit. The top legend indicates results of the wind speed.

the elliptical shape of the intersection of the cone with the water surface (see Fig. 5) provides the tilt and roll angles of the cone axis and thus of the lidar itself.

We adopt the results of the SSL method as a reference because they show the misalignment of lidar, scanner and support structure combined in a direct way. For this reason, the misalignment results from the SSL can be used in trajectory planning. Eventually, the data could also be used to calibrate the internal inclinometer or any other auxiliary inclinometer used in a campaign. The SSL is performed regularly to check if the alignment has changed.

To assess the robustness of the SSL and its performance against the internal inclinometer of the scanner system, we ran the SSL continuously for almost 18 d from 6–24 August 2020. Figure 6a and b show, respectively, the time series of tilt and roll obtained from the SSL and the internal inclinometer. Each time step represents the result of a full SSL scan (with a duration of about 2.5 min) and the corresponding mean value of the inclinometer data. In addition, the standard deviation of the inclinometer is shown as a band of  $\pm\sigma$ . The results show a good correlation between the two signals. The

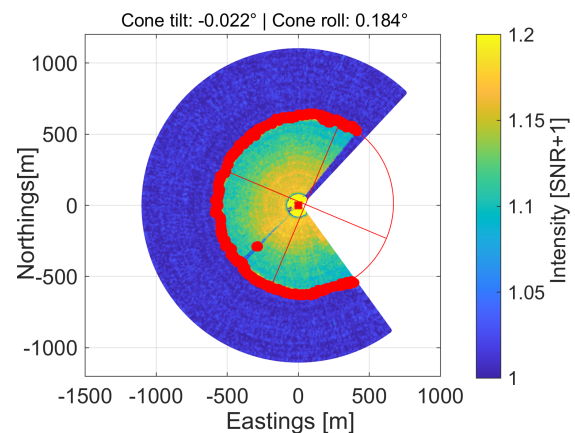


**Figure 5.** Example of backscattered signal intensity after SSL scanning. Red dots show the estimated water entrance. The red ellipse and its axes reveal a misalignment of the sensor. The blind area to the east is due to the turbine tower.

SSL indicates a different bias in each axis of the inclinometer, namely  $\text{tilt}_{\text{bias}} = -0.05^\circ$  and  $\text{roll}_{\text{bias}} = +0.05^\circ$ . A change

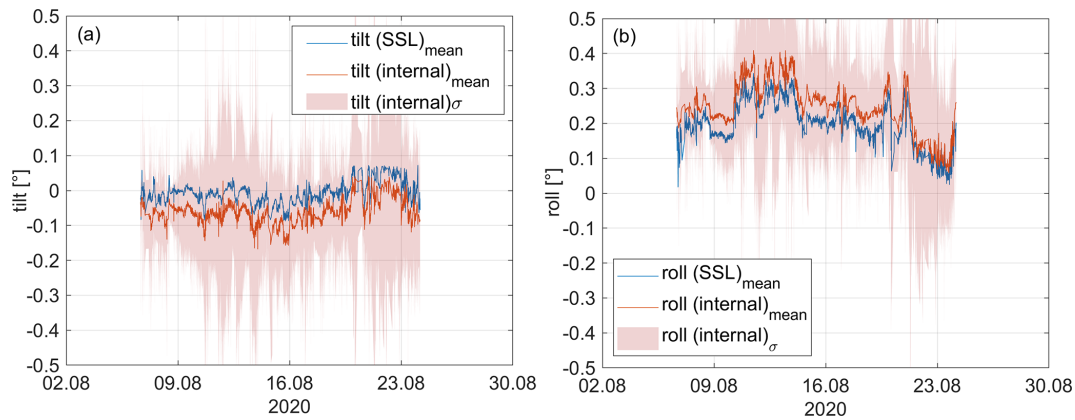


**Figure 6.** (a) Lidar tilt from internal inclinometer (internal, red) and from SSL (blue). The red band shows the standard deviation (SD) of the inclinometer tilt during each SSL scan. (b) Lidar roll from internal inclinometer (internal, red) and from SSL (blue). The red band shows the standard deviation ( $\sigma$ ) of the inclinometer roll during each SSL scan.

in mean tilt and roll over time can be observed. This is due to the varying conditions of the support structure. In particular, the thrust of the wind turbine changes the magnitude and direction of the tower inclination depending on the wind direction and wind speed. The error between the two sensors (now assuming SSL as the sensor) can be seen in Fig. 6a and b. After debiasing both errors, we obtain mean-square errors of  $\epsilon_{\text{tilt}} = 0.01^\circ$  and  $\epsilon_{\text{roll}} = 0.02^\circ$ . Finally, the variance of the inclinometer is a consequence of the system dynamics, which must be taken into account when assessing the accuracy of the scanner alignment. The total variance of the inclinometer signals is  $\sigma_{\text{tilt}} = 0.23^\circ$  and  $\sigma_{\text{roll}} = 0.24^\circ$ . It should be noted that in the absence of information on the calibration of this sensor, we assume this value to be conservative. This is based on the assumption not only that the sensor perfectly detects rotational changes but also that the resulting values are a superposition of rotational and translational movements.

## 2.2 Mesoscale model

Mesoscale simulations, including both undisturbed free wind conditions and the wake-disturbed wind field due to the surrounding wind farm, were performed using the WRF model (version 4.2.1) developed by the National Center of Atmospheric Research (Skamarock et al., 2019). In the WRF model, there are prognostic variables for the horizontal and vertical wind components, potential temperature, geopotential and surface pressure of dry air as well as several scalars such as cloud water and water vapor. The WRF model is well known and widely used in the wind energy community (Huang et al., 2014; Hahmann et al., 2020; Kibona, 2020), and in recent years also for wind farm wake simulations (Pryor et al., 2019; Siedersleben et al., 2018b).

Our set-up was optimized within several research projects for wind energy applications, especially with a focus on offshore conditions (Gottschall et al., 2018; Dörenkämper et al.,

2020; Gottschall and Dörenkämper, 2021). The studies by Gottschall et al. (2018) and Gottschall and Dörenkämper (2021) compare the mesoscale model data from a similar set-up against vertical lidar and mast measurements. The WRF model set-up is based on the extensive sensitivity studies carried out in the framework of the NEWA (New European Wind Atlas) project (Hahmann et al., 2020; Dörenkämper et al., 2020). The final set-up was validated against almost 300 masts in different terrain complexity. In low terrain complexity this set-up showed a bias of the mean wind speed of  $0.06 \text{ m s}^{-1} \pm 0.49 \text{ m s}^{-1}$  evaluated at 110 masts. To limit the number of grid points in the numerical calculations, a nesting technique is used. Three domains centered around the German Bight area are nested, each of a size of 120 grid points with resolutions of 18, 6 and 2 km. Figure 7a shows the distribution and size of the three domains around the site of interest.

The wind turbines were parameterized as momentum sinks and source of turbulence using the Fitch wind farm parameterization (Fitch et al., 2012). In every grid that intersects the rotor disk, the horizontal wind components are reduced to represent the drag of the wind turbine. Different thrust and power curves corresponding to all turbine types were applied. Figure 7b shows the locations of the turbines in the model simulations. Boundary conditions for the model were prescribed by the ERA5 dataset (ERA5 resolution,  $0.25^\circ \times 0.25^\circ$  ( $\sim 30 \text{ km}$ ), 6-hourly) for the atmospheric variables (Hersbach et al., 2020) and the OSTIA dataset for the sea surface variables (Donlon et al., 2012), which provides near-real-time global sea surface temperature at the grid resolution of  $1/20^\circ$  ( $\sim 6 \text{ km}$ ). The WRF version used in this study does account for the turbulent-kinetic-energy advection bug that was recently discovered (Archer et al., 2020).

We performed simulations with and without wind farms and extracted the time series from the WRF simulations at the position of the scanning lidar measurements for the same



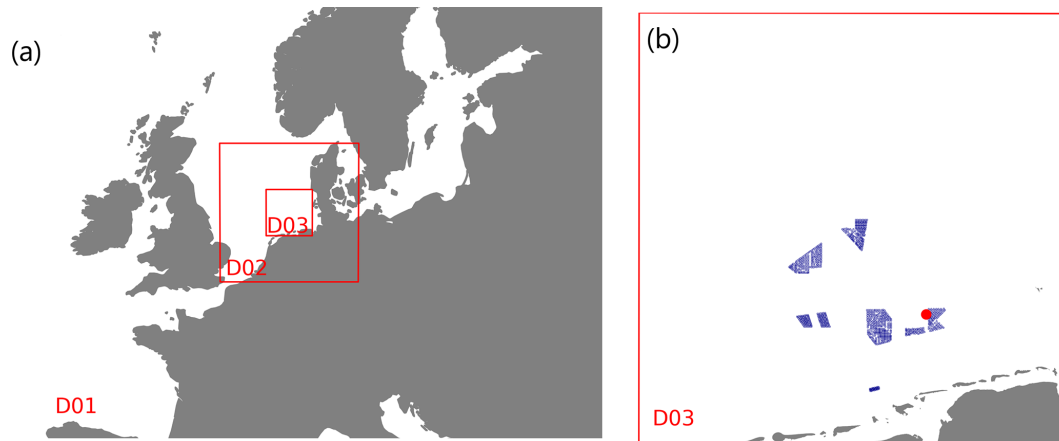


**Figure 7.** (a) Locations of the three WRF model domains (D01, D02, D03) with a grid sizes of 18, 6 and 2 km, respectively. The innermost domain (D03) of (a) is shown in detail in (b) with the locations of the wind turbines accounted for in the simulations and the location of the lidar measurements marked in red. Note that wind farms with a distance of more than 100 km from the site were ignored.

period. The most important settings of the mesoscale model configuration are summarized in Table 4.

### 2.3 Airborne measurements

The spatial extent of the wind farm wakes can be briefly investigated by considering one of the measurement flights carried out during the scanning wind lidar measurement period with the research aircraft Dornier DO-128 operated by the Technische Universität Braunschweig (Lampert et al., 2020).

Although the flight data are limited to a few hours within a single day, they provide an overview of the wind situation at different distances and vertical profiles both upstream and downstream of the wind farm clusters. The research aircraft is equipped with a nose boom to perform high-resolution measurements of the wind vector, temperature, humidity and pressure, sampling at a frequency of 100 Hz (Corsmeier et al., 2001). Sensors for measuring the surface temperature, a laser scanner for determining sea state characteristics and cameras were also integrated (Lampert et al., 2020). During the measurement flights, both the upstream and downstream areas of the wind farm clusters were investigated. The flight pattern included legs of 45 km length that were aligned perpendicular to the main wind direction, therefore crossing the wakes, and vertical profiles from around 15 m altitude up to 1000 m. The individual straight flight legs were horizontally spaced about 10 km from each other. The measurement height was 120 m above sea level, which corresponds to the hub height of the wind farms Gode Wind 1 and 2.

An example of a flight dataset showing multiple wake-transect profiles perpendicular to the mean wind direction, measured downstream of clusters N-2 and N-3 on 3 July 2020, is briefly presented in the next section.

## 3 Wind field modification by wind farm clusters

The strong modification of the wind field by the wind farm clusters is clearly evident in scanning lidar measurements, flight measurements and WRF simulations. Flight measurements enable an initial side-by-side evaluation of the WRF model over a larger spatial scale than is possible with just the scanning lidar system and illustrate the strength and extent of wind farm cluster wakes (Sect. 3.1). The lidar measurements are then compared with WRF model results with and without a wind farm parameterization for the different sectors and atmospheric stability conditions, which enables an evaluation of WRF performance for different upstream wind conditions (Sect. 3.2).

### 3.1 The spatial extension of cluster wakes

Because of the extended range of flight paths around the wind farm clusters, the flight measurements are presented here to complement the lidar measurements. We consider the wake situation of the N-2 and N-3 clusters on 3 July 2020 (10:24–13:02 UTC) when flight legs were performed perpendicular to the mean wind direction ( $\approx 230^\circ$ ) and taking on average 10 min per traversal. The cluster wake limits in Fig. 8a are defined as the physical cluster extent which expands with distance  $x$  at the rate of  $k_w = 0.04$  (wake decay constant for offshore as suggested by Sørensen et al., 2008).

The spatial distribution of the measured wind speed is inferred in Fig. 8a from the flight legs extending perpendicular to the wind direction. Darker colors, representing lower wind speed values, are evident directly behind the wind farms and more dense clusters of wind turbines. In particular, the strong reduction in wind speed downstream of cluster N-2, which is located to the west, but also the wind farms Gode Wind 1 and 2, which are located further to the east, can be clearly seen. Behind the northeastern edge of Gode Wind 2, the wind



**Table 4.** Relevant parameters of the mesoscale model set-up. The references for the different schemes and models are summarized in WRF Users Page (2020).

Parameter	Setting
WRF model version	4.2.1
Planetary boundary layer (PBL) scheme	MYNN level 2.5
Wind farm parametrization	Fitch et al. (2012)
Land use data	MODIS
Surface layer scheme	MYNN
Microphysics scheme	WRF single-moment five-class
Shortwave and long-wave radiation	RRTMG
Atmospheric boundary conditions	ERA5
Sea surface conditions	OSTIA
Horizontal resolution	18, 6 and 2 km
Vertical resolution	60 eta level
Nudging	Grid nudging above PBL
Model output interval	10 min
Nesting	One-way
Land surface model	Unified Noah Land Surface Model
Simulation duration	240 (+24 spin-up) hours

speed is about  $7.5 \text{ m s}^{-1}$ . Upstream of the wind farm, the wind speed is about  $11 \text{ m s}^{-1}$ , which corresponds to a reduction in wind speed of about 30%. Stability during this period was inferred from vertical temperature profiles outside the wake area influenced by the wind farm clusters by steep climbing and descending flight profiles up to an altitude of about 1000 m, which reveal, after an initial close-to-neutral period ( $-0.005 \text{ K m}^{-1}$ ), stable conditions (with a maximum value of  $0.01 \text{ K m}^{-1}$ ) for the last legs and thus explain the strong wakes detected.

Figure 8b shows the horizontal wind speed transect for the closest flight traversal (black line) upstream of the lidar measurement point ( $x = -0.33 \text{ km}$ ) compared with the mean wind speed according to the lidar (green diamond) and standard deviation for the duration of the flight leg (error bars), revealing a suitable agreement between the two measurements for this flight (mean bias =  $0.06 \text{ m s}^{-1}$ ). For this leg, the lapse rate was  $-0.003 \text{ K m}^{-1}$ , implying neutral conditions, which explains the relatively high turbulence signal in the 100 Hz data (gray line). The flight leg was performed between 11:27 and 11:37 UTC.

For comparison, the WRF-WF model results for the times 10:00 (red dotted curve), 11:00 (blue dotted curve) and 12:00 (purple dotted curve) UTC are shown for a transect corresponding to the flight coordinates. Note that for this particular time period, there is an approximate time delay of around 1 h, which is common in WRF results. The flight altitude corresponds to approximately 120 m, corresponding to the mean hub height of the N-2 and N-3 clusters and the mean wind direction of  $228^\circ$  for this transect. While these data also show a decrease in the wind speed between the limits of the cluster N-2, the wind speed of the wake minimum is about  $0.5 \text{ m s}^{-1}$  higher than the flight leg. The mean wind direction differ-

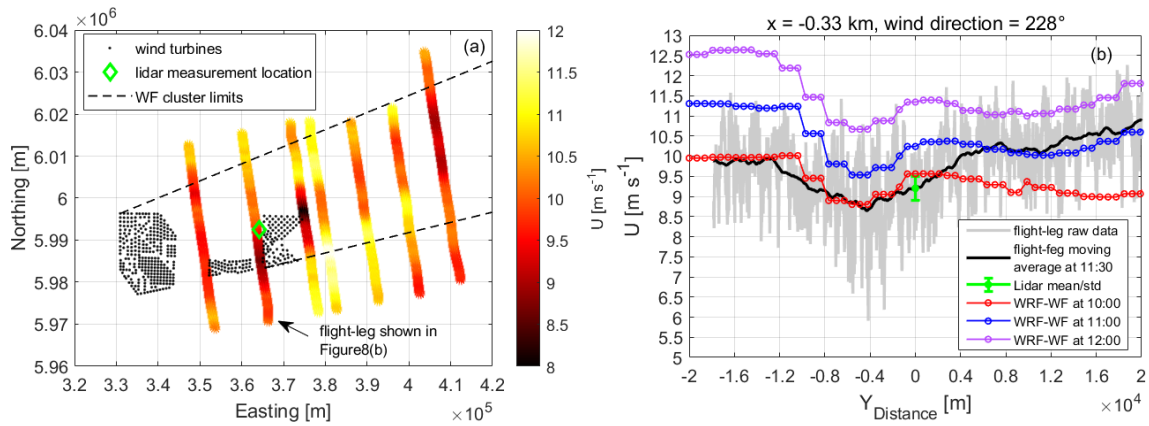
ence between the flight leg and the simulation is about  $10^\circ$ . It is worth mentioning that the WRF simulation does not take into account the wind farms located at about 15 km east of the cluster N-2 (Gemini wind farm), which could explain the difference of more than  $1 \text{ m s}^{-1}$  at the northern part of the wind farm wake (negative  $x$  axes).

Figure 9 shows the WRF-model-simulated horizontal wind field with the wind farm parameterization at mean hub height (120 m) and at different time steps.

Both the observations (Fig. 8a) and model (Fig. 9) show a wake extending at least 40 km downstream of the N-3 wind farm cluster, meaning this wake was long enough to reach the wind farm cluster N-4 (not shown) located about 60 km downstream of Gode Wind. In the spanwise direction, the wake has dimensions of approximately the maximum width of the wind farms. The simulations for different time steps indicate the temporal variability of the wind field well, which has to be considered for a flight duration of 4 h as well. As shown next, significant wake effects were detected by the scanning lidar for cases such as these for flow from the east.

### 3.2 Directional and stability dependence of cluster wakes

We evaluate the lidar-derived wind speed measurements by first dividing the wind direction into five unequal sectors within the cluster wakes (see Fig. 1). The lidar measurements are then compared with mesoscale model results without and with a wind farm parameterization for the different sectors, which enables (1) an estimation of the wind speed deficit when using the model without wind farm parameterization and (2) an evaluation of the model (with wind farm parameterization) performance for the different upstream conditions. Note that because the stability is also wind direction



**Figure 8.** (a) Flight path in the vicinity of the clusters N-2 and N-3 (individual turbines as black points) of the measured wind speed from the measurement flight on 3 July 2020 (10:24–13:02 UTC). The black dashed lines indicate the downstream boundaries of the clusters for the measured wind direction of  $230^\circ$ . The flight altitude during the traversals of the wake clusters was  $\approx 120$  m, and the coordinates refer to UTM WGS84, zone 32. (b) Horizontal wind speed transect for the closest flight traversal upstream of the lidar measurement point ( $x = -0.33$  km, where the negative sign refers to the left of the location of the measurements obtained by scanning lidar) and perpendicular to the wind direction. The gray line represents the 100 Hz data, the black line shows the data filtered by a moving average and the green diamond with error bars represents the lidar mean wind speed and its standard deviation for the duration of the flight leg ( $\approx 10$  min). The red, blue and purple dotted lines show the WRF results with a wind farm parameterization (WRF-WF) from a transect of the model results at 10:00, 11:00 and 12:00 UTC, respectively, based on the flight coordinates.

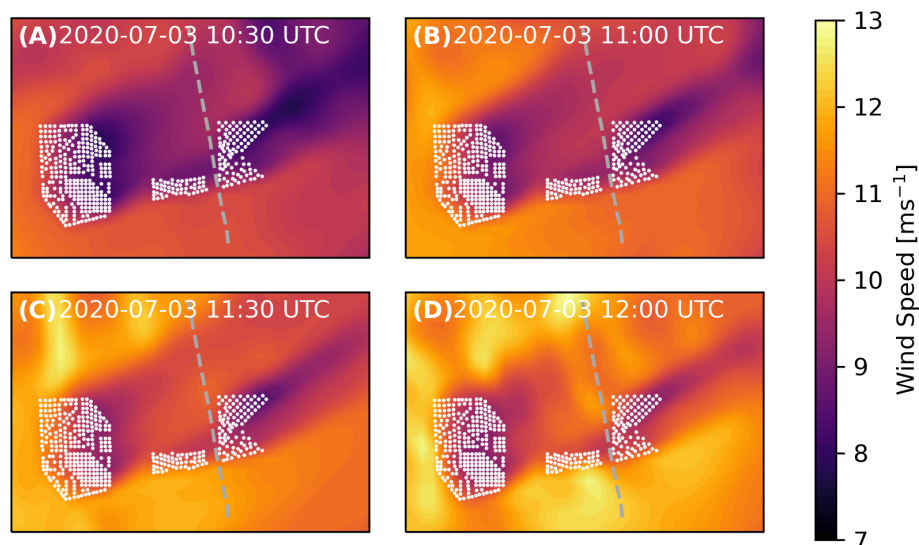


**Figure 9.** Spatial distribution of the modeled wind speed (see color bar) from the WRF simulation with a wind farm parameterization on 3 July 2020 at different time steps. The dashed gray line indicates the position of the flight leg shown in Fig. 8b.

dependent at this site, some sectors are affected more by certain stability conditions.

Figure 10a shows the wind rose from the lidar measurements together with the five wind direction regions R1–5, illustrating the predominance of a west-southwesterly wind direction for the data period presented here, which corresponds to the main meteorological wind direction in the German Bight area (Cañadillas et al., 2020). Figure 10b shows the Weibull distribution for the wind speed together with the scale parameter  $A$  and shape parameter  $k$  for each region

R1–5 at 120 m. This illustrates that meteorological conditions and wind speed distributions within a region are very different, so that a direct comparison of wind data between the different sectors does not make sense due to the different flow conditions found in each sector. (For a more detailed depiction of the lidar data distribution for different sectors, please refer to Appendix B.)

The wind roses derived from lidar data for different atmospheric stabilities are shown in Fig. 11, illustrating that a large part of the data obtained during stable atmospheric

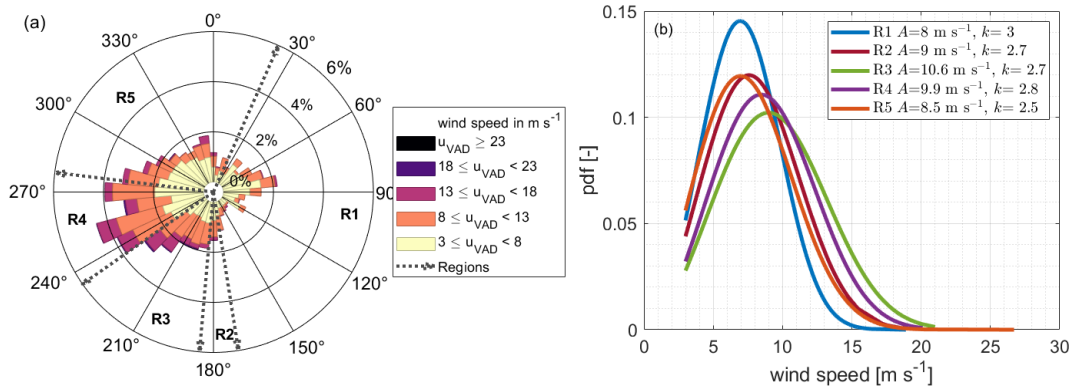


**Figure 10.** Wind rose (a) and Weibull distribution per regions R1–5 (b) at 120 m altitude measured by the scanning wind lidar for the period from May to September 2020.

stratification correspond to flow from the east. With neutral atmospheric stability, southwesterly winds prevail, while in unstable stratification northwesterly winds are predominant. Unstable and neutral conditions are associated with higher average wind speeds than stable conditions.

The wake-induced wind speed reduction at the position of the lidar measurements is investigated for each wind region using a polar plot for which the mesoscale simulation results (without wind farm parameterization) are used as the reference free wind speed. Since the model data represent an undisturbed state not influenced by wind farms, differences in the wind conditions are to be expected when comparing the two datasets. Especially in the regions R1, R3 and R4, which are directly influenced by the wind farm clusters, lower measured wind speed values are expected. Figure 12 shows the direct comparison of the wind speed values per wind direction of the lidar and the mesoscale model data at 120 m height for (a) unstable, (b) neutral and (c) stable atmospheric conditions. To aid visualization, the boundaries of the regions R1 to R5 and the individual positions of the wind turbines are also indicated.

Relatively good agreement is found between both datasets in unstable conditions and in region R2 in neutral conditions. The difference in wind speed in the other regions is also minimal under unstable stratification where the influence of the wind farms is difficult to detect in the measurements since wind farm wakes are not expected to be large. In contrast, a comparison of the datasets for neutral and stable atmospheric stratification shows a clear discrepancy between the measurements and model results, with this difference particularly evident in the regions R1, R3 and R4, which are directly influenced by wind farm clusters. The maximum difference is about  $4 \text{ m s}^{-1}$  in region R3 in stable stratification. Even with neutral stratification, a difference can be seen in the two wind speed datasets and the regions influenced by wind farms. In the free-wind region, however, both datasets agree very well. The strong fluctuations in the wind speed of the lidar data in region R1 are due to the very small amount of data in neu-

tral stratification (see Fig. 12). For region R5, in the case of stable atmospheric stratification, there are no or too few data available in some wind direction sectors. A comparison of the data from the free-wind sector is not possible here. Nevertheless, the reduction in wind speed caused by the wind farms in the other regions can be clearly seen.

To quantify the effects of the wind farm wake in the different regions, the wind speed deficit ( $\epsilon_{\text{WRF}}$ ) of the lidar-measured wind speed  $u_{\text{lidar}}$  with respect to the mesoscale wind speed  $u_{\text{WRF}}$  is defined as

$$\epsilon_{\text{WRF}} = \left( \frac{u_{\text{lidar}}}{u_{\text{WRF}}} - 1 \right) 100\% \quad (2)$$

and presented in Fig. 13a, which is computed as an average over all points in each wind direction region for unstable, neutral and stable conditions. The bars within a group represent the five measurement heights of 40, 80, 120, 160 and 200 m, and the number of 10 min lidar values within a bar is shown at the end of the bar.

The wind speed deficit  $\epsilon_{\text{WRF}}$  in region R5, the free-wind region, is small for neutral and unstable conditions ( $< 10\%$ ), especially for unstable stratification (1%–2%), for all measurement heights. For the second free-wind sector R2, only small differences between the WRF model and lidar data are evident in the case of unstable and neutral atmospheric stratification. However, the results in this sector vary strongly with height. One possible reason for this is that the lateral extent of the narrow undisturbed corridor in region R2 is too small, only about 3 km, and that the boundaries of the wake effects become wider with increasing distance to a wind farm due to the wake expansion. This effect is enhanced by a stable atmosphere. Even when the corridor was further narrowed by changing the region boundaries of R2, no effect similar to R5 was detected. The small horizontal extent of the corridor and the large distance of the lidar measurement site from this area make a differentiated evaluation of region R2 difficult.

The regions R1, R3 and R4 influenced by the wind turbines all show a relatively large wind speed deficit. As ex-

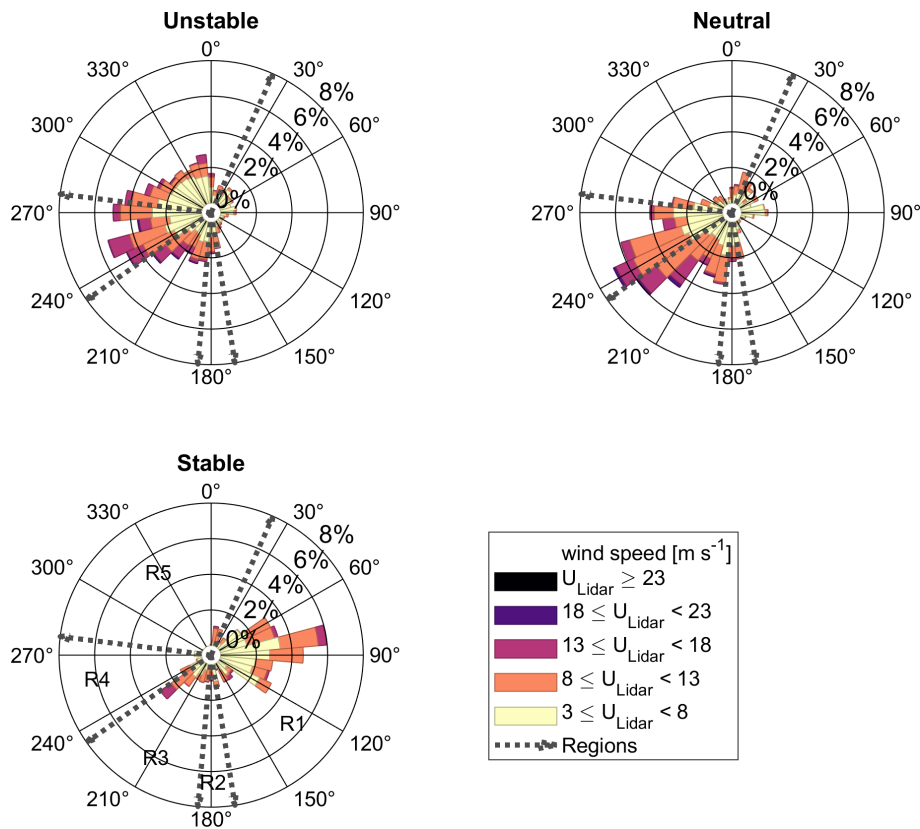


**Figure 11.** Wind roses measured by the scanning lidar for different atmospheric stabilities at 120 m above LAT. The regions R1–5 are indicated by dashed lines.

pected, the  $\epsilon_{\text{WRF}}$  values measured are generally lower (negative) than the values from the undisturbed computational model at all heights and stability conditions, particularly in stable stratification. In region R4 and at a measurement height of 120 m,  $\epsilon_{\text{WRF}} \approx -30\%$  in stable stratification. It is also noticeable that the reduction in wind speed shows a negative trend with increasing height. While the maximum height of the lidar measurements may be 200 m and most of the wind turbines in the surrounding area have a total height between 140 and 180 m, some interaction effects can also be detected above the wind farm due to vertical wake expansion (Siedersleben et al., 2018a; Larsén and Fischereit, 2021). However, as measurements at a height of 200 m are only partially influenced by the wind turbines, as they are no longer completely behind the rotor surface, this probably explains the lower wind speed deficit at 200 m.

The wind speed differences can be further emphasized for different atmospheric stability conditions within a region. Here it is noticeable that, in regions R4 and R3, a strong reduction in wind speed behind the wind farms with increasing atmospheric stability can be seen, but this is much less pronounced in region R1. As regions R3 and R4 have a larger distance to the measuring point of the lidar than region R1, it can be assumed that, in an unstable atmosphere, the wind

speed recovers more quickly in the wake of a wind farm than in stable conditions, as also shown in Cañadillas et al. (2020).

The lateral extent of a wind farm, i.e., the number of wind turbines in the flow direction as well as the wind turbine layout, also affects the strength of the change in wind conditions in the wake of a wind farm cluster. Region R3 is influenced by the wind farm Nordsee One. Here, a maximum of six to seven wind turbines are located behind each other in the flow direction. In region R4, which is influenced by the wind farm cluster N-2, the number of wind turbines in the direction of flow is 17 to 20 turbines, depending on the wind direction. This effect is evident when considering the wind speed differences in regions R3 and R4 under unstable atmospheric conditions. Although the distance of the wind farm in region R3 to the measurement location of the lidar is significantly smaller, the reduction in wind speed is smaller than in region R4. A possible reason for this is the size of the wind farm cluster in R4.

Figure 14 shows a polar plot comparing WRF results, both without and with wind farms, with the lidar measurements, for all atmospheric stabilities detected during the measurement period. To ensure a fair comparison between the mesoscale (WRF-WF) model and the lidar, hourly production data from energy charts (available at <https://www>.



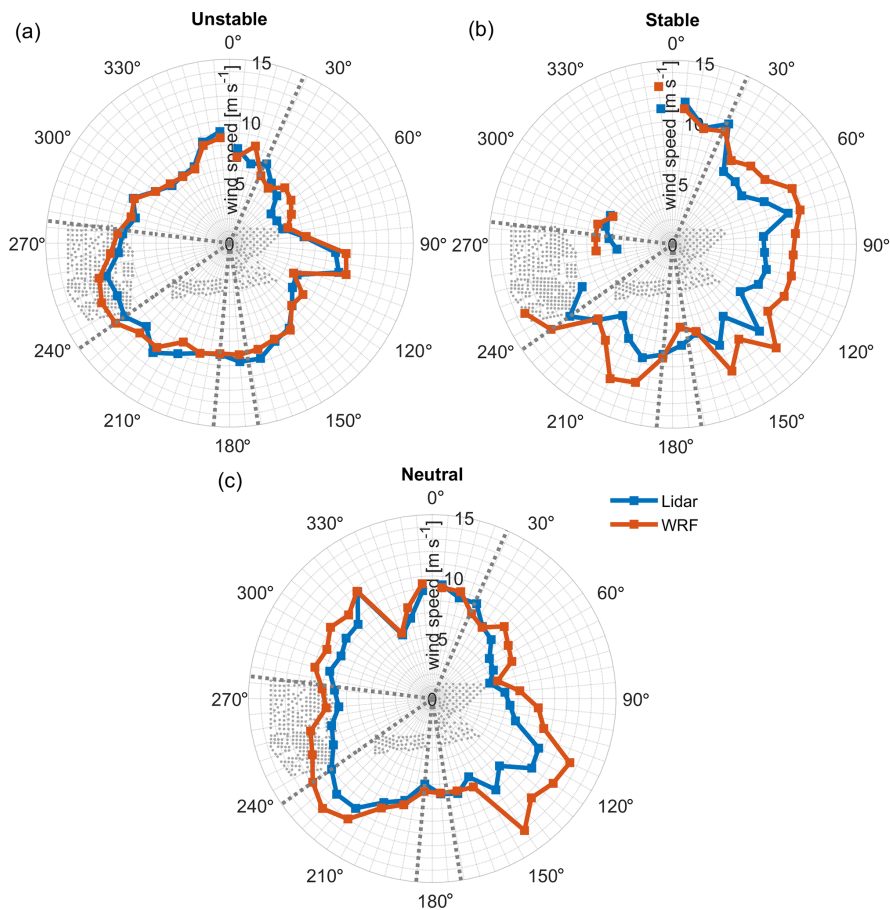


**Figure 12.** Wind speed polar plots of the lidar measurements and WRF results (without the wind farm parameterization) for (a) unstable, (b) stable and (c) neutral atmospheric stratification at the height of 120 m. Wind turbines are indicated by gray points and the regions R1–5 by dashed gray lines.

energy-charts.de/, last access: July 2021) were used for filtering purposes. Only wind farms in operation at the measurement times are included in the mesoscale simulations and thus considered in the comparison.

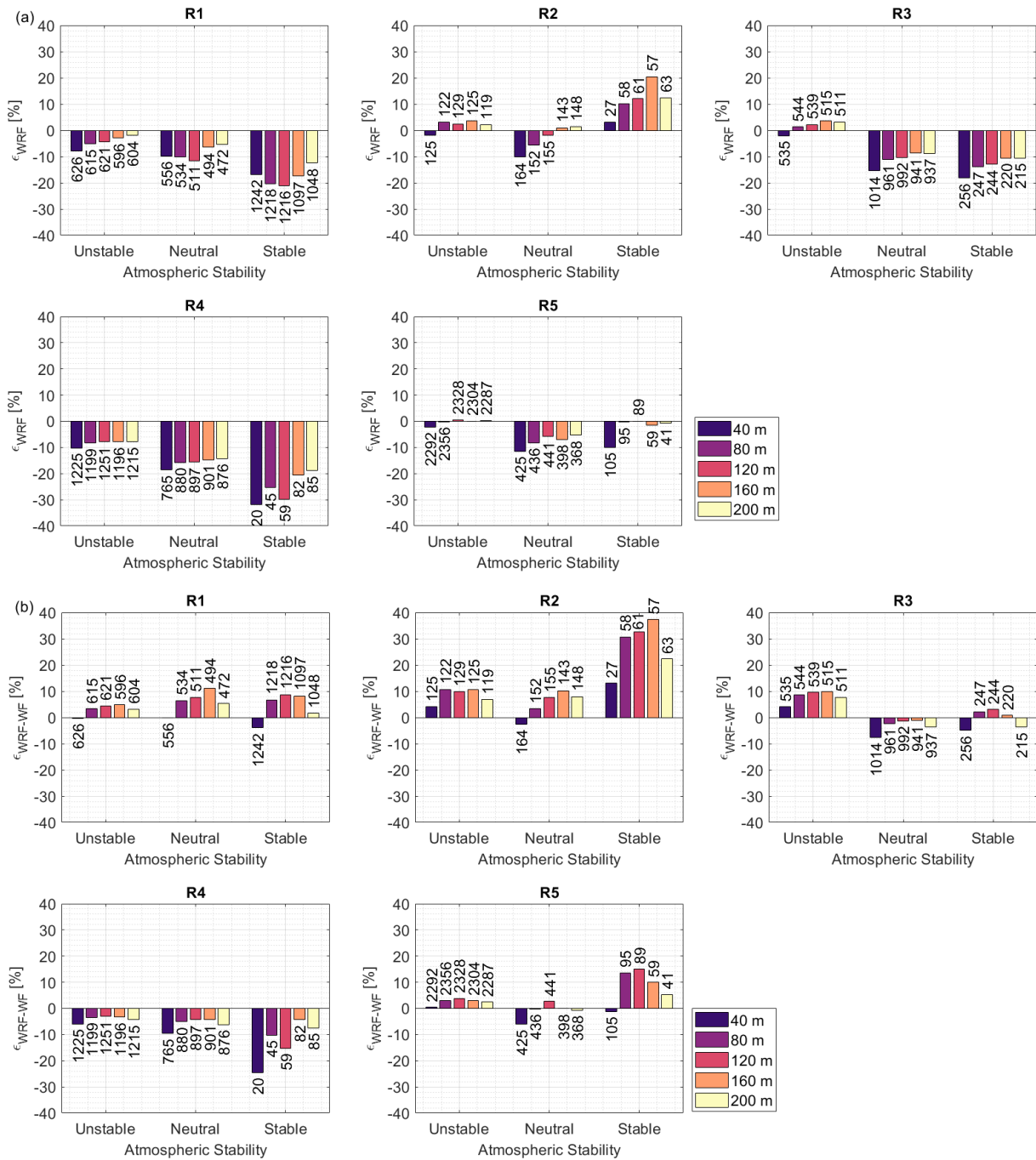
Wind speed deficits of up to about 30 % are shown for the easterly winds at a distance of 1.5 km and up to 15 % for the southwesterly flow at a distance of about 20 km. On the other hand, the lidar (blue) and WRF-WF (green) data show improved agreement between the two datasets for all directions with a difference in wind speed of about 2 %, indicating that the WRF-WF model with the wind farm parameterization included is capable of capturing the mean wake effects detected by the in situ measurements.

As for Fig. 12, the data presented in Fig. 14 are divided into unstable (a), stable (b) and neutral (c) conditions in Fig. 15 for the WRF model with the wind farm parameterization (green line) and for the scanning lidar (blue line). A good agreement is found for most of the regions (R1, R4 and R5) under unstable conditions with a wind speed difference of around 2 % in wind speed. The larger disagreements in wind speed (almost 15 %–20 %) are found under stable

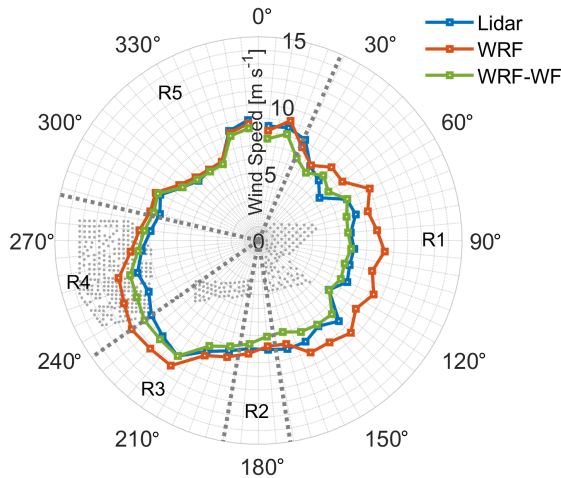
conditions for the regions R1 (downstream of the large wind farm clusters Gode Wind, N-2) and R2 and of around 10 % for the region R3 (downstream of the relatively small wind farm Nordsee One).

Figure 13 (lower panels) also presents the wind speed difference for the mesoscale model  $\epsilon_{\text{WRF-WF}}$ . In general, the wind farm parameterization reduces the absolute magnitude of the wind speed difference  $\epsilon_{\text{WRF-WF}}$  in the waked regions, especially for regions R1 and R4 to, respectively, the east and west of the lidar for all stability classes, and for region R3 to the southwest of the lidar, except for unstable conditions where the value of  $\epsilon_{\text{WRF-WF}}$  is more positive for all heights. This could be due to coastal effects to the south not being properly captured by the model (see also the southern part of the polar plot in Fig. 15a). The difference in the narrow region R2 to the south is also worsened by the wind farm parameterization, including for all stability classes. Our lidar measurements thus serve as a reference for further improvements in wind farm parameterizations.





**Figure 13.** The deficit  $\epsilon_{WRF}$  (Eq. 2) in the wind speed between the lidar measurements and WRF model for (a) no wind farm parameterization  $u_{diff}(WRF)$  and (b) with the wind farm parameterization  $\epsilon_{WRF-WF}$  for regions R1 to R5; for each measurement height 40, 80, 120, 160 and 200 m; and for each stability class. The number below and above each bar indicates the number of 10 min wind speed values.



**Figure 14.** Wind speed polar plot of the lidar (blue) and WRF model without (red) and with wind farm influences (WRF-WF, green) at 120 m. Wind turbines are indicated as gray points, and the sectors are indicated as dashed gray lines.

#### 4 Discussion

In this study measurements of wakes inside an offshore cluster are reported for the first time. Data of a lidar scanner installed on the transition piece of a wind turbine located within a cluster in the German Bight are collected and analyzed within a 5-month field campaign. As part of the goals of this study, a detailed description of the experimental setup and an uncertainty estimation have also been presented. We have implemented a method for obtaining a representative wind speed vertical profile with a single scanning lidar for areas nearby offshore wind farms. The method comprises two novelties in the application of scanning lidars offshore. First, we used a lidar VAD analysis to deliver wind characteristics in a domain between 1 and 2 km instead of concentrating on one-point measurements. Second, we used what we call partial VAD to derive area-equivalent wind speed and wind direction. We selected the area-equivalent approach to obtain more representative wind characteristics, especially across inhomogeneous flow. Moreover, we expected the spatial “averaging” effect to make the results more comparable to mesoscale models. The results presented in this paper support our hypothesis that such a measurement approach is also robust in wind farm wakes and can be applied for resource assessment. On the technical side, this is the first time, to our knowledge, that this type of scanning and data processing have been implemented. One usually obtains wind speed profiles with scanning lidars in the vicinity of wind farms using a dual-Doppler-lidar approach. This means that two scanning lidars operate simultaneously. With our approach we considerably reduce the campaign complexity and execution costs. This has advantages for the industry and is potentially an application for campaigns where fixed structures

and existing infrastructure can be used to install the scanning lidar. Finally, this could be an alternative to floating lidars for some measurement campaigns near wind farms. Moreover, these systems can be relatively easily installed on the TP of an offshore wind turbine. So far, there is no standard similar to that existing for other remote sensing systems, for instance, vertical ground-based lidars (e.g., as part of IEC-61400-12). In addition to the scanning lidar, we describe a novel way to easily estimate the stability of the atmosphere by installing air temperature and sea surface temperature sensors on the railing of the TP. Normally, air and sea temperature and humidity are not measured in close proximity to wind measurements at offshore locations when using a lidar system. However, several previous studies have shown that the stability of the atmosphere plays a decisive role in the value of the wake deficit, so it is necessary to have an estimate of this parameter. We used a WRF model to estimate the wind deficit as no undisturbed wind measurements are available during the scanning survey campaign in the area, which is a general problem of such an inner wind farm cluster analysis. High-fidelity WRF model simulations are used to (1) estimate the average wind speed deficit and (2) compare the inter-wake effects simulated by the model with the scanning lidar data. Analyses are performed for different in-flow directions based on the obstacle encountered at the measurement position (i.e., a wind farm in the case of Nordsee One or a wind farm cluster) and for different atmospheric stabilities. For the comparison of measurements to the WRF model, 10 min time series of wind simulations were extracted at the position of the scanning lidar measurements and without taking into account the effect of the turbines on the model. We have demonstrated that our lidar measurements are able to quantify wake effects within a modern offshore cluster. The dependency of the results is plausible in the sense of external parameters like atmospheric stability.

#### 5 Conclusions

Interaction effects between wind farm clusters N-2 and N-3 in the German Bight are demonstrated via the analysis of data from a scanning lidar, airborne measurements and a mesoscale model. Lidar measurements combined with meteorological sensors reveal the strong directional and stability dependence of the wake strength in the direct vicinity of wind farm clusters. For sectors without upstream wind farms, the scanning lidar data agree with the mesoscale simulations of the undisturbed flow in unstable, neutral and stable atmospheric conditions. In region R5 (sector free of wind farms to the north), the maximum wind speed deficit is about 2 %, whereas in region R4 a reduction of up to 30 % was observed. The magnitude of the deficit increases in all other regions with increasing atmospheric stability.

The wakes still have an influence at 200 m altitude, but it is much smaller than at hub height. This effect is also appar-

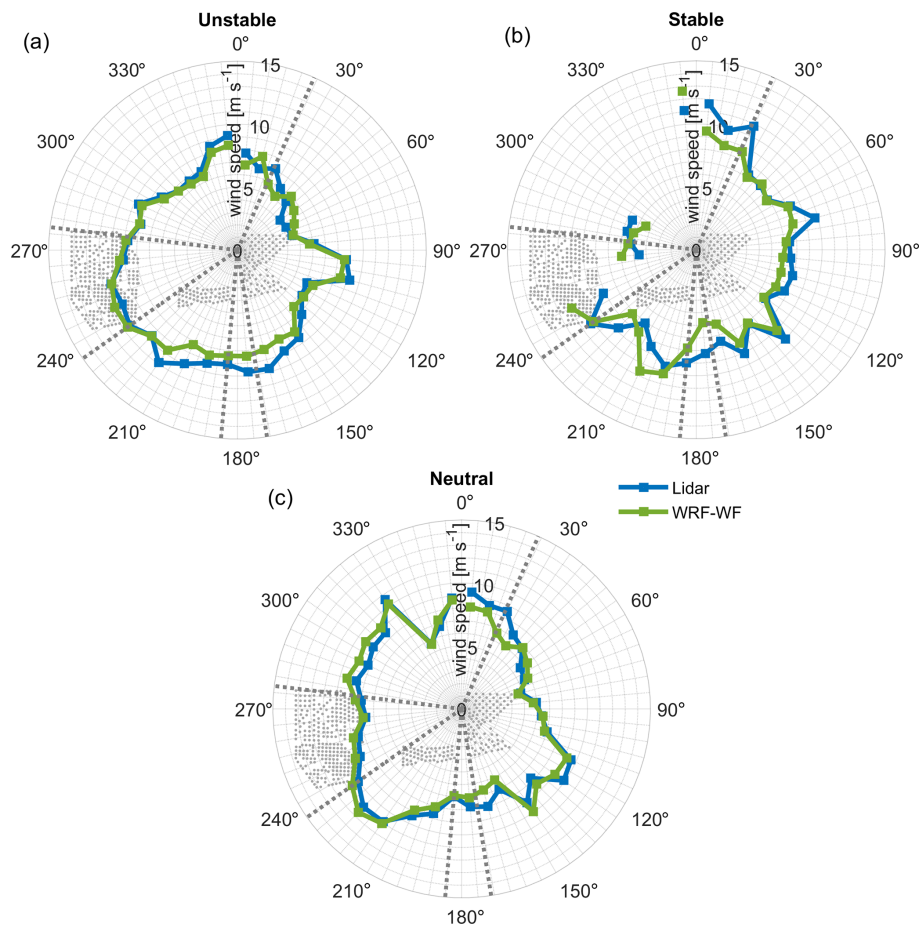


**Figure 15.** Wind speed polar plots of the lidar measurements and WRF-WF results (with the wind farm parameterization) for (a) unstable, (b) stable and (c) neutral stratification at the height of 120 m. Wind turbines are indicated by gray points and the regions R1–5 by dashed gray lines.

ent when examining the wind speed at other measurement heights.

This observational dataset allows for numerical model validations. Taking into account the mesoscale wind farm parameterization (WRF-WF), overall, the model performs reasonably well and is able to capture the wake trend. A good agreement is found for most of the regions (R2, R3 and R5) in unstable conditions, with a relative deviation of around 2 % in wind speed. As expected, the larger disagreements in wind speed (almost 20 %) are found for stable conditions for the regions R1 and R4, amounting to around 10 % for region R3. This means that mesoscale wake simulations still have deficiencies in correctly reproducing the atmospheric stratification and its influence on the development and decay of wind farm wakes. Scanning wind lidar measurements are therefore a powerful tool for the evaluation and improvement of wind model simulations and in particular wind farm parameterizations. We conclude that the scanning Doppler wind lidar is a flexible, accurate and robust tool for deployment inside wind farm clusters for the investigation of the flow phenom-

ena therein. Further work is ongoing to establish longer-term measurement campaigns and comparisons with standard industry models.

#### Appendix A: Quantification of scanning wind lidar uncertainties

Any field measurement has inherent uncertainties which have to be estimated. Typically, standards agreed on by the industry are used to quantify them. In the case of scanning wind lidar, no standard has yet been developed, so in this section we explain the uncertainties that we found to be relevant in the context of this study. In Table A1 we show the summary of uncertainty components. Where applicable, the analysis is based on the methods described in IEC-61400-12-1 (2017) and on industry-accepted best practice guidelines (Wagner et al., 2016; Franke, 2018). Each of the individual uncertainty components is explained in the following sections. Some of them are obtained by known procedures, while others are quantified based on procedures we derived

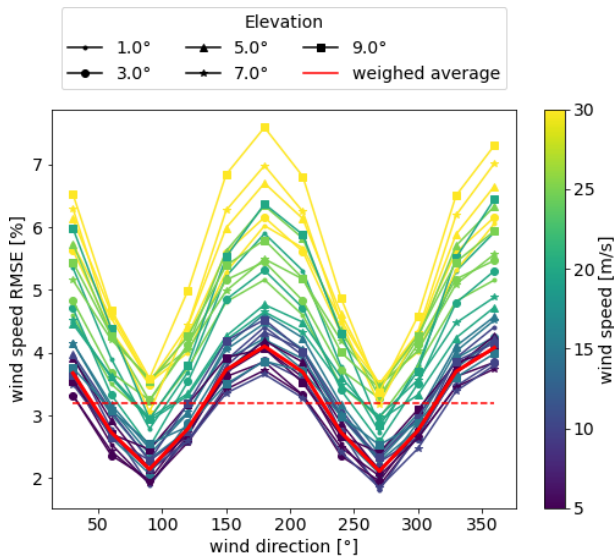


**Figure A1.** RMSE of simulated VAD. The resulting RMSE is calculated for 100 runs of each combination of parameters as shown in Table A2. Lines in red represent values weighed with the frequency distribution of wind speed and wind direction at the site. The dashed line represents the average of the continuous red line.

specifically for the set-up used in this campaign with a conservative approach.

#### A1 Calibration

Prior to offshore deployment of the lidar, a calibration of the system was performed using a reference measurement. For this campaign, the calibration of the system was performed according to the calibration procedure for conventional vertical profilers (IEC-61400-12-1, 2017) at UL's test field in Wehlens in northern Germany. This means that we reproduced the measurement performed by a short-range vertical profiler with an elevation angle of  $60^\circ$ . The uncertainties obtained in this way are assumed to be conservative if compared to a line-of-sight calibration, as suggested by Borraccino et al. (2016). This increased uncertainty is due to the large height span and associated wind shear within a single range gate. During the campaign, the maximum elevation angle was closer to  $7^\circ$ , and hence the height range covered by a single range gate is significantly smaller. Accordingly, the actual uncertainty is expected to be smaller than that obtained during the system verification.

#### A2 Beam positioning

Another uncertainty component is the lidar laser beam positioning, which describes the combined effect of the accuracy of the scanning head in the vertical direction and the vertical wind shear. Here we used scanning lidar precision as given

by the manufacturer and used a vertical power-law profile with an exponent  $\alpha = 0.14$ .

The error of the measurement height due to the curvature of the Earth is considered negligible at the range distance of the measurement location (1.5 km).

#### A3 Mounting error

The mounting error has been quantified by means of SSL. This has been taken into account in the scanning trajectory design to compensate for it. In this way we almost diminish this error; however there is still a very small remaining error.

#### A4 Platform vibration

Height variations in the measurement are caused by orientation changes in tilt and roll, due to platform vibration. An analysis of these signals from the internal inclinometer has been performed over the whole campaign. Finally, the effect of wind shear has been evaluated based on an assumption of a power-law profile with an exponent of  $\alpha = 0.14$ .

#### A5 Wind field inhomogeneity

The effect of inhomogeneous flow, mainly caused by partial wake effects, has been evaluated based on simulation results from Lundquist et al. (2015). The value is based on the assumption of a wake distance of nine rotor diameters downstream.

#### A6 Wind speed reconstruction

Additionally, as pointed out in Newsom et al. (2017) with respect to the VAD method, deviations from the perfect sinusoidal occur due to spatial and temporal fluctuations in the velocity field and instrumental errors, and in the context of the VAD algorithm, any departure from the perfect sinusoidal may be regarded as error. Due the lack of a proper physical set-up during this study, numerical simulations have been performed to assess the robustness of the calculation chain of the partial VAD. The results show an average of approximately 3% mean error due to wind field inhomogeneity on our partial VAD procedure. This can be seen as a conservative estimation of uncertainty in the wind field reconstruction.

The simulations were based on synthetic fields with a defined mean wind speed ( $U$ ) with superimposed Gaussian random noise  $\sigma/U = 10\%$ . The wind field was scanned with the same geometry as our partial VAD and for all combinations of parameters shown in Table A2.

The results in Fig. A1 show the root-mean-square error (RMSE) of simulations against the reference mean wind speed for 100 runs of each parameter combination. A dependence of the wind field reconstruction on both the azimuth opening angle of the scan trajectory and the wind speed can

**Table A1.** Summary of uncertainty components that contribute to the global uncertainty of the wind measurement with the scanning lidar and analysis techniques used during this project.

Component	Estimated value [%]	Remark
Calibration ( $u_1$ )	1.4–2.2	Conventional calibration as a vertical profiler
Beam positioning ( $u_2$ )	0.1	Based on scan head accuracy
Mounting error ( $u_3$ )	< 0.1	Accuracy of SSL
Platform vibration ( $u_4$ )	1.7	Conservative value from inclinometer variance over the measurement period
Wind field inhomogeneity ( $u_5$ )	< 2.5	Conservative value applicable for situations in wake; obtained from Lundquist et al. (2015)
Wind speed reconstruction ( $u_6$ )	< 3.0	Conservative value obtained from simulation of our partial VAD

**Table A2.** Parameter set-up for the VAD simulation.

Parameter	Range	Step
Wind speed ( $U$ ) [ $\text{m s}^{-1}$ ]	[5, 30]	5
Wind direction [ $^\circ$ ]	[0, 360]	30
Scanning elevation [ $^\circ$ ]	[1, 9]	2
Gaussian noise ( $\sigma/U$ ) [%]	10	–

be observed. An average value was obtained based on the dependencies and wind speed distribution.

Six sources of uncertainty have been identified that play a role in the overall uncertainty of the lidar wind speed. Assuming that these uncertainties are independent, they can be combined in quadrature to yield

$$u_{\text{lidar}}^2 = u_1^2 + u_2^2 + u_3^2 + u_4^2 + u_5^2 + u_6^2, \quad (\text{A1})$$

and therefore the overall lidar uncertainty in wind speed ranges between 4.4 % and 4.8 %, which is largely dominated by the wind field inhomogeneity and wind speed reconstruction. It is worth noting that these values are very conservative and are expected to be lower in the case of the wind-free sectors.

## Appendix B: Weibull probability density function of wind speed scanning lidar per wind sector area

Figure B1 is an extension of Fig. 10 in the main text that shows the probability density function of wind speed scanning lidar per wind sector area using the largest free-wind sector (related to region R5) as reference. The bars shown have a width of  $1 \text{ m s}^{-1}$ . The height of the bars corresponds to the normalized density function, i.e., the frequency of the measured values contained in a bar multiplied by the bar width.



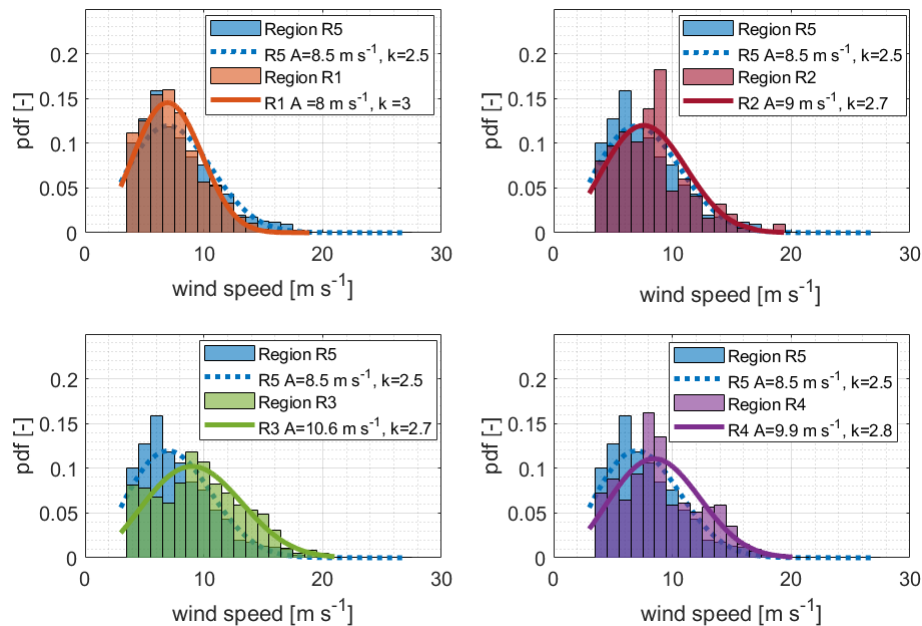


**Figure B1.** Weibull probability density function (pdf) of wind speed scanning lidar per wind sector area. The sector R5 is used as a reference.

**Code and data availability.** The airborne data will be published in PANGAEA after the end of the project X-Wakes. The WRF and scanning lidar data will be available upon request after the end of the project X-Wakes, and the mesoscale model itself is open source and can be obtained from <https://doi.org/10.5065/D6MK6B4K> (NCAR Users Page, 2021). Data from Figs. 12, 14 and 15 are available at <https://doi.org/10.6084/m9.figshare.19747252.v1> (Cañadillas, 2022).

**Author contributions.** BC wrote the manuscript with the support of RF and AL. MB and BC evaluated and prepared most of the figures. JJT together with BC processed the scanning lidar data and wrote the scanning lidar section. MD provided the WRF data and the description of the simulation. TN was involved in the funding acquisition and supervised the research. All authors contributed intensively to an internal review.

**Competing interests.** The contact author has declared that neither they nor their co-authors have any competing interests.

**Disclaimer.** Publisher's note: Copernicus Publications remains neutral with regard to jurisdictional claims in published maps and institutional affiliations.

**Acknowledgements.** The authors would like to thank Rolf Hankers, Thomas Feuerle, Helmut Schulz and Mark Bitter for coordinating and conducting the flight campaigns. Special thanks go to Alexander Tschirch, Hauke Decker and Richard Fruehmann from UL International GmbH for the logistics and installation of the scan-

ning wind lidar. We thank the operator of the wind farm Gode Wind (Oersted) for their support and help with the installation.

**Financial support.** This research has been performed under the X-Wakes project which has been funded by the Federal Ministry for Economic Affairs and Climate Action (BMWK) under grant number FKZ 03EE3008 (A-G) on the basis of a decision by the German Bundestag.

This open-access publication was funded by Technische Universität Braunschweig.

**Review statement.** This paper was edited by Johan Meyers and reviewed by two anonymous referees.

## References

- Ahsbahs, T., Badger, M., Volker, P., Hansen, K. S., and Hasager, C. B.: Applications of satellite winds for the offshore wind farm site Anholt, *Wind Energ. Sci.*, 3, 573–588, <https://doi.org/10.5194/wes-3-573-2018>, 2018.
- Ahsbahs, T., Nygaard, N., Newcombe, A., and Badger, M.: Wind Farm Wakes from SAR and Doppler Radar, *Remote Sensing*, 12, 462, <https://doi.org/10.3390/rs12030462>, 2020.
- Aitken, M. L., Banta, R. M., Pichugina, Y. L., and Lundquist, J. K.: Quantifying Wind Turbine Wake Characteristics from Scanning Remote Sensor Data, *J. Atmos. Ocean. Tech.*, 31, 765–787, <https://doi.org/10.1175/JTECH-D-13-00104.1>, 2014.
- Akhtar, N., Geyer, B., Rockel, B., Sommer, P. S., and Schrum, C.: Accelerating deployment of offshore wind energy alter wind cli-

- mate and reduce future power generation potentials, *Sci. Rep.*, 11, 11826, <https://doi.org/10.1038/s41598-021-91283-3>, 2021.
- Archer, C., Wu, S., Ma, Y., and Jimenez, P.: Two Corrections for Turbulent Kinetic Energy Generated by Wind Farms in the WRF Model, *Mon. Weather Rev.*, 148, 4823–4835, <https://doi.org/10.1175/MWR-D-20-0097.1>, 2020.
- Bastine, D., Wächter, M., Peinke, J., Trabucchi, D., and Kühn, M.: Characterizing Wake Turbulence with Staring Lidar Measurements, *Journal of Physics: Conference Series*, 625, 012006, <https://doi.org/10.1088/1742-6596/625/1/012006>, 2015.
- Cañadillas, B.: Figures wes-2021-159 manuscript, figshare [data set], <https://doi.org/10.6084/m9.figshare.19747252.v1>, 2022.
- Bingöl, F., Mann, J., and Larsen, G. C.: Light detection and ranging measurements of wake dynamics part I: one-dimensional scanning, *Wind Energy*, 13, 51–61, <https://doi.org/10.1002/we.352>, 2010.
- Borraccino, A., Courtney, M., and Wagner, R.: Generic Methodology for Field Calibration of Nacelle-Based Wind Lidars, *Remote Sensing*, 8, 6588–6596, <https://doi.org/10.3390/rs8110907>, 2016.
- Brower, M. and Robinson, N.: The OpenWind deep-array wake model: development and validation, Tech. rep., AWS Truepower, Albany, NY, USA, 2012.
- BSH: Flächenentwicklungsplan 2020 für die deutsche Nord- und Ostsee, Tech. Rep. 7608, BSH – Bundesamt für Seeschifffahrt und Hydrographie, [https://www.bsh.de/DE/THEMEN/Offshore/Meeresfachplanung/Fortschreibung/\\_Anlagen/Downloads/FEP\\_2020\\_Flaechenentwicklungsplan\\_2020.pdf?\\_\\_blob=publicationFile&v=6](https://www.bsh.de/DE/THEMEN/Offshore/Meeresfachplanung/Fortschreibung/_Anlagen/Downloads/FEP_2020_Flaechenentwicklungsplan_2020.pdf?__blob=publicationFile&v=6), last access: 1 April 2021.
- Cañadillas, B., Foreman, R., Barth, V., Siedersleben, S., Lampert, A., Platis, A., Djath, B., Schulz-Stellenfleth, J., Bange, J., Emeis, S., and Neumann, T.: Offshore wind farm wake recovery: Airborne measurements and its representation in engineering models, *Wind Energy*, 23, 1249–1265, <https://doi.org/10.1002/we.2484>, 2020.
- Christiansen, M. and Hasager, C.: Wake effects of large offshore wind farms identified from satellite SAR, *Remote Sens. Environ.*, 98, 251–268, <https://doi.org/10.1016/j.rse.2005.07.009>, 2005.
- Corsmeier, U., Hankers, R., and Wieser, A.: Airborne turbulence measurements in the lower troposphere onboard the research aircraft Dornier 128-6, *D-IBUF, Meteorol. Z.*, 10, 315–329, <https://doi.org/10.1127/0941-2948/2001/0010-0315>, 2001.
- Djath, B., Schulz-Stellenfleth, J., and Cañadillas, B.: Impact of atmospheric stability on X-band and C-band synthetic aperture radar imagery of offshore windpark wakes, *J. Renew. Sustain. Energ.*, 10, 043301, <https://doi.org/10.1063/1.5020437>, 2018.
- Donlon, C. J., Martin, M., Stark, J., Roberts-Jones, J., Fiedler, E., and Wimmer, W.: The Operational Sea Surface Temperature and Sea Ice Analysis (OSTIA) system, *Remote Sens. Environ.*, 116, 140–158, <https://doi.org/10.1016/j.rse.2010.10.017>, 2012.
- Dörenkämper, M., Olsen, B. T., Witha, B., Hahmann, A. N., Davis, N. N., Barcons, J., Ezber, Y., García-Bustamante, E., González-Rouco, J. F., Navarro, J., Sastre-Marugán, M., Sile, T., Trei, W., Žagar, M., Badger, J., Gottschall, J., Sanz Rodrigo, J., and Mann, J.: The Making of the New European Wind Atlas – Part 2: Production and evaluation, *Geosci. Model Dev.*, 13, 5079–5102, <https://doi.org/10.5194/gmd-13-5079-2020>, 2020.
- Emeis, S.: A simple analytical wind park model considering atmospheric stability, *Wind Energy*, 13, 459–469, <https://doi.org/10.1002/we.367>, 2010.
- Emeis, S.: *Wind Energy Meteorology: Atmospheric Physics for Wind Power Generation*, Springer International Publishing, 2 edn., <https://doi.org/10.1007/978-3-319-72859-9>, 2018.
- Fischler, M. A. and Bolles, R.: Random sample consensus: a paradigm for model fitting with applications to image analysis and automated cartography, *Communications of the ACM*, 24, 381–395, <https://doi.org/10.1145/358669.358692>, 1981.
- Fitch, A. C., Olson, J. B., Lundquist, J. K., Dudhia, J., Gupta, A. K., Michalakes, J., and Barstad, I.: Local and mesoscale impacts of wind farms as parameterized in a mesoscale nwp model, *Mon. Weather Rev.*, 140, 3017–3038, <https://doi.org/10.1175/MWR-D-11-00352.1>, 2012.
- Franke, K.: Summary of classification of remote sensing device, type: Leosphere WINDCUBE, techreport PP18030.A1, Deutsche WindGuard Consulting GmbH, Varel, DE, 2018.
- Frühmann, R., Neumann, T., and Decker, H.: Platform based infrared sea surface temperature measurement: experiences from a one year trial in the North Sea, in: *Deutsche Windenergie-Konferenz (DEWEK)*, 2018.
- Goit, J., Yamaguchi, A., and Ishihara, T.: Measurement and Prediction of Wind Fields at an Offshore Site by Scanning Doppler LiDAR and WRF, *Atmosphere*, 11, 1–20, <https://doi.org/10.3390/atmos11050442>, 2020.
- Gómez Arranz, P. and Courtney, M.: WPI – Literature Review: Scanning Lidar For Wind Turbine Power Performance Testing, 2021.
- Gottschall, J. and Dörenkämper, M.: Understanding and mitigating the impact of data gaps on offshore wind resource estimates, *Wind Energ. Sci.*, 6, 505–520, <https://doi.org/10.5194/wes-6-505-2021>, 2021.
- Gottschall, J., Catalano, E., Dörenkämper, M., and Witha, B.: The NEWA Ferry Lidar Experiment: Measuring Mesoscale Winds in the Southern Baltic Sea, *Remote Sensing*, 10, 1620, <https://doi.org/10.3390/rs10101620>, 2018.
- Hahmann, A. N., Sile, T., Witha, B., Davis, N. N., Dörenkämper, M., Ezber, Y., García-Bustamante, E., González-Rouco, J. F., Navarro, J., Olsen, B. T., and Söderberg, S.: The making of the New European Wind Atlas – Part 1: Model sensitivity, *Geosci. Model Dev.*, 13, 5053–5078, <https://doi.org/10.5194/gmd-13-5053-2020>, 2020.
- Herges, T. G., Maniaci, D. C., Naughton, B. T., Mikkelsen, T., and Sjöholm, M.: High resolution wind turbine wake measurements with a scanning lidar, in: *Journal of Physics Conference Series*, vol. 854 of *Journal of Physics Conference Series*, 854, 012021, <https://doi.org/10.1088/1742-6596/854/1/012021>, 2017.
- Hersbach, H., Bell, B., Berrisford, P., Hirahara, S., Horányi, A., Muñoz-Sabater, J., Nicolas, J., Peubey, C., Radu, R., Schepers, D., Simmons, A., Soci, C., Abdalla, S., Abellan, X., Balsamo, G., Bechtold, P., Biavati, G., Bidlot, J., Bonavita, M., De Chiara, G., Dahlgren, P., Dee, D., Diamantakis, M., Dragani, R., Flemming, J., Forbes, R., Fuentes, M., Geer, A., Haimberger, L., Healy, S., Hogan, R. J., Hólm, E., Janisková, M., Keeley, S., Laloyaux, P., Lopez, P., Lupu, C., Radnoti, G., de Rosnay, P., Rozum, I., Vamborg, F., Villaume, S., and Thépaut, J.-N.: The ERA5 global reanalysis, *Q. J. Roy. Meteorol. Soc.*, 146, 1999–2049, <https://doi.org/10.1002/qj.3803>, 2020.

- Huang, H.-P., Giannakopoulou, E.-M., and Nhili, R.: WRF Model Methodology for Offshore Wind Energy Applications, *Adv. Meteorol.*, 2014, 1687–9309, <https://doi.org/10.1155/2014/319819>, 2014.
- IEC-61400-12-1: Wind energy generation systems – Part 12-1: Power performance measurements of electricity producing wind turbines, International Standard IEC TC 29110-1:2016, International Electrotechnical Commission, Geneva, Switzerland, <https://webstore.iec.ch/publication/26603> (last access: 10 December 2021), 2017.
- Iungo, G. V. and Porté-Agel, F.: Volumetric Lidar Scanning of Wind Turbine Wakes under Convective and Neutral Atmospheric Stability Regimes, *J. Atmos. Ocean. Tech.*, 31, 2035–2048, <https://doi.org/10.1175/JTECH-D-13-00252.1>, 2014.
- Käsler, Y., Rahm, S., Simmet, R., and Kühn, M.: Wake Measurements of a Multi-MW Wind Turbine with Coherent Long-Range Pulsed Doppler Wind Lidar, *J. Atmos. Ocean. Tech.*, 27, 1529–1532, <https://doi.org/10.1175/2010JTECHA1483.1>, 2010.
- Kibona, T. E.: Application of WRF mesoscale model for prediction of wind energy resources in Tanzania, *Scientific African*, 7, e00302, <https://doi.org/10.1016/j.sciaf.2020.e00302>, 2020.
- Krishnamurthy, R., Reuder, J., Svoldal, B., Fernando, H., and Jakobsen, J.: Offshore Wind Turbine Wake characteristics using Scanning Doppler Lidar, *Energy Procedia*, 137, 428–442, <https://doi.org/10.1016/j.egypro.2017.10.367>, 2017.
- Lampert, A., Bärfuss, K., Platis, A., Siedersleben, S., Djath, B., Cañadillas, B., Hunger, R., Hankers, R., Bitter, M., Feuerle, T., Schulz, H., Rausch, T., Angermann, M., Schwithal, A., Bange, J., Schulz-Stellenfleth, J., Neumann, T., and Emeis, S.: In situ airborne measurements of atmospheric and sea surface parameters related to offshore wind parks in the German Bight, *Earth Syst. Sci. Data*, 12, 935–946, <https://doi.org/10.5194/essd-12-935-2020>, 2020.
- Larsén, X. G. and Fischereit, J.: A case study of wind farm effects using two wake parameterizations in the Weather Research and Forecasting (WRF) model (V3.7.1) in the presence of low-level jets, *Geosci. Model Dev.*, 14, 3141–3158, <https://doi.org/10.5194/gmd-14-3141-2021>, 2021.
- Lee, J. and Zhao, F.: Global wind report 2021, Tech. rep., Global Wind Energy Council (GWEC), Brussels, Belgium, 2021.
- Lundquist, J. K., Churchfield, M. J., Lee, S., and Clifton, A.: Quantifying error of lidar and sodar Doppler beam swinging measurements of wind turbine wakes using computational fluid dynamics, *Atmos. Meas. Tech.*, 8, 907–920, <https://doi.org/10.5194/amt-8-907-2015>, 2015.
- METEK-GmbH: Doppler Lidar Stream Line XR, Brochure, [https://metek.de/de/wp-content/uploads/sites/6/2016/01/20150410\\_DataSheet\\_StreamLineXR.pdf](https://metek.de/de/wp-content/uploads/sites/6/2016/01/20150410_DataSheet_StreamLineXR.pdf) (last access: 7 February 2022), 2021.
- NCAR Users Page: WRF Model User's Page, WRF Version 4.0.1, <https://doi.org/10.5065/D6MK6B4K>, 2021.
- Neumann, T., Nadillas, B. C., Trujillo, J., and Frühmann, R.: MO-DATA 33 – Meteorologische Messungen N-3.7 und N-3.8, Tech. rep., UL International GmbH, Wilhelmshaven, Germany, 2020.
- Newsom, R. K., Brewer, W. A., Wilczak, J. M., Wolfe, D. E., Oncley, S. P., and Lundquist, J. K.: Validating precision estimates in horizontal wind measurements from a Doppler lidar, *Atmos. Meas. Tech.*, 10, 1229–1240, <https://doi.org/10.5194/amt-10-1229-2017>, 2017.
- Nygaard, N. and Newcombe, A.: Wake behind an offshore wind farm observed with dual-Doppler radars, *Journal of Physics: Conference Series*, 1037, 072008, <https://doi.org/10.1088/1742-6596/1037/7/072008>, 2018.
- Patrick, V., Hahmann, A. N., and Badger, J.: Wake Effects of Large Offshore Wind Farms – a study of the Mesoscale Atmosphere, Ph.D. thesis, DTU Wind Energy, Denmark, 2014.
- Platis, A., Bange, J., Bärfuss, K., Cañadillas, B., Hundhausen, M., Djath, B., Lampert, A., Schulz-Stellenfleth, J., Siedersleben, S., Neumann, T., and Emeis, S.: Long-range modifications of the wind field by offshore wind parks – results of the project WIPAFF, *Meteorol. Z.*, 29, 355–376, <https://doi.org/10.1127/metz/2020/1023>, 2020.
- Platis, A., Hundhausen, M., Mauz, M., Siedersleben, S., Lampert, A., Emeis, S., and Bange, J.: The Role of Atmospheric Stability and Turbulence in Offshore Wind-Farm Wakes in the German Bight, *Bound.-Lay. Meteorol.*, 182, 1573–1472, <https://doi.org/10.1007/s10546-021-00668-4>, 2021.
- Pryor, S. C., Shepherd, T. J., Barthelmie, R. J., Hahmann, A. N., and Volker, P.: Wind Farm Wakes Simulated Using WRF, *J. Phys.: Conf. Ser.*, 1256, 012025, <https://doi.org/10.1088/1742-6596/1256/1/012025>, 2019.
- Rettenmeier, A., Schlipf, D., Würth, I., and Cheng, P. W.: Power Performance Measurements of the NREL CART-2 Wind Turbine Using a Nacelle-Based Lidar Scanner, *J. Atmos. Ocean. Tech.*, 31, 2029–2034, <https://doi.org/10.1175/JTECH-D-13-00154.1>, 2014.
- Rott, A., Schneemann, J., Theuer, F., Trujillo Quintero, J. J., and Kühn, M.: Alignment of scanning lidars in offshore wind farms, *Wind Energ. Sci.*, 7, 283–297, <https://doi.org/10.5194/wes-7-283-2022>, 2022.
- Schneemann, J., Rott, A., Dörenkämper, M., Steinfeld, G., and Kühn, M.: Cluster wakes impact on a far-distant offshore wind farm's power, *Wind Energ. Sci.*, 5, 29–49, <https://doi.org/10.5194/wes-5-29-2020>, 2020.
- Schneemann, J., Theuer, F., Rott, A., Dörenkämper, M., and Kühn, M.: Offshore wind farm global blockage measured with scanning lidar, *Wind Energ. Sci.*, 6, 521–538, <https://doi.org/10.5194/wes-6-521-2021>, 2021.
- Siedersleben, S. K., Lundquist, J. K., Platis, A., Bange, J., Bärfuss, K., Lampert, A., Cañadillas, B., Neumann, T., and Emeis, S.: Micrometeorological impacts of offshore wind farms as seen in observations and simulations, *Environ. Res. Lett.*, 13, 1–12, <https://doi.org/10.1088/1748-9326/aaea0b>, 2018a.
- Siedersleben, S. K., Platis, A., Lundquist, J. K., Lampert, A., Bärfuss, K., Cañadillas, B., Djath, B., Schulz-Stellenfleth, J., Bange, J., Neumann, T., and Emeis, S.: Evaluation of a Wind Farm Parametrization for Mesoscale Atmospheric Flow Models with Aircraft Measurements, *Meteorol. Z.*, 27, 401–415, <https://doi.org/10.1127/metz/2018/0900>, 2018b.
- Siedersleben, S. K., Platis, A., Lundquist, J. K., Djath, B., Lampert, A., Bärfuss, K., Cañadillas, B., Schulz-Stellenfleth, J., Bange, J., Neumann, T., and Emeis, S.: Turbulent kinetic energy over large offshore wind farms observed and simulated by the mesoscale model WRF (3.8.1), *Geosci. Model Dev.*, 13, 249–268, <https://doi.org/10.5194/gmd-13-249-2020>, 2020.
- Skamarock, W., Klemp, J., Dudhia, J., Gill, D., Liu, Z., Berner, J., Wang, W., Power, J., Duda, M., Barker, D., and Huang, X.-Y.: A description of the advanced research WRF version

- 3, Technical Report, 162 pages NCAR/TN-556+STR, NCAR - National Center for Atmospheric Research, Boulder, Colorado, USA, <https://doi.org/10.5065/1dfh-6p97>, 2019.
- Smalikho, I. N., Banakh, V. A., Pichugina, Y. L., Brewer, W. A., Banta, R. M., Lundquist, J. K., and Kelley, N. D.: Lidar Investigation of Atmosphere Effect on a Wind Turbine Wake, *J. Atmos. Ocean. Tech.*, 30, 2554–2570, <https://doi.org/10.1175/JTECH-D-12-00108.1>, 2013.
- Sørensen, T. L., Thøgersen, M. L., and Nielsen, P. M.: Adapting and calibration of existing wake models to meet the conditions inside offshore wind farms, EMD International A/S, 2008.
- Trujillo, J., Bingöl, F., Mann, J., and Larsen, G. C.: Light detection and ranging measurements of wake dynamics part I: one-dimensional scanning, *Wind Energy*, 13, 51–61, <https://doi.org/10.1002/we.352>, 2010.
- Volker, P. J. H., Badger, J., Hahmann, A. N., and Ott, S.: The Explicit Wake Parametrisation V1.0: a wind farm parametrisation in the mesoscale model WRF, *Geosci. Model Dev.*, 8, 3715–3731, <https://doi.org/10.5194/gmd-8-3715-2015>, 2015.
- Wagner, R., Courtney, M. S., Pedersen, T. F., and Davoust, S.: Uncertainty of power curve measurement with a two-beam nacelle-mounted lidar, *Wind Energy*, 19, 1269–1287, <https://doi.org/10.1002/we.1897>, 2016.
- Wang, H. and Barthelmie, R.: Wind turbine wake detection with a single Doppler wind lidar, *Journal of Physics: Conference Series*, 625, 012017, <https://doi.org/10.1088/1742-6596/625/1/012017>, 2015.
- Werner, C.: Lidar – Range-Resolved Optical Remote Sensing of the Atmosphere, chap. Doppler Wind Lidar, pp. 325–354, Springer-Verlag New York, 2005.
- WRF Users Page: WRF Model Physics Options and References, [https://www2.mmm.ucar.edu/wrf/users/phys\\_references.html](https://www2.mmm.ucar.edu/wrf/users/phys_references.html) (last access: 13 July 2020), 2020.
- Zhan, L., Letizia, S., and Valerio Iungo, G.: LiDAR measurements for an onshore wind farm: Wake variability for different incoming wind speeds and atmospheric stability regimes, *Wind Energy*, 23, 501–527, <https://doi.org/10.1002/we.2430>, 2020.



# Cluster wakes impact on a far-distant offshore wind farm's power

Jörg Schneemann<sup>1</sup>, Andreas Rott<sup>1</sup>, Martin Dörenkämper<sup>2</sup>, Gerald Steinfeld<sup>1</sup>, and Martin Kühn<sup>1</sup>

<sup>1</sup>ForWind, Institute of Physics, Carl von Ossietzky University Oldenburg,  
Küpkersweg 70, 26129 Oldenburg, Germany

<sup>2</sup>Fraunhofer Institute for Wind Energy Systems, Küpkersweg 70, 26129 Oldenburg, Germany

**Correspondence:** Jörg Schneemann [REDACTED]@uol.de)

Received: 5 July 2019 – Discussion started: 7 August 2019

Revised: 14 November 2019 – Accepted: 19 November 2019 – Published: 3 January 2020

**Abstract.** Our aim with this paper was the analysis of the influence of offshore cluster wakes on the power of a far-distant wind farm. We measured cluster wakes with long-range Doppler light detection and ranging (lidar) and satellite synthetic aperture radar (SAR) in different atmospheric stabilities and analysed their impact on the 400 MW offshore wind farm Global Tech I in the German North Sea using supervisory control and data acquisition (SCADA) power data. Our results showed clear wind speed deficits that can be related to the wakes of wind farm clusters up to 55 km upstream in stable and weakly unstable stratified boundary layers resulting in a clear reduction in power production. We discussed the influence of cluster wakes on the power production of a far-distant wind farm, cluster wake characteristics and methods for cluster wake monitoring. In conclusion, we proved the existence of wake shadowing effects with resulting power losses up to 55 km downstream and encouraged further investigations on far-reaching wake shadowing effects for optimized areal planning and reduced uncertainties in offshore wind power resource assessment.

## 1 Introduction

Wind energy utilization at sea is an increasingly important part for the transition of the mainly fossil-based energy system towards renewable electricity generation. By the end of 2018 offshore wind turbines with a capacity of 6382 MW were installed in German waters, 21 750 MW worldwide. A massive expansion of offshore wind energy utilization is expected in many countries. Germany alone aims at an installed capacity of 15 GW by the year 2030 (Mackensen, 2019). Most of this capacity will be installed in the North Sea and Baltic Sea mainly in large wind farm clusters. A wind farm cluster typically consists of several wind farms in the direct vicinity, often operated by different parties and featuring different wind turbine types and geometries. Here, we call a large accumulation of more than a hundred wind turbines a cluster.

Wind turbines extract energy from the atmosphere forming regions of reduced wind speed, so called wakes, behind them. Wakes of single wind turbines merge to a wind farm or

cluster wake (e.g. Nygaard, 2014). We use the term cluster wake for the merged wakes of a large number of wind turbines of either the same or different type with no individual wind turbine wake identifiable anymore. Downstream turbines within a wind farm (e.g. Barthelmie and Jensen, 2010) and in neighbouring downstream clusters (e.g. Nygaard and Hansen, 2016) experience reduced wind speeds and reduced power generation caused by wake shadowing effects. With a rising offshore wind energy utilization, cluster wake shadowing effects will occur to an increasing degree, leading to power losses and uncertainties in offshore wind resource assessment.

Wind turbine wakes were subject of intensive research in the last decade. Wake measurements were mainly performed using the remote-sensing technique Doppler lidar (e.g. Aitken et al., 2014; Trabucchi et al., 2017; Bodini et al., 2017; Fuertes et al., 2018; Beck and Kühn, 2019), power analysis on the basis of SCADA data (e.g. Barthelmie and Jensen, 2010) or Doppler radar (e.g. Hirth et al., 2014). Fur-



thermore, several numerical studies investigated wind turbine wakes using large eddy simulation (LES) (e.g. Churchfield et al., 2012; Abkar and Porté-Agel, 2015; Dörenkämper et al., 2015b; Lignarolo et al., 2016; Vollmer et al., 2016). In an unstable atmosphere, e.g. in cold air over warm water, vertical turbulence leads to a well mixed boundary layer and causes a faster wake recovery. In stable conditions, e.g. in warm air over cold water, wake deficits can last far downstream. Hansen et al. (2011), Dörenkämper et al. (2015b) and Lee et al. (2018) investigated wake recovery with respect to atmospheric stability and found an increased length of wakes in stable stratification. Optimized wind farm layouts on the basis of the prevailing wind rose and stability distribution to reduce wake effects are commonly used (e.g. Emeis, 2009; Turner et al., 2014; Schmidt and Stoevesandt, 2015).

Cluster wakes are recently coming into the scientific focus with an increased offshore wind energy utilization. Due to the large dimensions of cluster wakes experimental investigations have been made with measurement systems capable of covering large areas like satellite synthetic aperture radar (SAR) (e.g. Hasager et al., 2015), research aircraft (e.g. Platis et al., 2018) and Doppler radar (e.g. Nygaard and Newcombe, 2018). Numerical studies were carried out by implementing wind farms in mesoscale models (e.g. Fitch et al., 2012; Volker et al., 2015). Wakes of large offshore wind farm clusters over distances of more than 10 km were first observed using data from satellite SAR (Christiansen and Hasager, 2005). Li and Lehner (2013) and Hasager et al. (2015) analysed offshore wind farm wakes using SAR images and compared the long, visible wakes to results of mesoscale models. Nygaard and Hansen (2016) analysed the power production of an offshore wind farm before and after the commissioning of a wind farm located 3 km to the west on the basis of SCADA data and discovered power losses caused by wakes of the upstream wind farm in the first rows of the downstream wind farm. Nygaard and Newcombe (2018) used dual Doppler wind radar to measure the inflow and the wake of an offshore wind farm and found wind speed deficits up to the maximal achievable downstream distance of 17 km possible with the used setup. They analysed a case with steady wind direction and speed and observed the cluster wake for over 1 h; stability information was not available. Platis et al. (2018) used in situ measurements taken with a research aircraft at hub height behind offshore wind farm clusters in the German North Sea and identified wakes with lengths of up to 55 km under stable atmospheric conditions, up to 35 km in neutral conditions and up to 10 km in unstable conditions. Siedersleben et al. (2018b) used the same flight measurements as Platis et al. (2018) to evaluate a wind farm parametrization (Fitch et al., 2012) in the numerical Weather Research and Forecasting model (WRF) that is well established in wind energy applications (e.g. Pryor et al., 2018b; Witha et al., 2019; Dörenkämper et al., 2015a). Additionally they presented an analysis of aircraft wake measurements in five different heights

5 km downwind of the cluster. The wake deficit existed in all considered height levels, also 50 m above the upper tip height of the rotor. Siedersleben et al. (2018a) investigated the micro-meteorological consequences of cluster wakes due to mixing effects in the atmosphere using the flight measurements from Platis et al. (2018). Pryor et al. (2018a) evaluated the downstream impact of large onshore wind farms in North America using the wind farm parametrization by Fitch et al. (2012) in convection-permitting mesoscale WRF simulations. Lundquist et al. (2019) analysed the physical, economic and legal consequences of wake effects between large onshore wind farms with sizes of more than a hundred megawatt each.

Wind farm cluster wakes in the far field of more than 20 km downstream have not been measured over longer periods. Satellite SAR just offers the possibility to take snapshots of the wind field. Doppler radar has been deployed on the coast monitoring a nearshore wind farm (Nygaard and Newcombe, 2018) but not in an offshore wind farm to use the full measurement range for wake analysis. Doppler lidar, which successfully monitored wind turbine wakes, was considered not to be able to achieve the measurement range needed to investigate full cluster wakes. Furthermore, the influence of cluster wakes on the power production of far downstream wind farms has not been analysed. The influence of atmospheric stability on the development and recovery of cluster wakes has not been studied in detail.

The objective of this paper is to analyse whether offshore cluster wakes have a significant and continuous influence on the power generation of a far downstream wind farm and how this influence depends on atmospheric stability. For this purpose we investigated two exemplary cases of cluster wakes approaching the 400 MW wind farm Global Tech I in the North Sea during situations with different atmospheric stabilities by means of four synchronized data sets, namely

1. large-area satellite SAR wind data,
2. continuous platform-based long-range Doppler lidar wind monitoring,
3. operational data of the wind farm Global Tech I and
4. meteorological measurements for atmospheric stability characterization.

We follow Platis et al. (2018) in their definition of the cluster wake deficit as the difference in the wind speeds from the manually selected wake region and a neighbouring free-flow region since the inflow wind speed of the wake generating cluster as reference is typically not known. Furthermore, regional and temporal differences in the wind field distort a comparison of the far-distant points in front of and far behind a cluster. Therefore, the adjacent regions in and aside the wakes are compared. Wake and free-flow regions are identified manually in this analysis.

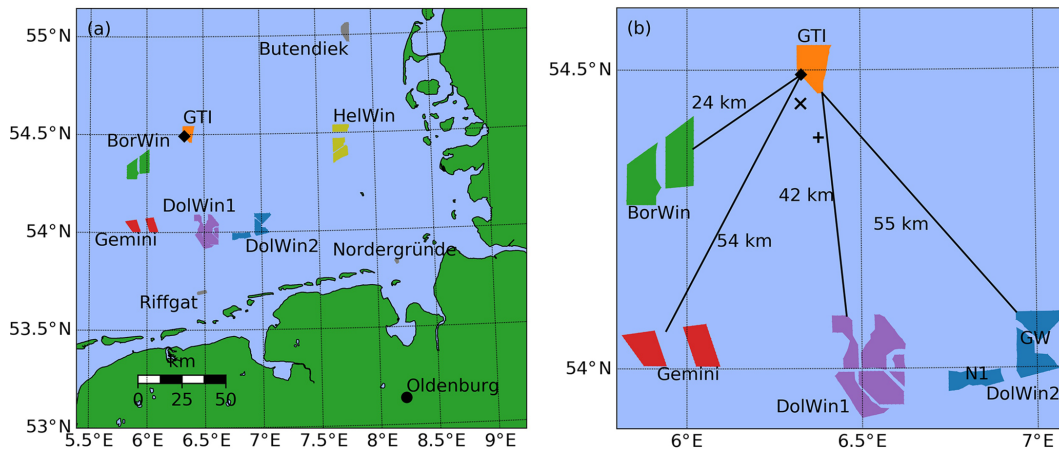


**Figure 1.** (a) Overview of the considered area in the southern North Sea with wind farms and clusters shown. (b) Close view on GT I and neighbouring wind farm clusters. The position of the lidar in GT I on turbine GT58 (filled  $\diamond$ ) and the offshore substation (OSS) “Hohe See” ( $\times$ ) and the transformer platform “BorWin gamma” ( $+$ ) are marked; distances to upstream clusters are also shown. We measured wakes of all clusters in (b) and exemplary present the wakes of the BorWin and the DolWin2 clusters in this work. Information on the wind farms and full names are listed in Table 1.

The paper is structured as follows. Section 2 introduces the experimental setup in the North Sea; measurements taken with lidar, SAR and meteorological sensors; and data processing. Section 3 presents two exemplary cluster wake cases affecting the wind farm Global Tech I. In Sect. 4 we discuss the influence of cluster wakes on the power production of a far downstream wind farm as well as cluster wake characteristics and methods for cluster wake monitoring. Section 5 concludes on the findings and closes the paper.

## 2 Methods

In this study different data sources have been used: meteorological measurements, wind farm production data (supervisory control and data acquisition, SCADA) and remote-sensing data from a Doppler lidar (light detection and ranging) measurement campaign, and satellite SAR (synthetic aperture radar) data. A description of these data sources is given in this section. Our measurement campaign started in late July 2018 and was planned to last 1 year. The measurements we present in this paper were taken on 11 October 2018 and 6 February 2019. All measurement data in this study were recorded in Coordinated Universal Time (UTC).

### 2.1 Wind farms and SCADA data

As of early 2019, several offshore wind farms were installed mainly in clusters in the German and Dutch North Sea. Focus of this work is on the effects on the 400 MW wind farm Global Tech I (GT I), which is one of the world’s most distant offshore wind farms with a coastal distance of more than 100 km. We analyse the impact of two large wind farm clusters, namely the 802 MW “BorWin” cluster located about

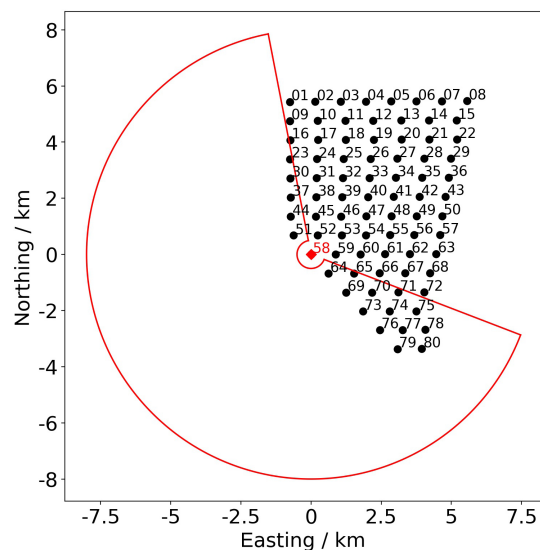


**Figure 2.** Layout of the wind farm Global Tech I with turbine numbers. The turbine GT58, where we positioned the lidar, is marked in red ( $\diamond$ ). The achievable sector for lidar measurements is drawn.

25 km southwest and the 914 MW “DolWin2” cluster 55 km southeast on the wind farm GT I.

Figure 1 gives an overview of the region around GT I while Fig. 2 displays its layout.

All coordinates in maps we show in the following, except Fig. 1, were transferred to the Gauss Krüger coordinate system and the origin was shifted to the lidar position at turbine GT58 in GT I (Fig. 2). Table 1 summarizes the main characteristics of the wind farms and clusters in the region. In the direct southwestern vicinity of GT I, the associated wind farms Hohe See and Albatros were under construction

**Table 1.** Overview of offshore wind farms considered in this work (as of June 2019). The wind farms Borkum Riffgrund 2 (Orsted, 2018) and “Merkur Offshore” (Merkur Offshore, 2018) were in the commissioning phase and partly fed into the grid during our measurements; therefore, they are marked with smaller symbols in the relevant plots in this paper.  $D$ : rotor diameter,  $h_H$ : hub height,  $P_r$ : rated power per turbine, No.: number of turbines per wind farm,  $\Sigma P_r$ : rated power of wind farm. The numbers for the hub height are related to different reference levels, namely lowest astronomical tide (LAT), mean sea level (MSL) or just “over water”. These differences are not further considered here since the difference between LAT and MSL is typically around 2 m in the North Sea.

Name	Short	Turbine	$D$ (m)	$h_H$ (m)	$P_r$ (MW)	No.	$\Sigma P_r$ (MW)
Global Tech I	GT I	AD 5–116	116	92	5.0	80	400
<i>BorWin Cluster (802 MW)</i>							
BARD Offshore 1	BO1	BARD 5.0	122	90	5.0	80	400
Veja Mate	VM	SWT-6.0-154	154	103	6.0	67	402
<i>Gemini Cluster (600 MW)</i>							
Buitengaats	BG	SWT-4.0-130	130	89	4.0	75	300
Zee Energie	ZE	SWT-4.0-130	130	89	4.0	75	300
<i>DolWin 1 Cluster (1416 MW)</i>							
Trianel Windpak Borkum	TWB	AD 5–116	116	92	5.0	40	200
alpha ventus	av	AD 5–116	116	90	5.0	6	30
		5M	126	92	5.0	6	30
Borkum Riffgrund 1	BR1	SWT-4.0-120	120	87	4.0	78	312
Borkum Riffgrund 2	BR2	V164-8.0	164	111	8.0	56	448
Merkur Offshore	MO	Haliade 150-6	150	103	6.0	66	396
<i>DolWin 2 Cluster (914 MW)</i>							
Nordsee One	N1	6.2M-126	126	90	6.15	54	332
Gode Wind 1 + 2	GW	SWT-6.0-154	154	110	6.0	97	582

during the period of our measurement campaign with several transition pieces and a substation but no wind turbine towers installed. The first turbine was erected on 6 April 2019 (EnBW, 2019). The position of the Hohe See offshore substation (OSS) is marked in the following plots ( $\times$ ). The installation of the 900 MW high-voltage direct current (HVDC) platform BorWin gamma in the southeast corner of Hohe See was completed on 11 October 2018 (Petrofac, 2018); we also mark its position ( $+$ ).

For the wind farm GT I, 10 min averaged SCADA data were available during the period of the measurements. Data of turbines in normal operation were considered; turbines with curtailed power below rated power were excluded from the analysis based on a SCADA status flag, a curtailment signal and consideration of pitch angles. For the wind farms BARD Offshore 1, Gode Wind 1 + 2 and Nordsee One we obtained hourly production data from Fraunhofer ISE (2019) and checked the operational status.

We analyse wind turbine power differences using the  $z$  score

$$z_{P_i} = \frac{P_i - \overline{P_{up}}}{\sigma_{P_{up}}} \quad (1)$$

with  $z_{P_i}$  being the difference in the  $i$ th turbine’s power  $P_i$  and the mean power of the turbines in the first row facing the wind direction (upstream turbines)  $\overline{P_{up}}$  normalized with the

standard deviation of the power of the upstream turbines  $\sigma_{P_{up}}$  within the considered time span. Advection through the farm is not considered. We use the upstream turbines to calculate the  $z$  score instead of the turbines of the whole farm to avoid distortion by inner-farm wake effects.

## 2.2 Lidar measurements

We used a scanning long-range Doppler lidar system of type Leosphere Windcube 200S (serial no. WLS200S-024) in this study. The lidar system emits laser pulses into the atmosphere and analyses the light backscattered by aerosols for a Doppler shift proportional to the radial wind velocity in beam direction  $v_r$ . The lidar is able to process wind speed information in  $> 200$  different ranges on the beam called range gates. For each range gate, the radial wind speed  $v_r$  and the carrier-to-noise ratio (CNR) as a measure of the signal quality are stored. The lidar’s scanner is able to point the beam in any desired direction in the hemisphere above and partly below the device.

We installed the lidar system on the transition piece (TP) of wind turbine GT58 in GT I (filled  $\diamond$  in Figs. 1 and 2). The height of its scanner was approximately 24.6 m a.m.s.l. (above mean sea level), 67.0 m below hub height and 9.0 m below lower blade tip height of the turbine. Figure 3 displays a picture of the lidar installed in GT I.

**Table 2.** Overview of the different settings for the lidar plan position indicator (PPI) scans. Both scenarios covered different sectors of  $150^\circ$  width. Range gates are listed as minimal range : spacing : maximal range. Range gates are also referred to as “measurement points” in the following.

Scenario	Pulse length (ns)	Acquisition time (s)	$\dot{\varphi}$ ( $^\circ \text{ s}^{-1}$ )	Scan duration (s)	Range gates (m)
A	400	8.0	0.25	600	1000 : 50 : 12 000
B	400	2.0	1.0	150	500 : 35 : 8000



**Figure 3.** Lidar system Windcube 200S on the transition piece of wind turbine GT58 in the offshore wind farm Global Tech I. On the right side of the image the tower of the turbine is visible while turbine GT51 northwest of GT58 can be seen in the background (cf. GT I layout in Fig. 2) (Stephan Voß, ForWind).

The lidar performed horizontal plan position indicator (PPI) scans (elevation angle  $\varphi$  was  $0^\circ$ ) with continuous scanner movement in different azimuthal sectors of  $150^\circ$  width upstream with two different settings, A and B, as listed in Table 2. We started with the slower scenario A aiming for a high measurement range. Later we optimized the measurements using scenario B, being 4 times faster and achieving similar ranges. In both scenarios the laser beam is scanned over an angle of  $2^\circ$  per measurement leading to spatial averaging perpendicular to the line of sight direction. After performing a scan, the lidar needs a few seconds to reset and start the next scan. Every few hours it performs a homing procedure of the scanner to assure precise orientation. The laser pulse length used in both scenarios was 400 ns, leading to a probe volume of approximately 70 m in the beam direction. The range gate spacing is listed in Table 2.

The offset in the azimuthal direction between geographic north and the lidar’s north was corrected by scanning distant wind turbines in GT I with known positions (“hard target-

ing”). The resulting error in the azimuthal orientation  $\Delta\varphi$  was smaller than  $0.1^\circ$  and is therefore neglected.

The lidar was well aligned on the pitch and roll axis; errors were checked using the method of sea surface levelling (Rott et al., 2017). The resulting maximal error in the elevation  $\Delta\vartheta$  was less than  $0.1^\circ$ . An additional error in the elevation angle of the lidar measurement occurs from a small movement of the TP due to the thrust on the rotor with a maximum of  $0.1^\circ$ .

When regarding the height of the measurement locations, the curvature of the earth must be taken into account for the ranges achieved. The error introduced raises quadratically with range and reaches  $\Delta h_8 = 5.02$  m for a distance of 8 km and of  $\Delta h_{10} = 7.85$  m for a distance of 10 km. The measurement errors we describe here can be neglected for the mainly qualitative analysis in this work.

### 2.3 Lidar data processing

Lidar scans were individually filtered on CNR minimal and maximal thresholds, a maximum range, and a minimal data density in the  $v_r$ -CNR plane (similar to Beck and Kühn, 2017). For each PPI scan, the mean wind direction was determined by fitting a cosine function to all radial speeds  $v_r$  of the scan over their azimuth angles  $\varphi$ . All  $v_r$  were then transformed back to the absolute wind speed  $v_a$  in mean wind direction assuming the perpendicular wind component to vanish using

$$v_a = v_r / \cos(\varphi_{\text{diff}}) \quad (2)$$

with  $\varphi_{\text{diff}}$  being the difference angle between the beam direction and the mean wind direction. Sectors with measurement ranges almost perpendicular to the wind direction ( $|\varphi_{\text{diff}}| > 75^\circ$ ) were excluded from the analysis because of an increasing error due to an overestimation of flow components perpendicular to the wind direction. We plot single lidar scans on their original polar grid. To obtain averaged lidar wind fields, we transferred the  $v_a$ -lidar data of each regarded scan to a Cartesian grid with a resolution of  $50 \text{ m} \times 50 \text{ m}$ , triangulating the data points and on each triangle performing linear barycentric interpolation to the grid points. We then calculated the cubic (or power) average on each grid point. Due to slightly changing wind directions in the averaging interval, points at the border of the scans were just included in the



**Table 3.** Classification of atmospheric stability as suggested by Sorbjan and Grachev (2010).

Stability category	Range
Very stable	$0.6 < \zeta < 2.0$
Stable	$0.2 < \zeta < 0.6$
Weakly stable	$0.02 < \zeta < 0.2$
Near neutral	$-0.02 < \zeta < 0.02$
Weakly unstable	$-0.2 < \zeta < -0.02$
Unstable	$-0.6 < \zeta < -0.2$
Very unstable	$-2.0 < \zeta < -0.6$

further analysis if no scan (scenario A) or less than 10 scans (scenario B) did not contribute at the grid point.

## 2.4 Atmospheric stability and meteorological data

Meteorological measurements of atmospheric stability are uncommon in offshore wind farms. Different methods for the derivation of stability exist (see Rodrigo et al., 2015 for an overview). We applied the *bulk Richardson method from profile measurements* according to Emeis (2018) based on the tropical observations of Grachev and Fairall (1997). We used the wind speed  $v_{\text{TP}}$ , the temperature  $T_{\text{TP}}$  on the height of the transition piece  $z_{\text{TP}}$ , and the difference in the virtual potential temperatures at the height of the TP and at sea level,  $\Delta\Theta_v = \Theta_{v,\text{TP}} - \Theta_{v,\text{SST}}$  (see Appendix A), to derive the dimensionless bulk Richardson number

$$Ri_b = \frac{g}{\Theta_{v,\text{TP}}} \frac{z_{\text{TP}} \Delta\Theta_v}{v_{\text{TP}}^2}, \quad (3)$$

where  $g$  is the gravity acceleration. The dimensionless stability parameter,

$$\zeta = \begin{cases} \frac{10Ri_b}{1-5Ri_b} & Ri_b > 0, \\ 10Ri_b & Ri_b \leq 0, \end{cases} \quad (4)$$

and the stability classification in Table 3 were chosen for stability categorization.

To be able to estimate  $\zeta$ , we operated sensors for air pressure (Vaisala PTB330) as well as temperature and relative humidity (Vaisala HMP155) on the TP of turbine GT58. In one case (see Sect. 3.2.1) we used meteorological measurements from the nacelle of turbine GT58 provided by the wind farm operator as a second source of data to derive the stability parameter at height of the nacelle  $\zeta_{\text{nac}}$  using the same methodology as described above. A buoy for the measurement of the sea surface temperature  $T_{\text{SST}}$  was available from 9 August 2018 until 31 January 2019. We compared the measurements with the OSTIA data set (Donlon et al., 2012), both re-sampled to a 30 min interval (mean values for the buoy data, linear interpolation for the daily available OSTIA data set), and found a mean difference of 0.19 K. Since the buoy was not available during the whole lidar measurement campaign,

we use  $T_{\text{SST}}$  from the OSTIA data set to derive  $\zeta$ . The wind speed on the height of the TP,  $v_{\text{TP}}$ , for the purpose of atmospheric stability analysis was calculated from horizontal lidar PPI scans as described in Sect. 2.3 using data with a measurement range less than 3000 m. These measurements took place within the approaching cluster wakes, when present. This influences the calculation of the stability parameter but we see the wake as part of the inflow and do not try to correct for it. We averaged meteorological measurements to 30 min intervals. Table 4 shows an overview of the available meteorological data.

For a comparison of the potential power  $P_{\text{pot}}$  in the wind with the power harvested by free-flow turbines, we had to transfer wind speeds from measurement heights ( $z_{\text{SAR}} = 10$  m,  $z_{\text{TP}} = 24.6$  m) to hub height  $z_{\text{hub}} = 91.6$  m. Following Emeis (2018), we used the logarithmic wind profile

$$u(z) = \frac{u_*}{\kappa} \cdot \left( \ln \frac{z}{z_0} - \Psi_m(z/L) \right) \quad (5)$$

with a correction function  $\Psi_m(z/L)$  to account for the atmospheric stability to calculate the vertical wind profile. We used mesoscale data with a setup very similar to the production runs of the New European Wind Atlas (NEWA; see Witha et al., 2019; NEWA, 2019) internally deriving the roughness length  $z_0$  using Charnock's relation. We obtained the Obukhov length  $L$  from the stability parameter  $\zeta = z_{\text{TP}}/L$ . The von Kármán constant reads as  $\kappa = 0.4$ . The friction velocity  $u_*$  was then calculated for the given pair of wind speed and height, e.g.  $z_{\text{TP}}$  and  $u_{\text{TP}}$  from Eq. (5). The wind speed on hub height was afterwards converted to the theoretical potential power  $P_{\text{pot}}$  using a power curve  $P_{\text{est}}(v) = c \cdot v^3$  with the constant  $c$  derived from power data in the partial load range. We do not curtail  $P_{\text{pot}}$  at rated wind speeds allowing it to be larger than rated power.

## 2.5 SAR wind data

Satellite SAR remotely measures the roughness of the sea surface. Using a geophysical model to estimate wind direction, wind speeds over the ocean can be derived. In this work, we use publicly available already processed wind data from the Copernicus SAR satellite Sentinel-1A. The algorithm for wind field processing is described in Mouche (2011), an overview of its performance is given in ESA (2019) and the data product including quality flags is described in Vincent et al. (2019). Wind data at 10 m height are processed on a grid with a spatial resolution of  $1 \text{ km} \times 1 \text{ km}$ . Wind speed estimates are in range from  $0$  to  $25 \text{ m s}^{-1}$  with a root mean square error (RMSE) smaller than  $2.0 \text{ m s}^{-1}$  and wind direction estimates have an RMSE below  $30^\circ$ . The spatial coverage of the SAR images and the processed wind fields is  $170 \text{ km} \times 80 \text{ km}$  minimum with a revisit time of the order of days. A quality flag for the wind estimate (*owiWindQuality*, 0: high quality, 1: medium quality, 2: low quality, 3: bad quality; see Vincent et al., 2019) is provided within the data



**Table 4.** Overview of the available meteorological quantities to derive the stability parameter  $\zeta$ . Availabilities disregard shorter data gaps. If no end time is stated, measurements are ongoing with date of 1 August 2019. Additional data from mesoscale simulations similar to the New European Wind Atlas (NEWA) data set were available but not listed in this table.

Quantity	Symbol	Sensor or source	Height	Availability period
Air temperature	$T_{TP}$	HMP155	$z_{TP} = 24.6$ m a.m.s.l.	23 Jul 2018
Air humidity	$RH_{TP}$	HMP155	$z_{TP} = 24.6$ m a.m.s.l.	23 Jul 2018
Air pressure	$P_{TP}$	PTB330	$z_{TP} = 24.6$ m a.m.s.l.	23 Jul 2018
Wind speed	$v_{TP, lidar}$	lidar PPI scans	$z_{TP} = 24.6$ m a.m.s.l.	17 Aug 2018 (dep. on scan scenario)
Sea surface temperature	$T_{SST, buoy}$	buoy next to GT58	sea surface	9 Aug 2018–31 Jan 2019
Sea surface temperature	$T_{SST, OSTIA}$	OSTIA data set	sea surface	2018–2019

product. We use data with a quality flag  $\leq 2$ . For the calculation of the potential power on hub height (see Sect. 2.4), we added constant wind speed values within the measurement accuracy to the SAR wind data to match the actual power production.

### 3 Results

In this section we present an analysis of wake situations of the BorWin cluster on 6 February 2019 and of the DolWin2 cluster on 11 October 2018 based on Sentinel-1 SAR wind data, lidar measurements and SCADA power data of the wind farm GT I.

#### 3.1 BorWin cluster wake on 6 February 2019

The BorWin cluster is located approximately 24 km upwind of GT I in southwesterly direction. We measured wakes from the cluster approaching GT I in stable stratified situations during our measurement campaign. Here we present a stably stratified situation in late winter 2018/2019 with low variation in the wind direction allowing us to analyse lidar scans of the same situation over a period of a couple of hours.

##### 3.1.1 Meteorological conditions

In Fig. 4 we plot the measured wind speed and direction, air pressure, temperature and humidity, and the sea surface temperature from the OSTIA data set and the derived stability parameter  $\zeta$  during 6 February 2019. On that day the frontal system of a cyclone southwest of Iceland crossed the German Bight. The warm front passed GT I in the morning, bringing air temperatures of about 6.9 °C in the warm sector over the 6.1 °C cold sea stabilizing the boundary layer. With decreasing humidity and disappearing fog, good lidar availability was achieved starting at approximately 10:00 UTC (short humid or foggy period of bad measurements around 12:00 UTC) with clear wakes of the BorWin cluster visible in the lidar scans. In the afternoon we choose a period with relatively constant wind direction from 13:35 to 16:12 UTC for analysing the averaged wake effects over a longer period of

about 2.5 h. The period with stable stratification ended with the passage of the cold front at approximately 17:15 UTC.

##### 3.1.2 SAR wind data

Figure 5 displays the analysis of a wind field derived from the measurement of the Copernicus satellite Sentinel-1A, which passed the German Bight at the end of the stable stratified period on 6 February 2019 as an overview of the wind field in the region around GT I. The wake of the BorWin cluster is clearly visible and extends approximately 24 km downstream until it partially hits the wind farm GT I. Further downstream of GT I an even higher wake deficit of the merged wakes of the BorWin cluster and GT I can be observed. The virtual wake cut (Fig. 5c) reveals a sharp transition from higher to lower wind speeds at the edge of the wake; a deficit in the SAR wind speed of  $0.9 \text{ m s}^{-1}$  is observed. Since the wake just partially hits GT I, it separates the farm into two regions: one in free flow and one affected by the wake. The turbines in free flow in the northwestern and southern corner of GT I produce significantly more power ( $> 2\sigma_p$ ) than the first upstream row of turbines produce on average (Fig. 5b). We confirm this result with the comparison of the 10 min power of the upstream-row turbines with the potential power on hub height derived from the inflow wind speed (Fig. 5d) which agrees well. Within the wake-affected region in GT I, typical inner-farm wake effects are visible through a power decrease in downstream direction (e.g. Barthelmie and Jensen, 2010, Fig. 5b) which are different in the northern and southern parts of the farm due to different turbine spacings in wind direction.

##### 3.1.3 Lidar wind fields

In Fig. 6 we present the analysis of a single lidar scan of the inflow of GT I. We observe a clear edge between high wind speeds in the undisturbed flow and lower wind speeds in the wake of the BorWin cluster, causing a clear separation of power production in the wind farm GT I in a free-flow and a wake region (Fig. 6b). The virtual wake cut in Fig. 6c illustrates the sharp transition region of just a few hundred metres width and highlights the wake deficit of  $3.9 \text{ m s}^{-1}$  or

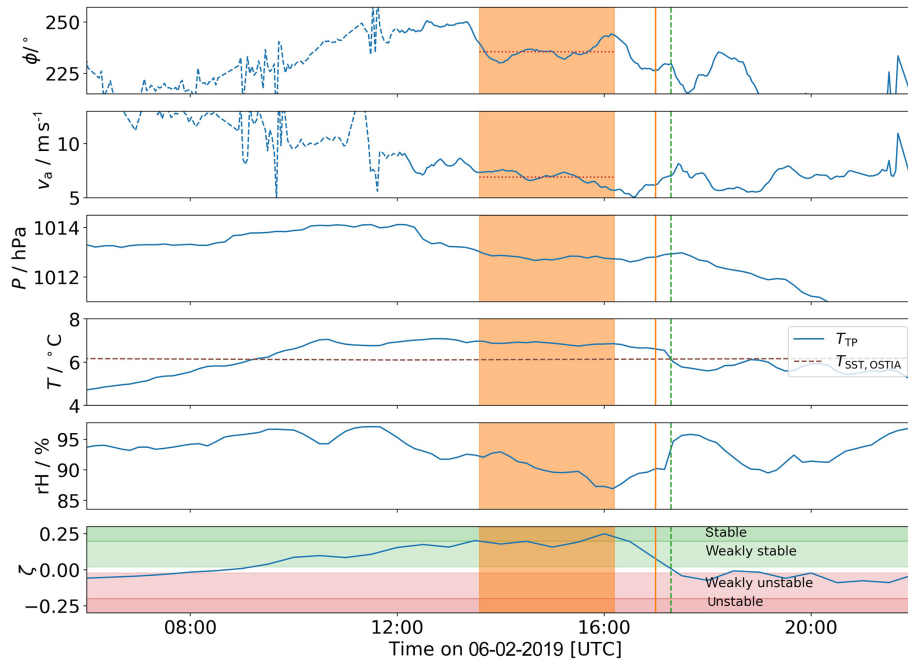


**Figure 4.** Meteorological data at the lidar location on the height of the TP (24.6 m a.m.s.l.) of turbine GT58 on 6 February 2019. Top to bottom: wind direction  $\phi_{\text{TP,lidar}}$ , wind speed  $v_{\text{TP,lidar}}$ , air pressure  $P_{\text{TP}}$ , air and sea surface temperature  $T_{\text{TP}}$  and  $T_{\text{SST,OSTIA}}$ , relative humidity  $\text{RH}_{\text{TP}}$ , and the dimensionless stability parameter  $\zeta_{\text{TP}}$ . Measurement times are marked as follows: vertical dashed line represents the SAR image (Fig. 5), vertical solid line represents the single lidar scan (Fig. 6), and shaded interval represents the averaged lidar wind field (Fig. 7). Mean wind speed and direction in the averaged lidar interval are marked by red horizontal dotted lines. Dashed lines in wind speed and direction indicate moist or foggy periods with reduced lidar data availability.

40.5 %. The potential power on hub height derived from the inflow wind speed corresponds well with the power generated by the upstream row of turbines in the regarded 10 min interval (Fig. 6d). The two northerly upstream turbines are in the region of free flow and produce, with  $> 2\sigma_p$ , significantly more power than the turbines being influenced by the BorWin wake.

In Fig. 7 we present an averaged lidar wind field calculated from 60 consecutive scans like the one in Fig. 6 in a period of approximately 157 min with relatively constant wind direction (see shaded areas in Fig. 4) to demonstrate the steadiness of the BorWin wake and its influence on power production. The wind speed along the virtual cut through the wind field in Fig. 7c reveals a strong average wake deficit of  $2.3 \text{ m s}^{-1}$ , equivalent to 24.7 %. The transition region from wake flow to free flow is about 3 km wide resulting from the small changes in wind direction and thus the slightly different positions of the wake during the averaging time. Aside from the clear visible northerly edge of the BorWin wake, the southerly edge can be observed in the southerly corner of the lidar wind field and correspondingly in the wake cut (Fig. 7c). Wind speeds recover on both sides of the wake to similar values just above  $9 \text{ m s}^{-1}$ . The average power of the GT I turbines reveals a clear reduction in the wake-affected region (Fig. 7b). The turbines in free flow produce ( $> 2\sigma_p$ ) above the average. Comparing the potential power on hub

height along the wake cut together with the average power of the upstream-row turbines (Fig. 7d), we find a slight overestimation of the potential power in the wake region and an overestimated increase in the turbine power in the transition region. The position of the transition onset in the estimated power from the wind field and the measured power from the turbines agree well.

### 3.2 DolWin2 cluster wake on 11 October 2018

The DolWin2 cluster is approximately 55 km upstream of GT I in southeasterly direction. We regularly have indications in our measurements for wakes from the cluster approaching GT I in stably stratified situations. Here we present a situation in autumn 2018 with a change of stability over the course of the day. We present a single lidar scan and an averaged lidar wind field from a period with low variation in the wind direction in stable stratification. A complementary SAR scan from the morning of the day during weakly unstable stratification is available as well and analysed here.

#### 3.2.1 Meteorological conditions

In Fig. 8 we plot the measured meteorological quantities on 11 October 2018. Since the lidar for measurements of wind speed and direction and the data of air temperature,

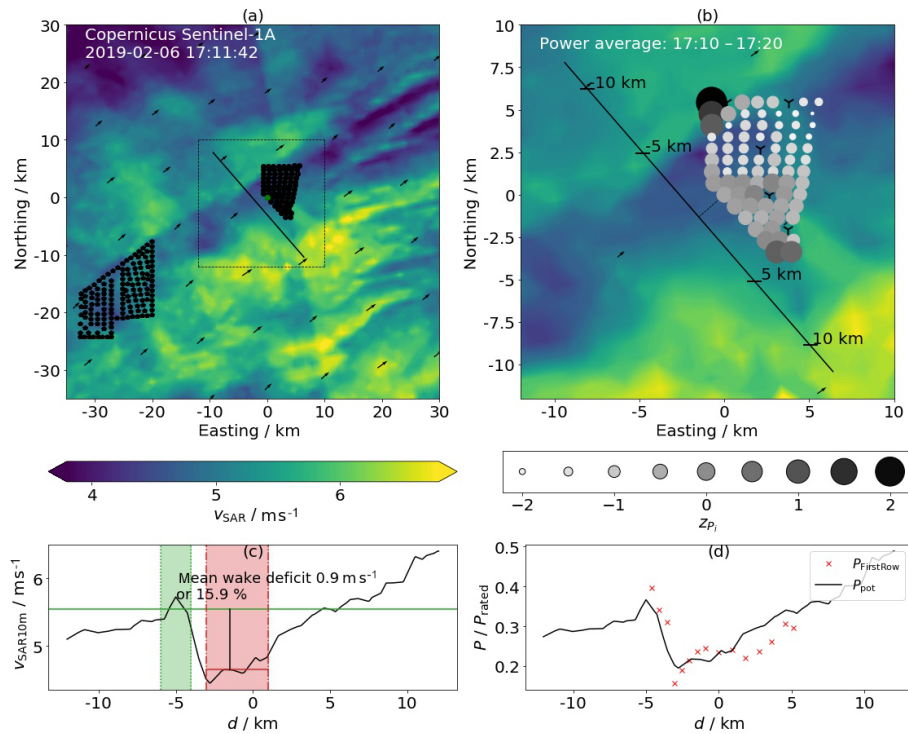


**Figure 5.** Sentinel-1A Ocean Wind Field (Copernicus Sentinel data (2019)), measurement taken 6 February 2019 17:11:42 UTC. (a) Overview of the BorWin cluster and Global Tech I. (b) Close look on the BorWin wake hitting GT I. The solid line marks a virtual wake cut 2000 m upstream of turbine GT58 on which the wind field is evaluated. Marked distances correspond to the  $x$  axis of (c) and (d). The  $z$  score of the turbine power  $z_{P_i}$  (see Eq. 1) is shown in greyscale for the relevant 10 min period (17:10–17:20 UTC); markers scale with  $z - z_{\min}$ . Numbers of upstream turbines to calculate the  $z$  score are 1, 9, 16, 23, 30, 37, 44, 51, 58, 64, 69, 73, 76, 79, and 80. Turbines not operating the full period or operating at curtailed power are excluded and marked (Y-shaped marker). (c) Wind speeds along the wake cut from (b). Wake and the free stream are shaded (regions selected manually). (d) Potential power on hub height along the wake cut (solid line) together with the power produced by the upstream turbines in GT I within the regarded 10 min interval with turbine positions projected to the wake cut. A constant value of  $1.0 \text{ m s}^{-1}$  was added to  $v_{\text{SAR},10\text{m}}$  for the calculation.

pressure and humidity at TP height were not available during the whole day we added the mesoscale data from the New European Wind Atlas (NEWA) and measurements from the nacelle of turbine GT58 to the plots. A cyclone southwest of Iceland and a strong high-pressure area over Russia dominated the weather during the day. The North Sea was positioned in the warm sector of the cyclone between the cold front over the UK and the warm front spanning from Iceland to Norway. Southeasterly winds prevailed in the southern North Sea raising the air temperature in GT I between 12:00 and 14:00 UTC above the temperature of the still quite warm North Sea (approximately  $16^\circ\text{C}$ ) stabilizing the boundary layer. In the morning a shallow (weakly) unstable boundary layer of some hundred metres height occurred because the surface layer over land cooled down during the night to temperatures below sea surface temperature and moved with the prevailing flow over the sea. Aside from the stability obtained from NEWA (weakly unstable) and the nacelle measurements (unstable), this finding is further supported by temperature profiles sounded with radiosondes at the stations in Bergen (no. 10238) and Ekofisk (no. 1400)

the same day. A weak inversion with temperatures of approximately  $13.5^\circ\text{C}$  up to 300 m height appears in the profile at Bergen, 04:00 UTC, with a stronger temperature inversion above. At the Ekofisk site the temperature profile at 11:00 UTC shows a similar behaviour with the upper inversion being less pronounced and sunken to approximately 230 m height. This allows for dry adiabatic convection up to heights between 200 and 300 m for the prevailing sea surface temperature.

We found a good general agreement between the NEWA data and the values measured in the wind farm. Especially the derived stability parameter  $\zeta$  agrees well. For the differences in the other quantities the different reference heights have to be considered. Half-hourly values of wind speed and direction from the NEWA data are not expected to cover small-scale fluctuations and to perfectly match a local measurement.

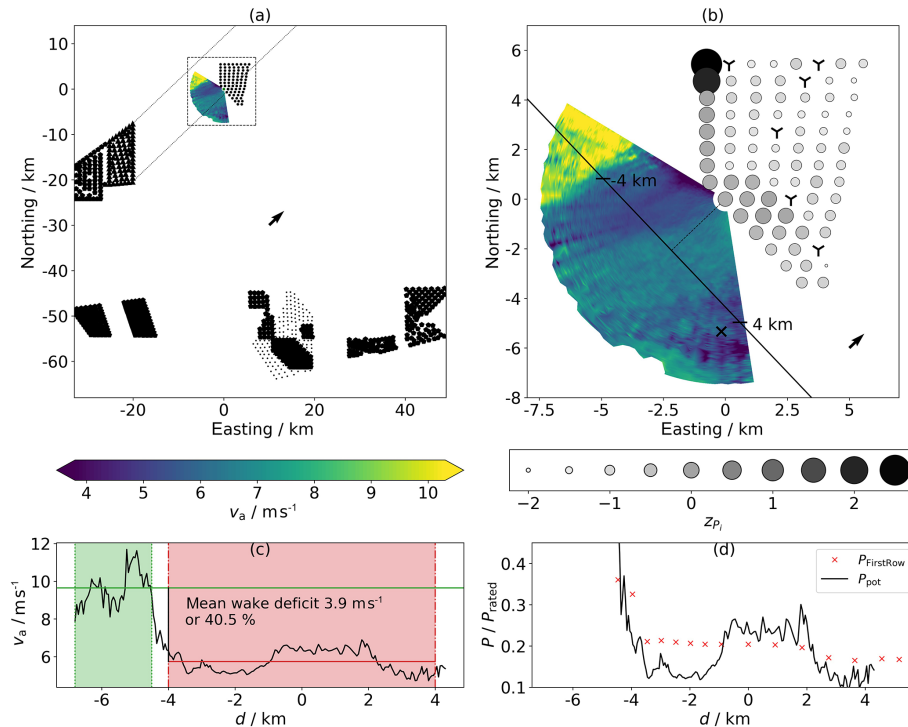


**Figure 6.** Lidar scan (scenario B from Table 2) on 6 February 2019 16:58–17:01 UTC: **(a)** overview of the situation in the German Bight with lines parallel to the wind direction retrieved from the lidar scan from the corners of the upstream wind farm cluster BorWin. Lidar wind speed is colour coded (left colour bar). **(b)** Close view of the lidar wind field and the wind farm GT I. The  $z$  score of the not curtailed wind turbines’ power in the current 10 min interval (16:50–17:00 UTC) is in greyscale (right colour bar), curtailed or non-operating turbines are marked (Y-shaped marker). Markers scale with  $z - z_{\min}$ . Turbine numbers to calculate the  $z$  score as in Fig. 5. The substation Hohe See (x) is marked. The solid line marks a virtual wake cut 3000 m upstream of turbine GT58 on which the wind field is evaluated and drawn in **(c)**. Areas of wake and free stream are shaded manually, the resulting wake deficit is stated. **(d)** Available power on hub height along the wake cut from **(b)** together with the power achieved from the upstream turbines in GT I with their positions projected to the wake cut.

### 3.2.2 SAR wind data

Figure 9a shows the wind field from the Copernicus satellite Sentinel-1A, which passed the German Bight in the morning of 11 October 2018, as an overview of the wind field in the region between GT I and the DolWin2 cluster. The stratification during the SAR snapshot was weakly unstable. Wakes of the Gemini, DolWin1 and DolWin2 clusters with lengths of at least 20, 40 and 55 km, respectively, are clearly visible. The wake originating in the DolWin2 cluster splits into two parts generated by “Gode Wind 1 + 2” (GW) and Nordsee One (N1); see Fig. 1. The GW wake extends far downstream until it hits the wind farm GT I after approximately 55 km. Further downstream a merged wake of the DolWin2 cluster and GT I can be observed extending out of the visible range after approximately 30 km. All wakes have the approximately same width as the generating cluster and become narrower downstream.

The virtual wake cut 9000 m upstream of GT58 reveals regions of different influence (Fig. 9c). On the southwest side of the cut we see a region of undisturbed flow ( $d \approx -15$  km,  $d$  is the distance on the wake cut from Fig. 9c) with

wind speeds decreasing towards northeast. The deficit between  $-5$  km  $< d < 0$  km originates in the wake of the wind farm N1 followed by the stronger deficit at  $0$  km  $< d < 10$  km of the GW wind farm. This wake deficit centrally hits GT I and affects its power production. Further east the wind speed remains approximately constant until it rises from  $d > 20$  km due to regional differences in the wind field. Regarding the marked wake and free-flow regions in Fig. 9c, we observe a wake deficit of  $0.6$  m s $^{-1}$  or 7.2 % in the SAR wind speed for the DolWin2 wake in 10 m height.

Differently from the wake situation of the BorWin cluster (Sect. 3.1), the wind farm GT I is affected by the DolWin wake centrally; therefore, we do not observe separated regions of power production within the farm. Nevertheless, the outer turbines on the western and northeastern corner of the wind farm produce significantly more power ( $2.6$  and  $1.7\sigma_P$  above average) than the average of the upstream row (Fig. 9b). Looking at the potential power on hub height calculated from the virtual wake cut (Fig. 9d), we find the increased power to result from the higher wind speeds at the sides of the DolWin2 wake deficit. This highlights the effect



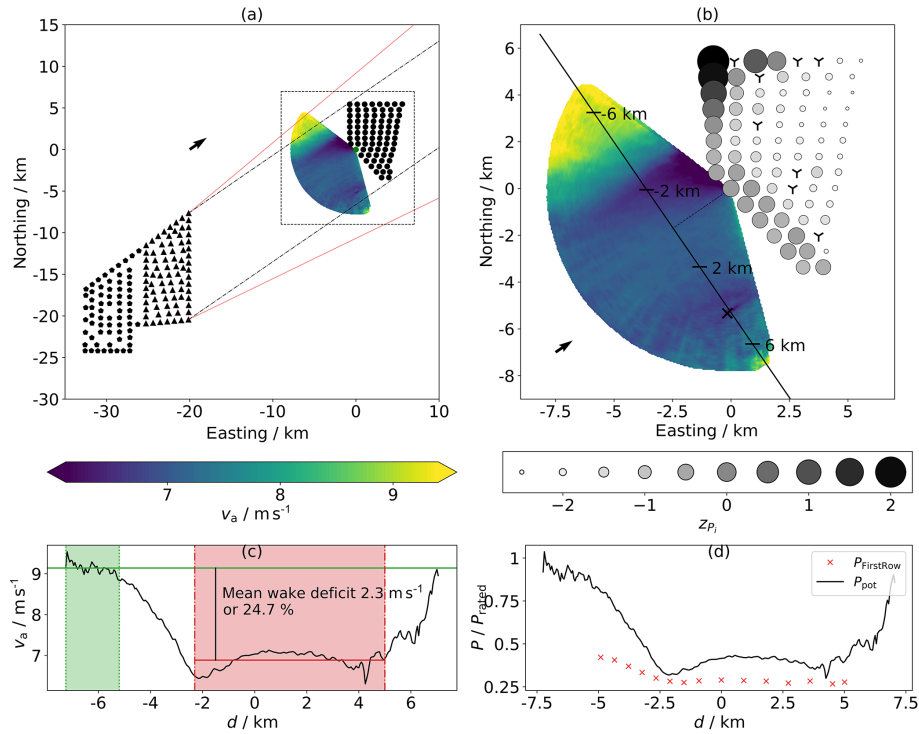


**Figure 7.** As in Fig. 6 but averaged over 60 consecutive lidar scans (scenario B) corresponding to a period of 157 min (13:35–16:12 UTC); power data averaged over 170 min (13:30–16:20 UTC). Red lines in (a) indicate minimal and maximal wind directions within the averaging interval.

of the wake on the power production even in weakly unstable conditions.

### 3.2.3 Lidar wind fields

In Fig. 10 we show a single lidar scan of the flow southwest of GT I. The stratification during the scan was stable (Fig. 8). We do not observe a sharp transition from wake to free-flow regions like for the BorWin wake (Fig. 6) but a steady decrease in wind speeds southwest to northeast, similar to the DolWin2 wake situation we found in the SAR data from the same morning in weakly unstable stratification (Fig. 9). Three more wakes appear in the wind field: one originating from a ship close to GT I, another one from the OSS Hohe See (×) and the third from the platform BorWin gamma (+). The latter wake extends at least 9 km downstream.

The virtual wake cut (Fig. 10c) highlights the different flow regions with lower wind speeds near GT I. The Hohe See OSS wake is located at  $d \approx -4$  km and the BorWin gamma wake between  $-6 \text{ km} < d < -5.5$  km. The wake deficit of the DolWin2 cluster amounts to  $3.3 \text{ m s}^{-1}$  or 26.4%. Comparing the potential power in the wind field with the power produced by the turbines of the upstream row, we find most turbines producing approximately rated power (Fig. 10d). The potential power in the west of the wind farm is slightly lower than the power of the upstream turbines. Even though during this lidar scan with high wind speeds the

wind farm’s power is not influenced by the DolWin2 wake due to the turbines curtailing power production above rated speed, we find clear indications for wake effects with reduced wind speeds at the position of GT I 55 km downstream the DolWin2 cluster.

Figure 11 highlights the steadiness of the DolWin2 wake situation on 11 October 2018. We averaged 16 consecutive lidar scans in a period of approximately 162 min (15:44 to 18:26 UTC; cf. shaded interval in Fig. 8) with a relatively constant wind direction. As for the single lidar scan we observe the same behaviour in the wind field with a wind speed decreasing along the virtual wake cut from southwest to northeast. The wake deficits of the Hohe See OSS and BorWin gamma are clearly visible in the averaged wind field (Fig. 11c). The relative wake deficit of the DolWin2 cluster is similar for the single and the averaged lidar scans (Fig. 10). Since the average wind speed within the averaging period is smaller than that at the time of the single scan (Fig. 8), the absolute deficit is smaller, too. The course of the potential power in the wind field (Fig. 11d) is continued by the power of the upstream-rows turbines. The wake effect of the DolWin2 cluster on the power of GT I is evident. The potential power in the wind about 4 km southwest of the wind farm reaches rated wind speed.



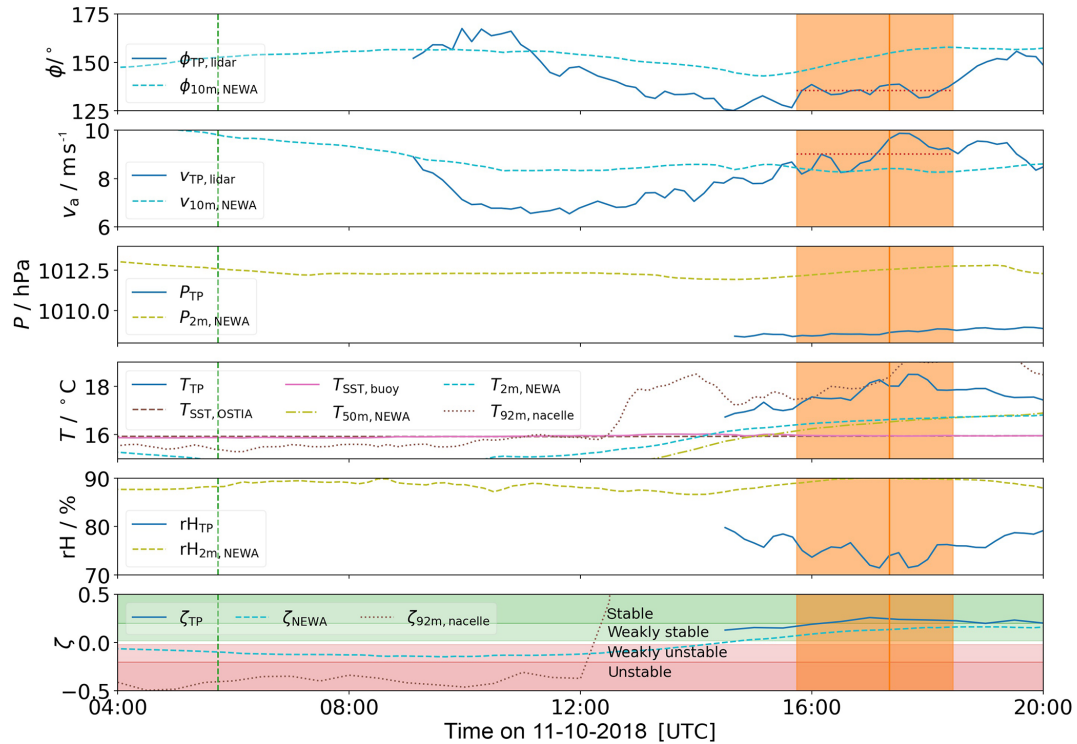


**Figure 8.** Meteorological data at the lidar location (turbine GT58) on 11 October 2018. Top to bottom: wind direction  $\phi_{TP, \text{lidar}}$ , wind speed  $v_{TP, \text{lidar}}$ , air pressure  $P_{TP}$ , air temperature  $T_{TP}$ , sea surface temperatures  $T_{SST, \text{OSTIA}}$  and  $T_{SST, \text{buoy}}$ , relative humidity  $RH_{TP}$ , and the dimensionless stability parameter  $\zeta_{TP}$  on the height of the TP of GT58 (24.6 m a.m.s.l.). Since the measurements are not available during the whole day, we added the 10 m wind speed  $v_{10m, \text{NEWA}}$  and direction  $\phi_{10m, \text{NEWA}}$ , 2 and 50 m temperature  $T_{2m, \text{NEWA}}$  and  $T_{50m, \text{NEWA}}$  and the stability parameter  $\zeta_{NEWA}$  from the NEWA data set (see Witha et al., 2019) as well as the temperature  $T_{92m, \text{nacelle}}$  and the derived stability parameter  $\zeta_{92m, \text{nacelle}}$  on hub height of turbine GT58. Measurement times are marked as follows: vertical dashed line represents the SAR image (Fig. 9), vertical solid line represents the single lidar scan (Fig. 10), and shaded interval represents the averaged lidar wind field (Fig. 11). Mean wind speed and direction in the averaged lidar interval are marked by red horizontal dotted lines.

## 4 Discussion

We found evidence of cluster wakes in the form of wind speed deficits with clear transition regions between slower wake flow and faster undisturbed flow in many lidar scans upstream of GT I for all neighbouring wind farm clusters in southeasterly to westerly wind directions, namely the DolWin2 (approximately 55 km), DolWin1 (approximately 42 km), Gemini (approximately 54 km) and BorWin (approximately 24 km) clusters. In some of the cases with available large-area SAR wind data, these alternative measurements supported the lidar cluster wake measurements. Power deficits in the wind farm agree with the wake regions found in lidar and SAR data. In this paper we present two exemplary wake cases: one for the BorWin cluster 24 km upstream and one for the DolWin2 cluster 55 km upstream, and both wake effects occurred steadily over more than 2.5 h and influenced the power production of GT I. We found cluster wakes mainly for positive values of the stability parameter  $\zeta$  (stable stratification) but also for  $\zeta$  slightly below zero (weakly unstable stratification, shallow boundary layer).

### 4.1 Influence of cluster wakes on power production of far downstream wind farms

The effect of cluster wakes on the operation of far downstream wind farms has not been investigated before. Nygaard and Hansen (2016) report about short-distance effects in the power production of wind farms in the direct vicinity (3.3 km gap) based on SCADA analysis. Nygaard and Newcombe (2018) analyse a cluster wake at hub height up to 17 km downstream a wind farm with dual Doppler radar from the coast. Platis et al. (2018) find long-reaching wake effects (wind speed difference of more than  $0.1 \text{ m s}^{-1}$  considered wakes) up to 55 km downstream in flight measurements but could not analyse their impact on distant wind farms. Here, our findings from combined satellite SAR and lidar measurements of cluster wakes existing over distances of up to 55 km downstream agree with the observation of Platis et al. (2018). Additionally, we confirm the assumption of negative effects of cluster wakes on the power production of a far downstream wind farm.

The evidence of the wake influence on wind farm power is obvious for the BorWin case where we find a clear distinc-

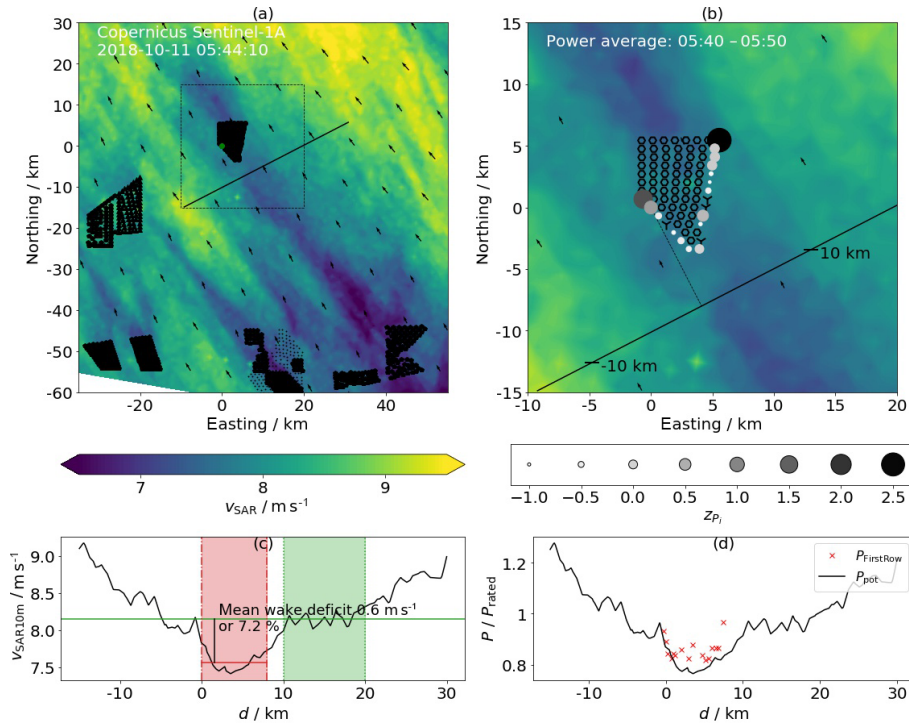


**Figure 9.** Sentinel-1A Ocean Wind Field (Copernicus Sentinel data (2018)); measurement taken 11 October 2018 05:44:10 UTC. We show power data of the upstream turbines in the interval 05:40–05:50 UTC, as in Fig. 5; positions of downstream turbines are marked (hexagon). In (d) we added an offset of  $2.0 \text{ m s}^{-1}$  to the SAR wind speeds on the virtual wake cut 9000 m upstream of GT58 before we transferred them to hub height and calculated the potential power. Numbers of considered upstream turbines to calculate the  $z$  score are 8, 15, 22, 29, 36, 43, 50, 68, 72, 80, 79, 76, 73, 64, 58, and 51.

tion of wake and free stream in the lidar and SAR wind measurements agreeing with the findings of Platis et al. (2018), who present a wake situation with a high wind speed gradient at one side of the cluster wake. In the BorWin case this edge of the wake continues in a separation of the wind farm turbines’ power production (Figs. 5–7). In the DolWin2 case we could argue whether the higher power of the outer turbines (Fig. 9b) result from flow effects at the farm corners leading to higher turbine efficiencies as found by Barthelmie and Jensen (2010) but the comparison of the potential power in the inflow with the turbine power (Fig. 9d) reveals a good agreement, suggesting that at least most of the effect originates in the wake-affected inflow conditions with the highest deficit reducing the power of the central turbines, while the outer turbines profit from higher wind speeds at the sides of the wake.

Wakes are expected to exist far downstream in stable stratifications but to recover much earlier in the unstable case. Platis et al. (2018) report about 41 measurement flights ( $24\times$  stable,  $12\times$  unstable,  $5\times$  neutral stratification) and find evidence for cluster wakes in stable boundary layers 55 km downstream, while the furthest evidence in an unstable case is found 10 km downstream. In our lidar measurements we find the most pronounced cluster wakes in stable situations supporting these findings. But we have evidence

for far-reaching wakes in neutral and weakly unstable conditions, too. All lidar measurements we present in this work were measured in stable situations but the SAR image of the DolWin2 case (Fig. 9) was taken earlier the same day in a shallow, weakly unstable boundary layer with cluster wakes appearing downstream of many clusters. Vertical momentum transport was possible in lower heights but was hindered by an inversion appearing at approximately 200 to 300 m. The rotor area of the GT I turbines extends up to 150 m height. The DolWin2 wake reaches 55 km downstream until it hits the wind farm GT I where the power production of the upstream-row turbines follows the potential power calculated from the inflow SAR wind. This finding proves the existence of long-reaching cluster wakes and their influence on power production of far downstream wind farms even in cases with weakly unstable stratification. In future work we plan to publish an analysis of the whole data set of the, at the time of writing, still ongoing lidar measurement campaign focusing on wakes in unstable conditions. Nevertheless, the DolWin2 case highlights the necessity to carefully characterize the boundary layer for stability analysis, since the unstable stratified layer in the boundary layer could be thin and limited by an inversion just above temperature measurement height and still within the rotor area.

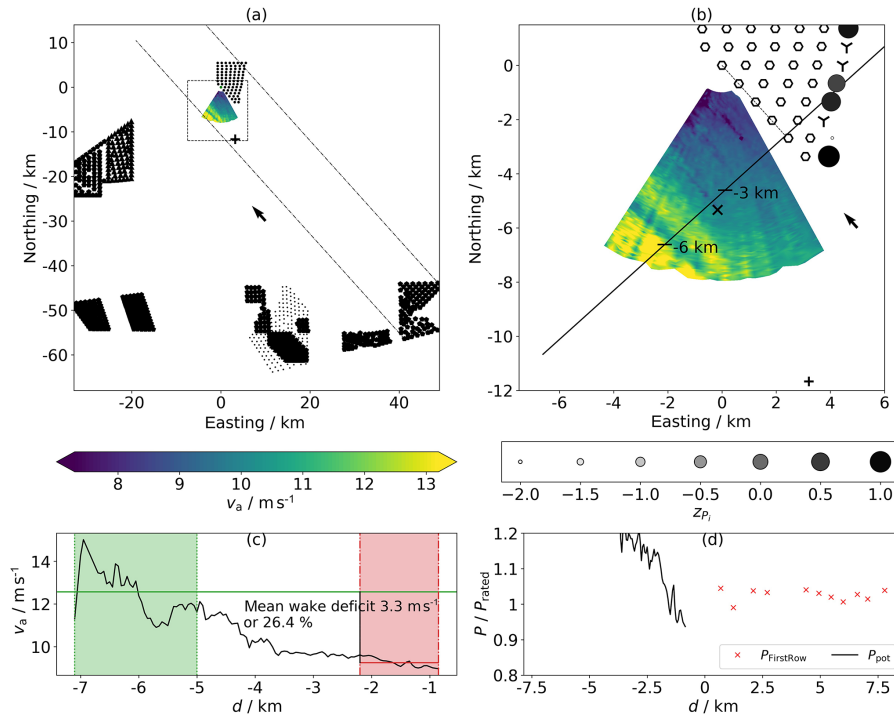


**Figure 10.** Lidar measurement (scenario A) of the wake of the DoWin2 cluster on 11 October 2018 17:16–17:20 UTC; power data of upstream turbines 17:10–17:20 UTC, as in Fig. 6. Downstream turbine positions marked (hexagon). Turbine numbers to calculate the  $z$  score are 8, 15, 22, 29, 36, 43, 50, 68, 72, 78, and 80. Additionally, we marked the converter platform BorWin gamma (+).

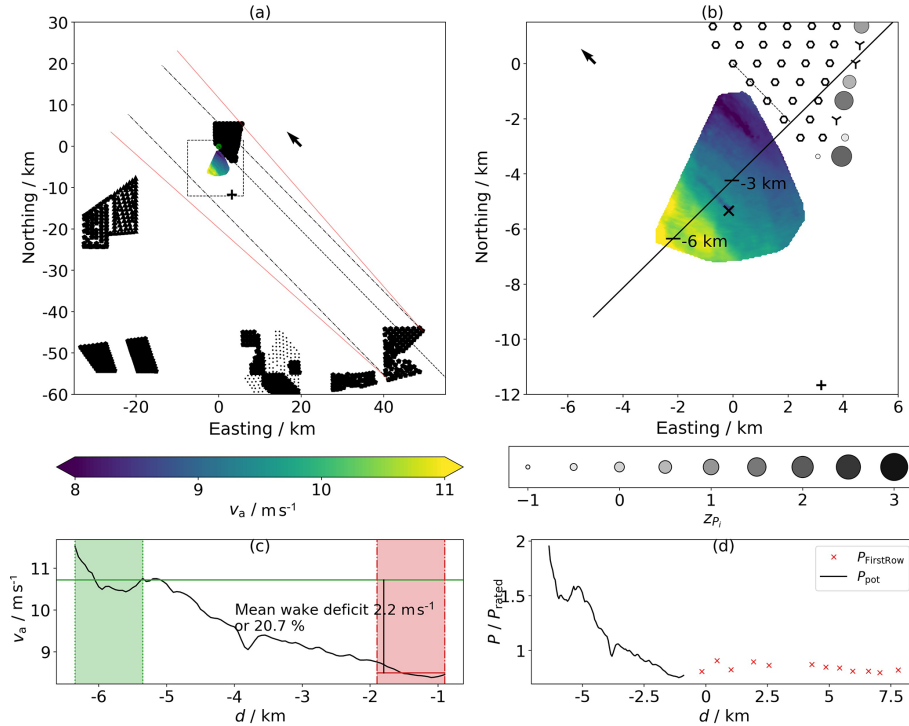


**Figure 11.** Wake of the DoWin2 cluster on 11 October 2018 as in Fig. 6 but averaged over 16 consecutive lidar scans (scan scenario A) in a period of 162 min (15:44–18:26 UTC); power data of upstream turbines averaged over 170 min (15:40–18:30 UTC); downstream turbines marked (hexagon). Turbine numbers to calculate the  $z$  score are 8, 15, 22, 29, 36, 43, 50, 68, 72, 78, 80, and 79.

In addition to the influence of a cluster wake on the wind farm GT I, we still observe inner-farm wake effects (Figs. 5 and 6) with decreasing power production downstream. Cluster wake and wind turbine wakes in the farm overlap. This supports the assumption of the cluster wake being a region of reduced wind speeds with no special characteristics of the original single turbine wakes remaining. We do not perform turbulence analysis comparing cluster wake turbulence to free-flow turbulence in this study. Platis et al. (2018) report a slender wake of increased turbulent kinetic energy (TKE) originating in one corner of the cluster. It was aligned with a stronger horizontal wind speed gradient at the border of the wake. The TKE was reduced in the wake deficit due to the lower wind speeds.

The influence of cluster wakes on the current power production of downstream wind farms could not easily be related to their influence on the annual energy production (AEP). To achieve this, a detailed assessment of the total influence during at least 1 year has to be conducted using, for example, validated wind farm parameterizations in mesoscale models. The local distribution of wind speed, direction and atmospheric stability has to be considered as well as farm and cluster geometries.

In many wake cases the wind speed in the wake deficit still exceeds rated wind speed of the downstream turbines without an effect on their power production. If the upstream cluster's turbines operate in wind speeds above rated speed, their thrust coefficient,  $c_T$ , decreases additionally, resulting in reduced wake deficits. We expect the total influence of cluster wakes on AEP to be smaller than wake effects from neighbouring wind farms (see Nygaard and Hansen, 2016) due to cluster wake recovery and a smaller wake-influenced wind direction sector. Our findings do not question wind energy utilization of any kind. Nevertheless, a detailed assessment of the influence of cluster wakes on AEP of downstream wind farms during their whole operational life time considering all planned wind energy activities in the region should be conducted in the future. This can improve power production, offshore resource assessment and consequently reduce the uncertainties in financing large offshore wind projects especially in regions with a high level of (planned) wind energy utilization. Therefore, further research is necessary to validate wind farm parameterizations in mesoscale weather models with appropriate wake, power and atmospheric measurements. Especially the influence of atmospheric stability on cluster wake recovery has to be investigated.

Aside from influence on power, the effect on additional wind turbine loads can be relevant. We did not perform analysis of the turbulence in the wake in this study or load simulations on wind turbines affected by far cluster wakes. Since we find sharp edges between wake flow and free stream continuing in the wind farm's power production (Fig. 6), future research should analyse turbine loads dependent on the cluster wake dynamics, e.g. when a turbine on the wake border

has to speed up and slow down fast caused by cluster wake dynamics.

#### 4.2 Cluster wake characteristics

Wind turbines are sensitive to the wind conditions over a wide range of heights defined by the swept rotor area. Therefore, the investigation of cluster wakes should cover the whole vertical wind profile at least from lower to upper tip height. Satellite SAR measurements at the sea surface are typically transferred to 10 m height. Platis et al. (2018) investigates cluster wakes at hub height with a research aircraft in stable stratification, and Siedersleben et al. (2018b) additionally presents measurements in five different height levels (60, 90, 120, 150, 220 m) from the same flight, revealing wake deficits in all regarded levels. This highlights a vertical expansion of the wake far above the rotor area (upper tip height: 150 m). We find evidence for cluster wake effects in SAR images (roughness measurement on the sea surface, interpolation to 10 m a.s.l. – above sea level), lidar measurements ( $\approx 24.6$  m a.m.s.l., 67.0 m below hub height and 9.0 m below lower blade tip height) and from the turbines' power production (rotor swept area spans from 33.6 m to 149.6 m a.m.s.l.). A quantitative comparison of the measured wake strengths is not possible with our data due to the very different type of the measurements. Nevertheless we obtain evidence for wake effects in the boundary layer from the sea surface to the upper tip height 24 and 55 km downstream, agreeing with the observed vertical wake extension closer to the generating cluster presented by Siedersleben et al. (2018b). For a future campaign we suggest the assessment of the development of the atmospheric boundary layer from the inflow through a cluster and in the cluster wake by means of, for example, lidar profilers, lidar range height indicator scans (RHI) or flight measurements for a better understanding of cluster wake development and recovery.

All previous investigations of cluster wakes with satellite SAR suffer from the fact that just one snapshot of the wake is available for a given situation and no wake dynamics or their steadiness could be analysed. Nygaard and Newcombe (2018) investigate a cluster wake at hub height up to 17 km downstream of a wind farm with dual Doppler radar from the coast and present a 1 h average wake field. The aircraft measurements performed by Platis et al. (2018) cover the whole area of the wake along the flight path taking several hours, indicating a constant behaviour of the wake. We find steady wake conditions in both presented examples for more than 2.5 h in the lidar data supported by the corresponding power data. This proves the existence of steady wake effects with a steady influence on the downstream wind farm for constant wind directions. Wake cases with changing wind directions are much harder to analyse since the wake just shortly influences the farm and will probably not even be detectable in wind measurements.



We did not find any evidence for single wind turbine wakes in the lidar inflow measurements of GT I. This is supported by the results by Nygaard and Newcombe (2018), who present dual Doppler radar cross stream flow cuts through a cluster wake at different downstream distances with disappearing signatures of the single turbines from 6 km downstream (unknown stability).

The shapes of the wakes we find could give further hints on the wake recovery process. While shorter wakes (i.e. from the BorWin cluster, Fig. 5) are as wide as the generating cluster, wakes originating further away often appear narrower in the lidar measurements as if they already recovered from the sides or if the whole wake widened with a resulting decrease in maximum wake deficit. This is supported by the shapes of the wakes seen in the SAR wind data in Fig. 9b where the highest wake deficits are narrower further downstream. A detailed analysis of this effect is difficult due to changes in the mesoscale wind field and wakes of neighbouring clusters overlapping with the cluster wake.

The width of the transition region between free flow and wake seems to (at least partly) depend on the downstream position of the wake. In the BorWin wake we sometimes find high wind speed gradients at the wake's border about 20 km downstream (Fig. 6), while in the DolWin wake 50 km downstream the transition region was several kilometres wide (Fig. 10).

The longevity of wakes in stable conditions is further supported by the investigation of two different converter platform wakes in our lidar measurements ranging at least 9 km downstream in one case (Fig. 10). Platform wakes have been observed before, e.g. Chunchuzov et al. (2000) reported a more than 60 km long wake of a 164 m tall offshore platform in very stable atmospheric conditions analysed with satellite SAR measurements. We did not investigate the effect of the wakes of wind farm converter platforms on the power of neighbouring or distant wind turbines but expect it to be fairly small compared to a wind turbine wake due to the lower heights and smaller cross sections of the platforms.

### 4.3 Cluster wake monitoring

Due to the large areas the cluster wakes take up, their investigation was mainly based on long-ranging remote-sensing techniques. Satellite SAR covers large areas and has been widely used to analyse cluster wakes (Hasager et al., 2015). Our analysis adds the potential power as a computed local quantity to the SAR analysis (Fig. 5d), confirming the wake shape acquired by SAR with turbine power data. This is another hint for the ability of satellite SAR to resolve flow structures, agreeing with the findings of Schneemann et al. (2015), who compared structures in concurrent SAR and lidar measurements indicating the general ability of SAR to resolve flow structures with the size of a few hundred metres.

Cluster wakes have not been measured with long-range lidar. With an achievable maximum range of 10 km with compact devices, lidar seemed not to be appropriate to measure far cluster wakes behind a wind farm. We used lidar to measure incoming far cluster wakes. As opposed to SAR, lidar allows for continuous measurements with scan repetition times in the order of a few minutes (2.5 and 10 min here). In some cases the lidar results are clear (e.g. Fig. 6) but in other cases it is difficult to interpret whether the wind field is influenced by a wake or not. Here, satellite SAR, when available, proves very useful to interpret wind monitoring by lidar offering the possibility to regard the lidar wind field in a wider context (e.g. the DolWin2 case, Sect. 3.2). Nevertheless, absolute wind speed measurements by satellite SAR are comparably imprecise. For the comparison of the shapes of the potential power in the inflow with the turbines' power, we had to correct individual offsets in the SAR wind speeds within the given measurement accuracy. Schneemann et al. (2015) had to correct for an offset in SAR winds, comparing it with lidar, as well. This inaccuracy could be possibly reduced by a SAR analysis tuned to the special case. We did not perform SAR wind calculations ourselves but used already processed wind data.

The analysis of SCADA data on power losses due to cluster wakes without additional flow information from remote sensing is difficult since obvious gradients in wind farm power (Fig. 6) due to cluster wakes are rare and not exactly stationary (e.g. washed out transition region in averaged lidar wind field, Fig. 7b). In the DolWin2 case (Fig. 9) it is hardly possible to judge the contributions of wake effects and effect of higher turbine efficiency at the farm corners (Barthelmie and Jensen, 2010) on the higher power of the turbines at the eastern and western corners of the farm.

For future research on cluster wakes and their influence on power generation, we propose a combination of different measurement techniques complementing with their advantages, namely satellite SAR, long-range lidar and flight measurements (aircrafts and drones). Doppler radar and non-compact lidar systems offering ranges larger than 15 km are available but have not been deployed in offshore wind farms so far due to high costs and technical hurdles in the deployment, orientation and operation of the container-size systems on offshore structures.

Another important aspect of measurements from offshore platforms like transition pieces of offshore wind turbines to be considered is platform movement and the resulting errors in measurement locations. We found platform tilts of up to  $0.1^\circ$  due to turbine thrust depending on wind speed and direction using the method of sea surface levelling (Rott et al., 2017). This value might be even higher for turbines on a commonly used monopile foundation compared to the tripod foundation used in GT I. With increasing measurement ranges, the location error in the measurements grows further.



## 5 Conclusions

This paper investigates the question of whether offshore cluster wakes have an influence on power generation of far downstream wind farms considering atmospheric stability. Therefore we analysed two different cases of 24 and 55 km long cluster wakes approaching the 400 MW offshore wind farm Global Tech I (GT I) by means of satellite SAR measurements, lidar wind monitoring and analysis of atmospheric stability and GT I power production.

Long-range Doppler lidar supported by satellite SAR proves to be a good combination for cluster wake measurements with the lidar providing accurate wind speed monitoring over long periods and SAR contributing with large-area wind fields for the overall picture.

We find that long-distance wake effects of a wind farm cluster exist at least 55 km downstream in stable and weakly unstable stratification. They persist for more than 2.5 h. During this measurement period the average wake deficits are  $2.3 \text{ m s}^{-1}$  or 25 % approximately 24 km downstream and  $2.2 \text{ m s}^{-1}$  or 21 % approximately 55 km downstream. Single lidar scans (2.5 min duration) reveal stronger wake deficits of up to  $3.9 \text{ m s}^{-1}$  or 41 % approximately 24 km downstream.

Clear transition regions like edges in the wind separate wake and free flow 24 km downstream and continue in the affected wind farm, splitting it into regions of higher power in undisturbed flow and reduced power in the wake deficit. Free-flow turbines produce more than two standard deviations,  $\sigma_P$ , more than the average of the upstream turbines.

This contribution proves the existence of steady power reductions in a far downstream wind farm caused by cluster wakes. We encourage further investigations on far-reaching wake shadowing effects for optimized areal planning at sea and reduced uncertainties in offshore wind power resource assessment.

**Data availability.** Lidar data and meteorological data are published (Schneemann et al., 2019). GT I SCADA data are confidential and therefore not available to the public. SAR wind data are available from <https://scihub.copernicus.eu/> (last access: 13 December 2019; Scihub, 2019). Hourly power data for several wind farms are available from <https://www.energy-charts.de/> (last access: 19 December 2019; Fraunhofer ISE, 2019). The New European Wind Atlas is published at <https://map.neweuropeanwindatlas.eu/> (last access: 19 December 2019; NEWA, 2019). The OSTIA data set can be obtained from <http://marine.copernicus.eu/> (last access: 13 December 2019; Copernicus marine service, 2019) and radiosonde soundings are available at <http://www.meteociel.fr/> (last access: 13 December 2019; meteociel.fr, 2019) or <http://weather.uwyo.edu> (last access: 13 December 2019; University of Wyoming, 2019).

## Appendix A: Calculation of virtual potential temperatures

We derived the virtual potential temperature used in Sect. 2.4 from the available measurements on the TP. We adapted the following methodology mainly from Etling (2008). We need the following:

- $R_d = 287 \text{ J K}^{-1} \text{ kg}^{-1}$  (specific gas constant of dry air);
- $R_v = 461 \text{ J K}^{-1} \text{ kg}^{-1}$  (specific gas constant of water vapour);
- $\epsilon = \frac{R_d}{R_v} = 0.622$  (ratio between the specific gas constants for dry air  $R_d$  and water vapour  $R_v$ );
- $\kappa_p = 0.286$  (Poisson constant in dry air).

The saturation vapour pressure in pascals (Pa) dependent on the temperature in kelvin (K) follows from the Magnus equation,

$$e_s(T) = 100.0 \cdot 6.1 \cdot 10^{\left(\frac{7.45 \cdot (T - 273.15)}{T - 38.15}\right)}. \quad (\text{A1})$$

The partial pressure of water vapour in the air dependant on the relative humidity RH reads as

$$e = \text{RH} \cdot e_s / 100.0, \quad (\text{A2})$$

while the mixing ratio is

$$r_v = \epsilon \cdot \left(\frac{e}{p - e}\right). \quad (\text{A3})$$

With the specific humidity

$$q = \frac{r_v}{1 + r_v} \quad (\text{A4})$$

and the potential temperature

$$\Theta = T \left(\frac{100000 \text{ Pa}}{p}\right)^{\kappa_p}, \quad (\text{A5})$$

we approximate the virtual potential temperature as

$$\Theta_v = \Theta \cdot (1.0 + 0.61 \cdot q). \quad (\text{A6})$$

While the virtual potential temperature at the TP,  $\Theta_{v, \text{TP}}$ , could be derived directly from the available measurements, we assume the relative humidity and the air temperature directly above the sea to be  $\text{RH}_0 = 100\%$  and  $T_0 = T_{\text{SST}}$ , respectively, to derive the virtual potential temperature at sea level,  $\Theta_{v, \text{SST}}$ . Furthermore we calculate the air pressure at sea level as

$$p_0 = p_{\text{TP}} \cdot \left(\frac{T_{\text{SST}} - \gamma \cdot z_{\text{TP}}}{T_{\text{SST}}}\right)^{\frac{-g}{\gamma R_d}}, \quad (\text{A7})$$

assuming a polytropic atmosphere and using the air temperature gradient

$$\gamma = \frac{T_{\text{SST}} - T_{\text{TP}}}{z_{\text{TP}}}. \quad (\text{A8})$$

**Author contributions.** JS conducted and supervised the measurement campaign, designed the research, performed the data analysis, made the figures, and planned and wrote the paper. AR and MK contributed to the research with intensive discussions and added to the paper with conceptual discussions and internal review. MD advised on the meteorological parts, participated in the conception of the paper and did an internal review. GS performed parts of the stability analysis and intensively reviewed the article.

**Competing interests.** The authors declare that they have no conflict of interest.

**Acknowledgements.** We acknowledge the wind farm operator Global Tech I Offshore Wind GmbH for providing SCADA data and their support of the work. Furthermore, we thank the European Space Agency (ESA) for making the Sentinel-1 data of the Copernicus programme available. Thanks to the Met Office for making the OSTIA data set available. We acknowledge the NEWA consortium for providing access to the New European Wind Atlas. Special thanks to Stephan Voß for his work on the measurement campaign and the picture from Fig. 3.

**Financial support.** The lidar measurements and parts of the work have been supported by the German Federal Ministry for Economic Affairs and Energy on the basis of a decision by the German Bundestag (OWP Control, grant no. 0324131A).

**Review statement.** This paper was edited by Rebecca Barthelmie and reviewed by Nicolai Gayle Nygaard and one anonymous referee.

## References

- Abkar, M. and Porté-Agel, F.: Influence of atmospheric stability on wind-turbine wakes: A large-eddy simulation study, *Phys. Fluids*, 27, 035104, <https://doi.org/10.1063/1.4913695>, 2015.
- Aitken, M. L., Banta, R. M., Pichugina, Y. L., and Lundquist, J. K.: Quantifying Wind Turbine Wake Characteristics from Scanning Remote Sensor Data, *J. Atmos. Ocean. Tech.*, 31, 765–787, <https://doi.org/10.1175/JTECH-D-13-00104.1>, 2014.
- Barthelmie, R. J. and Jensen, L. E.: Evaluation of wind farm efficiency and wind turbine wakes at the Nysted offshore wind farm, *Wind Energy*, 13, 573–586, <https://doi.org/10.1002/we.408>, 2010.
- Beck, H. and Kühn, M.: Dynamic Data Filtering of Long-Range Doppler LiDAR Wind Speed Measurements, *Remote Sens.*, 9, 561, <https://doi.org/10.3390/rs9060561>, 2017.
- Beck, H. and Kühn, M.: Temporal Up-Sampling of Planar Long-Range Doppler LiDAR Wind Speed Measurements Using Space-Time Conversion, *Remote Sens.*, 11, 867, <https://doi.org/10.3390/rs11070867>, 2019.
- Bodini, N., Zardi, D., and Lundquist, J. K.: Three-dimensional structure of wind turbine wakes as measured by scanning lidar, *Atmos. Meas. Tech.*, 10, 2881–2896, <https://doi.org/10.5194/amt-10-2881-2017>, 2017.
- Christiansen, M. B. and Hasager, C. B.: Wake effects of large offshore wind farms identified from satellite SAR, *Remote Sens. Environ.*, 98, 251–268, <https://doi.org/10.1016/j.rse.2005.07.009>, 2005.
- Chunchuzov, I., Vachon, P., and Li, X.: Analysis and Modeling of Atmospheric Gravity Waves Observed in RADARSAT SAR Images, *Remote Sens. Environ.*, 74, 343–361, [https://doi.org/10.1016/S0034-4257\(00\)00076-6](https://doi.org/10.1016/S0034-4257(00)00076-6), 2000.
- Churchfield, M. J., Lee, S., Michalakes, J., and Moriarty, P. J.: A numerical study of the effects of atmospheric and wake turbulence on wind turbine dynamics, *J. Turbulence*, 13, N14, <https://doi.org/10.1080/14685248.2012.668191>, 2012.
- Copernicus marine service: Copernicus Marine environment monitoring service, available at: <http://marine.copernicus.eu/>, last access: 13 December 2019.
- Donlon, C. J., Martin, M., Stark, J., Roberts-Jones, J., Fiedler, E., and Wimmer, W.: The Operational Sea Surface Temperature and Sea Ice Analysis (OSTIA) system, *Remote Sens. Environ.*, 116, 140–158, <https://doi.org/10.1016/j.rse.2010.10.017>, 2012.
- Dörenkämper, M., Optis, M., Monahan, A., and Steinfeld, G.: On the Offshore Advection of Boundary-Layer Structures and the Influence on Offshore Wind Conditions, *Bound.-Lay. Meteorol.*, 155, 459–482, <https://doi.org/10.1007/s10546-015-0008-x>, 2015a.
- Dörenkämper, M., Witha, B., Steinfeld, G., Heinemann, D., and Kühn, M.: The impact of stable atmospheric boundary layers on wind-turbine wakes within offshore wind farms, *J. Wind Eng. Indust. Aerodynam.*, 144, 146–153, <https://doi.org/10.1016/j.jweia.2014.12.011>, 2015b.
- Emeis, S.: A simple analytical wind park model considering atmospheric stability, *Wind Energy*, 13, 459–469, <https://doi.org/10.1002/we.367>, 2009.
- Emeis, S.: *Wind Energy Meteorology*, Springer International Publishing, 2nd Edn, Springer International Publishing AG, part of Springer Nature 2018, <https://doi.org/10.1007/978-3-319-72859-9>, 2018.
- EnBW: EnBW Hohe See and Albatros wind farms, The construction diary for Hohe available at: <https://www.enbw.com/renewable-energy/wind-energy/our-offshore-wind-farms/hohe-see/construction-diary.html>, (last access: 18 June 2019).
- ESA: Level 2 OCN Ocean Wind Field (OWI) Component, available at: <https://sentinel.esa.int/web/sentinel/ocean-wind-field-component>, last access: 19 June 2019.
- Etling, D.: *Theoretische Meteorologie*, 3rd Edn., Springer, Berlin, Heidelberg, <https://doi.org/10.1007/978-3-662-10430-9>, 2008.
- Fitch, A. C., Olson, J. B., Lundquist, J. K., Dudhia, J., Gupta, A. K., Michalakes, J., and Barstad, I.: Local and Mesoscale Impacts of Wind Farms as Parameterized in a Mesoscale NWP Model, *Mon. Weather Rev.*, 140, 3017–3038, <https://doi.org/10.1175/mwr-d-11-00352.1>, 2012.
- Fraunhofer ISE: Energy Charts, available at: <https://www.energy-charts.de/>, last access: 19 June 2019.
- Fuertes, F. C., Markfort, C., and Porté-Agel, F.: Wind Turbine Wake Characterization with Nacelle-Mounted Wind Lidars for Analytical Wake Model Validation, *Remote Sens.*, 10, 668, <https://doi.org/10.3390/rs10050668>, 2018.

- Grachev, A. A. and Fairall, C. W.: Dependence of the Monin–Obukhov Stability Parameter on the Bulk Richardson Number over the Ocean, *J. Appl. Meteorol.*, 36, 406–414, [https://doi.org/10.1175/1520-0450\(1997\)036<0406:dotmos>2.0.co;2](https://doi.org/10.1175/1520-0450(1997)036<0406:dotmos>2.0.co;2), 1997.
- Hansen, K. S., Barthelmie, R. J., Jensen, L. E., and Sommer, A.: The impact of turbulence intensity and atmospheric stability on power deficits due to wind turbine wakes at Horns Rev wind farm, *Wind Energy*, 15, 183–196, <https://doi.org/10.1002/we.512>, 2011.
- Hasager, C., Vincent, P., Badger, J., Badger, M., Bella, A. D., Peña, A., Husson, R., and Volker, P.: Using Satellite SAR to Characterize the Wind Flow around Offshore Wind Farms, *Energies*, 8, 5413–5439, <https://doi.org/10.3390/en8065413>, 2015.
- Hirth, B. D., Schroeder, J. L., Gunter, W. S., and Guynes, J. G.: Coupling Doppler radar-derived wind maps with operational turbine data to document wind farm complex flows, *Wind Energy*, 18, 529–540, <https://doi.org/10.1002/we.1701>, 2014.
- Lee, S., Vorobieff, P., and Poroseva, S.: Interaction of Wind Turbine Wakes under Various Atmospheric Conditions, *Energies*, 11, 1442, <https://doi.org/10.3390/en11061442>, 2018.
- Li, X. and Lehner, S.: Observation of TerraSAR-X for Studies on Offshore Wind Turbine Wake in Near and Far Fields, *IEEE J. Select. Top. Appl. Earth Obs. Remote Sens.*, 6, 1757–1768, <https://doi.org/10.1109/jstars.2013.2263577>, 2013.
- Lignarolo, L. E., Mehta, D., Stevens, R. J., Yilmaz, A. E., van Kuik, G., Andersen, S. J., Meneveau, C., Ferreira, C. J., Ragni, D., Meyers, J., van Bussel, G. J., and Holierhoek, J.: Validation of four LES and a vortex model against stereo-PIV measurements in the near wake of an actuator disc and a wind turbine, *Renewable Energy*, 94, 510–523, <https://doi.org/10.1016/j.renene.2016.03.070>, 2016.
- Lundquist, J. K., DuVivier, K. K., Kaffine, D., and Tomaszewski, J. M.: Costs and consequences of wind turbine wake effects arising from uncoordinated wind energy development, *Nat. Energy*, 4, 26–34, <https://doi.org/10.1038/s41560-018-0281-2>, 2019.
- Mackensen, R.: Windenergie Report Deutschland 2018, available at: [http://windmonitor.iee.fraunhofer.de/opencms/export/sites/windmonitor/img/Windmonitor-2018/WERD\\_2018.pdf](http://windmonitor.iee.fraunhofer.de/opencms/export/sites/windmonitor/img/Windmonitor-2018/WERD_2018.pdf), last access: 5 July 2019.
- Merkur Offshore: Sea Change: GE Installs The Last Turbine At One Of Germany’s Largest Offshore Wind Farms, available at: <https://www.merkur-offshore.com/progress/> (last access: 19 June 2019), 2018.
- meteociel.fr: Observation, Prévisions, Modèles, En temps réel, available at: <https://www.meteociel.fr/>, last access: 13 December 2019.
- Mouche, A.: Sentinel-1 Ocean Wind Fields (OWI) Algorithm Definition, Tech. Rep. CLS-DAR-NT-10-167 S1-TN-CLS-52-904, CLS/ESA, available at: [https://sentinel.esa.int/documents/247904/349449/S-1\\_L2\\_OWI\\_Detailed\\_Algorithm\\_Definition.pdf](https://sentinel.esa.int/documents/247904/349449/S-1_L2_OWI_Detailed_Algorithm_Definition.pdf) (last access: 22 February 2019), 2011.
- NEWA: New European Wind Atlas, available at: <https://map.neweuropeanwindatlas.eu/>, last access: 27 June 2019.
- Nygaard, N. G.: Wakes in very large wind farms and the effect of neighbouring wind farms, *J. Phys.: Conf. Ser.*, 524, 012162, <https://doi.org/10.1088/1742-6596/524/1/012162>, 2014.
- Nygaard, N. G. and Hansen, S. D.: Wake effects between two neighbouring wind farms, *J. Phys.: Conf. Ser.*, 753, 032020, <https://doi.org/10.1088/1742-6596/753/3/032020>, 2016.
- Nygaard, N. G. and Newcombe, A. C.: Wake behind an offshore wind farm observed with dual-Doppler radars, *J. Phys.: Conf. Ser.*, 1037, 072008, <https://doi.org/10.1088/1742-6596/1037/7/072008>, 2018.
- Orsted: Borkum Riffgrund 2, available at: <https://orsted.de/offshore-windenergie/unsere-offshore-windparks-nordsee/offshore-windpark-borkum-riffgrund-2> (last access: 19 June 2019), 2018.
- Petrofac: BorWin gamma platform topside touches down in the German North Sea, available at: <https://www.petrofac.com/en-gb/media/news/borwin-gamma-platform-topside-touches-down-in-the-german-north-sea/> (last access: 7 June 2019), 2018.
- Platis, A., Siedersleben, S. K., Bange, J., Lampert, A., Bärfuss, K., Hankers, R., Cañadillas, B., Foreman, R., Schulz-Stellenfleth, J., Djath, B., Neumann, T., and Emeis, S.: First in situ evidence of wakes in the far field behind offshore wind farms, *Scient. Rep.*, 8, 2163, <https://doi.org/10.1038/s41598-018-20389-y>, 2018.
- Pryor, S. C., Barthelmie, R. J., and Shepherd, T. J.: The Influence of Real-World Wind Turbine Deployments on Local to Mesoscale Climate, *J. Geophys. Res.-Atmos.*, 123, 5804–5826, <https://doi.org/10.1029/2017jd028114>, 2018a.
- Pryor, S. C., Shepherd, T. J., and Barthelmie, R. J.: Interannual variability of wind climates and wind turbine annual energy production, *Wind Energy. Sci.*, 3, 651–665, <https://doi.org/10.5194/wes-3-651-2018>, 2018b.
- Rodrigo, J. S., Cantero, E., García, B., Borbón, F., Irigoyen, U., Lozano, S., Fernande, P. M., and Chávez, R. A.: Atmospheric stability assessment for the characterization of offshore wind conditions, *J. Phys.: Conf. Ser.*, 625, 012044, <https://doi.org/10.1088/1742-6596/625/1/012044>, 2015.
- Rott, A., Schneemann, J., Trabucchi, D., Trujillo, J., and Kühn, M.: Accurate deployment of long range scanning lidar on offshore platforms by means of sea surface leveling, in: Poster presentation, NAWEA Windtech, available at: [http://windtechconferences.org/wp-content/uploads/2018/01/Windtech2017\\_AnRott-Poster.pdf](http://windtechconferences.org/wp-content/uploads/2018/01/Windtech2017_AnRott-Poster.pdf) (last access: 5 July 2019), 2017.
- Schmidt, J. and Stoevesandt, B.: The impact of wake models on wind farm layout optimization, *J. Phys.: Conf. Ser.*, 625, 012040, <https://doi.org/10.1088/1742-6596/625/1/012040>, 2015.
- Schneemann, J., Hieronimus, J., Jacobsen, S., Lehner, S., and Kühn, M.: Offshore wind farm flow measured by complementary remote sensing techniques: radar satellite TerraSAR-X and lidar windscanners, *J. Phys.: Conf. Ser.*, 625, 012015, <https://doi.org/10.1088/1742-6596/625/1/012015>, 2015.
- Schneemann, J., Voß, S., Rott, A., and Kühn, M.: Doppler wind lidar plan position indicator scans and atmospheric measurements at the offshore wind farm “Global Tech I”, PAN-GAEA – Data Publisher for Earth & Environmental Science, <https://doi.org/10.1594/PANGAEA.909721>, 2019.
- SciHub: ESA, Copernicus Open Access Hub, available at: <https://scihub.copernicus.eu/>, last access: 13 December 2019.
- Siedersleben, S. K., Lundquist, J. K., Platis, A., Bange, J., Bärfuss, K., Lampert, A., Cañadillas, B., Neumann, T., and Emeis, S.: Micrometeorological impacts of offshore wind farms as seen in observations and simulations, *Environ. Res. Lett.*, 13, 124012, <https://doi.org/10.1088/1748-9326/aaca0b>, 2018a.

- Siedersleben, S. K., Platis, A., Lundquist, J. K., Lampert, A., Bärfuss, K., Cañadillas, B., Djath, B., Schulz-Stellenfleth, J., Bange, J., Neumann, T., and Emeis, S.: Evaluation of a Wind Farm Parametrization for Mesoscale Atmospheric Flow Models with Aircraft Measurements, *Meteorol. Z.*, 27, 401–415, <https://doi.org/10.1127/metz/2018/0900>, 2018b.
- Sorbjan, Z. and Grachev, A. A.: An Evaluation of the Flux-Gradient Relationship in the Stable Boundary Layer, *Bound.-Lay. Meteorol.*, 135, 385–405, <https://doi.org/10.1007/s10546-010-9482-3>, 2010.
- Trabucchi, D., Trujillo, J.-J., and Kühn, M.: Nacelle-based Lidar Measurements for the Calibration of a Wake Model at Different Offshore Operating Conditions, *Energy Procedia*, 137, 77–88, <https://doi.org/10.1016/j.egypro.2017.10.335>, 2017.
- Turner, S., Romero, D., Zhang, P., Amon, C., and Chan, T.: A new mathematical programming approach to optimize wind farm layouts, *Renew. Energy*, 63, 674–680, <https://doi.org/10.1016/j.renene.2013.10.023>, 2014.
- University of Wyoming: Wyoming weather web, available at: <http://weather.uwyo.edu/>, last access: 13 December 2019.
- Vincent, P., Bourbigot, M., Johnsen, H., and Piantanida, R.: Sentinel-1 Product Specification, Tech. Rep. S1-RS-MDA-52-7441, ESA, available at: [https://sentinel.esa.int/web/sentinel/user-guides/sentinel-1-sar/document-library/-/asset\\_publisher/1dO7RF5fJMbd/content/sentinel-1-product-specification](https://sentinel.esa.int/web/sentinel/user-guides/sentinel-1-sar/document-library/-/asset_publisher/1dO7RF5fJMbd/content/sentinel-1-product-specification), last access: 13 December 2019.
- Volker, P. J. H., Badger, J., Hahmann, A. N., and Ott, S.: The Explicit Wake Parametrisation V1.0: a wind farm parametrisation in the mesoscale model WRF, *Geosci. Model Dev.*, 8, 3715–3731, <https://doi.org/10.5194/gmd-8-3715-2015>, 2015.
- Vollmer, L., Steinfeld, G., Heinemann, D., and Kühn, M.: Estimating the wake deflection downstream of a wind turbine in different atmospheric stabilities: an LES study, *Wind Energ. Sci.*, 1, 129–141, <https://doi.org/10.5194/wes-1-129-2016>, 2016.
- Witha, B., Hahmann, A., Sile, T., Dörenkämper, M., Ezber, Y., García-Bustamante, E., González-Rouco, J. F., Leroy, G., and Navarro, J.: WRF model sensitivity studies and specifications for the NEWA mesoscale wind atlas production runs, Technical report, The NEWA consortium, 73 pp., <https://doi.org/10.5281/zenodo.2682604>, 2019.

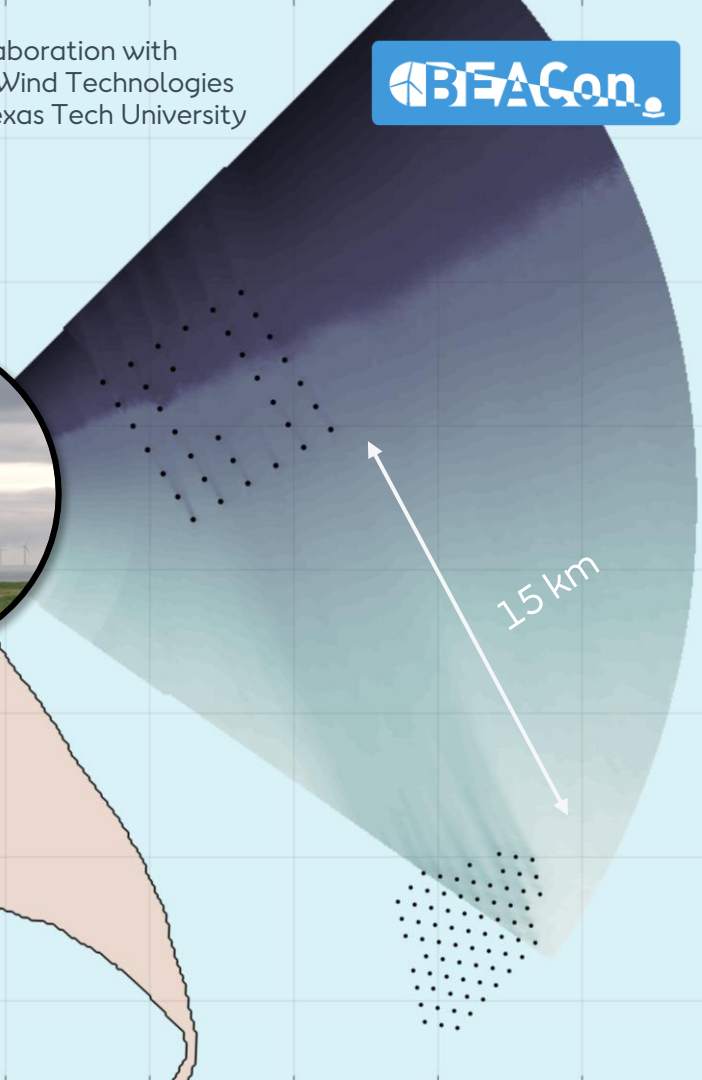
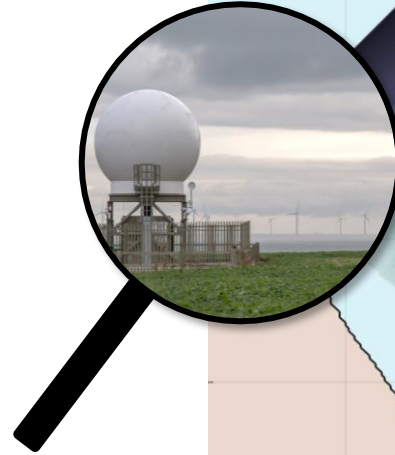
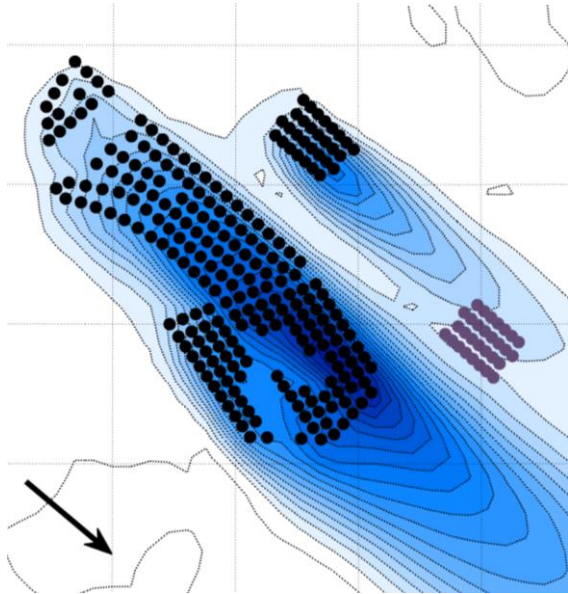


# Impact of long-distance wakes between offshore wind farms

Assessed using operational data

# Wakes between wind farms

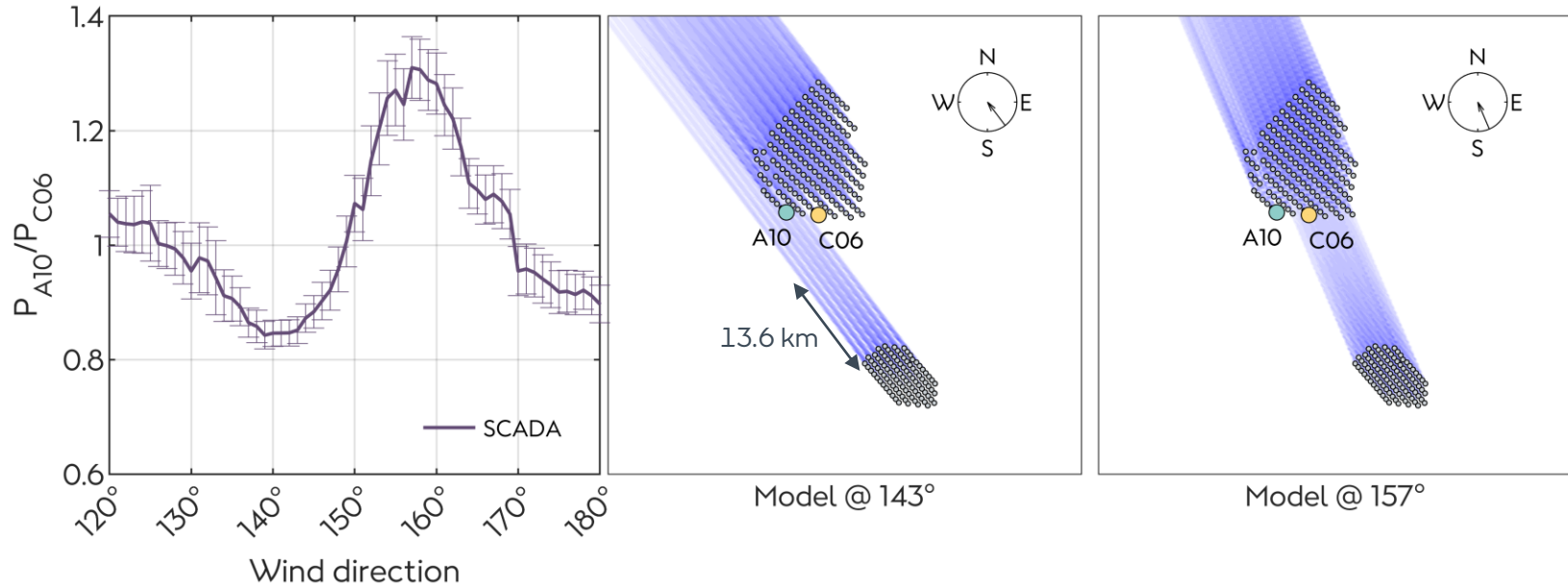
In collaboration with  
SmartWind Technologies  
and Texas Tech University



WRF modelling by Lina Poulsen, [MSc thesis](#)

# Detecting long-range wind farm wakes

Using power ratio of front-row turbines

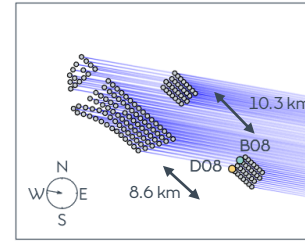
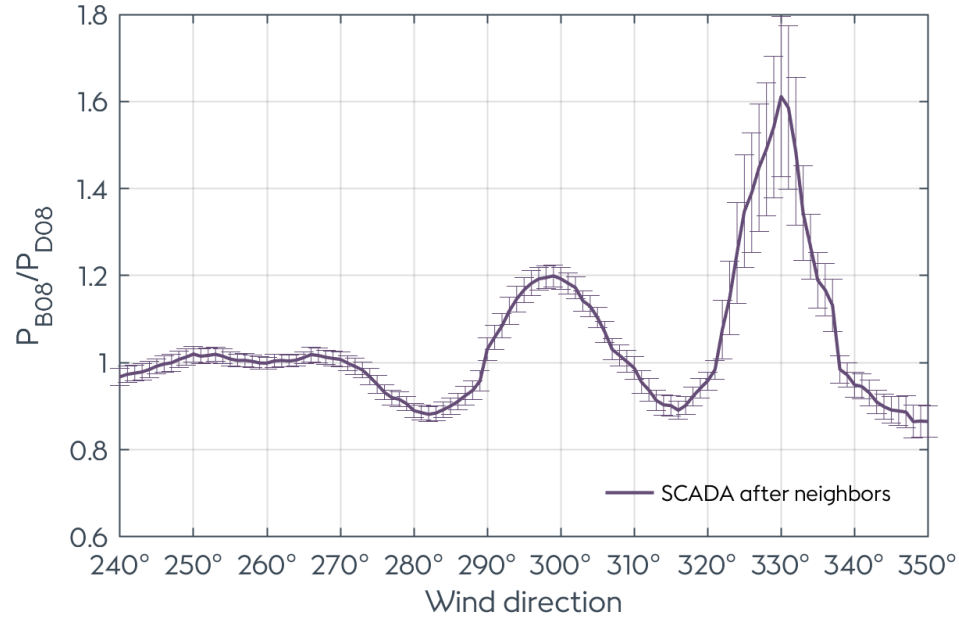


*Not indicative of impact on AEP*

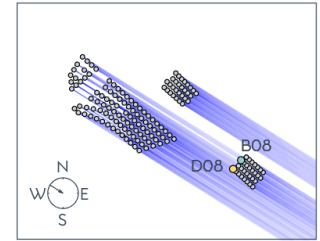
- *Single wind speed only*
- *Only few wind directions affected*
- *Results only shown for front row turbines*

# These are really wakes!

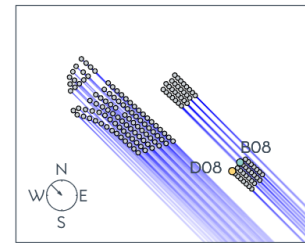
The effect is absent before the neighbors were built



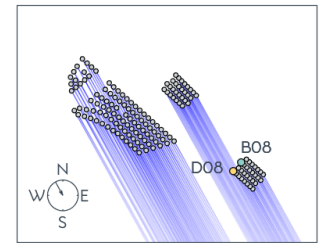
Model @ 280°



Model @ 302°



Model @ 315°

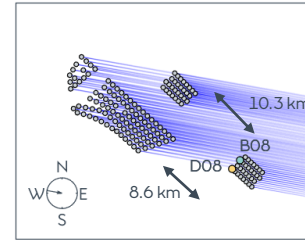
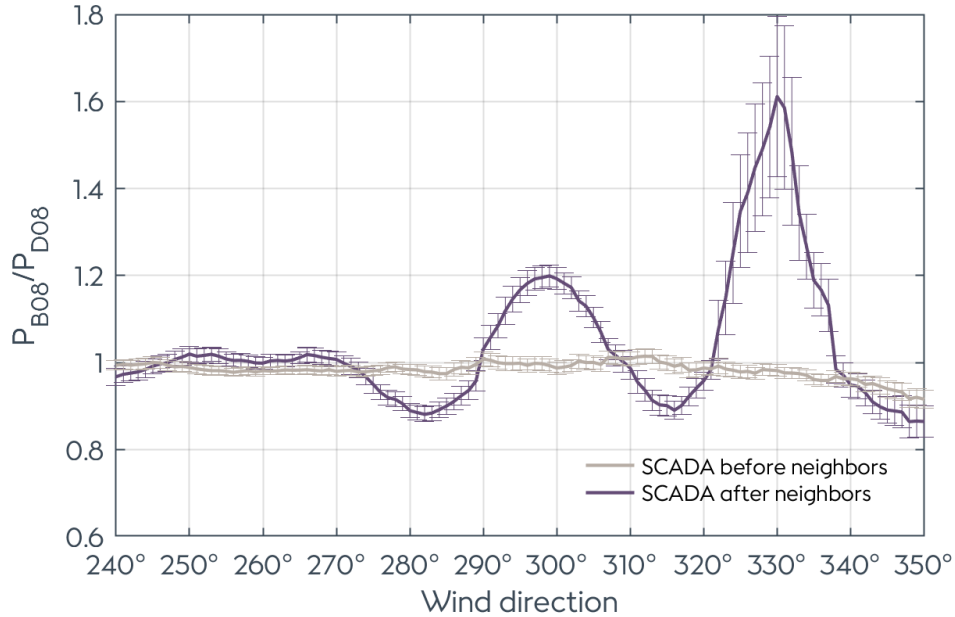


Model @ 331°

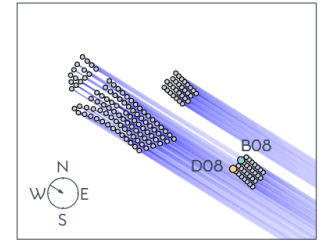


# These are really wakes!

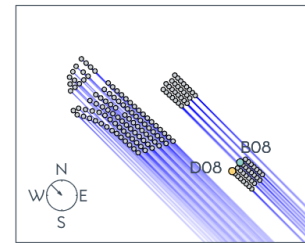
The effect is absent before the neighbors were built



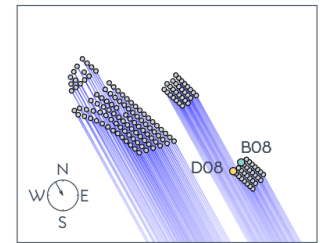
Model @ 280°



Model @ 302°



Model @ 315°

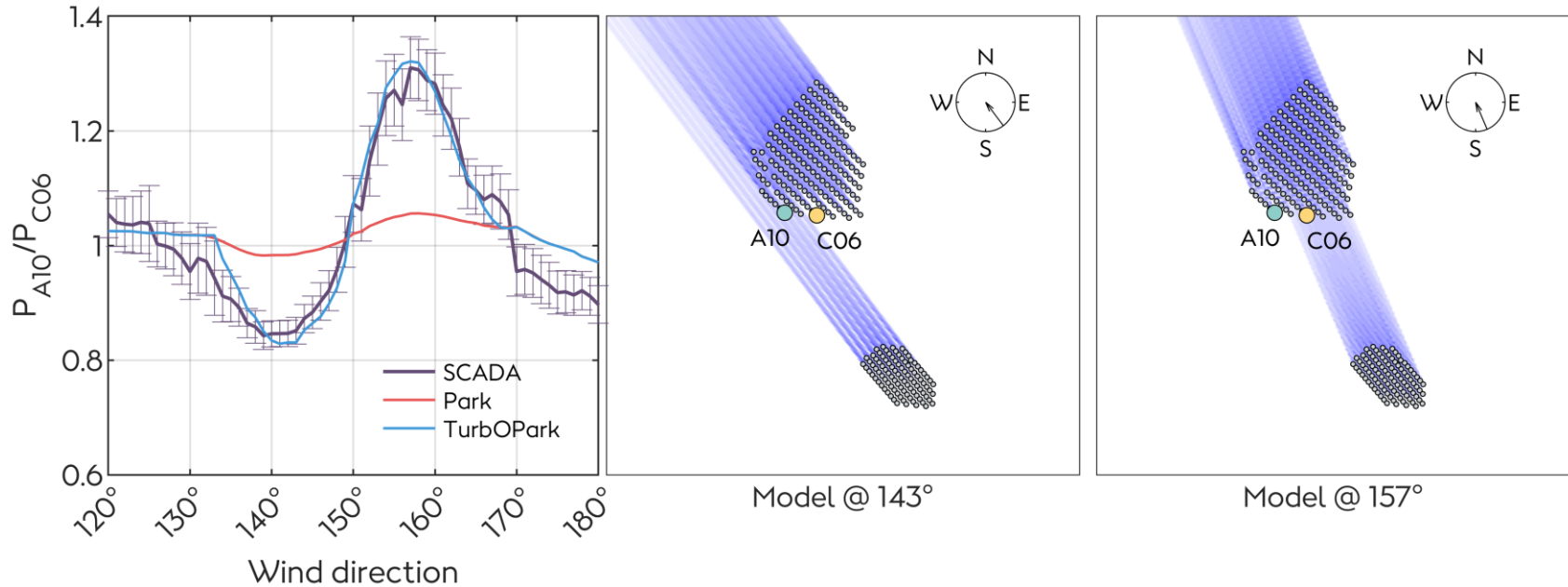


Model @ 331°



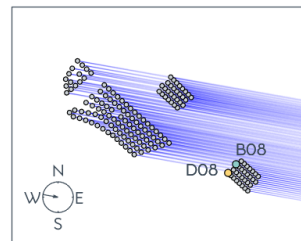
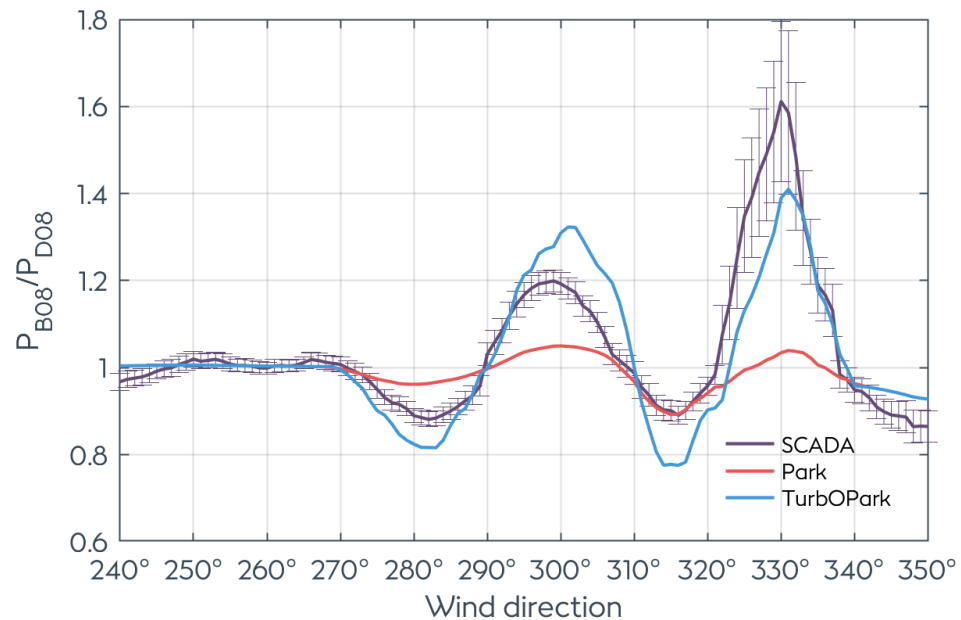
# Observed vs. modelled neighbor wake impact

## TurbOPark better captures long-distance wakes

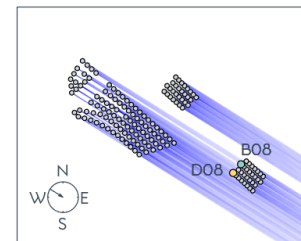


# Observed vs. modelled neighbor wake impact

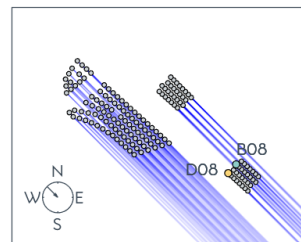
TurbOPark better captures long-distance wakes



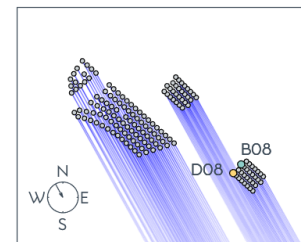
Model @ 280°



Model @ 302°



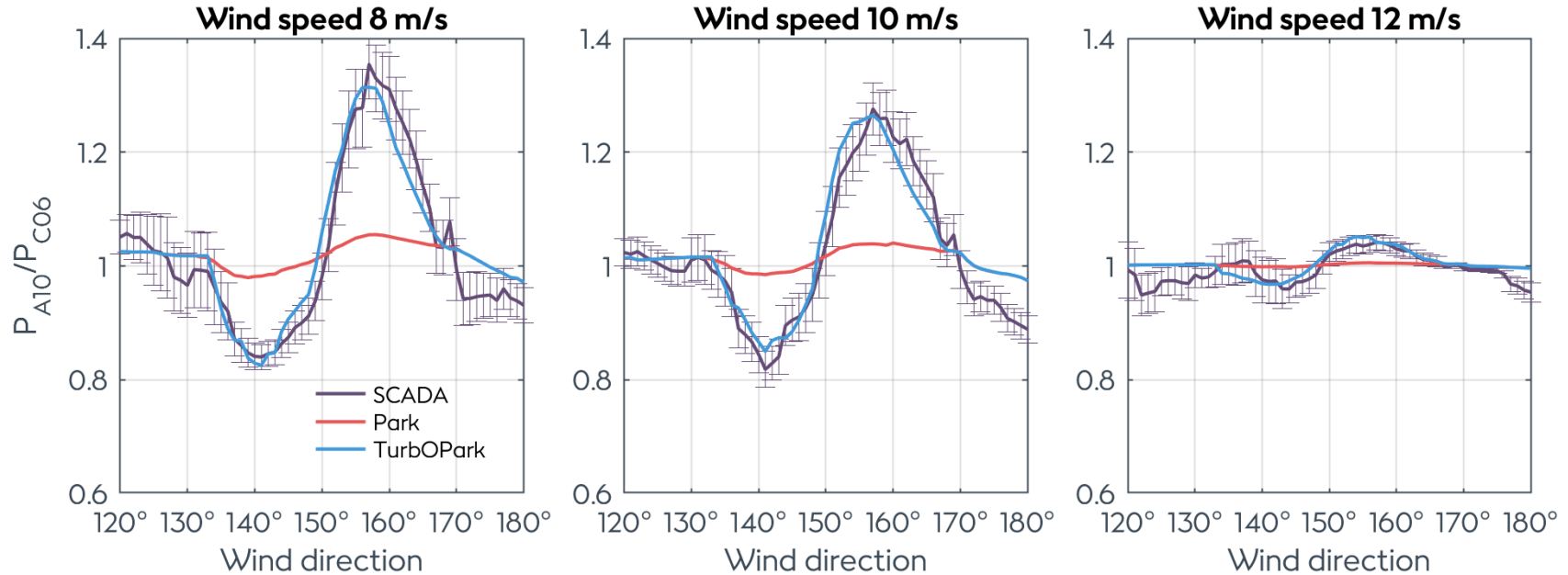
Model @ 315°



Model @ 331°

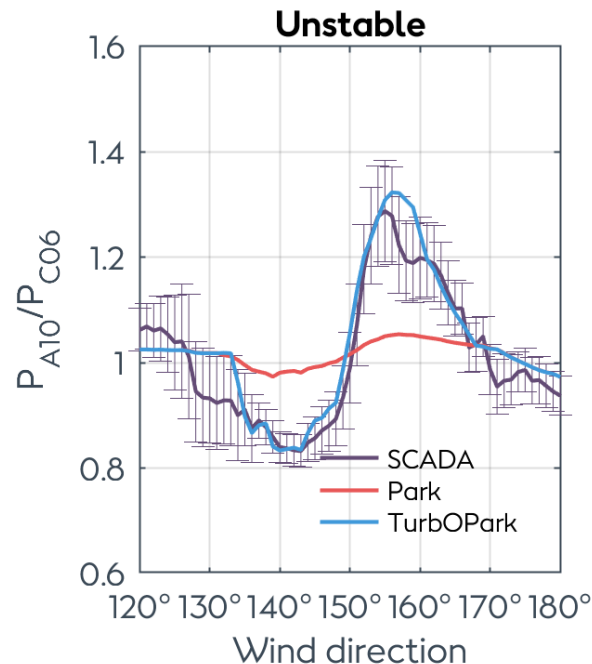
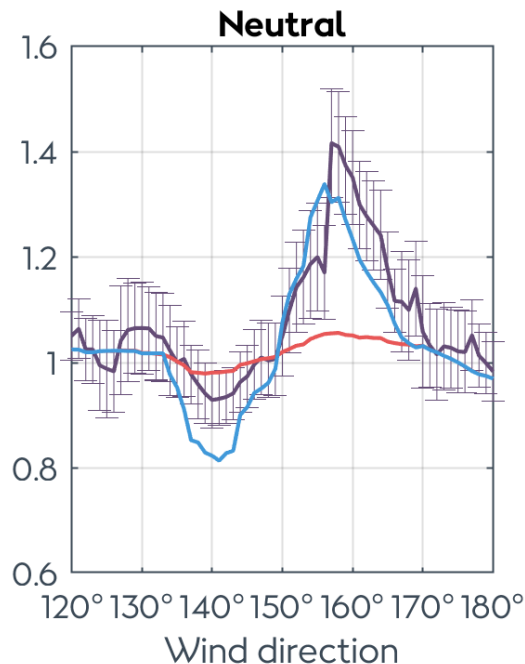
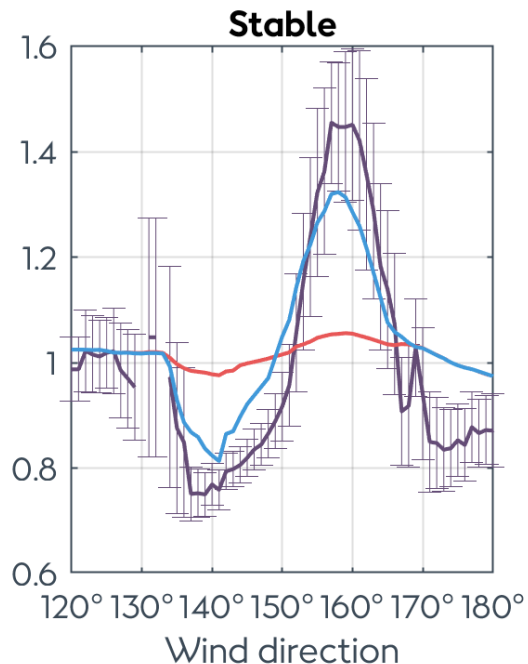
# Wind speed dependence

Higher wind speeds reduce the neighbor wake impact



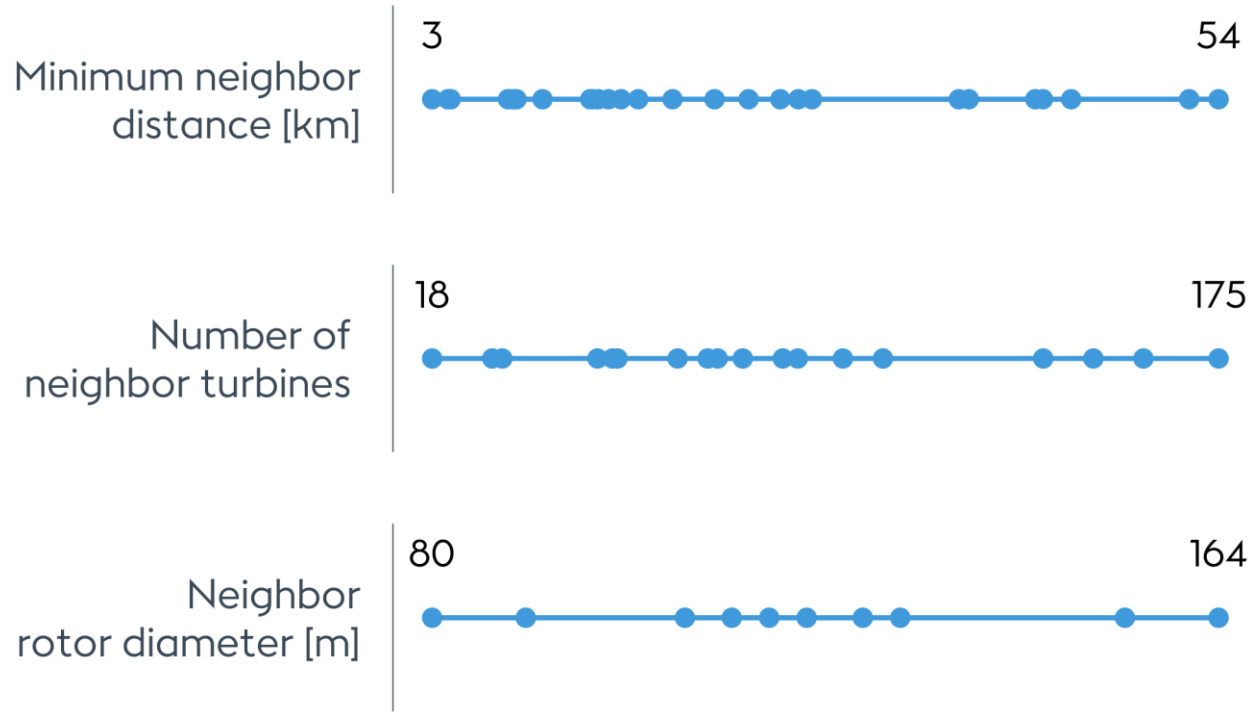
# Stability dependence @ 8 m/s

With Monin-Obukhov length estimated from ERA5 data



# Generalizing to multiple cases

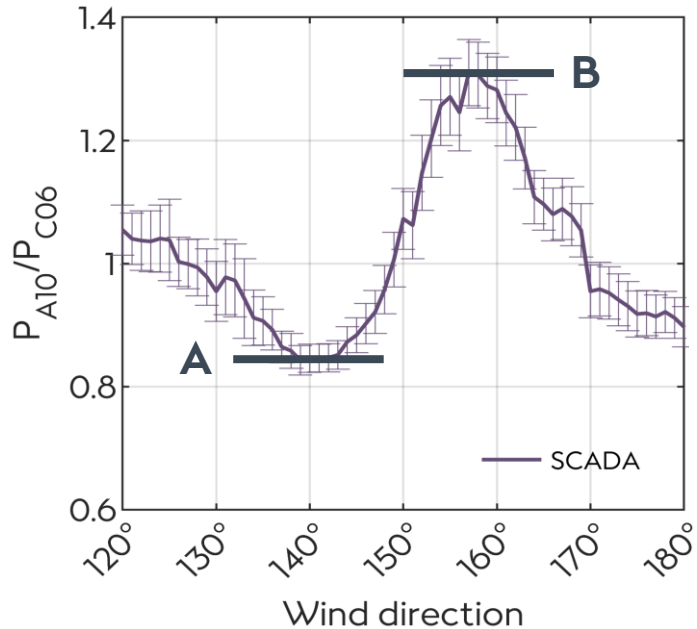
37 neighbor wind farms in Northern Europe





# Calculating the wake impact from the neighbor

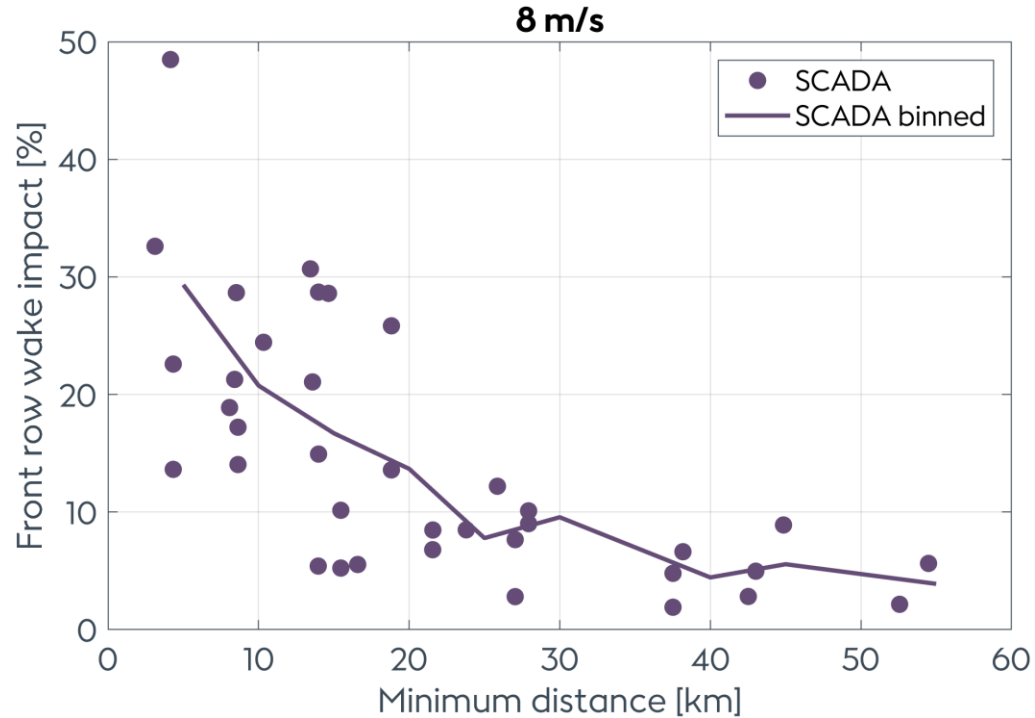
Only front row, only single wind speed



- Front row wake impact =  $1 - 0.5(A + B^{-1})$
- Determine this for
  - All 37 wind farm pairs
  - SCADA data
  - Park model
  - TurbOPark model

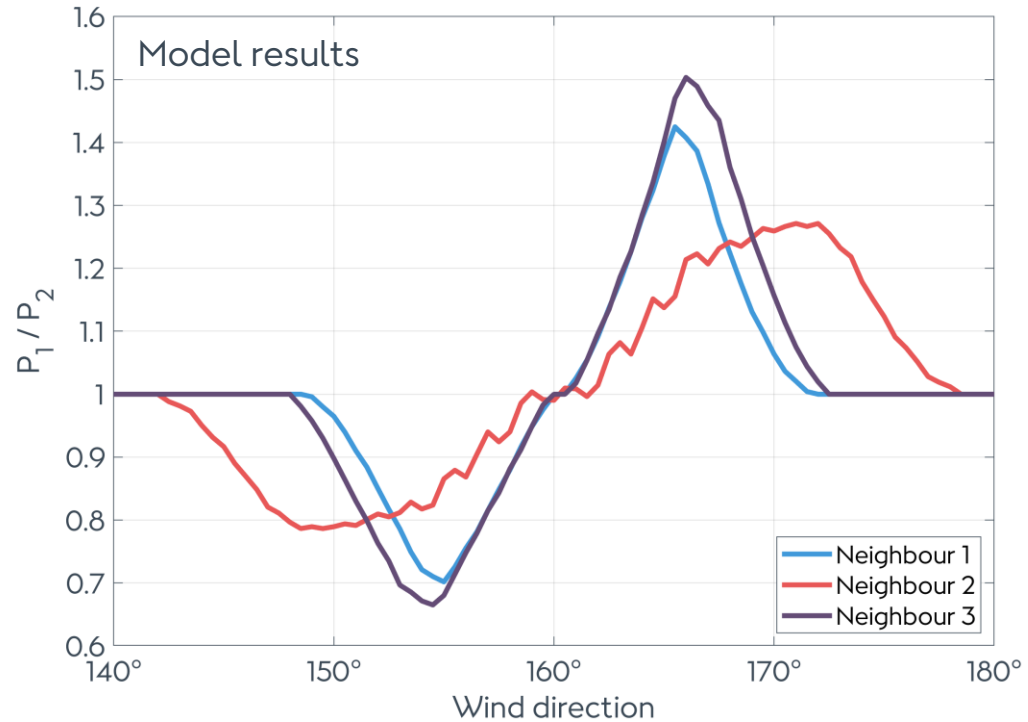
# Dependence on distance

Neighbor wake impact decreases at larger distances



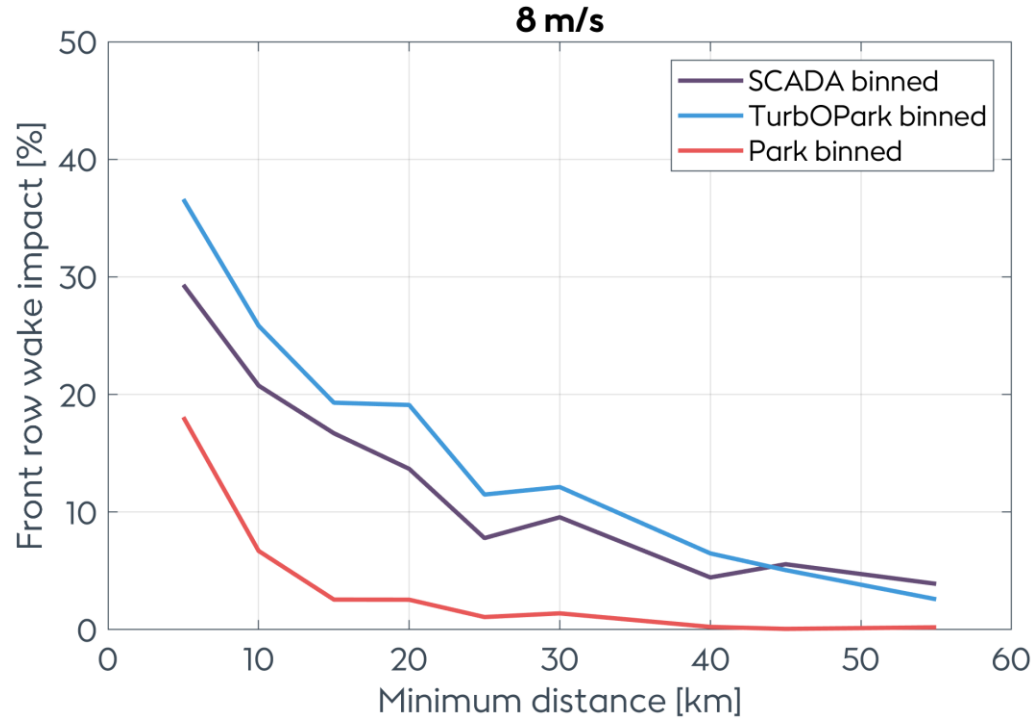
# Sensitivity to neighbour configuration

Same turbines, same distance, different shapes



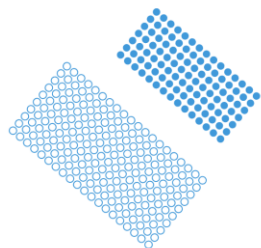
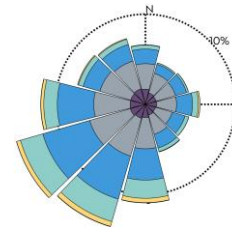
# Dependence on distance

TurbOPark agrees well. Park underestimates the impact

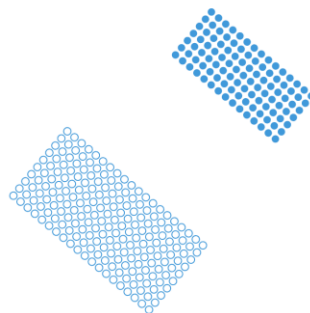


# Impact on annual energy production

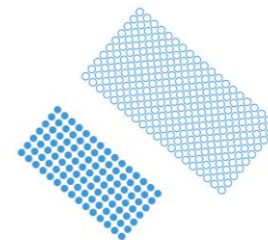
Hypothetical example



Separation 5 km  
External wake loss 7.8%



Separation 15 km  
External wake loss 3.8%

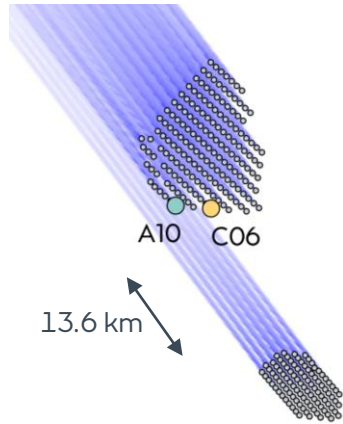


Separation 5 km  
External wake loss 3.4%

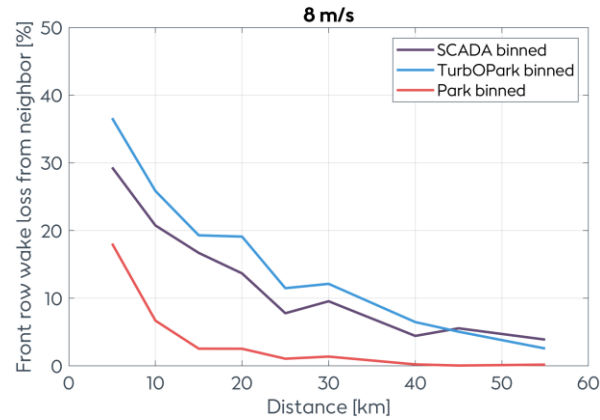
- Target
- Neighbour



# Conclusions



Cluster wakes detected



Cluster wakes extend >50 km

- Wind speed
  - Stability
  - Neighbour configuration
  - Wind rose
- Cluster wake dependencies

Orsted

Thank you  
for listening!

@orsted.com